Université de Montréal

Caractérisation et modélisation de l'évolution spectrale des étoiles naines blanches chaudes

par

Antoine Bédard

Département de physique
Faculté des arts et des sciences

Thèse présentée en vue de l'obtention du grade de
Philosophiæ Doctor (Ph.D.)
en Physique

Juillet 2022

Université de Montréal

Faculté des arts et des sciences

Cette thèse intitulée

Caractérisation et modélisation de l'évolution spectrale des étoiles naines blanches chaudes

présentée par

Antoine Bédard

a été évaluée par un jury composé des personnes suivantes :

Paul Charbonneau
(président-rapporteur)

Pierre Bergeron
(directeur de recherche)

Pierre Brassard
(codirecteur)

Patrick Dufour
(membre du jury)

Martin Barstow
(examinateur externe)

Max Mignotte
(représentant du doyen de la FESP)

Résumé

Cette thèse présente une étude empirique et théorique approfondie de l'évolution spectrale des étoiles naines blanches, avec un accent particulier sur les naines blanches chaudes. La composition atmosphérique (et donc l'apparence spectrale) de ces cadavres stellaires peut changer drastiquement avec le temps à mesure qu'ils se refroidissent. Ce phénomène est généralement interprété comme le résultat d'une compétition entre divers mécanismes de transport des éléments dans l'enveloppe stellaire (tels que la diffusion, la convection, les vents et l'accrétion), mais demeure mal compris à plusieurs égards. Il est impératif de remédier à cette situation pour être en mesure d'exploiter le potentiel immense des naines blanches pour notre compréhension du passé de la Galaxie.

Pour mieux caractériser l'incidence de l'évolution spectrale, nous effectuons tout d'abord une analyse spectroscopique exhaustive de près de 2000 naines blanches chaudes ($T_{\rm eff} \geq$ 30,000 K) observées par le relevé SDSS. Nous déterminons les propriétés atmosphériques (notamment la température effective et la composition de surface) de ces objets à l'aide d'un nouvel ensemble de modèles d'atmosphère calculé spécifiquement à cet effet. En examinant la fréquence relative des étoiles riches en hydrogène et riches en hélium en fonction de la température, nous obtenons pour la première fois un portrait empirique détaillé de l'évolution spectrale des naines blanches chaudes. Plus spécifiquement, nous déduisons (1) qu'environ une étoile sur quatre arrive sur la séquence de refroidissement avec une atmosphère d'hélium, et (2) qu'environ deux tiers de ces objets développent ultérieurement une atmosphère d'hydrogène. En outre, nous accordons une attention particulière aux naines blanches hybrides (qui montrent à la fois des traces d'hydrogène et d'hélium) de notre échantillon et à ce que ces objets distinctifs nous apprennent sur l'évolution spectrale.

Nous étudions ensuite l'évolution spectrale d'un point de vue théorique en modélisant les transformations chimiques qui s'opèrent dans les naines blanches. Pour ce faire, nous utilisons le code d'évolution stellaire STELUM, qui inclut un traitement cohérent et réaliste

du transport des éléments et nous permet donc de réaliser les simulations numériques d'évolution spectrale les plus sophistiquées à ce jour. Nous modélisons la diffusion de l'hydrogène résiduel dans une enveloppe d'hélium à haute température, qui mène ultimement à la formation d'une atmosphère d'hydrogène. Nous simulons également le mélange convectif de cette couche superficielle d'hydrogène avec la couche sous-jacente d'hélium à basse température, qui produit à nouveau une surface dominée par l'hélium. En outre, nous étudions le transport du carbone dans les étoiles riches en hélium, incluant à la fois le tri gravitationnel à haute température et le dragage convectif à basse température.

Ces calculs donnent lieu à plusieurs résultats astrophysiques d'intérêt. Nous obtenons notamment une contrainte inédite sur la quantité d'hydrogène résiduel contenue dans les naines blanches chaudes dominées par l'hélium. Nous démontrons aussi que la bifurcation observée dans le diagramme couleur−magnitude des naines blanches découvertes par le satellite Gaia est une signature du processus de mélange convectif à basse température. Par ailleurs, nos modèles fournissent de précieuses informations sur les propriétés des étoiles polluées par le carbone, en particulier sur leur masse et leur zone convective. Enfin, le résultat le plus important de cette thèse est la résolution définitive du problème le plus sérieux de la théorie de l'évolution spectrale, soit le problème de l'origine de l'hydrogène à la surface des naines blanches de type DBA.

Mots-clés : Étoiles naines blanches ; Étoiles DA ; Étoiles DB ; Étoiles DO ; Étoiles DQ ; Évolution stellaire tardive ; Atmosphères stellaires ; Composition atmosphérique ; Modèles d'évolution stellaire ; Diffusion stellaire ; Enveloppes stellaires convectives ; Vents stellaires

Abstract

This thesis presents an in-depth empirical and theoretical study of the spectral evolution of white dwarf stars, with a particular focus on hot white dwarfs. The atmospheric composition (and thus the spectral appearance) of these stellar remnants can change drastically over time as they cool. This phenomenon is generally interpreted as the result of an interplay between various element transport mechanisms in the stellar envelope (such as diffusion, convection, winds, and accretion), but remains poorly understood in several respects. It is imperative to remedy this situation to be able to exploit the immense potential of white dwarfs for our understanding of the past of the Galaxy.

To better characterize the incidence of spectral evolution, we first carry out an exhaustive spectroscopic analysis of nearly 2000 hot white dwarfs ($T_{\rm eff} \geq 30{,}000$ K) observed by the SDSS survey. We determine the atmospheric properties (in particular the effective temperature and surface composition) of these objects using a new set of model atmospheres calculated specifically for this purpose. By examining the relative frequency of hydrogen-rich and helium-rich stars as a function of temperature, we obtain for the first time a detailed empirical picture of the spectral evolution of hot white dwarfs. More specifically, we infer (1) that about one in four stars enters the cooling sequence with a helium atmosphere, and (2) that about two-thirds of these objects eventually develop a hydrogen atmosphere. Furthermore, we pay special attention to the hybrid white dwarfs (which exhibit traces of both hydrogen and helium) in our sample and to what can be learned about spectral evolution from these distinctive objects.

We then study spectral evolution from a theoretical point of view by modeling the chemical transformations that take place in white dwarfs. To do this, we use the stellar evolution code STELUM, which includes a consistent and realistic treatment of element transport and therefore allows us to perform the most sophisticated numerical simulations of spectral evolution to date. We model the diffusion of residual hydrogen in a helium envelope at high temperature, which ultimately leads to the formation of a hydrogen atmosphere. We also

simulate the convective mixing of this superficial hydrogen layer with the underlying helium layer at low temperature, which once again produces a helium-dominated surface. Furthermore, we study the transport of carbon in helium-rich stars, including both gravitational settling at high temperature and convective dredge-up at low temperature.

These calculations give rise to several astrophysical results of interest. In particular, we obtain an unprecedented constraint on the amount of residual hydrogen contained within hot helium-dominated white dwarfs. We also demonstrate that the bifurcation observed in the color−magnitude diagram of white dwarfs discovered by the Gaia satellite is a signature of the convective mixing process at low temperature. Furthermore, our models provide valuable information on the properties of carbon-polluted stars, in particular on their mass and convective zone. Finally, the most important result of this thesis is the definitive resolution of the most serious problem of the theory of spectral evolution, namely the problem of the origin of hydrogen at the surface of DBA-type white dwarfs.

Key words: White dwarf stars; DA stars; DB stars; DO stars; DQ stars; Late stellar evolution; Stellar atmospheres; Atmospheric composition; Stellar evolutionary models; Stellar diffusion; Stellar convective envelopes; Stellar winds

Table des matières

Liste des tableaux

Liste des figures

Liste des abréviations

4MOST	*4-meter Multi-Object Spectroscopic Telescope*
AB	Système photométrique absolu
AGB	Branche asymptotique des géantes (*asymptotic giant branch*)
DA	Naine blanche montrant des raies spectrales d'hydrogène
DB	Naine blanche montrant des raies spectrales d'hélium neutre
DC	Naine blanche ne montrant aucune raie spectrale
DESI	*Dark Energy Spectroscopic Instrument*
DO	Naine blanche montrant des raies spectrales d'hélium ionisé
DQ	Naine blanche montrant des raies spectrales de carbone
DR	*Data Release*
DZ	Naine blanche montrant des raies spectrales de métaux
EUV	Ultraviolet extrême (*extreme ultraviolet*)
FUV	Ultraviolet lointain (*far ultraviolet*)
Hα	Raie spectrale d'hydrogène à $\lambda = 6563$ Å
Hβ	Raie spectrale d'hydrogène à $\lambda = 4861$ Å
Hγ	Raie spectrale d'hydrogène à $\lambda = 4340$ Å
HR	Hertzsprung−Russell
LTE	Équilibre thermodynamique local (*local thermodynamic equilibirum*)
LTP	Pulse thermique tardif (*late thermal pulse*)
MESA	*Modules for Experiments in Stellar Astrophysics*
ML2	Version standard de la théorie de la longueur de mélange
MWDD	*Montreal White Dwarf Database*
O(H)	Pré-naine blanche montrant surtout des raies spectrales d'hydrogène
O(He)	Pré-naine blanche montrant surtout des raies spectrales d'hélium
OP	*Opacity Project*

OPAL	*Opacity Project at Livermore*
PG	Palomar-Green
PG 1159	Pré-naine blanche montrant des raies spectrales d'hélium et de carbone
PP	Proton-proton
RADAU5	Nom du code de résolution d'équations de Hairer & Wanner (1996)
RGB	Branche des géantes rouges (*red giant branch*)
SDSS	*Sloan Digital Sky Survey*
STELUM	*Stellar modeling from the University of Montreal*
SYNSPEC	Nom du code de spectres synthétiques de Hubeny & Lanz (1995)
TLUSTY	Nom du code de modèles d'atmosphère de Hubeny & Lanz (1995)
VLTP	Pulse thermique très tardif (*very late thermal pulse*)
WEAVE	*William-Herschel-Telescope Enhanced Area Velocity Explorer*

Notation

a	Premier paramètre géométrique de la théorie de la longueur de mélange
a_e	Rayon de la sphère d'électrons
A_i	Poids atomique de l'élément i
α	Paramètre de longueur de mélange
$\alpha_{\rm sc}$	Paramètre d'efficacité de la semi-convection
$\alpha_{\rm th}$	Paramètre d'efficacité de la convection thermohaline
b	Deuxième paramètre géométrique de la théorie de la longueur de mélange
B	Terme de Ledoux
c	Vitesse de la lumière
	Troisième paramètre géométrique de la théorie de la longueur de mélange
c_P	Chaleur spécifique à pression constante par unité de masse
χ_ρ	Dérivée de la pression par rapport à la densité à température constante
χ_T	Dérivée de la pression par rapport à la température à densité constante
D	Distance
	Coefficient de mélange
$D_{\rm conv}$	Coefficient de mélange dû à la convection ordinaire
$D_{\rm lim}$	Coefficient de mélange artificiel à la surface
$D_{\rm ov}$	Coefficient de mélange dû au dépassement convectif
$D_{\rm sc}$	Coefficient de mélange dû à la semi-convection
$D_{\rm th}$	Coefficient de mélange dû à la convection thermohaline
δ	Fonction delta de Dirac
e	Charge d'un électron
E	Champ électrique
E_1	Première fonction exponentielle intégrale
$\epsilon_{\rm grav}$	Taux de production d'énergie gravothermale par unité de masse

ϵ_{neu}	Taux de perte d'énergie due à l'émission de neutrinos par unité de masse
ϵ_{nuc}	Taux de production d'énergie nucléaire par unité de masse
$f_{\mathcal{N}}$	Facteur d'écrantage de la réaction nucléaire $\mathcal{N}$
f_{ν}	Flux monochromatique de radiation observée
f_{ov}	Paramètre d'efficacité du dépassement convectif
F_{ν}	Flux monochromatique de radiation
g	Accélération gravitationnelle de surface
g	Accélération gravitationnelle
	Magnitude apparente dans la bande SDSS-g
$g_{\mathrm{rad},i}$	Accélération radiative de l'élément i
G	Constante gravitationnelle
	Magnitude apparente dans la bande Gaia-G
G_{BP}	Magnitude apparente dans la bande Gaia-$\mathrm{G_{BP}}$
G_{RP}	Magnitude apparente dans la bande Gaia-$\mathrm{G_{RP}}$
Γ	Paramètre de couplage de Coulomb
Γ_{cr}	Paramètre de couplage de Coulomb critique pour la cristallisation
Γ_{e}	Paramètre de couplage de Coulomb des électrons
$\hbar$	Constante de Planck réduite
H	Fonction de Hopf
H_{ν}	Flux monochromatique d'Eddington
H_P	Hauteur caractéristique de pression
i	Indice identifiant un élément donné
	Magnitude apparente dans la bande SDSS-i
I	Nombre total d'éléments
k_B	Constante de Boltzmann
K_{ij}	Premier coefficient de résistance entre les éléments i et j
κ	Opacité moyenne de Rosseland
$\kappa_{\nu,i}$	Opacité monochromatique de l'élément i
l	Luminosité

$l_{\rm cr}$	Énergie produite par la cristallisation par unité de masse
$\ell_{\rm conv}$	Longueur de mélange
L	Luminosité totale
$L_\odot$	Luminosité totale du Soleil
λ	Longueur d'onde
m	Coordonnée de masse
$m_{\rm cr}$	Coordonnée de masse du front de cristallisation
m_e	Masse d'un électron
$m_{\rm lim}$	Coordonnée de masse de la frontière de transport
m_p	Masse d'un proton
M	Masse totale
$\dot{M}_{\rm acc}$	Taux d'accrétion de masse
$M_{\rm conv}$	Masse de la zone de convection
$M_{\rm env}$	Masse de l'enveloppe
M_G	Magnitude absolue dans la bande Gaia-G
M_i	Masse d'élément i
M_u	Magnitude absolue dans la bande SDSS-u
$\dot{M}_{\rm wind}$	Taux de perte de masse due au vent
$M_\odot$	Masse totale du Soleil
$\mu_{\rm ion}$	Poids moléculaire moyen par ion
n_e	Densité de nombre d'électrons
n_i	Densité de nombre d'atomes d'élément i
N_A	Nombre d'Avogadro
N_i	Nombre d'atomes d'élément i
∇	Gradient de température
$\nabla_{\rm ad}$	Gradient de température adiabatique
$\nabla_{\rm conv}$	Gradient de température convectif
$\nabla_{\rm rad}$	Gradient de température radiatif
ν	Fréquence

$\nu_{\mathcal{N}_i}$	Coefficient stoechiométrique de l'élément i dans la réaction nucléaire $\mathcal{N}$
P	Pression
P_i	Pression partielle de l'élément i
π	Constante mathématique usuelle
	Parallaxe trigonométrique
q	$\equiv 1 - m/M$
$q_{\rm conv}$	$\equiv M_{\rm conv}/M$
$q_{\rm env}$	$\equiv M_{\rm env}/M$
q_i	$\equiv M_i/M$
$q_{\rm lim}$	$\equiv 1 - m_{\rm lim}/M$
$Q_{\mathcal{L}}$	Taux de perte d'énergie par la réaction leptonique $\mathcal{L}$ par unité de volume
$Q_{\mathcal{N}}$	Énergie produite par la réaction nucléaire $\mathcal{N}$
r	Coordonnée radiale
	Magnitude apparente dans la bande SDSS-r
r_i	Flux résiduel de chaleur de l'élément i
R	Rayon total
$R_{\mathcal{N}}$	Taux de réaction de la réaction nucléaire $\mathcal{N}$ par unité de volume
$R_\odot$	Rayon total du Soleil
ρ	Densité de masse
ρ_i	Densité de masse d'élément i
$S_{{\rm acc},i}$	Terme source/puits associé à l'accrétion d'élément i à la surface
S/N	Rapport signal-sur-bruit spectral
$S_{{\rm nuc},i}$	Terme source/puits associé à la création/destruction d'élément i
$S_{{\rm wind},i}$	Terme source/puits associé à l'éjection d'élément i à la surface
σ	Constante de Stefan−Boltzmann
$\langle \sigma v \rangle_{\mathcal{N}}$	Section efficace de la réaction nucléaire $\mathcal{N}$
σ_x	Incertitude sur le paramètre x
t	Coordonnée temporelle
T	Température

$T_{\rm eff}$	Température effective
τ	Profondeur optique de Rosseland
$\tau_{\rm cool}$	Âge de refroidissement
u	Magnitude apparente dans la bande SDSS-u
u_i	Énergie interne d'élément i par unité de masse
$v_{\rm acc}$	Vitesse due à l'accrétion
$v_{\rm conv}$	Vitesse convective
v_i	Vitesse de diffusion des atomes d'élément i
$v_{\rm wind}$	Vitesse due au vent
W	Facteur de correction atmosphérique
X_i	Fraction de masse d'élément i
$X_{i,0}$	Fraction de masse initiale d'élément i
$X_{{\rm acc},i}$	Fraction de masse d'élément i accrétée
ξ	Coordonnée de masse modifiée
z	Magnitude apparente dans la bande SDSS-z
z_{ij}	Deuxième coefficient de résistance entre les éléments i et j
z'_{ij}	Troisième coefficient de résistance entre les éléments i et j
z''_{ij}	Quatrième coefficient de résistance entre les éléments i et j
Z_i	Charge des atomes d'élément i

Liste des contributions

Articles publiés dans des revues scientifiques avec comité de révision

(1) Bergeron, P., Dufour, P., Fontaine, G., Coutu, S., Blouin, S., Genest-Beaulieu, C., **Bédard, A.**, & Rolland, B. (2019). *On the Measurement of Fundamental Parameters of White Dwarfs in the Gaia Era*, The Astrophysical Journal, 876, 67.

(2) Kilic, M., **Bédard, A.**, Bergeron, P., & Kosakowski, A. (2020). *Two New Double-Lined Spectroscopic Binary White Dwarfs*, Monthly Notices of the Royal Astronomical Society, 493, 2805.

(3) Brown, W. R., Kilic, M., **Bédard, A.**, Kosakowski, A., & Bergeron, P. (2020). *A 1201 s Orbital Period Detached Binary : The First Double Helium Core White Dwarf LISA Verification Binary*, The Astrophysical Journal Letters, 892, L35.

(4) Blouin, S., Daligault, J., Saumon, D., **Bédard, A.**, & Brassard, P. (2020). *Toward Precision Cosmochronology : A New C/O Phase Diagram for White Dwarfs*, Astronomy & Astrophysics Letters, 640, L11.

(5) Klein, B., Blouin, S., Romani, D., Zuckerman, B., Melis, C., Xu, S., Dufour, P., Genest-Beaulieu, C., **Bédard, A.**, & Jura, M. (2020). *Atmospheric Temperature Inversions and He I 5876 Core Profile Structure in White Dwarfs*, The Astrophysical Journal, 900, 2.

(6) **Bédard, A.**, Bergeron, P., Brassard, P., & Fontaine, G. (2020). *On the Spectral Evolution of Hot White Dwarf Stars. I. A Detailed Model Atmosphere Analysis of Hot White Dwarfs from SDSS DR12*, The Astrophysical Journal, 901, 93.

(7) Gagné, J., David, T. J., Mamajek, E. E., Mann, A. W., Faherty, J. K., & **Bédard, A.** (2020). *The μ Tau Association : A 60 Myr Old Coeval Group at 150 pc from the Sun*, The Astrophysical Journal, 903, 96.

(8) Kaiser, B. C., Clemens, J. C., Blouin, S., Dufour, P., Hegedus, R. J., Reding, J. S., & **Bédard, A.** (2021). *Lithium Pollution of a White Dwarf Records the Accretion of an Extrasolar Planetesimal*, Science, 371, 168.

(9) Kilic, M., **Bédard, A.**, & Bergeron, P. (2021). *Hidden in Plain Sight : A Double-Lined White Dwarf Binary 26 pc Away and a Distant Cousin*, Monthly Notices of the Royal Astronomical Society, 502, 4972.

(10) Kilic, M., Bergeron, P., Blouin, S., & **Bédard, A.** (2021). *The Most Massive White Dwarfs in the Solar Neighbourhood*, Monthly Notices of the Royal Astronomical Society, 503, 5397.

(11) Kilic, M., Brown, W. R., **Bédard, A.**, & Kosakowski, A. (2021). *The Discovery of Two LISA Sources Within 0.5 kpc*, The Astrophysical Journal Letters, 918, L14.

(12) Barnett, J. W., Williams, K. A., **Bédard, A.**, & Bolte, M. (2021). *The Initial-Final Mass Relation for Hydrogen-Deficient White Dwarfs*, The Astronomical Journal, 162, 162.

(13) Bergeron, P., Wesemael, F., Fontaine, G., Lamontagne, R., Demers, S., **Bédard, A.**, Gingras, M.-J., Blouin, S., Irwin, M. J., & Kepler, S. O. (2021). *Hot Degenerates in the MCT Survey. III. A Sample of White Dwarf Stars in the Southern Hemisphere*, The Astronomical Journal, 162, 188.

(14) **Bédard, A.**, Brassard, P., Bergeron, P., & Blouin, S. (2022). *On the Spectral Evolution of Hot White Dwarf Stars. II. Time-dependent Simulations of Element Transport in Evolving White Dwarfs with STELUM*, The Astrophysical Journal, 927, 128.

(15) **Bédard, A.**, Bergeron, P., & Brassard, P. (2022). *On the Spectral Evolution of Hot White Dwarf Stars. III. The PG 1159-DO-DB-DQ Evolutionary Channel Revisited*, The Astrophysical Journal, 930, 8.

(16) Bergeron, P., Kilic, M., Blouin, S., **Bédard, A.**, Leggett, S. K., & Brown, W. R. (2022). *On the Nature of Ultracool White Dwarfs : Not so Cool after All*, The Astrophysical Journal, 934, 36.

(17) **Bédard, A.**, Bergeron, P., & Brassard, P. (2022). *On the Spectral Evolution of Hot White Dwarf Stars. IV. The Diffusion and Mixing of Residual Hydrogen in Helium-rich White Dwarfs*, soumis à The Astrophysical Journal.

Présentations orales à des conférences scientifiques

(1) *The Spectral Evolution of Hot White Dwarf Stars*, rencontre annuelle de la Société canadienne d'astronomie, Montréal, Québec, Canada, 17–20 juin 2019.

(2) *The Spectral Evolution of Hot White Dwarfs*, 357th Symposium of the International Astronomical Union (White Dwarfs as Probes of Fundamental Physics and Tracers of Planetary, Stellar, and Galactic Evolution), Hilo, Hawaii, USA, 21–25 octobre 2019.

(3) *Element Transport in Evolutionary Models : A New Look at the Spectral Evolution of White Dwarfs*, Online Meetings on Evolved Stars and Systems, à distance, 21 avril 2021.

(4) *A Detailed Modeling of the DO-to-DA Spectral Evolution and an Explanation for the Composition of DBA White Dwarfs*, 22nd European Workshop on White Dwarfs, Tübingen, Allemagne, 15–19 août 2022.

Présentations par affiche à des conférences scientifiques

(1) *Revisiting the White Dwarf Luminosity Function from the Palomar-Green Survey*, 21st European Workshop on White Dwarfs, Austin, Texas, USA, 23—27 juillet 2018.

(2) *A Non-LTE Model Atmosphere Analysis of Hot, Hydrogen-Deficient White Dwarfs*, Hydrogen-Deficient Stars 2018, Armagh, Northern Ireland, UK, 10–14 septembre 2018.

Remerciements

J'aimerais tout d'abord exprimer ma profonde gratitude envers mon directeur de recherche, Pierre Bergeron. Tu as non seulement su me transmettre ta grande passion des étoiles naines blanches, mais c'est aussi toi qui m'as appris les multiples rouages de la recherche scientifique et a ainsi fait de moi un chercheur accompli. Je te suis particulièrement reconnaissant de m'avoir confié un projet aussi fascinant et stimulant. Tes conseils, tes idées, tes encouragements et même tes nombreuses anecdotes ont été pour moi des sources essentielles d'inspiration et de motivation. Je me souviendrai longtemps de nos discussions passionnantes sur l'évolution spectrale, mais aussi de celles un peu moins passionnantes sur les erreurs internes et externes de la méthode spectroscopique ou encore sur la satanée question de savoir lequel de N ou α est constant.

Je tiens à rendre hommage à mon ancien codirecteur de recherche, Gilles Fontaine, tragiquement décédé d'un cancer en novembre 2019. C'est un immense privilège d'avoir eu ce professeur dévoué et monument de l'astrophysique comme mentor. Cette thèse représente en quelque sorte l'aboutissement d'un travail mené tout au long de sa carrière ; il n'en aura malheureusement pas été témoin, mais je suis convaincu qu'il en aurait été fier. Je suis profondément reconnaissant envers mon codirecteur actuel, Pierre Brassard, pour avoir accepté sans hésitation de prendre la relève dans ces circonstances difficiles. Sans son implication, une bonne partie de cette thèse aurait été impossible. Ses conseils m'ont été d'une très grande aide.

Je remercie chaleureusement mes collègues passés (Benoît, Cynthia, Simon B., Simon C. et Maude) et présents (François, Olivier, Patrick et Alexandre) du groupe des naines blanches. Vous avez fait de mon doctorat une aventure remplie de moments inoubliables, surtout lors des conférences auxquelles nous avons participé ensemble. Je pense notamment aux parties endiablées d'Avalon à Santa Fe, aux chauves-souris « silencieuses » d'Austin, aux tortues géantes de Hilo, ou encore aux bingos spéciaux de la rencontre du CRAQ, pour n'en nommer que quelques-uns. Un merci particulier à Simon B., qui est devenu un fidèle

collaborateur et qui m'invite continuellement à faire partie de ses projets, toujours plus intéressants les uns que les autres.

Je tiens à remercier ma garde rapprochée, maman, papa, Olivier, Denis, Nathalie et Gabriel, pour tous les beaux moments passés en famille, loin des tracas de la recherche. Vous occupez une place fondamentale dans ma vie et vous êtes une composante essentielle de mon bonheur. Un merci tout spécial à papa et maman d'avoir été et d'être encore des parents aussi exceptionnels. Votre support inconditionnel dans tous les aspects de ma vie m'est très précieux.

Enfin, mon plus vif remerciement va à Jasmine, non seulement mon amoureuse et meilleure amie, mais aussi ma partenaire de doctorat et collègue de télétravail. Je suis choyé d'avoir pu partager avec toi les hauts et les bas de cette folle aventure que sont les études supérieures. Merci d'avoir été le pilier de mon quotidien en cette époque insolite. Ton amour et ton soutien indéfectibles me sont inestimables, et ta résilience phénoménale est une source inépuisable d'inspiration. Au final, je sais que je repenserai toujours à cette période de notre vie avec beaucoup de bonheur, d'affection et de fierté.

À la mémoire de Gilles Fontaine.

Chapitre 1

Introduction

Ce premier chapitre vise à établir les bases conceptuelles de la problématique étudiée dans cette thèse, soit l'évolution spectrale des étoiles naines blanches. Tout d'abord, la section 1.1 présente les principales caractéristiques des naines blanches, puis la section 1.2 introduit le phénomène d'évolution spectrale et décrit ses diverses signatures observationnelles. Après une courte digression à la section 1.3 sur le transport des éléments dans les étoiles, la section 1.4 aborde notre compréhension théorique de l'évolution spectrale des naines blanches. Enfin, la section 1.5 détaille les objectifs et le contenu de cette thèse.

1.1. Les étoiles naines blanches

Pour une grande partie de leur vie, les étoiles sont en mesure de supporter leur propre poids grâce aux réactions nucléaires qui se produisent en leur cœur, fusionnant l'hydrogène en hélium, puis l'hélium en carbone et en oxygène. Lorsque le carburant nucléaire est épuisé, le noyau se contracte sous l'effet de la gravité, tandis que l'enveloppe est presque totalement expulsée par un vent stellaire, donnant ainsi lieu au phénomène de nébuleuse planétaire. L'objet résiduel, remarquablement dense et chaud, est une étoile naine blanche. Un tel cadavre stellaire est quasiment dépourvu de source d'énergie interne et est donc simplement condamné à se refroidir pendant des milliards d'années. On estime que cette destinée est celle de pas moins de 97% des étoiles de la Galaxie, incluant le Soleil (Fontaine et al., 2001). La présente section aborde les notions élémentaires relatives à la structure (section 1.1.1), l'évolution (section 1.1.2) et la classification spectrale (section 1.1.3) des étoiles naines blanches.

1.1.1. Structure

Les naines blanches sont des objets très compacts : elles contiennent une masse semblable à celle du Soleil dans un volume comparable à celui de la Terre. Plus précisément, une

naine blanche typique possède une masse de $\sim$0.6 $M_\odot$ et un rayon de $\sim$0.013 $R_\odot$, ce qui lui confère une énorme densité centrale de $\sim 10^6$ g cm^{-3} (Fontaine et al., 2001). Dans ces conditions extrêmes, les électrons sont fortement dégénérés. C'est ce phénomène quantique qui est responsable de l'existence même des naines blanches : la pression de dégénérescence des électrons permet de freiner l'effondrement gravitationnel provoqué par l'extinction des réactions nucléaires et subséquemment de maintenir l'état d'équilibre hydrostatique (Fowler, 1926).

Cette propriété fondamentale est aussi à l'origine du fait que les naines blanches obéissent à une relation masse−rayon bien particulière. En supposant que le gaz d'électrons est idéal et complètement dégénéré, il est possible de démontrer que l'équilibre entre la force gravitationnelle et le gradient de pression de dégénérescence implique que la masse M et le rayon R sont approximativement reliés par l'expression

$$R \approx \frac{\hbar^2}{G m_e m_p^{5/3}} \frac{1}{M^{1/3}}, \tag{1.1}$$

où $\hbar$ est la constante de Planck réduite, G est la constante gravitationnelle, et m_e et m_p sont les masses de l'électron et du proton (Hansen et al., 2004). On en déduit que les naines blanches plus massives sont plus petites, et vice versa. Ce comportement quelque peu contre-intuitif découle de l'équation d'état de la matière dégénérée non-relativiste, qui est de la forme $P \propto \rho^{5/3}$, où P et ρ symbolisent respectivement la pression et la densité. En effet, une masse plus grande se traduit par une gravité plus forte, et l'établissement d'une configuration stable requiert alors une pression de dégénérescence plus élevée. Or, selon l'équation d'état, une pression plus élevée ne peut être obtenue que via une densité plus élevée. Autrement dit, plus le poids à supporter est grand, plus l'étoile doit être compacte (Chandrasekhar, 1935). La relation masse−rayon est d'une immense utilité pour l'étude empirique des propriétés physiques des naines blanches : puisque la masse, le rayon et la gravité de surface ($g = GM/R^2$) sont reliés d'une manière relativement simple, il suffit de mesurer seulement l'un de ces trois paramètres pour connaître les deux autres.

L'équation 1.1 est une approximation assez grossière de la réalité et devient de moins en moins exacte pour les masses de plus en plus élevées, la raison étant que les électrons deviennent alors relativistes. Dans ce régime, l'équation d'état change et tend plutôt vers la forme $P \propto \rho^{4/3}$ dans la limite ultra-relativiste. Puisque la pression dépend plus faiblement de la densité, la capacité de l'étoile à contrebalancer sa propre gravité est réduite.

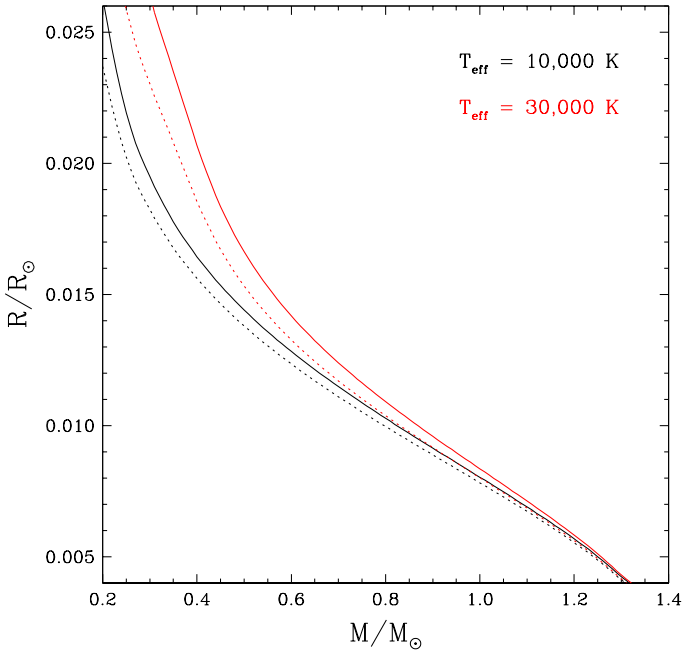

Figure 1.1 – Relations masse−rayon obtenues des modèles détaillés de naines blanches présentés à la section 2.3.2. Les courbes noires et rouges correspondent à des modèles de température effective $T_{\rm eff}$ = 10,000 et 30,000 K, respectivement. Les courbes pleines et pointillées correspondent à des modèles possédant une couche superficielle d'hydrogène de masse $M_{\rm H}/M = 10^{-4}$ et 10^{-10}, respectivement.

Une conséquence radicale de ce phénomène est qu'aucune naine blanche ne peut exister au-delà d'une masse limite, dite de Chandrasekhar, de $\sim$1.4 $M_{\odot}$ (Chandrasekhar, 1931). Par ailleurs, d'autres effets physiques doivent également être pris en compte pour obtenir une représentation réaliste de la relation masse−rayon. Parmi les plus importants, notons les effets de la température non-nulle du gaz d'électrons et des interactions électrostatiques entre les électrons et les ions sur l'équation d'état. Ces phénomènes font en sorte que la relation masse−rayon varie légèrement selon la température effective [1] et la composition chimique de l'étoile (Hamada & Salpeter, 1961). Ceci est illustré à la figure 1.1, qui montre la relation masse−rayon prédite par des modèles détaillés de naines blanches (voir la section 2.3.2) pour diverses températures effectives et épaisseurs d'enveloppe.

1. La température effective d'une étoile est définie comme la température qu'aurait un corps noir émettant la même quantité de radiation (intégrée sur toutes les longueurs d'onde) que cette étoile. La température effective diffère généralement très peu de la température de surface.

Quant à la structure chimique, la majorité des naines blanches possèdent un noyau de carbone et d'oxygène (les produits du brûlage nucléaire antérieur), entouré d'une mince enveloppe d'hélium, elle-même entourée d'une couche encore plus mince d'hydrogène. Typiquement, le noyau comprend ∼99% de la masse totale de l'étoile, tandis que les couches d'hélium et d'hydrogène en représentent seulement ∼0.99% et ∼0.01%, respectivement (Iben & Tutukov, 1984). L'enveloppe est généralement très opaque, de telle sorte qu'on ne peut en voir directement qu'une minuscule partie à la surface, nommée atmosphère ; la fraction de la masse stellaire contenue dans l'atmosphère est un infime $\sim 10^{-15}$. Une caractéristique remarquable des naines blanches est l'exceptionnelle pureté chimique de leur atmosphère, autre conséquence de leur grande compacité. En effet, puisque l'accélération gravitationnelle de surface est très élevée, c'est-à-dire de l'ordre de $\sim 10^8$ cm s^{-2}, le processus de tri gravitationnel des éléments chimiques est d'une formidable efficacité : en l'absence de mécanismes concurrents, tous les métaux [2] coulent très rapidement dans l'étoile, laissant uniquement l'élément le plus léger à la surface (Schatzman, 1958). Pour cette raison, la plupart des naines blanches montrent une atmosphère composée exclusivement d'hydrogène, sans aucune trace d'éléments plus lourds.

Il existe bien sûr quelques exceptions à cette composition archétypique. D'abord, on retrouve plutôt un noyau d'hélium dans les naines blanches de faible masse ($M \lesssim 0.45\ M_\odot$) et un noyau d'oxygène et de néon dans les naines blanches très massives ($M \gtrsim 1.1\ M_\odot$), résultat de leur historique de brûlage nucléaire différent (Althaus et al., 2010). De plus, une fraction appréciable (de l'ordre de 25%) des naines blanches connues possèdent une atmosphère constituée non pas d'hydrogène, mais plutôt d'hélium, ce qui signifie qu'elles ont perdu l'essentiel de leur couche superficielle d'hydrogène dans le passé. Enfin, la surface de nombreux objets est, contre toute attente, contaminée par une petite quantité d'un ou plusieurs éléments autres que le constituant principal (Fontaine & Wesemael, 1987). Nous aurons amplement l'occasion de revenir sur ces phénomènes au fil de cette thèse.

2. Dans un contexte astrophysique, le mot « métal » désigne tout élément autre que l'hydrogène et l'hélium. Cette convention découle du fait que l'hydrogène et l'hélium sont beaucoup plus abondants que le reste des éléments dans l'Univers.

1.1.2. Évolution

Étant donné la quasi-absence de sources et de puits d'énergie dans les naines blanches, celles-ci ne peuvent que rayonner leur énergie thermique dans le milieu interstellaire et ainsi se refroidir inexorablement. C'est pourquoi le terme « séquence de refroidissement » est communément employé pour décrire cette portion de l'évolution stellaire. Ce refroidissement n'affecte presque pas la structure de l'étoile, car la pression exercée par les électrons dégénérés dépend surtout de la densité et peu de la température. Autrement dit, l'évolution d'une naine blanche se résume en une décroissance continue de la température effective et de la luminosité[3], et ce à masse et rayon à peu près constants (Mestel, 1952). Les valeurs numériques vont de $T_{\rm eff} \sim 150{,}000$ K et $L \sim 10^3\ L_\odot$ pour les plus jeunes naines blanches, à $T_{\rm eff} \sim 3000$ K et $L \sim 10^{-5}\ L_\odot$ pour les plus vieilles, qui prennent environ 10 milliards d'années pour atteindre ce stade (Fontaine et al., 2001).

Deux notions entrent en jeu dans la description physique du refroidissement d'une naine blanche : la quantité d'énergie thermique que renferme dans le noyau, et le taux auquel cette énergie est transférée au milieu interstellaire via l'enveloppe. La première partie de la question est simplifiée par le fait que les électrons dégénérés contribuent faiblement au réservoir thermique, par définition même du concept de dégénérescence. Ainsi, la quasi-totalité de l'énergie thermique est emmagasinée dans les ions du noyau, qui eux demeurent non-dégénérés. La principale difficulté est que ceux-ci ne forment pas un gaz parfait et s'apparentent plutôt à un liquide ou même à un solide, donc il faut recourir à une équation d'état complexe pour évaluer le contenu thermique de l'étoile. La seconde partie du problème consiste à décrire les différents modes de transport de l'énergie à travers l'enveloppe, soit la radiation, la conduction et la convection. Ceci nécessite une connaissance approfondie des propriétés microscopiques de la matière, notamment son opacité (Fontaine et al., 2001).

En faisant quelques suppositions assez radicales, ce problème compliqué peut être réduit à une expression analytique illustrant, pour une composition donnée, la dépendance approximative de l'âge de refroidissement (ou temps de refroidissement) $\tau_{\rm cool}$ sur la masse et

3. La luminosité d'une étoile est définie comme la quantité d'énergie qu'émet cette étoile par unité de temps. La luminosité et la température effective sont reliées par la loi de Stefan−Boltzmann, $L = 4\pi R^2 \sigma T_{\rm eff}^4$, où σ est la constante de Stefan−Boltzmann.

la luminosité,

$$\tau_{\rm cool} \propto \left(\frac{M}{L}\right)^{5/7}. \tag{1.2}$$

D'une part, cette formule indique évidemment qu'un objet donné (M fixe) se refroidit avec l'âge, mais également que son taux de refroidissement diminue avec l'âge. Autrement dit, les naines blanches chaudes et lumineuses évoluent d'abord très rapidement, puis de plus en plus lentement à mesure que leur température et leur luminosité diminuent. D'autre part, cette relation implique qu'une étoile plus massive prend plus de temps pour atteindre un point donné de la séquence de refroidissement (L fixe), la raison étant simplement qu'à une plus grande masse est associé un plus grand contenu thermique (Mestel, 1952). Par ailleurs, mentionnons que la composition de l'étoile a aussi une influence considérable sur son évolution. Par exemple, le refroidissement est plus lent pour un noyau de carbone que pour un noyau d'oxygène, parce qu'une certaine masse de carbone contient plus d'ions (et donc d'énergie thermique) que la même masse d'oxygène. En outre, à basse température, une naine blanche dont l'enveloppe est constituée exclusivement d'hélium se refroidit plus rapidement qu'une naine blanche typique possédant une couche superficielle d'hydrogène, puisque l'hélium est moins opaque que l'hydrogène et permet donc un transfert d'énergie plus efficace (Fontaine et al., 2001).

L'idée d'un refroidissement tranquille et ininterrompu représente néanmoins un portrait hautement idéalisé de la réalité. En effet, à divers moments de la vie d'une naine blanche, des sources ou des puits d'énergie modifient son contenu thermique et affectent ainsi son taux de refroidissement. Dans les quelques premiers millions d'années, on recense trois processus d'intérêt : la contraction gravitationnelle résiduelle de l'étoile, le brûlage nucléaire résiduel dans l'enveloppe, et l'émission de neutrinos dans les régions centrales extrêmement chaudes. Ce dernier phénomène est le plus important et accélère significativement le refroidissement, puisque les neutrinos s'échappent sans interagir avec la matière et emportent ainsi une grande quantité d'énergie. À l'inverse, les deux premiers processus augmentent les réserves énergétiques de l'étoile, ce qui ralentit légèrement le refroidissement (Althaus et al., 2010). Plus tard dans l'évolution, soit après quelques milliards d'années, deux autres événements majeurs surviennent. Premièrement, la température du noyau devient tellement basse que les ions passent de la phase liquide à la phase solide : c'est la cristallisation du noyau. Cette transition de phase libère une quantité substantielle de chaleur latente, ce qui provoque un

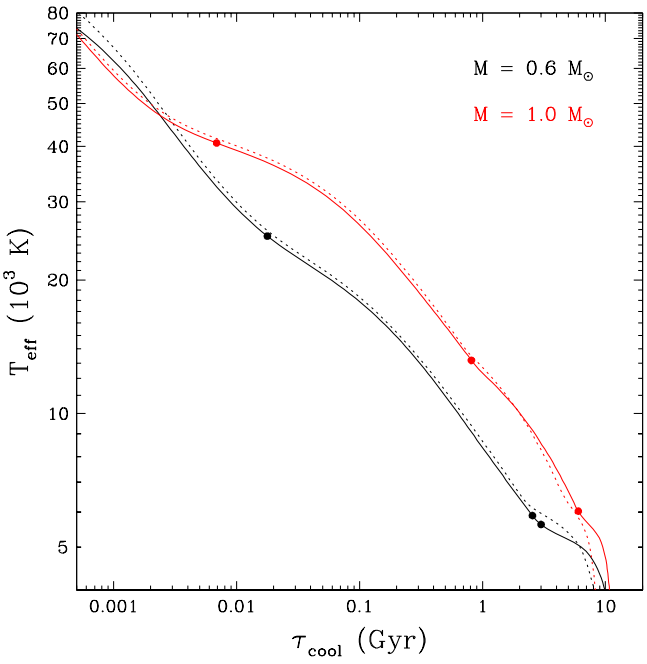

Figure 1.2 – Courbes de refroidissement (température effective en fonction de l'âge de refroidissement) obtenues des modèles détaillés de naines blanches présentés à la section 2.3.2. Les courbes noires et rouges correspondent à des modèles de masse $M = 0.6$ et 1.0 $M_\odot$, respectivement. Les courbes pleines et pointillées correspondent à des modèles possédant une couche superficielle d'hydrogène de masse $M_\mathrm{H}/M = 10^{-4}$ et 10^{-10}, respectivement. Sur les courbes pleines, des points indiquent, de gauche à droite, la fin du refroidissement par émission de neutrinos, le début de la cristallisation du noyau, et le début du couplage convectif entre le noyau et la surface.

délai dans le refroidissement. Deuxièmement, la zone de convection présente dans l'enveloppe atteint le noyau, ce qui résulte en un couplage direct entre le réservoir thermique et la surface de l'étoile, étant donné que les mouvements convectifs transportent l'énergie de manière très efficace. Ce couplage convectif se traduit ultimement par une accélération marquée du refroidissement (Fontaine et al., 2001).

La figure 1.2 présente la courbe de refroidissement (c'est-à-dire la variation de la température effective selon l'âge de refroidissement) obtenue de modèles détaillés de naines blanches (voir la section 2.3.2) de masse $M = 0.6$ et 1.0 $M_\odot$. Des points indiquent les événements les plus significatifs dans l'évolution : la fin du refroidissement par émission de neutrinos, le début de la cristallisation du noyau, et le début du couplage convectif entre le noyau et la

surface. La figure 1.2 montre que chacun de ces trois phénomènes provoque un changement de pente de la courbe de refroidissement, conformément à la description qualitative du paragraphe précédent. Malgré ces complications, on peut voir que l'affirmation ci-dessus selon laquelle une étoile plus massive prend plus de temps pour se refroidir à une température donnée est bel et bien valide sur une vaste portion de l'évolution. La figure 1.2 illustre également comment le refroidissement est affecté par une réduction de l'épaisseur de la couche superficielle d'hydrogène. Bien que l'effet puisse sembler petit à l'échelle du graphique, la différence d'âge peut atteindre jusqu'à deux milliards d'années à basse température.

De par leur statut de cadavre stellaire et leur évolution relativement simple, les naines blanches nous offrent une opportunité unique d'étudier le passé de la Galaxie. En effet, il est raisonnablement facile de déterminer l'âge d'une naine blanche : si sa température effective, sa masse et sa structure chimique sont connues, la courbe de refroidissement permet d'estimer son âge. Or, ce n'est pas le cas des autres types d'étoiles : en général, l'âge est l'une des propriétés stellaires les plus difficiles à mesurer. Dans ce contexte, les naines blanches peuvent être exploitées pour dater les populations stellaires auxquelles elles appartiennent. Cette technique, appelée cosmochronologie, est largement utilisée pour évaluer l'âge des différentes composantes de la Galaxie (Winget et al., 1987; Oswalt et al., 1996; Leggett et al., 1998; Fontaine et al., 2001; Hansen et al., 2002, 2007; García-Berro et al., 2010; Kalirai, 2012; Tremblay et al., 2014; Kilic et al., 2017). Toutefois, il ne faut pas oublier que la validité de cette approche repose entièrement sur notre capacité à déterminer l'âge des naines blanches. Cette tâche n'est pas exempte de défis : elle requiert de bien connaître non seulement leurs paramètres stellaires, mais aussi tous les processus physiques pouvant affecter leur refroidissement. Ainsi, notre compréhension de la structure et de l'évolution des naines blanches est d'une importance fondamentale pour la cosmochronologie.

1.1.3. Classification spectrale

Les raies d'absorption présentes dans le spectre d'une étoile renferment une mine d'information physique sur l'atmosphère de cette étoile. En effet, la nature et l'amplitude des raies spectrales observées sont entièrement déterminées par la température effective, la gravité de surface et la composition atmosphérique, qui sont collectivement appelées paramètres atmosphériques. Dans le cas spécifique des naines blanches, le large éventail de températures effectives et de compositions atmosphériques existantes se traduit par une grande diversité

de spectres. Pour s'y retrouver, il est indispensable de regrouper les différents spectres en catégories.

Le système de classification des naines blanches a été élaboré par Sion et al. (1983) et illustré en détail par Wesemael et al. (1993). Tout comme pour les autres types d'étoiles, ce système repose sur les caractéristiques spectrales observées dans la portion visible du spectre (3500 Å $\lesssim \lambda \lesssim$ 7000 Å, où λ est la longueur d'onde)[4]. À chaque objet est attribué un type spectral composé d'au moins deux lettres majuscules, la première lettre étant toujours « D » (pour souligner le caractère dégénéré de l'étoile) et la seconde lettre identifiant la nature des raies dominantes. Les principales classes spectrales et les raies qui leur sont associées sont les suivantes :

- DA : raies d'hydrogène ;
- DB : raies d'hélium neutre ;
- DC : aucune raie (spectre continu) ;
- DO : raies d'hélium ionisé ;
- DQ : raies de carbone ;
- DZ : raies d'autres métaux.

Des exemples de spectres de naines blanches appartenant à chacune de ces classes sont présentés à la figure 1.3.

Il est important de réaliser que le type spectral ne reflète pas toujours la nature du principal élément chimique présent à la surface de l'étoile. Par exemple, une naine blanche à atmosphère d'hydrogène pur est bel et bien de type DA sur la majeure partie de la séquence de refroidissement, mais est plutôt de type DC lorsque $T_{\rm eff} \lesssim 5000$ K étant donné que les raies d'hydrogène disparaissent à ces basses températures (car tous les atomes d'hydrogène demeurent alors dans leur état fondamental). De même, une naine blanche à atmosphère d'hélium pur appartient à la classe DO lorsque $T_{\rm eff} \gtrsim 45{,}000$ K, DB lorsque 45,000 K $\gtrsim T_{\rm eff} \gtrsim 11{,}000$ K, et DC lorsque $T_{\rm eff} \lesssim 11{,}000$ K. La transition de DO à DB est causée par la recombinaison des atomes d'hélium, tandis que la transition de DB à DC est due à la disparition des raies d'hélium (pour les mêmes raisons que les raies d'hydrogène).

4. Il y a toutefois une exception à cette règle : les naines blanches montrant des raies de carbone uniquement dans l'ultraviolet peuvent tout de même être assignées à la classe spectrale DQ.

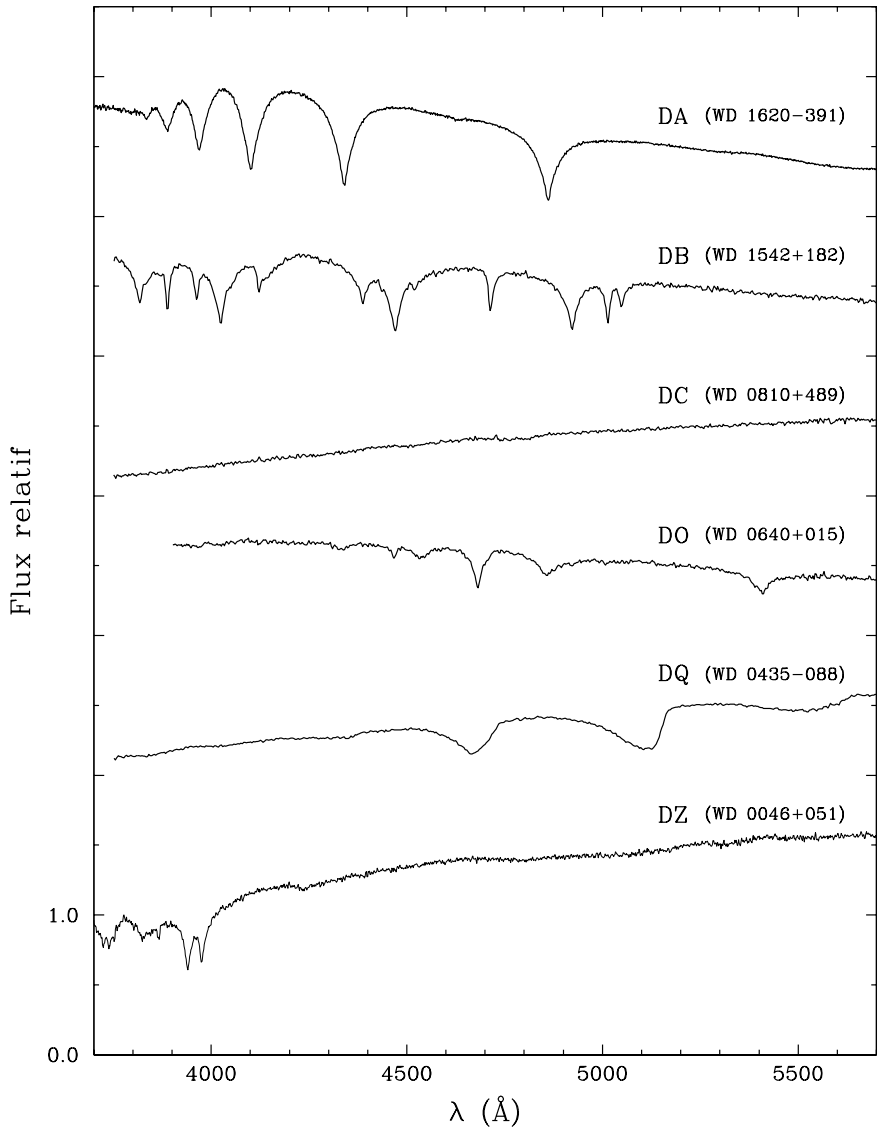

Figure 1.3 – Exemples de spectres (flux de radiation en fonction de la longueur d'onde) de naines blanches de types DA, DB, DC, DO, DQ et DZ. Les spectres sont normalisés à $\lambda = 5200$ Å et sont décalés verticalement par souci de clarté. Ces données sont tirées de Bergeron et al. (1997), Bergeron et al. (2011), Giammichele et al. (2012) et Subasavage et al. (2017).

Enfin, les étoiles de types DQ et DZ possèdent en fait une atmosphère composée majoritairement d'hélium, qui comporte seulement de petites quantités de carbone ou de métaux. Leur apparence spectrale s'explique par leurs basses températures effectives ($T_{\rm eff} \lesssim 11{,}000$ K) :

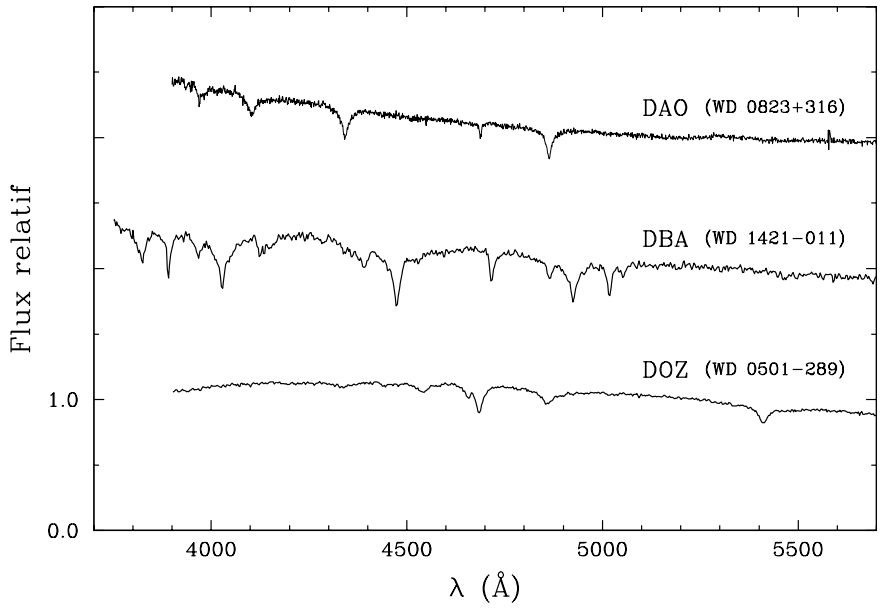

Figure 1.4 – Exemples de spectres (flux de radiation en fonction de la longueur d'onde) de naines blanches de types DAO, DBA et DOZ. Les spectres sont normalisés à $\lambda = 5200$ Å et sont décalés verticalement par souci de clarté. Ces données sont tirées de Bergeron et al. (2011) et Alam et al. (2015).

dans ces conditions, l'hélium est invisible tandis que les métaux demeurent visibles, même en faibles abondances [5].

Si une signature spectrale secondaire est également détectée, elle est spécifiée par l'ajout d'une troisième lettre majuscule. Par exemple, une naine blanche dont le spectre montre à la fois de fortes raies d'hydrogène et de faibles raies d'hélium ionisé se voit assigner le type spectral DAO. La même logique s'applique aux autres classes dites hybrides. Parmi les naines blanches riches en hydrogène, les types hybrides les plus communs sont DAO et DAZ. Parmi les naines blanches riches en hélium, on retrouve surtout les classes hybrides DBA, DBZ et DOZ. Quelques spectres hybrides typiques sont représentés à la figure 1.4 ; les raies secondaires que l'on peut y voir sont He II λ4686 dans le spectre DAO, H I λ4861 (Hβ) dans le spectre DBA, et C IV λ4658 dans le spectre DOZ.

5. Il existe quelques exceptions. D'une part, une petite fraction des naines blanches de type DQ possèdent une atmosphère dominée par le carbone (voir la section 1.2.3). D'autre part, parmi les naines blanches très froides, la classe DZ regroupe autant des atmosphères d'hydrogène que des atmosphères d'hélium (puisque les raies d'hydrogène disparaissent à leur tour à $T_{\rm eff} \lesssim 5000$ K).

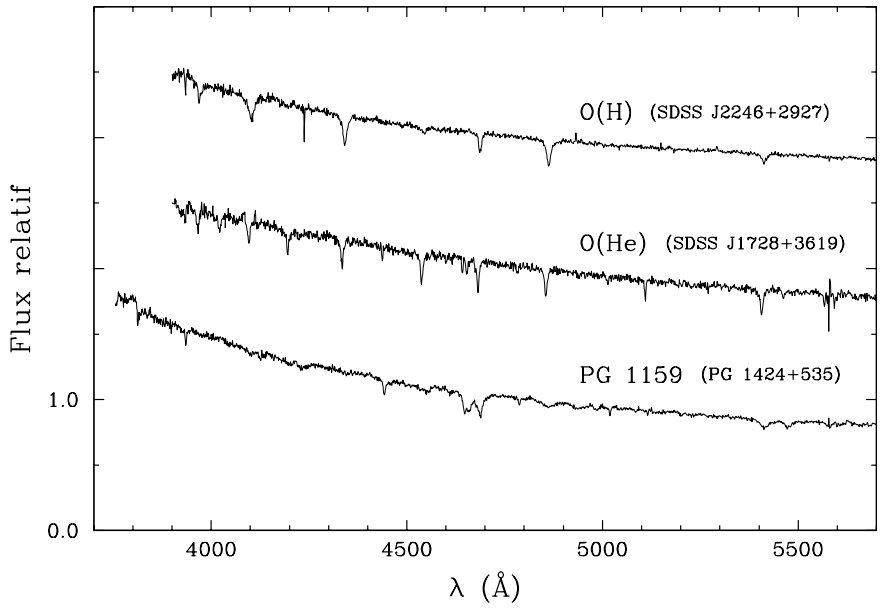

Figure 1.5 – Exemples de spectres (flux de radiation en fonction de la longueur d'onde) d'étoiles pré-naines blanches de types O(H), O(He) et PG 1159. Les spectres sont normalisés à $\lambda = 4800$ Å et sont décalés verticalement par souci de clarté. Ces données sont tirées de Alam et al. (2015).

Finalement, puisque cette thèse s'intéresse plus particulièrement aux naines blanches chaudes et donc jeunes, il est approprié de donner un bref aperçu des classes spectrales de leurs précurseurs directs, c'est-à-dire des étoiles que l'on retrouve juste avant la séquence de refroidissement. D'une part, la plupart de ces objets arborent un spectre de type O(H), qui comporte typiquement un mélange de raies d'hydrogène et d'hélium ionisé. Une telle apparence spectrale est caractéristique d'une atmosphère de composition solaire à très haute température. D'autre part, le reste des pré-naines blanches sont déficientes en hydrogène et peuvent être regroupées en deux catégories. Le type O(He) est défini par la présence quasi-exclusive de raies d'hélium ionisé et correspond donc à une atmosphère largement dominée par l'hélium. D'autres objets possèdent plutôt une atmosphère composée d'hélium, de carbone et d'oxygène dans des proportions similaires, qui se traduit spectroscopiquement par un mélange de raies d'hélium ionisé, de carbone ionisé (C IV) et d'oxygène ionisé (O VI) définissant la classe PG 1159 (d'après le prototype, PG 1159−035). Des exemples de spectres O(H), O(He) et PG 1159 sont illustrés à la figure 1.5. Étant donné l'effet purificateur du tri gravitationnel, on estime que les étoiles O(H) deviendront des naines blanches à atmosphère

d'hydrogène, tandis que les étoiles O(He) et PG 1159 deviendront des naines blanches à atmosphère d'hélium.

1.2. Un portrait empirique de l'évolution spectrale

Comme mentionné dans la section précédente, les raies spectrales d'une étoile contiennent beaucoup d'information sur ses propriétés atmosphériques. Pour extraire cette information, il faut recourir à des modèles d'atmosphère, qui permettent de prédire, à partir de principes physiques, le spectre d'une étoile pour un ensemble donné de paramètres atmosphériques (température effective, gravité de surface et composition atmosphérique). L'approche usuelle est de calculer un grand nombre de modèles couvrant un large éventail de valeurs de paramètres, puis de comparer quantitativement les spectres théoriques au spectre observé. Les valeurs de paramètres donnant le meilleur accord entre les raies prédites et observées peuvent alors être considérées comme représentatives de l'étoile à l'étude. En appliquant cette méthode dite spectroscopique à grande échelle, il est possible de déterminer la température effective, la gravité de surface et les abondances chimiques d'un grand nombre de naines blanches (Bergeron et al., 1992, 2011). Par ailleurs, notons qu'il existe une autre technique, dite photométrique et basée plutôt sur l'analyse de la distribution spectrale d'énergie, permettant d'estimer les paramètres atmosphériques des naines blanches, bien que sa capacité à contraindre la composition soit beaucoup plus limitée (Bergeron et al., 1997, 2001).

Étant donné la sédimentation des éléments chimiques par la gravité, il serait légitime de s'attendre à ce que toutes les naines blanches conservent une atmosphère d'hydrogène pur ou d'hélium pur tout au long de leur vie. Or, les analyses spectroscopiques et photométriques existantes révèlent que la réalité est loin d'être aussi simple. Non seulement la surface de nombreuses étoiles est polluée par des éléments traces, mais en outre, les proportions de naines blanches riches en hydrogène et riches en hélium varient selon la température effective. Puisque la température effective est étroitement reliée à l'âge de refroidissement, cette dernière constatation implique que le constituant atmosphérique principal d'un objet peut changer en fonction du temps. Bref, il s'avère que les naines blanches subissent des changements drastiques de composition de surface à mesure qu'elles se refroidissent. On donne à ce phénomène fascinant le nom d'évolution spectrale. Le but de la présente section est de donner un aperçu des preuves empiriques de l'évolution spectrale des naines blanches.

Pour dresser un portrait compréhensible de ce sujet riche en détails, nous mettrons d'abord l'accent sur les variations du constituant atmosphérique dominant (section 1.2.1), puis nous aborderons les tendances associées aux divers éléments traces (sections 1.2.2 et 1.2.3).

1.2.1. Constituant principal

Historiquement, les premiers indices de l'évolution spectrale remontent au relevé Palomar-Green (PG), qui a fourni des données spectroscopiques pour près de 500 naines blanches (Green et al., 1986). L'étude de cet échantillon a fait ressortir plusieurs tendances pouvant être résumées en quatre points.

(1) Parmi les naines blanches extrêmement chaudes, c'est-à-dire ayant $T_{\rm eff} \gtrsim 80{,}000$ K, on retrouve plusieurs étoiles riches en hélium, de type spectral DO, mais aucune étoile riche en hydrogène, de type spectral DA (Wesemael et al., 1985; Fleming et al., 1986). Ceci suggère que toutes les naines blanches ont une atmosphère dominée par l'hélium à leur entrée sur la séquence de refroidissement.

(2) Dans l'intervalle $80{,}000 \text{ K} \gtrsim T_{\rm eff} \gtrsim 45{,}000$ K, le rapport du nombre d'étoiles DO sur le nombre d'étoiles DA diminue graduellement à mesure que la température effective décroît (Fleming et al., 1986), ce qui indique que des atmosphères d'hélium se transforment en atmosphères d'hydrogène avec le temps.

(3) L'intervalle $45{,}000 \text{ K} \gtrsim T_{\rm eff} \gtrsim 30{,}000$ K contient uniquement des objets de type DA et est donc historiquement désigné comme la brèche des DB, ou *DB gap* en anglais (Wesemael et al., 1985; Liebert et al., 1986). Ce manque de naines blanches riches en hélium laisse croire que toutes les étoiles développent une couche superficielle d'hydrogène avant d'atteindre $T_{\rm eff} \sim 45{,}000$ K.

(4) Enfin, une petite fraction des objets ayant $T_{\rm eff} \lesssim 30{,}000$ K appartient à la classe DB, et cette fraction augmente à mesure que la température effective diminue (Liebert et al., 1986). Ceci indique que des atmosphères composées d'hydrogène dans la brèche des DB redeviennent subséquemment dominées par l'hélium.

La figure 1.6 montre la fraction des naines blanches à atmosphère d'hélium selon la température effective dans l'échantillon PG. On y remarque nettement les tendances décrites ci-dessus. De plus, d'autres études ont démontré que la proportion des naines blanches riches en hélium continue à augmenter à plus basse température effective ($T_{\rm eff} \lesssim 10{,}000$ K, non

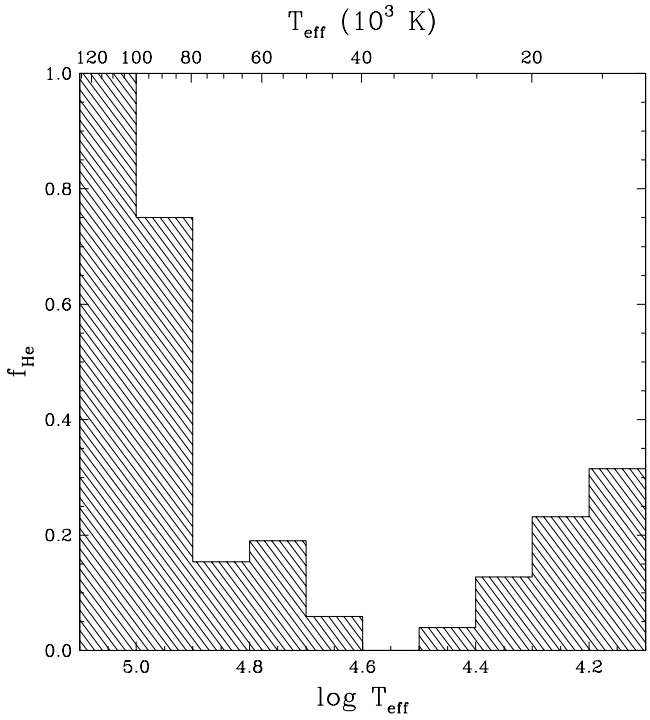

Figure 1.6 – Fraction des naines blanches à atmosphère d'hélium en fonction de la température effective dans le relevé PG. Ces résultats proviennent d'une réanalyse moderne non-publiée de l'échantillon PG, qui est basée sur les modèles et méthodes décrits dans Gianninas et al. (2011), Rolland et al. (2018), ainsi qu'au chapitre 2.

visible sur la figure 1.6) et atteint même plus de 50% parmi les étoiles les plus froides (Sion, 1984; Greenstein, 1986).

Des analyses plus poussées ont subséquemment corroboré la raréfaction des étoiles DA à très haute température et des étoiles DB dans la brèche des DB (Bergeron et al., 1994; Beauchamp et al., 1996; Dreizler & Werner, 1996). Toutefois, avec l'expansion de la population de naines blanches connues au fil des années, il est devenu clair que ces « trous » dans les distributions de types spectraux ne sont pas complètement vides. D'abord, un relevé spectroscopique d'étoiles pré-naines blanches a révélé de nombreux objets riches en hydrogène (Napiwotzki & Schönberner, 1995; Napiwotzki, 1999). Ceci implique que certaines étoiles possèdent déjà une atmosphère d'hydrogène à leur entrée sur la séquence de refroidissement, contrairement à ce que suggère l'échantillon PG. Ensuite, et surtout, l'avènement du *Sloan Digital Sky Survey* (SDSS) a révolutionné la recherche sur les naines blanches en portant à plus de 35,000 le nombre d'objets observés en spectroscopie (Kleinman et al., 2013; Kepler

et al., 2015, 2016, 2019). Ce vaste ensemble de données a permis la caractérisation détaillée d'une multitude de nouvelles étoiles DA (Tremblay et al., 2011; Genest-Beaulieu & Bergeron, 2019a), DO (Hügelmeyer et al., 2005, 2006; Reindl et al., 2014a; Werner et al., 2014) et DB (Koester & Kepler, 2015; Genest-Beaulieu & Bergeron, 2019b). Dans le contexte de l'évolution spectrale, l'un des principaux résultats d'intérêt est qu'une vingtaine d'objets riches en hélium ont été identifiés dans la brèche des DB (Eisenstein et al., 2006a). On peut donc en déduire que certaines naines blanches ne développent jamais de couche superficielle d'hydrogène et préservent plutôt une atmosphère d'hélium durant toute leur vie.

Il est important de souligner que, malgré ces découvertes, l'intervalle $T_{\rm eff} \gtrsim 80{,}000$ K demeure déficient en étoiles DA (Krzesinski et al., 2009; Werner et al., 2019), et l'intervalle 45,000 K $\gtrsim T_{\rm eff} \gtrsim$ 20,000 K demeure déficient en étoiles DB [6] (Eisenstein et al., 2006a; Bergeron et al., 2011). Ainsi, les transformations atmosphériques décrites ci-dessus doivent bel et bien se produire pour une fraction notable des naines blanches. En résumé, il y a vraisemblablement trois canaux évolutifs possibles :

(1) Certaines naines blanches possèdent une atmosphère d'hydrogène durant toute leur évolution.

(2) Certaines naines blanches possèdent initialement une atmosphère d'hélium, qui devient riche en hydrogène dans la brèche des DB, puis redevient dominée par l'hélium par la suite.

(3) Certaines naines blanches possèdent une atmosphère d'hélium durant toute leur évolution.

Dans les dernières années, de nombreuses études ont tenté d'obtenir un tableau plus précis de l'évolution spectrale en examinant la variation de la fraction des étoiles riches en hélium à basse température effective ($T_{\rm eff} \lesssim 30{,}000$ K ; Tremblay & Bergeron 2008; Giammichele et al. 2012; Limoges et al. 2015; Blouin et al. 2019; Genest-Beaulieu & Bergeron 2019b; Ourique et al. 2019; Cunningham et al. 2020; McCleery et al. 2020; López-Sanjuan et al. 2022). La figure 1.7 présente les résultats de quelques-unes des analyses les plus récentes. Bien qu'il y ait de légères différences d'une courbe à l'autre (qui sont associées à l'utilisation de divers échantillons d'étoiles, modèles d'atmosphère et techniques d'analyse), le consensus qui en

6. Grâce à l'échantillon SDSS, il a été établi que le déficit de naines blanches de type DB persiste jusqu'à $T_{\rm eff} \sim 20{,}000$ K, et non 30,000 K comme le laissait croire l'échantillon PG.

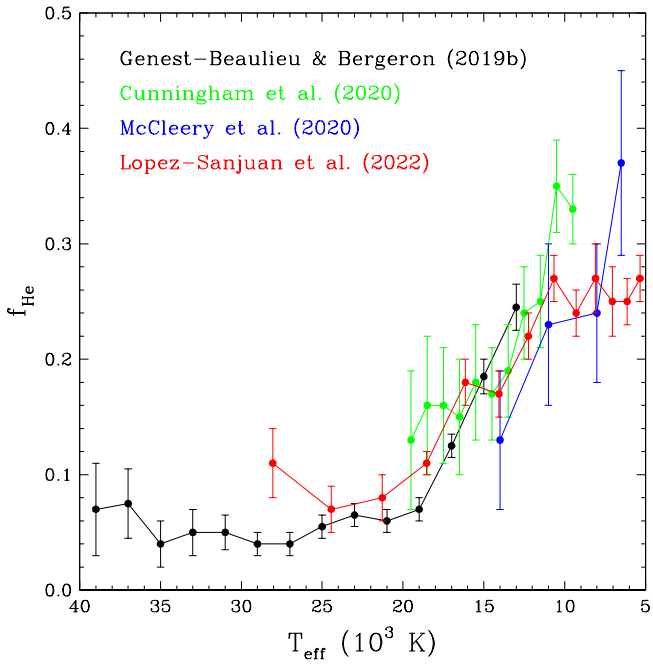

Figure 1.7 – Fraction des naines blanches à atmosphère d'hélium en fonction de la température effective selon quelques études récentes. Les points noirs, verts, bleus et rouges sont tirés de Genest-Beaulieu & Bergeron (2019b), Cunningham et al. (2020), McCleery et al. (2020) et López-Sanjuan et al. (2022), respectivement.

émerge est que la proportion des atmosphères d'hélium est environ 5−10% à $T_{\rm eff} \gtrsim 20{,}000$ K, puis augmente graduellement pour atteindre environ 20−40% à $T_{\rm eff} \lesssim 10{,}000$ K. En revanche, parmi les naines blanches chaudes ($T_{\rm eff} \gtrsim 30{,}000$ K), la variation de l'incidence des atmosphères d'hélium selon la température a été très peu étudiée depuis le relevé PG. Cette situation est essentiellement due à deux facteurs : les naines blanches chaudes sont beaucoup plus rares que leurs homologues froides puisqu'elles se refroidissent plus rapidement (Kleinman et al., 2013; Kepler et al., 2015, 2016, 2019), et leur atmosphère est plus complexe à modéliser à cause des effets hors-équilibre thermodynamique local (Lanz & Hubeny, 1995; Napiwotzki, 1997). La mise à jour de la figure 1.6 à haute température effective constitue une étape essentielle dans la quête d'un portrait moderne et complet de l'évolution spectrale.

1.2.2. Éléments traces : l'hydrogène et l'hélium

Certaines naines blanches montrent une surface composée à la fois d'hydrogène et d'hélium. Ces atmosphères mixtes se traduisent observationnellement par les types spectraux

hybrides DAB, DAO, DBA ou DOA, dépendamment de la température effective et des abondances d'hydrogène et d'hélium. De telles étoiles représentent vraisemblablement des manifestations directes des métamorphoses atmosphériques que subissent les naines blanches au fur et à mesure qu'elles se refroidissent. Ainsi, elles revêtent un intérêt particulier dans le cadre de cette thèse. Pour des raisons qui deviendront évidentes, la discussion qui suit est divisée en trois parties se rapportant à des intervalles de température distincts, soit $T_{\rm eff} \gtrsim 55{,}000$ K, $55{,}000$ K $\gtrsim T_{\rm eff} \gtrsim 35{,}000$ K, et $T_{\rm eff} \lesssim 35{,}000$ K.

Débutons par l'intervalle $T_{\rm eff} \gtrsim 55{,}000$ K. À ces températures, les atmosphères mixtes devraient donner lieu aux classes hybrides DAO et DOA, puisque l'hélium apparaît sous forme ionisée. D'une part, parmi les naines blanches riches en hydrogène, environ 15−30% des objets (ce qui représente actuellement une centaine d'étoiles) montrent aussi la raie He II λ4686 et sont donc de type DAO (Gianninas et al., 2010; Kepler et al., 2019). D'autre part, les naines blanches de type DOA sont pratiquement inexistantes, c'est-à-dire que presque toutes les étoiles dominées par l'hélium n'arborent aucune trace d'hydrogène. Cependant, il est probable que certaines naines blanches chaudes et riches en hélium soient bel et bien contaminées par un peu d'hydrogène, mais que celui-ci échappe à toute détection. En effet, un défi de nature observationnelle s'impose : chaque raie d'hydrogène se situe vis-à-vis une raie d'hélium ionisé, conséquence de la structure hydrogénoïde de l'ion He II. Pour cette raison, il est très difficile de déceler une petite quantité d'hydrogène dans une atmosphère d'hélium à haute température. Les meilleures analyses spectroscopiques ne peuvent qu'établir des limites supérieures peu contraignantes sur l'abondance d'hydrogène, soit $\log N_{\rm H}/N_{\rm He} \lesssim -1.5$, où $N_{\rm H}$ et $N_{\rm He}$ symbolisent les nombres d'atomes d'hydrogène et d'hélium (Werner, 1996a).

En revanche, les étoiles DAO sont relativement bien étudiées. Notamment, la question de la distribution de l'hélium selon la profondeur dans l'atmosphère de ces objets a été examinée en détail. Deux principales configurations peuvent être envisagées : l'hélium est soit distribué uniformément dans l'atmosphère (configuration homogène), soit située sous une couche d'hydrogène flottant à la surface (configuration stratifiée). La composition chimique est quantifiée différemment selon la distribution supposée : dans le premier cas, le paramètre utilisé est l'abondance d'hélium exprimée en ratio de nombres, $N_{\rm He}/N_{\rm H}$, tandis que dans le second cas, la quantité employée est la masse de la couche superficielle d'hydrogène, ou plutôt

le ratio de cette masse sur la masse stellaire totale, $M_{\rm H}/M$. À prime abord, la deuxième proposition semble plus réaliste étant donné l'influence présumée du tri gravitationnel dans les naines blanches. Les premiers calculs de modèles d'enveloppes chimiquement stratifiées ont démontré que la couche d'hydrogène doit être extrêmement mince, soit $\log M_{\rm H}/M \sim -16.0$, pour que l'hélium sous-jacent soit visible spectroscopiquement (Jordan & Koester, 1986; Vennes et al., 1988; Vennes & Fontaine, 1992). À titre de comparaison, la théorie standard de l'évolution stellaire prédit une valeur plus élevée par plusieurs ordres de grandeur, $\log M_{\rm H}/M \sim -4.0$ (Iben & Tutukov, 1984; Renedo et al., 2010). La configuration stratifiée a par la suite été testée via des analyses spectroscopiques détaillées d'étoiles DAO. Plus spécifiquement, le profil de la raie He II λ4686 est sensible à la distribution de l'hélium dans les couches externes et permet donc de discriminer entre les configurations homogènes et stratifiées (Bergeron et al., 1994). En exploitant cette sensibilité, il a été déterminé que la totalité des naines blanches DAO ayant $T_{\rm eff} \gtrsim 55{,}000$ K possèdent en fait une atmosphère chimiquement homogène (Bergeron et al., 1994). La conclusion qui s'impose est que la composition de surface de ces objets n'est pas régie uniquement par le tri gravitationnel : un autre processus physique est responsable du maintien et du mélange de l'hélium dans les couches externes.

Les abondances d'hélium mesurées à l'aide de modèles d'atmosphères homogènes couvrent l'intervalle $-3.5 \lesssim \log N_{\rm He}/N_{\rm H} \lesssim -0.5$ (Napiwotzki, 1999; Good et al., 2004; Gianninas et al., 2010; Tremblay et al., 2011). En outre, l'abondance d'hélium est corrélée avec la luminosité de l'étoile : plus la luminosité est faible, plus la quantité d'hélium à la surface est petite (Napiwotzki, 1999). Cette tendance suggère que le mécanisme physique à l'origine de la classe DAO est d'abord très efficace au tout début de la séquence de refroidissement, puis s'estompe avec le temps.

Passons maintenant au deuxième intervalle de température, $55{,}000 \text{ K} \gtrsim T_{\rm eff} \gtrsim 35{,}000$ K, où la situation est significativement différente. Dans cette partie de la séquence de refroidissement, les naines blanches hybrides sont beaucoup plus rares : seule une poignée d'objets, tous de type DAO, étaient connus avant l'arrivée du SDSS. En dépit de sa taille réduite, cet échantillon a tout de même apporté son lot de découvertes. Par exemple, il a été établi de manière décisive que l'étoile PG 1305−017, contrairement à toutes ses homologues, est dotée d'une atmosphère chimiquement stratifiée (Bergeron et al., 1994; Manseau et al.,

2016). Les valeurs modernes des paramètres atmosphériques de PG 1305−017 ($T_{\rm eff} = 44{,}900$ K, $\log g = 7.9$ et $\log M_{\rm H}/M = -16.1$) indiquent que cet objet se situe à la limite chaude de la brèche des DB et possède une couche d'hydrogène excessivement mince (Manseau et al., 2016). Une autre étoile intéressante est PG 1210+533, dont le spectre est variable dans le temps et est mal reproduit par les modèles d'atmosphère actuels, autant homogènes que stratifiés (Bergeron et al., 1994; Gianninas et al., 2010).

Le SDSS a révélé une quinzaine de nouvelles naines blanches similaires à PG 1305−017 : leur spectre est caractéristique d'une atmosphère chimiquement stratifiée et leur température avoisine la frontière chaude de la brèche des DB (Manseau et al., 2016). Tous les types spectraux hybrides possibles (DAB, DAO, DBA et DOA) sont représentés parmi ces étoiles, notamment parce que la masse de la couche d'hydrogène varie passablement d'un objet à l'autre ($-18.0 \lesssim \log M_{\rm H}/M \lesssim -15.5$) : plus la couche d'hydrogène est mince, plus les raies d'hélium dominent le spectre, et vice versa (Manseau et al., 2016). La stratification de l'hydrogène et l'hélium laisse croire que le tri gravitationnel joue ici un rôle prépondérant. Ainsi, ces étoiles n'ont probablement rien à voir, d'un point de vue physique, avec les étoiles DAO plus chaudes et chimiquement homogènes discutées précédemment. Cette idée est appuyée par le fait que ces deux groupes sont, à quelques exceptions près, nettement séparés dans le diagramme $\log g - T_{\rm eff}$, tel que l'illustre la figure 1.8.

Enfin, attardons-nous aux propriétés des naines blanches hybrides dans le dernier intervalle de température effective, $T_{\rm eff} \lesssim 35{,}000$ K. Parmi ces objets plus froids, seules les classes DAB et DBA peuvent être observées, puisque l'hélium à la surface n'est plus ionisé. D'un côté, les naines blanches DAB sont très peu communes (Gianninas et al., 2011; Kepler et al., 2019). En fait, la plupart des spectres de type DAB sont produits par des systèmes binaires non-résolus formés d'une étoile DA et d'une étoile DB (Wesemael et al., 1994; Bergeron & Liebert, 2002; Limoges & Bergeron, 2010). Quant aux quelques « vraies » naines blanches DAB, des études spectroscopiques suggèrent qu'elles sont plutôt singulières. Plus spécifiquement, les deux objets les mieux connus, GD 323 (Koester et al., 1994; Pereira et al., 2005) et HS 0209+0832 (Heber et al., 1997; Wolff et al., 2000), ne peuvent être expliqués par les modèles d'atmosphère conventionnels et montrent en outre des variations spectroscopiques (tout comme PG 1210+533 à plus haute température).

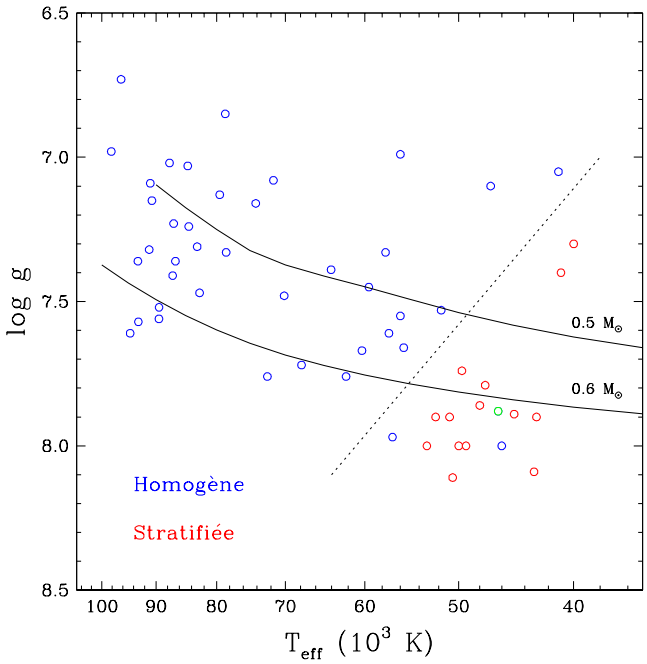

Figure 1.8 – Gravité de surface en fonction de la température effective pour un échantillon de naines blanches chaudes hybrides. Les points bleus et rouges dénotent respectivement les atmosphères homogènes et stratifiées. Le point vert correspond à l'étoile particulière PG 1210+533. Les paramètres atmosphériques sont tirés de Gianninas et al. (2010), Tremblay et al. (2011) et Manseau et al. (2016). Les courbes pleines représentent des séquences évolutives de masse $M = 0.5$ et $0.6\ M_{\odot}$ basées sur les modèles détaillés de naines blanches présentés à la section 2.3.2. Le trait pointillé délimite approximativement les régions occupées par les atmosphères homogènes et stratifiées.

En revanche, les naines blanches froides de type DBA sont la règle plutôt que l'exception. En effet, pas moins de 60−75% des étoiles à atmosphère d'hélium montrent des traces d'hydrogène à basse température (Koester & Kepler, 2015; Rolland et al., 2018). Puisque ces objets ont des enveloppes convectives (voir la section 1.3.3), l'hydrogène est ici distribué de manière homogène dans les couches externes. Les propriétés des naines blanches DBA ont été examinées minutieusement via de nombreuses analyses spectroscopiques, basées soit sur de petits échantillons (entre 30 et 80 objets) de très haute qualité (Beauchamp et al., 1996; Voss et al., 2007; Bergeron et al., 2011; Rolland et al., 2018), soit sur l'échantillon beaucoup plus gros (environ 900 objets) mais de moindre qualité issu du SDSS (Koester & Kepler, 2015; Genest-Beaulieu & Bergeron, 2019b). Ces études ont démontré que la grande majorité

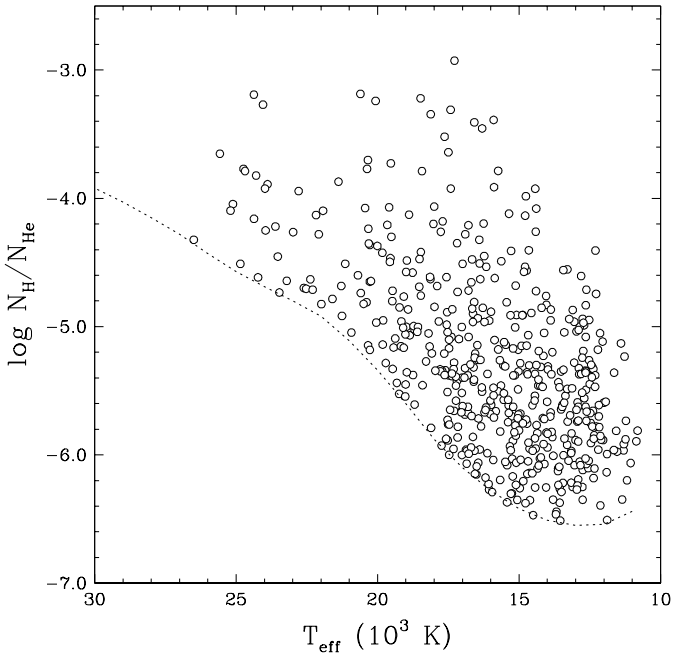

Figure 1.9 – Abondance d'hydrogène (exprimée en ratio de nombres) en fonction de la température effective pour un échantillon de naines blanches de type DBA. Les paramètres atmosphériques sont tirés de Rolland et al. (2018) et Genest-Beaulieu & Bergeron (2019b), et seuls les objets dont le rapport signal-sur-bruit spectral est supérieur à 20 sont montrés. La courbe pointillée correspond à la limite de détection de l'hydrogène dans une atmosphère d'hélium (dans la portion visible du spectre).

des étoiles DBA sont caractérisées par $T_{\rm eff} \lesssim 20{,}000$ K et $-6.5 \lesssim \log N_{\rm H}/N_{\rm He} \lesssim -4.0$, tel que l'illustre la figure 1.9.

1.2.3. Éléments traces : les métaux

En plus de l'hydrogène et/ou l'hélium, l'atmosphère de nombreuses naines blanches contient aussi des éléments lourds en petite quantité. Ces étoiles peuvent être divisées en deux groupes : celles montrant uniquement des traces de carbone, et celles montrant des traces d'autres métaux.

On sait depuis longtemps que le premier groupe est formé en quasi-totalité de naines blanches froides ($T_{\rm eff} \lesssim 10{,}000$ K) et riches en hélium (Koester et al., 1982; Wegner & Yackovich, 1984; Weidemann & Koester, 1995). Puisque l'hélium est spectroscopiquement invisible à basse température, leur spectre ne comporte que des raies atomiques et/ou des

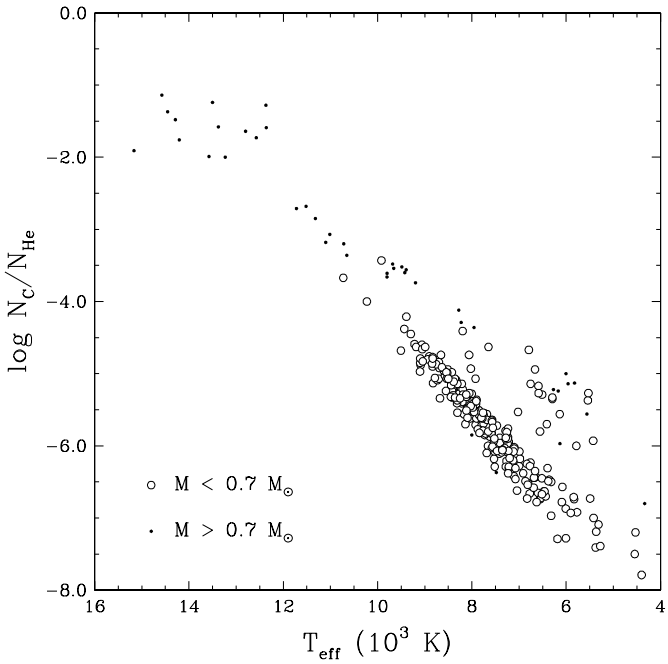

Figure 1.10 – Abondance de carbone (exprimée en ratio de nombres) en fonction de la température effective pour un échantillon de naines blanches de type DQ. Les paramètres atmosphériques sont tirés de Coutu et al. (2019) et Blouin & Dufour (2019), et seuls les objets dont la parallaxe trigonométrique est plus précise que 10% sont montrés. Les gros cercles représentent les étoiles ayant une masse typique ($M < 0.7\ M_\odot$), tandis que les petits points correspondent aux étoiles anormalement massives ($M > 0.7\ M_\odot$).

bandes moléculaires dues au carbone, même si celui-ci est un constituant trace. Ces objets appartiennent donc à la classe spectrale DQ. Une particularité des étoiles de type DQ est que le carbone est le seul contaminant détecté dans leur atmosphère : elles sont en général complètement dépourvues d'hydrogène et d'autres métaux (Dufour, 2011; Coutu et al., 2019). Une autre caractéristique importante des naines blanches DQ est qu'il existe une corrélation très claire entre leur abondance de carbone et leur température effective : plus l'étoile est froide, plus la quantité de carbone à la surface est petite (Dufour et al., 2005; Koester & Knist, 2006; Koester & Kepler, 2019; Coutu et al., 2019). Cette tendance est illustrée à la figure 1.10.

En plus de ces étoiles DQ typiques, la famille des naines blanches polluées par le carbone comprend également une autre catégorie d'objets présentant plusieurs anomalies : ils sont plus massifs, plus chauds et plus riches en carbone que la moyenne (Dufour et al., 2007, 2008;

Dufour, 2011; Coutu et al., 2019; Koester & Kepler, 2019). Ces naines blanches DQ atypiques sont beaucoup plus rares et ont donc été découvertes relativement récemment grâce au SDSS. On peut voir à la figure 1.10 qu'elles forment une deuxième séquence, nettement distincte de la première, dans le diagramme abondance−température. Fait intéressant, l'atmosphère des étoiles DQ les plus chaudes ($T_{\rm eff} \sim 20{,}000 - 25{,}000$ K, non visibles sur la figure 1.10) comporte en fait plus de carbone que d'hélium (Dufour et al., 2007, 2008; Koester & Kepler, 2019).

Pour leur part, les naines blanches contaminées par d'autres éléments lourds sont présentes sur l'ensemble de la séquence de refroidissement, et ce, à la fois parmi les objets riches en hydrogène et les objets riches en hélium. Elles appartiennent donc à des classes spectrales variées, telles que DAZ, DBZ, DOZ et DZ. Il est même fréquent qu'une étoile dominée par l'hélium montre simultanément des traces d'hydrogène et de métaux, ce qui donne notamment lieu aux types spectraux DBAZ et DBZA. On évalue qu'au moins 25% (et peut-être jusqu'à 50%) des naines blanches ont de petites quantités d'éléments lourds dans leur atmosphère, et ce, à toute température effective (Zuckerman et al., 2003, 2010; Barstow et al., 2014; Koester et al., 2014a).

Dans les naines blanches chaudes ($T_{\rm eff} \gtrsim 30{,}000$ K), il est plutôt rare que les métaux soient assez abondants pour produire des raies dans la portion visible du spectre. Pour les détecter, il faut alors sonder l'ultraviolet. Des données spectroscopiques ultraviolettes ont révélé la présence de nombreuses espèces chimiques à la surface des étoiles chaudes, notamment le carbone, l'oxygène, le silicium, le phosphore, le soufre, le fer et le nickel (Holberg et al., 1993; Werner & Dreizler, 1994; Dreizler & Werner, 1996; Dreizler, 1999; Barstow et al., 2003b, 2014; Good et al., 2005; Vennes et al., 2006; Werner et al., 2017; Preval et al., 2019), mais aussi des éléments plus exotiques comme l'argon, le chrome, le manganèse, le cobalt, le zinc, le gallium, le germanium, l'arsenic, le sélénium, le brome, le krypton, l'étain, le tellure, l'iode et le xénon (Chayer et al., 2005; Vennes et al., 2005; Werner et al., 2007, 2012, 2018; Hoyer et al., 2017, 2018; Löbling et al., 2020). Les abondances mesurées couvrent plusieurs ordres de grandeur ($-9.0 \lesssim \log N_{\rm Z}/N_{\rm H}\,, \log N_{\rm Z}/N_{\rm He} \lesssim -3.0$, où Z désigne un métal quelconque) et peuvent être très différentes dans deux objets ayant pourtant des paramètres atmosphériques similaires. Malgré cette dispersion, quelques tendances globales ont pu être établies. Premièrement, les abondances semblent augmenter légèrement avec la température effective. Deuxièmement, à

une température donnée, un objet riche en hélium comporte plus d'éléments lourds qu'un objet riche en hydrogène (Dreizler & Werner, 1996; Dreizler, 1999; Barstow et al., 2003b, 2014; Good et al., 2005; Vennes et al., 2006).

Bien que les raies métalliques apparaissent surtout dans l'ultraviolet, les métaux peuvent se manifester indirectement dans le visible par leur influence sur les raies d'hydrogène et d'hélium. En particulier, les naines blanches DA les plus chaudes sont affectées par ce qui a été nommé le problème des raies de Balmer : les modèles atmosphériques composés d'hydrogène pur échouent à reproduire correctement les spectres observés, plus précisément le cœur des raies Hα et Hβ (Napiwotzki, 1992; Napiwotzki & Rauch, 1994; Napiwotzki, 1999; Gianninas et al., 2010). Une difficulté analogue affecte les raies d'hélium ionisé des naines blanches DO très chaudes (Werner et al., 1995a, 2014; Dreizler & Werner, 1996). Il a été démontré que cette incohérence est causée par l'omission des éléments lourds dans les modèles d'atmosphère. En effet, les métaux modifient la structure thermodynamique de l'atmosphère, qui à son tour influence les profils des raies de Balmer, ce qui mène à un meilleur accord entre les modèles et les observations (Bergeron et al., 1993; Werner, 1996b; Gianninas et al., 2010). Détail intéressant, le problème des raies de Balmer est plus fréquent chez les étoiles DAO que chez les étoiles DA, ce qui indique que leur contenu métallique est en moyenne plus élevée (Bergeron et al., 1994; Napiwotzki, 1999; Good et al., 2005; Gianninas et al., 2010). Une explication possible de cette corrélation est que l'hélium et les éléments lourds sont maintenus dans les couches externes par un seul et même mécanisme.

À plus basse température effective ($T_{\rm eff} \lesssim 30{,}000$ K), les spectres visibles montrant des raies métalliques sont plus courants, non pas parce que les métaux sont plus abondants, mais bien parce que le gaz d'hydrogène ou d'hélium est plus transparent. Le calcium est l'élément le plus fréquemment détecté, mais le magnésium et le fer sont également observés dans certains cas. Les mesures d'abondances de calcium sont généralement comprises dans l'intervalle $-11.0 \lesssim \log N_{\rm Ca}/N_{\rm H}\,, \log N_{\rm Ca}/N_{\rm He} \lesssim -6.0$ et ne montrent aucune corrélation avec la température effective ou avec la nature du principal constituant atmosphérique (Liebert et al., 1987; Zuckerman & Reid, 1998; Zuckerman et al., 2003; Koester et al., 2005, 2011; Koester & Kepler, 2015; Dufour et al., 2007; Hollands et al., 2017; Coutu et al., 2019; Blouin & Xu, 2022). Tout comme pour les naines blanches chaudes, la spectroscopie ultraviolette nous permet de déceler une panoplie d'autres éléments lourds, dont les plus communs sont

l'oxygène, l'aluminium, le silicium, le titane, le chrome, le manganèse et le nickel (Zuckerman et al., 2007; Klein et al., 2010, 2011; Dufour et al., 2012; Gänsicke et al., 2012; Farihi et al., 2013; Xu et al., 2014, 2017).

1.3. Les mécanismes de transport des éléments

À la lumière des résultats rapportés à la section précédente, il ne fait aucun doute que l'évolution chimique des étoiles naines blanches ne se limite pas à un simple processus de tri gravitationnel. En effet, il est évident que des phénomènes physiques perturbant la sédimentation des éléments sont à l'œuvre dans les couches externes des naines blanches. Pour tenter d'expliquer les tendances observées, il faut d'abord comprendre les divers mécanismes gouvernant le transport des éléments dans les étoiles. La présente section introduit les processus couramment invoqués dans le cadre de l'évolution spectrale des naines blanches, soit la diffusion (section 1.3.1), la lévitation radiative (section 1.3.2), la convection (section 1.3.3), les vents stellaires (section 1.3.4) et l'accrétion (section 1.3.5).

1.3.1. Diffusion

De manière générale, la diffusion désigne le mouvement net des constituants microscopiques d'un fluide occasionné par la présence d'un gradient spatial dans l'une des propriétés physiques du système. On peut distinguer trois principaux types de diffusion. Premièrement, l'exemple le plus familier est évidemment le mélange de deux espèces de particules, initialement distribuées de façon inhomogène, à la suite des multiples collisions interparticulaires. Ce procédé, que nous nommerons diffusion chimique, est régi par le gradient de concentration chimique et tend à uniformiser la composition du fluide (c'est-à-dire à aplanir ce même gradient). Deuxièmement, la diffusion peut également être causée par un gradient de pression. C'est ce phénomène qui est communément appelé sédimentation ou tri gravitationnel et que nous avons déjà évoqué à quelques reprises. Puisqu'un gradient de pression est effectivement une force, ce type de diffusion reflète l'influence des forces en jeu sur les différents atomes. Dans une étoile, ce sont les champs gravitationnels et électriques qui dominent la dynamique au niveau microscopique. Ces interactions induisent une séparation des éléments : les particules plus lourdes migrent vers les régions de plus haute pression, c'est-à-dire vers l'intérieur de l'étoile. Troisièmement, un transport diffusif peut aussi être provoqué par un gradient de température. On parle alors de diffusion thermique, dont l'effet net est un déplacement

des atomes plus lourds vers les régions de plus haute température, soit encore une fois vers l'intérieur de l'étoile. Ainsi, dans un plasma stellaire, le tri gravitationnel et la diffusion thermique tendent à séparer les éléments selon leur masse (les plus lourds coulent, les plus légers flottent), tandis que la diffusion chimique s'oppose à ce processus et tend plutôt à mélanger les éléments (Thoul et al., 1994; Michaud et al., 2015).

Dans les naines blanches, l'intense champ gravitationnel fait en sorte que le tri gravitationnel est extrêmement efficace dans les couches externes. Ainsi, en l'absence de tout autre mécanisme de transport, on s'attend à ce qu'une séparation complète des éléments s'opère dans le haut de l'enveloppe, et ce en un temps très court. Autrement dit, le temps caractéristique associé à la diffusion est beaucoup plus petit que le temps caractéristique associé à l'évolution de l'étoile. Par exemple, on estime que des métaux déposés sur une naine blanche (et soumis uniquement au tri gravitationnel) coulent sous la surface en moins d'une année, c'est-à-dire pratiquement instantanément à l'échelle de temps du refroidissement (Schatzman, 1958; Paquette et al., 1986a; Dupuis et al., 1992; Koester, 2009). Toutefois, il est important de mentionner que le temps caractéristique de diffusion augmente avec la profondeur dans l'étoile, ce qui signifie que le tri gravitationnel est beaucoup moins rapide dans le bas de l'enveloppe des naines blanches (Fontaine & Michaud, 1979; Dehner & Kawaler, 1995). Par ailleurs, les deux autres types de diffusion ont aussi un impact, quoique plus marginal, sur la structure chimique. La diffusion thermique, bien que beaucoup moins efficace que le tri gravitationnel, contribue au processus de séparation des éléments dans les naines blanches chaudes ($T_{\rm eff} \gtrsim 20{,}000$ K ; Althaus & Córsico 2004). Pour sa part, la diffusion chimique fait en sorte qu'il existe une zone de transition entre deux couches de compositions différentes (par exemple, une couche d'hydrogène au-dessus d'une couche d'hélium) où l'on retrouve un mélange des deux éléments (Arcoragi & Fontaine, 1980; Vennes et al., 1988).

1.3.2. Lévitation radiative

Dans l'enveloppe des étoiles chaudes, l'énergie est transportée essentiellement par la radiation, c'est-à-dire via la propagation des photons. Sur leur chemin, ceux-ci interagissent avec la matière : ils sont absorbés puis réémis à de multiples reprises. Or, un photon transporte aussi une certaine quantité de mouvement, qu'il peut transmettre à un atome lorsqu'il est absorbé par celui-ci. Ce gain de quantité de mouvement se traduit par une force nette

s'opposant à la gravité, puisque les photons se déplacent en moyenne de l'intérieur vers l'extérieur. Une espèce chimique sujette à une telle force radiative peut, si le champ de radiation est suffisamment intense, déjouer le tri gravitationnel et demeurer en petite quantité dans les couches externes d'une étoile. Il s'agit du phénomène de lévitation radiative (Chayer et al., 1995; Michaud et al., 2015).

Ce mécanisme de transport peut être quantifié par l'accélération radiative que subissent les particules. L'accélération radiative d'un certain type d'ions i, dénotée $g_{\mathrm{rad},i}$, est donnée par

$$g_{\mathrm{rad},i} = \frac{1}{cX_i} \int_0^\infty \kappa_{\nu,i} F_\nu \, d\nu, \tag{1.3}$$

où c est la vitesse de la lumière, X_i est la fraction de masse des ions i dans le plasma, ν est la fréquence, $\kappa_{\nu,i}$ est l'opacité monochromatique[7] des ions i, et F_ν est le flux radiatif monochromatique. Cette équation met en évidence les deux principaux ingrédients physiques de la lévitation radiative, soit la quantité de photons disponibles (F_ν) et la capacité de la matière à absorber ces photons ($\kappa_{\nu,i}$). Pour obtenir une accélération radiative significative, ces deux quantités doivent non seulement être grandes, mais elles doivent l'être dans le même intervalle de fréquence. Dans le cas contraire, les atomes absorbent de façon efficace là où il y a peu de radiation, et vice versa, donc l'intégrale de l'équation 1.3 vaut près de 0 (Chayer et al., 1995; Michaud et al., 2015).

Dans le domaine des naines blanches, les travaux théoriques qui se sont intéressés à l'influence de la lévitation radiative sur la structure chimique supposent un équilibre strict entre l'accélération gravitationnelle et l'accélération radiative à toutes les profondeurs. L'équation 1.3 fournit alors, pour une espèce chimique donnée, le profil d'abondance (ici exprimée en fraction de masse). De tels calculs ont prouvé que des éléments traces peuvent effectivement être maintenus par lévitation radiative dans l'enveloppe des étoiles DA et DO/DB chaudes ($T_{\mathrm{eff}} \gtrsim 30{,}000$ K). C'est particulièrement le cas des métaux, dont les nombreuses raies spectrales situées dans l'ultraviolet (là où le flux de radiation est maximal) procurent un support radiatif appréciable (Chayer et al., 1995; Dreizler, 1999).

7. L'opacité représente une mesure de la capacité de la matière à absorber la radiation. Elle est exprimée en $\mathrm{cm}^2\ \mathrm{g}^{-1}$ et correspond donc à une section efficace par unité de masse.

1.3.3. Convection

La diffusion et la lévitation radiative sont des processus de transport microscopiques, qui affectent les différents types d'atomes de façon sélective. Il existe aussi des processus de transport macroscopiques, qui induisent un déplacement global du plasma stellaire. L'un de ceux-ci est la convection, qui désigne le mouvement vertical de parcelles de matière occasionné par une instabilité hydrodynamique. Dans une étoile, ce phénomène se manifeste lorsque le transfert d'énergie par radiation devient inefficace, notamment si l'opacité de la matière est très grande. Les mouvements convectifs prennent alors le relai : des bulles de fluide chaud s'élèvent et des bulles de fluide froid plongent de manière cyclique, résultant en un transport net de chaleur vers la surface. Plus quantitativement, une région devient convective si elle satisfait le critère de Schwarzschild, qui est donné par

$$\left|\frac{\partial T}{\partial r}\right| > \left|\frac{\partial T}{\partial r}\right|_{\mathrm{ad}}, \tag{1.4}$$

où r est la coordonnée radiale, T est la température, et « ad » signifie « adiabatique ». En mots, la convection apparaît lorsque le gradient de température dans l'étoile est plus abrupt que le gradient de température caractérisant une bulle de matière qui subirait une ascension adiabatique. En plus de jouer un rôle important dans le transport de l'énergie, la convection exerce une influence considérable sur le transport des particules et donc sur la composition chimique. En fait, il est évident que l'advection du plasma par les cellules convectives provoque très rapidement un mélange complet des divers éléments. Ainsi, les régions convectives des étoiles sont chimiquement homogènes (Cox & Giuli, 1968; Eggleton, 1972; Kippenhahn et al., 2012).

Au cours du refroidissement d'une naine blanche, une zone de convection se développe dans son enveloppe lorsque l'espèce chimique dominante, qui était précédemment ionisée, commence à se recombiner. C'est l'opacité très élevée du gaz partiellement ionisé qui est à l'origine de l'instabilité convective (Fontaine & van Horn, 1976). Dans une enveloppe d'hydrogène, la recombinaison H II $\rightarrow$ H I débute à $T_{\mathrm{eff}} \sim 15{,}000$ K et progresse avec le refroidissement, de telle sorte que la région convective devient de plus en plus profonde à mesure que la température diminue (Tassoul et al., 1990; Tremblay et al., 2015; Rolland et al., 2018). Ce comportement est illustré à la figure 1.11, qui montre l'étendue verticale (mesurée en termes de masse) de la zone de convection d'hydrogène en fonction de la température

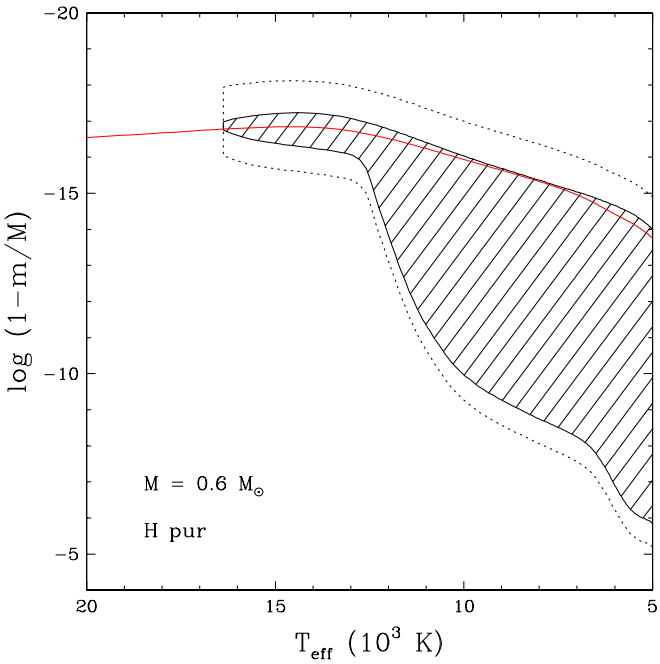

Figure 1.11 – Étendue verticale de la région soumise au mélange causé par la convection en fonction de la température effective, dans une naine blanche de masse $M = 0.6\ M_{\odot}$ dont l'enveloppe est composée d'hydrogène. La profondeur dans l'étoile est mesurée en termes de la fraction de la masse totale au-dessus d'un point donné. La zone hachurée représente la région formellement convective selon le critère de Schwarzschild, tandis que la courbe pointillée délimite approximativement la région de dépassement convectif (qui s'étend ici sur deux hauteurs caractéristiques de pression). Le trait rouge indique la position de la photosphère. Ces résultats sont basés sur les modèles détaillés de naines blanches présentés à la section 2.3.2.

effective. Dans une enveloppe d'hélium, deux processus de recombinaison ont lieu : He III → He II à partir de $T_{\rm eff} \sim 60{,}000$ K, puis He II → He I à partir de $T_{\rm eff} \sim 30{,}000$ K. L'évolution de la région convective correspondante est présentée à la figure 1.12. On peut voir que la zone de convection d'hélium est initialement confinée à l'atmosphère, puis plonge profondément dans l'enveloppe à $T_{\rm eff} \sim 20{,}000$ K (Tassoul et al., 1990; Rolland et al., 2018; Cukanovaite et al., 2019).

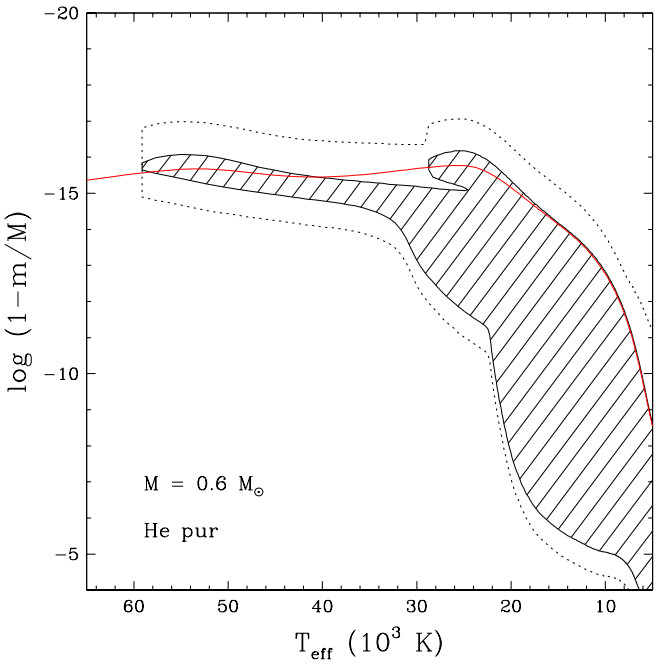

Figure 1.12 – Similaire à la figure 1.11, mais dans une naine blanche de masse $M = 0.6$ $M_\odot$ dont l'enveloppe est composée d'hélium.

Dans les modèles stellaires, la convection est généralement décrite à l'aide de la théorie dite de la longueur de mélange, qui est une approximation très grossière de la réalité (Böhm-Vitense, 1958; Cox & Giuli, 1968). L'une des limitations de ce formalisme est que celui-ci prédit que le mélange des éléments se borne à la région formellement convective selon le critère de Schwarzschild. Or, on s'attend à ce que les mouvements convectifs aient une quantité de mouvement non-nulle à la frontière de la zone de convection et transportent donc la matière au-delà de cette frontière. Ce dépassement convectif, ou *convective overshoot* en anglais, a pour effet d'augmenter l'étendue de la région chimiquement homogène (Zahn, 1991; Freytag et al., 1996). Dans les naines blanches, des simulations hydrodynamiques ont démontré que le dépassement convectif est très important : il peut mélanger les éléments jusqu'à quelques hauteurs caractéristiques de pression au-dessus et en-dessous de la zone de convection (Freytag et al., 1996; Tremblay et al., 2015; Kupka et al., 2018; Cunningham et al., 2019). À titre indicatif, la profondeur correspondant à deux hauteurs caractéristiques de pression au-dessus et en-dessous de la région formellement convective est mise en évidence sur les figures 1.11 et 1.12.

1.3.4. Vents stellaires

À la surface des étoiles les plus lumineuses, le champ de radiation peut devenir tellement intense que la force radiative peut surpasser la force gravitationnelle. L'équilibre hydrostatique n'étant plus possible, l'atmosphère se met alors globalement en mouvement vers l'extérieur, formant ce qui est appelé un vent stellaire radiatif. Les couches externes sont successivement expulsées de l'étoile, qui subit donc une perte de masse (Kudritzki & Puls, 2000; Michaud et al., 2015). Les vents ont un impact fondamental sur l'évolution stellaire : ils sont responsables, entre autres, de l'écart substantiel entre la masse initiale d'un objet sur la séquence principale et sa masse finale sur la séquence de refroidissement (Salaris et al., 2009; Choi et al., 2016). En outre, un tel transport macroscopique de matière peut affecter sensiblement la structure chimique.

Le paramètre le plus fréquemment employé pour mesurer l'intensité d'un vent stellaire est le taux auquel la masse est éjectée de l'étoile. Pour un taux de perte de masse $\dot{M}_{\text{wind}}$ donné, on peut évaluer la vitesse du vent v_{wind} à une certaine altitude via la relation

$$v_{\text{wind}} = -\frac{\dot{M}_{\text{wind}}}{4\pi r^2 \rho}, \tag{1.5}$$

où r est la coordonnée radiale et ρ est la densité de masse. Puisque la masse de l'étoile diminue ($\dot{M}_{\text{wind}} < 0$), la vitesse est orientée vers l'extérieur ($v_{\text{wind}} > 0$), comme il se doit. Près de la surface, toutes les particules, indépendamment de leur nature, sont transportées par le vent à cette même vitesse. Ainsi, l'effet d'un vent stellaire est d'empêcher la séparation des éléments et donc de maintenir une composition chimique uniforme dans les couches externes, tout comme la convection (Charbonneau, 1993; Unglaub & Bues, 2000; Hu et al., 2011).

À première vue, l'idée que les naines blanches soient en mesure de propulser un vent radiatif semble peu plausible, étant donné leur gravité de surface élevée. Néanmoins, certains indices observationnels supportent l'existence de vents très faibles au tout début de la séquence de refroidissement ($T_{\text{eff}} \gtrsim 60{,}000$ K). Nous reviendrons sur ce sujet à la section 1.4. De plus, quelques études ont appliqué la théorie des vents radiatifs aux naines blanches et ont trouvé qu'un vent très faible est bel et bien possible dans les naines blanches très chaudes et riches en éléments lourds (Unglaub & Bues, 2000). Les taux de perte de masse prédits par ces calculs sont initialement de l'ordre de 10^{-12} $M_{\odot}$ an^{-1} et décroissent rapidement avec le

temps, conséquence du fait que l'intensité d'un vent radiatif dépend surtout de la luminosité de l'étoile (Blöcker, 1995a; Kudritzki & Puls, 2000).

1.3.5. Accrétion

Si une étoile peut perdre de la masse via un vent, elle peut également en gagner en interagissant avec son environnement immédiat. Une telle accrétion de matière représente un autre mécanisme pouvant altérer sa composition chimique de surface. Il existe principalement deux types d'interactions possibles : l'étoile peut accréter le gaz ténu du milieu interstellaire (qui est constitué en majeure partie d'hydrogène), ou encore la matière provenant d'un éventuel compagnon stellaire ou planétaire (Michaud et al., 2015).

Évidemment, l'accrétion modifie directement la composition atmosphérique, mais elle peut aussi avoir un impact indirect sur la structure chimique sous-jacente : l'ajout de matière à la surface perturbe l'équilibre hydrostatique, ce qui entraîne un déplacement global du plasma vers l'intérieur de l'étoile. Puisque ce processus est exactement l'inverse du transport généré par un vent stellaire, la vitesse due à l'accrétion $v_{\rm acc}$ est reliée au taux d'accrétion $\dot{M}_{\rm acc}$ par une expression analogue à l'équation 1.5, c'est-à-dire par

$$v_{\rm acc} = -\frac{\dot{M}_{\rm acc}}{4\pi r^2 \rho}. \tag{1.6}$$

Par contre, on a ici $\dot{M}_{\rm acc} > 0$ et donc $\dot{v}_{\rm acc} < 0$ (Turcotte & Charbonneau, 1993).

Dans le cas des naines blanches, on pensait à l'origine que l'accrétion d'hydrogène et de métaux en provenance du milieu interstellaire était chose courante (Vauclair et al., 1979; Alcock & Illarionov, 1980; MacDonald & Vennes, 1991; Dupuis et al., 1993b). Cependant, un changement radical de paradigme s'est opéré dans la dernière décennie : il s'avère que les naines blanches accrètent en fait des corps rocheux, tels que des comètes, des astéroïdes ou même des planètes, qui sont détruits sur leur orbite par les forces de marée (Zuckerman et al., 2010; Farihi et al., 2010; Farihi, 2016; Jura & Young, 2014). Ce phénomène se manifeste par plusieurs signatures observationnelles, notamment par la présence d'éléments lourds dans l'atmosphère stellaire (Coutu et al., 2019), d'un disque de débris circumstellaire (Manser et al., 2020), ou même parfois d'un compagnon planétaire en train de se désintégrer (Vanderburg et al., 2015). Les taux d'accrétion mesurés sont généralement compris entre 10^{-20} et 10^{-16} $M_\odot$ an^{-1} (Koester et al., 2014a; Wyatt et al., 2014; Hollands et al., 2018; Blouin & Xu, 2022).

1.4. Un portrait théorique de l'évolution spectrale

L'objectif de cette section est de rassembler les morceaux du casse-tête : comment les processus de transport discutés à la section 1.3 se combinent-ils pour donner lieu à l'évolution spectrale telle que décrite à la section 1.2 ? C'est là la question centrale que cherche à élucider la théorie de l'évolution spectrale des étoiles naines blanches. Après un court segment consacré à la formation des objets pré-naines blanches pauvres en hydrogène (section 1.4.1), nous décrirons les divers mécanismes physiques invoqués pour expliquer les transformations atmosphériques observées le long de la séquence de refroidissent (section 1.4.2). Nous compléterons ensuite cette section en abordant l'origine des étoiles hybrides (section 1.4.3) et des étoiles polluées par des métaux (section 1.4.4).

1.4.1. La formation d'atmosphères pauvres en hydrogène

Comme mentionné précédemment, les modèles standards d'évolution stellaire prédisent qu'une étoile devenue naine blanche devrait être dotée d'une couche superficielle d'hydrogène de masse $\log M_{\rm H}/M \sim -4.0$ (Iben & Tutukov, 1984; Renedo et al., 2010) et devrait donc montrer une atmosphère d'hydrogène. Dès lors, comment se fait-il que certains objets possèdent plutôt une atmosphère d'hélium à leur arrivée sur la séquence de refroidissement ? Ces étoiles ont vraisemblablement subi, dans les phases évolutives précédentes, des événements particulièrement violents les ayant dépouillées de tout (ou presque tout) leur hydrogène. Comme nous l'avons vu à la section 1.1, il existe deux groupes d'objets pré-naines blanches pauvres en hydrogène, soit les étoiles de type O(He), dont la surface est dominée par l'hélium, et les étoiles de type PG 1159, dont l'atmosphère est composée d'un mélange d'hélium, de carbone et d'oxygène. On pense que deux phénomènes distincts sont à l'origine de ces deux classes spectrales.

Commençons par les étoiles PG 1159, qui sont plus communes et mieux comprises. L'existence de ces objets est généralement expliquée par le scénario dit de renaissance, ou *born-again scenario* en anglais. Lorsqu'une naine blanche nouvellement formée amorce son processus de refroidissement, il est possible, dans certaines circonstances, que les réactions nucléaires se rallument de façon explosive dans la couche d'hélium, un événement appelé flash tardif de l'hélium. Métaphoriquement parlant, une étoile en route vers sa « mort » connaît une brève « renaissance », d'où le nom donné au phénomène. L'évolution subséquente se déroule

extrêmement rapidement, c'est-à-dire sur une période de quelques années seulement. À cause de l'apparition soudaine d'une source d'énergie à un endroit localisé dans l'étoile, le gradient de température y devient de plus en plus abrupt. Conformément au critère de Schwarzschild (équation 1.4), une zone de convection se développe et atteint tôt ou tard la couche d'hydrogène à la surface. Il s'ensuit un mélange très efficace dans l'entièreté de l'enveloppe, qui a deux conséquences importantes. D'une part, l'hydrogène est englouti à une profondeur où la température est suffisamment élevée pour qu'il soit brûlé. D'autre part, une quantité notable de carbone et d'oxygène est transporté du noyau à la surface. Par conséquent, suite au flash, l'atmosphère de l'étoile est dénuée d'hydrogène et comporte plutôt de l'hélium, du carbone et de l'oxygène dans des proportions similaires (Iben et al., 1983; Herwig et al., 1999; Althaus et al., 2005b; Werner & Herwig, 2006). Lorsque les réactions nucléaires cessent, l'étoile recommence à se refroidir et devient donc, pour de bon cette fois-ci, une naine blanche.

Les objets de type O(He) sont moins nombreux et plus mystérieux. Deux principaux scénarios ont été proposés pour expliquer leur atmosphère riche en hélium. La première suggestion est qu'un vent stellaire très puissant éjecte la couche d'hydrogène dans la phase pré-naine blanche (Rauch et al., 1998; Miller Bertolami & Althaus, 2006; Reindl et al., 2014b). Le problème de cette hypothèse est que les taux de perte de masse nécessaires sont beaucoup plus élevés que ce que prédit la théorie des vents radiatifs (Pauldrach et al., 1988). La deuxième suggestion fait intervenir la fusion de deux naines blanches de faible masse, un événement que l'on croit assez violent pour entraîner le brûlage quasi-complet de l'hydrogène à la surface des deux objets (Rauch et al., 2006; Zhang & Jeffery, 2012; Reindl et al., 2014b). Bien que ce scénario comporte lui aussi certaines lacunes, il est actuellement considéré comme le plus vraisemblable.

1.4.2. Le modèle de Fontaine & Wesemael (1987)

Le premier modèle global de l'évolution spectrale des naines blanches a été proposé par Fontaine & Wesemael (1987) dans la foulée du relevé PG. Rappelons qu'à cette époque, on ne connaissait aucun objet de type DA dans l'intervalle $T_{\rm eff} \gtrsim 80{,}000$ K et aucun objet de type DB dans l'intervalle $45{,}000 \text{ K} \gtrsim T_{\rm eff} \gtrsim 30{,}000$ K (voir la figure 1.6). D'abord, le scénario original de Fontaine & Wesemael (1987) postule que les étoiles PG 1159 sont les précurseurs de la totalité des naines blanches, ce qui explique naturellement l'absence d'étoiles riches en hydrogène au début de la séquence de refroidissement. En outre, il suppose également

qu'une toute petite quantité d'hydrogène survit au flash tardif de l'hélium mais est initialement diluée dans l'enveloppe d'hélium, demeurant ainsi spectroscopiquement invisible. Avec le temps, cet hydrogène résiduel remonte vers la surface sous l'effet du tri gravitationnel, formant ultimement une mince couche superficielle d'hydrogène. Ce phénomène est communément appelé le flottement, ou *float-up* en anglais, de l'hydrogène. Par conséquent, les atmosphères d'hélium se transforment progressivement en atmosphères d'hydrogène, d'où l'augmentation du nombre d'étoiles DA et la diminution du nombre d'étoiles DO à mesure que la température effective décroît. La brèche des DB est alors interprétée comme la conséquence du fait que toutes les naines blanches développent une couche d'hydrogène englobant complètement l'atmosphère ($\log M_{\rm H}/M \gtrsim -15.0$) avant d'atteindre $T_{\rm eff} \sim 45{,}000$ K.

À plus basse température effective, Fontaine & Wesemael (1987) suggèrent que le processus physique responsable de la réapparition des étoiles à atmosphère d'hélium et de la réaugmentation de leur incidence dans la population de naines blanches est la convection. En fait, deux mécanismes similaires mais distincts sont invoqués. D'une part, si la couche superficielle d'hydrogène est suffisamment mince ($\log M_{\rm H}/M \lesssim -14.0$), une zone de convection apparaît dans l'enveloppe sous-jacente d'hélium à $T_{\rm eff} \sim 30{,}000$ K et devient de plus en plus profonde avec le refroidissement (voir la figure 1.12). Les mouvements convectifs érodent la couche d'hydrogène par-dessous, de telle sorte que l'hydrogène se retrouve complètement dilué dans le réservoir d'hélium. Ce phénomène est appelé la dilution convective. D'autre part, si la couche superficielle d'hydrogène est plus épaisse ($\log M_{\rm H}/M \gtrsim -14.0$), la convection dans l'enveloppe d'hélium est inhibée. Toutefois, la couche d'hydrogène devient elle-même convective à $T_{\rm eff} \sim 15{,}000$ K, et la zone de convection prend de l'expansion à mesure que l'étoile se refroidit (voir la figure 1.11). Inévitablement, il arrive un moment où les mouvements convectifs atteignent l'enveloppe sous-jacente d'hélium, ce qui provoque un mélange complet des couches d'hydrogène et d'hélium. Ce processus est appelé le mélange convectif. Plus la couche d'hydrogène est épaisse, plus le mélange se produit à basse température effective (voir la figure 1.11). Tant la dilution convective que le mélange convectif engendrent une atmosphère dominée par l'hélium, puisque la petite quantité d'hydrogène jadis présente à la surface se retrouve noyée dans un réservoir d'hélium beaucoup plus massif. Selon Fontaine & Wesemael (1987), ce sont ces deux mécanismes qui sont à l'origine de la frontière froide

de la brèche des DB et de l'augmentation de la proportion des atmosphères d'hélium parmi les naines blanches froides.

À l'époque où il a été imaginé, le modèle de Fontaine & Wesemael (1987) avait pour principal attrait d'expliquer de manière cohérente plusieurs facettes de l'évolution spectrale à partir du concept simple et unificateur selon lequel toutes les naines blanches ont une origine commune. Cependant, il avait aussi pour conséquence révolutionnaire de remettre en question la théorie standard de l'évolution stellaire (pourtant un jalon solide de l'astrophysique théorique), de par sa prémisse que l'ensemble des naines blanches contiennent remarquablement peu d'hydrogène. Les avancées réalisées dans les années subséquentes ont mis en évidence quelques failles dans le scénario de Fontaine & Wesemael (1987). D'abord, la découverte par Napiwotzki & Schönberner (1995) d'objets riches en hydrogène à l'entrée de la séquence de refroidissement est venue infirmer l'hypothèse selon laquelle les étoiles PG 1159 sont les précurseurs de la totalité des naines blanches. Ces étoiles DA très chaudes constituent la preuve de l'existence d'un canal évolutif standard, associé à des objets vraisemblablement caractérisés par une couche d'hydrogène « épaisse » ($\log M_{\rm H}/M \sim -4.0$). De telles naines blanches conservent leur type spectral DA durant toute leur vie, puisqu'aucun des mécanismes de transport évoqués à la section 1.3 ne peut altérer un réservoir d'hydrogène aussi imposant. De plus, la découverte par Eisenstein et al. (2006a) d'étoiles riches en hélium dans la brèche des DB a réfuté l'idée selon laquelle le flash tardif de l'hélium laisse toujours un peu d'hydrogène intact. En effet, ces naines blanches DB doivent être pratiquement dépourvues d'hydrogène, car autrement elles se seraient transformées en naines blanches DA sous l'action du tri gravitationnel. Néanmoins, il est important de rappeler qu'à l'heure actuelle, des déficits d'étoiles DA et DB sont toujours observés dans les intervalles $T_{\rm eff} \gtrsim 80{,}000$ K et $45{,}000$ K $\gtrsim T_{\rm eff} \gtrsim 20{,}000$ K, respectivement. Ainsi, le canal évolutif de type DO/DB $\rightarrow$ DA $\rightarrow$ DB/DC s'applique probablement à une fraction non-négligeable de la population de naines blanches. Plus précisément, les analyses empiriques modernes à basse température effective ($T_{\rm eff} \lesssim 30{,}000$ K) indiquent qu'entre 15 et 30 % des naines blanches subissent une telle évolution spectrale (voir la figure 1.7).

En outre, les trois mécanismes physiques proposés par Fontaine & Wesemael (1987), soit le flottement de l'hydrogène, la dilution convective et le mélange convectif, sont encore aujourd'hui invoqués très fréquemment dans la littérature pour expliquer les transformations

atmosphériques. La description originale de Fontaine & Wesemael (1987) étant essentiellement qualitative, des études ultérieures ont développé des modèles quantitatifs de ces phénomènes afin d'asseoir la théorie de l'évolution spectrale sur des bases plus solides. À haute température, Unglaub & Bues (1998, 2000) sont à peu près les seuls à avoir modéliser la diffusion de l'hydrogène résiduel dans une enveloppe d'hélium. À basse température, la dilution convective et le mélange convectif ont fait l'objet de plusieurs travaux théoriques, notamment par Baglin & Vauclair (1973), Koester (1976), D'Antona & Mazzitelli (1989), MacDonald & Vennes (1991), Althaus & Benvenuto (1998), Chen & Hansen (2011) et Rolland et al. (2018, 2020). Toutefois, il convient de mentionner que toutes ces études sont approximatives. En effet, l'approche idéale pour modéliser l'évolution spectrale des naines blanches consiste à effectuer des calculs d'évolution stellaire dans lesquels le transport des éléments est pris en compte de manière exacte et cohérente. Or, puisque de telles simulations sont numériquement très exigeantes (à cause, entre autres, de la disparité des temps caractéristiques d'évolution et de transport), les modèles que l'on retrouve dans la littérature reposent sur diverses approximations plus ou moins réalistes. Parmi les plus répandues, notons l'emploi de modèles stellaires statiques (qui négligent l'impact des changements de composition sur le refroidissement) et un traitement simplifié du transport des éléments (équilibre diffusif, mélange instantané, etc.). Ainsi, il y a certainement place à l'amélioration dans la description quantitative du flottement de l'hydrogène, de la dilution convective et du mélange convectif.

1.4.3. L'origine des atmosphères hybrides

Le modèle d'évolution spectrale de Fontaine & Wesemael (1987) a également la vertu d'offrir des éclaircissements quant à l'existence de naines blanches possédant une atmosphère hybride, c'est-à-dire composée à la fois d'hydrogène et d'hélium. D'une part, à haute température, le processus de flottement donne inévitablement lieu à une période de transition lors de laquelle la couche superficielle d'hydrogène nouvellement formée est tellement mince que l'enveloppe sous-jacente d'hélium est toujours visible, produisant ainsi un spectre hybride. Insistons ici sur le fait que l'atmosphère mixte ainsi formée est chimiquement stratifiée, étant donné l'effet du tri gravitationnel. Par conséquent, les naines blanches relativement chaudes (55,000 K $\gtrsim T_{\rm eff} \gtrsim$ 35,000 K) dont le spectre est bien reproduit par des modèles d'atmosphères stratifiées peuvent être interprétées comme des objets qui sont en train de subir la transformation de DO/DB à DA par flottement de l'hydrogène résiduel (Bergeron et al.,

1994; Manseau et al., 2016). D'autre part, à basse température, la dilution ou le mélange de la couche d'hydrogène dans l'enveloppe d'hélium par la convection engendre une atmosphère dominée par l'hélium mais aussi pourvue d'une petite quantité d'hydrogène, qui se traduit encore une fois par un spectre hybride. En particulier, le phénomène de dilution convective semble à première vue fournir une explication toute naturelle à l'existence de nombreuses étoiles froides ($T_{\rm eff} \lesssim 20{,}000$ K) de type DBA (MacDonald & Vennes, 1991; Bergeron et al., 2011; Rolland et al., 2018). Par ailleurs, les naines blanches comme PG 1210+533, GD 323 et HS 0209+0832, qui montrent des variations spectroscopiques, peuvent être interprétées comme des manifestations en temps réel de l'évolution spectrale.

Ceci dit, les mécanismes physiques proposés par Fontaine & Wesemael (1987) ne rendent pas compte de toutes les caractéristiques observées des naines blanches hybrides. Tout d'abord, nous avons vu à la section 1.2.2 qu'en plus des deux groupes d'objets mentionnés dans le paragraphe précédent, il existe un troisième groupe d'étoiles hybrides : les naines blanches DAO très chaudes ($T_{\rm eff} \gtrsim 55{,}000$ K) dont l'atmosphère est chimiquement homogène. Cette dernière propriété indique que ces objets ne sont pas le produit du flottement de l'hydrogène, qui donne plutôt lieu à une atmosphère chimiquement stratifiée. Autrement dit, les naines blanches DAO très chaudes ne représentent pas une phase intermédiaire dans la transition spectrale de DO et DA (MacDonald & Vennes, 1991; Bergeron et al., 1994). Il n'y a donc aucune raison de penser que leur contenu total d'hydrogène est significativement réduit : il est plus probable qu'elles appartiennent au canal évolutif associé à une couche d'hydrogène standard ($\log M_{\rm H}/M \sim -4.0$) et qu'un peu d'hélium est maintenu à leur surface par un quelconque processus de transport à très haute température effective. Parmi les mécanismes décrits à la section 1.3, la lévitation radiative et les vents stellaires sont les deux candidats les plus plausibles. Or, on sait depuis longtemps que la quantité d'hélium supportée par lévitation radiative dans une enveloppe d'hydrogène est nettement inférieure (par deux ordres de grandeur environ) aux abondances mesurées dans les étoiles DAO (Vennes et al., 1988; MacDonald & Vennes, 1991). En revanche, ces observations sont très bien reproduites par un modèle dans lequel un vent radiatif entrave l'action du tri gravitationnel. De surcroît, puisque le taux de perte de masse est déterminé principalement par la luminosité de l'étoile, ce paradigme mène spontanément à une corrélation entre l'abondance d'hélium et la luminosité, telle qu'observée dans les naines blanches DAO (Unglaub & Bues, 1998,

2000). En outre, notons que d'autres caractéristiques de ces objets, notamment leurs masses plus faibles et leurs contenus métalliques plus élevés que la moyenne, sont également compatibles avec l'idée d'un vent radiatif (Napiwotzki, 1999; Good et al., 2005; Gianninas et al., 2010). En particulier, une plus grande quantité d'éléments lourds se traduit par un vent plus fort et donc une abondance d'hélium plus élevée, ce qui explique pourquoi les étoiles DAO comportent à la fois plus d'hélium et de métaux que les étoiles DA.

Finalement, à plus basse température effective, notre compréhension de l'origine des naines blanches de type DBA est, encore à ce jour, loin d'être satisfaisante. En effet, l'interprétation selon laquelle ces étoiles sont le produit de la dilution convective comporte un problème majeur. Celui-ci concerne l'abondance d'hydrogène dans l'enveloppe d'hélium une fois la dilution convective complétée. Supposons qu'une couche d'hydrogène de masse $\log M_{\rm H}/M \sim -14.0$ est entièrement diluée dans la zone convective d'hélium, dont la masse est $\log M_{\rm conv}/M \sim -5.0$ à basse température (voir la figure 1.12). La fraction de masse d'hydrogène dans l'enveloppe devrait donc être $\log X_{\rm H} \sim \log M_{\rm H}/M_{\rm conv} \sim -9.0$, ce qui correspond à un ratio de nombres $\log N_{\rm H}/N_{\rm He} \sim -8.4$. Or, les abondances d'hydrogènes observées à la surface des étoiles DBA sont beaucoup plus élevées ($-6.5 \lesssim \log N_{\rm H}/N_{\rm He} \lesssim -4.0$; voir la figure 1.9). Autrement dit, le scénario de dilution convective prédit des abondances d'hydrogène beaucoup trop faibles, ce qui signifie que les naines blanches DBA bénéficient d'une source additionnelle d'hydrogène (en plus de la mince couche jadis présente à la surface). Ce problème, dont l'existence a été confirmée par des modèles plus détaillés que le calcul simple effectué ci-dessus, est l'un des plus importants de la théorie de l'évolution spectrale (MacDonald & Vennes, 1991; Voss et al., 2007; Bergeron et al., 2011; Koester & Kepler, 2015; Rolland et al., 2018, 2020).

Une solution couramment suggérée dans la littérature est que les étoiles DBA accrètent de l'hydrogène de l'extérieur, soit via le gaz du milieu interstellaire (MacDonald & Vennes, 1991; Voss et al., 2007), soit sous forme de comètes, d'astéroïdes ou de planètes riches en eau (Farihi et al., 2013; Veras et al., 2014; Raddi et al., 2015; Gentile Fusillo et al., 2017). Cependant, cette hypothèse n'est pas sans difficulté : elle requiert que l'accrétion ne débute qu'après le processus de dilution convective. Dans le cas contraire, la couche superficielle d'hydrogène accumulée par accrétion devient rapidement trop épaisse pour que la dilution convective se produise, ce qui empêche la formation d'une atmosphère riche en hélium (Bergeron et al.,

2011; Koester & Kepler, 2015; Rolland et al., 2018). Puisque cette éventualité semble peu probable, une tout autre solution a été proposée récemment par Rolland et al. (2020). Selon eux, la source supplémentaire d'hydrogène des naines blanches DBA est interne. Plus spécifiquement, ils suggèrent que l'hydrogène résiduel situé profondément dans l'enveloppe n'a pas eu le temps de flotter, puisque le temps caractéristique de diffusion y est très long. Ainsi, la couche superficielle d'hydrogène formée par tri gravitationnel ne représente qu'une petite fraction de l'hydrogène présent dans l'étoile. Une fois la dilution convective achevée, le réservoir interne d'hydrogène est mélangé dans la zone convective d'hélium et contribue donc à la composition atmosphérique. Les modèles préliminaires de Rolland et al. (2020) ont démontré que cette idée est très prometteuse et mérite donc un examen plus approfondi.

1.4.4. L'origine des atmosphères polluées par des métaux

Nous avons vu précédemment qu'il existe deux classes distinctes de naines blanches polluées par des éléments lourds, soit celles montrant uniquement des traces de carbone (de type DQ) et celles montrant des traces d'autres métaux (de types DAZ, DBZ, DOZ et DZ). Dans les deux cas, la présence d'éléments lourds dans l'atmosphère implique nécessairement qu'un ou plusieurs mécanismes de transport rivalisent avec le tri gravitationnel. Toutefois, il est évident que ces processus ne sont pas les mêmes pour les deux groupes, puisque ceux-ci ont des propriétés atmosphériques passablement différentes.

Tel que rapporté à la section 1.2.3, les étoiles DQ « classiques » sont froides ($T_{\rm eff} \lesssim 10{,}000$ K) et riches en hélium. De tels objets possèdent une zone de convection s'étendant très profondément dans l'enveloppe (voir la figure 1.12). Ceci a très tôt inspiré la suggestion que le carbone détecté dans l'atmosphère des naines blanches DQ proviendrait du noyau et serait transporté jusqu'à la surface par les mouvements convectifs (Koester et al., 1982; Fontaine et al., 1984). On parle alors de dragage convectif, ou *convective dredge-up* en anglais. Les calculs élaborés de Pelletier et al. (1986) ont démontré que ce phénomène engendre bel et bien la composition atmosphérique des étoiles DQ, pourvu que l'enveloppe d'hélium soit suffisamment mince ($\log M_{\rm He}/M \sim -3.5$). Les modèles de Pelletier et al. (1986) ont aussi révélé que la décroissance de l'abondance de carbone avec le refroidissement (voir la figure 1.10) est due à un effet d'ionisation : à mesure que la température diminue, la recombinaison du carbone fait en sorte que celui-ci coule graduellement sous la zone de convection. Malgré ce succès, la nécessité d'une couche d'hélium nettement moins massive que prévu par les modèles

d'évolution pré-naine blanche ($\log M_{\rm He}/M \sim -2.0$; Iben & Tutukov 1984; Miller Bertolami & Althaus 2006) constituait une difficulté de taille pour le scénario original de dragage convectif. La solution à ce problème réside dans la structure chimique des précurseurs directs des naines blanches DQ. Les calculs de Pelletier et al. (1986) supposent que ces prédécesseurs sont des étoiles DB formées simplement d'une enveloppe d'hélium et d'un noyau de carbone. Autrement dit, ils présument que le tri gravitationnel a complètement séparé l'hélium et le carbone avant que le dragage convectif ne débute. Il s'avère que cette hypothèse est incorrecte. En simulant la transformation d'une étoile PG 1159 en naine blanche DB causée par la diffusion, Dehner & Kawaler (1995) ont réalisé que la séparation des éléments demeure incomplète : une couche d'hélium pur apparaît bel et bien en surface, mais la composition du bas de l'enveloppe demeure inchangée, puisque le temps caractéristique de diffusion y est très long. Les naines blanches DB possèdent donc une enveloppe en double couche : un plasma d'hélium pur au-dessus, et un mélange d'hélium, de carbone et d'oxygène en-dessous. D'autres études théoriques ont subséquemment démontré que c'est en fait dans cette couche située dans le bas de l'enveloppe, et non dans le noyau, que la zone de convection vient ultimement puiser le carbone donnant lieu à la classe spectrale DQ (Althaus et al., 2005b; Dufour et al., 2005; Fontaine & Brassard, 2005; Scóccola et al., 2006; Brassard et al., 2007; Camisassa et al., 2017). Dans ce nouveau paradigme, il n'est donc plus nécessaire d'invoquer une enveloppe mince pour expliquer la composition atmosphérique des étoiles DQ.

Pour leur part, les quelques naines blanches DQ atypiques, qui sont plus massives, plus chaudes et plus riches en carbone, sont moins bien comprises. On pense qu'elles sont elles aussi le produit du dragage convectif, mais dans une enveloppe contenant remarquablement peu d'hélium ($\log M_{\rm He}/M \sim -8.0$; Althaus et al. 2009a). Dans ce cas-ci, il y a une bonne raison de croire que ce déficit d'hélium est réel : les propriétés cinématiques et magnétiques des étoiles DQ massives suggèrent que celles-ci résultent de la fusion de deux naines blanches, un événement pouvant réduire significativement le contenu total d'hélium (Dunlap & Clemens, 2015; Cheng et al., 2019; Coutu et al., 2019). Néanmoins, les modèles actuels de dragage convectif ne parviennent toujours pas à reproduire correctement la séquence que forment ces objets dans le diagramme abondance−température (Brassard et al., 2007; Coutu et al., 2019).

Les naines blanches dont la surface est contaminée par un mélange de plusieurs éléments lourds sont le produit d'un tout autre phénomène. Tout d'abord, à basse température effective ($T_{\rm eff} \lesssim 30{,}000$ K), le seul mécanisme pouvant générer une telle composition atmosphérique est l'accrétion de matière. Qui plus est, puisque les métaux coulent extrêmement rapidement dans l'étoile sous l'effet du tri gravitationnel, leur détection implique que l'épisode d'accrétion est actuellement en cours, ou à tout le moins très récent. Comme mentionné à la section 1.3.5, on a longtemps pensé que ces éléments lourds avaient pour origine le milieu interstellaire (Vauclair et al., 1979; Alcock & Illarionov, 1980; Dupuis et al., 1993b; Koester et al., 2005), mais on sait maintenant qu'ils proviennent plutôt de comètes, d'astéroïdes ou de planètes qui viennent s'écraser à la surface de l'étoile (Zuckerman et al., 2010; Farihi et al., 2010; Farihi, 2016; Jura & Young, 2014). Dans ce contexte, les naines blanches froides nous offrent une fenêtre unique sur la structure interne des corps rocheux situés au-delà du système solaire. En effet, en modélisant simultanément les processus d'accrétion et de diffusion des métaux dans l'enveloppe stellaire, il est possible de déterminer la composition chimique des objets accrétés (Dupuis et al., 1993a,b; Koester, 2009; Fontaine et al., 2015b). Par ailleurs, rappelons que la pollution métallique des naines blanches froides est un phénomène essentiellement aléatoire selon la température effective et la nature du constituant atmosphérique dominant ; ceci est une conséquence directe du fait que la source d'éléments lourds est externe.

À plus haute température effective ($T_{\rm eff} \gtrsim 30{,}000$ K), la situation est plus complexe, car l'accrétion de matière n'est pas le seul phénomène pouvant mener à la présence d'éléments lourds dans l'atmosphère. En effet, une autre possibilité est que les métaux primordiaux de l'étoile sont maintenus à la surface par lévitation radiative ou encore par un vent stellaire. La lévitation radiative était initialement considérée comme l'hypothèse la plus vraisemblable, mais les travaux théoriques de Chayer et al. (1995) et Dreizler (1999) ont démontré qu'un modèle supposant un équilibre strict entre les forces gravitationnelles et radiatives échoue à reproduire les abondances métalliques observées. Par conséquent, la perte de masse est maintenant le processus généralement favorisé, du moins pour les naines blanches très chaudes ($T_{\rm eff} \gtrsim 60{,}000$ K). Cette idée est notamment cohérente avec le fait que les mesures d'abondances ont tendance à être plus élevées dans les étoiles plus chaudes et plus riches en hélium. Cependant, elle ne peut pas être invoquée à des températures plus basses, où les vents radiatifs sont très probablement impossibles ($T_{\rm eff} \lesssim 60{,}000$ K). De surcroît, elle n'explique pas

pourquoi des objets ayant des paramètres atmosphériques similaires peuvent montrer des quantités d'éléments lourds très différentes. Pour ces raisons, une autre suggestion a été mise de l'avant par Barstow et al. (2014) : les abondances métalliques des naines blanches chaudes seraient en fait dues à une combinaison entre l'accrétion de matière et le support radiatif, d'où le caractère semi-aléatoire du phénomène.

1.5. Contenu de cette thèse

1.5.1. Objectifs et structure

Le but de cette thèse est d'améliorer notre compréhension de l'évolution spectrale des étoiles naines blanches, à la fois sur les plans empirique et théorique. Comme l'indique le titre de ce travail, nous mettrons l'accent principalement sur les naines blanches chaudes ($T_{\rm eff} \gtrsim 30{,}000$ K), mais nous nous intéresserons aussi aux naines blanches plus froides en maintes occasions. Les motivations derrière ce projet sont nombreuses. Tout d'abord, l'étude de l'évolution spectrale est d'une importance capitale pour la cosmochronologie, étant donné que le taux de refroidissement des naines blanches dépend de la composition de leur enveloppe. En outre, cette avenue de recherche représente une excellente façon d'en apprendre plus sur les processus physiques à l'œuvre non seulement sur la séquence de refroidissement, mais aussi dans les phases évolutives précédentes, puisque celles-ci déterminent largement la structure chimique des naines blanches. Enfin, l'évolution spectrale est un phénomène fascinant en lui-même, faisant intervenir un mélange unique de physique et d'astronomie ; le simple plaisir de comprendre constitue donc ici une motivation significative, comme il devrait l'être pour tout travail scientifique.

Du côté empirique, nous avons vu que l'évolution spectrale peut être caractérisée en examinant la variation de la proportion des naines blanches à atmosphère d'hélium en fonction de la température effective. Or, si cette fonction est relativement bien contrainte à basse température, elle ne l'est pas à haute température, où nos connaissances reposent sur des études désuètes et demeurent donc insuffisantes. Plus spécifiquement, pour obtenir un portrait complet et à jour de l'évolution spectrale, il est essentiel d'évaluer avec précision : (1) quelle fraction des étoiles possèdent une atmosphère d'hélium à leur arrivée sur la séquence de refroidissement, (2) quelle fraction d'entre elles développent une atmosphère d'hydrogène avec le temps, et (3) dans quel intervalle de température effective ces transformations se

produisent. Ce sont là les objectifs du chapitre 2, qui est une adaptation de l'article intitulé *On the Spectral Evolution of Hot White Dwarf Stars. I. A Detailed Model Atmosphere Analysis of Hot White Dwarfs from SDSS DR12*, publié dans *The Astrophysical Journal* en octobre 2020 (Bédard et al., 2020). Dans ce chapitre, nous présentons une analyse spectroscopique détaillée d'un échantillon de près de 2000 naines blanches chaudes ($T_{\rm eff} \gtrsim 30{,}000$ K) observées par le SDSS. Nous calculons tout d'abord un nouvel ensemble de modèles d'atmosphère appropriés pour ces objets, que nous utilisons ensuite pour analyser les données spectroscopiques et ainsi déterminer les propriétés atmosphériques de notre échantillon. Nous sommes donc en mesure, pour la première fois, de caractériser précisément l'incidence des étoiles riches en hélium à haute température et ainsi d'apporter des réponses aux questions soulevées ci-dessus. De surcroît, nous accordons une attention particulière à la centaine de naines blanches hybrides incluses dans notre étude et à ce que ces objets distinctifs nous apprennent sur l'évolution spectrale.

Du côté théorique, nous avons vu que les transformations atmosphériques peuvent être expliquées par divers mécanismes physiques associés au transport des éléments dans l'enveloppe stellaire, notamment le flottement de l'hydrogène, la dilution convective et le mélange convectif. Or, jusqu'à présent, ces processus n'ont été modélisés qu'approximativement, une situation à laquelle il est impératif de remédier pour faire progresser la théorie de l'évolution spectrale des naines blanches. Dans ce contexte, les chapitres 3, 4 et 5 présentent les simulations numériques d'évolution spectrale les plus sophistiquées à ce jour, en ce sens qu'elles incorporent un traitement élaboré du transport des éléments et tiennent compte de l'impact des changements de composition sur le refroidissement de manière cohérente. Tout d'abord, le chapitre 3 est une adaptation de l'article intitulé *On the Spectral Evolution of Hot White Dwarf Stars. II. Time-dependent Simulations of Element Transport in Evolving White Dwarfs with STELUM*, publié dans *The Astrophysical Journal* en mars 2022 (Bédard et al., 2022b). L'objet de ce chapitre est d'introduire le code d'évolution stellaire STELUM, qui est utilisé pour réaliser l'ensemble de nos simulations. Dans un premier temps, nous donnons une description détaillée des ingrédients physiques et des techniques numériques employés par le programme pour modéliser l'évolution stellaire et le transport des éléments. Dans un

second temps, nous démontrons les capacités du code en présentant deux exemples de calculs d'évolution spectrale, dont l'un constitue le tout premier modèle complet et cohérent du flottement de l'hydrogène à haute température et du mélange convectif à basse température.

Ensuite, les chapitres 4 et 5 présentent plusieurs autres simulations similaires à celles du chapitre 3 afin d'examiner l'effet de divers paramètres physiques sur l'évolution spectrale. Le chapitre 4 est une adaptation de l'article intitulé *On the Spectral Evolution of Hot White Dwarf Stars. III. The PG 1159−DO−DB−DQ Evolutionary Channel Revisited*, publié dans *The Astrophysical Journal* en mai 2022 (Bédard et al., 2022a). Nous y étudions la transformation des étoiles PG 1159 en naines blanches DO/DB par tri gravitationnel puis en naines blanches DQ par dragage convectif. Plus spécifiquement, nous quantifions la dépendance de l'abondance atmosphérique de carbone sur certains paramètres stellaires (comme la masse totale et l'épaisseur de l'enveloppe) et mécanismes de transport (comme le vent radiatif et le dépassement convectif). Ces calculs nous permettent d'en apprendre davantage sur les propriétés des étoiles DO, DB et DQ, notamment sur l'étendue du dépassement convectif dans les naines blanches froides. Pour sa part, le chapitre 5 est une version préliminaire d'un article en préparation intitulé *On the Spectral Evolution of Hot White Dwarf Stars. IV. The Diffusion and Mixing of Residual Hydrogen in Helium-rich White Dwarfs*, qui sera bientôt soumis à *The Astrophysical Journal*. Nous y présentons plusieurs simulations du phénomène de flottement de l'hydrogène résiduel dans une enveloppe d'hélium, dans le but de donner une interprétation physique aux résultats empiriques du chapitre 2. En comparant nos modèles à l'évolution spectrale observée à haute température, nous obtenons une contrainte inédite sur le contenu en hydrogène des naines blanches riches en hélium. Par ailleurs, nous explorons aussi la dilution de l'hydrogène dans la zone convective d'hélium à plus basse température et démontrons que nos calculs offrent une solution claire au problème de l'origine de l'hydrogène dans les étoiles DBA.

Enfin, le chapitre 6 résume les conclusions de cette thèse.

1.5.2. Déclaration de l'étudiant

C'est moi qui ai rédigé l'entièreté du texte et créé toutes les figures de cette thèse, ce qui inclut autant l'introduction que les articles constituant les chapitres subséquents. J'ai également effectué l'ensemble du travail scientifique présenté dans ce document. D'abord, c'est moi qui ai réalisé tous les calculs de modèles d'atmosphère et d'évolution. J'ai employé

les codes de modélisation atmosphérique TLUSTY et SYNSPEC, qui sont publiquement accessibles, ainsi que le code de modélisation évolutive STELUM, qui m'a été fourni par ses auteurs Pierre Brassard et Gilles Fontaine. Dans les deux cas, ma tâche a largement dépassé la simple utilisation : j'ai corrigé de nombreux bogues et apporté des modifications substantielles pour mener à bien mes projets. De plus, j'ai aussi effectué l'intégralité de l'analyse des données observationnelles et des simulations numériques. Concernant plus spécifiquement l'analyse du chapitre 2, j'ai rassemblé les données spectroscopiques, photométriques et astrométriques nécessaires à partir des archives publiques des relevés SDSS et Gaia, et j'ai adapté à mes besoins une méthode d'ajustement originalement conçue par Pierre Bergeron. Enfin, c'est moi qui ai en majeure partie développé l'interprétation astrophysique des résultats. Par ailleurs, en plus de m'avoir fourni les outils mentionnés ci-dessus, Pierre Bergeron, Pierre Brassard et Gilles Fontaine ont participé aux diverses étapes du travail de recherche via leurs précieux conseils. Je leur dois également l'idée initiale du projet qui forme le corps de cette thèse.

Chapitre 2

On the Spectral Evolution of Hot White Dwarf Stars. I. A Detailed Model Atmosphere Analysis of Hot White Dwarfs from SDSS DR12

A. Bédard[1], P. Bergeron[1], P. Brassard[1], & G. Fontaine[1]

[1] Département de Physique, Université de Montréal, Montréal, QC H3C 3J7, Canada

Published in *The Astrophysical Journal*
October 2020, Volume 901, Article 93
DOI: 10.3847/1538-4357/abafbe

Abstract

As they evolve, white dwarfs undergo major changes in surface composition, a phenomenon known as spectral evolution. In particular, some stars enter the cooling sequence with helium atmospheres (type DO) but eventually develop hydrogen atmospheres (type DA), most likely through the upward diffusion of residual hydrogen. Our empirical knowledge of this process remains scarce: the fractions of white dwarfs that are born helium rich and that experience the DO-to-DA transformation are poorly constrained. We tackle this issue by performing a detailed model-atmosphere investigation of 1806 hot ($T_{\rm eff} \geq 30{,}000$ K) white dwarfs observed spectroscopically by the Sloan Digital Sky Survey. We first introduce our new generations of model atmospheres and theoretical cooling tracks, both appropriate for hot white dwarfs. We then present our spectroscopic analysis, from which we determine the atmospheric and stellar parameters of our sample objects. We find that $\sim$24% of white dwarfs begin their degenerate life as DO stars, among which $\sim$2/3 later become DA stars. We also infer that the DO-to-DA transition occurs at substantially different temperatures

(75,000 K $>$ $T_{\rm eff}$ $>$ 30,000 K) for different objects, implying a broad range of hydrogen content within the DO population. Furthermore, we identify 127 hybrid white dwarfs, including 31 showing evidence of chemical stratification, and we discuss how these stars fit in our understanding of the spectral evolution. Finally, we uncover significant problems in the spectroscopic mass scale of very hot ($T_{\rm eff}$ $>$ 60,000 K) white dwarfs.

Key words: White dwarf stars; Late stellar evolution; Stellar atmospheres; Atmospheric composition

2.1. Introduction

White dwarf stars form a remarkably homogeneous class of objects, and yet they exhibit a surprisingly diverse variety of faces. On one hand, all stars with initial masses lower than $\sim$8 $M_{\odot}$ (that is, $\sim$97% of the stars in the Galaxy) are destined to evolve into white dwarfs, all sharing the same fundamental, defining property: an exceptionally high density, reaching up to $\sim 10^6 - 10^8$ g cm^{-3} in the stellar core (Fontaine et al., 2001). Indeed, following the exhaustion of nuclear energy sources, gravitational contraction proceeds unimpeded until it is eventually halted by electron degeneracy pressure, thus producing a highly compact stellar remnant, condemned to simply cool off with time. Such an object is characterized by an extreme surface gravity field of typically $\sim 10^8$ cm s^{-2}, in which the process of gravitational settling is predicted to be so efficient that all heavy elements should sink into the star on very short timescales, leaving only the lightest element at the surface (Paquette et al., 1986a; Dupuis et al., 1992). Consequently, all white dwarfs are expected to have a stratified chemical structure: a core made of carbon and oxygen, surrounded by a thin pure-helium envelope, itself surrounded by an even thinner pure-hydrogen layer encompassing the observable atmosphere (Fontaine et al., 2001).

On the other hand, while this simple picture provides a fairly accurate description of reality, it does not reflect the numerous details uncovered by decades of observational and theoretical investigations. It is well known that although most white dwarfs have canonical hydrogen-rich atmospheres, a significant fraction of them instead have helium-rich atmospheres. Furthermore, in several instances, small traces of elements other than the main constituent are detected at the surface. Even more surprising is the fact that the atmospheric composition of a star can change radically as it evolves on the cooling sequence, a

phenomenon referred to as the spectral evolution of white dwarfs. This empirical evidence indicates that various transport mechanisms, such as ordinary diffusion, thermal diffusion, radiative levitation, convective mixing, convective overshooting, stellar winds, and accretion, compete with gravitational settling in determining the chemical appearance of degenerate stars.

More than three decades ago, Fontaine & Wesemael (1987) laid the foundations of this most interesting field of research aiming at providing a complete, consistent theory of spectral evolution, which would identify the predominant physical processes and explain the observed chemical peculiarities. Such an endeavor is of course crucial to our understanding of white dwarf evolution, but also of stellar evolution in general, to which white dwarfs, as the ultimate fate of the vast majority of stars, hold important clues. We now review the progress that has been made over the years toward the achievement of this goal. Because it would be impossible to cover the whole subject in detail, in the present paper we restrict our attention to the early phases of degenerate evolution, more specifically to hot white dwarfs with effective temperatures $T_{\rm eff} \geq 30{,}000$ K. The reader is referred to Rolland et al. (2018, 2020), Ourique et al. (2019, 2020), Blouin et al. (2019), Genest-Beaulieu & Bergeron (2019b), Coutu et al. (2019), and Cunningham et al. (2020) for recent studies of the spectral evolution of cooler remnants.

In the 1980s, white dwarf research was stimulated by the advent of the Palomar-Green (PG) survey (Green et al., 1986), which revealed a few intriguing features. First, at the very hot end of the cooling sequence ($T_{\rm eff} > 80{,}000$ K), a lack of hydrogen-atmosphere white dwarfs of spectral type DA, with respect to their helium-atmosphere counterparts of spectral type DO, was discovered (Fleming et al., 1986). Second, it was found that the helium-dominated white dwarf sequence was interrupted by the so-called DB gap in the range $45{,}000 \text{ K} > T_{\rm eff} > 30{,}000$ K, between the hot DO stars and cooler DB stars, where all objects had hydrogen-dominated atmospheres (Wesemael et al., 1985; Liebert et al., 1986). Between the former and latter regimes, the ratio of hydrogen-rich to helium-rich white dwarfs showed a monotonic rise with decreasing effective temperature.

In light of these results, Fontaine & Wesemael (1987) devised a model of spectral evolution based on the unifying paradigm that all white dwarfs shared a common origin. In their scenario, the extremely hot hydrogen-deficient PG 1159 stars were the progenitors of the

entire white dwarf population, which naturally explained the paucity of DA stars with $T_{\rm eff} >$ 80,000 K. It was already believed at that time that PG 1159 stars were the product of a late helium-shell flash, during which the superficial hydrogen inherited from previous evolutionary phases had been ingested in the stellar envelope and burned (Iben et al., 1983). However, Fontaine & Wesemael (1987) postulated that a small amount of hydrogen had survived this violent episode while remaining thoroughly mixed in the envelope and thus invisible. They suggested that this residual hydrogen then gradually diffused upward under the influence of gravitational settling, building up a thicker and thicker hydrogen layer at the surface, and ultimately transforming all helium-atmosphere white dwarfs into hydrogen-atmosphere white dwarfs. This idea accounted for both the increase of the DA-to-DO ratio along the cooling sequence and the existence of the blue edge of the DB gap at $T_{\rm eff} \sim$ 45,000 K. Finally, the reappearance of DB stars beyond the red edge of the DB gap at $T_{\rm eff} \sim$ 30,000 K was interpreted as the consequence of the dilution of the hydrogen layer by the growing convection zone in the underlying helium envelope.

One striking implication of this so-called float-up model was that the mass of the hydrogen layer in DA white dwarfs had to be extremely small, of the order of $q_{\rm H} \equiv M_{\rm H}/M \sim 10^{-16} - 10^{-10}$ (Fontaine & Wesemael, 1987), many orders of magnitude smaller than the standard value of 10^{-4} predicted by evolutionary calculations (Iben & Tutukov, 1984). Nevertheless, further evidence in favor of such thin hydrogen layers was obtained independently from spectral studies of hot DA stars. Indeed, a number of these objects were found to exhibit X-ray and extreme-ultraviolet (EUV) flux deficiencies with respect to what was expected from pure-hydrogen atmospheres (Vennes et al. 1988 and references therein). The additional short-wavelength opacity was first assumed to be provided by minute traces of helium, supported in the outer layers by radiative levitation. This hypothesis was motivated by the detection of helium in the optical spectra of some hot hydrogen-rich white dwarfs, mostly through a weak He II λ4686 feature, defining the spectral class DAO. However, Vennes et al. (1988) demonstrated that the amount of helium supported by radiation pressure was insufficient to explain the measured flux deficiencies. Instead, they showed that the short-wavelength observations could be successfully reproduced by a model in which a very thin hydrogen layer ($q_{\rm H} \sim 10^{-15} - 10^{-13}$) floated on top of the helium envelope in diffusive equilibrium. In this context, DAO stars could naturally be interpreted as transitional

objects currently undergoing the DO-to-DA transformation through the upward diffusion of hydrogen envisioned by Fontaine & Wesemael (1987).

In the following years, several challenges to the float-up model emerged. Analyses of far-ultraviolet (FUV) spectra of hot white dwarfs conclusively revealed the presence of traces of numerous heavy elements (mainly carbon, nitrogen, oxygen, silicon, iron, and nickel) in the atmospheres of these objects (Vennes et al., 1992; Holberg et al., 1993; Werner & Dreizler, 1994; Werner et al., 1995b). It then became quite clear that metals, rather than helium, were responsible for the X-ray and EUV opacity in hot DA stars, and thin hydrogen layers were therefore no longer required. Another major discovery was made by Napiwotzki & Schönberner (1995) through their survey of old central stars of planetary nebulae. They identified a large number of hydrogen-atmosphere objects with $T_{\rm eff} > 80{,}000$ K, implying that a significant proportion of the white dwarf population was born hydrogen rich, thus dismissing the assertion of Fontaine & Wesemael (1987) that all white dwarfs descended from PG 1159 stars. The two latter findings pointed to the existence of an evolutionary channel involving white dwarfs characterized by canonical thick hydrogen layers ($q_{\rm H} \sim 10^{-4}$) and hence retaining their DA spectral type throughout their entire evolution. Nonetheless, the idea that DO stars had to turn into DA stars with thin hydrogen layers in the DB gap, perhaps via the DAO stage, remained relevant.

In that respect, of particular importance was the detailed investigation of the float-up model conducted by MacDonald & Vennes (1991), who studied the combined effect of gravitational settling, ordinary diffusion, radiative levitation, and convective mixing in hydrogen−helium white dwarf envelopes. They concluded that the float-up hypothesis effectively accounted for the key observational features uncovered by the PG survey for hydrogen-layer masses of $q_{\rm H} \sim 10^{-15} - 10^{-13}$, but they also encountered a few inconsistencies. They noted that the amount of hydrogen had to be much smaller in DO white dwarfs than in DAO white dwarfs, without any known intermediate object in between, suggesting that these two spectral groups did not actually share an evolutionary link. In addition, they found that the hydrogen abundances measured in the cooler DBA stars were much higher than those predicted by the convective dilution scenario. These two results led them to invoke accretion of hydrogen from the interstellar medium as the main driving force behind the spectral evolution of white dwarfs.

Another decisive step was taken by Bergeron et al. (1994), who carried out an in-depth model-atmosphere analysis of a sample of hot DA and DAO stars. In particular, they analyzed their DAO white dwarfs with two sets of models differing by the assumed chemical structure: a homogeneous configuration, with hydrogen and helium uniformly distributed throughout the atmosphere, and a stratified configuration, with hydrogen floating on top of helium in diffusive equilibrium. They showed that the optical spectra of all objects but one (PG 1305−017) were better reproduced by homogeneous models rather than stratified models. Moreover, for most DAO stars, they obtained effective temperatures considerably higher than the hot boundary of the DB gap. This outcome confirmed that the DAO phenomenon could not be viewed as a transitional stage between the DO and DA stars resulting from the upward diffusion of hydrogen. Nevertheless, one DAO white dwarf, PG 1305−017, remained consistent with this picture, as it lied precisely at the blue edge of the DB gap and displayed convincing signs of chemical stratification. Bergeron et al. (1994) also noted that the bulk of their DAO sample was afflicted by the so-called Balmer-line problem, the lower lines of the Balmer series being predicted as too shallow by their models. They argued that atmospheric pollution by heavy elements, and omission of the corresponding opacities in the model-atmosphere calculations, was the most probable cause of this issue, which was later corroborated by Werner (1996b) and Gianninas et al. (2010). Consequently, they proposed that a weak stellar wind, possibly driven by metals, was responsible for maintaining helium at the surface of DAO white dwarfs as well as homogenizing the composition of the external layers.

In subsequent years, overwhelming evidence in favor of the occurrence of winds in some of the hottest ($T_{\rm eff} \gtrsim 60{,}000$ K) white dwarfs accumulated. Napiwotzki (1999) found that DAO stars followed a correlation of decreasing helium abundance with decreasing luminosity, which was indeed expected if the helium content was sustained by a steadily fading wind. Additionally, while it was initially believed that heavy elements were radiatively levitated in the atmospheres of hot DA and DO stars, the elaborate theoretical work of Chayer et al. (1995) and Dreizler (1999) compellingly demonstrated that the observed abundance patterns were poorly reproduced under the assumption of an equilibrium between gravitational and radiative forces. As more and more metals (including elements beyond the iron group) were discovered and improved abundance determinations were made available, this disagreement

became even more evident (Dreizler & Werner, 1996; Barstow et al., 2003b, 2014; Chayer et al., 2005; Good et al., 2005; Vennes et al., 2006; Werner et al., 2007, 2012). In most cases, mass loss was put forward as the most plausible alternative mechanism (with the recent exception of Barstow et al. 2014, who instead invoked an interplay between accretion of planetary debris and radiative levitation). Finally, Werner et al. (1995a) and Dreizler et al. (1995) exposed the puzzling phenomenon of the ultra-high-excitation absorption lines in the optical spectra of a few hot helium-rich objects. Because the formation of these peculiar features, arising from very high ionization stages of light metals, required excessively high temperatures, a photospheric origin was definitely ruled out. Based on the asymmetric shape and the slight blueshift of some ultra-high-excitation lines, they speculated that such features were generated in a shock-heated circumstellar wind, a conjecture validated only recently by Reindl et al. (2019).

The wind interpretation was put on more quantitative grounds by Unglaub & Bues (1998, 2000), who carried out time-dependent simulations of diffusion and mass loss in white dwarf envelopes. Adopting a metal-driven wind model, they calculated that mass-loss rates of the order of $\dot{M}_{\rm wind} \sim 10^{-12} - 10^{-11}\ M_{\odot}\ {\rm yr}^{-1}$ effectively gave rise to helium pollution of hydrogen-rich envelopes with surface abundances similar to those measured in DAO stars. This support mechanism was shown to be efficient only above a certain line in the $\log g - T_{\rm eff}$ diagram called the wind limit, beyond which mass loss vanished and gravitational settling rapidly transformed DAO stars into DA stars. These results underlined the essential role played by stellar winds in the DAO phenomenon. However, a significant discrepancy remained between the theoretical and empirical wind limits, found at $T_{\rm eff} \sim$ 85,000 and 60,000 K, respectively, for normal-mass objects (Gianninas et al., 2010). In addition, Unglaub & Bues (2000) demonstrated that mass loss was mandatory to explain the presence of large amounts of carbon and oxygen in the atmospheres of PG 1159 stars, a conclusion also reached by Quirion et al. (2012) from their investigation of the GW Vir instability strip.

The next major developments in our understanding of the spectral evolution were made possible by the Sloan Digital Sky Survey (SDSS; York et al. 2000), which revolutionized the white dwarf field by increasing the number of spectroscopically identified white dwarfs more than tenfold (Eisenstein et al., 2006b; Kleinman et al., 2013; Kepler et al., 2015, 2016, 2019). On the basis of a model-atmosphere analysis of the Data Release (DR) 4 sample, Eisenstein

et al. (2006a) reported the striking discovery of a small number of helium-rich objects in the DB gap, indicating that not all DO stars inevitably evolved into DA stars. In other words, these hot DB stars had to be the outcome of a different evolutionary channel, in which white dwarfs were born almost completely devoid of hydrogen and thus permanently preserved helium-dominated atmospheres. Nevertheless, Eisenstein et al. (2006a) estimated that a substantial deficit of helium-rich stars persisted in the range 45,000 K $> T_{\rm eff} >$ 20,000 K with respect to higher and lower effective temperatures, suggesting that such hydrogen-free evolution occurred quite rarely. Therefore, the notion of a DB gap was replaced by that of a DB deficiency, whose cool boundary was ∼10,000 K cooler than previously believed, a result also obtained by Bergeron et al. (2011) from their assessment of the PG luminosity function.

Finally, Manseau et al. (2016) recently took advantage of the large SDSS DR12 sample to search for new hybrid white dwarfs (exhibiting traces of both hydrogen and helium) with chemically layered atmospheres, similar to the unique such star PG 1305−017 known at the time. They successfully identified about a dozen objects that were better modeled assuming stratified atmospheres, with typical hydrogen masses of $q_{\rm H} \sim 10^{-17} - 10^{-16}$. Considering that the derived effective temperatures fell in the range 55,000 K $> T_{\rm eff} >$ 40,000 K, coinciding with the onset of the DB deficiency, this finding proved that the float-up of hydrogen and the corresponding DO-to-DA transition indeed occurred for an important fraction of all hot helium-rich white dwarfs. Furthermore, Manseau et al. (2016) stressed the fact that their new stratified candidates, of rather diverse spectral types (DAB, DAO, DBA, or DOA), were well separated from the classical, hotter, chemically homogeneous DAO stars in the $\log g - T_{\rm eff}$ diagram, reflecting the fundamentally different physical processes at work in the two groups of objects.

This completes our historical overview of the state of knowledge regarding the spectral evolution of hot white dwarfs. Despite the latest advances, we wish to point out that the extensive spectroscopic dataset provided by the SDSS has never been fully exploited in terms of the subject at hand. In fact, several model-atmosphere studies of the hot white dwarfs in the SDSS have been published (Hügelmeyer et al., 2005, 2006; Eisenstein et al., 2006a,b; Tremblay et al., 2011; Kleinman et al., 2013; Reindl et al., 2014a; Werner et al., 2014; Kepler et al., 2015, 2016, 2019; Manseau et al., 2016; Genest-Beaulieu & Bergeron, 2019a), but

they all suffer from either one of the two following limitations. First, most of them do not include all relevant spectral classes (DA, DB, DO, plus the various subtypes) simultaneously, rendering it difficult to establish a global picture of the spectral evolution. Second, the few of them that do consider all spectral types are geared toward classification purposes and hence provide only coarse atmospheric parameter estimates. In particular, they make use of model atmospheres assuming local thermodynamic equilibrium (LTE), a poor approximation at high effective temperatures (Napiwotzki, 1997).

In light of this situation, the primary aim of the present paper is to improve our understanding of the spectral evolution of hot white dwarfs by performing an exhaustive, homogeneous, state-of-the-art model-atmosphere analysis of a large sample of stars drawn from the SDSS. Ultimately, we seek to answer a number of questions that remain unsettled to this day: what fraction of all white dwarfs are born with a helium atmosphere? Among those, how many eventually develop a hydrogen-rich atmosphere, and how many retain a helium-rich atmosphere throughout their life? How does the number of hybrid white dwarfs, both with homogeneous and stratified atmospheres, vary with effective temperature? What does this imply about the role of stellar winds and the helium-to-hydrogen transition? What is the total hydrogen content of these various groups of white dwarfs, and how will it impact their future spectral evolution?

The paper is organized as follows. In Section 2.2, we describe our sample selection as well as the observational data used in our analysis. In Section 2.3, we outline our theoretical framework consisting of new white dwarf model atmospheres and evolutionary sequences. Section 2.4 is dedicated to our spectroscopic analysis, including the description of the fitting method and the presentation of representative fits. In Section 2.5, we report our results regarding the physical properties of our sample and discuss their implications for the theory of the spectral evolution of white dwarfs. Finally, our conclusions are summarized in Section 2.6.

2.2. Sample

We constructed our sample of hot white dwarfs (which, we remind the reader, are defined here as those with $T_{\rm eff} \geq 30{,}000$ K) starting from the available SDSS white dwarf catalogs, up

to DR12[1] (Kleinman et al., 2013; Kepler et al., 2015, 2016). In a first step, we selected only the bluest objects by applying the following simple color criteria to the *ugriz* photometry given in the catalogs: $u - g < 0$, $u < 21$, and $g < 21$. These restrictions resulted in a raw sample of 6270 stars. In a second step, we retrieved the optical spectra of these objects from the SDSS database and performed preliminary fits to all spectra with both our pure-hydrogen and pure-helium model atmospheres (see Sections 2.3 and 2.4) in order to clean up our initial sample. Several stars turned out to be hot subdwarfs with $\log g < 6.5$ or white dwarfs with $T_{\rm eff} < 30{,}000$ K, and were thus rejected. We assigned spectral types to the remaining objects based on a careful visual inspection of each spectrum. Our final sample contains 1806 white dwarfs, including 1638 DA, 95 DO, and 73 DB stars[2]. Among these, we identified 127 hybrid white dwarfs (whose spectra show both hydrogen and helium lines), namely, 96 DAO, 6 DAB, 8 DOA, and 17 DBA stars. In addition, 29 of our DO white dwarfs exhibit traces of metals through a weak C IV λ4658 feature and are therefore members of the DOZ spectral class. Finally, 185 objects in our sample have M dwarf companions that contaminate the red portion of their optical spectra.

Figure 2.1 shows the distribution of signal-to-noise ratios (S/Ns) of the spectroscopic observations, computed in the featureless range 5100 Å $< \lambda <$ 5300 Å. As expected, our sample is dominated by faint objects and hence low-S/N data. Indeed, in the SDSS, the brightness and S/N are correlated, because the same exposure time is set for all targets on a given plate. We note that 1467 of our 1806 white dwarf spectra have S/N $\geq$ 10.

In addition to spectroscopy, we also gathered *ugriz* photometry from the SDSS database for all stars in our sample with the aim of studying their spectral energy distribution. We chose not to rely further on the *ugriz* magnitudes given in the white dwarf catalogs mentioned above, because the SDSS photometric calibration has been updated since their publication. Furthermore, we cross-matched our sample with the Gaia DR2 catalog (Gaia Collaboration

1. Note that the most recent data release of the SDSS is DR16 (Ahumada et al., 2020).

2. In the canonical classification scheme, helium-atmosphere white dwarfs are assigned the spectral type DB if they show only He I lines or the spectral type DO if they show at least one He II line, whatever its strength (Sion et al., 1983; Wesemael et al., 1993). In the present paper, we adopt a slightly different convention. If both He I and He II features are present in a spectrum, our spectral designation is based on the strongest set of lines: we use the letter B if the He I lines dominate or the letter O if the He II lines dominate. Note that a similar approach was used by Krzesiński et al. (2004) and Manseau et al. (2016).

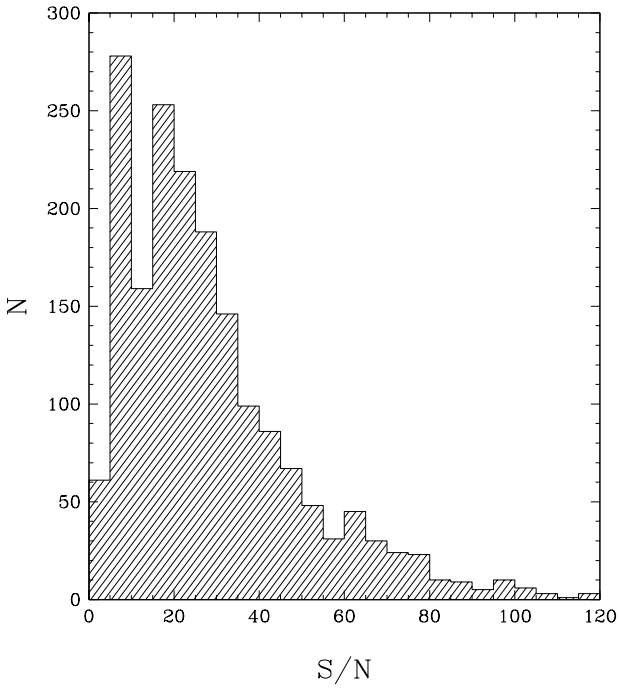

Figure 2.1 – Distribution of spectral signal-to-noise ratios for our sample of 1806 white dwarfs.

et al., 2018a) and could retrieve trigonometric parallax measurements for 1721 objects, including 824 with $\sigma_\pi/\pi \leq 25\%$. In the remainder of the paper, when we make use of the astrometric and photometric observations, we confine our attention to the latter subset with high-quality data. We obtained distance estimates by simply inverting the parallaxes as this procedure agrees well with more sophisticated probabilistic methods for small parallax uncertainties (Bailer-Jones, 2015; Bailer-Jones et al., 2018). Using the extinction maps of Schlafly & Finkbeiner (2011) together with the Gaia distances, we dereddened the *ugriz* magnitudes following the approach outlined in Harris et al. (2006). We also applied the SDSS-to-AB system corrections to the u, i, and z bands suggested by Eisenstein et al. (2006b).

Figure 2.2 displays the distribution of distances for our subsample of objects with precise parallax measurements. Unsurprisingly, our hot white dwarfs are on average quite distant: most of them are located between 200 and 1000 pc from the Sun (and none of them are part of the 100 pc solar neighborhood). Besides, the large-distance tail of the histogram is certainly underestimated as a result of our parallax error cut. The shape of the distribution originates from two competing factors: on one hand, hot white dwarfs are locally much rarer

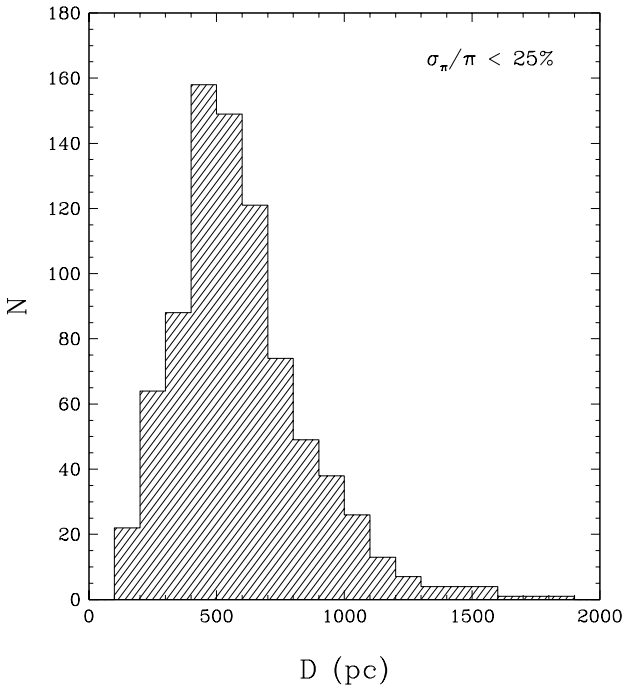

Figure 2.2 – Distribution of distances for our subsample of 824 white dwarfs with $\sigma_\pi/\pi \leq 25\%$.

than their cooler counterparts because of their shorter evolutionary timescales; on the other hand, they are intrinsically more luminous and can thus be detected farther away. Figure 2.2 underlines the fact that interstellar reddening probably affects our entire sample.

The dereddened M_u vs. $u-g$ color−magnitude diagram for the same subsample is presented in Figure 2.3, where hydrogen-rich and helium-rich white dwarfs are shown in blue and red, respectively. Also displayed are sequences of theoretical colors for both pure-hydrogen and pure-helium atmospheres, computed using our new model atmospheres and cooling tracks introduced in Section 2.3 below. Most hydrogen-rich and helium-rich objects cluster around the corresponding 0.6 $M_\odot$ sequences, as expected. However, there is a clear distinction between the two rightmost panels of Figure 2.3: the DA population contains a significant number of overluminous stars, which are either very low-mass white dwarfs or unresolved double degenerate systems, while very few such objects are found in the DO/DB population. This dichotomy is also observed in cooler white dwarf samples (Bergeron et al., 2019; Genest-Beaulieu & Bergeron, 2019a) and probably means that evolutionary processes

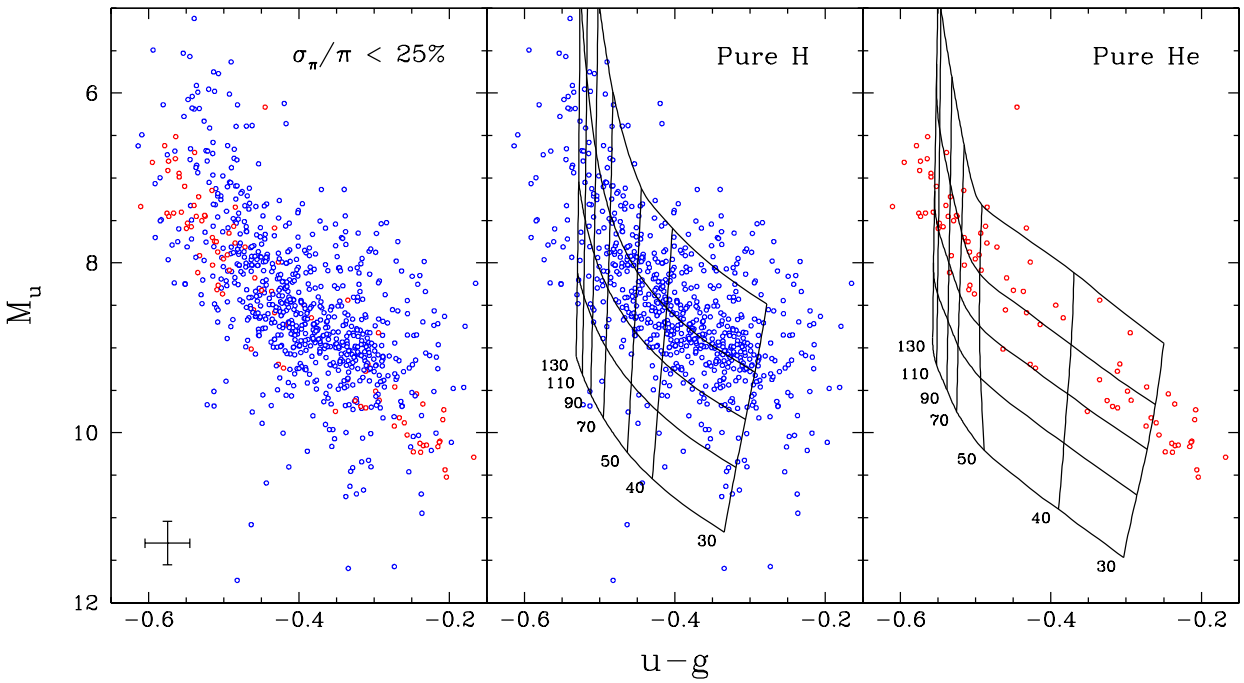

Figure 2.3 – Dereddened M_u vs. $u-g$ color−magnitude diagram for our subsample of 824 white dwarfs with $\sigma_\pi/\pi \leq 25\%$. Hydrogen-rich and helium-rich objects are shown in blue and red, respectively. The error bars represent the average uncertainties. The middle and right panels display sequences of theoretical colors for pure-hydrogen and pure-helium atmospheres, respectively, with masses of 0.4, 0.6, 0.8, 1.0, and 1.2 $M_\odot$ (from top to bottom) and effective temperatures indicated in units of 10^3 K.

producing low-mass white dwarfs or double degenerate binaries almost always lead to the formation of hydrogen atmospheres.

Because hot stars emit most of their light in the ultraviolet, optical photometry samples the Rayleigh-Jeans tail of their spectral energy distribution and is therefore extremely weakly sensitive to their effective temperature. This is highlighted by the theoretical sequences illustrated in Figure 2.3: the synthetic $u-g$ color index varies very slowly with temperature (for a 0.6 $M_\odot$ hydrogen-atmosphere white dwarf, the difference in $u-g$ between $T_{\rm eff}$ = 50,000 and 100,000 K is a mere 0.06 mag) and even tends asymptotically to a minimum value at the hot end. Consequently, the *ugriz* magnitudes cannot be employed to measure the effective temperatures of the objects in our sample. Nonetheless, when coupled with parallax measurements, they can still provide information on the stellar masses: for

a given temperature, the synthetic M_u absolute magnitude strongly depends on the mass, as shown in the color−magnitude diagram. In other words, for our hot white dwarfs, the combination of SDSS photometry and Gaia astrometry cannot be used to determine the effective temperatures but can be used to estimate the masses (or, alternatively, the surface gravities) if the temperatures are known from another source, such as spectroscopy.

A curious aspect of Figure 2.3 is that some stars have a $u - g$ color index redder than that corresponding to our low-temperature selection limit of $T_{\rm eff} = 30{,}000$ K, or bluer than the high-temperature asymptotic value. In the former case, the main cause is the well-established disparity between the spectroscopic and photometric temperature scales: while all selected white dwarfs have $T_{\rm eff} \geq 30{,}000$ K based on spectroscopy, some of them may have $T_{\rm eff} < 30{,}000$ K based on photometry, as photometric temperatures are on average lower than spectroscopic temperatures by 5−10% (Bergeron et al., 2019; Genest-Beaulieu & Bergeron, 2019a; Tremblay et al., 2019a). In addition, a few white dwarfs look redder than they really are because their g magnitudes are contaminated by main-sequence companions. In the latter case, the reason why the bluest objects appear too blue is most likely related to the SDSS-to-AB system correction of $\Delta u = -0.04$ mag taken from Eisenstein et al. (2006b). While this correction is adequate for the majority of the stars in our sample, Figure 2.3 indicates that it is too large for the hottest white dwarfs, an outcome that is not too surprising given that the offset between the SDSS and AB magnitude systems was calibrated using cooler objects (Eisenstein et al., 2006b).

2.3. Theoretical Framework

2.3.1. Model Atmospheres

We employed the publicly available codes TLUSTY and SYNSPEC (Hubeny & Lanz, 1995, 2017a,b,c) to compute non-LTE model atmospheres and synthetic spectra of hot white dwarfs. We considered one-dimensional, plane-parallel structures in hydrostatic, statistical, and radiative equilibrium. This last assumption, namely, ignoring the convective energy transport, is appropriate in the present context, with a small exception discussed below.

Starting from version 205 of TLUSTY and version 51 of SYNSPEC, we made two major improvements to the codes regarding the treatment of the He I opacity. First, we incorporated the state-of-the-art Stark profiles of Beauchamp et al. (1997) for He I lines. These profiles,

which supersede the best option offered until now (a combination of data from Shamey 1969, Barnard et al. 1974 and Dimitrijevic & Sahal-Brechot 1984), are essential to properly model the broad absorption features of helium-rich white dwarfs. Second, we refined the implementation of the occupation probability formalism of Hummer & Mihalas (1988) and the corresponding pseudo-continuum opacity by dropping the assumption of a hydrogenic ion (see Beauchamp 1995 for details). Regarding other important ionic species, we used the detailed Stark profiles of Tremblay & Bergeron (2009) and Schöning & Butler (1989) for H I and He II lines, both already included in TLUSTY and SYNSPEC. Note that we applied the Hummer−Mihalas formalism to these two ions as well.

We calculated a pure-hydrogen grid and a pure-helium grid, which both cover the following parameter space: 30,000 K $\leq T_{\rm eff} \leq$ 150,000 K (in steps of 2500 K for 30,000 − 60,000 K, 5000 K for 60,000 − 90,000 K, and 10,000 K for 90,000 − 150,000 K) and $6.5 \leq \log g \leq 9.5$ (in steps of 0.5 dex). In the pure-hydrogen models, ignoring convection is an excellent approximation over the entire temperature range of interest here, because the atmospheres of DA stars become convective only for $T_{\rm eff} \lesssim$ 15,000 K (see Figure 5 of Tremblay et al. 2010). However, this is not true for the pure-helium models: a thin convection zone develops in the atmospheres of DO/DB stars for $T_{\rm eff} \lesssim$ 60,000 K due to the partial ionization of He II (see Figure 3 of Bergeron et al. 2011). Unfortunately, strong numerical instabilities arise when convective energy transport and non-LTE effects are included simultaneously in helium-rich TLUSTY models. Nevertheless, the LTE calculations performed by Bergeron et al. (2011) indicate that convection becomes truly significant only close to the low-temperature limit of our grid, where non-LTE effects are unimportant. For instance, in their pure-helium models with $\log g = 8.0$, the convective flux accounts for at most 0.02%, 6%, and 57% of the total flux at $T_{\rm eff} =$ 45,000, 40,000, and 35,000 K, respectively. Consequently, for our pure-helium grid, we adopted the following strategy: we employ the non-LTE, strictly radiative models of TLUSTY/SYNSPEC for $T_{\rm eff} >$ 40,000 K, and the LTE, convective models of Bergeron et al. (2011) for $T_{\rm eff} \leq$ 40,000 K. We verified that the two sets of synthetic spectra are in good agreement at the branching point for every $\log g$ value, as illustrated in Figure 2.4 for $\log g = 8.0$.

For the purpose of analyzing our hybrid white dwarfs, we also calculated model atmospheres containing both hydrogen and helium. We constructed two separate grids differing

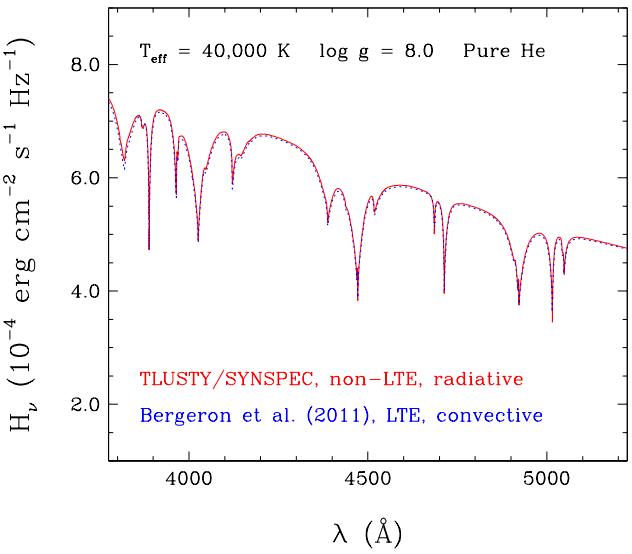

Figure 2.4 – Comparison of synthetic optical spectra generated from two different white dwarf model atmospheres with $T_{\rm eff} = 40{,}000$ K, $\log g = 8.0$, and a pure-helium composition: a non-LTE, strictly radiative model computed with the codes TLUSTY/SYNSPEC (solid red line) and an LTE, convective model computed with the code of Bergeron et al. (2011, dotted blue line).

by the assumed chemical configuration, which we refer to as homogeneous and stratified. In our chemically homogeneous models, hydrogen and helium are mixed uniformly in the atmosphere, in which case the helium-to-hydrogen number ratio ($N_{\rm He}/N_{\rm H}$) is a free parameter. Our homogeneous grid spans the same effective temperatures and surface gravities as our pure-composition grids, as well as abundances of $-5.0 \leq \log N_{\rm He}/N_{\rm H} \leq 5.0$ (in steps of 1.0 dex). For helium-rich ($\log N_{\rm He}/N_{\rm H} > 0$) models, we adopted the same compromise between non-LTE effects and convection as above.

In our chemically stratified models, a thin hydrogen layer floats on top of a helium envelope in diffusive equilibrium, in which case the mass of the superficial hydrogen layer ($q_{\rm H} \equiv M_{\rm H}/M$) is a free parameter. The equilibrium chemical profile was obtained from the formalism of Vennes et al. (1988), as implemented in TLUSTY and SYNSPEC by Barstow & Hubeny (1998). To our knowledge, this is the first time that an exhaustive set of such non-LTE stratified model atmospheres is presented. The parameter space covered by our stratified grid is 30,000 K $\leq T_{\rm eff} \leq$ 90,000 K (in steps of 2500 K for 30,000 − 60,000 K, and 5000 K for 60,000 − 90,000 K), $7.0 \leq \log g \leq 9.0$ (in steps of 0.5 dex), and $-13.0 \leq Q \leq -5.0$

(in steps of 1.0), where $Q \equiv 3 \log g + 2 \log q_{\rm H}$. The introduction of the quantity Q allows us to consider a different range of $\log q_{\rm H}$ values for each $\log g$ value, and its definition is such that synthetic spectra with a given Q value look fairly similar to each other (Manseau et al., 2016). For example, at $\log g = 8.0$, hydrogen-layer masses span the range $-18.5 \leq \log q_{\rm H} \leq -14.5$. Note that we could not follow our usual approach for taking convection into account, because no convective stratified models are available in the literature. Hence, one must keep in mind that the cool ($T_{\rm eff} \lesssim 40{,}000$ K) models of our stratified grid are approximate (see Manseau et al. 2016 for a discussion of the occurrence of convection in chemically layered atmospheres).

Finally, we relied on the non-LTE model atmospheres and synthetic spectra introduced by Gianninas et al. (2010) to analyze the objects afflicted by the Balmer-line problem. These models, also computed with TLUSTY and SYNSPEC, contain carbon, nitrogen, and oxygen at solar abundances (in a homogeneous configuration) and incorporate the appropriate Stark broadening for these elements, as prescribed by Werner (1996b). While this addition effectively solves the Balmer-line problem, we stress that such a large amount of CNO is not observed in hot white dwarfs and simply acts as a proxy for all metals here. It should be mentioned that our own calculations and those of Gianninas et al. (2010) made use of the same input physics, with the obvious exception of our improvements to the TLUSTY and SYNSPEC codes described above. However, these modifications only affect the He I opacity, which is negligible in the hot, hydrogen-rich stars suffering from the Balmer-line problem.

Figure 2.5 presents some of our synthetic spectra at $\log g = 8.0$, for selected effective temperatures and atmospheric compositions. The top-left and top-right panels show spectra generated from, respectively, pure-hydrogen and pure-helium models (typical of DA and DO/DB white dwarfs). As the temperature decreases, the spectral appearance reflects the changing ionization balance: the H I lines strengthen continuously; the He II lines first strengthen, reach a maximum intensity around $T_{\rm eff} \sim 65{,}000$ K, and then weaken; the He I lines appear around $T_{\rm eff} \sim 75{,}000$ K and then strengthen steadily. The middle and bottom panels display spectra corresponding to, respectively, homogeneous and stratified models. In each instance, the left panel shows spectra dominated by hydrogen features (typical of DAO/DAB stars), whereas the right panel shows spectra exhibiting primarily helium features (typical of DOA/DBA stars). The chemical structure of the atmosphere clearly influences the shape of the absorption lines, which are much broader and shallower in the stratified

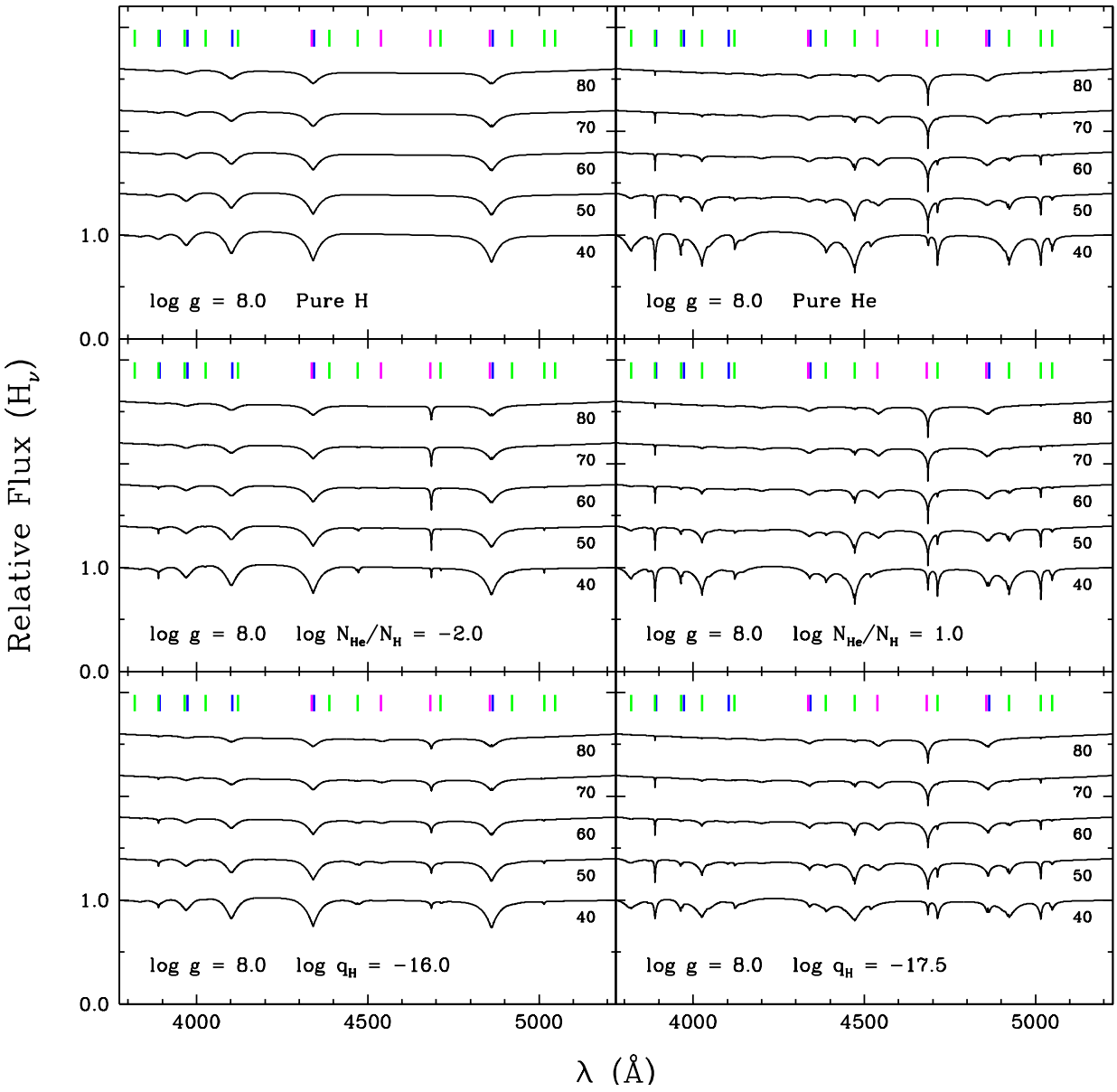

Figure 2.5 – Synthetic optical spectra of white dwarf model atmospheres at $\log g = 8.0$ for various effective temperatures and chemical compositions. The temperatures are indicated in units of 10^3 K, and the compositions are pure hydrogen (top-left panel), pure helium (top-right panel), hydrogen and helium in a homogeneous configuration (middle panels), and hydrogen and helium in a stratified configuration (bottom panels). The spectra are normalized to a continuum set to unity and offset vertically from each other by 0.4 for clarity. The positions of the H I, He I, and He II lines are marked by blue, green, and magenta ticks, respectively.

case than in the homogeneous case (see Manseau et al. 2016 for more on this topic). Finally, the right panels of Figure 2.5 highlight the well-known difficulty of detecting a small amount of hydrogen in a hot helium-rich atmosphere, every H I feature being blended with a He II feature (Werner, 1996a).

2.3.2. Evolutionary Cooling Sequences

In order to convert atmospheric parameters (effective temperature and surface gravity) into stellar properties (mass, radius, luminosity, and cooling age), one needs a set of detailed white dwarf evolutionary sequences. The Montreal sequences, first introduced by Fontaine et al. (2001) and available online at `http://www.astro.umontreal.ca/~bergeron/CoolingModels/` (in the section titled "Evolutionary Sequences"), are widely employed in the literature for that purpose. However, in their latest version, they are not suitable for the present work, because their validity is restricted to relatively cool ($T_{\rm eff} \lesssim 30{,}000$ K) degenerates. The main reason is that they were computed starting from static white dwarf models, which represent a poor approximation at high effective temperatures, when gravitational contraction and neutrino emission are still significant. Therefore, we decided to calculate a whole new set of white dwarf cooling tracks using more realistic models as initial conditions and thus extending to much higher effective temperatures.

To generate our starting models, we relied on the public stellar-evolution code Modules for Experiments in Stellar Astrophysics (MESA; Paxton et al. 2011, 2013, 2015, 2018, 2019). We evolved 14 stellar models with different initial masses from the zero-age main sequence to the beginning of the white dwarf stage. We considered initial masses ranging from 0.4 to 11 $M_{\odot}$ (corresponding to final masses ranging from 0.306 to 1.223 $M_{\odot}$) and an initial metallicity of 0.02 in all cases. We adopted the mass-loss prescriptions of Reimers (1975) on the red giant branch (RGB) and Blöcker (1995b) on the asymptotic giant branch (AGB), both with an efficiency parameter (η) of 0.5, except for stars with high initial masses ($\geq$4 $M_{\odot}$), for which we increased the AGB efficiency parameter to 20. As pointed out in previous studies utilizing MESA, this artificial enhancement of mass loss is necessary to avoid numerical difficulties associated with the occurrence of thermal pulses on the AGB (Paxton et al., 2013; Lauffer et al., 2018). Other computational settings were chosen similar to those of the test-suite case `1M_pre_ms_to_wd`.

Next, to calculate state-of-the-art white dwarf cooling sequences, we turned to our own evolutionary code, designed specifically for the modeling of white dwarfs. We used a revamped, modern implementation of our code named STELUM, for STELlar modeling from the Université de Montréal. This program offers a variety of applications geared mostly toward chemical evolution and asteroseismology (see Brassard & Fontaine 2018 for an early report). An elaborate description of STELUM is clearly beyond the scope of this work and is thus postponed to a future publication (A. Bédard et al., in preparation). It is nonetheless worth mentioning that STELUM produces and evolves complete models of stars, down from the center up to the very surface. The constitutive physics of our code is broadly similar to that outlined in Fontaine et al. (2001) and Van Grootel et al. (2013), apart from the treatment of the conductive opacities, which are now taken from Cassisi et al. (2007) instead of from Hubbard & Lampe (1969) and Itoh et al. (1983, 1984, 1993). The effects of this improvement on the cooling process are discussed below.

We chose to follow the same approach as in Fontaine et al. (2001), that is, to compute evolutionary tracks with pre-specified masses and chemical compositions (as opposed to those obtained from the MESA calculations). We assumed a core made of a uniform mixture of carbon and oxygen in equal proportions ($X_{\rm C} = X_{\rm O} = 0.5$), surrounded by a helium mantle and an outermost hydrogen layer. We considered two standard envelope compositions differing by the thickness of the hydrogen layer, which we refer to as thick ($q_{\rm He} = 10^{-2}$, $q_{\rm H} = 10^{-4}$) and thin ($q_{\rm He} = 10^{-2}$, $q_{\rm H} = 10^{-10}$). For each of these two chemical profiles, we considered 23 mass values covering the range $0.2\ M_{\odot} \leq M \leq 1.3\ M_{\odot}$ (in steps of $0.05\ M_{\odot}$), for a total of 46 cooling tracks. Of course, low-mass ($M \lesssim 0.45\ M_{\odot}$) and high-mass ($M \gtrsim 1.1\ M_{\odot}$) degenerates are expected to harbor helium cores and oxygen/neon cores, respectively, instead of carbon/oxygen cores; for these masses, our computations should hence be viewed with caution. To produce a given sequence, we proceeded as follows. We first built an approximate initial model by combining a pre-white dwarf thermodynamic structure obtained from MESA (interpolated at the desired mass) with our fixed chemical structure. This model was then fed into STELUM and relaxed for a few iterations to allow the thermodynamic structure to adjust to the new chemical structure. Finally, this self-consistent model was used as input for the calculation of the detailed evolutionary sequence. In order to keep the composition constant with cooling, diffusive equilibrium was assumed (that is,

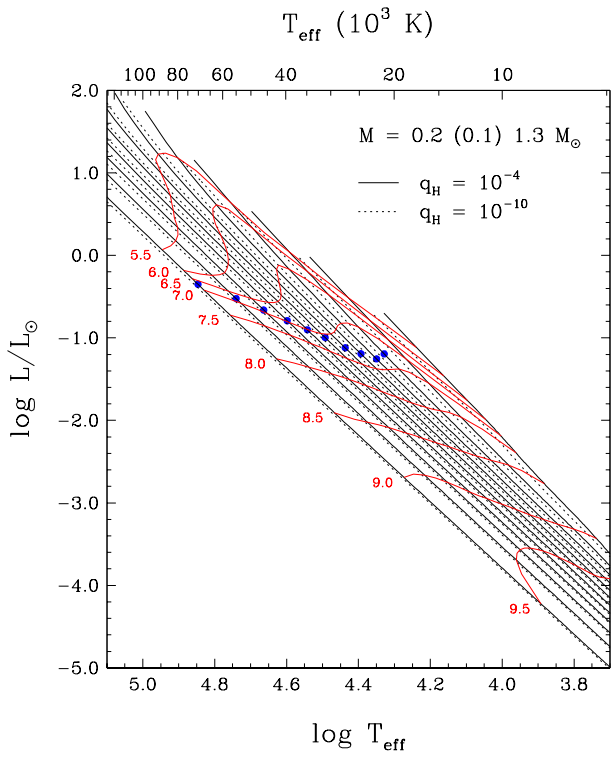

Figure 2.6 – Evolutionary sequences of white dwarf models in the theoretical Hertzsprung−Russell diagram, for masses of $0.2 - 1.3$ $M_{\odot}$ in steps of 0.1 $M_{\odot}$ (from top to bottom), and for thick (solid black lines) and thin (dotted black lines) hydrogen layers. Also shown, for the thick-layer models only, are isochrones labeled in units of $\log \tau_{\rm cool}$, where $\tau_{\rm cool}$ is the white dwarf cooling age in years (solid red lines), as well as the location of the transition between the neutrino and thermal cooling phases (blue dots).

transport mechanisms were turned off) and residual nuclear burning was ignored. While the strategy of forcing a specific chemical profile might seem somewhat arbitrary, it does have the advantage of minimizing the dependence of our results on the numerous uncertainties of pre-white dwarf evolution, most notably regarding core convective overshooting, helium-burning reaction rates, and wind mass-loss rates (Salaris et al., 2010; De Gerónimo et al., 2017).

Figure 2.6 shows some of our new evolutionary tracks, for various masses and for both envelope compositions, in the theoretical Hertzsprung−Russell (HR) diagram, together with representative isochrones for the thick-layer models only. It is readily seen that our sequences now extend to much higher effective temperatures than before, most of them beginning at

$T_{\rm eff} > 100{,}000$ K (except, of course, for the low-mass models, which never reach such high temperatures in their evolution). The cooling of a young, hot white dwarf is essentially driven by the emission of neutrinos formed in large numbers in the hot stellar core. These weakly interacting particles escape directly from the central regions to the outer space, thus providing an extremely efficient energy-loss mechanism and making this early evolution quite rapid. As cooling proceeds, the neutrino luminosity decreases and eventually drops below the photon luminosity, at which point the evolution becomes dominated by the much slower process of thermal cooling. The location of this transition on the evolutionary tracks is shown by the blue dots in Figure 2.6, again for the thick-layer models only. (Note that no blue dots are displayed on the very low-mass sequences, because the photon luminosity always exceeds the neutrino luminosity in these models.) As a white dwarf leaves the neutrino cooling phase and enters the thermal cooling phase, its evolutionary rate slows down, as illustrated by the tightening of the isochrones near the blue dots in Figure 2.6. The effective temperature of the transition sensitively depends on the stellar mass: for more massive stars, the neutrino-to-photon luminosity ratio declines at higher temperatures, which explains the shape of the isochrones in the theoretical HR diagram.

For completeness, we now make a brief digression from our main subject to discuss differences between our old and new evolutionary sequences at low effective temperatures ($T_{\rm eff} < 30{,}000$ K). To this end, as an illustrative example, we display in Figure 2.7 the percentage change of various physical quantities (namely, the surface gravity, the cooling age, the central temperature, and the neutrino luminosity) as a function of effective temperature for the typical case $M = 0.6\ M_{\odot}$, $q_{\rm H} = 10^{-4}$. The primary source of discrepancy between our previous and current generations of calculations at low temperatures is the inclusion of the conductive opacities of Cassisi et al. (2007) in STELUM. On one hand, this improvement has absolutely no effect on the mechanical properties of white dwarf models. In fact, for all cooling tracks, the changes in surface gravity, radius, and luminosity are smaller than 0.5% over the entire temperature range of validity of our old models. This is illustrated in the first panel of Figure 2.7 for the particular case of the surface gravity in our reference sequence. Therefore, the theoretical mass−radius relation is basically unaltered, and the conclusions achieved by recent studies on its accuracy remain intact (Bédard et al., 2017; Parsons et al., 2017; Genest-Beaulieu & Bergeron, 2019a; Tremblay et al., 2019a).

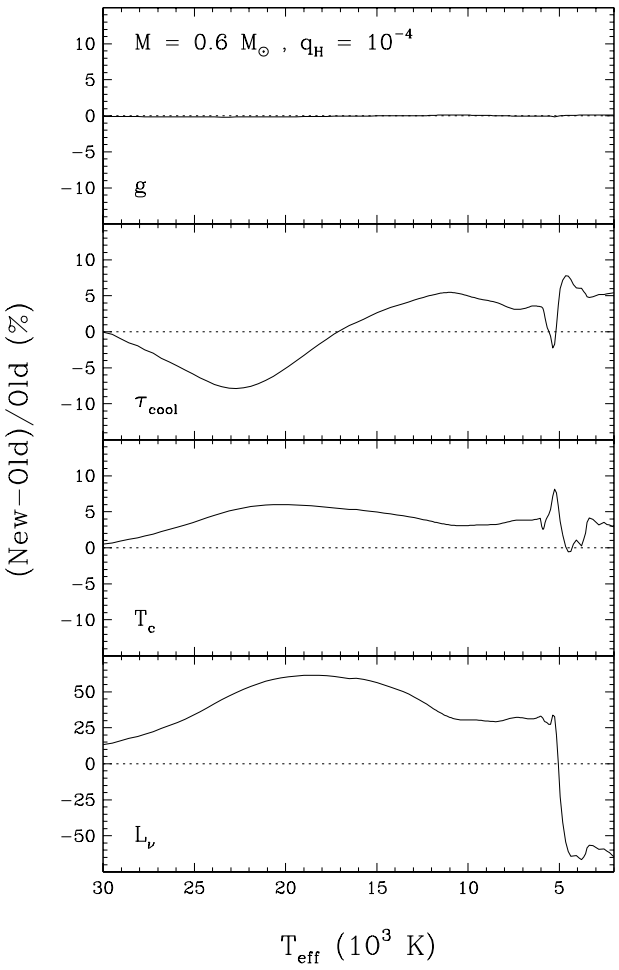

Figure 2.7 – Percentage difference in surface gravity, cooling age, central temperature, and neutrino luminosity (from top to bottom) as a function of effective temperature, between our old and new 0.6 $M_{\odot}$, thick-layer evolutionary sequences, which differ in the treatment of the conductive opacity.

On the other hand, the new conductive opacities substantially impact the thermal properties of white dwarf models. As shown by Salaris et al. (2013), the opacities of Cassisi et al. (2007) are larger than those of Hubbard & Lampe (1969) and Itoh et al. (1983, 1984, 1993), both in the carbon/oxygen core and the helium envelope. One could naively expect the enhanced opacity to simply slow down the cooling, as a result of the reduced efficiency of radiative transfer throughout the star. In other words, it would be reasonable to expect the cooling time required to reach a given effective temperature to be longer. This hypothesis is proven wrong by the second panel of Figure 2.7: the cooling age is actually shorter at high

temperatures and longer at low temperatures, by as much as ∼10%. The correct explanation for this behavior was first put forward by Salaris et al. (2013). The updated conductive opacities cause the core temperature to rise by a few percent, as displayed in the third panel of Figure 2.7. Because neutrino production rates strongly depend on temperature, this in turn leads to an increase in neutrino luminosity as large as ∼50%, as shown in the fourth panel of Figure 2.7. Consequently, at high effective temperatures, when neutrino emission is still the main energy sink, the cooling process is actually faster. However, as the temperature decreases and thermal cooling becomes dominant, the enhanced opacity translates into a slower evolution, as anticipated from the simple argument made above.

Finally, it is worth mentioning that these changes in the thermal properties of our models obviously have repercussions on the crystallization process. More specifically, for most masses, the net effect of the improved conductive opacities is to shift the onset of core crystallization to slightly lower effective temperatures. This difference between our old and new sequences manifests itself as small spikes near $T_{\rm eff} \sim 5500$ K in the two middle panels of Figure 2.7. Nevertheless, we want to emphasize that these shifts are small (typically a few hundred Kelvin) and hence do not affect the conclusions drawn by Tremblay et al. (2019b) and Bergeron et al. (2019) about the so-called Gaia crystallization sequence using our previous generation of evolutionary tracks.

As before, we make our new white dwarf cooling sequences available to the community online at `http://www.astro.umontreal.ca/~bergeron/CoolingModels/`, as well as through the Montreal White Dwarf Database (Dufour et al., 2017) at `https://www.montrealwhitedwarfdatabase.org/evolution.html`.

2.4. Spectroscopic Analysis

2.4.1. Standard Fitting Procedure

Our next task was to analyze the SDSS optical spectra with our model atmospheres in order to derive the effective temperature, surface gravity, and atmospheric composition of each star in our sample. For objects showing spectral lines from only one element, we simply assumed a pure composition (that is, we applied our pure-hydrogen and pure-helium models to the analysis of DA and DO/DB white dwarfs, respectively), leaving only $T_{\rm eff}$ and $\log g$ to be determined. Note that we also included in this category the few DOZ stars, for which we

employed our pure-helium models as well, because we did not calculate metal-rich models, admittedly more adequate here but much more computationally expensive. The study of hybrid white dwarfs, whose chemical configuration is a priori unknown, required a more elaborate approach, the description of which is deferred to the next subsection.

We relied on a two-step fitting method wherein the observed and synthetic spectra were first normalized to a continuum set to unity and then compared to each other, so that the atmospheric parameters were constrained solely from the information contained in the line profiles (Bergeron et al., 1992, 2011; Liebert et al., 2005). The most critical aspect of the normalization process was to properly define the continuum of the observed spectrum. To do so, we fitted the observed spectrum with the grid of theoretical spectra, convolved with a Gaussian instrumental profile and multiplied by a sixth-order polynomial in wavelength designed to account for interstellar reddening and flux calibration errors. The optimization was carried out using the nonlinear least-squares Levenberg−Marquardt algorithm. Although the resulting fit did not yield reliable values of $T_{\rm eff}$ and $\log g$ due to the large number of free parameters, it provided a smooth fitting function defining the continuum of the observed spectrum. Normal points were fixed at the value of this function at a few chosen wavelengths and used to normalize the spectrum to a continuum set to unity. Then, we fitted this normalized spectrum with the grid of normalized synthetic spectra, still convolved with a Gaussian instrumental profile, again employing the Levenberg−Marquardt algorithm. This time, we obtained physically meaningful atmospheric parameters, because only $T_{\rm eff}$ and $\log g$ were allowed to vary in the optimization procedure. Finally, each fit was visually inspected to ensure the quality of the results.

Figures 2.8 and 2.9 display our spectroscopic solutions for some DA and DO/DB white dwarfs, respectively, with high-S/N observations (S/N $>$ 30). Note that in each fit, the whole optical spectrum, up to $\lambda = 7000$ Å, was taken into account, but we show here only the blue part for presentation purposes. In the vast majority of cases, our pure-hydrogen and pure-helium models provide excellent matches to the spectroscopic data. For the 29 DOZ stars, our pure-helium models obviously fail to reproduce the weak C IV λ4658 feature detected in the spectra, as illustrated for two objects in Figure 2.9. In such instances, we simply excluded this narrow wavelength region from the fits. We are confident that ignoring the carbon opacity in our models only marginally impacts the derived values of $T_{\rm eff}$ and $\log g$.

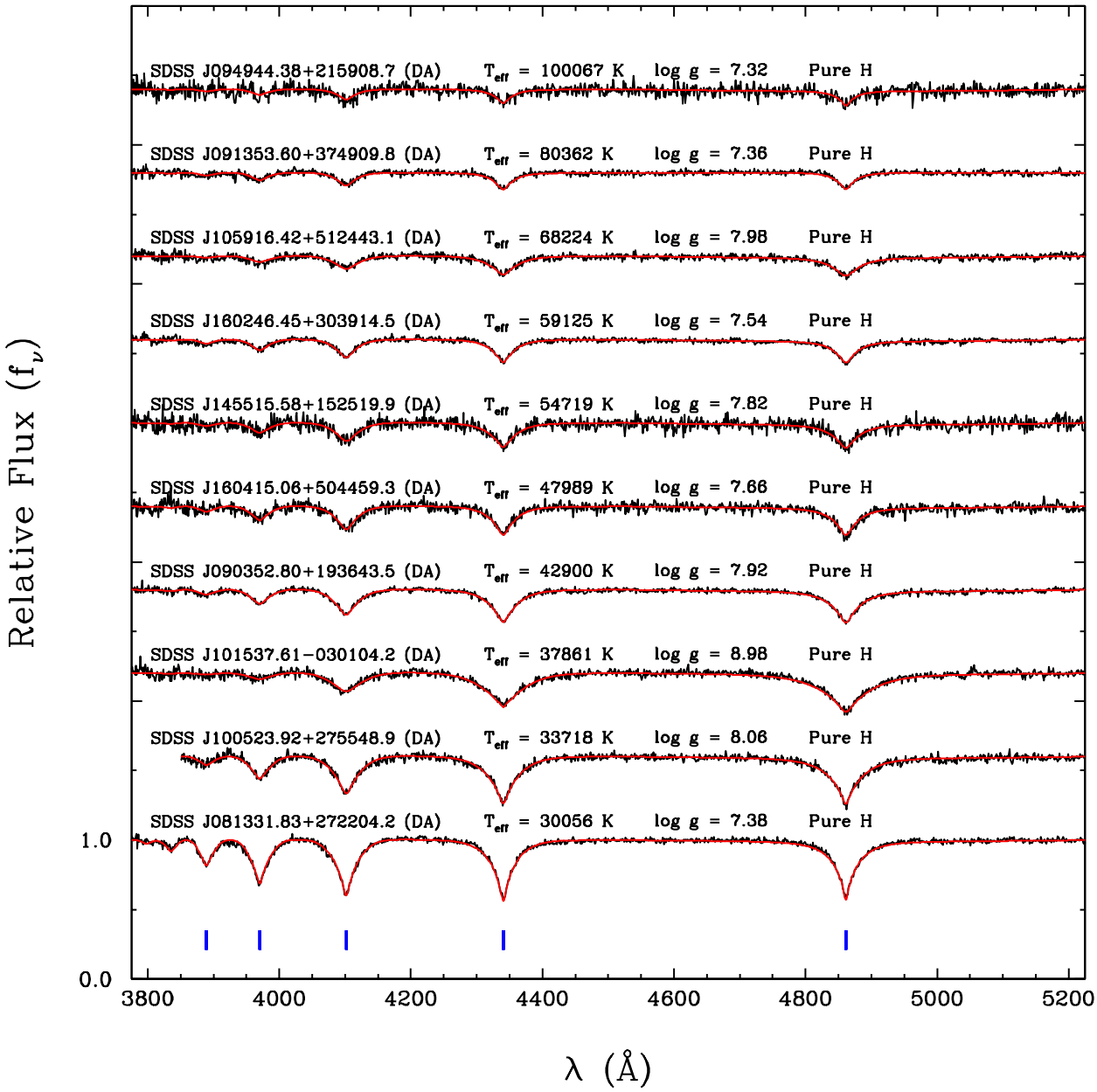

Figure 2.8 – Best model-atmosphere fits to the optical spectra of DA white dwarfs with high signal-to-noise observations (S/N > 30). The observed and synthetic spectra, normalized to a continuum set to unity, are displayed as black and red lines, respectively. The fits are offset vertically from each other by 0.6 for clarity. The SDSS name, the spectral type, and the best-fitting atmospheric parameters are given for each object. The positions of the H I lines are marked by blue ticks.

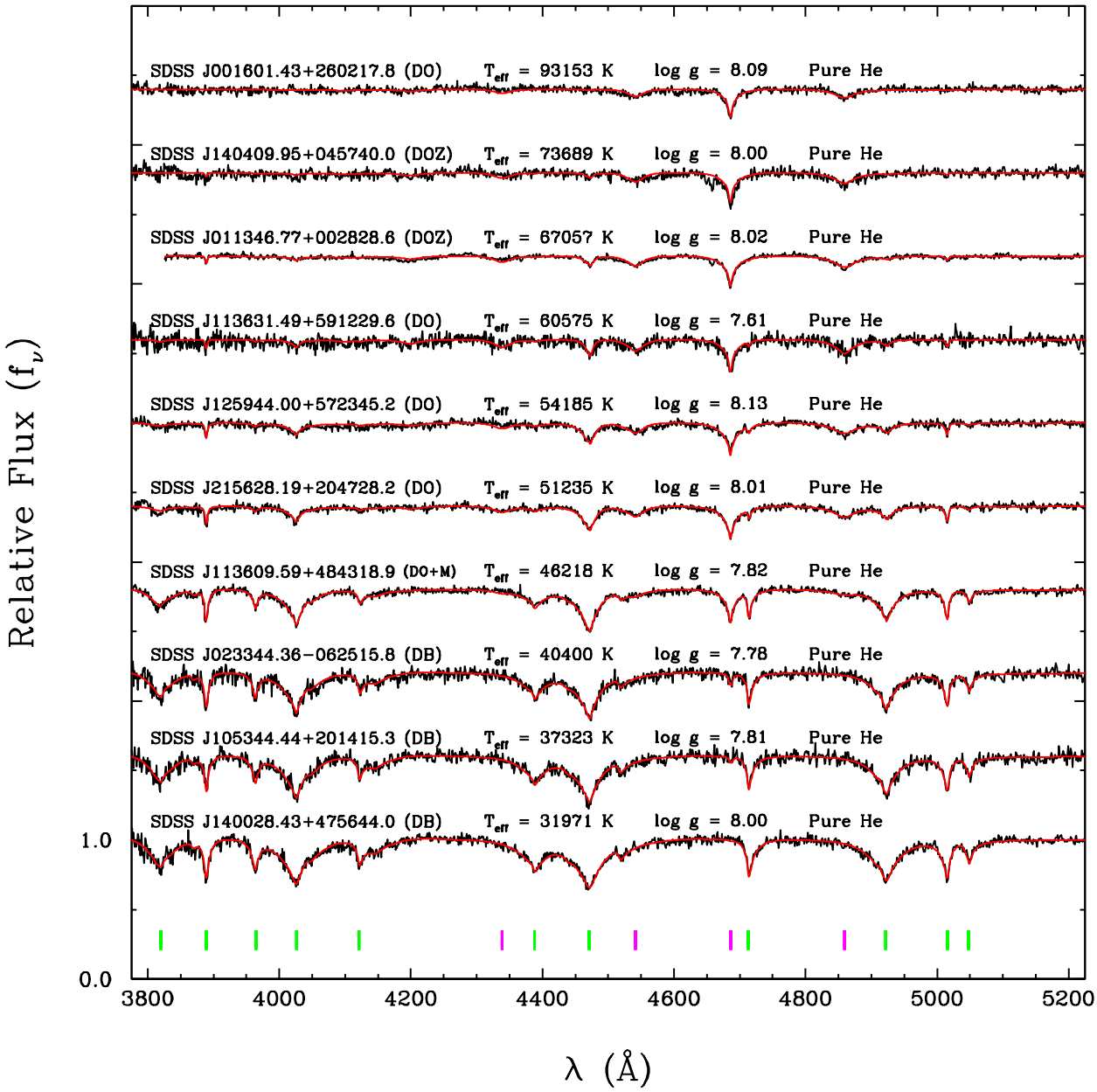

Figure 2.9 – Same as Figure 2.8, but for DO/DB white dwarfs. The positions of the He I and He II lines are marked by green and magenta ticks, respectively.

Indeed, the carbon abundances measured in DOZ white dwarfs typically fall in the range $-3.0 < \log N_{\rm C}/N_{\rm He} < -2.0$ (Dreizler & Werner, 1996; Reindl et al., 2014a; Werner et al., 2014), and the corresponding opacity barely influences the He I and He II line profiles at high temperatures according to the model-atmosphere calculations of Reindl et al. (2018).

2.4.2. Hybrid White Dwarfs

Special care was needed to properly analyze the 127 stars in our sample exhibiting both hydrogen and helium spectral features. As indicated by Figure 2.5, the great sensitivity of the spectrum to the chemical structure of the atmosphere can be exploited to discriminate between homogeneous and stratified distributions of hydrogen and helium (Bergeron et al., 1994; Manseau et al., 2016). To this end, we fitted the optical spectra of our hybrid white dwarfs with both our homogeneous and stratified model-atmosphere grids. The physical quantity used to measure the composition (the helium-to-hydrogen number ratio $N_{\rm He}/N_{\rm H}$ in the homogeneous case, the fractional mass of the hydrogen layer $q_{\rm H}$ in the stratified case) was treated as an additional free parameter in the optimization process. We then compared the two solutions and adopted the best-fitting one.

Figure 2.10 contrasts the homogeneous and stratified solutions for four hybrid white dwarfs in our sample. Once again, while only the blue optical spectra are displayed here, redder wavelengths, up to $\lambda = 7000$ Å, were included in the fits as well. For each star, the parameters corresponding to the adopted chemical configuration are highlighted in red. The top two white dwarfs are relatively hot, in which situation the comparison rests largely on the He II λ4686 line and to a lesser extent on the He I λ4471 line. We can safely assert that the first object has a homogeneous atmosphere, because our stratified models produce a He II λ4686 feature that is too shallow. Conversely, the second object bears the signature of a stratified atmosphere, the He II λ4686 profile predicted by our homogeneous models being too deep. The bottom two panels show cooler stars, for which the distinction between both types of chemical structure is more evident. In this temperature range, most observed hydrogen and helium lines are sensitive to the chemical configuration, especially Hα, Hβ, and Hγ, as well as He I λ4471, λ5876, and λ6678. Moreover, when stratified white dwarfs are fitted with homogeneous models, the best solution often predicts sharp He II λ4686 and λ5412 features that are definitely not observed. This can be seen for the bottom two objects, which undoubtedly have stratified external layers. We want to point out that the four stars presented in Figure 2.10 all exhibit both hydrogen and helium lines of at least moderate strength, which makes the disparity between homogeneous and stratified atmospheres quite obvious. However, this is not always the case: the difference can be more subtle when the

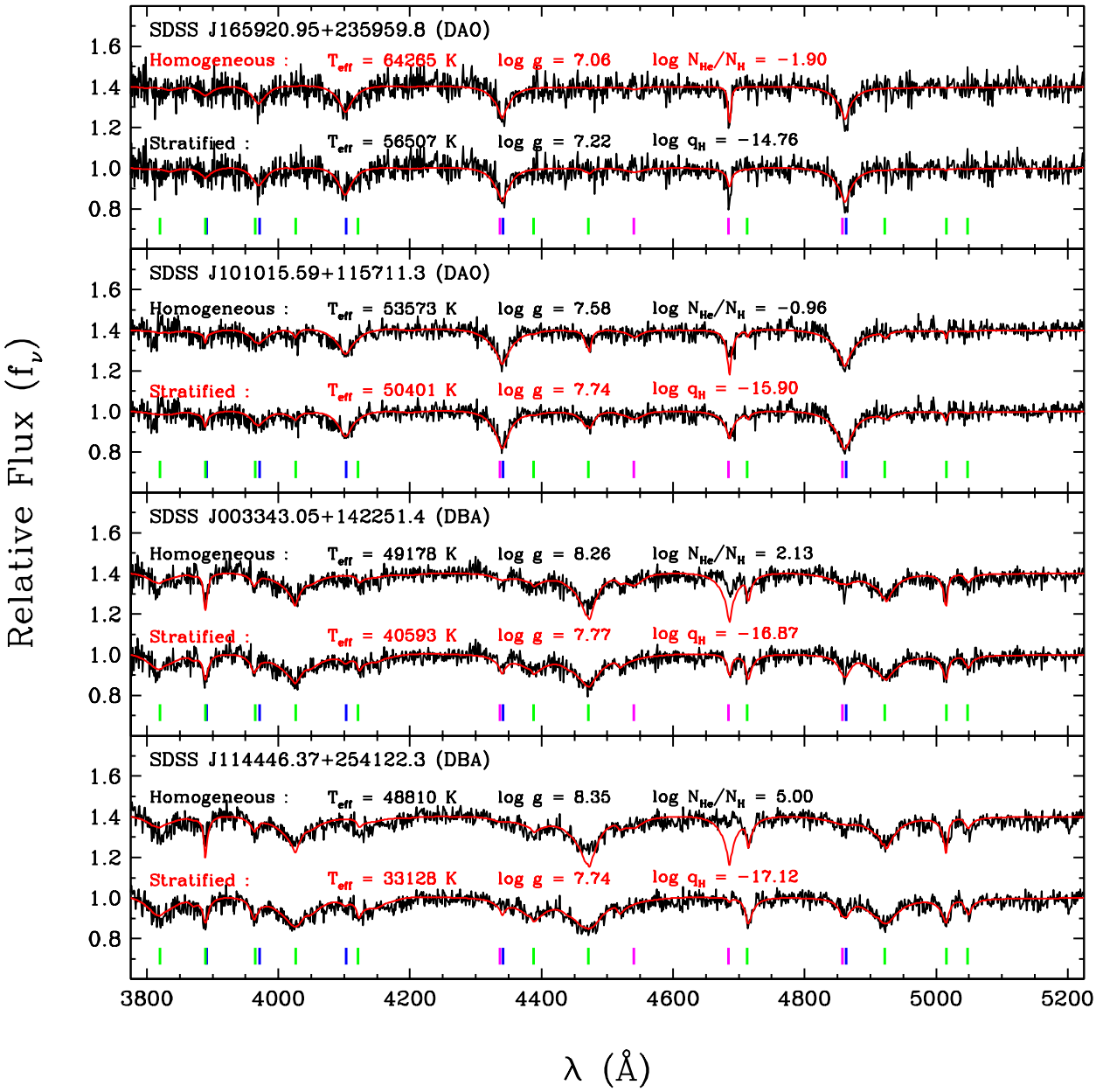

Figure 2.10 – Same as Figure 2.8, but for hybrid white dwarfs analyzed assuming in turn a chemically homogeneous and stratified atmosphere. The adopted solution is highlighted in red. The positions of the H I, He I, and He II lines are marked by blue, green, and magenta ticks, respectively.

lines of one species are much weaker than those of the other species (see Figure 13 of Manseau et al. 2016).

Out of our 127 hybrid stars, 31 show evidence of atmospheric chemical stratification (in five cases, the evidence is somewhat ambiguous). Therefore, besides retrieving the 15 stratified white dwarfs of Manseau et al. (2016), we further identified 16 new such objects. The latter were missed by Manseau et al. (2016) most likely because their search algorithm targeted SDSS white dwarfs exhibiting the He II λ4686 feature and consequently ignored the cooler candidates. For the stars in common, a quick comparison reveals that our effective temperatures are on average slightly lower, an effect that is probably due to our improved non-LTE model atmospheres. We note that all of our stratified white dwarfs have $T_{\rm eff} <$ 55,000 K, whereas most of our homogeneous white dwarfs have $T_{\rm eff} >$ 55,000 K. Furthermore, our estimates of the masses of hydrogen floating at the surface of stratified objects span the narrow range $-18.25 < \log q_{\rm H} < -15.25$. Of course, this result does not mean that white dwarfs with slightly lower and higher values of $q_{\rm H}$ do not exist, but rather that such stars simply show pure DO/DB and pure DA spectra, respectively, because the transition region between the hydrogen and helium layers is located far away from the photosphere. We also want to stress that the quantity $q_{\rm H}$ evaluated here cannot be interpreted as the total hydrogen content, but rather as the instantaneous amount of hydrogen floating at the surface at the present time. In fact, it is highly plausible that much more hydrogen is still diluted in the underlying helium envelope.

Finally, we mention that for two hybrid white dwarfs, SDSS J163757.58+190526.1 (DBA) and SDSS J221703.09+223330.8 (DAO), neither homogeneous nor stratified models yielded satisfactory fits to all observed spectral lines simultaneously. These two objects are actually DA+DB and DA+DO binary systems. A proper model-atmosphere study of these double degenerate binaries will be reported elsewhere.

2.4.3. White Dwarfs with Main-sequence Companions

For some 185 white dwarfs in our sample, the optical spectra suffer from contamination by M dwarf companions, which can jeopardize the accuracy of the atmospheric parameters obtained from our fitting method. To overcome this problem, we applied the procedure developed by Gianninas et al. (2011) to remove the contribution of the main-sequence stars from the observed spectra before proceeding with our standard analysis.

Briefly, we combined our white dwarf synthetic spectra with the M dwarf spectral templates of Bochanski et al. (2007), and we fitted each observed spectrum with a function given

by

$$F_{\rm obs} = [F_{\rm WD}(T_{\rm eff}, \log g) + f \times F_{\rm M}({\rm type})] \times \left[a_0 + a_1\lambda + a_2\lambda^2 + a_3\lambda^3\right]. \quad (2.1)$$

In this equation, the flux of the white dwarf $F_{\rm WD}$ depends only on $T_{\rm eff}$ and $\log g$ (for an assumed atmospheric composition), while the flux of the M dwarf $F_{\rm M}$ depends only on its spectral type, between M0 and M9. Besides these three parameters, the function also contains a scaling factor f setting the relative contributions of the two stars and the four coefficients $a_0 - a_3$ of a third-order polynomial in wavelength. These eight parameters were all allowed to vary in the fitting process in order to reproduce the observed spectrum as well as possible. We took advantage of the fact that the SDSS spectroscopic data cover the near-infrared and extended the fitted wavelength range up to $\lambda = 9200$ Å to put tight constraints on the M dwarf type. Once achieved, the solution provided us with the individual contributions of the white dwarf and the M dwarf to the composite spectrum. We then subtracted the synthetic flux of the main-sequence component from the observed spectrum. Finally, this decontaminated spectrum was analyzed using our standard technique outlined above to derive reliable atmospheric parameters for the white dwarf.

Figure 2.11 displays an example of our decontamination method. In general, we obtained excellent fits to the composite spectra, which resulted in very clean white dwarf spectra after subtraction of the M dwarf contribution, as illustrated in the top and bottom panels of Figure 2.11. In some cases where the cores of the absorption features are filled in with reprocessed emission from the main-sequence star, we simply excluded the line centers from our fits, as this effect was not taken into account in our binary modeling and thereby could not be corrected for.

2.4.4. Problematic Objects

Through our visual inspection, we identified 70 DA and 53 (homogeneous) DAO stars affected by the Balmer-line problem. For these objects, the Hα and Hβ line cores predicted by our hydrogen−helium models are not as deep as in the observed features, which constitutes an indirect indication of the presence of metals in the atmospheres. Therefore, to improve our atmospheric parameter determination, we reanalyzed these DA and DAO white dwarfs with the CNO-rich models of Gianninas et al. (2010), which generally yielded better fits (see Gianninas et al. 2010 for graphical examples). The most important effect of these models is to

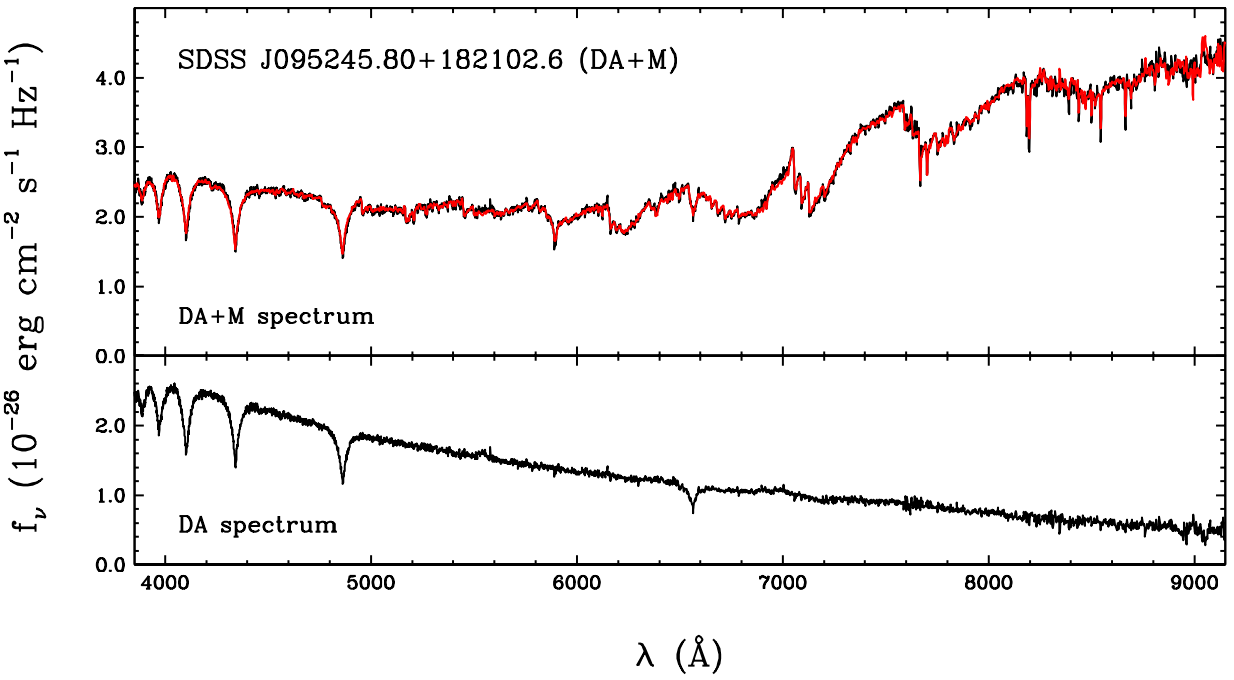

Figure 2.11 – Top panel: best model-atmosphere fit to the optical and near-infrared spectrum of a white dwarf + M dwarf binary system. The observed and synthetic spectra are displayed as black and red lines, respectively. Bottom panel: decontaminated white dwarf spectrum obtained by subtracting the best-fitting M dwarf template from the observed composite spectrum.

increase the surface gravities by $\sim$0.1$-$0.2 dex with respect to those obtained from metal-free models. The Balmer-line problem, found mainly at very high effective temperatures, has an incidence of 34% among our hydrogen-rich white dwarfs with $T_{\rm eff} > 60{,}000$ K. Nonetheless, it is clear that our ability to detect such subtle discrepancies in the line cores depends quite sensitively on the S/N of the spectroscopic data: for instance, the proportion rises to 56% if we restrict ourselves to S/N > 30. Thus, the Balmer-line problem would likely be more common if we had access to higher-S/N observations. This implies that the atmospheric parameters of some of our very hot DA and DAO stars might suffer from systematic errors. We come back to this point in Section 2.5 below.

Furthermore, a small number of hot DO and DOZ white dwarfs in our sample are peculiar in that their optical spectra show exceedingly broad and deep He II absorption features that cannot be matched by any of our models. An example of fit for such a strange object is

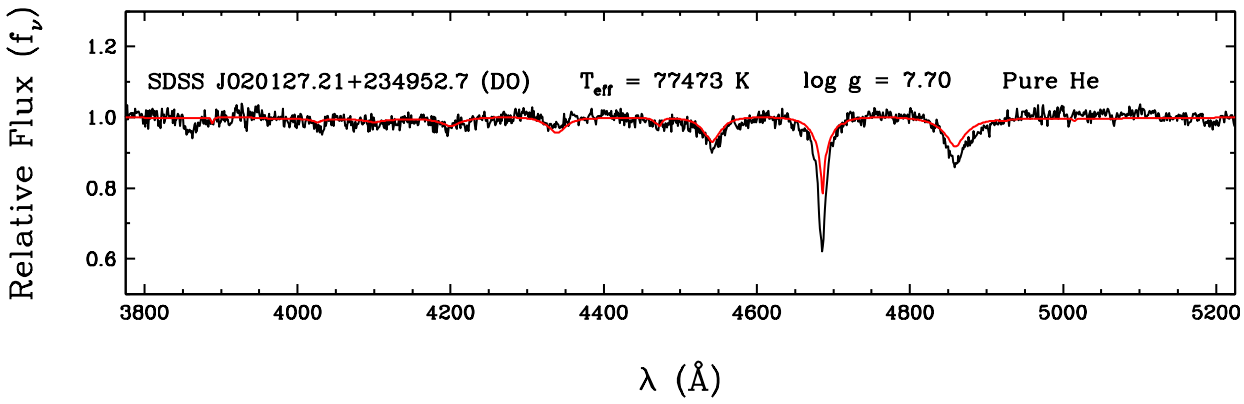

Figure 2.12 – Same as Figure 2.8, but for a peculiar DO white dwarf showing abnormally strong He II lines.

displayed in Figure 2.12, where the He II λ4686 and λ4859 lines are clearly problematic. In all cases, the issue was already known from previous spectroscopic investigations (see Reindl et al. 2014a for a compilation). These abnormally strong He II features are often accompanied by so-called ultra-high-ionization features, believed to be produced by extremely high ionization stages of carbon, nitrogen, oxygen, and neon. For instance, the depression near $\lambda \sim 3850$ Å in the spectrum shown in Figure 2.12 is attributed to N VII or O VII by Reindl et al. (2014a). The formation of these ions requires temperatures well in excess of 500,000 K, uncharacteristic of a static stellar atmosphere. Hence, the currently favored explanation for this puzzling phenomenon is the presence of a shock-heated circumstellar wind, possibly trapped in a weak magnetic field, around these stars (Werner et al., 2018; Reindl et al., 2019). The reason why such extreme winds occur almost exclusively in helium-dominated white dwarfs still remains a mystery. To assess the atmospheric parameters as well as possible in the circumstances, we rejected the affected He II lines and assigned a higher weight to the He I λ4471, λ5876, and λ6678 lines (which persist up to $T_{\rm eff} \sim 75{,}000$ K) in our fits. Indeed, while it is uncertain whether the He II features are formed primarily in the hot wind or in the cooler, static atmosphere, the He I features must necessarily originate from the latter and can thereby serve as fairly reliable effective temperature indicators. The peculiar DO and DOZ stars all have $T_{\rm eff} > 60{,}000$ K and represent 24% of our helium-rich sample in this temperature range.

2.5. Results and Discussion

2.5.1. Physical Properties

For each star in our sample, we converted the atmospheric parameters into stellar parameters through our white dwarf evolutionary sequences[3]. We used our thick-layer and thin-layer models for hydrogen-rich and hydrogen-deficient objects, respectively. The results are reported in Table 2.1 (see the Appendix), where we give for each white dwarf the SDSS name, spectral type, signal-to-noise ratio (S/N), effective temperature ($T_{\rm eff}$), surface gravity ($\log g$), atmospheric composition (either pure H, pure He, $\log N_{\rm He}/N_{\rm H}$, or $\log q_{\rm H}$, depending on the adopted chemical structure), mass (M), radius (R), luminosity (L), and cooling age ($\tau_{\rm cool}$)[4]. The confidence intervals correspond to the internal uncertainties taken directly from the covariance matrix of the fitting procedure. As discussed below, we warn the reader that the derived properties of our hottest objects ($T_{\rm eff} \gtrsim 60{,}000$ K for DA stars and $T_{\rm eff} \gtrsim 50{,}000$ K for DO/DB stars) are inaccurate to some degree due to significant systematic effects.

2.5.1.1. *Examination of the* $\log g - T_{\rm eff}$ *Diagram*

The atmospheric parameters obtained from our spectroscopic analysis are summarized in the $\log g - T_{\rm eff}$ diagram presented in Figure 2.13, where blue and red circles symbolize hydrogen-rich and helium-rich stars, respectively. Also displayed as solid and dotted lines are our cooling tracks for thick and thin hydrogen layers, respectively. On one hand, at low effective temperatures, most DA and DO/DB white dwarfs form a continuous sequence, essentially parallel to the curves of constant mass and tightly centered around $M \sim 0.55\ M_{\odot}$, as expected from our knowledge of degenerate evolution. We also notice a small population of very low-mass DA stars with $T_{\rm eff} < 40{,}000$ K, which are probably remnants of common-envelope binary evolution, as the Galaxy is not old enough for such objects to have been produced through canonical single-star evolution. On the other hand, at high effective

3. For the few high-temperature and low-gravity white dwarfs lying outside the parameter space covered by our cooling tracks (see Figure 2.13), we used a quadratic extrapolation to estimate the stellar properties, which should thus be viewed with caution. Nevertheless, we verified that these extrapolated sequences behave similarly to existing evolutionary calculations, such as those of Althaus et al. (2009b) and Renedo et al. (2010).

4. Very short cooling ages ($\log \tau_{\rm cool} \lesssim 5$) are sensitive to the zero points set by the initial models of our sequences. In such cases, we state an upper limit ($\log \tau_{\rm cool} < 5$) rather than our derived value.

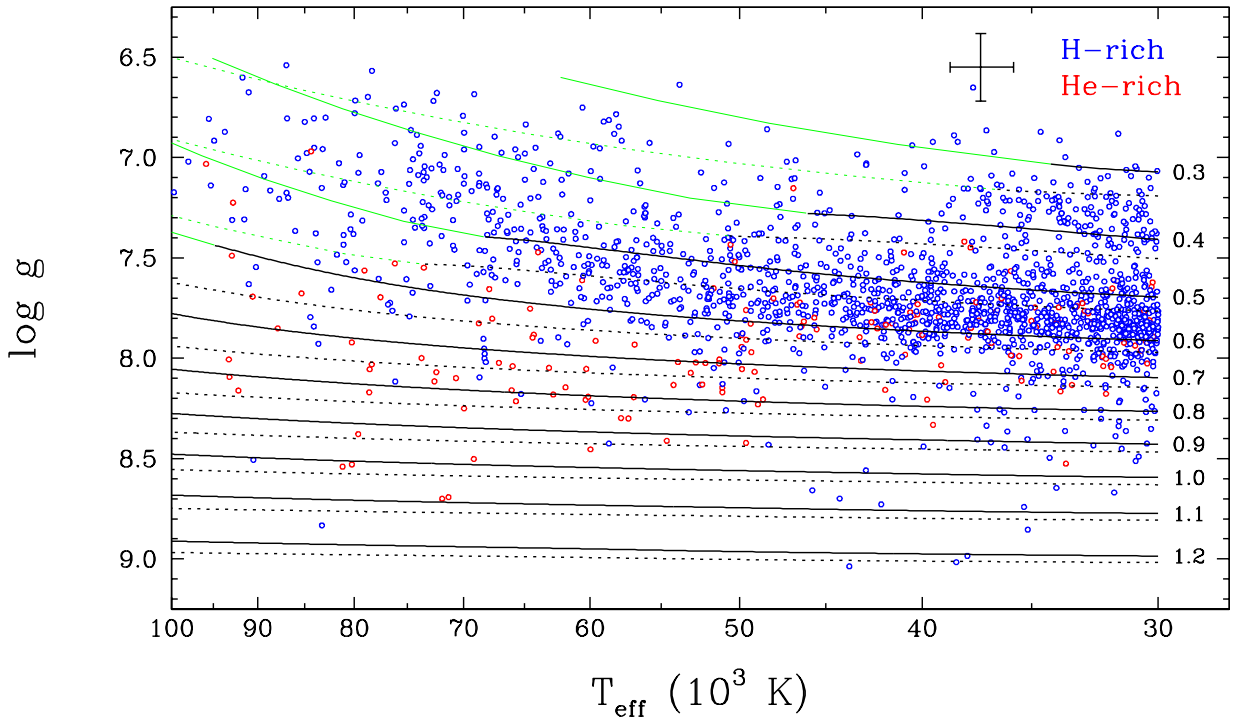

Figure 2.13 – Location of our sample of 1806 white dwarfs in the $\log g - T_{\rm eff}$ diagram, as determined from our spectroscopic analysis. Hydrogen-rich and helium-rich objects are shown in blue and red, respectively. The error bars represent the average uncertainties. Our white dwarf evolutionary sequences for thick and thin hydrogen layers are displayed as solid and dotted black lines, respectively, with masses indicated in units of $M_{\odot}$. The green extensions represent the extrapolated parts of our sequences.

temperatures, our results are much more puzzling: DA white dwarfs with $T_{\rm eff} \gtrsim 60{,}000$ K have lower-than-average surface gravities, and DO white dwarfs with $T_{\rm eff} \gtrsim 50{,}000$ K have higher-than-average surface gravities. Consequently, the hydrogen-dominated sequence bends upward toward low masses, whereas the helium-dominated sequence abruptly drops toward high masses. These features are definitely at odds with the well-established facts that white dwarfs evolve at constant mass and that the DA and DB spectral classes are characterized by similar mean masses (Genest-Beaulieu & Bergeron, 2019a; Ourique et al., 2019; Tremblay et al., 2019a).

The problem is illustrated more quantitatively in Figure 2.14, where we show the cumulative mass distributions for hydrogen-atmosphere and helium-atmosphere objects. Each group is divided into a low-temperature sample and a high-temperature sample (based on

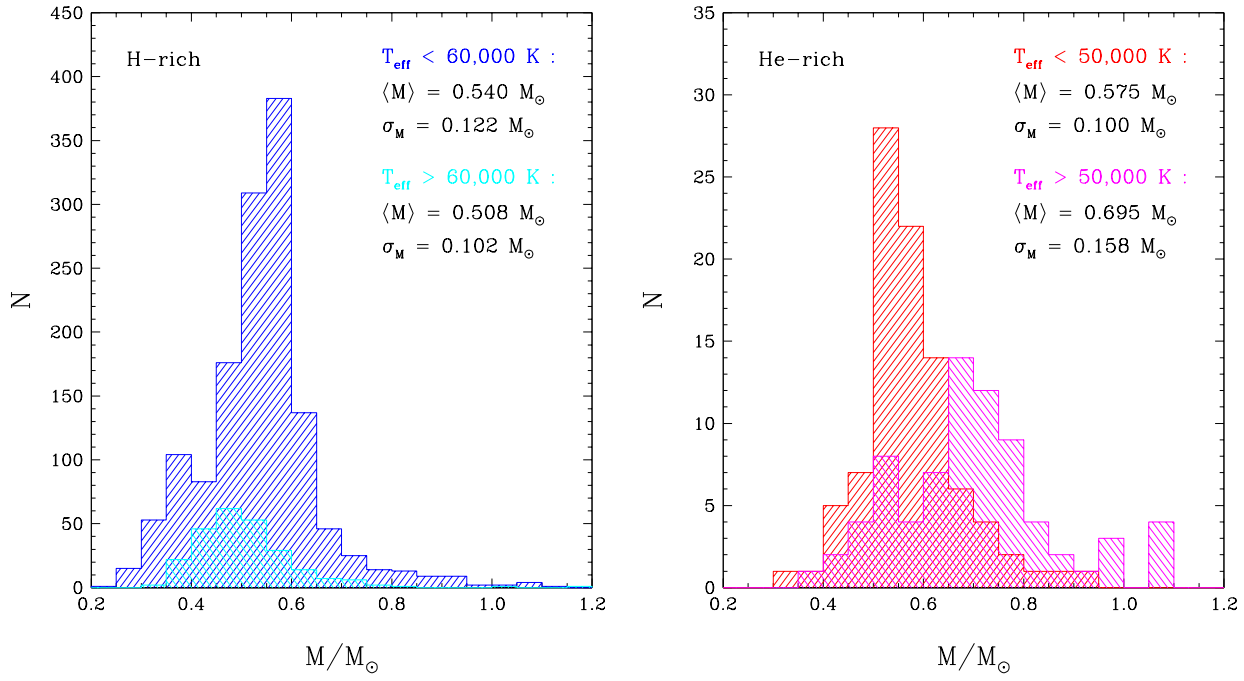

Figure 2.14 – Cumulative mass distributions of hydrogen-rich (left panel) and helium-rich (right panel) objects in our sample of 1806 white dwarfs, as determined from our spectroscopic analysis. Each group is divided into a low-temperature subgroup (blue and red histograms in the left and right panels, respectively) and a high-temperature subgroup (cyan and magenta histograms in the left and right panels, respectively) based on the trends seen in Figure 2.13. The average and standard deviation of the various distributions are given in the panels.

Figure 2.13, the boundary is set at $T_{\rm eff}$ = 60,000 K for DA stars and at $T_{\rm eff}$ = 50,000 K for DO/DB stars). As anticipated from Figure 2.13, the mass distribution of the hottest DA white dwarfs is slightly shifted toward lower masses with respect to that of their cooler counterparts. Accordingly, the mean mass is slightly lower at $T_{\rm eff} > 60{,}000$ K ($\langle M \rangle = 0.508\ M_{\odot}$) than at $T_{\rm eff} < 60{,}000$ K ($\langle M \rangle = 0.540\ M_{\odot}$). For helium-rich objects, the discrepancy between the high-temperature and low-temperature regimes is even more severe: the mass distribution of hot DO stars is flatter and displaced to considerably higher masses. This translates into significantly larger values of the average and the standard deviation at $T_{\rm eff} > 50{,}000$ K ($\langle M \rangle = 0.695\ M_{\odot}$) than at $T_{\rm eff} < 50{,}000$ K ($\langle M \rangle = 0.575\ M_{\odot}$). On a more encouraging note, the low-temperature DA and DO/DB mass distributions are comparable (with the exception of a small low-mass peak in the DA histogram associated with post-common-envelope white

dwarfs), as expected. We are thus confident that our gravity and mass determinations are relatively reliable in this temperature range, where the bulk of our sample lies.

It should be mentioned that the mass issues raised here are not unique to our study. In their recent spectroscopic analyses of SDSS DA white dwarfs, Kepler et al. (2019, see their Figure 2) and Genest-Beaulieu & Bergeron (2019a, see their Figure 7) also found a trend of decreasing mass with increasing effective temperature at the hot end of their samples. Furthermore, from their compilation of spectroscopic parameters of SDSS DO stars, Reindl et al. (2014a, see their Figure 5) also obtained a mass distribution with a peak at $M \sim 0.675\ M_{\odot}$. They argue that this high-mass peak is real, but the striking contrast between the DO and DB mass distributions suggests otherwise. Therefore, it seems clear that the spectroscopic masses of very hot SDSS white dwarfs are afflicted by generalized problems that are not restricted to our own model atmospheres, cooling tracks, or fitting technique.

2.5.1.2. *Insight from Photometric and Astrometric Data*

Our assertion that the high-temperature mass offsets are artificial can be proven by deriving alternative mass estimates through an independent method. This is where the *ugriz* photometry and Gaia parallaxes can be useful. Indeed, the photometric energy distribution of a white dwarf principally depends on its effective temperature $T_{\rm eff}$ and solid angle $\pi(R/D)^2$, and thereby on its radius R (and mass M via the mass−radius relation) if the distance D is known from a parallax measurement (Bergeron et al., 1997, 2001). For each of the 824 objects in our astrometric subsample ($\sigma_{\pi}/\pi \leq 25\%$), we transformed the dereddened and SDSS-to-AB corrected *ugriz* magnitudes into observed average fluxes, which we then fitted with theoretical average fluxes predicted from our model atmospheres using the Levenberg−Marquardt algorithm. In the fitting procedure, only the radius was treated as a free parameter, while we assumed the effective temperature and atmospheric composition obtained from our spectroscopic analysis. This approach was motivated by the fact that the optical energy distribution of hot stars is very weakly sensitive to effective temperature, as shown in Section 2.2. For white dwarfs with main-sequence companions, the latter often contribute considerably to the measured *riz* magnitudes (and sometimes to the *g* magnitude

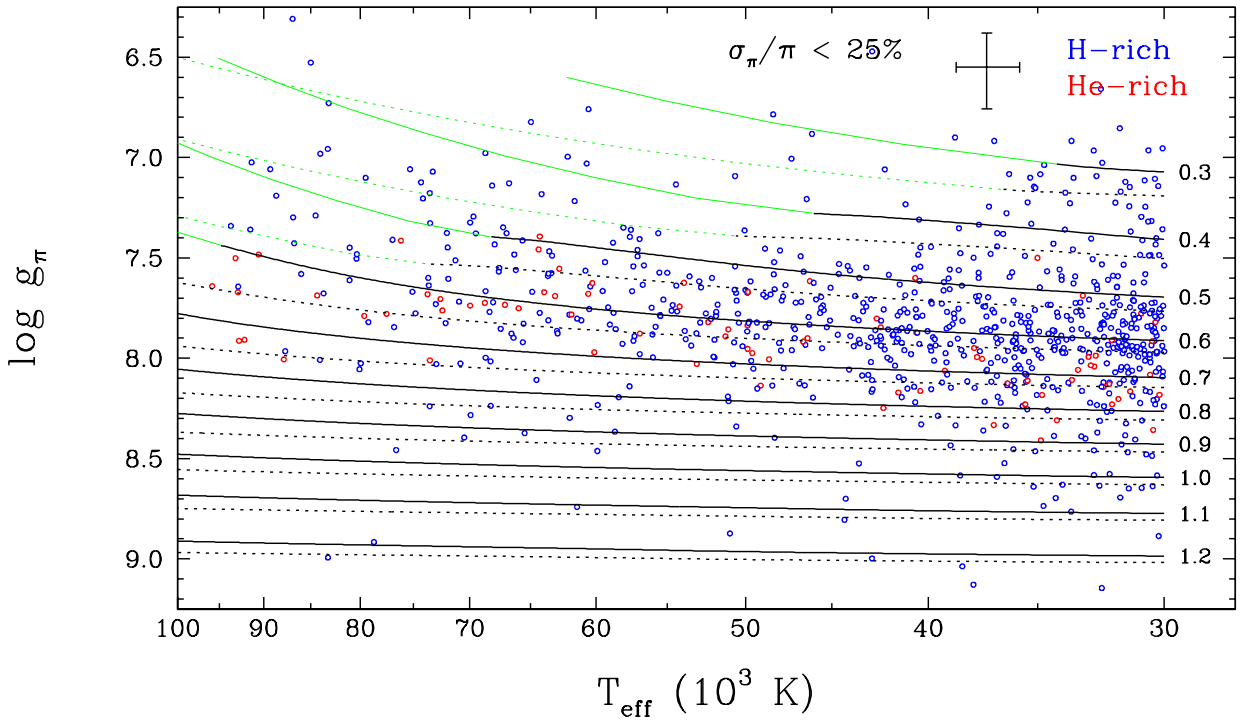

Figure 2.15 – Same as Figure 2.13, but for our subsample of 824 white dwarfs with $\sigma_\pi/\pi \leq 25\%$, and as determined from our photometric analysis.

as well), which were consequently excluded from the fits. Finally, we employed our evolutionary sequences to convert the inferred radius into surface gravity and mass, henceforth denoted as $\log g_\pi$ and M_π.

The results of this photometric analysis are presented in Figures 2.15 and 2.16, which are exactly analogous to Figures 2.13 and 2.14, but with $\log g_\pi$ and M_π in place of $\log g$ and M. This time, the hot DA and DO white dwarfs form a smooth, constant-mass extension of the low-temperature cooling sequence in the $\log g - T_{\rm eff}$ diagram. Accordingly, the high-temperature and low-temperature mass distributions are now in markedly better agreement, for both hydrogen-atmosphere and helium-atmosphere objects. We still notice a small average offset of $\sim$0.05 $M_\odot$ between the hot and cool helium-rich samples, but the corresponding histograms now largely overlap and have similar shapes, two notable improvements over the spectroscopic case. On another note, comparing the photometric and spectroscopic mass distributions in the low-temperature regime (where the reliability of our atmospheric parameters is likely highest), it can be seen that the two mass scales are shifted by $\sim$0.07 $M_\odot$ with respect to each other, for both DA and DO/DB stars. This disparity was already

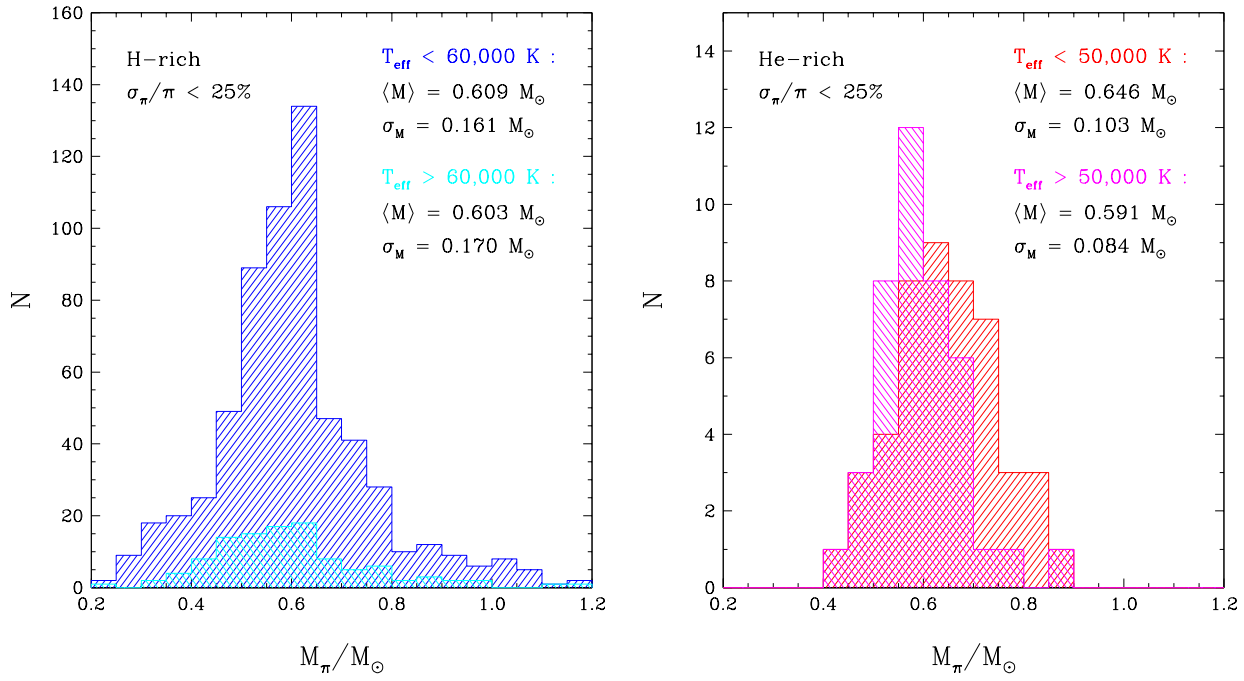

Figure 2.16 – Same as Figure 2.14, but for our subsample of 824 white dwarfs with $\sigma_\pi/\pi \leq 25\%$, and as determined from our photometric analysis.

exposed in previous investigations of SDSS white dwarfs and was attributed to problems in the calibration of the SDSS spectra causing the surface gravities measured spectroscopically to be slightly too low (Tremblay et al., 2011; Genest-Beaulieu & Bergeron, 2014, 2019a).

2.5.1.3. *Possible Error Sources*

The above test clearly demonstrates that the systematic shifts observed at the hot end of our spectroscopic $\log g - T_{\rm eff}$ diagram are not real. Then, what is wrong with the spectroscopic gravities and masses of very hot white dwarfs? The answer to this question is certainly not identical for DA and DO stars, because we found opposite trends for these two groups. Nevertheless, in both instances, the issue must be related to the spectral line profiles, as we showed that the overall energy distribution is not affected.

In the case of DA white dwarfs, valuable insight can be gained from a comparison with the work of Gianninas et al. (2010), who contrarily obtained normal surface gravities (see their Figure 14). There are two primary differences between their study and ours. First, they conducted their own spectroscopic survey and hence did not rely on SDSS observations. Second, thanks to their high-S/N spectra, they detected the Balmer-line problem in a

significant fraction of their objects with $T_{\rm eff} > 60{,}000$ K, which they consequently analyzed with CNO-rich model atmospheres. We believe that our use of both SDSS data and metal-free models contributed to the mass shift encountered here. First, as mentioned above, it is now well documented that the SDSS spectra suffer from a small calibration issue, which leads to slightly underestimated $\log g$ values. This effect is probably aggravated at higher temperatures by the lower sensitivity of the H I line profiles to the atmospheric parameters. Second, as discussed in Section 2.4, only 34% of our DA and DAO stars with $T_{\rm eff} > 60{,}000$ K exhibit the Balmer-line problem, but this proportion rises to 56% if we only consider objects with S/N > 30. Therefore, the presence of small amounts of atmospheric metals might be rather frequent among our hottest hydrogen-dominated white dwarfs, in line with the conclusions of FUV studies (Barstow et al., 2003b, 2014; Good et al., 2005). Yet the corresponding Balmer-line problem sometimes remains imperceptible, buried in the noise of the SDSS data, in which situation our analysis relying on hydrogen−helium models likely underevaluated the surface gravities. To further investigate this idea, we performed an experiment in which we fitted all of our hot DA and DAO spectra with the CNO-rich models of Gianninas et al. (2010). The outcome was that the high-temperature mean mass increased to $\langle M \rangle = 0.520\ M_{\odot}$, closer to (but still a bit lower than) the low-temperature mean mass of $\langle M \rangle = 0.540\ M_{\odot}$, in accordance with our expectations.

In the case of DO white dwarfs, the significantly too high $\log g$ values point to a severe problem in the modeling of He II line broadening. A simple explanation would be that the Stark broadening profiles of Schöning & Butler (1989), used in all modern analyses of DO stars, are inadequate for some unknown reason. There is, however, another conceivable possibility. As mentioned in Section 2.4, a nonnegligible fraction of the hottest helium-atmosphere white dwarfs show extremely broad and deep He II features stemming from an ultrahot circumstellar wind (Werner et al., 2018; Reindl et al., 2019). Given our results, it is tempting to generalize this concept and to suggest that most DO stars with $T_{\rm eff} \gtrsim 50{,}000$ K are afflicted by this phenomenon, albeit to a lower degree. The wind would then act as an additional line-broadening mechanism, obviously not included in our static model-atmosphere calculations and thus inducing a spuriously high surface gravity. Still, this interpretation seems a little far-fetched, and we believe that the current modeling of Stark broadening of He II features should be looked into first.

Given the above considerations about the surface gravities, one may legitimately ask, how trustworthy are the effective temperatures? This question is of fundamental importance for our forthcoming discussion of the spectral evolution of hot white dwarfs, which is largely based on our spectroscopically derived $T_{\rm eff}$ values. Several works have cast doubts on the accuracy of the temperature scale of very hot white dwarfs as measured from optical spectroscopy (Barstow et al. 1998, 2003a; Good et al. 2004; Werner et al. 2017, 2019; see also Latour et al. 2015 in the context of hot subdwarfs). Accordingly, we recognize that our effective temperatures probably suffer from sizable systematic errors in the range $T_{\rm eff} \gtrsim 75{,}000$ K, a caveat that we bear in mind when assessing the spectral evolution below. Nevertheless, we have good reasons to trust our effective temperatures in the range $T_{\rm eff} \lesssim 75{,}000$ K. In the case of DA stars, a comparison of Figures 2.13 and 2.15 indicates that the $\log g$ offset remains rather small and thus that our spectroscopic solutions are only marginally affected in this temperature regime. Moreover, while switching from CNO-free to CNO-rich models causes conspicuous changes in $\log g$, the corresponding changes in $T_{\rm eff}$ are typically minor (see Figure 11 of Gianninas et al. 2010). In the case of DO/DB stars, even if the $\log g$ shift is substantially worse, the effective temperatures are still robustly constrained by the simultaneous presence of He I and He II features in the optical spectra for $T_{\rm eff} \lesssim 75{,}000$ K. This is because the ionization balance of helium, which determines the relative strength of the two sets of lines, is strongly temperature dependent and weakly gravity dependent. As an illustrative experiment, if we fit a $T_{\rm eff} = 65{,}000$ K, $\log g = 7.8$, pure-helium synthetic spectrum with our full grid of pure-helium synthetic spectra while forcing the surface gravity to the much higher value $\log g = 8.2$, the resulting effective temperature is $T_{\rm eff} = 65{,}730$ K, only 1.1% higher than the true value. In short, despite the shortcomings of our analysis, we are confident that our spectroscopic temperature scale is reliable up to $T_{\rm eff} \sim 75{,}000$ K.

2.5.1.4. *Parameters of Hybrid White Dwarfs*

We end this subsection by addressing the properties of the hybrid white dwarfs in our sample. The location of these stars in the $\log g - T_{\rm eff}$ diagram is highlighted in Figure 2.17, where chemically homogeneous and stratified atmospheres are shown in blue and red, respectively. On one hand, the bulk of our homogeneous objects have hydrogen-rich atmospheres containing small traces of helium and populate the high-temperature, low-gravity part of the $\log g - T_{\rm eff}$ diagram. Those belong to the group of classical DAO white dwarfs, which

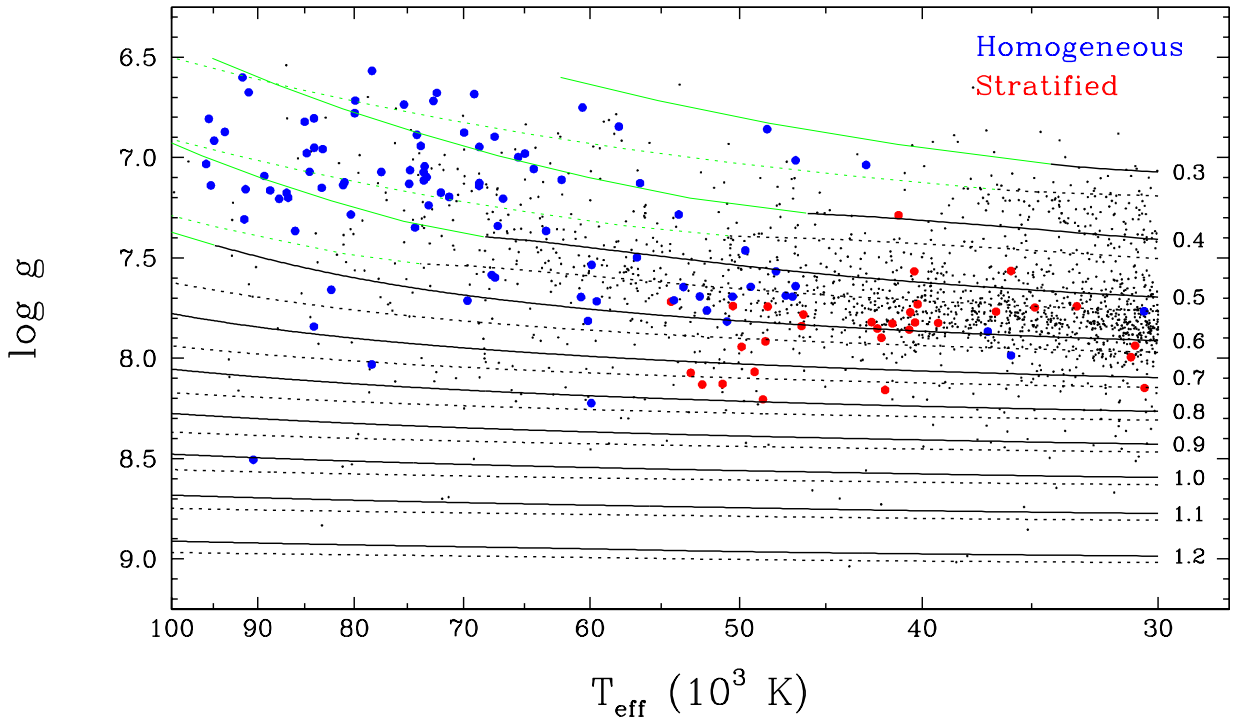

Figure 2.17 – Same as Figure 2.13, but with emphasis on the 125 single hybrid white dwarfs in our sample (we exclude the two double degenerate systems mentioned in Section 2.4). Objects with chemically homogeneous and stratified atmospheres are shown as large blue and red circles, respectively. For comparison purposes, the rest of the stars in our sample are represented as small black dots.

have been known for a long time and extensively studied over the years (Bergeron et al., 1994; Napiwotzki, 1999; Good et al., 2005; Gianninas et al., 2010; Tremblay et al., 2011; Kepler et al., 2019). Similarly to our hot DA stars, the surface gravities and masses of our hot homogeneous DAO stars are obviously underestimated. Nonetheless, we can still deduce from Figure 2.17 that these objects truly have mildly low masses in a relative sense (that is, compared to DA stars of the same temperature), a trend also noticed in most papers just cited. On the other hand, the stratified white dwarfs, which were discovered in significant numbers only recently by Manseau et al. (2016), are located in a completely different part of the $\log g - T_{\rm eff}$ diagram: they all have $T_{\rm eff} < 55{,}000$ K and more typical masses. Furthermore, as stated in Section 2.4, they are characterized by hydrogen-layer masses in the full range $-18.25 < \log q_{\rm H} < -15.25$ and hence exhibit all varieties of spectra from helium-line dominated (spectral type DOA/DBA) to hydrogen-line dominated (spectral type DAO/DAB).

This evidence strongly supports the idea that homogeneous and stratified white dwarfs form two fundamentally distinct populations, as pointed out by Manseau et al. (2016).

2.5.2. Spectral Evolution

We are now ready to address the central purpose of the paper, which is to improve our understanding of the spectral evolution of hot white dwarfs. To do so, we rely essentially on the effective temperatures and atmospheric compositions inferred from our spectroscopic analysis. Because we want our picture of the spectral evolution to be as faithful as possible, from now on we only consider the objects with S/N $\geq$ 10 (1467 out of 1806 stars), a restriction that offers a good compromise between the size and quality of the ensuing sample.

2.5.2.1. *Selection Bias Corrections*

Ideally, one could study the spectral evolution by simply counting the numbers of hydrogen-atmosphere and helium-atmosphere objects in several effective temperature bins and examining how these numbers change along the white dwarf cooling sequence. However, in the present work, there are two potentially important selection effects that might render this approach inadequate and therefore must be discussed before going further.

First, a possible variation of the SDSS spectroscopic completeness with temperature and/or composition could seriously distort the results. Fortunately for us, this is not an issue for our sample. By virtue of their very blue colors, most of our objects were likely observed as part of the so-called "hot-standard" target class of the SDSS, independently of their specific atmospheric properties (Eisenstein et al., 2006b). However, it is important to note that such a bias was actually induced by our own sample selection process. Indeed, it is well known that the hydrogen-deficient white dwarf population comprises not only the helium-rich DO stars, but also the helium-, carbon-, and oxygen-rich PG 1159 stars at the very hot end of the cooling sequence ($T_{\rm eff} \gtrsim$ 80,000 K; Werner & Herwig 2006). In our initial color-selected sample (see Section 2.2), we identified 17 PG 1159 stars but did not retain them in our final sample given that our hydrogen−helium model atmospheres are not appropriate for their analysis. In the following, we take these 17 objects into account by using atmospheric parameters from the literature (Dreizler & Heber, 1998; Hügelmeyer et al., 2006; Nagel et al., 2006; Werner et al., 2014; Kepler et al., 2016).

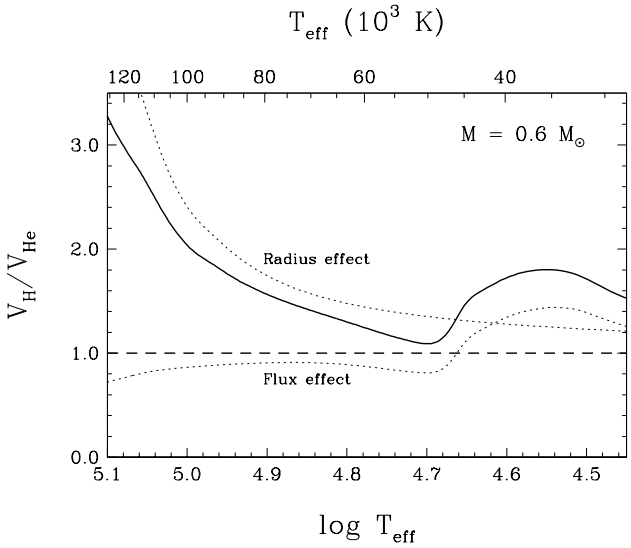

Figure 2.18 – Ratio of the volumes of space sampled by hydrogen-atmosphere and helium-atmosphere white dwarfs (with $M = 0.6\ M_{\odot}$) in a g-band magnitude-limited survey as a function of effective temperature. The dotted lines show the individual contributions of the flux and radius differences to the total ratio.

Second, because the SDSS is a magnitude-limited survey and because intrinsically brighter stars are more preferentially detected, hotter white dwarfs are inevitably overrepresented in our sample. This selection effect can be partly eliminated by working with fractions or ratios of objects rather than with absolute numbers, because at a given temperature, white dwarfs of different surface compositions have similar luminosities and are thus affected to a comparable extent by this bias. Consequently, we choose here to discuss the spectral evolution in terms of fractions of stars of some types (for instance, the fraction of helium-atmosphere white dwarfs). Still, these fractions must be corrected for the fact that hydrogen-rich and helium-rich white dwarfs with identical atmospheric parameters do not have strictly equal luminosities. This is because they do not have the same emergent fluxes (due to their different atmospheric opacities) and radii (due to their different hydrogen-layer masses). To account for this phenomenon, we rely on the so-called maximum-volume method (Schmidt, 1975). More specifically, we estimate the volumes $V_{\rm H}$ and $V_{\rm He}$ corresponding to the maximum distances at which DA and DO/DB stars of a given temperature would still be observed in a g-band magnitude-limited survey such as the SDSS. We use pure-hydrogen

atmospheres and thick-layer cooling tracks for the calculation of $V_{\rm H}$, whereas we use pure-helium atmospheres and thin-layer cooling tracks for the calculation of $V_{\rm He}$. We also simply assume $M = 0.6\ M_{\odot}$ throughout. The ratio $V_{\rm H}/V_{\rm He}$ of the volumes probed by each type of objects represents the quantitative factor by which the detection rates of hydrogen-dominated and helium-dominated white dwarfs are expected to differ. Figure 2.18 shows this ratio, as well as the individual contributions of the flux and radius effects mentioned above, as a function of effective temperature. The combination of both effects leads to $V_{\rm H}/V_{\rm He} > 1$ over the entire temperature range considered here, meaning that a DA star is always brighter and hence seen up to a farther distance than an analogous DO/DB star. To compensate for this bias, we assign a modified weight of $V_{\rm H}/V_{\rm He}$ to each helium-rich white dwarf, as opposed to a weight of 1 to each hydrogen-rich white dwarf, in our statistical analysis. See Eisenstein et al. (2006a), Tremblay & Bergeron (2008), and Blouin et al. (2019) for similar applications of this method.

2.5.2.2. *Constraints from Helium-rich White Dwarfs*

Figure 2.19 presents the fraction of helium-rich objects (corrected for the selection effects described above) as a function of decreasing effective temperature. Focusing first on the high-temperature part of the histogram, we notice that as much as $\sim$85$-$90% of white dwarfs have hydrogen-deficient atmospheres at the very beginning of the cooling sequence. Then, this proportion drops sharply to $\sim$25% below $T_{\rm eff} \sim$ 90,000 K. This glaring lack of extremely hot DA stars is a long-standing problem of spectral evolution theory (Fleming et al., 1986; Krzesinski et al., 2009; Werner et al., 2019). Taken at face value, this result seems to imply that the vast majority of all white dwarfs are initially born with helium-rich atmospheres, but then develop hydrogen-rich atmospheres quite early in their evolution through some mechanism, as originally suggested by Fontaine & Wesemael (1987). Nonetheless, this interpretation is rather doubtful for two reasons. First, as mentioned earlier, the temperature scale of these very hot objects suffer from significant uncertainties, which certainly impact the statistics reported in Figure 2.19, although to an unclear extent. Second, as proposed many years ago by Fleming et al. (1986) and more recently by Werner et al. (2019), the deficiency of DA white dwarfs with $T_{\rm eff} >$ 90,000 K might be an artifact of the different evolutionary rates of hydrogen-dominated and helium-dominated objects. Indeed,

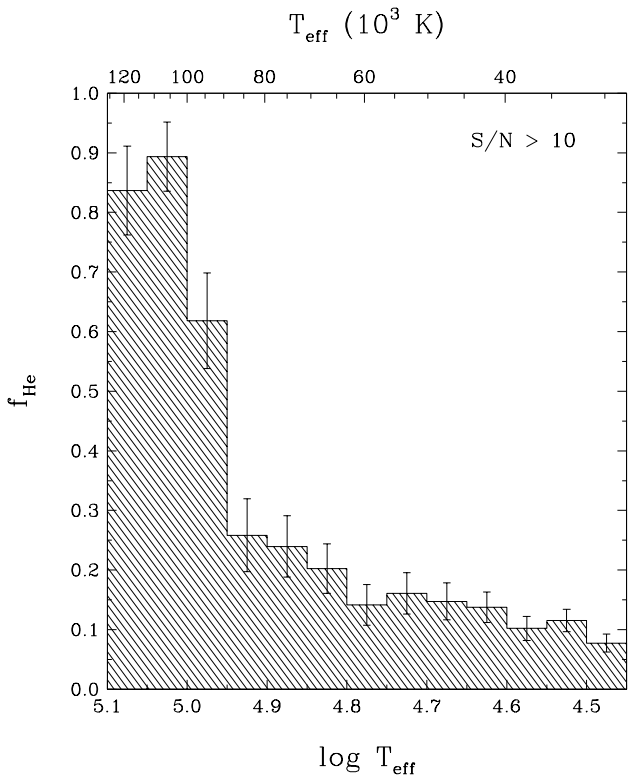

Figure 2.19 – Fraction of helium-rich white dwarfs (corrected for the selection effects discussed in the text) as a function of effective temperature for our subsample of 1467 objects with S/N $\geq$ 10. The error bars represent the Poisson statistics of each bin.

at the entrance of the cooling sequence, nuclear burning switches off more rapidly in hydrogen envelopes than in helium envelopes, causing the former to sustain a high luminosity for a shorter time than the latter (Iben & Tutukov, 1984). Therefore, it is entirely plausible that the apparent paucity of extremely hot hydrogen-rich white dwarfs is not due to some kind of atmospheric transformation, but rather to the fact that DA stars pass through this high-temperature phase faster than their DO (and PG 1159) counterparts[5]. We note in

5. According to this argument, our implicit assumption that the effective temperature is a good proxy for the cooling age in our discussion of the spectral evolution, although valid over most of the cooling sequence, fails for $T_{\rm eff} > 90{,}000$ K. However, using the cooling age as the independent variable is not a viable alternative, for several reasons: (1) our evolutionary tracks do not include residual nuclear burning and the associated difference in cooling rate between models with thick and thin hydrogen layers; (2) for very young white dwarfs ($\log \tau_{\rm cool} \lesssim 5$), our cooling ages are sensitive to the zero points defined by the initial models of our tracks; (3) because $\tau_{\rm cool}$ depends on both $T_{\rm eff}$ and $\log g$, the systematic errors on our surface gravities cast doubts on the reliability of our cooling ages at very high effective temperatures.

passing that such a difference in cooling timescale between hydrogen-envelope and helium-envelope pre-white dwarfs is actually predicted by the evolutionary calculations of Althaus et al. (2009b) and Renedo et al. (2010), as shown in Figure 11 of Werner et al. (2019). In the end, we simply refrain from drawing any firm conclusion on the spectral evolution based on our results at very high effective temperatures.

Fortunately, the statistics for cooler stars are not subject to these difficulties. As argued earlier, for $T_{\rm eff} \lesssim 75{,}000$ K, our temperature scale rests on more solid grounds. Moreover, at these temperatures, the cooling ages of hydrogen-rich and helium-rich white dwarfs become similar, as the longer evolutionary timescale makes the initial difference completely negligible. Thus, the fraction of helium-dominated objects at $T_{\rm eff} \sim 75{,}000$ K, which is $\sim$24% according to Figure 2.19, accurately reflects the actual population of very hot white dwarfs. In other words, we can confidently assert that $\sim$24% of all white dwarfs are born with hydrogen-deficient atmospheres.

Going down in effective temperature, we see in Figure 2.19 that the proportion of helium-rich white dwarfs gradually declines from $\sim$24% at $T_{\rm eff} \sim 75{,}000$ K to $\sim$8% at $T_{\rm eff} \sim 30{,}000$ K. In that respect, our results smoothly merge with those of Ourique et al. (2019, see their Figure 10) and Genest-Beaulieu & Bergeron (2019b, see their Figure 23) at lower temperatures. Unlike the sharp drop at $T_{\rm eff} \sim 90{,}000$ K, there are no reasons for this continuous decrease not to be real, which suggests that spectral evolution does occur here. More specifically, among the $\sim$24% of DO stars at $T_{\rm eff} \sim 75{,}000$ K, $\sim$1/3 remain helium rich while $\sim$2/3 become hydrogen rich by the time they reach $T_{\rm eff} \sim 30{,}000$ K. From the results of Ourique et al. (2019) and Genest-Beaulieu & Bergeron (2019b), we can even argue that those persisting DB stars at $T_{\rm eff} \sim 30{,}000$ K will always remain so at lower temperatures, because the fraction of helium-atmosphere white dwarfs does not decrease further for $T_{\rm eff} < 30{,}000$ K (it stays roughly constant down to $T_{\rm eff} \sim 20{,}000$ K and then increases). Our findings indicate that the concept of a DB gap, historically seen as a hole with sharp boundaries, must be definitely abandoned: this so-called gap not only contains a few DB stars, as first discovered by Eisenstein et al. (2006a), but also has a fuzzy blue edge, considering that the deficiency of helium-rich white dwarfs grows progressively over a very broad range of effective temperatures ($75{,}000$ K $> T_{\rm eff} > 30{,}000$ K).

The most likely physical explanation for the transformation of DO stars into DA stars is provided by the so-called float-up model of Fontaine & Wesemael (1987). This scenario begins with a PG 1159 star, whose peculiar surface chemistry is the result of a late helium-shell flash, during which the superficial hydrogen is deeply mixed in the helium envelope and almost entirely burned, while significant quantities of carbon and oxygen are dredged up to the surface (Herwig et al., 1999; Althaus et al., 2005b; Werner & Herwig, 2006). The basic assumption of Fontaine & Wesemael (1987) is that a small amount of hydrogen survives this event but initially remains undetectable, because it is diluted in the whole envelope. As gravitational settling starts to operate, carbon and oxygen rapidly sink out of the atmosphere, and the PG 1159 star becomes a DO white dwarf. Then, the residual hydrogen slowly diffuses upward and accumulates at the surface, building up a thicker and thicker superficial hydrogen layer, and eventually turning the DO star into a DA star.

Although the float-up model offers a relevant description of the DO-to-DA transition, we stress that some aspects of the original proposition of Fontaine & Wesemael (1987) no longer hold today. Based on the absence of DA stars with $T_{\rm eff} > 80{,}000$ K and of DB stars with $45{,}000\ {\rm K} > T_{\rm eff} > 30{,}000$ K in the PG survey, they argued that the entire white dwarf population descends from PG 1159 stars and undergoes the float-up of residual hydrogen. We now know that this is not the case. First, as discussed above, the deficiency of extremely hot hydrogen-rich white dwarfs is probably only apparent, and the true fraction of helium-rich white dwarfs at the beginning of the cooling sequence is likely closer to $\sim$24%. Second, the PG 1159 stars are not the sole precursors of DO stars. In fact, the helium-dominated white dwarf population is also fed by a second evolutionary channel associated with a different progenitor: the so-called O(He) stars, which display almost pure-helium atmospheres and are believed to be formed through merger or common-envelope processes (Rauch et al., 1998; Reindl et al., 2014a,b). Third, not all DO stars evolve into DA stars: $\sim$8% of all white dwarfs never become hydrogen-rich at any point during their life.

In the framework of the float-up model, the results presented in Figure 2.19 can be interpreted as follows. Among the DO stars at $T_{\rm eff} \sim 75{,}000$ K, $\sim$2/3 (or $\sim$16% of the whole white dwarf population) contain residual hydrogen that diffuses to the surface and turns them into DA stars before they reach $T_{\rm eff} \sim 30{,}000$ K, whereas the remaining $\sim$1/3 (or $\sim$8% of the whole white dwarf population) do not possess a sufficient amount of hydrogen for this

transformation to happen. The fact that the fraction of helium-dominated objects declines very gradually with decreasing effective temperature then suggests that a broad range of total hydrogen content exists within the DO/DB population. Qualitatively, the larger the quantity of residual hydrogen, the faster the float-up process, and the earlier the helium-to-hydrogen atmospheric transition. Quantitatively, estimating total hydrogen masses from our results would require detailed time-dependent simulations of diffusion in evolving white dwarfs. Indeed, when the spectral type of a star changes from DO to DA, it merely means that enough hydrogen has accumulated at the surface so as to enclose the full line-forming region, which corresponds to a lower limit of $q_{\rm H} \gtrsim 10^{-15}$. It is almost certain that much more hydrogen is still hidden deeper in the envelope, where the diffusion timescales are extremely long and the composition profile thereby remains far from diffusive equilibrium (Dehner & Kawaler, 1995; Althaus & Córsico, 2004; Rolland et al., 2020). This hydrogen reservoir, which can only be probed through theoretical calculations of gravitational settling, might play a fundamental role in the spectral evolution of cooler white dwarfs (Rolland et al., 2020).

As for the objects that always retain helium-rich atmospheres, there is simply no way to tell whether they represent the tail of the $q_{\rm H}$ distribution and thus contain hydrogen in an amount too small to ever be detected, as alleged by Koester & Kepler (2015), or arise from a distinct evolutionary path that made them completely devoid of hydrogen, as claimed by Bergeron et al. (2011). Nevertheless, it is interesting to note that our two groups of DO white dwarfs (those that eventually become hydrogen rich and those that do not) are somewhat reminiscent of the two known formation channels of DO white dwarfs, involving respectively the PG 1159 and O(He) stars. It is not unreasonable to speculate that the two types of progenitors lead to two different spectral evolution scenarios, with and without residual hydrogen.

It is worth mentioning that several works have attempted to infer the total hydrogen content of cooler degenerates from measured atmospheric compositions (MacDonald & Vennes, 1991; Tremblay & Bergeron, 2008; Koester & Kepler, 2015; Rolland et al., 2018, 2020; Genest-Beaulieu & Bergeron, 2019b; Cunningham et al., 2020; Koester et al., 2020). Briefly, the increase in the fraction of helium-atmosphere objects for 20,000 K $> T_{\rm eff} >$ 6000 K implies hydrogen masses in the range $10^{-16} < q_{\rm H} < 10^{-8}$ for $\sim$15$-$30% of all white dwarfs. If a

DA star is characterized by $q_{\rm H} \lesssim 10^{-14}$, it will transform into a DB star as a consequence of the so-called convective dilution process, by which the thin hydrogen layer is eroded from below by the much thicker convective helium envelope. Otherwise, a DA white dwarf still has the opportunity to develop a helium-rich atmosphere when the superficial hydrogen layer in turn becomes convective and mixes with the underlying helium mantle, a phenomenon referred to as convective mixing. The thicker the hydrogen layer, the lower the transition temperature, hence a range of $q_{\rm H}$ values translates into a range of $T_{\rm eff}$ values over which white dwarfs experience convective dilution or mixing. However, the quantitative results cited above must be taken with caution, because they were obtained under the questionable assumption that all the hydrogen has had enough time to float to the surface. Once again, we emphasize that this is likely not the case, given the very long diffusion timescales at the base of white dwarf envelopes. In fact, the parameter $q_{\rm H}$ reported in the literature should be viewed as the amount of hydrogen residing in the outer envelope at a given time and not as the total amount of hydrogen present in the star. Because of this widespread confusion, we refrain from further discussing the matter until the evolution of the inner chemical structure is better understood.

2.5.2.3. *Constraints from Hybrid White Dwarfs*

Finally, we turn our attention to the hybrid white dwarfs. Such objects represent direct manifestations of the atmospheric metamorphoses occurring along the cooling sequence and are therefore of central interest for the theory of the spectral evolution. Because chemically homogeneous and stratified atmospheres arise from different physical mechanisms, we consider these two groups of stars separately. We show in Figure 2.20 the fractions of homogeneous and stratified white dwarfs in our sample as a function of decreasing effective temperature. The statistics are corrected for the selection effects described above, under the assumption (motivated by our findings) of thick and thin hydrogen layers for the homogeneous and stratified objects, respectively. Note that Figures 2.19 and 2.20 use different horizontal and vertical scales; the histogram from the former is reproduced in the latter for ease of comparison.

The homogeneous white dwarfs, the bulk of which are DAO stars characterized by hydrogen-dominated atmospheres containing uniform traces of helium, exhibit a clear trend of declining incidence with decreasing effective temperature. They constitute more than

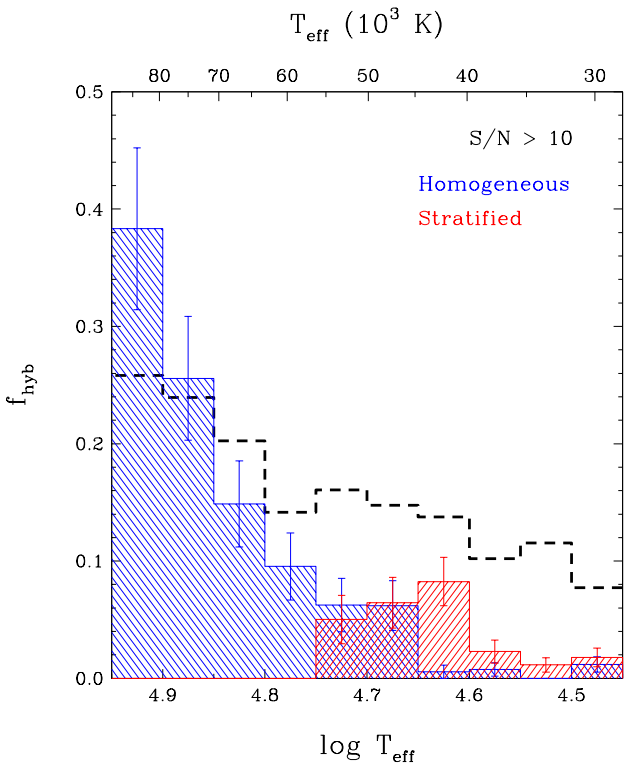

Figure 2.20 – Fraction of hybrid white dwarfs (corrected for the selection effects discussed in the text) as a function of effective temperature for our subsample of 1467 objects with S/N $\geq$ 10. The blue and red histograms correspond to stars with chemically homogeneous and stratified atmospheres, respectively. The error bars represent the Poisson statistics of each bin. For comparison purposes, the histogram of Figure 2.19 is reproduced here as the dashed black line.

one-third of the white dwarf population at $T_{\rm eff} > 80{,}000$ K (although the shortcomings associated with this temperature range should be kept in mind), whereas they exist in very small numbers at $T_{\rm eff} < 60{,}000$ K. The abrupt, continuous drop between the two regimes indicates that the physical process responsible for maintaining helium homogeneously in the outer hydrogen-rich layers rapidly becomes ineffective with cooling. The transport mechanism that best fits this description is a weak metal-driven stellar wind, as also alleged in previous studies of hot DAO white dwarfs (Bergeron et al., 1994; Napiwotzki, 1999; Gianninas et al., 2010). Furthermore, other properties of these objects are consistent with the wind hypothesis: they typically have low masses and high metal contents (resulting in severe forms of the Balmer-line problem), two factors that stimulate mass loss and thereby helium

contamination (Puls et al., 2000). The idea of a steadily fading wind also implies a correlation between the helium abundance and the luminosity, as observed by Napiwotzki (1999) and predicted by Unglaub & Bues (2000); we did not find such a correlation in our analysis, possibly because our ability to detect weak He II lines varies wildly from star to star, given the large range of S/N values among the SDSS spectra.

Anyhow, we reaffirm that residual stellar winds drive the spectral evolution of the hottest white dwarfs. At the beginning of the cooling sequence, trace species, that is, helium in hydrogen-rich objects as well as heavy elements in both hydrogen-rich and helium-rich objects, are supported uniformly in the outer envelope by this weak mass loss. Consequently, several members of the DA population (preferentially those with low masses and/or high primordial metal content) actually appear as homogeneous DAO stars. As the strength of metal-driven winds depends mostly on the luminosity (Puls et al., 2000), the cooling causes the wind to cease and thus the contaminants to settle: ultimately, homogeneous DAO stars become genuine DA stars. (Note that according to this interpretation, hybrid objects with homogeneous atmospheres should possess standard thick hydrogen layers, because they are the precursors of normal DA white dwarfs.) The calculations of Unglaub & Bues (2000) predict that this transition should happen at $T_{\rm eff} \sim 85{,}000$ K for normal-mass objects. The fact that we observe a few homogeneous DAO stars down to lower effective temperatures implies that a small number of white dwarfs have stronger winds than expected, perhaps because they hold larger amounts of primordial heavy elements. Besides, we note that the occurrence of mass loss in extremely hot white dwarfs is in agreement with our previous claim that the sharp drop in the fraction of helium-dominated atmospheres at $T_{\rm eff} \sim 90{,}000$ K seen in Figure 2.19 is not due to some sort of spectral evolution. Indeed, gravitational settling does not operate in presence of a wind, hence it is highly implausible that a large number of objects experience a sudden DO-to-DA transformation through the float-up of residual hydrogen at such a high temperature. For this reason, we believe that our estimate of $\sim$24% for the fraction of helium-rich stars at $T_{\rm eff} \sim 75{,}000$ K is likely representative of the hotter white dwarf population as well.

The stratified white dwarfs are of a markedly different nature than their homogeneous counterparts. Figure 2.20 shows that they are much rarer, which explains why only one such object (PG 1305$-$017) was known prior to the SDSS (Bergeron et al., 1994; Manseau et al.,

2016). They also tend to be cooler: they are all found in the effective temperature range where the fraction of helium-rich white dwarfs slowly decreases. Most importantly, the very fact that their atmospheres are chemically layered underlines that gravitational settling plays a dominant role here. Put together, these properties strongly suggest that stratified white dwarfs are transitional objects currently undergoing the DO-to-DA conversion, as advocated by Manseau et al. (2016) and references therein. They are DO stars caught in the process of turning into DA stars through the upward diffusion of residual hydrogen, at that short-lived moment when the newly formed superficial hydrogen layer is so thin that the underlying helium layer is still visible. With time, as more hydrogen initially diluted in the envelope reaches the surface, they will evolve into DA white dwarfs with thin hydrogen layers.

The existence of objects with stratified atmospheres constitutes another clear proof that spectral evolution takes place among hot white dwarfs. Furthermore, these snapshots of the float-up process are found over a broad range of effective temperatures, which confirms that the temperature of the DO-to-DA transformation can differ significantly from star to star. On this topic, we note that all of our stratified white dwarfs have $T_{\rm eff} < 55{,}000$ K, while we should also have discovered some with $75{,}000\ {\rm K} > T_{\rm eff} > 55{,}000$ K, given that we observe a decline in the fraction of helium-rich objects in this range as well. We believe that this nondetection is due to observational challenges rather than to a true absence. In fact, the spectroscopic distinction between homogeneous and stratified atmospheres becomes very subtle at high effective temperatures (see Figure 13 of Manseau et al. 2016). Therefore, it is possible that some hot hybrid stars classified as homogeneous in this work will turn out to be stratified when observed at higher S/N. Furthermore, detecting a small amount of hydrogen in a hot helium-rich atmosphere is a difficult task even at high S/N, given that each H I line is blended with a He II line (see Section 2.3). Yet another conceivable explanation would be that the DO-to-DA conversion occurs faster at higher temperatures, thus reducing our chances of catching it in the act.

2.6. Summary and Conclusion

We performed a comprehensive model-atmosphere analysis of 1806 hot ($T_{\rm eff} \geq 30{,}000$ K) white dwarfs, including 1638 DA, 95 DO, and 73 DB stars, observed spectroscopically by the SDSS. We first presented new non-LTE model atmospheres and synthetic spectra

computed with the codes TLUSTY and SYNSPEC, in which we implemented for the first time the detailed He I line profiles of Beauchamp et al. (1997). We also introduced our next generation of evolutionary cooling sequences, which now extend to much higher effective temperatures and make use of more recent conductive opacities compared to our previous calculations. Our model atmospheres allowed us to analyze the SDSS optical spectra of all the objects in our sample and thus to homogeneously determine their atmospheric parameters, which were then converted into stellar parameters through our cooling tracks.

At low effective temperature, most hydrogen-rich and helium-rich white dwarfs form a tight sequence around $M \sim 0.55\ M_{\odot}$ in the $\log g - T_{\rm eff}$ diagram, with the exception of a few low-mass DA stars likely produced through common-envelope evolution. At high effective temperature, we found that the accuracy of the spectroscopic mass scale is compromised by significant systematic errors. On one hand, DA stars with $T_{\rm eff} \gtrsim 60{,}000$ K have lower-than-average masses, an effect that is possibly due to an improper calibration of the SDSS spectroscopic data as well as to the undetected presence of atmospheric metals in some objects. On the other hand, DO stars with $T_{\rm eff} \gtrsim 50{,}000$ K suffer from an opposite and even more severe problem, their masses being much too high, which we tentatively attributed to issues in the current modeling of He II line broadening.

Furthermore, we identified 127 white dwarfs exhibiting hybrid spectra, which we analyzed with two types of model atmospheres, assuming respectively homogeneous and stratified distributions of hydrogen and helium. We uncovered signs of atmospheric chemical stratification in 31 objects, thereby doubling the number of such white dwarfs known. We provided strong support to the idea that homogeneous and stratified objects constitute two fundamentally distinct groups, the former typically being considerably hotter and slightly less massive than the latter.

On the basis of our results, we were able to establish an exhaustive picture of the spectral evolution of hot white dwarfs, placing improved quantitative constraints on the theory of spectral evolution. In particular, we are now in position to address the many outstanding questions raised in the Introduction:

(1) What fraction of all white dwarfs are born with a helium atmosphere? At $T_{\rm eff} \sim 75{,}000$ K, $\sim$24% of white dwarfs are characterized by a helium-dominated surface composition. At the very highest effective temperatures ($T_{\rm eff} > 90{,}000$ K), this proportion is

markedly larger, but we believe this to be an artifact of the different cooling rates of extremely hot hydrogen-rich and helium-rich objects. This interpretation is consistent with the occurrence, at the very beginning of the cooling sequence, of weak stellar winds preventing any major changes in atmospheric composition. Our statistics at $T_{\rm eff} \sim 75{,}000$ K are not affected by the above-mentioned evolutionary effect and are therefore more representative of the actual population of hot white dwarfs. In essence, our findings indicate that approximately one in four white dwarfs are born hydrogen deficient.

(2) Among those, how many eventually develop a hydrogen-rich atmosphere, and how many retain a helium-rich atmosphere throughout their life? The fraction of helium-dominated white dwarfs gradually decreases from $\sim$24% at $T_{\rm eff} \sim 75{,}000$ K to $\sim$8% at $T_{\rm eff} \sim 30{,}000$ K. From this result, it can be deduced that $\sim$2/3 of the DO stars turn into DA stars through the float-up of residual hydrogen before they cool down to $T_{\rm eff} \sim 30{,}000$ K, and that the transformation takes place at different effective temperatures for different objects, depending on their total hydrogen content. As for the remaining $\sim$1/3, they most likely do not contain enough residual hydrogen for the DO-to-DA transition to happen and thus preserve a helium-dominated surface composition throughout their whole life. These two spectral evolution channels account for $\sim$16% and $\sim$8% of the total white dwarf population, respectively.

(3) How does the number of hybrid white dwarfs, both with homogeneous and stratified atmospheres, vary with effective temperature? On one hand, homogeneous objects exist abundantly at $T_{\rm eff} > 80{,}000$ K, where they represent more than one-third of our white dwarf sample. This proportion drops sharply with decreasing effective temperature, so that they become rather uncommon among cooler stars. On the other hand, stratified objects, which are intrinsically rarer than their homogeneous counterparts, concentrate mostly in the range $55{,}000 \text{ K} > T_{\rm eff} > 40{,}000$ K, where they constitute $\sim$5$-$10% of the white dwarf population, but a few of them are found down to $T_{\rm eff} \sim 30{,}000$ K as well.

(4) What does this imply about the role of stellar winds and the helium-to-hydrogen transition? In the case of the very hot DAO stars with homogeneous atmospheres, the trend uncovered in our study confirms that residual stellar winds govern the spectral

appearance of the hottest white dwarfs. In particular, a weak mass loss initially causes small amounts of helium and heavier elements to be maintained uniformly in the external layers of hydrogen-rich objects, perhaps more efficiently in those having lower masses and/or higher metal contents. As cooling proceeds and winds accordingly fade, the trace species sink, thereby turning DAO stars into typical DA stars. For their part, the cooler white dwarfs showing stratified atmospheres are transitional objects in the process of undergoing the DO-to-DA conversion through the float-up of residual hydrogen. Their existence over a broad range of effective temperatures corroborates our assertion that the timing of this transformation varies substantially from one star to another.

(5) What is the total hydrogen content of these various groups of white dwarfs, and how will it impact their future spectral evolution? The total masses of hydrogen characterizing the white dwarf population and giving rise to the observed spectral evolution cannot be precisely determined from our analysis alone. We may, however, speculate on the future spectral evolution specific to each channel identified here by connecting our findings to those obtained at lower effective temperatures ($T_{\rm eff} < 30{,}000$ K). Approximately three in four white dwarfs are born as DA stars (or DAO stars if their wind is strong enough) and most likely possess canonical thick hydrogen layers ($q_{\rm H} \sim 10^{-4}$). Because no physical mechanism can alter such massive hydrogen layers along the cooling sequence, these objects will retain a hydrogen-dominated surface composition throughout their entire life (Tremblay & Bergeron, 2008; Rolland et al., 2018; Cunningham et al., 2020). The remaining one in four white dwarfs are born as DO stars with much smaller amounts of hydrogen, which probably span many orders of magnitude. Most of them have enough hydrogen to transform into DA stars as a consequence of gravitational settling, but this state is only temporary. If the superficial hydrogen layer is sufficiently thin ($q_{\rm H} \lesssim 10^{-14}$), the convective dilution process will make the outer envelope helium rich again before the star reaches $T_{\rm eff} \sim 15{,}000$ K, and the spectral type will accordingly change to DB or DBA, and later on to DC (MacDonald & Vennes, 1991; Bergeron et al., 2011; Koester & Kepler, 2015; Rolland et al., 2018, 2020; Genest-Beaulieu & Bergeron, 2019b). Otherwise ($q_{\rm H} \gtrsim 10^{-14}$), the

white dwarf will still develop a helium-dominated atmosphere at a lower effective temperature via the convective mixing process, hence directly turning into a DC star or a helium-rich DA star (MacDonald & Vennes, 1991; Tremblay & Bergeron, 2008; Chen & Hansen, 2011; Rolland et al., 2018; Blouin et al., 2019; Cunningham et al., 2020). Finally, it is believed that those DO white dwarfs that are almost completely devoid of hydrogen will preserve essentially pure-helium atmospheres down to $T_{\rm eff} \sim 10{,}000$ K, at which point they will evolve into DQ stars through the convective dredge-up of primordial carbon (Pelletier et al., 1986; Dufour et al., 2005; Koester & Knist, 2006; Koester & Kepler, 2019; Koester et al., 2020; Coutu et al., 2019).

It is not an exaggeration to say that the spectral evolution of white dwarfs is now very well characterized from an empirical perspective, largely thanks to the advent of the SDSS and more recently of the Gaia mission. For this reason, we feel that the time is ripe for advances on the theoretical front, more specifically in the modeling of the dynamical phenomena invoked to explain the spectral evolution. This endeavor will require full-fledged evolutionary calculations, in which the appropriate chemical transport mechanisms (such as gravitational settling, convective mixing, and stellar winds, just to name a few) are self-consistently coupled to the cooling of a white dwarf. Only through such simulations will we gain the ability to answer the fundamental question at the center of spectral evolution theory: how much hydrogen is there in white dwarfs?

Acknowledgements

This work was supported by the Natural Sciences and Engineering Research Council (NSERC) of Canada and the Fonds de Recherche du Québec − Nature et Technologie (FRQNT).

Funding for the Sloan Digital Sky Survey (https://www.sdss.org) has been provided by the Alfred P. Sloan Foundation, the U.S. Department of Energy Office of Science, and the Participating Institutions. SDSS-IV acknowledges support and resources from the Center for High-Performance Computing at the University of Utah and is managed by the Astrophysical Research Consortium for the Participating Institutions of the SDSS Collaboration (Blanton et al., 2017).

This work has made use of data from the European Space Agency mission Gaia (https://www.cosmos.esa.int/gaia), processed by the Gaia Data Processing and Analysis Consortium (DPAC). Funding for the DPAC has been provided by national institutions, in particular the institutions participating in the Gaia Multilateral Agreement (Gaia Collaboration et al., 2018a).

This research has also made use of the NASA Astrophysics Data System Bibliographic Services; the Montreal White Dwarf Database (Dufour et al., 2017); the SIMBAD database, operated at the Centre de Données astronomiques de Strasbourg (Wenger et al., 2000); and the NASA/IPAC Infrared Science Archive, operated at the California Institute of Technology.

Appendix: Atmospheric and Stellar Parameters

Table 2.1 – Atmospheric and stellar parameters of hot white dwarfs from SDSS DR12

SDSS Name	Type	S/N	$T_{\rm eff}$ (K)	$\log g$	Composition	$M/M_{\odot}$	$R/R_{\odot}$	$\log L/L_{\odot}$	$\log \tau_{\rm cool}$	Notes
J000007.16−094339.9	DA	6.4	30,469 (866)	7.64 (0.22)	Pure H	0.48 (0.09)	0.0174 (0.0029)	−0.63 (0.15)	6.85 (0.17)	
J000310.36+071801.1	DA	33.8	30,532 (191)	7.87 (0.05)	Pure H	0.58 (0.02)	0.0146 (0.0005)	−0.78 (0.03)	6.92 (0.01)	
J000419.93+235000.2	DA	14.9	38,163 (1447)	7.70 (0.19)	Pure H	0.52 (0.08)	0.0169 (0.0025)	−0.26 (0.15)	6.59 (0.12)	
J000509.93+003809.6	DO	35.2	51,049 (564)	8.17 (0.11)	Pure He	0.74 (0.06)	0.0117 (0.0009)	−0.07 (0.07)	6.28 (0.04)	
J000622.61+010958.8	DA	29.6	38,060 (578)	7.67 (0.08)	Pure H	0.51 (0.03)	0.0174 (0.0010)	−0.24 (0.06)	6.58 (0.07)	
J000733.15−092121.0	DA	4.8	31,087 (1325)	7.90 (0.32)	Pure H	0.60 (0.16)	0.0143 (0.0035)	−0.76 (0.22)	6.90 (0.14)	
J000739.68+244534.7	DA	6.1	46,253 (5478)	7.59 (0.47)	Pure H	0.51 (0.18)	0.0189 (0.0071)	0.17 (0.39)	6.23 (0.43)	
J000825.77−054122.3	DA	17.0	44,257 (2098)	7.61 (0.19)	Pure H	0.51 (0.07)	0.0185 (0.0029)	0.07 (0.16)	6.32 (0.27)	
J000829.71+245900.8	DA	14.0	34,208 (776)	7.54 (0.14)	Pure H	0.45 (0.05)	0.0190 (0.0021)	−0.35 (0.10)	6.57 (0.26)	
J001043.54+253829.1	DA	42.0	32,874 (217)	7.79 (0.04)	Pure H	0.55 (0.02)	0.0156 (0.0005)	−0.59 (0.03)	6.81 (0.01)	
J001053.41+251207.3	DA	7.5	45,519 (4257)	7.61 (0.37)	Pure H	0.51 (0.14)	0.0185 (0.0055)	0.12 (0.31)	6.29 (0.33)	
J001137.32−102509.1	DA	6.0	36,594 (2721)	7.64 (0.40)	Pure H	0.50 (0.16)	0.0177 (0.0055)	−0.30 (0.30)	6.60 (0.25)	
J001529.74+010521.3	DB	28.4	39,203 (913)	7.79 (0.09)	Pure He	0.53 (0.04)	0.0153 (0.0010)	−0.30 (0.07)	6.62 (0.05)	
J001549.43+245604.8	DA	38.1	37,396 (467)	7.81 (0.07)	Pure H	0.57 (0.03)	0.0156 (0.0008)	−0.37 (0.05)	6.65 (0.02)	
J001601.43+260217.8	DO	66.4	93,153 (4152)	8.09 (0.12)	Pure He	0.75 (0.06)	0.0129 (0.0014)	1.05 (0.12)	5.54 (0.09)	
J001749.24−000955.5	DA+M	55.6	54,642 (2093)	7.64 (0.14)	Pure H	0.55 (0.05)	0.0186 (0.0021)	0.44 (0.12)	6.10 (0.20)	1,2
J002153.32+083141.9	DBA	20.3	30,854 (2262)	7.94 (0.12)	$\log q_{\rm H} = -18.13$	0.58 (0.06)	0.0136 (0.0012)	−0.82 (0.15)	6.95 (0.11)	3
J002203.58+152908.0	DA	34.2	48,386 (1240)	7.55 (0.10)	Pure H	0.50 (0.03)	0.0197 (0.0016)	0.28 (0.08)	6.05 (0.35)	
J002223.92−000324.1	DA	6.3	31,214 (1253)	7.33 (0.30)	Pure H	0.38 (0.09)	0.0221 (0.0049)	−0.38 (0.21)	6.14 (0.97)	
J002227.79+151920.9	DA	61.8	31,430 (107)	8.21 (0.03)	Pure H	0.77 (0.01)	0.0114 (0.0002)	−0.94 (0.02)	6.98 (0.03)	
J002534.73−102426.6	DA	7.2	31,208 (1076)	7.25 (0.26)	Pure H	0.36 (0.08)	0.0234 (0.0044)	−0.33 (0.18)	5.75 (0.96)	
J002545.95+161435.0	DA	19.5	38,683 (908)	7.83 (0.12)	Pure H	0.58 (0.05)	0.0154 (0.0014)	−0.32 (0.09)	6.61 (0.03)	
J002844.19+241511.1	DAO	44.2	77,399 (5185)	7.07 (0.16)	$\log N_{\rm He}/N_{\rm H} = -2.16$	0.45 (0.04)	0.0325 (0.0049)	1.53 (0.18)	<5.00	4,5
J003005.38−001949.0	DA+M	20.5	66,837 (4550)	6.98 (0.20)	Pure H	0.40 (0.05)	0.0339 (0.0059)	1.31 (0.20)	<5.00	1
J003122.28+080920.3	DA	9.3	45,031 (3536)	8.14 (0.32)	Pure H	0.75 (0.17)	0.0122 (0.0031)	−0.26 (0.26)	6.39 (0.10)	
J003211.99+004843.0	DA	22.5	30,153 (293)	7.81 (0.08)	Pure H	0.55 (0.04)	0.0153 (0.0009)	−0.76 (0.05)	6.93 (0.02)	
J003306.20+153627.5	DA	4.0	34,781 (2750)	8.06 (0.48)	Pure H	0.69 (0.25)	0.0128 (0.0048)	−0.67 (0.35)	6.74 (0.34)	
J003343.05+142251.4	DBA	43.9	40,593 (1051)	7.77 (0.09)	$\log q_{\rm H} = -16.87$	0.52 (0.04)	0.0156 (0.0010)	−0.22 (0.07)	6.57 (0.07)	3
J003445.36+152456.7	DA	6.9	31,754 (971)	7.57 (0.22)	Pure H	0.46 (0.08)	0.0184 (0.0031)	−0.51 (0.16)	6.73 (0.27)	
J003512.75+003738.1	DA	5.3	33,513 (1852)	7.88 (0.36)	Pure H	0.59 (0.17)	0.0146 (0.0040)	−0.62 (0.26)	6.79 (0.16)	
J003602.59+070047.1	DA+M	43.1	32,636 (278)	7.93 (0.06)	Pure H	0.61 (0.03)	0.0141 (0.0006)	−0.69 (0.04)	6.83 (0.01)	1,2
J003925.22+254823.6	DA+M	52.6	35,986 (327)	7.82 (0.05)	Pure H	0.57 (0.02)	0.0153 (0.0006)	−0.45 (0.04)	6.70 (0.01)	1
J004054.80+235044.8	DA	39.9	36,908 (423)	7.23 (0.06)	Pure H	0.36 (0.02)	0.0242 (0.0010)	−0.01 (0.04)	5.11 (0.32)	
J004123.98+070819.1	DA	6.6	32,967 (1672)	7.71 (0.34)	Pure H	0.51 (0.14)	0.0166 (0.0044)	−0.53 (0.24)	6.78 (0.16)	
J004138.68+151105.0	DA+M	8.1	35,236 (1904)	7.42 (0.32)	Pure H	0.42 (0.10)	0.0210 (0.0050)	−0.21 (0.23)	6.21 (0.99)	1
J004537.46+010700.2	DA	16.5	31,029 (491)	7.98 (0.12)	Pure H	0.64 (0.06)	0.0135 (0.0012)	−0.82 (0.08)	6.91 (0.03)	
J005011.78+135612.6	DA	19.1	39,615 (1084)	7.64 (0.13)	Pure H	0.51 (0.05)	0.0178 (0.0018)	−0.15 (0.10)	6.50 (0.16)	
J005149.40+064705.9	DA	30.8	42,295 (986)	7.82 (0.10)	Pure H	0.58 (0.04)	0.0156 (0.0012)	−0.15 (0.08)	6.50 (0.03)	
J005443.83+070921.2	DA+M	26.6	32,636 (324)	7.67 (0.07)	Pure H	0.50 (0.03)	0.0170 (0.0009)	−0.53 (0.05)	6.78 (0.04)	1
J005510.54+010838.3	DA+M	9.6	33,411 (948)	8.06 (0.19)	Pure H	0.69 (0.10)	0.0128 (0.0018)	−0.74 (0.13)	6.80 (0.06)	1
J005540.12−100643.3	DA+M	15.2	76,988 (8049)	7.17 (0.29)	Pure H	0.47 (0.07)	0.0294 (0.0077)	1.44 (0.30)	<5.00	1
J005547.78−084507.2	DA	72.9	76,903 (2514)	7.21 (0.08)	Pure H	0.48 (0.02)	0.0284 (0.0020)	1.41 (0.09)	<5.00	5
J010322.19−002047.7	DA	24.7	60,442 (2730)	7.70 (0.16)	Pure H	0.58 (0.05)	0.0178 (0.0024)	0.58 (0.14)	6.03 (0.14)	
J010530.28+004009.9	DA	53.6	61,988 (1464)	7.41 (0.08)	Pure H	0.49 (0.03)	0.0229 (0.0014)	0.85 (0.07)	<5.00	
J010946.99−090742.1	DA	49.7	51,935 (1039)	7.68 (0.07)	Pure H	0.55 (0.03)	0.0178 (0.0011)	0.32 (0.06)	6.20 (0.06)	

Table 2.1 – Atmospheric and stellar parameters of hot white dwarfs from SDSS DR12 (continued)

SDSS Name	Type	S/N	$T_{\rm eff}$ (K)	$\log g$	Composition	$M/M_{\odot}$	$R/R_{\odot}$	$\log L/L_{\odot}$	$\log \tau_{\rm cool}$	Notes
J011042.01−010839.3	DA+M	22.5	60,419 (2689)	7.54 (0.15)	Pure H	0.53 (0.05)	0.0205 (0.0026)	0.70 (0.14)	5.74 (0.58)	1,2
J011206.92+272743.2	DA	16.2	38,049 (985)	7.87 (0.13)	Pure H	0.60 (0.06)	0.0149 (0.0015)	−0.38 (0.10)	6.63 (0.03)	
J011346.77+002828.6	DOZ	116.2	67,057 (637)	8.02 (0.06)	Pure He	0.69 (0.03)	0.0134 (0.0006)	0.51 (0.04)	6.02 (0.02)	6
J011447.52+254229.7	DA+M	69.0	35,505 (215)	7.76 (0.04)	Pure H	0.54 (0.02)	0.0161 (0.0004)	−0.43 (0.03)	6.71 (0.01)	1,2
J011622.02+261112.3	DA	11.8	44,957 (2864)	7.55 (0.26)	Pure H	0.49 (0.09)	0.0195 (0.0040)	0.15 (0.21)	6.14 (0.62)	
J011650.71+202253.1	DA+M	23.6	70,059 (4155)	6.79 (0.15)	Pure H	0.37 (0.03)	0.0404 (0.0054)	1.55 (0.17)	<5.00	1
J011923.88+401212.7	DA	5.9	37,125 (3160)	7.41 (0.44)	Pure H	0.42 (0.14)	0.0213 (0.0072)	−0.11 (0.33)	6.04 (1.21)	7
J012003.60+392141.6	DA	12.6	37,489 (1243)	7.46 (0.17)	Pure H	0.44 (0.06)	0.0204 (0.0027)	−0.13 (0.13)	6.23 (0.57)	
J012039.72+383934.0	DA	19.6	43,620 (1367)	7.38 (0.13)	Pure H	0.43 (0.04)	0.0222 (0.0022)	0.20 (0.10)	5.47 (0.65)	2
J012158.41+381346.6	DA	17.7	37,103 (931)	7.64 (0.13)	Pure H	0.50 (0.05)	0.0176 (0.0018)	−0.28 (0.10)	6.59 (0.14)	
J012339.94+405241.9	DA	6.0	39,559 (2892)	7.50 (0.34)	Pure H	0.46 (0.12)	0.0199 (0.0052)	−0.06 (0.26)	6.23 (0.76)	
J012341.91+383810.6	DA+M	9.8	32,072 (860)	7.82 (0.19)	Pure H	0.56 (0.09)	0.0153 (0.0022)	−0.65 (0.13)	6.85 (0.06)	1
J012344.77−084208.6	DA	16.7	51,080 (2658)	7.51 (0.19)	Pure H	0.49 (0.06)	0.0205 (0.0031)	0.41 (0.16)	5.80 (0.82)	
J012517.87+080657.6	DA	32.9	31,340 (240)	8.04 (0.06)	Pure H	0.67 (0.03)	0.0129 (0.0005)	−0.84 (0.04)	6.90 (0.02)	
J012828.98+385436.5	DA	91.2	68,247 (1336)	8.00 (0.06)	Pure H	0.72 (0.03)	0.0140 (0.0007)	0.59 (0.06)	5.91 (0.03)	5
J012959.98+231211.1	DA	25.6	41,366 (956)	7.71 (0.10)	Pure H	0.54 (0.04)	0.0169 (0.0014)	−0.12 (0.08)	6.51 (0.07)	
J013112.65−095819.9	DA	22.8	30,269 (313)	7.85 (0.08)	Pure H	0.57 (0.04)	0.0148 (0.0009)	−0.78 (0.06)	6.93 (0.02)	
J013215.36+144755.9	DA	18.3	32,067 (510)	7.52 (0.11)	Pure H	0.44 (0.04)	0.0191 (0.0017)	−0.46 (0.08)	6.66 (0.18)	
J013314.21+235247.3	DOZ	16.2	70,658 (5420)	8.10 (0.44)	Pure He	0.73 (0.21)	0.0126 (0.0046)	0.55 (0.34)	5.93 (0.19)	6
J013328.62+142459.4	DA+M	24.5	38,475 (816)	7.96 (0.11)	Pure H	0.64 (0.05)	0.0139 (0.0011)	−0.42 (0.08)	6.61 (0.03)	1
J013348.55+001649.7	DA	28.4	34,763 (391)	7.84 (0.07)	Pure H	0.57 (0.03)	0.0151 (0.0008)	−0.52 (0.05)	6.75 (0.02)	
J013428.72+232119.8	DAO	23.8	46,686 (1649)	7.64 (0.16)	$\log N_{\rm He}/N_{\rm H} = -1.06$	0.52 (0.06)	0.0181 (0.0024)	0.15 (0.13)	6.30 (0.18)	4
J013443.62−093807.6	DA	10.9	43,930 (2765)	8.06 (0.26)	Pure H	0.70 (0.14)	0.0130 (0.0027)	−0.25 (0.21)	6.44 (0.08)	
J013518.24+065324.8	DA	34.7	32,439 (250)	7.82 (0.05)	Pure H	0.56 (0.02)	0.0153 (0.0006)	−0.63 (0.04)	6.83 (0.01)	
J013812.73+010350.7	DA	38.7	73,989 (4051)	7.09 (0.12)	Pure H	0.45 (0.03)	0.0317 (0.0037)	1.43 (0.15)	<5.00	5
J013920.41+131120.7	DA	22.7	61,957 (2903)	7.36 (0.15)	Pure H	0.47 (0.05)	0.0239 (0.0030)	0.88 (0.14)	<5.00	
J014019.09+134142.2	DA	17.6	36,021 (876)	7.75 (0.14)	Pure H	0.54 (0.06)	0.0162 (0.0017)	−0.40 (0.10)	6.69 (0.06)	
J014024.08−090814.7	DAO	20.8	84,767 (12,460)	6.98 (0.36)	$\log N_{\rm He}/N_{\rm H} = -1.19$	0.46 (0.09)	0.0364 (0.0123)	1.79 (0.41)	<5.00	4
J014259.20−102225.0	DA	31.9	32,403 (326)	7.19 (0.07)	Pure H	0.34 (0.02)	0.0245 (0.0012)	−0.22 (0.05)	5.35 (0.32)	
J014523.66+234239.4	DA	30.3	31,200 (246)	8.36 (0.06)	Pure H	0.86 (0.04)	0.0101 (0.0005)	−1.06 (0.04)	7.26 (0.13)	
J015037.49+223259.5	DA	30.0	37,355 (573)	7.23 (0.08)	Pure H	0.36 (0.03)	0.0243 (0.0014)	0.01 (0.06)	5.07 (0.42)	
J015221.11−003037.3	DA	36.1	35,984 (356)	7.87 (0.06)	Pure H	0.59 (0.03)	0.0148 (0.0006)	−0.48 (0.04)	6.70 (0.01)	
J015329.95+054531.7	DA	104.1	36,106 (135)	7.77 (0.02)	Pure H	0.55 (0.01)	0.0160 (0.0003)	−0.41 (0.02)	6.69 (0.01)	
J015445.79+142412.8	DA	4.6	36,766 (2932)	7.09 (0.43)	Pure H	0.32 (0.11)	0.0268 (0.0090)	0.07 (0.32)	<5.00	
J015939.47−005415.9	DA	33.6	56,879 (1591)	7.51 (0.10)	Pure H	0.51 (0.03)	0.0207 (0.0016)	0.61 (0.09)	5.75 (0.50)	
J020127.21+234952.7	DO	69.2	77,473 (2738)	7.70 (0.16)	Pure He	0.58 (0.06)	0.0178 (0.0024)	1.01 (0.13)	5.72 (0.19)	8
J020245.67+122201.4	DA	19.2	57,426 (3186)	7.32 (0.19)	Pure H	0.44 (0.06)	0.0241 (0.0038)	0.76 (0.17)	<5.00	
J020326.13+223828.1	DA	11.8	30,106 (441)	7.97 (0.12)	Pure H	0.63 (0.06)	0.0136 (0.0012)	−0.87 (0.08)	6.95 (0.03)	
J020847.63+224814.4	DA+M	14.5	48,850 (2702)	7.71 (0.21)	Pure H	0.56 (0.08)	0.0172 (0.0030)	0.18 (0.18)	6.30 (0.15)	1
J020848.27+121332.6	DA	15.5	30,416 (517)	7.41 (0.13)	Pure H	0.40 (0.04)	0.0207 (0.0021)	−0.48 (0.09)	6.53 (0.41)	
J021358.81+060644.9	DO	9.9	49,602 (1498)	7.76 (0.43)	Pure He	0.54 (0.19)	0.0160 (0.0052)	0.15 (0.29)	6.32 (0.39)	
J021650.67−091916.1	DA+M	7.4	65,262 (9776)	7.36 (0.48)	Pure H	0.48 (0.14)	0.0242 (0.0103)	0.98 (0.46)	<5.00	1
J023344.36−062515.8	DB	40.0	40,400 (320)	7.78 (0.05)	Pure He	0.53 (0.02)	0.0155 (0.0006)	−0.24 (0.04)	6.58 (0.03)	
J023520.01−093456.2	DA	29.1	30,805 (283)	7.25 (0.07)	Pure H	0.36 (0.02)	0.0234 (0.0012)	−0.35 (0.05)	5.77 (0.34)	
J023944.39+281534.8	DA	27.4	37,624 (661)	7.81 (0.09)	Pure H	0.57 (0.04)	0.0156 (0.0011)	−0.36 (0.07)	6.65 (0.03)	
J024854.96+334548.2	DA	34.0	34,003 (314)	7.20 (0.06)	Pure H	0.35 (0.02)	0.0245 (0.0010)	−0.14 (0.04)	5.25 (0.28)	
J024958.71+334249.9	DAO+M	46.6	49,316 (1133)	7.64 (0.09)	$\log N_{\rm He}/N_{\rm H} = -2.21$	0.53 (0.03)	0.0182 (0.0014)	0.25 (0.08)	6.24 (0.13)	1,4,7
J025123.33−011314.4	DA+M	32.8	33,306 (335)	7.87 (0.07)	Pure H	0.59 (0.03)	0.0147 (0.0007)	−0.62 (0.05)	6.80 (0.01)	1
J025202.46−010515.7	DA	79.5	63,587 (1038)	7.34 (0.05)	Pure H	0.47 (0.02)	0.0243 (0.0011)	0.94 (0.05)	<5.00	
J025206.82+350322.6	DA	19.9	33,165 (471)	7.26 (0.09)	Pure H	0.36 (0.03)	0.0235 (0.0016)	−0.22 (0.07)	5.61 (0.48)	

Table 2.1 – Atmospheric and stellar parameters of hot white dwarfs from SDSS DR12 (continued)

SDSS Name	Type	S/N	$T_{\rm eff}$ (K)	$\log g$	Composition	$M/M_{\odot}$	$R/R_{\odot}$	$\log L/L_{\odot}$	$\log \tau_{\rm cool}$	Notes
J025303.74+350737.2	DA	22.3	39,527 (1169)	7.53 (0.14)	Pure H	0.47 (0.04)	0.0195 (0.0021)	−0.08 (0.11)	6.30 (0.36)	7
J025622.18+330944.7	DAO	9.2	73,763 (14,363)	6.94 (0.57)	$\log N_{\rm He}/N_{\rm H} = -1.65$	0.41 (0.14)	0.0360 (0.0185)	1.54 (0.58)	<5.00	4
J025624.75+003557.9	DA	45.7	41,587 (516)	7.47 (0.05)	Pure H	0.45 (0.02)	0.0206 (0.0009)	0.06 (0.04)	6.01 (0.21)	
J025758.04+341748.0	DB	5.1	31,638 (4326)	7.61 (0.47)	Pure He	0.44 (0.19)	0.0172 (0.0058)	−0.57 (0.38)	6.77 (0.57)	
J025807.08+332202.9	DA	22.1	45,065 (1449)	7.28 (0.13)	Pure H	0.40 (0.04)	0.0240 (0.0023)	0.33 (0.10)	<5.00	
J025817.89+010945.9	DA+M	29.2	33,185 (430)	7.75 (0.09)	Pure H	0.53 (0.04)	0.0161 (0.0010)	−0.55 (0.06)	6.79 (0.03)	1,2
J025935.27−011405.0	DA	63.2	50,463 (729)	7.51 (0.05)	Pure H	0.49 (0.02)	0.0204 (0.0009)	0.39 (0.05)	5.84 (0.27)	
J030024.57−002342.1	DAO+M	51.6	87,666 (5105)	7.21 (0.16)	$\log N_{\rm He}/N_{\rm H} = -2.54$	0.51 (0.04)	0.0296 (0.0045)	1.67 (0.17)	<5.00	1,4,5
J030107.21+375120.7	DA	11.9	31,417 (598)	7.64 (0.14)	Pure H	0.48 (0.05)	0.0173 (0.0018)	−0.58 (0.10)	6.81 (0.10)	
J030130.10+050802.9	DOZ	32.3	49,869 (340)	7.88 (0.12)	Pure He	0.59 (0.05)	0.0146 (0.0013)	0.07 (0.08)	6.37 (0.02)	6
J030141.63+043820.0	DA	12.1	44,815 (2614)	7.45 (0.23)	Pure H	0.46 (0.08)	0.0211 (0.0039)	0.21 (0.19)	5.74 (0.96)	
J030340.66+380031.2	DA	6.4	43,908 (5212)	7.80 (0.49)	Pure H	0.58 (0.22)	0.0159 (0.0063)	−0.07 (0.40)	6.46 (0.42)	
J031050.04+420807.6	DA	24.0	36,057 (503)	8.37 (0.08)	Pure H	0.87 (0.05)	0.0101 (0.0006)	−0.80 (0.06)	6.82 (0.11)	
J031422.21+001025.1	DA	10.2	33,767 (838)	7.46 (0.16)	Pure H	0.43 (0.05)	0.0201 (0.0025)	−0.32 (0.12)	6.45 (0.45)	
J031445.00+411722.7	DA	8.6	42,285 (3014)	7.76 (0.31)	Pure H	0.56 (0.13)	0.0163 (0.0040)	−0.11 (0.25)	6.49 (0.22)	
J031456.03+403327.1	DA	5.1	31,305 (1550)	8.11 (0.37)	Pure H	0.71 (0.21)	0.0123 (0.0035)	−0.88 (0.26)	6.93 (0.21)	
J031829.90−072746.6	DA	13.9	50,019 (5130)	7.98 (0.39)	Pure H	0.67 (0.19)	0.0140 (0.0044)	0.04 (0.33)	6.29 (0.16)	2
J031919.11+400920.0	DA	5.2	36,962 (3639)	7.22 (0.52)	Pure H	0.36 (0.15)	0.0244 (0.0100)	0.00 (0.39)	5.05 (1.47)	
J032425.60+044803.3	DA	22.0	51,967 (1781)	7.78 (0.13)	Pure H	0.59 (0.05)	0.0164 (0.0017)	0.25 (0.11)	6.25 (0.06)	
J032614.49−001138.2	DA	36.7	33,963 (286)	8.65 (0.05)	Pure H	1.03 (0.03)	0.0080 (0.0004)	−1.11 (0.04)	7.61 (0.09)	
J032706.26−062828.5	DA	19.8	42,179 (1257)	7.50 (0.13)	Pure H	0.47 (0.04)	0.0202 (0.0021)	0.06 (0.11)	6.08 (0.45)	2
J032726.25−071149.9	DA	25.7	49,995 (1676)	7.50 (0.12)	Pure H	0.49 (0.04)	0.0206 (0.0021)	0.38 (0.11)	5.77 (0.61)	
J033133.89+010327.8	DA	78.3	35,375 (158)	7.91 (0.03)	Pure H	0.61 (0.01)	0.0143 (0.0003)	−0.54 (0.02)	6.72 (0.01)	
J033236.86−004936.9	DA	89.9	34,313 (126)	7.83 (0.02)	Pure H	0.57 (0.01)	0.0152 (0.0003)	−0.54 (0.02)	6.76 (0.01)	
J033257.67−070435.0	DA	36.2	42,012 (728)	7.83 (0.08)	Pure H	0.59 (0.03)	0.0154 (0.0009)	−0.18 (0.06)	6.51 (0.02)	
J033622.01−000146.7	DA	25.1	49,306 (1842)	7.76 (0.14)	Pure H	0.58 (0.06)	0.0165 (0.0019)	0.16 (0.12)	6.31 (0.08)	2
J034101.38+005352.8	DO	32.7	53,897 (846)	8.02 (0.13)	Pure He	0.66 (0.07)	0.0132 (0.0014)	0.12 (0.09)	6.27 (0.03)	
J034227.62−072213.2	DOA	39.1	48,583 (228)	8.21 (0.08)	$\log q_{\rm H} = -18.05$	0.76 (0.05)	0.0114 (0.0007)	−0.19 (0.05)	6.33 (0.02)	3
J034314.35+102938.3	DA	69.6	83,219 (1736)	8.83 (0.07)	Pure H	1.16 (0.03)	0.0068 (0.0005)	0.31 (0.07)	5.43 (0.04)	
J034319.08+101237.9	DA	25.2	32,461 (414)	8.43 (0.09)	Pure H	0.91 (0.05)	0.0096 (0.0007)	−1.04 (0.07)	7.29 (0.21)	
J034356.12−050758.7	DA	38.7	47,151 (854)	7.78 (0.07)	Pure H	0.58 (0.03)	0.0163 (0.0009)	0.07 (0.06)	6.37 (0.03)	
J034428.27−003814.0	DA	52.4	30,964 (128)	7.88 (0.03)	Pure H	0.59 (0.02)	0.0145 (0.0003)	−0.76 (0.02)	6.90 (0.01)	
J034831.33+004616.2	DAO	77.8	86,718 (2998)	7.20 (0.10)	$\log N_{\rm He}/N_{\rm H} = -2.24$	0.51 (0.02)	0.0297 (0.0028)	1.65 (0.11)	<5.00	4,5
J035343.66−000434.2	DA	96.4	36,850 (175)	7.67 (0.03)	Pure H	0.51 (0.01)	0.0173 (0.0003)	−0.30 (0.02)	6.62 (0.02)	
J040854.60−043354.6	DB	10.2	38,897 (2794)	8.12 (0.27)	Pure He	0.70 (0.15)	0.0120 (0.0024)	−0.52 (0.22)	6.64 (0.10)	
J041053.63−063027.7	DA	12.4	64,026 (6578)	7.45 (0.33)	Pure H	0.51 (0.10)	0.0223 (0.0065)	0.88 (0.31)	5.13 (1.33)	2
J041945.51+055008.9	DA	7.7	36,259 (2010)	7.27 (0.30)	Pure H	0.37 (0.09)	0.0236 (0.0054)	−0.06 (0.22)	5.39 (1.11)	
J042437.67+063408.2	DA+M	12.0	45,552 (3334)	7.76 (0.29)	Pure H	0.57 (0.12)	0.0164 (0.0039)	0.02 (0.24)	6.40 (0.22)	1,2
J043917.78+104247.9	DA	7.6	37,396 (2243)	8.40 (0.32)	Pure H	0.90 (0.18)	0.0098 (0.0025)	−0.77 (0.25)	6.77 (0.39)	
J043939.03+095927.0	DB	5.0	39,087 (4260)	8.04 (0.42)	Pure He	0.65 (0.22)	0.0128 (0.0041)	−0.46 (0.34)	6.64 (0.22)	
J044031.65−055906.7	DA	18.5	46,551 (2029)	7.49 (0.17)	Pure H	0.47 (0.06)	0.0206 (0.0028)	0.26 (0.14)	5.83 (0.73)	7
J044051.96−053017.8	DA	9.0	30,673 (1054)	7.80 (0.26)	Pure H	0.55 (0.12)	0.0155 (0.0031)	−0.72 (0.18)	6.91 (0.11)	
J044052.29−052516.4	DA	13.4	32,474 (849)	8.00 (0.18)	Pure H	0.65 (0.10)	0.0134 (0.0018)	−0.75 (0.13)	6.84 (0.05)	
J044556.05−000419.2	DO	7.8	45,506 (941)	7.86 (0.34)	Pure He	0.57 (0.16)	0.0148 (0.0040)	−0.07 (0.23)	6.46 (0.17)	
J044641.97−043242.8	DA	8.9	39,071 (2338)	7.28 (0.29)	Pure H	0.39 (0.09)	0.0236 (0.0052)	0.07 (0.22)	5.23 (1.11)	
J044751.43−050904.1	DA	24.8	32,370 (408)	9.26 (0.09)	Pure H	1.29 (0.03)	0.0044 (0.0004)	−1.71 (0.08)	8.33 (0.07)	
J052901.34+624325.2	DA	9.4	34,276 (1192)	7.57 (0.22)	Pure H	0.46 (0.08)	0.0186 (0.0031)	−0.37 (0.16)	6.61 (0.31)	
J053108.37+633108.5	DA	12.1	36,141 (1562)	7.57 (0.24)	Pure H	0.47 (0.08)	0.0187 (0.0035)	−0.27 (0.18)	6.54 (0.34)	
J053653.54−000534.4	DA+M	13.5	32,033 (914)	7.62 (0.18)	Pure H	0.48 (0.07)	0.0177 (0.0025)	−0.53 (0.13)	6.77 (0.18)	1,7
J053831.60+001537.9	DA	24.3	44,241 (1877)	8.70 (0.18)	Pure H	1.07 (0.09)	0.0077 (0.0012)	−0.69 (0.16)	6.88 (0.50)	2

Table 2.1 – Atmospheric and stellar parameters of hot white dwarfs from SDSS DR12 (continued)

SDSS Name	Type	S/N	$T_{\rm eff}$ (K)	$\log g$	Composition	$M/M_{\odot}$	$R/R_{\odot}$	$\log L/L_{\odot}$	$\log \tau_{\rm cool}$	Notes
J054043.26+835726.8	DA	11.7	44,556 (2454)	7.62 (0.22)	Pure H	0.51 (0.08)	0.0184 (0.0033)	0.08 (0.19)	6.33 (0.27)	
J054430.97+825608.8	DA+M	20.2	32,437 (554)	8.01 (0.12)	Pure H	0.66 (0.06)	0.0133 (0.0012)	−0.76 (0.08)	6.84 (0.03)	1,2
J055844.80+644122.2	DA	21.0	30,262 (324)	7.69 (0.08)	Pure H	0.50 (0.03)	0.0168 (0.0010)	−0.67 (0.06)	6.89 (0.04)	
J055946.70+641238.2	DA	28.3	48,496 (1256)	7.66 (0.10)	Pure H	0.54 (0.04)	0.0180 (0.0015)	0.21 (0.09)	6.27 (0.12)	
J060059.17+632736.0	DA	5.8	35,690 (2139)	7.59 (0.34)	Pure H	0.48 (0.13)	0.0183 (0.0048)	−0.31 (0.25)	6.59 (0.30)	
J060501.39+840152.6	DA	8.5	30,818 (923)	7.57 (0.23)	Pure H	0.45 (0.08)	0.0183 (0.0032)	−0.56 (0.16)	6.78 (0.26)	
J060914.17+633740.5	DA	7.1	34,031 (1632)	7.21 (0.30)	Pure H	0.35 (0.09)	0.0244 (0.0055)	−0.14 (0.21)	5.28 (1.10)	
J061938.24+635656.4	DAO	80.5	74,105 (3063)	6.89 (0.09)	$\log N_{\rm He}/N_{\rm H} = -3.36$	0.40 (0.02)	0.0378 (0.0030)	1.59 (0.11)	<5.00	4,5
J062049.47+641325.5	DA	5.8	33,747 (1795)	7.28 (0.34)	Pure H	0.37 (0.10)	0.0232 (0.0059)	−0.20 (0.24)	5.66 (1.14)	
J064027.98+370818.6	DA	25.6	35,616 (566)	7.81 (0.09)	Pure H	0.56 (0.04)	0.0155 (0.0011)	−0.46 (0.07)	6.71 (0.03)	
J064400.79+372022.7	DOZ	40.2	64,260 (1510)	7.88 (0.15)	Pure He	0.62 (0.06)	0.0149 (0.0018)	0.53 (0.11)	6.07 (0.07)	6
J064500.91+380121.0	DA	11.9	33,877 (962)	7.90 (0.18)	Pure H	0.60 (0.09)	0.0144 (0.0020)	−0.61 (0.13)	6.78 (0.04)	
J064653.21+285030.4	DA	8.4	31,152 (684)	7.83 (0.17)	Pure H	0.56 (0.08)	0.0151 (0.0018)	−0.71 (0.11)	6.89 (0.05)	
J064724.43+370713.7	DA	23.2	30,163 (281)	7.74 (0.07)	Pure H	0.52 (0.03)	0.0161 (0.0009)	−0.71 (0.05)	6.91 (0.03)	
J064743.70+270906.1	DA	56.3	46,472 (556)	7.97 (0.05)	Pure H	0.67 (0.02)	0.0139 (0.0005)	−0.09 (0.04)	6.38 (0.02)	
J064746.52+382230.5	DA	23.2	65,455 (3147)	7.47 (0.16)	Pure H	0.52 (0.05)	0.0220 (0.0029)	0.90 (0.15)	5.24 (0.89)	
J065146.31+271927.3	DB	28.8	37,826 (1166)	7.90 (0.09)	Pure He	0.58 (0.05)	0.0141 (0.0010)	−0.43 (0.08)	6.69 (0.04)	
J065745.82+834958.4	DO	20.1	85,312 (12,012)	7.68 (0.51)	Pure He	0.58 (0.18)	0.0184 (0.0082)	1.21 (0.46)	5.49 (0.53)	
J070407.12+401941.8	DA	17.5	62,382 (4384)	6.88 (0.21)	Pure H	0.36 (0.05)	0.0361 (0.0065)	1.25 (0.21)	<5.00	
J071335.68+393419.1	DA	7.8	32,472 (953)	7.82 (0.20)	Pure H	0.56 (0.09)	0.0153 (0.0023)	−0.63 (0.14)	6.83 (0.07)	
J071340.55+385037.0	DA	9.6	59,125 (6329)	7.69 (0.37)	Pure H	0.58 (0.14)	0.0179 (0.0055)	0.55 (0.33)	6.05 (0.29)	
J071415.56+395937.3	DA	5.1	52,475 (7336)	8.13 (0.52)	Pure H	0.76 (0.26)	0.0124 (0.0054)	0.02 (0.45)	6.20 (0.18)	
J071644.59+395808.9	DO	30.6	66,018 (2324)	8.16 (0.21)	Pure He	0.75 (0.11)	0.0120 (0.0021)	0.39 (0.16)	5.98 (0.08)	
J071837.12+373805.3	DA	11.8	41,029 (1711)	7.86 (0.19)	Pure H	0.60 (0.09)	0.0151 (0.0022)	−0.23 (0.15)	6.54 (0.06)	
J071841.33+314412.3	DA	24.4	50,951 (1562)	7.71 (0.11)	Pure H	0.56 (0.04)	0.0174 (0.0016)	0.26 (0.10)	6.24 (0.09)	
J071924.87+320758.9	DA	27.7	38,370 (489)	7.78 (0.06)	Pure H	0.56 (0.03)	0.0159 (0.0008)	−0.31 (0.05)	6.62 (0.02)	
J072025.52+370336.3	DO	31.7	52,733 (990)	8.02 (0.12)	Pure He	0.66 (0.06)	0.0132 (0.0012)	0.08 (0.09)	6.29 (0.03)	
J072607.91+395111.9	DA	44.1	36,089 (303)	7.83 (0.05)	Pure H	0.57 (0.02)	0.0153 (0.0005)	−0.45 (0.03)	6.70 (0.01)	
J072611.03+380402.6	DA	18.5	32,561 (426)	7.69 (0.09)	Pure H	0.51 (0.04)	0.0168 (0.0011)	−0.54 (0.06)	6.79 (0.05)	
J072620.78+370537.6	DA	11.5	47,194 (2854)	7.76 (0.24)	Pure H	0.57 (0.10)	0.0166 (0.0032)	0.09 (0.20)	6.36 (0.17)	
J072621.21+363311.5	DOA	41.8	46,352 (401)	7.84 (0.11)	$\log q_{\rm H} = -16.89$	0.57 (0.05)	0.0150 (0.0012)	−0.03 (0.07)	6.44 (0.03)	3
J072752.76+321416.0	DA	40.6	57,037 (1397)	7.55 (0.08)	Pure H	0.52 (0.03)	0.0202 (0.0015)	0.59 (0.08)	5.88 (0.31)	
J072942.69+392636.0	DA	36.9	43,122 (720)	7.50 (0.07)	Pure H	0.47 (0.02)	0.0201 (0.0011)	0.10 (0.06)	6.06 (0.26)	
J072953.54+150147.5	DA	11.5	32,414 (648)	7.82 (0.14)	Pure H	0.56 (0.06)	0.0153 (0.0016)	−0.63 (0.10)	6.84 (0.04)	
J073114.93+385530.4	DA	38.8	72,914 (2851)	7.64 (0.12)	Pure H	0.59 (0.04)	0.0193 (0.0022)	0.98 (0.12)	5.72 (0.16)	
J073204.80+401658.4	DA	21.9	30,802 (309)	7.85 (0.08)	Pure H	0.57 (0.04)	0.0148 (0.0008)	−0.75 (0.05)	6.91 (0.02)	
J073511.19+265708.4	DA	49.8	33,226 (180)	7.78 (0.04)	Pure H	0.54 (0.02)	0.0158 (0.0004)	−0.56 (0.03)	6.80 (0.01)	
J073533.46+295945.9	DA	6.7	33,667 (1309)	8.12 (0.25)	Pure H	0.72 (0.14)	0.0123 (0.0024)	−0.76 (0.18)	6.80 (0.12)	
J073616.39+152106.8	DAO	16.8	90,469 (13,613)	8.51 (0.49)	$\log N_{\rm He}/N_{\rm H} = -1.47$	1.01 (0.23)	0.0093 (0.0042)	0.72 (0.47)	5.34 (0.29)	4
J073655.00+161805.1	DA	36.5	56,573 (1717)	7.59 (0.11)	Pure H	0.53 (0.03)	0.0195 (0.0018)	0.55 (0.10)	5.98 (0.25)	
J073705.71+282449.0	DA	5.4	40,444 (2885)	8.19 (0.33)	Pure H	0.77 (0.19)	0.0117 (0.0031)	−0.48 (0.26)	6.53 (0.17)	
J073715.08+402707.1	DA	8.8	31,789 (1006)	8.03 (0.23)	Pure H	0.67 (0.12)	0.0130 (0.0022)	−0.81 (0.16)	6.88 (0.10)	
J073727.33+263158.3	DA	27.5	68,898 (3494)	7.58 (0.16)	Pure H	0.57 (0.06)	0.0202 (0.0028)	0.92 (0.16)	5.77 (0.17)	
J073741.49+470421.1	DA	32.6	58,225 (1971)	7.45 (0.12)	Pure H	0.49 (0.04)	0.0220 (0.0020)	0.70 (0.10)	5.27 (0.82)	
J073756.44+390753.2	DA	30.8	62,156 (2209)	7.53 (0.12)	Pure H	0.53 (0.04)	0.0207 (0.0021)	0.76 (0.11)	5.65 (0.51)	
J073849.46+485126.6	DO	29.8	60,320 (1848)	8.21 (0.19)	Pure He	0.77 (0.11)	0.0115 (0.0018)	0.20 (0.14)	6.07 (0.08)	
J073849.67+463603.0	DA	20.4	33,308 (470)	7.76 (0.09)	Pure H	0.54 (0.04)	0.0160 (0.0011)	−0.55 (0.07)	6.79 (0.03)	
J073924.85+280722.8	DA	26.2	32,686 (358)	7.20 (0.08)	Pure H	0.34 (0.02)	0.0245 (0.0013)	−0.21 (0.05)	5.34 (0.35)	
J073938.21+212730.5	DOZ	16.2	117,073 (8014)	7.80 (0.78)	Pure He	0.69 (0.27)	0.0173 (0.0133)	1.70 (0.63)	5.08 (0.78)	6
J074023.82+653418.6	DA	16.0	60,069 (3530)	7.57 (0.20)	Pure H	0.54 (0.07)	0.0200 (0.0033)	0.67 (0.18)	5.84 (0.49)	

Table 2.1 – Atmospheric and stellar parameters of hot white dwarfs from SDSS DR12 (continued)

SDSS Name	Type	S/N	$T_{\rm eff}$ (K)	$\log g$	Composition	$M/M_{\odot}$	$R/R_{\odot}$	$\log L/L_{\odot}$	$\log \tau_{\rm cool}$	Notes
J074059.11+380810.1	DA	47.8	36,995 (326)	7.87 (0.05)	Pure H	0.59 (0.02)	0.0149 (0.0005)	−0.43 (0.03)	6.67 (0.01)	
J074203.59+493333.8	DO	92.8	61,812 (611)	8.14 (0.06)	Pure He	0.74 (0.03)	0.0121 (0.0006)	0.28 (0.05)	6.07 (0.03)	
J074216.66+325123.3	DA	15.3	31,248 (445)	7.85 (0.11)	Pure H	0.57 (0.05)	0.0149 (0.0012)	−0.72 (0.07)	6.89 (0.02)	
J074243.40+442231.5	DA	49.4	63,619 (1841)	7.55 (0.09)	Pure H	0.54 (0.03)	0.0205 (0.0016)	0.79 (0.09)	5.71 (0.35)	5
J074307.18+330049.8	DA	19.3	48,655 (2023)	7.38 (0.16)	Pure H	0.44 (0.05)	0.0226 (0.0027)	0.41 (0.13)	5.10 (0.86)	
J074319.77+654806.7	DA	28.8	34,412 (485)	7.78 (0.09)	Pure H	0.55 (0.04)	0.0158 (0.0010)	−0.50 (0.06)	6.75 (0.03)	
J074320.32+160752.8	DAO	62.1	83,230 (4934)	7.15 (0.13)	$\log N_{\rm He}/N_{\rm H} = -1.14$	0.49 (0.03)	0.0308 (0.0038)	1.61 (0.16)	<5.00	4,5
J074325.12+275452.3	DA	10.2	51,778 (2669)	7.50 (0.19)	Pure H	0.49 (0.06)	0.0207 (0.0031)	0.44 (0.16)	5.75 (0.84)	
J074333.94+482113.3	DA	43.1	33,195 (213)	7.88 (0.04)	Pure H	0.59 (0.02)	0.0146 (0.0005)	−0.63 (0.03)	6.81 (0.01)	
J074353.83+192543.5	DA	7.2	39,944 (2442)	8.44 (0.29)	Pure H	0.92 (0.17)	0.0096 (0.0023)	−0.68 (0.24)	6.64 (0.33)	
J074403.80+495439.9	DA	32.2	36,681 (550)	9.36 (0.08)	Pure H	1.32 (0.03)	0.0040 (0.0003)	−1.59 (0.08)	8.27 (0.08)	
J074448.78+455916.7	DA	15.0	43,961 (2232)	7.86 (0.21)	Pure H	0.61 (0.10)	0.0152 (0.0025)	−0.11 (0.17)	6.46 (0.08)	
J074458.75+380301.5	DA	48.8	53,079 (973)	7.82 (0.07)	Pure H	0.61 (0.03)	0.0159 (0.0009)	0.26 (0.06)	6.23 (0.03)	5
J074517.54+351151.8	DA	14.7	30,621 (456)	7.90 (0.12)	Pure H	0.60 (0.06)	0.0143 (0.0012)	−0.79 (0.08)	6.92 (0.03)	
J074520.04+234223.8	DA+M	36.9	72,090 (3536)	7.04 (0.13)	Pure H	0.43 (0.03)	0.0329 (0.0040)	1.42 (0.14)	<5.00	1
J074532.89+225914.2	DA	64.7	56,591 (1039)	7.55 (0.06)	Pure H	0.53 (0.02)	0.0200 (0.0010)	0.57 (0.06)	5.91 (0.19)	5
J074538.16+312205.3	DBA	8.7	41,854 (4661)	8.16 (0.40)	$\log q_{\rm H} = -17.76$	0.72 (0.22)	0.0117 (0.0037)	−0.42 (0.33)	6.53 (0.18)	3
J074542.98+150756.0	DA	76.4	31,914 (105)	7.91 (0.02)	Pure H	0.60 (0.01)	0.0142 (0.0003)	−0.72 (0.02)	6.86 (0.01)	
J074553.09+252540.5	DA+M	29.6	33,785 (357)	7.81 (0.07)	Pure H	0.56 (0.03)	0.0154 (0.0008)	−0.55 (0.05)	6.78 (0.02)	1
J074609.53+335720.2	DA	4.2	32,005 (1577)	7.70 (0.35)	Pure H	0.51 (0.14)	0.0167 (0.0045)	−0.58 (0.25)	6.82 (0.17)	
J074612.67+654207.6	DA	9.1	35,773 (1543)	7.45 (0.24)	Pure H	0.43 (0.08)	0.0204 (0.0038)	−0.21 (0.18)	6.30 (0.78)	
J074632.00+415210.1	DA	23.4	76,567 (4496)	7.72 (0.19)	Pure H	0.63 (0.06)	0.0180 (0.0030)	1.00 (0.18)	5.69 (0.15)	
J074638.20+331652.9	DA	40.6	31,163 (186)	7.88 (0.04)	Pure H	0.58 (0.02)	0.0146 (0.0005)	−0.74 (0.03)	6.89 (0.01)	
J074641.88+170746.0	DO	4.7	71,301 (16,046)	8.69 (1.12)	Pure He	1.06 (0.52)	0.0077 (0.0084)	0.14 (0.97)	5.74 (0.60)	
J074717.79+190445.6	DA	13.9	59,058 (4194)	7.62 (0.24)	Pure H	0.55 (0.09)	0.0190 (0.0039)	0.60 (0.22)	5.97 (0.33)	
J074741.72+230558.4	DA	12.1	41,627 (1718)	7.66 (0.18)	Pure H	0.52 (0.07)	0.0176 (0.0025)	−0.08 (0.15)	6.46 (0.16)	
J074803.65+140558.6	DA	18.3	41,373 (1209)	7.63 (0.13)	Pure H	0.51 (0.05)	0.0180 (0.0019)	−0.07 (0.10)	6.43 (0.19)	
J074807.22+205814.2	DA+M	40.9	73,586 (3848)	7.22 (0.12)	Pure H	0.47 (0.03)	0.0278 (0.0032)	1.31 (0.14)	<5.00	1,5
J074815.28+380845.8	DA+M	8.1	30,029 (797)	7.73 (0.21)	Pure H	0.52 (0.09)	0.0162 (0.0026)	−0.72 (0.14)	6.92 (0.10)	1
J074816.59+292321.0	DA	33.7	49,909 (1011)	7.55 (0.08)	Pure H	0.51 (0.02)	0.0196 (0.0012)	0.33 (0.07)	6.04 (0.27)	
J074816.73+161200.8	DA	30.7	39,338 (661)	7.60 (0.08)	Pure H	0.49 (0.03)	0.0183 (0.0012)	−0.14 (0.06)	6.46 (0.12)	
J074854.06+133806.8	DA	19.2	67,248 (4434)	7.18 (0.20)	Pure H	0.44 (0.05)	0.0282 (0.0051)	1.17 (0.20)	<5.00	
J074859.06+215445.7	DA	5.3	30,897 (1203)	7.65 (0.29)	Pure H	0.48 (0.12)	0.0173 (0.0039)	−0.61 (0.21)	6.84 (0.18)	
J074904.12+500431.8	DA	29.8	38,397 (611)	7.77 (0.08)	Pure H	0.55 (0.03)	0.0160 (0.0010)	−0.30 (0.06)	6.62 (0.03)	
J074906.14+421939.8	DA	4.8	31,186 (1541)	7.06 (0.38)	Pure H	0.30 (0.10)	0.0267 (0.0075)	−0.22 (0.26)	<5.00	
J074907.55+211124.1	DA	28.8	32,171 (263)	8.26 (0.06)	Pure H	0.80 (0.04)	0.0110 (0.0005)	−0.93 (0.04)	6.98 (0.07)	
J074924.23+240227.0	DA	30.9	33,059 (308)	7.91 (0.06)	Pure H	0.60 (0.03)	0.0143 (0.0007)	−0.65 (0.04)	6.81 (0.01)	
J074927.91+132107.9	DA	37.1	34,280 (290)	7.88 (0.05)	Pure H	0.59 (0.03)	0.0147 (0.0006)	−0.57 (0.04)	6.76 (0.01)	
J074934.85+365205.0	DA	13.2	35,499 (972)	7.29 (0.16)	Pure H	0.38 (0.05)	0.0232 (0.0027)	−0.11 (0.11)	5.56 (0.74)	
J074935.02+314315.5	DA	15.3	44,463 (1813)	7.48 (0.17)	Pure H	0.47 (0.06)	0.0206 (0.0027)	0.17 (0.14)	5.89 (0.67)	
J075013.07+494743.2	DAO	45.1	81,080 (5874)	7.14 (0.19)	$\log N_{\rm He}/N_{\rm H} = -1.67$	0.48 (0.05)	0.0309 (0.0054)	1.57 (0.21)	<5.00	4,5
J075106.51+301726.4	DA	77.0	32,669 (101)	7.93 (0.02)	Pure H	0.61 (0.01)	0.0141 (0.0002)	−0.69 (0.01)	6.83 (0.01)	
J075121.22+192026.7	DAO	15.5	95,529 (14,837)	6.81 (0.41)	$\log N_{\rm He}/N_{\rm H} = -1.38$	0.46 (0.10)	0.0445 (0.0174)	2.17 (0.46)	<5.00	4
J075124.21+410920.7	DA	26.7	46,835 (1405)	7.21 (0.12)	Pure H	0.38 (0.03)	0.0255 (0.0024)	0.45 (0.10)	<5.00	
J075219.42+264157.9	DA	47.4	30,039 (124)	7.67 (0.03)	Pure H	0.49 (0.01)	0.0170 (0.0004)	−0.67 (0.02)	6.89 (0.02)	
J075235.28+160913.0	DA	29.6	66,521 (2901)	7.61 (0.14)	Pure H	0.57 (0.05)	0.0195 (0.0024)	0.83 (0.14)	5.85 (0.14)	
J075254.64+182046.4	DA	23.7	50,570 (1797)	7.49 (0.13)	Pure H	0.49 (0.04)	0.0208 (0.0022)	0.41 (0.11)	5.70 (0.67)	
J075315.56+162323.8	DA	4.0	32,734 (1979)	7.72 (0.41)	Pure H	0.52 (0.17)	0.0165 (0.0053)	−0.55 (0.29)	6.80 (0.20)	
J075321.56+334308.2	DA	49.0	36,513 (314)	7.13 (0.05)	Pure H	0.33 (0.01)	0.0259 (0.0009)	0.03 (0.03)	<5.00	
J075325.99+102457.3	DA	16.6	42,370 (1366)	7.62 (0.14)	Pure H	0.50 (0.05)	0.0183 (0.0020)	−0.01 (0.11)	6.38 (0.23)	

Table 2.1 – Atmospheric and stellar parameters of hot white dwarfs from SDSS DR12 (continued)

SDSS Name	Type	S/N	$T_{\rm eff}$ (K)	$\log g$	Composition	$M/M_{\odot}$	$R/R_{\odot}$	$\log L/L_{\odot}$	$\log \tau_{\rm cool}$	Notes
J075343.46+334451.5	DA	6.8	32,828 (1163)	7.77 (0.24)	Pure H	0.54 (0.11)	0.0159 (0.0029)	−0.58 (0.17)	6.81 (0.10)	
J075405.34+132708.6	DA	61.7	74,783 (2080)	7.79 (0.08)	Pure H	0.65 (0.03)	0.0169 (0.0011)	0.91 (0.08)	5.77 (0.05)	5
J075409.25+485058.1	DA	20.9	35,217 (647)	7.71 (0.11)	Pure H	0.52 (0.04)	0.0167 (0.0014)	−0.41 (0.08)	6.70 (0.06)	
J075426.46+242220.9	DA	17.2	32,346 (612)	7.88 (0.13)	Pure H	0.59 (0.06)	0.0145 (0.0014)	−0.68 (0.09)	6.84 (0.03)	
J075505.42+245832.7	DA	3.4	35,175 (3060)	7.63 (0.51)	Pure H	0.49 (0.20)	0.0177 (0.0070)	−0.36 (0.37)	6.65 (0.31)	
J075535.95+441333.9	DA	7.1	34,981 (1481)	8.03 (0.25)	Pure H	0.67 (0.14)	0.0131 (0.0025)	−0.63 (0.18)	6.74 (0.08)	
J075537.50+382306.5	DA	5.8	41,775 (4043)	8.00 (0.43)	Pure H	0.67 (0.21)	0.0136 (0.0046)	−0.30 (0.34)	6.51 (0.18)	
J075540.93+400917.9	DOZ	31.7	92,873 (10,405)	7.49 (0.32)	Pure He	0.54 (0.10)	0.0218 (0.0063)	1.50 (0.33)	<5.00	6
J075556.92+113917.8	DA	4.9	31,046 (1307)	7.82 (0.32)	Pure H	0.56 (0.15)	0.0152 (0.0036)	−0.71 (0.22)	6.89 (0.15)	
J075606.36+421613.0	DO+M	19.6	51,596 (1413)	7.65 (0.22)	Pure He	0.50 (0.09)	0.0175 (0.0030)	0.29 (0.16)	6.07 (0.52)	1
J075611.24+124715.2	DA	3.3	32,185 (2559)	7.27 (0.56)	Pure H	0.37 (0.17)	0.0232 (0.0099)	−0.29 (0.39)	5.76 (1.39)	
J075633.77+163359.0	DO	23.7	56,820 (2031)	7.93 (0.23)	Pure He	0.63 (0.11)	0.0142 (0.0026)	0.28 (0.17)	6.22 (0.09)	
J075725.91+164756.9	DA	9.6	53,684 (4892)	7.75 (0.33)	Pure H	0.58 (0.13)	0.0169 (0.0046)	0.33 (0.29)	6.19 (0.33)	
J075726.87+112416.2	DA	29.1	38,693 (604)	8.15 (0.08)	Pure H	0.74 (0.04)	0.0121 (0.0007)	−0.53 (0.06)	6.59 (0.02)	
J075757.09+124112.7	DA	40.8	55,534 (1444)	7.47 (0.09)	Pure H	0.49 (0.03)	0.0215 (0.0015)	0.60 (0.08)	5.45 (0.65)	
J075757.68+324815.4	DA	12.6	64,512 (6342)	7.37 (0.32)	Pure H	0.49 (0.09)	0.0238 (0.0065)	0.95 (0.30)	<5.00	
J075813.94+475657.8	DA	20.1	31,578 (437)	7.78 (0.10)	Pure H	0.54 (0.04)	0.0157 (0.0012)	−0.65 (0.07)	6.86 (0.03)	
J075818.03+163346.6	DA	29.8	36,009 (433)	7.97 (0.07)	Pure H	0.64 (0.04)	0.0137 (0.0007)	−0.54 (0.05)	6.70 (0.02)	
J075842.45+170950.5	DA+M	16.7	32,223 (568)	7.96 (0.12)	Pure H	0.63 (0.06)	0.0138 (0.0013)	−0.73 (0.09)	6.85 (0.03)	1
J075857.46+092559.9	DAO	84.2	83,133 (5862)	6.96 (0.13)	$\log N_{\rm He}/N_{\rm H} = -1.03$	0.45 (0.03)	0.0369 (0.0046)	1.77 (0.18)	<5.00	4,5
J075930.84+270804.3	DA	17.5	46,119 (2003)	7.74 (0.17)	Pure H	0.56 (0.07)	0.0167 (0.0023)	0.06 (0.14)	6.38 (0.11)	
J080007.45+521820.8	DO	5.4	49,277 (1891)	7.97 (0.69)	Pure He	0.63 (0.33)	0.0136 (0.0075)	−0.01 (0.47)	6.38 (0.45)	
J080022.65+115022.9	DA+M	14.8	35,118 (1288)	7.30 (0.22)	Pure H	0.38 (0.07)	0.0230 (0.0037)	−0.14 (0.15)	5.65 (0.90)	1
J080045.51+481212.2	DA	22.0	33,880 (499)	7.20 (0.09)	Pure H	0.35 (0.03)	0.0246 (0.0016)	−0.14 (0.06)	5.23 (0.43)	
J080104.28+110617.8	DB	5.7	40,239 (2706)	7.78 (0.42)	Pure He	0.53 (0.19)	0.0155 (0.0049)	−0.25 (0.30)	6.58 (0.33)	
J080135.96+100417.1	DA	8.3	57,512 (7333)	7.70 (0.45)	Pure H	0.57 (0.18)	0.0177 (0.0065)	0.49 (0.39)	6.08 (0.56)	
J080229.13+103946.1	DA	10.0	56,116 (5500)	8.21 (0.36)	Pure H	0.80 (0.19)	0.0117 (0.0034)	0.09 (0.31)	6.09 (0.14)	
J080318.61+124726.5	DA+M	4.4	58,252 (13,533)	6.88 (0.74)	Pure H	0.35 (0.19)	0.0353 (0.0204)	1.11 (0.68)	<5.00	1
J080403.05+083030.7	DA	16.8	75,275 (6879)	7.26 (0.26)	Pure H	0.49 (0.07)	0.0269 (0.0065)	1.32 (0.27)	<5.00	
J080417.37+055402.2	DA	6.7	32,338 (1081)	7.52 (0.23)	Pure H	0.44 (0.08)	0.0192 (0.0034)	−0.44 (0.17)	6.64 (0.39)	
J080428.54+081910.2	DA	18.7	30,001 (251)	7.77 (0.07)	Pure H	0.53 (0.03)	0.0158 (0.0008)	−0.74 (0.05)	6.93 (0.02)	
J080435.87+061333.9	DA	33.2	70,510 (3037)	7.06 (0.12)	Pure H	0.43 (0.03)	0.0321 (0.0035)	1.36 (0.13)	<5.00	
J080439.20+212729.5	DA	19.5	35,044 (550)	7.93 (0.09)	Pure H	0.62 (0.05)	0.0141 (0.0010)	−0.57 (0.07)	6.73 (0.02)	
J080450.02+282545.5	DA	6.9	47,866 (4973)	7.65 (0.40)	Pure H	0.53 (0.16)	0.0180 (0.0057)	0.19 (0.33)	6.29 (0.28)	
J080614.32+455304.8	DA	15.8	48,280 (2392)	7.58 (0.19)	Pure H	0.51 (0.06)	0.0191 (0.0029)	0.25 (0.16)	6.16 (0.37)	
J080623.51+142315.8	DA	29.7	30,821 (229)	7.76 (0.06)	Pure H	0.53 (0.02)	0.0159 (0.0007)	−0.69 (0.04)	6.89 (0.02)	
J080652.50+232855.9	DA	21.2	56,057 (2395)	7.72 (0.15)	Pure H	0.58 (0.05)	0.0174 (0.0022)	0.43 (0.14)	6.12 (0.13)	
J080658.33+325501.8	DA	5.2	38,307 (3662)	6.92 (0.48)	Pure H	0.29 (0.12)	0.0308 (0.0115)	0.26 (0.37)	<5.00	
J080700.43+143731.1	DA	24.9	41,485 (1084)	8.11 (0.12)	Pure H	0.73 (0.06)	0.0124 (0.0011)	−0.39 (0.09)	6.50 (0.04)	
J080713.87+505306.4	DA	37.4	49,885 (1008)	7.56 (0.08)	Pure H	0.51 (0.03)	0.0196 (0.0013)	0.33 (0.07)	6.06 (0.28)	5
J080730.55+121827.4	DAO	72.4	54,349 (728)	7.72 (0.07)	$\log q_{\rm H} = -15.58$	0.53 (0.03)	0.0167 (0.0010)	0.34 (0.06)	6.16 (0.12)	3
J080751.84+443030.4	DA	7.5	35,402 (1707)	7.87 (0.28)	Pure H	0.59 (0.13)	0.0148 (0.0032)	−0.51 (0.20)	6.72 (0.11)	
J080758.46+341151.0	DA	26.5	67,778 (3345)	7.55 (0.16)	Pure H	0.55 (0.05)	0.0207 (0.0028)	0.91 (0.15)	5.67 (0.39)	
J080758.75+134419.1	DA	51.2	35,181 (264)	8.40 (0.04)	Pure H	0.89 (0.03)	0.0098 (0.0004)	−0.87 (0.03)	6.95 (0.09)	
J080759.46+273823.8	DA+M	25.7	33,647 (379)	7.32 (0.07)	Pure H	0.38 (0.02)	0.0225 (0.0012)	−0.23 (0.05)	5.88 (0.37)	1
J080810.24+262614.4	DA	17.8	41,780 (1353)	7.81 (0.14)	Pure H	0.58 (0.06)	0.0157 (0.0017)	−0.17 (0.11)	6.52 (0.05)	
J080824.44+304726.5	DA	16.4	30,269 (391)	7.76 (0.10)	Pure H	0.53 (0.04)	0.0159 (0.0012)	−0.72 (0.07)	6.91 (0.04)	
J080844.34+540348.5	DA	10.0	30,822 (739)	7.67 (0.18)	Pure H	0.49 (0.07)	0.0170 (0.0023)	−0.63 (0.13)	6.86 (0.12)	
J080846.59+182558.1	DA+M	16.9	31,143 (617)	8.12 (0.15)	Pure H	0.72 (0.09)	0.0122 (0.0014)	−0.90 (0.10)	6.94 (0.10)	1,2
J080855.37+561503.3	DA	48.8	47,836 (719)	7.73 (0.06)	Pure H	0.56 (0.02)	0.0170 (0.0008)	0.13 (0.05)	6.33 (0.03)	

Table 2.1 – Atmospheric and stellar parameters of hot white dwarfs from SDSS DR12 (continued)

SDSS Name	Type	S/N	$T_{\rm eff}$ (K)	$\log g$	Composition	$M/M_{\odot}$	$R/R_{\odot}$	$\log L/L_{\odot}$	$\log \tau_{\rm cool}$	Notes
J080913.04−075310.2	DA	57.7	52,082 (1089)	7.41 (0.08)	Pure H	0.46 (0.03)	0.0223 (0.0013)	0.52 (0.06)	5.06 (0.52)	5
J080921.89+192400.0	DAO	67.5	85,973 (3969)	7.37 (0.12)	$\log N_{\rm He}/N_{\rm H} = -2.76$	0.55 (0.03)	0.0255 (0.0028)	1.50 (0.13)	<5.00	4,5
J080942.21+063535.8	DA	4.1	30,720 (1601)	9.34 (0.40)	Pure H	1.32 (0.16)	0.0041 (0.0017)	−1.88 (0.36)	8.48 (0.35)	
J081001.29+315607.3	DA	5.0	31,017 (1233)	7.73 (0.29)	Pure H	0.52 (0.12)	0.0163 (0.0035)	−0.66 (0.20)	6.87 (0.14)	7
J081002.57+230046.3	DA	61.5	31,302 (136)	7.89 (0.03)	Pure H	0.59 (0.02)	0.0145 (0.0003)	−0.74 (0.02)	6.89 (0.01)	
J081018.08+311034.0	DA	15.3	34,661 (890)	8.04 (0.16)	Pure H	0.67 (0.09)	0.0131 (0.0015)	−0.65 (0.11)	6.75 (0.04)	
J081031.30+451832.6	DA	18.0	56,927 (3447)	7.58 (0.21)	Pure H	0.53 (0.07)	0.0196 (0.0034)	0.56 (0.19)	5.96 (0.40)	
J081044.90−064319.4	DA	15.3	39,387 (1229)	7.72 (0.15)	Pure H	0.54 (0.06)	0.0167 (0.0019)	−0.22 (0.11)	6.57 (0.09)	
J081048.45+491423.7	DA	11.1	50,507 (3592)	7.40 (0.26)	Pure H	0.46 (0.08)	0.0223 (0.0046)	0.46 (0.22)	5.14 (1.18)	
J081051.06−060043.0	DA	28.1	71,754 (4600)	7.06 (0.18)	Pure H	0.43 (0.04)	0.0321 (0.0052)	1.39 (0.19)	<5.00	
J081051.27+465226.2	DA	5.7	36,683 (2276)	7.60 (0.33)	Pure H	0.48 (0.13)	0.0182 (0.0047)	−0.27 (0.25)	6.56 (0.29)	
J081114.88+473019.1	DA+M	54.9	65,808 (1782)	7.36 (0.09)	Pure H	0.48 (0.03)	0.0241 (0.0018)	0.99 (0.08)	<5.00	1
J081115.08+270621.8	DO	35.0	46,603 (213)	7.73 (0.06)	Pure He	0.52 (0.02)	0.0163 (0.0008)	0.05 (0.04)	6.37 (0.08)	
J081116.95+482640.4	DA	42.7	33,510 (243)	7.83 (0.05)	Pure H	0.57 (0.02)	0.0151 (0.0005)	−0.58 (0.03)	6.79 (0.01)	
J081121.10+150440.8	DA	18.2	69,672 (5178)	7.54 (0.24)	Pure H	0.56 (0.08)	0.0210 (0.0043)	0.97 (0.23)	5.63 (0.45)	
J081127.75+315233.1	DA	19.5	31,293 (391)	7.87 (0.09)	Pure H	0.58 (0.05)	0.0146 (0.0010)	−0.73 (0.06)	6.89 (0.02)	
J081136.33+461156.4	DA	6.5	30,236 (948)	7.93 (0.25)	Pure H	0.61 (0.13)	0.0140 (0.0026)	−0.83 (0.17)	6.94 (0.09)	
J081147.05+352138.3	DA	35.1	30,463 (193)	7.82 (0.05)	Pure H	0.55 (0.02)	0.0152 (0.0006)	−0.74 (0.03)	6.92 (0.01)	
J081148.47+140330.0	DA	10.8	30,013 (524)	7.86 (0.14)	Pure H	0.57 (0.07)	0.0148 (0.0015)	−0.80 (0.09)	6.94 (0.04)	
J081152.51+383155.5	DA	14.7	35,739 (928)	7.74 (0.15)	Pure H	0.53 (0.06)	0.0163 (0.0018)	−0.41 (0.11)	6.70 (0.07)	
J081207.51+125707.7	DA	35.9	43,808 (895)	7.49 (0.08)	Pure H	0.47 (0.03)	0.0203 (0.0014)	0.14 (0.07)	5.99 (0.33)	
J081215.18−001019.8	DA	14.8	42,867 (1504)	7.93 (0.15)	Pure H	0.64 (0.07)	0.0143 (0.0017)	−0.21 (0.12)	6.48 (0.04)	
J081226.91+145618.4	DA	16.8	63,531 (5112)	7.12 (0.25)	Pure H	0.42 (0.06)	0.0293 (0.0064)	1.10 (0.25)	<5.00	
J081231.32+562221.1	DBA	11.2	40,356 (4277)	7.82 (0.33)	$\log q_{\rm H} = -17.58$	0.55 (0.15)	0.0150 (0.0038)	−0.27 (0.29)	6.60 (0.30)	3
J081308.50+480642.3	DA	64.9	32,164 (137)	7.85 (0.03)	Pure H	0.58 (0.01)	0.0149 (0.0003)	−0.67 (0.02)	6.85 (0.01)	
J081320.00+215259.2	DA+M	6.0	30,641 (1033)	7.98 (0.26)	Pure H	0.64 (0.14)	0.0135 (0.0026)	−0.84 (0.18)	6.93 (0.12)	1
J081329.45+260550.3	DA	3.6	31,991 (1990)	8.13 (0.45)	Pure H	0.73 (0.25)	0.0121 (0.0042)	−0.86 (0.32)	6.90 (0.27)	
J081331.83+272204.2	DA	82.3	30,056 (74)	7.38 (0.02)	Pure H	0.39 (0.01)	0.0212 (0.0003)	−0.48 (0.01)	6.44 (0.07)	
J081406.15+521715.4	DA+M	65.6	41,040 (375)	7.55 (0.04)	Pure H	0.48 (0.01)	0.0193 (0.0006)	−0.02 (0.03)	6.29 (0.10)	1
J081429.56+215140.4	DA	18.3	62,532 (4892)	7.47 (0.24)	Pure H	0.51 (0.08)	0.0218 (0.0044)	0.82 (0.23)	5.36 (1.16)	5
J081458.13+034352.1	DA	3.9	57,099 (15,240)	7.81 (0.94)	Pure H	0.62 (0.39)	0.0161 (0.0140)	0.40 (0.85)	6.14 (0.99)	
J081505.17+224109.7	DA	19.3	33,502 (480)	7.70 (0.09)	Pure H	0.51 (0.04)	0.0168 (0.0012)	−0.49 (0.07)	6.76 (0.05)	
J081509.14+392912.2	DA	22.7	31,295 (335)	7.91 (0.08)	Pure H	0.60 (0.04)	0.0143 (0.0008)	−0.75 (0.05)	6.89 (0.02)	
J081514.43+511312.1	DA	34.6	68,654 (3202)	8.10 (0.15)	Pure H	0.77 (0.07)	0.0130 (0.0016)	0.53 (0.14)	5.88 (0.08)	5
J081522.56+265451.4	DA	4.5	35,837 (2899)	7.99 (0.46)	Pure H	0.65 (0.23)	0.0136 (0.0049)	−0.56 (0.34)	6.70 (0.28)	
J081533.08+264646.4	DO	5.4	57,259 (8157)	8.30 (0.91)	Pure He	0.82 (0.43)	0.0106 (0.0084)	0.04 (0.71)	6.10 (1.60)	
J081546.08+244603.2	DO	15.0	46,468 (580)	7.89 (0.15)	Pure He	0.59 (0.07)	0.0144 (0.0016)	−0.06 (0.10)	6.45 (0.03)	
J081546.09−070648.2	DA	9.8	42,823 (2992)	7.03 (0.30)	Pure H	0.32 (0.07)	0.0289 (0.0068)	0.40 (0.24)	<5.00	
J081559.30+464655.4	DA	15.5	32,290 (559)	7.82 (0.12)	Pure H	0.56 (0.06)	0.0152 (0.0014)	−0.64 (0.08)	6.84 (0.03)	
J081613.71+322330.7	DO	11.5	67,844 (6249)	7.66 (0.58)	Pure He	0.54 (0.22)	0.0181 (0.0086)	0.80 (0.44)	5.67 (0.62)	
J081618.17+131620.5	DAO	74.6	62,112 (1653)	7.11 (0.08)	$\log N_{\rm He}/N_{\rm H} = -2.40$	0.41 (0.02)	0.0295 (0.0020)	1.07 (0.08)	<5.00	4,5
J081618.79+034234.2	DAO	14.9	50,419 (3205)	7.69 (0.26)	$\log N_{\rm He}/N_{\rm H} = -1.18$	0.55 (0.10)	0.0175 (0.0037)	0.25 (0.22)	6.25 (0.18)	4
J081625.47−002815.4	DOZ	51.5	90,555 (5824)	7.69 (0.19)	Pure He	0.60 (0.06)	0.0183 (0.0030)	1.31 (0.19)	5.43 (0.44)	6
J081632.53+205700.3	DA	4.5	31,463 (1680)	7.81 (0.39)	Pure H	0.55 (0.18)	0.0154 (0.0046)	−0.68 (0.27)	6.87 (0.25)	
J081640.52+365130.2	DA	7.8	30,413 (830)	8.43 (0.21)	Pure H	0.90 (0.13)	0.0096 (0.0017)	−1.15 (0.16)	7.47 (0.39)	
J081642.90+064740.4	DB	4.5	39,768 (4362)	8.21 (0.53)	Pure He	0.75 (0.29)	0.0113 (0.0047)	−0.54 (0.41)	6.60 (0.34)	
J081643.85−003955.1	DA	2.6	34,794 (2580)	7.53 (0.45)	Pure H	0.45 (0.16)	0.0191 (0.0065)	−0.32 (0.32)	6.54 (0.48)	
J081656.49+335032.4	DA	5.6	37,945 (2481)	7.84 (0.33)	Pure H	0.58 (0.15)	0.0152 (0.0039)	−0.37 (0.25)	6.64 (0.18)	7
J081709.70+143923.0	DA	16.7	50,662 (2798)	6.93 (0.20)	Pure H	0.33 (0.04)	0.0326 (0.0054)	0.80 (0.18)	<5.00	
J081716.98+054223.6	DA+M	12.5	35,402 (1228)	7.94 (0.20)	Pure H	0.63 (0.10)	0.0140 (0.0021)	−0.56 (0.15)	6.72 (0.05)	1,2

Table 2.1 – Atmospheric and stellar parameters of hot white dwarfs from SDSS DR12 (continued)

SDSS Name	Type	S/N	$T_{\rm eff}$ (K)	$\log g$	Composition	$M/M_{\odot}$	$R/R_{\odot}$	$\log L/L_{\odot}$	$\log \tau_{\rm cool}$	Notes
J081739.99+163117.1	DO	17.1	59,964 (2619)	8.45 (0.27)	Pure He	0.92 (0.15)	0.0094 (0.0021)	0.01 (0.21)	6.00 (0.08)	
J081740.08+002959.8	DA	9.7	51,586 (3478)	8.05 (0.25)	Pure H	0.71 (0.13)	0.0132 (0.0027)	0.05 (0.21)	6.24 (0.09)	
J081757.63+314805.8	DA	33.6	35,829 (397)	7.91 (0.06)	Pure H	0.61 (0.03)	0.0144 (0.0007)	−0.51 (0.05)	6.71 (0.01)	
J081806.88+121155.3	DA	52.6	31,986 (192)	8.15 (0.04)	Pure H	0.73 (0.03)	0.0120 (0.0004)	−0.87 (0.03)	6.90 (0.03)	
J081819.51+225349.9	DA	38.5	33,858 (279)	7.24 (0.05)	Pure H	0.36 (0.02)	0.0239 (0.0009)	−0.17 (0.04)	5.43 (0.28)	
J081820.41+270532.6	DA	112.3	81,046 (1753)	7.39 (0.05)	Pure H	0.54 (0.02)	0.0247 (0.0011)	1.38 (0.06)	<5.00	5
J081840.74+204748.0	DA+M	16.6	31,296 (470)	7.68 (0.11)	Pure H	0.50 (0.04)	0.0168 (0.0014)	−0.61 (0.08)	6.84 (0.06)	1,2
J081841.59+454538.0	DA	36.3	30,112 (200)	7.37 (0.05)	Pure H	0.39 (0.02)	0.0214 (0.0009)	−0.47 (0.04)	6.40 (0.22)	
J081849.41+190928.9	DA	4.2	30,181 (1315)	8.04 (0.35)	Pure H	0.67 (0.19)	0.0129 (0.0034)	−0.90 (0.24)	6.96 (0.20)	
J081900.46+393637.9	DA	40.2	39,773 (494)	7.78 (0.06)	Pure H	0.56 (0.02)	0.0160 (0.0007)	−0.24 (0.04)	6.57 (0.02)	
J081918.31+060714.0	DA	4.6	38,922 (3832)	7.53 (0.47)	Pure H	0.46 (0.17)	0.0195 (0.0072)	−0.11 (0.36)	6.33 (0.64)	
J082020.86+444433.0	DA	41.5	36,760 (387)	7.94 (0.06)	Pure H	0.63 (0.03)	0.0140 (0.0006)	−0.49 (0.04)	6.67 (0.01)	
J082026.55−000517.5	DA	23.8	31,687 (319)	7.89 (0.07)	Pure H	0.59 (0.04)	0.0145 (0.0008)	−0.72 (0.05)	6.87 (0.01)	
J082034.19+005139.1	DA	9.9	62,214 (7937)	6.90 (0.38)	Pure H	0.36 (0.09)	0.0356 (0.0117)	1.23 (0.38)	<5.00	
J082134.94+173919.3	DOZ	26.3	64,545 (2659)	7.75 (0.27)	Pure He	0.57 (0.11)	0.0166 (0.0036)	0.63 (0.20)	5.98 (0.19)	6,8
J082153.01+190659.1	DAB	23.5	39,236 (3086)	7.82 (0.25)	$\log q_{\rm H} = -16.51$	0.55 (0.11)	0.0150 (0.0028)	−0.32 (0.22)	6.63 (0.21)	3
J082200.49+273050.3	DA	12.1	41,928 (1904)	7.87 (0.20)	Pure H	0.61 (0.09)	0.0150 (0.0023)	−0.20 (0.16)	6.51 (0.07)	
J082257.56+575011.0	DA	43.2	67,526 (2010)	7.51 (0.10)	Pure H	0.54 (0.03)	0.0214 (0.0017)	0.93 (0.09)	5.45 (0.55)	
J082300.81+821539.1	DAO	13.2	124,615 (25,235)	6.42 (0.34)	$\log N_{\rm He}/N_{\rm H} = -1.28$	0.49 (0.11)	0.0713 (0.0243)	3.04 (0.52)	<5.00	4
J082321.79+245140.4	DA	41.7	56,115 (1524)	7.30 (0.09)	Pure H	0.43 (0.03)	0.0244 (0.0018)	0.73 (0.08)	<5.00	5
J082346.14+245345.6	DA	105.2	33,428 (98)	7.72 (0.02)	Pure H	0.52 (0.01)	0.0164 (0.0002)	−0.52 (0.01)	6.77 (0.01)	
J082346.47+541546.1	DA	14.4	36,327 (946)	7.67 (0.14)	Pure H	0.51 (0.05)	0.0173 (0.0019)	−0.33 (0.11)	6.63 (0.13)	
J082451.87+225332.6	DA	18.6	48,459 (2143)	7.72 (0.17)	Pure H	0.56 (0.07)	0.0170 (0.0023)	0.16 (0.14)	6.32 (0.12)	
J082529.12+110413.8	DA	16.2	35,169 (797)	8.85 (0.14)	Pure H	1.14 (0.07)	0.0066 (0.0009)	−1.22 (0.12)	7.84 (0.17)	
J082538.04+180522.7	DAO	16.7	48,442 (1915)	7.92 (0.26)	$\log q_{\rm H} = -16.31$	0.60 (0.12)	0.0142 (0.0029)	−0.00 (0.19)	6.40 (0.10)	3
J082613.22+393846.2	DA	27.5	46,208 (1190)	8.06 (0.10)	Pure H	0.71 (0.05)	0.0130 (0.0011)	−0.16 (0.08)	6.37 (0.04)	
J082613.32+262850.8	DA	6.1	36,407 (2096)	7.73 (0.32)	Pure H	0.53 (0.13)	0.0165 (0.0041)	−0.36 (0.24)	6.67 (0.15)	
J082628.10+145558.2	DA	26.3	33,729 (350)	7.84 (0.07)	Pure H	0.57 (0.03)	0.0151 (0.0008)	−0.58 (0.05)	6.79 (0.01)	
J082636.85+470124.3	DA	6.5	62,749 (9593)	7.45 (0.50)	Pure H	0.51 (0.16)	0.0222 (0.0098)	0.84 (0.47)	5.22 (1.54)	
J082638.54+193210.7	DA	2.2	30,808 (2401)	7.46 (0.59)	Pure H	0.42 (0.21)	0.0200 (0.0090)	−0.49 (0.41)	6.63 (0.67)	
J082647.68−042123.9	DBA	45.9	42,254 (800)	7.85 (0.07)	$\log q_{\rm H} = -18.24$	0.56 (0.03)	0.0147 (0.0008)	−0.20 (0.06)	6.55 (0.03)	3
J082704.44+184624.3	DA	21.9	30,612 (352)	7.18 (0.09)	Pure H	0.33 (0.03)	0.0245 (0.0015)	−0.32 (0.06)	5.48 (0.39)	
J082705.53+313008.2	DAO	99.1	74,279 (1868)	7.35 (0.06)	$\log N_{\rm He}/N_{\rm H} = -2.43$	0.50 (0.02)	0.0249 (0.0014)	1.23 (0.07)	<5.00	4,5
J082724.45+585851.6	DO	35.5	92,751 (8459)	7.22 (0.25)	Pure He	0.47 (0.07)	0.0276 (0.0061)	1.71 (0.26)	<5.00	8
J082726.43+444530.9	DA	23.3	48,744 (1909)	7.10 (0.15)	Pure H	0.36 (0.03)	0.0280 (0.0034)	0.60 (0.13)	<5.00	
J082730.35+062301.6	DA	8.0	53,182 (5423)	8.27 (0.38)	Pure H	0.84 (0.20)	0.0111 (0.0035)	−0.05 (0.33)	6.14 (0.15)	
J082750.50+373831.1	DA	21.1	46,927 (1717)	7.74 (0.14)	Pure H	0.56 (0.06)	0.0168 (0.0019)	0.09 (0.12)	6.36 (0.10)	7
J082753.81+140619.9	DA	7.0	39,968 (2821)	7.77 (0.33)	Pure H	0.56 (0.14)	0.0161 (0.0042)	−0.22 (0.26)	6.57 (0.21)	
J082758.51+242859.8	DA	14.4	35,987 (883)	7.70 (0.14)	Pure H	0.52 (0.05)	0.0169 (0.0018)	−0.37 (0.10)	6.67 (0.09)	
J082800.94−042204.4	DA	29.1	49,519 (1340)	7.48 (0.10)	Pure H	0.48 (0.03)	0.0209 (0.0017)	0.37 (0.09)	5.70 (0.54)	
J082819.56+122919.5	DA	15.0	33,096 (642)	7.73 (0.13)	Pure H	0.52 (0.05)	0.0164 (0.0016)	−0.54 (0.09)	6.79 (0.06)	
J082857.94+324855.2	DA	32.2	30,135 (228)	7.85 (0.06)	Pure H	0.57 (0.03)	0.0149 (0.0007)	−0.78 (0.04)	6.94 (0.01)	
J082944.46+530101.1	DA	32.4	30,398 (215)	7.82 (0.06)	Pure H	0.56 (0.03)	0.0152 (0.0006)	−0.75 (0.04)	6.92 (0.01)	
J083022.88+272244.3	DA	28.0	55,274 (1986)	7.33 (0.12)	Pure H	0.44 (0.04)	0.0238 (0.0024)	0.68 (0.11)	<5.00	
J083029.76+061844.0	DA	6.7	51,573 (6248)	7.15 (0.43)	Pure H	0.38 (0.12)	0.0272 (0.0098)	0.67 (0.38)	<5.00	
J083038.79+470246.9	DA+M	18.2	39,127 (1333)	7.94 (0.17)	Pure H	0.63 (0.08)	0.0142 (0.0018)	−0.37 (0.13)	6.59 (0.04)	1,2
J083056.12+315941.9	DA+M	10.9	30,360 (797)	7.69 (0.21)	Pure H	0.50 (0.08)	0.0167 (0.0026)	−0.67 (0.14)	6.88 (0.12)	1,2
J083058.23+262110.7	DA	6.8	30,864 (889)	7.79 (0.22)	Pure H	0.55 (0.10)	0.0155 (0.0025)	−0.71 (0.15)	6.90 (0.08)	
J083115.33−051815.8	DA	40.5	35,402 (287)	7.85 (0.05)	Pure H	0.58 (0.02)	0.0151 (0.0005)	−0.49 (0.03)	6.72 (0.01)	
J083130.03+131038.2	DA	4.4	33,108 (2034)	8.00 (0.41)	Pure H	0.65 (0.21)	0.0133 (0.0042)	−0.72 (0.29)	6.81 (0.26)	

Table 2.1 – Atmospheric and stellar parameters of hot white dwarfs from SDSS DR12 (continued)

SDSS Name	Type	S/N	$T_{\rm eff}$ (K)	$\log g$	Composition	$M/M_{\odot}$	$R/R_{\odot}$	$\log L/L_{\odot}$	$\log \tau_{\rm cool}$	Notes
J083135.86+083124.1	DA	5.2	30,834 (1069)	7.98 (0.27)	Pure H	0.64 (0.14)	0.0135 (0.0027)	−0.83 (0.18)	6.92 (0.12)	
J083200.78+172628.5	DA	40.1	39,087 (450)	7.58 (0.05)	Pure H	0.48 (0.02)	0.0187 (0.0008)	−0.13 (0.04)	6.43 (0.10)	
J083219.95+153727.9	DA	27.6	55,060 (1939)	7.55 (0.12)	Pure H	0.52 (0.04)	0.0200 (0.0020)	0.52 (0.11)	5.93 (0.37)	
J083228.27+441441.8	DA	15.1	69,977 (7062)	7.13 (0.29)	Pure H	0.44 (0.07)	0.0300 (0.0079)	1.29 (0.30)	<5.00	
J083253.66+233121.2	DA+M	16.2	51,359 (3025)	7.85 (0.22)	Pure H	0.62 (0.09)	0.0155 (0.0028)	0.18 (0.19)	6.27 (0.10)	1,2
J083255.84+542353.8	DA	15.4	39,270 (1250)	7.58 (0.15)	Pure H	0.48 (0.05)	0.0187 (0.0023)	−0.12 (0.12)	6.42 (0.30)	
J083300.12+272254.5	DA	20.6	31,258 (413)	7.76 (0.10)	Pure H	0.53 (0.04)	0.0159 (0.0012)	−0.66 (0.07)	6.87 (0.03)	
J083317.76+025015.8	DA	17.9	63,901 (4515)	7.20 (0.22)	Pure H	0.43 (0.06)	0.0275 (0.0053)	1.06 (0.22)	<5.00	
J083324.56+041916.5	DA	49.9	31,284 (156)	7.32 (0.04)	Pure H	0.38 (0.01)	0.0223 (0.0006)	−0.37 (0.03)	6.09 (0.18)	
J083345.75+295748.3	DA	33.9	37,800 (483)	7.85 (0.07)	Pure H	0.59 (0.03)	0.0151 (0.0007)	−0.38 (0.05)	6.64 (0.02)	
J083420.39+231600.6	DB	6.3	37,713 (7145)	7.45 (0.52)	Pure He	0.40 (0.18)	0.0198 (0.0075)	−0.15 (0.48)	5.91 (1.48)	
J083423.38+184940.1	DA	4.8	48,978 (7870)	8.16 (0.62)	Pure H	0.77 (0.31)	0.0120 (0.0063)	−0.12 (0.53)	6.28 (0.40)	
J083443.94+074947.6	DA	18.2	37,356 (864)	7.80 (0.12)	Pure H	0.56 (0.05)	0.0157 (0.0014)	−0.36 (0.09)	6.65 (0.04)	
J083502.97+410639.9	DA	47.9	31,598 (162)	8.39 (0.04)	Pure H	0.88 (0.02)	0.0099 (0.0003)	−1.05 (0.03)	7.27 (0.09)	
J083504.76+090111.7	DOZ	23.5	71,863 (3551)	8.70 (0.25)	Pure He	1.06 (0.13)	0.0076 (0.0017)	0.15 (0.22)	5.72 (0.08)	6
J083531.68+315503.2	DA	8.3	32,873 (1150)	8.08 (0.24)	Pure H	0.69 (0.13)	0.0126 (0.0023)	−0.77 (0.17)	6.83 (0.11)	
J083540.95+155224.8	DA	5.4	46,999 (4562)	7.82 (0.38)	Pure H	0.60 (0.16)	0.0157 (0.0049)	0.04 (0.32)	6.38 (0.29)	
J083549.96+475516.6	DA	21.7	44,549 (1460)	7.70 (0.13)	Pure H	0.54 (0.05)	0.0172 (0.0019)	0.02 (0.11)	6.41 (0.10)	
J083600.33+060853.4	DA	41.5	32,791 (215)	7.34 (0.04)	Pure H	0.39 (0.01)	0.0220 (0.0008)	−0.30 (0.03)	6.09 (0.22)	
J083610.09+160558.7	DO	38.0	106,807 (5367)	7.37 (0.27)	Pure He	0.53 (0.08)	0.0251 (0.0062)	1.87 (0.23)	<5.00	
J083629.26−040640.2	DB	14.2	33,841 (1791)	7.82 (0.19)	Pure He	0.53 (0.09)	0.0148 (0.0020)	−0.59 (0.15)	6.81 (0.11)	
J083633.86+210436.1	DA	23.1	56,610 (2440)	7.67 (0.15)	Pure H	0.56 (0.05)	0.0182 (0.0023)	0.49 (0.14)	6.07 (0.20)	
J083650.27+155326.4	DA	54.8	50,581 (710)	7.74 (0.05)	Pure H	0.57 (0.02)	0.0169 (0.0007)	0.23 (0.04)	6.27 (0.03)	
J083659.21+062204.8	DA	59.5	37,323 (282)	7.77 (0.04)	Pure H	0.55 (0.02)	0.0160 (0.0005)	−0.35 (0.03)	6.65 (0.01)	
J083700.70+193154.7	DA	4.6	34,325 (1907)	8.09 (0.35)	Pure H	0.70 (0.19)	0.0125 (0.0033)	−0.71 (0.25)	6.77 (0.16)	
J083716.93+094540.9	DA	6.6	37,009 (2407)	7.26 (0.34)	Pure H	0.37 (0.10)	0.0237 (0.0062)	−0.02 (0.26)	5.30 (1.18)	
J083736.58+143643.7	DA	5.8	31,209 (1136)	7.81 (0.27)	Pure H	0.55 (0.12)	0.0154 (0.0031)	−0.69 (0.19)	6.88 (0.11)	
J083755.46+023516.9	DA	32.6	31,630 (254)	7.85 (0.06)	Pure H	0.57 (0.03)	0.0149 (0.0006)	−0.70 (0.04)	6.87 (0.01)	
J083808.01+530254.2	DA+M	10.8	45,331 (3105)	7.17 (0.27)	Pure H	0.37 (0.08)	0.0260 (0.0056)	0.41 (0.22)	<5.00	1
J083838.52+065240.1	DA	53.2	63,528 (1567)	7.36 (0.08)	Pure H	0.48 (0.02)	0.0240 (0.0015)	0.93 (0.07)	<5.00	5
J083840.30+095325.3	DA	6.1	36,176 (2256)	8.44 (0.35)	Pure H	0.92 (0.20)	0.0095 (0.0027)	−0.85 (0.27)	6.95 (0.56)	
J083843.64+145500.4	DA	6.0	39,665 (3149)	7.82 (0.38)	Pure H	0.58 (0.17)	0.0155 (0.0046)	−0.27 (0.29)	6.58 (0.23)	
J083917.93+531542.0	DA	9.8	30,863 (714)	7.54 (0.18)	Pure H	0.44 (0.06)	0.0188 (0.0025)	−0.54 (0.12)	6.75 (0.27)	
J083942.74+552438.5	DO	18.8	73,479 (5883)	7.55 (0.43)	Pure He	0.51 (0.15)	0.0198 (0.0072)	1.01 (0.34)	<5.00	8
J083959.93+142857.9	DO	14.6	111,220 (9423)	8.66 (0.62)	Pure He	1.06 (0.27)	0.0079 (0.0047)	0.94 (0.52)	5.01 (0.25)	
J084008.72+325114.5	DOZ	15.6	80,224 (8371)	8.53 (0.42)	Pure He	0.97 (0.22)	0.0089 (0.0033)	0.47 (0.37)	5.59 (0.19)	6
J084019.99+402730.8	DA	28.7	30,469 (238)	7.77 (0.06)	Pure H	0.53 (0.03)	0.0158 (0.0007)	−0.71 (0.04)	6.91 (0.02)	
J084109.08+292135.9	DA	11.3	30,262 (454)	8.35 (0.12)	Pure H	0.85 (0.07)	0.0102 (0.0010)	−1.10 (0.09)	7.33 (0.24)	
J084135.55+581348.3	DA	94.9	56,668 (693)	7.65 (0.04)	Pure H	0.55 (0.01)	0.0184 (0.0007)	0.50 (0.04)	6.06 (0.04)	
J084153.73+035732.4	DA	18.7	42,834 (1643)	7.84 (0.16)	Pure H	0.59 (0.07)	0.0154 (0.0020)	−0.14 (0.13)	6.49 (0.06)	
J084156.75+401512.5	DAO	39.8	69,679 (5270)	7.71 (0.22)	$\log N_{\rm He}/N_{\rm H} = -0.58$	0.61 (0.08)	0.0180 (0.0034)	0.84 (0.22)	5.82 (0.29)	4,5
J084211.05+130306.9	DA	18.0	65,296 (3928)	7.24 (0.19)	Pure H	0.45 (0.05)	0.0268 (0.0044)	1.07 (0.18)	<5.00	
J084214.20+440238.0	DA	14.7	33,399 (648)	7.73 (0.13)	Pure H	0.53 (0.05)	0.0163 (0.0016)	−0.52 (0.09)	6.78 (0.06)	
J084223.14+375900.1	DOZ	44.2	76,126 (2820)	7.53 (0.18)	Pure He	0.50 (0.06)	0.0202 (0.0030)	1.09 (0.14)	<5.00	6,8
J084229.66+525417.7	DA+M	10.2	39,975 (1823)	7.90 (0.21)	Pure H	0.61 (0.10)	0.0146 (0.0024)	−0.31 (0.16)	6.57 (0.06)	1
J084239.97+023621.5	DA	38.7	43,365 (975)	7.78 (0.10)	Pure H	0.57 (0.04)	0.0161 (0.0012)	−0.09 (0.08)	6.47 (0.04)	7
J084308.07+474815.9	DA	7.9	31,589 (970)	7.23 (0.22)	Pure H	0.35 (0.07)	0.0239 (0.0039)	−0.29 (0.15)	5.58 (0.91)	
J084324.58+393151.5	DA	2.8	43,724 (7721)	9.04 (0.79)	Pure H	1.23 (0.38)	0.0056 (0.0043)	−0.99 (0.72)	7.69 (1.26)	
J084330.81+201049.1	DA	29.3	100,362 (7635)	7.87 (0.22)	Pure H	0.73 (0.08)	0.0164 (0.0034)	1.39 (0.23)	5.34 (0.21)	
J084353.63+174626.6	DA	5.1	40,868 (4664)	7.08 (0.51)	Pure H	0.33 (0.14)	0.0275 (0.0112)	0.28 (0.41)	<5.00	

Table 2.1 – Atmospheric and stellar parameters of hot white dwarfs from SDSS DR12 (continued)

SDSS Name	Type	S/N	$T_{\rm eff}$ (K)	$\log g$	Composition	$M/M_\odot$	$R/R_\odot$	$\log L/L_\odot$	$\log \tau_{\rm cool}$	Notes
J084353.75+021654.5	DA	5.5	53,549 (10,352)	7.48 (0.69)	Pure H	0.49 (0.24)	0.0211 (0.0124)	0.52 (0.61)	5.59 (1.38)	
J084404.83+070942.8	DA	75.6	32,011 (116)	7.84 (0.03)	Pure H	0.57 (0.01)	0.0151 (0.0003)	−0.67 (0.02)	6.85 (0.01)	
J084418.72+005309.9	DA	28.8	36,337 (487)	7.84 (0.07)	Pure H	0.58 (0.03)	0.0152 (0.0008)	−0.44 (0.05)	6.69 (0.02)	
J084443.43+555403.9	DA+M	10.1	37,528 (2221)	7.77 (0.31)	Pure H	0.55 (0.13)	0.0161 (0.0038)	−0.34 (0.23)	6.64 (0.17)	1
J084512.14+203049.2	DOZ	15.2	78,549 (8992)	8.17 (0.50)	Pure He	0.77 (0.24)	0.0120 (0.0053)	0.69 (0.42)	5.76 (0.19)	6
J084535.15+234806.0	DA+M	8.5	42,380 (3123)	7.76 (0.32)	Pure H	0.56 (0.13)	0.0163 (0.0042)	−0.11 (0.26)	6.49 (0.23)	1
J084608.35+413852.7	DA	33.0	37,042 (473)	7.90 (0.07)	Pure H	0.61 (0.03)	0.0145 (0.0007)	−0.45 (0.05)	6.67 (0.02)	
J084618.45+154419.9	DA	45.5	38,915 (383)	7.89 (0.05)	Pure H	0.61 (0.02)	0.0147 (0.0005)	−0.35 (0.04)	6.60 (0.01)	
J084639.27+091406.7	DA	57.4	40,352 (396)	7.83 (0.04)	Pure H	0.58 (0.02)	0.0154 (0.0005)	−0.24 (0.03)	6.56 (0.01)	
J084652.38+170208.7	DA	8.9	55,993 (5759)	7.43 (0.36)	Pure H	0.48 (0.11)	0.0220 (0.0066)	0.63 (0.32)	5.16 (1.31)	
J084823.52+033216.7	DB	11.8	33,864 (2006)	7.75 (0.21)	Pure He	0.50 (0.09)	0.0157 (0.0024)	−0.54 (0.17)	6.78 (0.18)	
J084836.65+511942.8	DA	18.4	44,561 (1535)	7.70 (0.14)	Pure H	0.54 (0.05)	0.0172 (0.0019)	0.02 (0.12)	6.41 (0.11)	
J084846.09+062816.3	DA	8.0	44,782 (3443)	7.26 (0.31)	Pure H	0.39 (0.09)	0.0243 (0.0060)	0.33 (0.25)	<5.00	7
J084848.12+310811.8	DA	8.0	34,944 (1356)	7.57 (0.23)	Pure H	0.47 (0.08)	0.0186 (0.0034)	−0.33 (0.17)	6.59 (0.32)	
J084907.26+113925.6	DA	89.5	35,327 (149)	7.22 (0.03)	Pure H	0.36 (0.01)	0.0243 (0.0004)	−0.08 (0.02)	5.20 (0.13)	
J084922.68+142603.9	DA	30.0	36,321 (451)	7.14 (0.07)	Pure H	0.33 (0.02)	0.0258 (0.0013)	0.02 (0.05)	<5.00	
J084951.91+071112.9	DA	8.8	52,043 (4088)	7.75 (0.29)	Pure H	0.58 (0.11)	0.0168 (0.0040)	0.27 (0.25)	6.24 (0.25)	
J084953.09+105621.2	DB	63.2	31,970 (468)	8.18 (0.05)	Pure He	0.72 (0.03)	0.0115 (0.0004)	−0.91 (0.04)	6.95 (0.04)	
J085029.21+060040.8	DA	8.9	64,890 (8720)	6.83 (0.38)	Pure H	0.36 (0.09)	0.0379 (0.0125)	1.36 (0.39)	<5.00	
J085052.22+034443.8	DAB	15.5	31,013 (2410)	8.00 (0.36)	$\log q_{\rm H} = -16.83$	0.61 (0.19)	0.0131 (0.0035)	−0.85 (0.27)	6.95 (0.25)	3
J085129.86+220932.7	DA	8.8	30,639 (701)	7.78 (0.17)	Pure H	0.54 (0.08)	0.0156 (0.0019)	−0.71 (0.12)	6.90 (0.06)	7
J085134.87+114217.7	DB	15.6	33,449 (1371)	7.96 (0.15)	Pure He	0.60 (0.08)	0.0134 (0.0014)	−0.69 (0.12)	6.84 (0.06)	
J085142.17+182653.2	DA+M	11.2	63,713 (7057)	7.91 (0.38)	Pure H	0.67 (0.16)	0.0150 (0.0049)	0.52 (0.34)	6.01 (0.27)	1
J085148.55+095035.1	DA	21.1	61,685 (3546)	7.93 (0.18)	Pure H	0.68 (0.08)	0.0148 (0.0022)	0.45 (0.17)	6.04 (0.07)	5
J085152.99+195146.7	DA	18.6	50,826 (2630)	8.26 (0.20)	Pure H	0.83 (0.11)	0.0112 (0.0018)	−0.12 (0.17)	6.21 (0.08)	
J085213.49+011706.8	DB	7.2	38,000 (4130)	7.42 (0.30)	Pure He	0.39 (0.10)	0.0202 (0.0042)	−0.11 (0.27)	5.73 (1.13)	
J085230.99+533901.8	DA	36.8	53,425 (1614)	7.89 (0.11)	Pure H	0.64 (0.05)	0.0151 (0.0014)	0.22 (0.10)	6.22 (0.04)	5
J085302.05+174843.1	DA	49.8	63,367 (1894)	7.53 (0.09)	Pure H	0.53 (0.03)	0.0209 (0.0016)	0.80 (0.09)	5.60 (0.42)	5
J085305.11+461013.0	DA	5.5	48,078 (5674)	7.71 (0.45)	Pure H	0.56 (0.19)	0.0171 (0.0063)	0.15 (0.38)	6.32 (0.48)	
J085308.98−001605.5	DA	22.3	38,942 (907)	7.82 (0.11)	Pure H	0.58 (0.05)	0.0154 (0.0013)	−0.31 (0.09)	6.60 (0.03)	
J085318.60+032444.6	DB	3.6	43,174 (8218)	7.89 (0.80)	Pure He	0.59 (0.38)	0.0143 (0.0091)	−0.19 (0.63)	6.53 (0.99)	
J085402.36+100443.1	DA+M	13.8	31,325 (556)	7.85 (0.13)	Pure H	0.57 (0.06)	0.0149 (0.0014)	−0.72 (0.09)	6.88 (0.03)	1
J085403.81+101705.2	DA	19.6	35,452 (555)	8.10 (0.09)	Pure H	0.71 (0.05)	0.0125 (0.0009)	−0.65 (0.07)	6.72 (0.03)	
J085404.89+244848.8	DA	5.0	42,060 (4548)	8.73 (0.49)	Pure H	1.09 (0.24)	0.0075 (0.0033)	−0.80 (0.43)	7.19 (0.84)	
J085421.57+231156.8	DA	10.2	50,696 (3597)	7.35 (0.26)	Pure H	0.44 (0.08)	0.0231 (0.0048)	0.50 (0.22)	<5.00	
J085430.09+243018.4	DA	9.0	30,968 (695)	7.68 (0.17)	Pure H	0.50 (0.07)	0.0169 (0.0022)	−0.63 (0.12)	6.85 (0.10)	
J085440.04+602603.6	DA	15.2	58,114 (5297)	6.78 (0.29)	Pure H	0.32 (0.06)	0.0382 (0.0090)	1.18 (0.27)	<5.00	
J085459.07+355755.7	DA	8.8	49,723 (4372)	8.21 (0.34)	Pure H	0.80 (0.18)	0.0116 (0.0032)	−0.13 (0.28)	6.25 (0.12)	
J085502.99+063548.3	DA	8.0	44,178 (3210)	7.45 (0.30)	Pure H	0.46 (0.10)	0.0210 (0.0049)	0.18 (0.24)	5.78 (1.10)	
J085528.43+610211.2	DA	86.4	35,160 (180)	7.31 (0.03)	Pure H	0.39 (0.01)	0.0228 (0.0005)	−0.15 (0.02)	5.72 (0.16)	
J085616.06+003138.8	DA	6.4	34,642 (1852)	7.88 (0.33)	Pure H	0.60 (0.16)	0.0146 (0.0036)	−0.56 (0.23)	6.75 (0.13)	
J085634.52+502748.2	DA	50.8	33,555 (207)	7.99 (0.04)	Pure H	0.65 (0.02)	0.0135 (0.0004)	−0.68 (0.03)	6.79 (0.01)	
J085644.71+102713.2	DA	20.5	54,746 (2460)	7.84 (0.16)	Pure H	0.62 (0.07)	0.0157 (0.0021)	0.30 (0.14)	6.19 (0.07)	
J085722.69+241809.9	DA	24.8	40,922 (835)	7.92 (0.09)	Pure H	0.63 (0.05)	0.0144 (0.0010)	−0.28 (0.07)	6.54 (0.03)	
J085746.18+034255.3	DA	34.4	41,128 (750)	7.40 (0.08)	Pure H	0.43 (0.03)	0.0216 (0.0014)	0.08 (0.06)	5.76 (0.38)	
J085824.95+590012.9	DB	25.1	30,322 (613)	7.81 (0.07)	Pure He	0.52 (0.03)	0.0149 (0.0007)	−0.77 (0.06)	6.96 (0.03)	
J085833.37+443429.1	DO	18.2	69,134 (4178)	8.50 (0.33)	Pure He	0.95 (0.18)	0.0091 (0.0025)	0.23 (0.26)	5.81 (0.11)	8
J085847.47+371115.5	DA+M	5.2	76,097 (19,607)	8.12 (0.87)	Pure H	0.79 (0.37)	0.0129 (0.0107)	0.70 (0.82)	5.73 (0.88)	1
J085903.96+184042.5	DA	20.5	40,193 (1125)	7.93 (0.13)	Pure H	0.63 (0.06)	0.0143 (0.0014)	−0.32 (0.10)	6.56 (0.04)	
J085904.40+122622.1	DA	27.8	31,525 (239)	7.83 (0.06)	Pure H	0.57 (0.03)	0.0151 (0.0006)	−0.69 (0.04)	6.87 (0.01)	

Table 2.1 – Atmospheric and stellar parameters of hot white dwarfs from SDSS DR12 (continued)

SDSS Name	Type	S/N	$T_{\rm eff}$ (K)	$\log g$	Composition	$M/M_{\odot}$	$R/R_{\odot}$	$\log L/L_{\odot}$	$\log \tau_{\rm cool}$	Notes
J085906.22+011936.4	DA	20.6	58,548 (3206)	7.76 (0.19)	Pure H	0.60 (0.07)	0.0169 (0.0027)	0.48 (0.17)	6.09 (0.14)	
J085923.49+035733.1	DA+M	21.6	52,816 (2224)	7.79 (0.15)	Pure H	0.60 (0.06)	0.0163 (0.0020)	0.27 (0.13)	6.23 (0.08)	1
J085929.56+150721.1	DA	30.5	45,876 (1092)	7.89 (0.10)	Pure H	0.63 (0.04)	0.0148 (0.0011)	−0.06 (0.08)	6.40 (0.03)	
J085931.59+314813.4	DA	6.5	48,257 (4683)	8.43 (0.38)	Pure H	0.92 (0.21)	0.0097 (0.0031)	−0.34 (0.33)	6.27 (0.31)	
J085943.39+642243.5	DA	16.0	50,695 (2856)	7.40 (0.21)	Pure H	0.46 (0.07)	0.0223 (0.0036)	0.47 (0.17)	5.10 (1.04)	
J085944.19+504050.9	DA	66.2	31,557 (113)	7.83 (0.03)	Pure H	0.56 (0.01)	0.0152 (0.0003)	−0.69 (0.02)	6.87 (0.01)	
J085947.99+092515.6	DA	6.4	53,785 (8390)	6.64 (0.51)	Pure H	0.28 (0.11)	0.0420 (0.0164)	1.12 (0.46)	<5.00	
J085955.88+234649.0	DA	30.4	30,114 (184)	7.97 (0.05)	Pure H	0.63 (0.03)	0.0136 (0.0005)	−0.86 (0.03)	6.95 (0.01)	
J090023.89+234353.2	DA	28.5	50,925 (1787)	7.41 (0.13)	Pure H	0.46 (0.05)	0.0222 (0.0023)	0.47 (0.11)	5.16 (0.78)	5
J090031.99+295741.0	DO	6.7	93,221 (44,228)	8.01 (1.33)	Pure He	0.72 (0.50)	0.0139 (0.0196)	1.12 (1.40)	5.59 (1.78)	
J090039.62+160131.2	DA+M	26.8	39,633 (694)	7.72 (0.08)	Pure H	0.54 (0.03)	0.0168 (0.0011)	−0.20 (0.06)	6.56 (0.05)	1
J090051.50+210450.3	DA	4.4	43,701 (6332)	7.40 (0.60)	Pure H	0.44 (0.20)	0.0218 (0.0105)	0.19 (0.49)	5.58 (1.48)	
J090112.44+025244.4	DA	26.2	43,914 (1237)	7.75 (0.12)	Pure H	0.56 (0.05)	0.0164 (0.0015)	−0.04 (0.10)	6.45 (0.06)	
J090116.64+301035.2	DA	37.6	63,109 (2262)	7.51 (0.11)	Pure H	0.53 (0.04)	0.0211 (0.0020)	0.80 (0.11)	5.56 (0.53)	5
J090129.26+472831.8	DA	44.0	30,774 (154)	7.89 (0.04)	Pure H	0.59 (0.02)	0.0145 (0.0004)	−0.77 (0.03)	6.91 (0.01)	
J090136.11+162704.1	DA	63.0	47,882 (567)	7.82 (0.05)	Pure H	0.60 (0.02)	0.0157 (0.0006)	0.07 (0.04)	6.35 (0.02)	
J090227.65+125206.0	DOZ	44.0	65,943 (1349)	8.04 (0.13)	Pure He	0.69 (0.06)	0.0132 (0.0013)	0.47 (0.10)	6.03 (0.04)	6
J090237.58+474448.1	DA	5.7	41,489 (3785)	8.21 (0.41)	Pure H	0.78 (0.23)	0.0116 (0.0038)	−0.45 (0.33)	6.49 (0.25)	
J090305.47+564218.5	DA	8.2	30,433 (893)	7.75 (0.23)	Pure H	0.53 (0.10)	0.0159 (0.0027)	−0.71 (0.16)	6.91 (0.10)	
J090316.74+092303.1	DA	16.3	32,492 (628)	7.28 (0.13)	Pure H	0.37 (0.04)	0.0230 (0.0023)	−0.27 (0.09)	5.80 (0.63)	2
J090320.15+351249.9	DA	43.1	37,346 (329)	7.74 (0.05)	Pure H	0.54 (0.02)	0.0165 (0.0006)	−0.32 (0.03)	6.64 (0.02)	
J090321.05+064427.0	DA	13.7	76,361 (8568)	7.76 (0.36)	Pure H	0.64 (0.13)	0.0174 (0.0056)	0.97 (0.34)	5.73 (0.37)	
J090322.45+834549.9	DB	29.2	30,439 (559)	7.92 (0.07)	Pure He	0.57 (0.03)	0.0138 (0.0007)	−0.83 (0.05)	6.97 (0.03)	
J090332.50+162601.0	DA	66.3	39,170 (267)	7.77 (0.03)	Pure H	0.55 (0.01)	0.0161 (0.0004)	−0.26 (0.03)	6.59 (0.01)	
J090338.97+011143.5	DA	7.2	30,542 (982)	8.15 (0.25)	Pure H	0.73 (0.14)	0.0119 (0.0023)	−0.96 (0.17)	7.00 (0.20)	
J090352.80+193643.5	DA	101.0	42,900 (297)	7.92 (0.03)	Pure H	0.63 (0.01)	0.0144 (0.0003)	−0.20 (0.02)	6.48 (0.01)	
J090359.59+374018.3	DA	52.7	42,238 (492)	7.68 (0.05)	Pure H	0.53 (0.02)	0.0174 (0.0007)	−0.06 (0.04)	6.46 (0.04)	
J090429.15+382249.3	DA	16.8	41,480 (1396)	7.70 (0.15)	Pure H	0.53 (0.06)	0.0171 (0.0020)	−0.11 (0.12)	6.50 (0.11)	
J090456.12+525029.8	DBA	21.2	36,558 (2439)	7.77 (0.14)	$\log q_{\rm H} = -17.74$	0.51 (0.06)	0.0155 (0.0016)	−0.41 (0.15)	6.70 (0.13)	3
J090500.41+355850.3	DA	19.9	33,840 (546)	7.88 (0.10)	Pure H	0.59 (0.05)	0.0147 (0.0011)	−0.59 (0.07)	6.78 (0.02)	
J090504.34+381344.7	DA	14.7	31,250 (516)	7.78 (0.12)	Pure H	0.54 (0.05)	0.0157 (0.0014)	−0.68 (0.08)	6.88 (0.04)	
J090545.56+324038.6	DA	29.3	30,964 (269)	7.83 (0.07)	Pure H	0.56 (0.03)	0.0151 (0.0007)	−0.73 (0.04)	6.90 (0.01)	
J090549.77+163111.6	DA	22.2	45,617 (1551)	7.59 (0.13)	Pure H	0.51 (0.05)	0.0188 (0.0021)	0.14 (0.11)	6.25 (0.30)	
J090609.91+041931.3	DA	50.6	54,686 (1160)	7.58 (0.07)	Pure H	0.53 (0.02)	0.0195 (0.0012)	0.48 (0.07)	6.02 (0.18)	5
J090611.00+414114.3	DA	56.8	44,670 (489)	7.89 (0.04)	Pure H	0.62 (0.02)	0.0148 (0.0005)	−0.10 (0.04)	6.44 (0.01)	
J090613.36+425002.9	DA	43.7	32,239 (231)	7.83 (0.05)	Pure H	0.57 (0.02)	0.0151 (0.0006)	−0.65 (0.03)	6.84 (0.01)	
J090709.13+420150.5	DA	6.6	37,586 (2101)	8.18 (0.29)	Pure H	0.76 (0.16)	0.0118 (0.0027)	−0.60 (0.22)	6.64 (0.17)	
J090759.99+223232.3	DA	22.8	32,458 (424)	7.38 (0.09)	Pure H	0.40 (0.03)	0.0213 (0.0015)	−0.34 (0.06)	6.29 (0.35)	
J090823.14+124703.9	DAO	47.5	48,302 (800)	7.74 (0.09)	$\log q_{\rm H} = -15.80$	0.53 (0.03)	0.0162 (0.0011)	0.11 (0.07)	6.34 (0.11)	3
J090905.54+024411.9	DA	27.2	32,283 (353)	7.89 (0.08)	Pure H	0.60 (0.04)	0.0144 (0.0008)	−0.69 (0.05)	6.84 (0.02)	
J090958.98+011105.4	DOA	74.7	49,866 (162)	7.94 (0.05)	$\log q_{\rm H} = -17.52$	0.62 (0.03)	0.0139 (0.0006)	0.03 (0.04)	6.37 (0.01)	3
J091003.15+422859.7	DA	18.9	35,112 (619)	7.67 (0.10)	Pure H	0.50 (0.04)	0.0172 (0.0014)	−0.39 (0.08)	6.68 (0.08)	
J091022.51+272843.7	DA	44.5	66,356 (1785)	7.38 (0.09)	Pure H	0.49 (0.03)	0.0238 (0.0017)	1.00 (0.08)	<5.00	
J091028.84+331005.0	DA	24.1	31,264 (315)	8.03 (0.08)	Pure H	0.67 (0.04)	0.0130 (0.0007)	−0.84 (0.05)	6.90 (0.02)	
J091120.85+305312.6	DA	45.5	58,582 (1234)	7.70 (0.07)	Pure H	0.58 (0.03)	0.0178 (0.0011)	0.53 (0.07)	6.06 (0.06)	
J091215.43+011958.8	DA	62.3	49,646 (736)	7.81 (0.06)	Pure H	0.60 (0.02)	0.0159 (0.0007)	0.14 (0.05)	6.31 (0.02)	
J091235.59+265828.6	DA	79.3	48,574 (468)	7.87 (0.04)	Pure H	0.62 (0.02)	0.0151 (0.0005)	0.06 (0.03)	6.34 (0.01)	5
J091322.68+380116.8	DA	21.9	56,652 (2696)	7.50 (0.16)	Pure H	0.51 (0.06)	0.0210 (0.0028)	0.61 (0.15)	5.66 (0.82)	
J091326.18+623006.0	DA	12.8	31,932 (507)	7.79 (0.11)	Pure H	0.55 (0.05)	0.0156 (0.0013)	−0.64 (0.08)	6.85 (0.03)	
J091353.60+374909.8	DA	79.9	80,362 (1620)	7.36 (0.06)	Pure H	0.53 (0.02)	0.0253 (0.0013)	1.38 (0.06)	<5.00	

Table 2.1 – Atmospheric and stellar parameters of hot white dwarfs from SDSS DR12 (continued)

SDSS Name	Type	S/N	$T_{\rm eff}$ (K)	$\log g$	Composition	$M/M_{\odot}$	$R/R_{\odot}$	$\log L/L_{\odot}$	$\log \tau_{\rm cool}$	Notes
J091357.21+125026.7	DA	18.7	30,756 (355)	7.38 (0.09)	Pure H	0.39 (0.03)	0.0212 (0.0014)	−0.44 (0.06)	6.41 (0.33)	
J091359.81+040149.0	DA	32.9	43,151 (845)	7.84 (0.08)	Pure H	0.59 (0.04)	0.0154 (0.0010)	−0.13 (0.07)	6.48 (0.03)	
J091433.60+581238.0	DO	38.8	69,965 (1900)	8.25 (0.15)	Pure He	0.81 (0.08)	0.0112 (0.0014)	0.43 (0.12)	5.87 (0.07)	
J091442.44+590706.6	DA+M	7.0	65,264 (13,941)	8.18 (0.74)	Pure H	0.80 (0.34)	0.0121 (0.0082)	0.38 (0.68)	5.91 (0.61)	1
J091442.69+041455.9	DA	20.9	85,684 (7180)	7.00 (0.18)	Pure H	0.47 (0.04)	0.0357 (0.0062)	1.79 (0.22)	<5.00	
J091445.93+115643.5	DA	8.0	37,194 (2050)	7.96 (0.29)	Pure H	0.64 (0.15)	0.0138 (0.0031)	−0.48 (0.22)	6.66 (0.08)	
J091507.88+253041.4	DAO	41.1	80,952 (5029)	7.12 (0.15)	$\log N_{\rm He}/N_{\rm H} = -2.53$	0.48 (0.04)	0.0313 (0.0044)	1.58 (0.17)	<5.00	4,5
J091522.91+165754.0	DA	18.6	40,999 (1180)	7.76 (0.13)	Pure H	0.56 (0.05)	0.0163 (0.0016)	−0.17 (0.10)	6.53 (0.07)	
J091539.67+143854.8	DA	39.9	37,147 (404)	7.20 (0.06)	Pure H	0.35 (0.02)	0.0247 (0.0010)	0.02 (0.04)	<5.00	
J091601.87+200758.0	DA	65.8	31,839 (112)	7.24 (0.03)	Pure H	0.36 (0.01)	0.0236 (0.0004)	−0.29 (0.02)	5.65 (0.13)	
J091606.66+115821.1	DA	8.2	50,936 (5073)	8.02 (0.38)	Pure H	0.70 (0.18)	0.0135 (0.0041)	0.04 (0.32)	6.26 (0.13)	
J091609.18+543734.9	DA	53.2	30,278 (124)	7.86 (0.03)	Pure H	0.58 (0.02)	0.0147 (0.0003)	−0.78 (0.02)	6.93 (0.01)	
J091621.81+052119.0	DO+M	38.0	56,877 (896)	8.19 (0.10)	Pure He	0.76 (0.06)	0.0116 (0.0009)	0.10 (0.07)	6.14 (0.04)	1
J091709.23+094157.3	DA	3.3	39,489 (6571)	6.92 (0.80)	Pure H	0.29 (0.20)	0.0310 (0.0187)	0.32 (0.60)	<5.00	
J091709.46−005041.8	DA	5.1	31,478 (1676)	8.34 (0.39)	Pure H	0.85 (0.23)	0.0103 (0.0032)	−1.03 (0.29)	7.18 (0.53)	
J091719.14+195438.5	DA	92.4	33,123 (123)	7.80 (0.03)	Pure H	0.55 (0.01)	0.0155 (0.0003)	−0.58 (0.02)	6.80 (0.01)	
J091725.51+483354.9	DA	26.6	32,594 (346)	7.71 (0.07)	Pure H	0.51 (0.03)	0.0166 (0.0009)	−0.55 (0.05)	6.80 (0.04)	
J091730.74+182309.7	DA	45.6	68,652 (1956)	7.46 (0.09)	Pure H	0.52 (0.03)	0.0223 (0.0016)	1.00 (0.08)	5.11 (0.66)	
J091757.25+093455.3	DA	31.1	32,123 (290)	8.00 (0.06)	Pure H	0.65 (0.03)	0.0134 (0.0006)	−0.76 (0.04)	6.86 (0.01)	
J091800.74−005049.7	DA	69.3	32,390 (127)	7.85 (0.03)	Pure H	0.58 (0.01)	0.0149 (0.0003)	−0.66 (0.02)	6.84 (0.01)	
J091833.06+195307.8	DA	84.3	75,275 (1621)	7.42 (0.05)	Pure H	0.53 (0.02)	0.0236 (0.0011)	1.21 (0.06)	<5.00	5
J091841.84+061701.9	DA	101.5	43,147 (284)	7.55 (0.03)	Pure H	0.49 (0.01)	0.0193 (0.0004)	0.07 (0.02)	6.22 (0.08)	
J091842.60+591804.2	DA	34.7	46,106 (918)	7.54 (0.08)	Pure H	0.49 (0.03)	0.0197 (0.0014)	0.20 (0.07)	6.07 (0.31)	5
J091845.55+612215.1	DA	36.5	30,191 (184)	7.85 (0.05)	Pure H	0.57 (0.02)	0.0149 (0.0005)	−0.78 (0.03)	6.93 (0.01)	
J091916.08+294420.4	DA+M	13.2	30,494 (602)	7.24 (0.15)	Pure H	0.35 (0.05)	0.0235 (0.0026)	−0.36 (0.10)	5.76 (0.68)	1
J091918.37+581447.0	DA	24.6	39,865 (893)	7.69 (0.11)	Pure H	0.52 (0.04)	0.0172 (0.0014)	−0.17 (0.08)	6.53 (0.09)	
J091927.00+180950.4	DA	27.6	30,722 (237)	7.91 (0.06)	Pure H	0.60 (0.03)	0.0142 (0.0006)	−0.79 (0.04)	6.91 (0.01)	
J091927.44+085133.2	DA+M	20.3	30,182 (367)	8.02 (0.10)	Pure H	0.66 (0.05)	0.0131 (0.0009)	−0.89 (0.07)	6.96 (0.03)	1,2
J091929.47+411803.2	DA	28.1	40,389 (727)	7.96 (0.08)	Pure H	0.65 (0.04)	0.0139 (0.0009)	−0.33 (0.06)	6.55 (0.02)	
J091938.40+580731.3	DA	15.9	47,415 (2280)	7.72 (0.19)	Pure H	0.55 (0.07)	0.0171 (0.0026)	0.12 (0.16)	6.34 (0.13)	
J091940.97+025801.1	DA	5.0	54,942 (9834)	7.47 (0.63)	Pure H	0.49 (0.21)	0.0214 (0.0115)	0.57 (0.56)	5.50 (1.47)	
J091944.26+421132.9	DAO	28.3	59,878 (3552)	7.54 (0.18)	$\log N_{\rm He}/N_{\rm H} = -3.12$	0.53 (0.06)	0.0205 (0.0031)	0.69 (0.17)	5.74 (0.64)	4,5
J092010.54+045721.1	DA	36.8	61,093 (1647)	7.37 (0.09)	Pure H	0.47 (0.03)	0.0236 (0.0017)	0.84 (0.08)	<5.00	
J092048.04+105734.4	DA+M	36.3	64,126 (2138)	6.95 (0.10)	Pure H	0.38 (0.02)	0.0342 (0.0030)	1.25 (0.10)	<5.00	1
J092121.19+431847.0	DA	22.4	57,970 (2940)	7.42 (0.17)	Pure H	0.48 (0.06)	0.0225 (0.0031)	0.71 (0.15)	5.00 (1.05)	
J092126.72+055734.0	DA	7.5	31,207 (820)	8.02 (0.20)	Pure H	0.66 (0.11)	0.0132 (0.0019)	−0.83 (0.14)	6.90 (0.08)	
J092135.03+351100.8	DA	17.7	39,584 (1198)	7.69 (0.14)	Pure H	0.52 (0.06)	0.0171 (0.0019)	−0.19 (0.11)	6.54 (0.11)	
J092220.93+204540.6	DA	4.6	33,834 (2511)	6.91 (0.49)	Pure H	0.27 (0.12)	0.0301 (0.0110)	0.03 (0.34)	<5.00	
J092242.42+011422.8	DA	4.5	32,390 (1512)	7.38 (0.32)	Pure H	0.40 (0.10)	0.0214 (0.0052)	−0.34 (0.23)	6.28 (0.99)	
J092256.80+562843.6	DA	8.3	32,678 (1136)	7.60 (0.24)	Pure H	0.47 (0.09)	0.0180 (0.0033)	−0.48 (0.17)	6.73 (0.23)	
J092302.96+021031.6	DA	7.6	32,511 (1033)	7.86 (0.22)	Pure H	0.58 (0.10)	0.0149 (0.0024)	−0.65 (0.15)	6.83 (0.07)	
J092332.77+154404.1	DA	32.6	42,848 (840)	8.56 (0.09)	Pure H	0.99 (0.05)	0.0087 (0.0007)	−0.64 (0.07)	6.62 (0.18)	5
J092405.73+304900.2	DA	36.2	35,636 (364)	7.77 (0.06)	Pure H	0.55 (0.03)	0.0159 (0.0007)	−0.43 (0.04)	6.71 (0.02)	
J092406.26+012411.5	DA+M	28.0	61,399 (3189)	7.28 (0.17)	Pure H	0.45 (0.05)	0.0253 (0.0036)	0.91 (0.16)	<5.00	1,2
J092429.06+010448.3	DA+M	4.4	32,286 (1883)	7.78 (0.41)	Pure H	0.54 (0.18)	0.0158 (0.0050)	−0.61 (0.29)	6.83 (0.21)	1
J092433.91+213342.4	DA	9.7	32,062 (831)	7.93 (0.18)	Pure H	0.61 (0.09)	0.0141 (0.0019)	−0.73 (0.13)	6.86 (0.04)	
J092454.56+543422.2	DA	50.3	30,289 (146)	7.32 (0.04)	Pure H	0.37 (0.01)	0.0222 (0.0006)	−0.43 (0.03)	6.16 (0.18)	
J092457.51+083316.7	DA	22.1	30,423 (276)	7.82 (0.07)	Pure H	0.56 (0.03)	0.0152 (0.0008)	−0.75 (0.05)	6.92 (0.02)	
J092534.54+330516.4	DA	8.5	33,374 (1294)	7.14 (0.26)	Pure H	0.33 (0.07)	0.0256 (0.0048)	−0.14 (0.18)	5.03 (0.96)	
J092539.55−013330.0	DA	29.5	44,683 (1280)	7.77 (0.12)	Pure H	0.57 (0.05)	0.0162 (0.0015)	−0.02 (0.10)	6.43 (0.05)	

Table 2.1 – Atmospheric and stellar parameters of hot white dwarfs from SDSS DR12 (continued)

SDSS Name	Type	S/N	$T_{\rm eff}$ (K)	$\log g$	Composition	$M/M_{\odot}$	$R/R_{\odot}$	$\log L/L_{\odot}$	$\log \tau_{\rm cool}$	Notes
J092544.40+414803.2	DB	8.0	40,907 (1795)	7.47 (0.30)	Pure He	0.42 (0.11)	0.0196 (0.0042)	−0.01 (0.20)	5.81 (1.11)	
J092644.52+124759.5	DA	27.3	44,681 (1173)	7.72 (0.11)	Pure H	0.55 (0.04)	0.0169 (0.0014)	0.01 (0.09)	6.42 (0.07)	
J092737.42+095207.4	DA+M	19.4	35,691 (714)	7.79 (0.11)	Pure H	0.56 (0.05)	0.0157 (0.0014)	−0.44 (0.08)	6.71 (0.04)	1
J092757.93+163913.4	DA	6.1	34,468 (1948)	7.59 (0.35)	Pure H	0.47 (0.13)	0.0183 (0.0049)	−0.37 (0.25)	6.63 (0.30)	
J092841.73+193328.9	DA+M	5.7	47,034 (5195)	7.70 (0.43)	Pure H	0.55 (0.18)	0.0173 (0.0060)	0.12 (0.36)	6.34 (0.45)	1
J092905.45+061118.6	DA	38.2	39,336 (483)	7.76 (0.06)	Pure H	0.55 (0.02)	0.0162 (0.0007)	−0.25 (0.05)	6.58 (0.02)	
J092933.07+411057.9	DA	23.1	68,205 (4526)	7.46 (0.21)	Pure H	0.52 (0.07)	0.0222 (0.0041)	0.98 (0.20)	5.14 (1.08)	
J093000.39+113805.0	DA	19.4	34,219 (579)	7.74 (0.11)	Pure H	0.53 (0.04)	0.0163 (0.0013)	−0.48 (0.08)	6.75 (0.05)	
J093006.79+522803.3	DA	50.2	34,543 (295)	7.63 (0.05)	Pure H	0.49 (0.02)	0.0176 (0.0007)	−0.40 (0.04)	6.67 (0.05)	
J093008.73+244708.8	DA	17.2	46,420 (1864)	7.85 (0.16)	Pure H	0.61 (0.07)	0.0154 (0.0019)	−0.00 (0.13)	6.39 (0.06)	
J093041.79+011508.4	DB	18.2	34,822 (1050)	7.85 (0.11)	Pure He	0.55 (0.05)	0.0146 (0.0011)	−0.55 (0.09)	6.78 (0.05)	
J093047.08+160012.7	DA	64.7	33,987 (157)	7.91 (0.03)	Pure H	0.61 (0.01)	0.0143 (0.0003)	−0.61 (0.02)	6.78 (0.01)	
J093058.91+074454.4	DA	45.5	32,097 (166)	7.98 (0.04)	Pure H	0.64 (0.02)	0.0136 (0.0004)	−0.75 (0.03)	6.86 (0.01)	
J093103.33+333948.2	DA	39.4	30,109 (139)	7.91 (0.04)	Pure H	0.60 (0.02)	0.0142 (0.0004)	−0.83 (0.02)	6.94 (0.01)	
J093113.64−012238.9	DA	21.8	31,158 (323)	7.93 (0.08)	Pure H	0.61 (0.04)	0.0140 (0.0008)	−0.78 (0.05)	6.90 (0.02)	
J093211.04+132903.3	DA+M	48.1	33,215 (234)	7.75 (0.05)	Pure H	0.53 (0.02)	0.0162 (0.0006)	−0.54 (0.03)	6.79 (0.02)	1,2
J093211.47−003515.6	DA	4.9	31,360 (1213)	7.61 (0.29)	Pure H	0.47 (0.11)	0.0178 (0.0039)	−0.56 (0.20)	6.79 (0.23)	
J093213.38+055845.6	DA	12.3	41,895 (1766)	7.90 (0.19)	Pure H	0.62 (0.09)	0.0146 (0.0021)	−0.23 (0.15)	6.51 (0.05)	
J093311.39+412223.5	DA	8.4	36,559 (1804)	7.78 (0.27)	Pure H	0.55 (0.12)	0.0159 (0.0033)	−0.39 (0.20)	6.68 (0.14)	
J093332.55+183915.9	DA	4.4	39,940 (4582)	7.48 (0.53)	Pure H	0.45 (0.19)	0.0203 (0.0085)	−0.02 (0.41)	6.14 (0.99)	
J093342.91+073153.6	DA	19.6	116,234 (21,750)	6.97 (0.21)	Pure H	0.56 (0.09)	0.0406 (0.0088)	2.43 (0.43)	<5.00	
J093358.28+174252.4	DA	22.1	31,404 (327)	7.85 (0.08)	Pure H	0.57 (0.04)	0.0148 (0.0008)	−0.71 (0.05)	6.88 (0.02)	
J093401.13+004742.2	DA	27.5	55,108 (2246)	7.65 (0.14)	Pure H	0.55 (0.05)	0.0184 (0.0022)	0.45 (0.13)	6.10 (0.21)	
J093420.05+051209.3	DA+M	22.3	61,062 (3008)	7.41 (0.16)	Pure H	0.49 (0.05)	0.0229 (0.0031)	0.82 (0.15)	<5.00	1
J093431.10+132814.6	DA	26.7	33,685 (414)	8.14 (0.08)	Pure H	0.73 (0.05)	0.0121 (0.0007)	−0.77 (0.06)	6.81 (0.03)	
J093432.48+031348.8	DA+M	31.4	31,278 (239)	7.66 (0.06)	Pure H	0.49 (0.02)	0.0171 (0.0007)	−0.60 (0.04)	6.83 (0.04)	1,2
J093515.98+562042.4	DA	49.1	38,423 (382)	7.83 (0.05)	Pure H	0.58 (0.02)	0.0154 (0.0006)	−0.33 (0.04)	6.62 (0.01)	
J093544.57+525741.0	DA	23.7	33,844 (450)	7.93 (0.08)	Pure H	0.62 (0.04)	0.0141 (0.0009)	−0.63 (0.06)	6.78 (0.02)	
J093607.96+001435.9	DA	78.7	32,836 (136)	8.26 (0.03)	Pure H	0.80 (0.02)	0.0110 (0.0002)	−0.90 (0.02)	6.93 (0.03)	
J093608.88+382200.4	DA	41.8	37,608 (384)	7.71 (0.05)	Pure H	0.53 (0.02)	0.0168 (0.0007)	−0.30 (0.04)	6.62 (0.03)	
J093740.17−011520.5	DA	44.0	36,053 (376)	7.44 (0.06)	Pure H	0.43 (0.02)	0.0206 (0.0010)	−0.19 (0.04)	6.25 (0.19)	
J093749.03+000212.9	DAO	32.0	46,868 (1319)	7.69 (0.12)	$\log N_{\rm He}/N_{\rm H} = -1.59$	0.54 (0.04)	0.0174 (0.0017)	0.12 (0.10)	6.34 (0.10)	4
J093759.51+091653.2	DB	17.2	31,766 (977)	8.04 (0.11)	Pure He	0.64 (0.06)	0.0126 (0.0010)	−0.83 (0.09)	6.92 (0.05)	
J093806.87+444647.9	DA	5.9	41,290 (3506)	8.02 (0.38)	Pure H	0.68 (0.20)	0.0133 (0.0040)	−0.33 (0.30)	6.52 (0.12)	
J093837.85+614909.1	DA	7.2	50,666 (5448)	7.56 (0.40)	Pure H	0.51 (0.14)	0.0196 (0.0063)	0.36 (0.34)	6.05 (0.53)	
J093844.96+021755.6	DB	2.8	33,916 (6319)	7.94 (0.68)	Pure He	0.59 (0.34)	0.0136 (0.0071)	−0.66 (0.55)	6.83 (1.20)	
J093920.69+033524.1	DA	42.9	50,543 (963)	7.70 (0.07)	Pure H	0.56 (0.03)	0.0174 (0.0010)	0.25 (0.06)	6.25 (0.05)	
J093921.82+264401.0	DA	44.9	55,978 (1280)	7.82 (0.08)	Pure H	0.62 (0.03)	0.0160 (0.0011)	0.35 (0.07)	6.17 (0.03)	
J093922.00+635831.7	DA	15.9	33,158 (699)	7.95 (0.14)	Pure H	0.63 (0.07)	0.0139 (0.0015)	−0.68 (0.10)	6.81 (0.03)	
J093937.90+173953.6	DAO+M	52.4	74,735 (3863)	7.06 (0.12)	$\log N_{\rm He}/N_{\rm H} = -2.20$	0.44 (0.03)	0.0325 (0.0038)	1.47 (0.14)	<5.00	1,4,5
J093941.74+281110.8	DA	18.8	35,767 (688)	7.93 (0.11)	Pure H	0.62 (0.06)	0.0141 (0.0012)	−0.53 (0.08)	6.71 (0.03)	
J093957.05+644634.1	DA	57.7	32,352 (149)	7.30 (0.03)	Pure H	0.38 (0.01)	0.0226 (0.0005)	−0.30 (0.02)	5.92 (0.17)	
J094002.83+074444.4	DA	15.4	39,565 (1230)	7.57 (0.15)	Pure H	0.48 (0.05)	0.0189 (0.0022)	−0.10 (0.12)	6.39 (0.31)	
J094022.65+502105.8	DA	100.0	36,497 (161)	7.76 (0.02)	Pure H	0.54 (0.01)	0.0161 (0.0003)	−0.38 (0.02)	6.68 (0.01)	
J094111.40+423921.2	DA	13.8	43,006 (1863)	7.63 (0.18)	Pure H	0.51 (0.07)	0.0181 (0.0027)	0.00 (0.15)	6.39 (0.21)	
J094132.96+224804.8	DA	5.2	30,721 (1298)	8.49 (0.32)	Pure H	0.94 (0.19)	0.0091 (0.0025)	−1.17 (0.25)	7.57 (0.52)	
J094209.63+300444.2	DA	22.9	34,660 (595)	7.95 (0.11)	Pure H	0.63 (0.05)	0.0140 (0.0011)	−0.60 (0.07)	6.75 (0.02)	
J094218.96+154131.3	DA	30.2	31,024 (271)	7.86 (0.07)	Pure H	0.57 (0.03)	0.0148 (0.0007)	−0.74 (0.04)	6.90 (0.01)	
J094303.61+462913.7	DB	7.0	43,109 (4504)	8.01 (0.39)	Pure He	0.64 (0.20)	0.0131 (0.0040)	−0.27 (0.32)	6.52 (0.22)	
J094510.19+172907.2	DA	15.0	30,031 (385)	7.76 (0.10)	Pure H	0.53 (0.05)	0.0158 (0.0012)	−0.74 (0.07)	6.93 (0.04)	

Table 2.1 – Atmospheric and stellar parameters of hot white dwarfs from SDSS DR12 (continued)

SDSS Name	Type	S/N	$T_{\rm eff}$ (K)	$\log g$	Composition	$M/M_{\odot}$	$R/R_{\odot}$	$\log L/L_{\odot}$	$\log \tau_{\rm cool}$	Notes
J094636.14+090437.4	DA	12.9	34,925 (915)	7.84 (0.16)	Pure H	0.58 (0.07)	0.0151 (0.0018)	−0.51 (0.11)	6.74 (0.04)	
J094720.94+111734.7	DAO+M	23.7	54,159 (2536)	7.71 (0.19)	$\log N_{\rm He}/N_{\rm H} = -2.24$	0.57 (0.07)	0.0174 (0.0027)	0.37 (0.16)	6.16 (0.15)	1,4
J094722.49+101523.6	DOZ	36.1	68,722 (2301)	7.83 (0.21)	Pure He	0.60 (0.08)	0.0157 (0.0027)	0.70 (0.16)	5.96 (0.10)	6,8
J094748.40+073310.6	DA+M	18.5	31,385 (545)	7.75 (0.12)	Pure H	0.53 (0.05)	0.0160 (0.0014)	−0.65 (0.08)	6.86 (0.05)	1,7
J094853.94+573957.8	DA+M	33.4	39,567 (673)	7.66 (0.08)	Pure H	0.51 (0.03)	0.0175 (0.0011)	−0.17 (0.06)	6.52 (0.08)	1,2
J094900.27+014746.4	DA+M	16.1	36,333 (897)	7.73 (0.14)	Pure H	0.53 (0.06)	0.0165 (0.0017)	−0.37 (0.10)	6.67 (0.07)	1,2
J094927.58+042508.3	DA	58.0	38,139 (309)	7.76 (0.04)	Pure H	0.55 (0.02)	0.0162 (0.0005)	−0.30 (0.03)	6.62 (0.02)	
J094932.63+324228.8	DA	28.5	52,060 (1546)	7.64 (0.11)	Pure H	0.54 (0.04)	0.0183 (0.0017)	0.35 (0.10)	6.17 (0.15)	
J094940.36+032425.5	DA	54.1	47,931 (741)	7.59 (0.06)	Pure H	0.51 (0.02)	0.0189 (0.0009)	0.23 (0.05)	6.19 (0.14)	
J094944.38+215908.7	DA	37.3	100,067 (6781)	7.32 (0.15)	Pure H	0.59 (0.05)	0.0278 (0.0039)	1.84 (0.18)	<5.00	
J095005.29+495548.9	DA	57.4	31,771 (145)	7.98 (0.03)	Pure H	0.64 (0.02)	0.0135 (0.0003)	−0.77 (0.02)	6.87 (0.01)	
J095019.72−010423.3	DAO	63.4	91,347 (3632)	7.16 (0.13)	$\log N_{\rm He}/N_{\rm H} = -1.52$	0.52 (0.03)	0.0314 (0.0038)	1.79 (0.13)	<5.00	4,5
J095021.37+305048.2	DA	14.0	30,747 (415)	7.99 (0.10)	Pure H	0.64 (0.06)	0.0134 (0.0010)	−0.84 (0.07)	6.92 (0.03)	
J095043.95+391541.6	DA+M	34.4	41,462 (2694)	7.57 (0.29)	Pure H	0.49 (0.10)	0.0189 (0.0043)	−0.02 (0.23)	6.33 (0.46)	1,2
J095108.97+040601.9	DA+M	12.6	60,058 (6041)	7.49 (0.34)	Pure H	0.51 (0.11)	0.0213 (0.0061)	0.73 (0.31)	5.55 (1.08)	1,2
J095211.55+001839.9	DA	76.0	44,606 (513)	7.73 (0.05)	Pure H	0.55 (0.02)	0.0168 (0.0007)	0.00 (0.04)	6.42 (0.02)	7
J095211.96+113321.8	DA	23.1	56,367 (2422)	7.81 (0.15)	Pure H	0.61 (0.06)	0.0161 (0.0020)	0.37 (0.13)	6.16 (0.08)	
J095229.03+150350.5	DA	17.1	63,685 (4581)	7.46 (0.24)	Pure H	0.51 (0.07)	0.0221 (0.0044)	0.86 (0.22)	5.23 (1.17)	
J095231.88+120544.8	DA	28.7	30,582 (237)	7.38 (0.06)	Pure H	0.39 (0.02)	0.0211 (0.0010)	−0.45 (0.04)	6.43 (0.22)	
J095245.58+020938.9	DA	62.7	42,902 (374)	7.75 (0.04)	Pure H	0.56 (0.02)	0.0165 (0.0005)	−0.08 (0.03)	6.48 (0.02)	
J095245.80+182102.6	DA+M	33.6	31,150 (103)	7.72 (0.03)	Pure H	0.51 (0.01)	0.0164 (0.0003)	−0.64 (0.02)	6.86 (0.01)	1
J095256.68+015407.6	DB	48.5	33,326 (320)	8.13 (0.03)	Pure He	0.70 (0.02)	0.0119 (0.0003)	−0.81 (0.03)	6.86 (0.02)	
J095303.33+070307.2	DA	13.6	40,013 (1706)	7.50 (0.20)	Pure H	0.46 (0.07)	0.0200 (0.0031)	−0.03 (0.16)	6.19 (0.63)	
J095321.84+133920.6	DA	19.9	39,315 (885)	7.85 (0.11)	Pure H	0.59 (0.05)	0.0151 (0.0013)	−0.31 (0.08)	6.59 (0.03)	
J095329.06+092409.5	DA	51.6	35,249 (214)	7.77 (0.04)	Pure H	0.55 (0.02)	0.0160 (0.0004)	−0.45 (0.03)	6.72 (0.01)	
J095333.14+333014.3	DA	19.7	43,018 (1377)	8.01 (0.14)	Pure H	0.68 (0.07)	0.0135 (0.0014)	−0.25 (0.11)	6.47 (0.04)	
J095437.82+360617.0	DA	35.5	60,144 (1630)	7.53 (0.09)	Pure H	0.53 (0.03)	0.0206 (0.0016)	0.70 (0.08)	5.72 (0.39)	
J095440.46+120917.1	DBA	22.3	35,898 (1440)	7.57 (0.11)	$\log q_{\rm H} = -18.02$	0.44 (0.04)	0.0180 (0.0015)	−0.31 (0.10)	6.47 (0.30)	3
J095503.14+214455.5	DA	26.9	50,566 (1655)	7.45 (0.12)	Pure H	0.47 (0.04)	0.0214 (0.0020)	0.43 (0.10)	5.47 (0.69)	
J095553.01+182014.2	DA	3.9	32,848 (1937)	7.67 (0.40)	Pure H	0.50 (0.16)	0.0171 (0.0053)	−0.51 (0.28)	6.77 (0.21)	
J095630.14+224311.5	DOZ	45.7	79,610 (2782)	8.38 (0.15)	Pure He	0.89 (0.08)	0.0101 (0.0013)	0.57 (0.12)	5.65 (0.07)	6
J095705.99+615254.2	DA+M	15.4	37,944 (1328)	7.66 (0.18)	Pure H	0.51 (0.07)	0.0174 (0.0024)	−0.25 (0.14)	6.57 (0.16)	1
J095843.47+015927.7	DA	27.5	36,146 (482)	7.21 (0.07)	Pure H	0.36 (0.02)	0.0244 (0.0013)	−0.04 (0.05)	5.11 (0.37)	
J095926.43+523459.1	DA	30.5	39,113 (634)	7.66 (0.08)	Pure H	0.51 (0.03)	0.0176 (0.0011)	−0.19 (0.06)	6.53 (0.08)	
J095944.57+062209.6	DA	32.8	62,264 (2155)	7.50 (0.12)	Pure H	0.52 (0.04)	0.0213 (0.0021)	0.79 (0.11)	5.51 (0.60)	
J095951.65+622626.6	DA	16.2	55,289 (3582)	7.42 (0.22)	Pure H	0.47 (0.07)	0.0222 (0.0041)	0.62 (0.20)	5.04 (1.09)	
J100015.29+240724.7	DBA	44.8	41,488 (823)	7.83 (0.07)	$\log q_{\rm H} = -17.29$	0.55 (0.03)	0.0150 (0.0008)	−0.22 (0.06)	6.57 (0.03)	3
J100015.39+140758.8	DA	41.2	38,469 (444)	7.80 (0.06)	Pure H	0.57 (0.03)	0.0157 (0.0007)	−0.31 (0.04)	6.62 (0.02)	
J100033.66+475414.0	DA	3.9	35,470 (2531)	7.89 (0.41)	Pure H	0.60 (0.20)	0.0146 (0.0047)	−0.52 (0.30)	6.72 (0.23)	
J100050.65+685505.5	DA	12.1	45,593 (2472)	7.33 (0.21)	Pure H	0.42 (0.07)	0.0231 (0.0039)	0.32 (0.18)	5.05 (1.04)	
J100100.10+313413.1	DO	5.8	46,815 (1421)	7.15 (0.60)	Pure He	0.32 (0.17)	0.0249 (0.0110)	0.43 (0.38)	<5.00	
J100132.79+013058.4	DA	17.7	33,366 (560)	7.89 (0.11)	Pure H	0.60 (0.05)	0.0145 (0.0012)	−0.63 (0.08)	6.80 (0.02)	
J100144.03+003721.1	DA	8.5	30,691 (717)	7.88 (0.18)	Pure H	0.59 (0.09)	0.0145 (0.0019)	−0.77 (0.12)	6.91 (0.05)	
J100144.41+453047.3	DA	18.7	42,996 (1400)	7.66 (0.14)	Pure H	0.52 (0.05)	0.0177 (0.0020)	−0.02 (0.11)	6.42 (0.14)	
J100145.03+364257.3	DA	6.7	40,869 (3687)	7.16 (0.41)	Pure H	0.35 (0.11)	0.0258 (0.0083)	0.22 (0.32)	<5.00	
J100222.50+292754.9	DA	78.8	60,783 (1047)	7.65 (0.05)	Pure H	0.57 (0.02)	0.0186 (0.0009)	0.63 (0.05)	5.98 (0.07)	5
J100242.40+700054.2	DB	6.8	32,106 (2785)	7.99 (0.30)	Pure He	0.61 (0.16)	0.0131 (0.0029)	−0.78 (0.24)	6.90 (0.17)	
J100326.98+055931.0	DA	19.4	30,662 (318)	7.75 (0.08)	Pure H	0.53 (0.03)	0.0160 (0.0009)	−0.69 (0.05)	6.90 (0.03)	
J100409.75+470519.8	DAO+M	44.4	73,057 (4415)	7.24 (0.15)	$\log N_{\rm He}/N_{\rm H} = -2.99$	0.47 (0.04)	0.0274 (0.0037)	1.28 (0.17)	<5.00	1,4,5
J100413.27+285856.1	DAO	42.6	46,247 (834)	7.78 (0.08)	$\log q_{\rm H} = -15.26$	0.54 (0.03)	0.0157 (0.0010)	0.00 (0.06)	6.42 (0.06)	3

Table 2.1 – Atmospheric and stellar parameters of hot white dwarfs from SDSS DR12 (continued)

SDSS Name	Type	S/N	$T_{\rm eff}$ (K)	$\log g$	Composition	$M/M_{\odot}$	$R/R_{\odot}$	$\log L/L_{\odot}$	$\log \tau_{\rm cool}$	Notes
J100508.75+570602.5	DA	20.8	30,329 (321)	7.78 (0.08)	Pure H	0.54 (0.04)	0.0157 (0.0010)	−0.73 (0.06)	6.92 (0.03)	
J100523.92+275548.9	DA	57.5	33,718 (159)	8.06 (0.03)	Pure H	0.68 (0.02)	0.0128 (0.0003)	−0.72 (0.02)	6.79 (0.01)	
J100543.92+304744.6	DA	78.5	57,327 (750)	7.55 (0.04)	Pure H	0.53 (0.01)	0.0201 (0.0008)	0.59 (0.04)	5.89 (0.13)	
J100605.29+450404.2	DA	60.8	38,555 (258)	7.84 (0.03)	Pure H	0.59 (0.02)	0.0152 (0.0004)	−0.34 (0.02)	6.62 (0.01)	
J100612.77+252833.5	DA	6.1	90,976 (22,149)	7.63 (0.69)	Pure H	0.64 (0.23)	0.0202 (0.0140)	1.40 (0.73)	5.30 (1.07)	
J100614.75+441906.2	DA	74.6	48,775 (496)	7.62 (0.04)	Pure H	0.52 (0.01)	0.0185 (0.0006)	0.24 (0.04)	6.23 (0.07)	5
J100628.33+624814.9	DA	21.3	42,842 (1316)	7.87 (0.13)	Pure H	0.61 (0.06)	0.0151 (0.0015)	−0.16 (0.10)	6.49 (0.04)	
J100646.27+314602.9	DA	7.6	34,888 (1499)	8.26 (0.26)	Pure H	0.80 (0.15)	0.0110 (0.0022)	−0.79 (0.19)	6.79 (0.20)	
J100734.34+271410.7	DA	20.8	39,309 (839)	7.75 (0.10)	Pure H	0.55 (0.04)	0.0164 (0.0013)	−0.24 (0.08)	6.58 (0.05)	
J100811.87+162450.4	DAO+M	36.7	59,515 (2093)	7.72 (0.12)	$\log N_{\rm He}/N_{\rm H} = -2.87$	0.58 (0.04)	0.0176 (0.0018)	0.54 (0.11)	6.05 (0.10)	1,2,4
J100822.39+015307.4	DA	8.4	56,089 (7605)	7.28 (0.42)	Pure H	0.43 (0.12)	0.0249 (0.0090)	0.74 (0.40)	<5.00	7
J100829.65+113550.5	DA	21.0	38,237 (876)	7.62 (0.11)	Pure H	0.49 (0.04)	0.0180 (0.0016)	−0.20 (0.09)	6.52 (0.15)	
J100854.06+002248.0	DA	19.8	30,619 (354)	7.83 (0.09)	Pure H	0.56 (0.04)	0.0151 (0.0010)	−0.74 (0.06)	6.91 (0.02)	
J100856.94+393838.4	DA+M	19.2	37,481 (900)	7.77 (0.12)	Pure H	0.55 (0.05)	0.0160 (0.0015)	−0.34 (0.09)	6.65 (0.05)	1
J100925.88+625631.3	DA	5.9	32,853 (1675)	7.78 (0.34)	Pure H	0.55 (0.15)	0.0157 (0.0042)	−0.59 (0.24)	6.81 (0.15)	
J100935.48+625022.0	DA	7.5	37,245 (2148)	7.16 (0.30)	Pure H	0.34 (0.08)	0.0255 (0.0059)	0.05 (0.22)	<5.00	
J101015.59+115711.3	DAO	43.9	50,401 (919)	7.74 (0.11)	$\log q_{\rm H} = -15.90$	0.53 (0.04)	0.0163 (0.0015)	0.19 (0.08)	6.28 (0.14)	3
J101035.46+262946.8	DA	17.8	32,698 (501)	7.12 (0.11)	Pure H	0.32 (0.03)	0.0258 (0.0019)	−0.16 (0.07)	5.03 (0.39)	
J101038.12+503631.4	DA	16.8	40,960 (1295)	7.70 (0.14)	Pure H	0.53 (0.06)	0.0171 (0.0019)	−0.13 (0.11)	6.51 (0.11)	
J101049.87+025100.3	DA	25.6	30,420 (253)	7.56 (0.07)	Pure H	0.45 (0.02)	0.0184 (0.0009)	−0.58 (0.05)	6.79 (0.06)	
J101141.22+354844.6	DA	10.2	37,704 (1390)	7.67 (0.19)	Pure H	0.51 (0.07)	0.0174 (0.0026)	−0.26 (0.14)	6.58 (0.15)	
J101144.74+110840.1	DA	7.6	30,057 (744)	7.92 (0.20)	Pure H	0.61 (0.10)	0.0141 (0.0020)	−0.84 (0.13)	6.95 (0.06)	
J101205.62+615651.8	DA	49.5	36,759 (305)	7.79 (0.04)	Pure H	0.56 (0.02)	0.0157 (0.0005)	−0.39 (0.03)	6.67 (0.01)	
J101240.60−003334.2	DA	33.6	58,529 (2014)	7.65 (0.12)	Pure H	0.56 (0.04)	0.0186 (0.0019)	0.56 (0.11)	6.02 (0.17)	
J101249.37+044135.9	DA	7.6	59,938 (7894)	7.07 (0.42)	Pure H	0.39 (0.11)	0.0304 (0.0111)	1.03 (0.40)	<5.00	
J101250.81+225104.8	DA	20.7	36,086 (622)	7.72 (0.10)	Pure H	0.53 (0.04)	0.0166 (0.0012)	−0.38 (0.07)	6.67 (0.05)	
J101254.81+581003.2	DA	25.0	32,052 (321)	7.83 (0.07)	Pure H	0.56 (0.03)	0.0151 (0.0008)	−0.66 (0.05)	6.85 (0.02)	
J101324.49+275513.2	DA	25.2	43,475 (1142)	7.74 (0.11)	Pure H	0.56 (0.04)	0.0166 (0.0014)	−0.05 (0.09)	6.46 (0.06)	
J101328.16+061207.3	DA	79.0	43,532 (381)	7.81 (0.04)	Pure H	0.58 (0.02)	0.0157 (0.0005)	−0.10 (0.03)	6.47 (0.01)	5
J101347.20+523022.5	DA	17.8	56,615 (3542)	7.06 (0.21)	Pure H	0.38 (0.05)	0.0300 (0.0054)	0.92 (0.20)	<5.00	
J101355.61−001306.4	DAO	28.3	59,901 (3026)	8.22 (0.25)	$\log N_{\rm He}/N_{\rm H} = -0.66$	0.82 (0.13)	0.0116 (0.0024)	0.19 (0.20)	6.00 (0.09)	4
J101532.10+042507.5	DA	49.7	33,846 (220)	7.30 (0.04)	Pure H	0.38 (0.01)	0.0228 (0.0007)	−0.21 (0.03)	5.79 (0.23)	
J101537.61−030104.2	DA	61.3	37,861 (286)	8.98 (0.04)	Pure H	1.20 (0.02)	0.0058 (0.0002)	−1.20 (0.04)	7.87 (0.05)	
J101558.34−020333.9	DA	38.3	39,860 (560)	7.66 (0.07)	Pure H	0.51 (0.02)	0.0175 (0.0009)	−0.16 (0.05)	6.51 (0.07)	
J101653.82+300538.0	DA	6.2	37,640 (2525)	7.42 (0.34)	Pure H	0.43 (0.11)	0.0211 (0.0055)	−0.09 (0.26)	6.06 (1.10)	
J101700.39+190110.0	DA	35.0	68,032 (2570)	7.28 (0.12)	Pure H	0.47 (0.03)	0.0260 (0.0027)	1.12 (0.11)	<5.00	
J101804.30+253308.0	DA+M	57.7	34,298 (183)	7.75 (0.03)	Pure H	0.53 (0.01)	0.0161 (0.0004)	−0.49 (0.02)	6.75 (0.01)	1
J101818.98+040427.3	DA	19.1	33,011 (498)	7.85 (0.10)	Pure H	0.58 (0.05)	0.0149 (0.0011)	−0.62 (0.07)	6.81 (0.02)	
J101819.45+174702.3	DA+M	38.8	31,777 (228)	7.43 (0.05)	Pure H	0.41 (0.02)	0.0205 (0.0008)	−0.41 (0.04)	6.49 (0.15)	1
J101840.93+470352.7	DA	5.1	45,744 (5457)	8.66 (0.49)	Pure H	1.05 (0.25)	0.0080 (0.0035)	−0.60 (0.44)	6.60 (0.83)	
J101847.14+304018.0	DA	15.6	38,376 (1221)	9.02 (0.17)	Pure H	1.22 (0.07)	0.0057 (0.0009)	−1.20 (0.15)	7.88 (0.20)	
J101932.62+062627.3	DA	7.1	33,026 (1144)	7.37 (0.23)	Pure H	0.40 (0.07)	0.0217 (0.0038)	−0.30 (0.16)	6.18 (0.83)	
J101935.68+254103.0	DO	48.1	122,147 (2157)	8.21 (0.24)	Pure He	0.84 (0.10)	0.0119 (0.0025)	1.46 (0.18)	<5.00	
J102111.93+271522.0	DA	38.9	65,552 (1932)	7.63 (0.10)	Pure H	0.57 (0.03)	0.0192 (0.0016)	0.79 (0.09)	5.89 (0.09)	
J102131.55+511622.9	DB+M	20.1	40,847 (950)	7.98 (0.15)	Pure He	0.62 (0.08)	0.0134 (0.0015)	−0.35 (0.10)	6.59 (0.03)	1
J102313.67+250617.6	DA	6.1	33,840 (1790)	7.25 (0.34)	Pure H	0.36 (0.10)	0.0238 (0.0060)	−0.18 (0.24)	5.48 (1.15)	
J102343.66+094336.5	DA	79.8	53,781 (732)	7.75 (0.05)	Pure H	0.58 (0.02)	0.0168 (0.0007)	0.33 (0.04)	6.20 (0.03)	5
J102349.41+094929.6	DA	34.7	66,402 (2668)	7.37 (0.12)	Pure H	0.49 (0.04)	0.0240 (0.0024)	1.00 (0.11)	<5.00	5
J102414.25+584147.2	DA	36.3	49,765 (1074)	7.68 (0.08)	Pure H	0.55 (0.03)	0.0177 (0.0012)	0.24 (0.07)	6.26 (0.07)	
J102430.93−003207.0	DA	29.3	41,735 (964)	7.73 (0.10)	Pure H	0.54 (0.04)	0.0167 (0.0013)	−0.12 (0.08)	6.50 (0.06)	

Table 2.1 – Atmospheric and stellar parameters of hot white dwarfs from SDSS DR12 (continued)

SDSS Name	Type	S/N	$T_{\rm eff}$ (K)	$\log g$	Composition	$M/M_\odot$	$R/R_\odot$	$\log L/L_\odot$	$\log \tau_{\rm cool}$	Notes
J102453.03+103336.5	DA+M	7.2	37,555 (2897)	7.59 (0.40)	Pure H	0.48 (0.15)	0.0184 (0.0056)	−0.21 (0.30)	6.51 (0.36)	1
J102549.71+003906.1	DA	102.3	37,660 (172)	7.77 (0.02)	Pure H	0.55 (0.01)	0.0161 (0.0003)	−0.33 (0.02)	6.64 (0.01)	
J102624.04+091554.8	DA	52.6	83,845 (4598)	7.38 (0.12)	Pure H	0.55 (0.04)	0.0251 (0.0028)	1.45 (0.14)	<5.00	5
J102654.04+044342.2	DA	17.5	30,696 (405)	7.88 (0.10)	Pure H	0.59 (0.05)	0.0145 (0.0011)	−0.77 (0.07)	6.91 (0.02)	
J102655.43+530610.4	DB	29.8	37,698 (1352)	7.85 (0.10)	Pure He	0.55 (0.05)	0.0147 (0.0011)	−0.41 (0.09)	6.69 (0.05)	
J102751.15+075955.4	DA	49.8	30,706 (159)	7.88 (0.04)	Pure H	0.58 (0.02)	0.0146 (0.0004)	−0.77 (0.03)	6.91 (0.01)	
J102752.92+082738.6	DA	32.9	32,560 (316)	7.25 (0.07)	Pure H	0.36 (0.02)	0.0236 (0.0011)	−0.25 (0.05)	5.60 (0.34)	
J102840.85−025243.8	DA	53.9	67,458 (1886)	7.37 (0.09)	Pure H	0.49 (0.03)	0.0239 (0.0018)	1.03 (0.08)	<5.00	
J102907.31+254008.3	DOZ	64.1	63,924 (1372)	7.47 (0.14)	Pure He	0.46 (0.05)	0.0206 (0.0023)	0.80 (0.10)	<5.00	6,8
J102915.70+314829.4	DA	19.1	35,438 (623)	7.33 (0.10)	Pure H	0.39 (0.03)	0.0224 (0.0017)	−0.15 (0.07)	5.83 (0.50)	
J102945.26+450704.9	DA	64.5	36,894 (250)	7.81 (0.04)	Pure H	0.57 (0.02)	0.0155 (0.0004)	−0.40 (0.03)	6.67 (0.01)	
J103016.65+494520.6	DA	56.8	38,972 (323)	7.67 (0.04)	Pure H	0.52 (0.02)	0.0174 (0.0005)	−0.20 (0.03)	6.55 (0.03)	
J103032.43+633317.6	DA	60.3	41,146 (406)	7.74 (0.04)	Pure H	0.55 (0.02)	0.0165 (0.0005)	−0.15 (0.03)	6.52 (0.02)	5
J103041.44+401312.6	DO	44.4	57,770 (824)	8.30 (0.09)	Pure He	0.82 (0.05)	0.0107 (0.0008)	0.06 (0.07)	6.09 (0.03)	
J103048.75+015109.9	DAO	27.5	71,250 (7075)	7.20 (0.25)	$\log N_{\rm He}/N_{\rm H} = -1.59$	0.46 (0.07)	0.0283 (0.0065)	1.27 (0.28)	<5.00	4,5
J103136.88+212123.6	DA	8.9	42,021 (2105)	7.74 (0.22)	Pure H	0.55 (0.09)	0.0166 (0.0029)	−0.11 (0.17)	6.50 (0.13)	
J103142.34+561601.9	DA	23.3	33,278 (369)	7.94 (0.07)	Pure H	0.62 (0.04)	0.0140 (0.0008)	−0.67 (0.05)	6.80 (0.02)	
J103306.41+475938.0	DA	23.2	31,096 (338)	7.71 (0.08)	Pure H	0.51 (0.03)	0.0166 (0.0010)	−0.64 (0.06)	6.86 (0.04)	
J103307.23+162237.6	DA	9.2	30,273 (621)	7.15 (0.16)	Pure H	0.32 (0.05)	0.0250 (0.0029)	−0.32 (0.11)	5.38 (0.66)	
J103455.90+240905.8	DOA	43.6	49,081 (242)	8.07 (0.08)	$\log q_{\rm H} = -17.68$	0.68 (0.04)	0.0126 (0.0008)	−0.08 (0.06)	6.36 (0.02)	3
J103500.91+023008.7	DA+M	24.8	73,427 (4323)	7.30 (0.17)	Pure H	0.49 (0.05)	0.0260 (0.0040)	1.25 (0.18)	<5.00	1
J103551.87+500707.6	DA	4.3	34,923 (2519)	7.60 (0.43)	Pure H	0.48 (0.17)	0.0182 (0.0060)	−0.35 (0.31)	6.62 (0.31)	
J103555.51+421043.8	DBA	25.0	34,868 (2172)	7.75 (0.11)	$\log q_{\rm H} = -17.50$	0.50 (0.05)	0.0157 (0.0012)	−0.48 (0.13)	6.75 (0.11)	3
J103559.29+335209.6	DA+M	8.3	46,913 (4995)	7.11 (0.41)	Pure H	0.36 (0.11)	0.0277 (0.0092)	0.52 (0.35)	<5.00	1
J103641.83+050807.0	DA	17.3	47,560 (2305)	7.30 (0.18)	Pure H	0.41 (0.06)	0.0238 (0.0034)	0.42 (0.15)	<5.00	
J103651.42+420727.5	DA	36.7	47,619 (869)	7.82 (0.07)	Pure H	0.60 (0.03)	0.0157 (0.0009)	0.06 (0.06)	6.36 (0.02)	
J103659.54+192655.4	DA	48.8	59,003 (1538)	7.51 (0.08)	Pure H	0.52 (0.03)	0.0209 (0.0014)	0.68 (0.08)	5.68 (0.41)	5
J103715.76+443013.3	DA	8.0	31,826 (908)	7.96 (0.21)	Pure H	0.63 (0.11)	0.0138 (0.0021)	−0.75 (0.14)	6.87 (0.06)	
J103756.67+221934.3	DA	22.7	34,244 (492)	8.50 (0.09)	Pure H	0.95 (0.05)	0.0091 (0.0007)	−0.99 (0.07)	7.27 (0.22)	
J103836.11+301126.7	DA	5.6	31,787 (1467)	7.67 (0.33)	Pure H	0.49 (0.13)	0.0170 (0.0043)	−0.57 (0.23)	6.81 (0.18)	
J103837.22+015058.4	DA	37.7	33,798 (236)	7.83 (0.04)	Pure H	0.57 (0.02)	0.0152 (0.0005)	−0.57 (0.03)	6.78 (0.01)	7
J103854.78+160544.3	DA	18.4	31,494 (459)	6.88 (0.11)	Pure H	0.26 (0.02)	0.0306 (0.0026)	−0.08 (0.08)	<5.00	
J103924.72+192614.1	DA	23.1	34,954 (517)	7.58 (0.09)	Pure H	0.47 (0.03)	0.0184 (0.0013)	−0.34 (0.07)	6.61 (0.12)	
J103944.75+470652.5	DA	36.5	31,741 (237)	7.84 (0.05)	Pure H	0.57 (0.03)	0.0150 (0.0006)	−0.68 (0.04)	6.86 (0.01)	
J104107.66+092103.3	DA+M	24.2	50,069 (1643)	7.55 (0.12)	Pure H	0.50 (0.04)	0.0197 (0.0020)	0.34 (0.11)	6.02 (0.45)	1
J104237.73+301800.0	DA	24.3	46,817 (1324)	7.95 (0.11)	Pure H	0.66 (0.05)	0.0142 (0.0012)	−0.06 (0.09)	6.37 (0.04)	
J104253.99+652425.8	DA	20.6	40,159 (2068)	7.88 (0.24)	Pure H	0.61 (0.11)	0.0148 (0.0027)	−0.29 (0.19)	6.57 (0.08)	
J104332.50+295703.4	DA	10.1	30,127 (708)	8.26 (0.19)	Pure H	0.80 (0.11)	0.0109 (0.0016)	−1.05 (0.13)	7.17 (0.29)	
J104332.61+445328.9	DA	72.0	48,925 (567)	7.72 (0.04)	Pure H	0.56 (0.02)	0.0170 (0.0006)	0.18 (0.04)	6.30 (0.02)	
J104423.24+565506.9	DB	21.3	34,196 (998)	7.80 (0.10)	Pure He	0.53 (0.05)	0.0150 (0.0011)	−0.55 (0.08)	6.80 (0.05)	
J104528.53+314516.0	DA	5.0	36,977 (2799)	7.61 (0.40)	Pure H	0.49 (0.15)	0.0182 (0.0056)	−0.26 (0.30)	6.55 (0.31)	
J104534.45+315740.6	DA+M	46.9	68,007 (2094)	7.38 (0.10)	Pure H	0.50 (0.03)	0.0237 (0.0019)	1.03 (0.09)	<5.00	1,2
J104604.39+214018.5	DA+M	25.4	41,222 (890)	7.77 (0.10)	Pure H	0.56 (0.04)	0.0161 (0.0012)	−0.17 (0.08)	6.53 (0.04)	1
J104614.75+045523.6	DA	22.2	62,069 (3645)	7.18 (0.19)	Pure H	0.42 (0.05)	0.0276 (0.0045)	1.01 (0.18)	<5.00	
J104616.00+202127.9	DA	82.6	79,946 (2375)	7.56 (0.07)	Pure H	0.59 (0.02)	0.0211 (0.0014)	1.21 (0.08)	5.45 (0.15)	5
J104921.97+102343.7	DA	43.2	54,429 (1185)	7.46 (0.08)	Pure H	0.49 (0.03)	0.0214 (0.0013)	0.56 (0.07)	5.45 (0.56)	
J104944.65+085512.0	DA+M	18.6	51,599 (2747)	7.74 (0.20)	Pure H	0.57 (0.08)	0.0169 (0.0027)	0.26 (0.17)	6.24 (0.14)	1
J104956.66+501109.4	DA	19.2	34,801 (581)	7.87 (0.10)	Pure H	0.59 (0.05)	0.0148 (0.0011)	−0.54 (0.07)	6.75 (0.02)	
J105040.87+464704.5	DA	16.7	51,210 (2734)	7.72 (0.20)	Pure H	0.56 (0.07)	0.0172 (0.0028)	0.27 (0.17)	6.24 (0.15)	
J105042.63−010830.4	DA	7.0	56,166 (9742)	7.29 (0.54)	Pure H	0.43 (0.16)	0.0246 (0.0115)	0.73 (0.51)	<5.00	7

Table 2.1 – Atmospheric and stellar parameters of hot white dwarfs from SDSS DR12 (continued)

SDSS Name	Type	S/N	$T_{\rm eff}$ (K)	$\log g$	Composition	$M/M_{\odot}$	$R/R_{\odot}$	$\log L/L_{\odot}$	$\log \tau_{\rm cool}$	Notes
J105052.55+641517.5	DA	7.0	39,697 (2667)	7.57 (0.31)	Pure H	0.48 (0.11)	0.0189 (0.0046)	−0.10 (0.25)	6.39 (0.44)	
J105100.53+484019.4	DA	11.3	36,440 (1218)	7.57 (0.18)	Pure H	0.47 (0.06)	0.0186 (0.0027)	−0.26 (0.14)	6.53 (0.31)	
J105101.97+010826.7	DA	44.5	42,379 (617)	7.73 (0.06)	Pure H	0.55 (0.03)	0.0167 (0.0008)	−0.09 (0.05)	6.48 (0.03)	
J105207.12+134445.8	DA	27.4	31,240 (256)	7.88 (0.06)	Pure H	0.58 (0.03)	0.0146 (0.0007)	−0.74 (0.04)	6.89 (0.01)	
J105211.30+274743.0	DA	35.4	30,685 (191)	7.92 (0.05)	Pure H	0.60 (0.02)	0.0141 (0.0005)	−0.80 (0.03)	6.92 (0.01)	
J105344.44+201415.3	DB	34.9	37,323 (724)	7.81 (0.06)	Pure He	0.54 (0.03)	0.0151 (0.0007)	−0.40 (0.05)	6.69 (0.03)	
J105414.62+542349.5	DA	17.2	32,193 (554)	7.84 (0.12)	Pure H	0.57 (0.06)	0.0150 (0.0014)	−0.66 (0.08)	6.85 (0.03)	
J105424.73+092258.2	DA+M	27.4	31,469 (277)	7.74 (0.07)	Pure H	0.52 (0.03)	0.0161 (0.0008)	−0.64 (0.04)	6.86 (0.02)	1
J105427.18+350004.5	DA	36.3	55,559 (1447)	7.40 (0.09)	Pure H	0.47 (0.03)	0.0225 (0.0015)	0.64 (0.08)	<5.00	
J105427.62+092128.8	DA	48.7	47,268 (805)	7.42 (0.07)	Pure H	0.45 (0.02)	0.0219 (0.0011)	0.33 (0.05)	5.40 (0.38)	
J105429.59+535829.4	DA	20.5	32,327 (421)	7.92 (0.09)	Pure H	0.61 (0.05)	0.0142 (0.0010)	−0.70 (0.06)	6.84 (0.02)	
J105442.84+611925.8	DA	31.8	34,339 (396)	7.93 (0.07)	Pure H	0.62 (0.04)	0.0141 (0.0008)	−0.61 (0.05)	6.76 (0.02)	
J105443.06+285032.7	DA+M	14.3	35,348 (919)	7.78 (0.15)	Pure H	0.55 (0.07)	0.0159 (0.0018)	−0.45 (0.11)	6.72 (0.06)	1
J105445.16+013525.5	DA	24.0	39,544 (889)	7.77 (0.11)	Pure H	0.56 (0.05)	0.0161 (0.0013)	−0.25 (0.08)	6.58 (0.04)	
J105448.41+025124.7	DA	15.2	33,473 (888)	7.30 (0.17)	Pure H	0.38 (0.05)	0.0228 (0.0029)	−0.23 (0.12)	5.82 (0.76)	2
J105555.24+484739.8	DA	65.9	73,469 (2822)	7.35 (0.09)	Pure H	0.50 (0.03)	0.0248 (0.0020)	1.21 (0.10)	<5.00	5
J105608.07+050458.9	DA	21.7	40,931 (1140)	7.80 (0.13)	Pure H	0.57 (0.05)	0.0158 (0.0015)	−0.20 (0.10)	6.54 (0.05)	
J105608.94+283048.9	DA	9.3	41,270 (2152)	7.56 (0.23)	Pure H	0.48 (0.08)	0.0191 (0.0035)	−0.02 (0.19)	6.31 (0.47)	
J105656.16+194458.4	DA+M	15.1	39,429 (1069)	7.88 (0.13)	Pure H	0.61 (0.06)	0.0148 (0.0015)	−0.32 (0.10)	6.59 (0.03)	1
J105731.96+531354.7	DA	20.3	30,031 (354)	7.07 (0.10)	Pure H	0.30 (0.03)	0.0265 (0.0018)	−0.29 (0.06)	5.09 (0.32)	
J105751.26+602318.7	DA	9.4	43,529 (2144)	7.61 (0.21)	Pure H	0.50 (0.07)	0.0185 (0.0031)	0.05 (0.17)	6.33 (0.30)	
J105845.61+151959.8	DA	32.6	35,845 (461)	7.08 (0.07)	Pure H	0.32 (0.02)	0.0269 (0.0015)	0.03 (0.05)	<5.00	
J105916.42+512443.1	DA	66.0	68,224 (1247)	7.98 (0.06)	Pure H	0.71 (0.03)	0.0143 (0.0007)	0.60 (0.06)	5.92 (0.02)	
J110150.90+360559.4	DA+M	6.2	31,887 (1308)	7.44 (0.29)	Pure H	0.41 (0.10)	0.0204 (0.0045)	−0.41 (0.21)	6.51 (0.68)	1
J110320.28+085645.8	DA	21.1	30,044 (293)	7.86 (0.08)	Pure H	0.57 (0.04)	0.0148 (0.0008)	−0.79 (0.05)	6.94 (0.02)	
J110330.36+342740.0	DA	18.5	52,606 (2619)	7.88 (0.18)	Pure H	0.63 (0.08)	0.0152 (0.0022)	0.20 (0.16)	6.24 (0.07)	
J110414.06+521435.2	DA	44.0	33,588 (249)	7.32 (0.05)	Pure H	0.39 (0.01)	0.0224 (0.0008)	−0.24 (0.03)	5.93 (0.25)	
J110435.25+291757.5	DA	8.0	31,715 (991)	7.80 (0.23)	Pure H	0.55 (0.10)	0.0154 (0.0026)	−0.66 (0.16)	6.86 (0.09)	
J110437.97+235641.4	DA	71.1	31,365 (106)	7.84 (0.03)	Pure H	0.57 (0.01)	0.0150 (0.0003)	−0.71 (0.02)	6.88 (0.01)	
J110459.36+035847.9	DA	15.6	37,399 (999)	7.62 (0.14)	Pure H	0.49 (0.05)	0.0179 (0.0019)	−0.25 (0.11)	6.56 (0.18)	
J110500.81+023504.7	DA	30.3	41,319 (885)	7.83 (0.10)	Pure H	0.59 (0.04)	0.0154 (0.0011)	−0.21 (0.08)	6.53 (0.03)	
J110549.24+024352.4	DA	27.8	47,774 (1272)	7.79 (0.10)	Pure H	0.58 (0.04)	0.0162 (0.0013)	0.09 (0.09)	6.35 (0.04)	
J110627.67−010514.6	DA+M	49.6	30,502 (186)	7.42 (0.05)	Pure H	0.41 (0.01)	0.0205 (0.0007)	−0.48 (0.03)	6.56 (0.14)	1,2
J110634.39+073712.2	DA+M	51.5	36,034 (232)	7.67 (0.04)	Pure H	0.51 (0.01)	0.0172 (0.0005)	−0.35 (0.03)	6.65 (0.03)	1
J110747.86+383550.8	DO	47.0	60,268 (1008)	8.05 (0.11)	Pure He	0.69 (0.06)	0.0129 (0.0011)	0.30 (0.08)	6.13 (0.04)	
J110748.70−163650.1	DA	27.5	37,064 (604)	7.72 (0.09)	Pure H	0.53 (0.04)	0.0166 (0.0011)	−0.33 (0.06)	6.64 (0.05)	
J110826.47+092721.5	DA+M	29.6	39,581 (769)	7.64 (0.09)	Pure H	0.50 (0.03)	0.0178 (0.0013)	−0.15 (0.07)	6.50 (0.11)	1
J110843.57+115515.8	DA+M	41.9	37,082 (365)	7.77 (0.05)	Pure H	0.55 (0.02)	0.0160 (0.0006)	−0.36 (0.04)	6.66 (0.02)	1
J110845.04−152414.6	DAO	58.6	88,642 (3666)	7.16 (0.12)	$\log N_{\rm He}/N_{\rm H} = -2.15$	0.51 (0.03)	0.0309 (0.0037)	1.73 (0.13)	<5.00	4,5
J110849.07+395105.1	DA	18.6	31,895 (413)	7.77 (0.09)	Pure H	0.54 (0.04)	0.0159 (0.0011)	−0.63 (0.06)	6.85 (0.03)	
J110944.28+095944.9	DA	8.9	32,959 (895)	7.82 (0.18)	Pure H	0.56 (0.08)	0.0152 (0.0021)	−0.61 (0.13)	6.81 (0.06)	
J111044.62+231405.0	DA	33.8	35,046 (332)	7.67 (0.06)	Pure H	0.50 (0.02)	0.0172 (0.0007)	−0.40 (0.04)	6.68 (0.04)	
J111045.90+321447.2	DA+M	42.0	69,924 (2546)	7.09 (0.11)	Pure H	0.43 (0.02)	0.0310 (0.0029)	1.32 (0.11)	<5.00	1
J111048.83+265544.7	DA	22.6	64,956 (4066)	7.11 (0.17)	Pure H	0.42 (0.04)	0.0298 (0.0046)	1.16 (0.18)	<5.00	5
J111058.51+502053.2	DA	47.1	39,832 (481)	7.77 (0.06)	Pure H	0.56 (0.02)	0.0161 (0.0007)	−0.23 (0.04)	6.57 (0.02)	
J111059.42−170954.2	DA	39.3	52,226 (1513)	7.63 (0.11)	Pure H	0.54 (0.04)	0.0185 (0.0016)	0.36 (0.09)	6.16 (0.16)	
J111127.30+395628.0	DA	32.1	62,572 (2465)	7.64 (0.13)	Pure H	0.57 (0.04)	0.0189 (0.0022)	0.69 (0.12)	5.93 (0.16)	
J111139.64+534752.0	DA	46.7	35,948 (278)	7.77 (0.04)	Pure H	0.55 (0.02)	0.0160 (0.0005)	−0.41 (0.03)	6.70 (0.01)	
J111305.09+155545.8	DAO	32.2	72,622 (6562)	6.72 (0.19)	$\log N_{\rm He}/N_{\rm H} = -1.57$	0.36 (0.05)	0.0436 (0.0074)	1.68 (0.23)	<5.00	4,5
J111345.02−162134.2	DA	9.0	59,759 (9399)	6.95 (0.50)	Pure H	0.37 (0.12)	0.0337 (0.0142)	1.12 (0.47)	<5.00	

Table 2.1 – Atmospheric and stellar parameters of hot white dwarfs from SDSS DR12 (continued)

SDSS Name	Type	S/N	$T_{\rm eff}$ (K)	$\log g$	Composition	$M/M_{\odot}$	$R/R_{\odot}$	$\log L/L_{\odot}$	$\log \tau_{\rm cool}$	Notes
J111351.80+315621.7	DA	24.0	31,091 (316)	7.88 (0.08)	Pure H	0.59 (0.04)	0.0145 (0.0008)	−0.75 (0.05)	6.90 (0.02)	
J111356.48+131614.4	DA	52.4	45,488 (623)	7.60 (0.06)	Pure H	0.51 (0.02)	0.0188 (0.0009)	0.13 (0.05)	6.26 (0.13)	5
J111444.70+200114.6	DA	38.7	41,904 (622)	7.83 (0.07)	Pure H	0.59 (0.03)	0.0154 (0.0008)	−0.18 (0.05)	6.52 (0.02)	5
J111501.15−124217.9	DA	27.4	38,835 (717)	7.57 (0.09)	Pure H	0.48 (0.03)	0.0188 (0.0013)	−0.14 (0.07)	6.43 (0.17)	
J111511.30+192032.5	DA	17.9	56,079 (3270)	7.28 (0.20)	Pure H	0.43 (0.06)	0.0249 (0.0041)	0.74 (0.18)	<5.00	
J111603.77+494343.9	DA	38.0	43,484 (621)	7.70 (0.06)	Pure H	0.54 (0.02)	0.0171 (0.0008)	−0.03 (0.05)	6.44 (0.04)	
J111617.04+155941.8	DA	21.8	31,924 (335)	7.69 (0.08)	Pure H	0.50 (0.03)	0.0168 (0.0009)	−0.58 (0.05)	6.82 (0.04)	
J111718.07+403644.0	DA	53.8	83,657 (3944)	7.52 (0.11)	Pure H	0.59 (0.03)	0.0220 (0.0022)	1.33 (0.12)	5.26 (0.32)	5
J111810.19+131338.4	DA+M	24.0	32,307 (648)	7.96 (0.14)	Pure H	0.63 (0.07)	0.0138 (0.0014)	−0.73 (0.10)	6.85 (0.03)	1,2
J111909.78+334224.7	DAO	20.0	56,661 (3941)	7.50 (0.27)	$\log N_{\rm He}/N_{\rm H} = -1.08$	0.51 (0.09)	0.0210 (0.0046)	0.61 (0.23)	5.67 (0.95)	4,5
J111949.35+092205.9	DA	40.5	37,071 (392)	7.83 (0.06)	Pure H	0.58 (0.03)	0.0153 (0.0006)	−0.40 (0.04)	6.67 (0.01)	
J111959.92−105056.0	DA	10.8	31,595 (784)	7.52 (0.18)	Pure H	0.44 (0.06)	0.0191 (0.0027)	−0.48 (0.13)	6.68 (0.32)	
J112059.66−001942.3	DA	17.8	32,446 (474)	7.17 (0.10)	Pure H	0.33 (0.03)	0.0250 (0.0018)	−0.21 (0.07)	5.22 (0.43)	
J112151.24+655159.3	DA	16.2	33,020 (631)	7.58 (0.13)	Pure H	0.46 (0.05)	0.0184 (0.0018)	−0.44 (0.09)	6.68 (0.16)	
J112215.98+671145.9	DA	66.2	51,724 (652)	7.66 (0.05)	Pure H	0.55 (0.02)	0.0181 (0.0007)	0.32 (0.04)	6.19 (0.04)	
J112316.80+291558.4	DA	15.6	30,898 (409)	7.71 (0.10)	Pure H	0.51 (0.04)	0.0164 (0.0012)	−0.65 (0.07)	6.87 (0.05)	
J112406.90+305053.1	DA	26.1	40,942 (869)	7.75 (0.10)	Pure H	0.55 (0.04)	0.0164 (0.0012)	−0.17 (0.08)	6.53 (0.05)	
J112520.99+563544.9	DA	33.4	31,193 (243)	7.79 (0.06)	Pure H	0.55 (0.03)	0.0155 (0.0007)	−0.69 (0.04)	6.88 (0.02)	
J112523.65+115243.1	DA	26.9	40,701 (682)	7.80 (0.08)	Pure H	0.57 (0.03)	0.0158 (0.0009)	−0.21 (0.06)	6.55 (0.02)	
J112536.82+084504.5	DA	24.5	30,165 (290)	7.90 (0.08)	Pure H	0.60 (0.04)	0.0143 (0.0008)	−0.82 (0.05)	6.94 (0.02)	
J112543.23+230654.1	DA	21.6	30,005 (238)	7.86 (0.06)	Pure H	0.57 (0.03)	0.0148 (0.0007)	−0.80 (0.04)	6.94 (0.01)	
J112605.64+623450.9	DA	27.6	32,563 (324)	7.82 (0.07)	Pure H	0.56 (0.03)	0.0152 (0.0008)	−0.63 (0.05)	6.83 (0.02)	
J112613.88−020536.2	DA	5.7	30,606 (1206)	8.02 (0.31)	Pure H	0.66 (0.16)	0.0132 (0.0030)	−0.86 (0.21)	6.93 (0.16)	
J112658.82+631650.6	DA	27.1	30,000 (242)	7.84 (0.06)	Pure H	0.57 (0.03)	0.0149 (0.0007)	−0.79 (0.04)	6.94 (0.01)	
J112722.04−062332.1	DA	11.4	30,415 (605)	7.92 (0.16)	Pure H	0.61 (0.08)	0.0141 (0.0016)	−0.82 (0.11)	6.93 (0.04)	
J112815.60+171408.8	DA	55.0	58,731 (1036)	7.65 (0.06)	Pure H	0.56 (0.02)	0.0185 (0.0010)	0.57 (0.06)	6.01 (0.07)	
J112906.29+331431.0	DA	23.4	39,584 (812)	7.62 (0.10)	Pure H	0.50 (0.03)	0.0180 (0.0014)	−0.14 (0.08)	6.48 (0.13)	
J112927.52−081527.0	DA+M	19.3	41,796 (1296)	7.52 (0.13)	Pure H	0.47 (0.04)	0.0197 (0.0021)	0.03 (0.11)	6.19 (0.41)	1
J112953.05+222506.6	DA	57.0	57,506 (1130)	7.54 (0.06)	Pure H	0.52 (0.02)	0.0203 (0.0011)	0.61 (0.06)	5.84 (0.23)	5
J112954.78+510000.2	DA	41.1	57,728 (1662)	6.92 (0.09)	Pure H	0.35 (0.02)	0.0342 (0.0026)	1.07 (0.09)	<5.00	5
J113115.56+113230.4	DA	20.7	38,469 (944)	7.67 (0.12)	Pure H	0.51 (0.05)	0.0174 (0.0017)	−0.22 (0.09)	6.56 (0.12)	
J113129.22−084726.6	DA	10.8	59,259 (4810)	7.11 (0.28)	Pure H	0.40 (0.07)	0.0293 (0.0069)	0.98 (0.26)	<5.00	7
J113144.67+630320.0	DA	7.3	38,615 (2091)	7.77 (0.27)	Pure H	0.55 (0.11)	0.0161 (0.0033)	−0.28 (0.20)	6.61 (0.15)	
J113151.33+204735.1	DA	39.1	36,358 (329)	7.34 (0.05)	Pure H	0.40 (0.02)	0.0224 (0.0008)	−0.10 (0.04)	5.76 (0.26)	
J113153.30+003146.9	DO	11.8	80,237 (11,293)	7.92 (0.61)	Pure He	0.66 (0.26)	0.0147 (0.0079)	0.91 (0.51)	5.80 (0.66)	
J113219.73−075442.0	DA	19.6	34,102 (539)	7.58 (0.10)	Pure H	0.47 (0.03)	0.0184 (0.0014)	−0.38 (0.07)	6.64 (0.13)	
J113303.70+290222.9	DA	45.0	72,743 (2282)	7.26 (0.09)	Pure H	0.48 (0.02)	0.0268 (0.0023)	1.26 (0.10)	<5.00	
J113316.26+270747.5	DA+M	46.9	70,798 (2455)	7.46 (0.11)	Pure H	0.53 (0.04)	0.0225 (0.0020)	1.06 (0.10)	5.11 (0.79)	1
J113408.25+485601.8	DA	35.3	80,790 (5241)	7.52 (0.16)	Pure H	0.58 (0.05)	0.0219 (0.0031)	1.27 (0.17)	5.35 (0.52)	5
J113431.17+523533.9	DA	26.4	32,078 (288)	7.83 (0.06)	Pure H	0.56 (0.03)	0.0151 (0.0007)	−0.66 (0.04)	6.85 (0.01)	
J113609.59+484318.9	DO+M	61.7	46,218 (119)	7.82 (0.04)	Pure He	0.56 (0.02)	0.0152 (0.0004)	−0.02 (0.02)	6.43 (0.01)	1
J113611.51+213246.6	DA	16.4	34,962 (716)	7.69 (0.12)	Pure H	0.51 (0.05)	0.0169 (0.0016)	−0.41 (0.09)	6.70 (0.08)	
J113627.04+220910.3	DA	46.6	41,045 (479)	7.80 (0.05)	Pure H	0.58 (0.02)	0.0157 (0.0006)	−0.20 (0.04)	6.54 (0.02)	
J113631.49+591229.6	DO	34.9	60,575 (1461)	7.61 (0.17)	Pure He	0.51 (0.07)	0.0185 (0.0023)	0.62 (0.12)	5.69 (0.77)	
J113643.40+475847.5	DA	23.3	54,492 (2070)	7.90 (0.14)	Pure H	0.65 (0.06)	0.0150 (0.0017)	0.25 (0.12)	6.20 (0.05)	
J113656.32+005835.5	DA	23.9	31,895 (412)	7.09 (0.09)	Pure H	0.31 (0.03)	0.0262 (0.0017)	−0.19 (0.06)	5.00 (0.32)	
J113816.30+382635.1	DO	28.3	81,140 (4647)	8.54 (0.23)	Pure He	0.98 (0.13)	0.0088 (0.0018)	0.48 (0.20)	5.57 (0.11)	
J113836.32+475510.0	DA	58.1	48,787 (680)	7.55 (0.05)	Pure H	0.50 (0.02)	0.0196 (0.0009)	0.29 (0.05)	6.07 (0.19)	
J113919.17+211934.3	DA	33.5	39,626 (686)	7.80 (0.08)	Pure H	0.57 (0.04)	0.0157 (0.0010)	−0.26 (0.06)	6.58 (0.03)	
J114010.15+094030.4	DA	32.5	30,938 (212)	7.88 (0.05)	Pure H	0.59 (0.03)	0.0145 (0.0006)	−0.76 (0.04)	6.90 (0.01)	

Table 2.1 – Atmospheric and stellar parameters of hot white dwarfs from SDSS DR12 (continued)

SDSS Name	Type	S/N	$T_{\rm eff}$ (K)	$\log g$	Composition	$M/M_{\odot}$	$R/R_{\odot}$	$\log L/L_{\odot}$	$\log \tau_{\rm cool}$	Notes
J114012.10+301308.8	DA+M	5.8	32,255 (1232)	7.79 (0.27)	Pure H	0.55 (0.12)	0.0156 (0.0031)	−0.63 (0.19)	6.84 (0.11)	1
J114100.88+325525.1	DA	26.4	36,164 (528)	7.61 (0.08)	Pure H	0.49 (0.03)	0.0181 (0.0011)	−0.30 (0.06)	6.59 (0.10)	
J114108.78+160436.7	DA	36.8	30,694 (180)	7.26 (0.04)	Pure H	0.36 (0.01)	0.0232 (0.0008)	−0.37 (0.03)	5.84 (0.23)	
J114152.62+253533.9	DA	50.0	43,301 (507)	7.73 (0.05)	Pure H	0.55 (0.02)	0.0168 (0.0006)	−0.05 (0.04)	6.46 (0.02)	
J114303.49+670224.7	DA	13.3	32,079 (546)	7.69 (0.12)	Pure H	0.50 (0.05)	0.0168 (0.0015)	−0.57 (0.08)	6.81 (0.07)	
J114402.10+310926.1	DA	18.6	40,475 (1118)	7.61 (0.13)	Pure H	0.50 (0.04)	0.0183 (0.0019)	−0.09 (0.10)	6.43 (0.21)	
J114446.37+254122.3	DBA	36.3	33,128 (1808)	7.74 (0.08)	$\log q_{\rm H} = -17.12$	0.50 (0.03)	0.0157 (0.0009)	−0.57 (0.11)	6.81 (0.09)	3
J114450.58+372527.7	DA	20.3	42,831 (1294)	7.58 (0.13)	Pure H	0.49 (0.04)	0.0189 (0.0020)	0.03 (0.11)	6.29 (0.30)	
J114511.78+062235.6	DA	20.5	30,795 (332)	7.06 (0.08)	Pure H	0.30 (0.02)	0.0268 (0.0016)	−0.24 (0.06)	<5.00	
J114723.19+240735.7	DA	24.1	36,022 (578)	7.81 (0.09)	Pure H	0.56 (0.04)	0.0155 (0.0011)	−0.44 (0.07)	6.70 (0.03)	
J114727.72+141923.7	DA	23.5	34,077 (435)	7.80 (0.08)	Pure H	0.56 (0.04)	0.0155 (0.0009)	−0.53 (0.06)	6.77 (0.02)	
J114734.57+142658.9	DA+M	29.0	53,197 (1786)	7.53 (0.12)	Pure H	0.51 (0.04)	0.0203 (0.0020)	0.47 (0.11)	5.88 (0.54)	1
J114852.77+430753.1	DA	5.8	45,470 (5645)	7.28 (0.49)	Pure H	0.40 (0.14)	0.0241 (0.0097)	0.35 (0.41)	<5.00	
J114924.06+375045.8	DA	5.4	42,203 (5317)	7.61 (0.50)	Pure H	0.50 (0.19)	0.0184 (0.0072)	−0.01 (0.41)	6.37 (0.43)	7
J115012.28+480905.9	DA	40.7	55,615 (1462)	7.68 (0.09)	Pure H	0.56 (0.03)	0.0179 (0.0013)	0.44 (0.08)	6.11 (0.08)	5
J115036.12+464521.4	DAO	31.7	78,290 (12,480)	6.57 (0.26)	$\log N_{\rm He}/N_{\rm H} = -0.93$	0.35 (0.07)	0.0511 (0.0120)	1.95 (0.39)	<5.00	4,5
J115106.71+315322.6	DA	34.0	35,315 (345)	7.79 (0.06)	Pure H	0.56 (0.03)	0.0156 (0.0007)	−0.46 (0.04)	6.72 (0.02)	
J115120.14+472922.2	DA	40.5	30,249 (144)	7.86 (0.04)	Pure H	0.58 (0.02)	0.0147 (0.0004)	−0.79 (0.03)	6.93 (0.01)	
J115145.63+375152.8	DA	4.3	39,984 (3604)	7.81 (0.42)	Pure H	0.58 (0.19)	0.0156 (0.0052)	−0.25 (0.33)	6.57 (0.28)	
J115216.64+060438.4	DA	17.1	56,140 (3343)	7.25 (0.20)	Pure H	0.42 (0.06)	0.0256 (0.0043)	0.77 (0.18)	<5.00	
J115218.69−024915.8	DO	21.5	49,587 (429)	7.91 (0.15)	Pure He	0.60 (0.07)	0.0143 (0.0016)	0.05 (0.10)	6.37 (0.02)	
J115232.85+035410.5	DA	27.4	45,112 (1354)	7.67 (0.12)	Pure H	0.53 (0.04)	0.0176 (0.0017)	0.06 (0.10)	6.38 (0.12)	
J115237.82+331221.3	DA	32.9	35,756 (459)	7.57 (0.07)	Pure H	0.47 (0.03)	0.0186 (0.0011)	−0.29 (0.06)	6.56 (0.11)	
J115300.86+042417.4	DA	24.5	37,280 (697)	7.15 (0.10)	Pure H	0.34 (0.03)	0.0256 (0.0018)	0.06 (0.07)	<5.00	
J115317.33+191152.7	DA	46.7	43,044 (593)	7.74 (0.06)	Pure H	0.55 (0.02)	0.0166 (0.0008)	−0.07 (0.05)	6.47 (0.03)	
J115321.03+645557.7	DA	5.0	48,134 (7662)	7.35 (0.60)	Pure H	0.43 (0.19)	0.0230 (0.0115)	0.41 (0.51)	<5.00	
J115338.12+362721.6	DA	22.5	41,325 (1011)	7.74 (0.11)	Pure H	0.55 (0.04)	0.0165 (0.0014)	−0.15 (0.09)	6.52 (0.06)	
J115411.77+543251.3	DA+M	17.5	40,323 (1606)	7.97 (0.18)	Pure H	0.65 (0.09)	0.0139 (0.0020)	−0.34 (0.14)	6.55 (0.05)	1,2
J115538.56+254135.2	DB	11.8	36,765 (2157)	7.92 (0.21)	Pure He	0.59 (0.11)	0.0139 (0.0022)	−0.50 (0.17)	6.72 (0.09)	
J115553.96+105255.1	DA+M	29.3	33,404 (435)	7.72 (0.08)	Pure H	0.52 (0.04)	0.0164 (0.0011)	−0.52 (0.06)	6.77 (0.04)	1,2
J115616.00+505039.9	DA	34.4	40,541 (596)	7.59 (0.07)	Pure H	0.49 (0.02)	0.0186 (0.0010)	−0.08 (0.05)	6.40 (0.12)	
J115744.83+485618.2	DAO+M	28.9	86,881 (6139)	7.18 (0.18)	$\log N_{\rm He}/N_{\rm H} = -0.81$	0.51 (0.04)	0.0304 (0.0053)	1.68 (0.20)	<5.00	1,2,4
J115816.52−012309.7	DA	6.0	38,902 (2993)	7.35 (0.37)	Pure H	0.41 (0.12)	0.0223 (0.0064)	0.01 (0.28)	5.67 (1.21)	
J115853.98+380917.5	DA	23.9	34,737 (491)	7.77 (0.09)	Pure H	0.54 (0.04)	0.0159 (0.0010)	−0.48 (0.06)	6.74 (0.03)	
J115857.33+152921.4	DA+M	10.4	32,561 (1261)	7.69 (0.27)	Pure H	0.50 (0.11)	0.0168 (0.0034)	−0.54 (0.19)	6.79 (0.14)	1,2
J120048.14+390329.1	DA	45.3	37,462 (345)	7.82 (0.05)	Pure H	0.57 (0.02)	0.0154 (0.0006)	−0.37 (0.04)	6.65 (0.01)	
J120128.77+340632.7	DA	34.9	43,827 (816)	7.68 (0.08)	Pure H	0.53 (0.03)	0.0175 (0.0011)	0.01 (0.06)	6.41 (0.07)	
J120132.65+594034.1	DA	48.2	41,784 (545)	7.70 (0.06)	Pure H	0.53 (0.02)	0.0171 (0.0008)	−0.09 (0.05)	6.49 (0.04)	5
J120238.18+602003.6	DA	16.2	33,189 (510)	8.09 (0.10)	Pure H	0.70 (0.06)	0.0125 (0.0010)	−0.77 (0.07)	6.82 (0.04)	
J120329.36+271548.1	DA	28.2	47,727 (1268)	7.51 (0.10)	Pure H	0.49 (0.03)	0.0203 (0.0017)	0.28 (0.09)	5.91 (0.45)	
J120351.02+631528.6	DA	23.1	31,542 (331)	7.61 (0.08)	Pure H	0.47 (0.03)	0.0178 (0.0010)	−0.55 (0.05)	6.78 (0.06)	
J120408.53+031324.6	DA+M	20.9	39,586 (1063)	7.41 (0.13)	Pure H	0.43 (0.04)	0.0214 (0.0021)	0.01 (0.10)	5.90 (0.55)	1
J120416.39−010924.9	DA	28.3	32,350 (278)	7.59 (0.06)	Pure H	0.47 (0.02)	0.0181 (0.0008)	−0.49 (0.04)	6.73 (0.06)	
J120525.01+303444.7	DA	79.0	30,015 (73)	7.81 (0.02)	Pure H	0.55 (0.01)	0.0153 (0.0002)	−0.77 (0.01)	6.94 (0.01)	
J120547.96+071259.6	DA	81.9	47,760 (500)	7.50 (0.04)	Pure H	0.48 (0.01)	0.0205 (0.0007)	0.29 (0.04)	5.84 (0.22)	5
J120649.27+210148.5	DA	51.4	35,885 (234)	7.77 (0.04)	Pure H	0.55 (0.02)	0.0159 (0.0004)	−0.42 (0.03)	6.70 (0.01)	
J120719.77+452305.5	DA	77.4	72,957 (1756)	7.43 (0.06)	Pure H	0.53 (0.02)	0.0232 (0.0012)	1.14 (0.06)	<5.00	5
J120738.03+134427.1	DA	5.0	36,816 (3032)	7.81 (0.44)	Pure H	0.57 (0.20)	0.0156 (0.0054)	−0.40 (0.33)	6.67 (0.22)	
J120803.24+625815.4	DA	5.9	68,693 (14,358)	7.08 (0.61)	Pure H	0.43 (0.16)	0.0312 (0.0172)	1.29 (0.62)	<5.00	
J120806.33+084641.8	DA	22.8	35,366 (591)	7.69 (0.10)	Pure H	0.51 (0.04)	0.0169 (0.0013)	−0.39 (0.07)	6.68 (0.06)	

Table 2.1 – Atmospheric and stellar parameters of hot white dwarfs from SDSS DR12 (continued)

SDSS Name	Type	S/N	$T_{\rm eff}$ (K)	$\log g$	Composition	$M/M_{\odot}$	$R/R_{\odot}$	$\log L/L_{\odot}$	$\log \tau_{\rm cool}$	Notes
J120924.26+095256.5	DA	57.3	42,415 (433)	7.68 (0.04)	Pure H	0.53 (0.02)	0.0174 (0.0006)	−0.05 (0.04)	6.45 (0.04)	
J120927.93−030206.2	DAO	40.0	73,225 (4132)	7.10 (0.14)	$\log N_{\rm He}/N_{\rm H} = -2.16$	0.45 (0.03)	0.0313 (0.0041)	1.40 (0.16)	<5.00	4,5
J121014.95+193310.4	DA	9.7	30,421 (566)	7.71 (0.14)	Pure H	0.51 (0.06)	0.0165 (0.0018)	−0.68 (0.10)	6.89 (0.07)	
J121135.64+181040.1	DB	6.8	39,482 (2622)	8.33 (0.29)	Pure He	0.82 (0.17)	0.0103 (0.0023)	−0.64 (0.23)	6.62 (0.23)	
J121156.86+041113.8	DA	23.1	34,821 (457)	7.81 (0.08)	Pure H	0.56 (0.04)	0.0155 (0.0009)	−0.50 (0.06)	6.74 (0.02)	
J121215.86+231550.3	DA	23.2	44,506 (1310)	7.57 (0.12)	Pure H	0.49 (0.04)	0.0191 (0.0019)	0.11 (0.10)	6.22 (0.33)	
J121229.82+505401.5	DA	44.7	55,489 (1293)	7.57 (0.08)	Pure H	0.53 (0.03)	0.0198 (0.0014)	0.53 (0.07)	5.96 (0.25)	
J121258.20−030713.8	DA	22.1	34,371 (419)	7.19 (0.08)	Pure H	0.35 (0.02)	0.0247 (0.0013)	−0.12 (0.05)	5.17 (0.35)	
J121405.11+453818.5	DA	32.5	34,294 (341)	7.81 (0.06)	Pure H	0.56 (0.03)	0.0155 (0.0007)	−0.53 (0.04)	6.76 (0.02)	
J121637.85+380914.6	DA	20.2	36,647 (845)	6.97 (0.13)	Pure H	0.29 (0.03)	0.0293 (0.0029)	0.14 (0.10)	<5.00	
J121731.42+610521.1	DA	33.7	39,871 (590)	7.68 (0.07)	Pure H	0.52 (0.03)	0.0172 (0.0009)	−0.17 (0.05)	6.53 (0.06)	
J121743.13+623118.2	DAO	74.4	84,010 (5597)	6.95 (0.11)	$\log N_{\rm He}/N_{\rm H} = -0.92$	0.45 (0.03)	0.0373 (0.0040)	1.79 (0.16)	<5.00	4,5
J121749.16+155446.8	DA	7.8	30,100 (628)	7.45 (0.17)	Pure H	0.41 (0.05)	0.0200 (0.0025)	−0.53 (0.12)	6.66 (0.39)	
J121756.19+021046.4	DA	51.8	65,633 (1696)	7.53 (0.08)	Pure H	0.54 (0.03)	0.0209 (0.0014)	0.86 (0.08)	5.60 (0.38)	5
J121813.58+461806.0	DB	28.4	42,599 (644)	7.72 (0.07)	Pure He	0.51 (0.03)	0.0163 (0.0009)	−0.10 (0.05)	6.47 (0.09)	
J121939.34+094956.4	DBA	38.7	30,517 (766)	7.77 (0.05)	$\log N_{\rm He}/N_{\rm H} = 3.51$	0.50 (0.02)	0.0153 (0.0006)	−0.73 (0.06)	6.93 (0.04)	4
J122105.33+492720.5	DA+M	60.2	35,487 (216)	7.87 (0.04)	Pure H	0.59 (0.02)	0.0148 (0.0004)	−0.50 (0.03)	6.72 (0.01)	1,2
J122111.37+112408.0	DA	47.9	53,206 (880)	7.66 (0.06)	Pure H	0.55 (0.02)	0.0181 (0.0009)	0.37 (0.05)	6.16 (0.05)	
J122154.02+545048.5	DA	29.7	44,016 (872)	7.68 (0.08)	Pure H	0.53 (0.03)	0.0174 (0.0011)	0.01 (0.07)	6.41 (0.07)	
J122218.55+584722.4	DA	48.8	63,585 (2546)	7.29 (0.12)	Pure H	0.46 (0.04)	0.0253 (0.0026)	0.97 (0.12)	<5.00	5
J122255.00+004046.9	DA	3.8	31,146 (1708)	7.98 (0.41)	Pure H	0.64 (0.21)	0.0136 (0.0043)	−0.81 (0.29)	6.90 (0.30)	
J122302.34+313842.2	DA	49.4	31,128 (131)	7.83 (0.03)	Pure H	0.56 (0.01)	0.0152 (0.0004)	−0.71 (0.02)	6.89 (0.01)	
J122303.63+103839.6	DA	55.6	35,313 (226)	7.83 (0.04)	Pure H	0.57 (0.02)	0.0152 (0.0004)	−0.49 (0.03)	6.73 (0.01)	
J122625.94+002700.2	DA	3.6	35,333 (3148)	8.74 (0.53)	Pure H	1.09 (0.26)	0.0074 (0.0035)	−1.12 (0.45)	7.68 (0.77)	
J122650.17+360426.4	DA	28.7	30,309 (197)	7.82 (0.05)	Pure H	0.56 (0.02)	0.0151 (0.0006)	−0.76 (0.03)	6.93 (0.01)	
J122722.84+021507.4	DA	39.6	31,724 (200)	8.09 (0.05)	Pure H	0.70 (0.03)	0.0125 (0.0004)	−0.84 (0.03)	6.89 (0.02)	
J123051.02+511208.5	DA	15.9	30,723 (443)	7.86 (0.11)	Pure H	0.57 (0.05)	0.0148 (0.0012)	−0.76 (0.08)	6.91 (0.03)	
J123117.87+112736.1	DA	26.3	30,348 (233)	7.83 (0.06)	Pure H	0.56 (0.03)	0.0151 (0.0007)	−0.76 (0.04)	6.93 (0.01)	
J123127.15+004133.0	DA+M	6.6	35,956 (2520)	7.21 (0.39)	Pure H	0.36 (0.11)	0.0244 (0.0074)	−0.05 (0.29)	5.12 (1.28)	1
J123151.81+613013.8	DA	25.2	31,928 (297)	7.79 (0.07)	Pure H	0.54 (0.03)	0.0156 (0.0008)	−0.64 (0.05)	6.85 (0.02)	
J123159.51+670918.9	DA	33.1	36,778 (716)	7.54 (0.10)	Pure H	0.46 (0.03)	0.0191 (0.0016)	−0.22 (0.08)	6.47 (0.21)	2
J123246.31+093348.7	DA	19.8	73,676 (7377)	7.30 (0.24)	Pure H	0.49 (0.07)	0.0258 (0.0057)	1.25 (0.27)	<5.00	5
J123459.31+131903.3	DA+M	36.6	32,368 (200)	7.77 (0.04)	Pure H	0.54 (0.02)	0.0158 (0.0005)	−0.61 (0.03)	6.83 (0.01)	1
J123516.33+233423.7	DA	63.5	48,282 (536)	7.68 (0.04)	Pure H	0.54 (0.02)	0.0177 (0.0006)	0.18 (0.04)	6.30 (0.03)	
J123519.06+575949.5	DA	21.3	48,252 (1826)	7.79 (0.15)	Pure H	0.59 (0.06)	0.0161 (0.0019)	0.10 (0.12)	6.34 (0.07)	
J123524.29−011547.4	DO	8.0	50,546 (3021)	7.43 (0.51)	Pure He	0.42 (0.17)	0.0205 (0.0080)	0.39 (0.35)	<5.00	
J123750.46+085526.0	DB	21.9	32,308 (856)	7.75 (0.09)	Pure He	0.50 (0.04)	0.0155 (0.0010)	−0.63 (0.07)	6.85 (0.06)	
J123827.81+312139.0	DA	29.8	57,420 (1855)	7.50 (0.11)	Pure H	0.51 (0.04)	0.0211 (0.0019)	0.64 (0.10)	5.64 (0.65)	
J123836.34−004042.2	DA+M	29.0	44,511 (976)	7.72 (0.09)	Pure H	0.55 (0.04)	0.0169 (0.0012)	0.00 (0.07)	6.42 (0.05)	1
J123846.72+170620.7	DA	40.3	31,475 (144)	7.78 (0.03)	Pure H	0.54 (0.02)	0.0156 (0.0004)	−0.66 (0.02)	6.87 (0.01)	
J123925.15+370957.2	DA	31.1	38,311 (599)	7.84 (0.08)	Pure H	0.59 (0.04)	0.0152 (0.0009)	−0.35 (0.06)	6.63 (0.02)	
J123928.35+133738.5	DA	31.6	34,940 (411)	7.26 (0.07)	Pure H	0.37 (0.02)	0.0236 (0.0012)	−0.12 (0.05)	5.45 (0.38)	
J124134.21+422126.9	DA	24.9	38,944 (734)	7.78 (0.09)	Pure H	0.56 (0.04)	0.0159 (0.0011)	−0.28 (0.07)	6.60 (0.03)	
J124253.38+162200.1	DA	29.3	35,963 (463)	7.73 (0.07)	Pure H	0.53 (0.03)	0.0164 (0.0009)	−0.39 (0.05)	6.68 (0.03)	
J124258.45+292405.5	DA	22.8	46,573 (1366)	7.69 (0.12)	Pure H	0.54 (0.04)	0.0175 (0.0016)	0.11 (0.10)	6.35 (0.11)	
J124331.37−063455.4	DB	9.7	30,235 (1969)	7.64 (0.23)	Pure He	0.45 (0.09)	0.0167 (0.0029)	−0.68 (0.19)	6.87 (0.29)	
J124407.66+582351.8	DA	38.1	31,607 (175)	7.98 (0.04)	Pure H	0.64 (0.02)	0.0136 (0.0004)	−0.78 (0.03)	6.88 (0.01)	
J124420.56+070057.2	DA	45.7	46,714 (747)	7.65 (0.06)	Pure H	0.53 (0.02)	0.0180 (0.0009)	0.14 (0.05)	6.31 (0.08)	
J124427.44+630057.6	DA	17.4	36,450 (854)	7.69 (0.13)	Pure H	0.51 (0.05)	0.0170 (0.0017)	−0.34 (0.10)	6.64 (0.10)	
J124455.15+040220.4	DA	12.2	74,500 (8511)	7.67 (0.36)	Pure H	0.61 (0.13)	0.0188 (0.0060)	0.99 (0.35)	5.69 (0.47)	

Table 2.1 – Atmospheric and stellar parameters of hot white dwarfs from SDSS DR12 (continued)

SDSS Name	Type	S/N	$T_{\rm eff}$ (K)	$\log g$	Composition	$M/M_{\odot}$	$R/R_{\odot}$	$\log L/L_{\odot}$	$\log \tau_{\rm cool}$	Notes
J124506.94+601019.1	DAO	93.2	71,974 (1814)	7.17 (0.06)	$\log N_{\rm He}/N_{\rm H} = -3.01$	0.46 (0.01)	0.0290 (0.0017)	1.31 (0.07)	<5.00	4,5
J124518.94+303623.1	DA	6.8	38,905 (2654)	7.88 (0.33)	Pure H	0.60 (0.16)	0.0148 (0.0039)	−0.34 (0.25)	6.61 (0.17)	
J124553.58+222032.7	DA	43.4	35,336 (279)	7.81 (0.05)	Pure H	0.56 (0.02)	0.0155 (0.0005)	−0.47 (0.03)	6.72 (0.01)	
J124601.73+155922.3	DA	6.8	30,931 (842)	8.03 (0.21)	Pure H	0.66 (0.11)	0.0131 (0.0020)	−0.85 (0.14)	6.92 (0.09)	7
J124741.84−081041.9	DA	24.1	39,862 (865)	7.71 (0.10)	Pure H	0.53 (0.04)	0.0169 (0.0013)	−0.19 (0.08)	6.55 (0.07)	
J124902.39+391028.9	DA	27.2	35,815 (503)	7.71 (0.08)	Pure H	0.52 (0.03)	0.0167 (0.0010)	−0.38 (0.06)	6.68 (0.05)	
J124906.90+432543.0	DA	30.1	37,403 (490)	8.26 (0.07)	Pure H	0.81 (0.04)	0.0111 (0.0006)	−0.66 (0.05)	6.66 (0.03)	
J124915.21+062052.7	DA	50.7	40,041 (424)	7.70 (0.05)	Pure H	0.53 (0.02)	0.0171 (0.0007)	−0.17 (0.04)	6.53 (0.03)	
J124959.76+035726.5	DAO+M	26.2	53,842 (8265)	7.28 (0.56)	$\log N_{\rm He}/N_{\rm H} = -3.22$	0.42 (0.16)	0.0246 (0.0117)	0.66 (0.49)	<5.00	1,2,4
J125029.50+505317.3	DAO	25.8	72,330 (8957)	6.68 (0.24)	$\log N_{\rm He}/N_{\rm H} = -1.27$	0.35 (0.06)	0.0451 (0.0094)	1.70 (0.31)	<5.00	4,5
J125206.13+181921.1	DA	7.0	32,480 (1329)	7.77 (0.28)	Pure H	0.54 (0.12)	0.0158 (0.0034)	−0.60 (0.20)	6.82 (0.12)	
J125232.05+423210.8	DA	30.0	37,562 (555)	7.83 (0.08)	Pure H	0.58 (0.03)	0.0153 (0.0009)	−0.38 (0.06)	6.65 (0.02)	
J125240.05+230456.7	DA	5.7	35,568 (1921)	8.19 (0.31)	Pure H	0.76 (0.18)	0.0116 (0.0028)	−0.71 (0.23)	6.73 (0.17)	
J125309.62+634242.4	DA	19.5	30,370 (279)	7.87 (0.07)	Pure H	0.58 (0.04)	0.0146 (0.0008)	−0.79 (0.05)	6.93 (0.02)	
J125400.29+581948.0	DA	40.3	35,727 (301)	7.79 (0.05)	Pure H	0.55 (0.02)	0.0158 (0.0006)	−0.44 (0.03)	6.71 (0.01)	
J125612.69+362235.8	DA	54.9	34,963 (223)	7.83 (0.04)	Pure H	0.57 (0.02)	0.0152 (0.0004)	−0.51 (0.03)	6.74 (0.01)	
J125715.80+311127.5	DA	22.5	33,187 (357)	7.74 (0.07)	Pure H	0.53 (0.03)	0.0162 (0.0009)	−0.54 (0.05)	6.79 (0.03)	
J125721.06+192451.7	DA	56.5	45,654 (565)	7.66 (0.05)	Pure H	0.53 (0.02)	0.0178 (0.0007)	0.09 (0.04)	6.35 (0.05)	
J125724.04+422054.2	DA	45.0	42,180 (597)	7.65 (0.06)	Pure H	0.52 (0.02)	0.0177 (0.0009)	−0.05 (0.05)	6.44 (0.07)	5
J125730.31−001150.9	DA	22.0	30,327 (316)	7.59 (0.08)	Pure H	0.46 (0.03)	0.0180 (0.0011)	−0.61 (0.06)	6.82 (0.07)	
J125740.04+130514.3	DA+M	21.3	43,653 (1210)	7.54 (0.12)	Pure H	0.48 (0.04)	0.0195 (0.0018)	0.09 (0.10)	6.17 (0.35)	1
J125921.51+192111.5	DA	8.8	37,903 (2248)	7.81 (0.30)	Pure H	0.57 (0.13)	0.0155 (0.0036)	−0.35 (0.23)	6.64 (0.16)	
J125938.06+603859.9	DA	78.3	37,233 (243)	7.82 (0.03)	Pure H	0.57 (0.02)	0.0154 (0.0004)	−0.39 (0.03)	6.66 (0.01)	
J125943.99+680400.9	DA	60.6	31,134 (111)	7.87 (0.03)	Pure H	0.58 (0.01)	0.0146 (0.0003)	−0.74 (0.02)	6.89 (0.01)	
J125944.00+572345.2	DO	69.8	54,185 (382)	8.13 (0.06)	Pure He	0.72 (0.03)	0.0121 (0.0006)	0.06 (0.04)	6.23 (0.03)	
J125952.17−014529.1	DA	4.6	35,528 (2573)	7.80 (0.42)	Pure H	0.56 (0.19)	0.0156 (0.0051)	−0.46 (0.31)	6.72 (0.20)	
J130033.82+661600.6	DA	78.1	33,232 (113)	7.82 (0.02)	Pure H	0.56 (0.01)	0.0153 (0.0003)	−0.59 (0.02)	6.80 (0.01)	
J130052.12+192931.6	DA	81.4	45,453 (398)	7.65 (0.04)	Pure H	0.52 (0.01)	0.0180 (0.0006)	0.09 (0.03)	6.34 (0.05)	5
J130234.43+101238.9	DA	56.4	40,440 (409)	7.92 (0.05)	Pure H	0.63 (0.02)	0.0144 (0.0005)	−0.30 (0.04)	6.55 (0.01)	
J130249.00−013309.5	DO	9.4	48,888 (840)	8.23 (0.34)	Pure He	0.77 (0.19)	0.0112 (0.0030)	−0.19 (0.24)	6.32 (0.04)	
J130332.01+541224.3	DA	95.1	34,942 (157)	8.10 (0.03)	Pure H	0.71 (0.02)	0.0124 (0.0003)	−0.68 (0.02)	6.74 (0.01)	
J130500.23+074225.2	DA	14.5	37,336 (1199)	7.74 (0.17)	Pure H	0.54 (0.07)	0.0164 (0.0021)	−0.33 (0.13)	6.64 (0.08)	
J130608.49+012838.0	DA+M	16.9	30,701 (426)	7.17 (0.11)	Pure H	0.33 (0.03)	0.0248 (0.0019)	−0.31 (0.07)	5.40 (0.45)	1
J130645.85+485628.8	DA	32.3	70,616 (3252)	7.22 (0.14)	Pure H	0.46 (0.03)	0.0277 (0.0035)	1.24 (0.14)	<5.00	
J130717.27+004151.6	DOZ	30.0	87,820 (9575)	7.85 (0.34)	Pure He	0.65 (0.13)	0.0158 (0.0047)	1.13 (0.32)	5.65 (0.37)	6
J130740.47+021523.9	DA	24.0	77,714 (4477)	7.13 (0.15)	Pure H	0.47 (0.03)	0.0308 (0.0044)	1.50 (0.17)	<5.00	
J130814.29+060221.5	DA	16.4	30,559 (353)	7.85 (0.09)	Pure H	0.57 (0.04)	0.0149 (0.0010)	−0.76 (0.06)	6.92 (0.02)	
J130815.21−015904.3	DAB	64.8	42,049 (698)	7.90 (0.06)	$\log q_{\rm H} = -16.26$	0.58 (0.03)	0.0142 (0.0007)	−0.24 (0.05)	6.56 (0.02)	3
J130846.75+493000.7	DA	43.0	31,880 (171)	7.79 (0.04)	Pure H	0.55 (0.02)	0.0155 (0.0004)	−0.65 (0.03)	6.85 (0.01)	
J131033.24+644032.8	DA	24.8	40,499 (883)	6.94 (0.10)	Pure H	0.30 (0.02)	0.0307 (0.0025)	0.36 (0.08)	<5.00	
J131033.51+533032.4	DA+M	21.7	38,304 (939)	7.72 (0.12)	Pure H	0.53 (0.05)	0.0167 (0.0016)	−0.27 (0.09)	6.60 (0.08)	1
J131142.79+391550.8	DA	49.0	35,547 (267)	7.80 (0.04)	Pure H	0.56 (0.02)	0.0156 (0.0005)	−0.46 (0.03)	6.72 (0.01)	
J131336.49+025237.0	DA	6.9	35,828 (1337)	8.02 (0.21)	Pure H	0.67 (0.11)	0.0132 (0.0021)	−0.59 (0.15)	6.70 (0.05)	
J131351.70+051054.4	DB	28.1	32,611 (734)	7.82 (0.08)	Pure He	0.53 (0.03)	0.0148 (0.0008)	−0.65 (0.06)	6.86 (0.04)	
J131445.05−031415.5	DA	18.0	45,991 (1934)	7.79 (0.17)	Pure H	0.58 (0.07)	0.0161 (0.0021)	0.02 (0.14)	6.40 (0.08)	
J131511.88+121512.3	DA	17.4	53,734 (3141)	7.61 (0.21)	Pure H	0.53 (0.07)	0.0190 (0.0033)	0.43 (0.18)	6.09 (0.29)	
J131557.48+100424.8	DA	33.7	40,433 (686)	7.92 (0.08)	Pure H	0.63 (0.04)	0.0144 (0.0009)	−0.30 (0.06)	6.56 (0.02)	
J131615.27−013436.1	DA	18.7	30,335 (372)	7.87 (0.10)	Pure H	0.58 (0.05)	0.0146 (0.0010)	−0.79 (0.07)	6.93 (0.02)	
J131619.24+055238.6	DA	34.1	31,672 (217)	7.96 (0.05)	Pure H	0.63 (0.03)	0.0138 (0.0005)	−0.76 (0.03)	6.87 (0.01)	
J131724.75+000237.3	DOZ	106.3	63,073 (749)	8.05 (0.08)	Pure He	0.69 (0.04)	0.0130 (0.0008)	0.38 (0.06)	6.08 (0.02)	6,8

Table 2.1 – Atmospheric and stellar parameters of hot white dwarfs from SDSS DR12 (continued)

SDSS Name	Type	S/N	$T_{\rm eff}$ (K)	$\log g$	Composition	$M/M_{\odot}$	$R/R_{\odot}$	$\log L/L_{\odot}$	$\log \tau_{\rm cool}$	Notes
J131739.30+523943.9	DA	3.8	30,062 (1308)	8.17 (0.35)	Pure H	0.75 (0.20)	0.0117 (0.0031)	−1.00 (0.24)	7.05 (0.30)	
J131751.70+673159.2	DA+M	56.1	79,476 (9756)	6.99 (0.29)	Pure H	0.44 (0.07)	0.0354 (0.0097)	1.65 (0.34)	<5.00	1,2
J131837.45+042806.5	DA	16.7	59,986 (4893)	7.21 (0.27)	Pure H	0.42 (0.07)	0.0266 (0.0061)	0.92 (0.25)	<5.00	
J131925.47+231304.0	DA	34.9	39,910 (638)	7.64 (0.07)	Pure H	0.50 (0.03)	0.0179 (0.0011)	−0.14 (0.06)	6.48 (0.09)	
J131937.73+595257.1	DA	35.7	71,234 (2587)	7.24 (0.11)	Pure H	0.47 (0.02)	0.0272 (0.0027)	1.24 (0.11)	<5.00	
J132010.47+340249.9	DA	35.5	32,567 (220)	7.90 (0.05)	Pure H	0.60 (0.02)	0.0144 (0.0005)	−0.68 (0.03)	6.83 (0.01)	
J132018.32+632416.9	DA	10.6	62,980 (6975)	7.03 (0.34)	Pure H	0.39 (0.08)	0.0318 (0.0094)	1.16 (0.33)	<5.00	
J132308.62+055900.9	DA	20.9	38,685 (965)	7.48 (0.12)	Pure H	0.45 (0.04)	0.0203 (0.0020)	−0.08 (0.10)	6.20 (0.39)	2
J132419.77+254931.6	DA	29.4	30,304 (210)	7.91 (0.05)	Pure H	0.60 (0.03)	0.0142 (0.0006)	−0.81 (0.04)	6.93 (0.01)	
J132436.24+185721.3	DA	27.1	30,068 (193)	7.91 (0.05)	Pure H	0.60 (0.03)	0.0142 (0.0005)	−0.83 (0.03)	6.95 (0.01)	
J132441.13+135330.7	DA	31.4	67,202 (2596)	7.16 (0.12)	Pure H	0.44 (0.03)	0.0289 (0.0030)	1.19 (0.12)	<5.00	
J132546.98+100218.8	DA	45.0	42,375 (612)	7.72 (0.06)	Pure H	0.54 (0.02)	0.0169 (0.0008)	−0.08 (0.05)	6.48 (0.04)	
J132619.23+041701.9	DA	17.4	51,208 (3016)	7.67 (0.22)	Pure H	0.55 (0.08)	0.0179 (0.0032)	0.30 (0.19)	6.21 (0.20)	
J132629.58+571131.5	DAO	15.3	91,677 (20,574)	6.60 (0.37)	$\log N_{\rm He}/N_{\rm H} = -1.79$	0.41 (0.11)	0.0529 (0.0184)	2.25 (0.56)	<5.00	4
J132724.68+590402.9	DA	13.4	31,752 (572)	7.78 (0.13)	Pure H	0.54 (0.06)	0.0157 (0.0015)	−0.65 (0.09)	6.86 (0.04)	
J132725.72+505711.0	DA+M	26.6	44,287 (1210)	7.58 (0.11)	Pure H	0.50 (0.04)	0.0189 (0.0017)	0.09 (0.09)	6.25 (0.28)	1
J132732.30+611556.8	DA+M	29.1	74,462 (4036)	7.01 (0.14)	Pure H	0.43 (0.03)	0.0340 (0.0044)	1.51 (0.16)	<5.00	1
J132752.90+253145.0	DB	19.5	40,001 (892)	7.88 (0.12)	Pure He	0.57 (0.06)	0.0143 (0.0013)	−0.32 (0.09)	6.62 (0.04)	
J132924.03+140458.0	DA	30.9	30,748 (202)	7.89 (0.05)	Pure H	0.59 (0.03)	0.0144 (0.0005)	−0.78 (0.03)	6.91 (0.01)	
J132926.96+562425.5	DA	19.2	30,846 (389)	7.84 (0.10)	Pure H	0.57 (0.05)	0.0149 (0.0011)	−0.74 (0.07)	6.90 (0.02)	
J132936.59+155716.7	DA	27.1	53,767 (1618)	7.71 (0.11)	Pure H	0.57 (0.04)	0.0175 (0.0016)	0.36 (0.10)	6.17 (0.08)	
J132959.71+462828.0	DA	5.6	33,206 (1567)	7.33 (0.31)	Pure H	0.39 (0.10)	0.0224 (0.0052)	−0.26 (0.22)	5.96 (1.04)	
J133039.51+152305.9	DA	19.3	31,078 (378)	7.82 (0.09)	Pure H	0.56 (0.04)	0.0152 (0.0010)	−0.71 (0.06)	6.89 (0.02)	
J133136.97+001127.4	DA	23.8	34,568 (455)	7.87 (0.08)	Pure H	0.59 (0.04)	0.0148 (0.0009)	−0.55 (0.06)	6.75 (0.02)	
J133137.06+010632.3	DA	46.1	35,940 (272)	7.79 (0.04)	Pure H	0.55 (0.02)	0.0158 (0.0005)	−0.43 (0.03)	6.70 (0.01)	
J133137.57+184354.3	DA	61.7	34,009 (162)	7.83 (0.03)	Pure H	0.57 (0.01)	0.0152 (0.0003)	−0.56 (0.02)	6.77 (0.01)	
J133154.10+354503.9	DA	66.6	35,962 (185)	7.87 (0.03)	Pure H	0.59 (0.01)	0.0148 (0.0003)	−0.48 (0.02)	6.70 (0.01)	
J133154.15+004119.4	DA	41.2	36,162 (389)	7.71 (0.06)	Pure H	0.52 (0.02)	0.0167 (0.0008)	−0.37 (0.04)	6.67 (0.03)	
J133303.87+624655.4	DA	29.2	39,099 (591)	7.74 (0.07)	Pure H	0.54 (0.03)	0.0164 (0.0009)	−0.25 (0.06)	6.59 (0.03)	
J133514.53+505012.4	DA	62.8	37,855 (263)	7.81 (0.04)	Pure H	0.57 (0.02)	0.0156 (0.0004)	−0.35 (0.03)	6.64 (0.01)	
J133545.03+530048.8	DA	27.3	50,669 (1212)	7.72 (0.09)	Pure H	0.56 (0.03)	0.0171 (0.0012)	0.24 (0.08)	6.26 (0.06)	
J133549.64+033048.0	DA	17.3	32,145 (539)	7.66 (0.12)	Pure H	0.49 (0.05)	0.0172 (0.0015)	−0.55 (0.08)	6.79 (0.08)	
J133554.30+260949.5	DA	30.3	30,697 (214)	7.29 (0.05)	Pure H	0.37 (0.02)	0.0228 (0.0009)	−0.38 (0.04)	5.97 (0.27)	
J133608.11+602505.1	DA	22.0	31,096 (333)	7.85 (0.08)	Pure H	0.57 (0.04)	0.0148 (0.0009)	−0.73 (0.06)	6.89 (0.02)	
J133620.79+352325.0	DA	62.6	67,557 (1305)	7.27 (0.06)	Pure H	0.47 (0.01)	0.0262 (0.0014)	1.11 (0.06)	<5.00	
J133633.21−013116.5	DO+M	19.8	52,116 (1839)	8.02 (0.19)	Pure He	0.66 (0.10)	0.0131 (0.0019)	0.06 (0.14)	6.30 (0.06)	1
J133739.64+455833.3	DA	34.8	30,748 (175)	7.76 (0.04)	Pure H	0.53 (0.02)	0.0159 (0.0005)	−0.69 (0.03)	6.89 (0.01)	
J133824.20−021454.2	DA	10.7	32,180 (867)	7.10 (0.19)	Pure H	0.31 (0.05)	0.0261 (0.0036)	−0.18 (0.13)	5.01 (0.70)	
J133824.20+115430.3	DA	61.3	36,052 (251)	7.80 (0.04)	Pure H	0.56 (0.02)	0.0156 (0.0005)	−0.43 (0.03)	6.70 (0.01)	
J133830.53+153502.9	DA	5.2	58,629 (14,515)	6.81 (0.77)	Pure H	0.33 (0.20)	0.0374 (0.0211)	1.17 (0.71)	<5.00	
J133929.64+082024.8	DA	7.6	30,503 (908)	7.64 (0.23)	Pure H	0.48 (0.09)	0.0173 (0.0030)	−0.63 (0.16)	6.85 (0.16)	
J134017.70+594552.5	DA	19.7	34,720 (647)	7.17 (0.11)	Pure H	0.34 (0.03)	0.0251 (0.0020)	−0.08 (0.08)	5.04 (0.48)	
J134100.03+602610.4	DA+M	61.5	43,514 (622)	7.63 (0.06)	Pure H	0.51 (0.02)	0.0181 (0.0009)	0.02 (0.05)	6.38 (0.09)	1,2
J134101.66+210616.9	DAO	17.1	73,424 (6989)	7.04 (0.30)	$\log N_{\rm He}/N_{\rm H} = -2.32$	0.44 (0.07)	0.0329 (0.0089)	1.45 (0.30)	<5.00	4
J134120.09+092918.2	DAO	57.9	93,680 (4241)	6.87 (0.13)	$\log N_{\rm He}/N_{\rm H} = -1.70$	0.47 (0.03)	0.0416 (0.0053)	2.08 (0.14)	<5.00	4,5
J134131.47+045446.7	DAO	100.9	69,099 (2415)	6.68 (0.07)	$\log N_{\rm He}/N_{\rm H} = -1.23$	0.34 (0.02)	0.0441 (0.0027)	1.60 (0.09)	<5.00	4,5
J134135.22+612128.5	DB+M	9.4	33,969 (2795)	7.83 (0.29)	Pure He	0.54 (0.14)	0.0148 (0.0032)	−0.58 (0.24)	6.81 (0.22)	1
J134422.63+271009.7	DA	53.7	30,724 (132)	7.31 (0.03)	Pure H	0.37 (0.01)	0.0224 (0.0006)	−0.39 (0.02)	6.07 (0.17)	
J134426.84+440833.2	DA	71.2	76,759 (1671)	7.73 (0.07)	Pure H	0.63 (0.02)	0.0179 (0.0011)	1.00 (0.07)	5.70 (0.06)	
J134509.49−005731.3	DA	50.1	38,770 (383)	7.78 (0.05)	Pure H	0.56 (0.02)	0.0159 (0.0006)	−0.29 (0.04)	6.61 (0.02)	

Table 2.1 – Atmospheric and stellar parameters of hot white dwarfs from SDSS DR12 (continued)

SDSS Name	Type	S/N	$T_{\rm eff}$ (K)	$\log g$	Composition	$M/M_{\odot}$	$R/R_{\odot}$	$\log L/L_{\odot}$	$\log \tau_{\rm cool}$	Notes
J134515.39+000837.8	DA+M	25.6	51,890 (1749)	7.71 (0.12)	Pure H	0.56 (0.05)	0.0174 (0.0018)	0.30 (0.11)	6.22 (0.10)	1
J134559.13+074854.1	DA	25.6	45,275 (1359)	7.53 (0.12)	Pure H	0.48 (0.04)	0.0198 (0.0019)	0.17 (0.10)	6.07 (0.43)	
J134604.41+494957.3	DA	23.1	32,281 (414)	7.40 (0.09)	Pure H	0.40 (0.03)	0.0211 (0.0015)	−0.36 (0.06)	6.35 (0.32)	
J134820.41−011224.7	DA	25.4	31,191 (277)	7.36 (0.07)	Pure H	0.39 (0.02)	0.0216 (0.0011)	−0.40 (0.05)	6.28 (0.28)	
J134839.80+660511.3	DA	23.5	61,407 (3450)	7.72 (0.19)	Pure H	0.59 (0.07)	0.0175 (0.0029)	0.59 (0.18)	6.02 (0.16)	
J134853.50+505428.1	DA	35.7	45,592 (852)	7.78 (0.08)	Pure H	0.58 (0.03)	0.0162 (0.0010)	0.01 (0.06)	6.41 (0.03)	
J134920.67+273508.3	DA	64.0	30,273 (87)	7.84 (0.02)	Pure H	0.57 (0.01)	0.0150 (0.0003)	−0.77 (0.02)	6.93 (0.01)	
J135105.31+144004.1	DA	18.6	31,964 (418)	7.20 (0.09)	Pure H	0.34 (0.03)	0.0244 (0.0016)	−0.25 (0.06)	5.40 (0.43)	
J135149.27+452756.1	DA	16.0	35,951 (845)	7.86 (0.13)	Pure H	0.59 (0.06)	0.0149 (0.0015)	−0.47 (0.10)	6.70 (0.03)	
J135155.65+075458.0	DA	36.6	48,167 (1008)	7.52 (0.08)	Pure H	0.49 (0.03)	0.0202 (0.0013)	0.30 (0.07)	5.93 (0.35)	
J135228.13+091039.0	DA	27.1	35,276 (558)	7.39 (0.09)	Pure H	0.41 (0.03)	0.0215 (0.0015)	−0.19 (0.07)	6.09 (0.39)	2
J135342.67+255201.7	DA	36.1	30,757 (196)	7.82 (0.05)	Pure H	0.56 (0.02)	0.0152 (0.0005)	−0.73 (0.03)	6.90 (0.01)	
J135356.88−025630.3	DAO	51.0	50,762 (1037)	7.82 (0.08)	$\log N_{\rm He}/N_{\rm H} = -1.87$	0.60 (0.03)	0.0159 (0.0010)	0.18 (0.07)	6.28 (0.03)	4
J135406.24+075747.9	DA	30.0	39,351 (620)	7.82 (0.08)	Pure H	0.58 (0.03)	0.0155 (0.0009)	−0.29 (0.06)	6.59 (0.02)	
J135423.07+114010.1	DA	16.4	37,826 (1033)	7.72 (0.14)	Pure H	0.53 (0.06)	0.0167 (0.0018)	−0.29 (0.11)	6.61 (0.09)	
J135442.14+215519.6	DA	8.9	51,282 (5553)	7.27 (0.39)	Pure H	0.41 (0.11)	0.0246 (0.0080)	0.58 (0.34)	<5.00	
J135446.88+083930.3	DA	30.3	64,859 (2477)	7.41 (0.12)	Pure H	0.50 (0.04)	0.0230 (0.0024)	0.93 (0.11)	<5.00	
J135523.91+085645.3	DA	33.9	33,504 (284)	7.33 (0.05)	Pure H	0.39 (0.02)	0.0223 (0.0009)	−0.25 (0.04)	5.96 (0.28)	
J135525.20+221632.1	DA	18.2	31,650 (412)	7.99 (0.09)	Pure H	0.64 (0.05)	0.0134 (0.0009)	−0.79 (0.07)	6.88 (0.02)	
J135539.47+262928.0	DA	28.7	35,392 (412)	7.81 (0.07)	Pure H	0.56 (0.03)	0.0155 (0.0008)	−0.47 (0.05)	6.72 (0.02)	
J135654.77+343617.2	DA	6.9	36,678 (2050)	7.89 (0.30)	Pure H	0.61 (0.15)	0.0146 (0.0034)	−0.46 (0.22)	6.68 (0.11)	
J135717.44+081548.5	DA	17.9	31,651 (419)	8.67 (0.10)	Pure H	1.04 (0.05)	0.0078 (0.0007)	−1.26 (0.08)	7.79 (0.13)	
J135734.72+280111.1	DA	59.7	31,454 (111)	7.89 (0.03)	Pure H	0.59 (0.01)	0.0144 (0.0003)	−0.74 (0.02)	6.88 (0.01)	
J135852.89+474757.3	DA	28.6	34,456 (485)	7.76 (0.09)	Pure H	0.54 (0.04)	0.0160 (0.0010)	−0.49 (0.06)	6.75 (0.03)	
J135902.13+520926.0	DA	12.2	41,207 (2115)	7.63 (0.23)	Pure H	0.50 (0.08)	0.0181 (0.0033)	−0.07 (0.18)	6.43 (0.25)	
J135948.12+182452.0	DA	16.4	33,606 (630)	8.36 (0.12)	Pure H	0.86 (0.07)	0.0102 (0.0010)	−0.93 (0.09)	7.02 (0.23)	
J140008.88+145247.1	DA	61.2	34,846 (215)	7.97 (0.04)	Pure H	0.64 (0.02)	0.0137 (0.0004)	−0.60 (0.03)	6.74 (0.01)	
J140015.81−025830.5	DA+M	31.1	39,288 (739)	7.90 (0.09)	Pure H	0.61 (0.04)	0.0146 (0.0010)	−0.34 (0.07)	6.59 (0.02)	1
J140028.43+475644.0	DB	61.3	31,971 (323)	8.00 (0.03)	Pure He	0.62 (0.02)	0.0130 (0.0003)	−0.80 (0.03)	6.91 (0.01)	
J140034.78+161451.9	DA+M	14.6	53,009 (3629)	7.50 (0.24)	Pure H	0.50 (0.08)	0.0207 (0.0041)	0.48 (0.21)	5.76 (0.92)	1
J140115.23+183334.8	DA	24.9	33,656 (409)	7.32 (0.08)	Pure H	0.38 (0.02)	0.0225 (0.0013)	−0.23 (0.06)	5.89 (0.39)	
J140122.45+024024.9	DAO	31.1	60,660 (3331)	7.70 (0.17)	$\log N_{\rm He}/N_{\rm H} = -3.02$	0.58 (0.06)	0.0179 (0.0026)	0.59 (0.16)	6.02 (0.16)	4,5
J140159.08+022126.8	DBA	18.1	35,898 (3429)	7.99 (0.23)	$\log N_{\rm He}/N_{\rm H} = 1.60$	0.62 (0.12)	0.0132 (0.0022)	−0.58 (0.23)	6.75 (0.13)	4
J140247.53+493321.3	DAO	22.7	67,403 (5102)	6.90 (0.22)	$\log N_{\rm He}/N_{\rm H} = -1.85$	0.38 (0.05)	0.0364 (0.0071)	1.39 (0.23)	<5.00	4
J140327.75+002119.5	DA	68.8	58,770 (1150)	7.54 (0.06)	Pure H	0.53 (0.02)	0.0204 (0.0011)	0.65 (0.06)	5.80 (0.23)	5
J140350.78+321859.8	DA	45.8	34,201 (210)	7.82 (0.04)	Pure H	0.56 (0.02)	0.0153 (0.0004)	−0.54 (0.03)	6.77 (0.01)	
J140409.95+045740.0	DOZ	46.8	73,689 (2119)	8.00 (0.15)	Pure He	0.68 (0.07)	0.0137 (0.0017)	0.70 (0.12)	5.91 (0.05)	6
J140611.25+662806.4	DA	28.4	34,141 (401)	7.67 (0.07)	Pure H	0.50 (0.03)	0.0172 (0.0010)	−0.44 (0.05)	6.72 (0.05)	
J140615.81+562725.9	DBA	16.2	40,644 (2576)	7.86 (0.25)	$\log q_{\rm H} = -16.98$	0.56 (0.12)	0.0146 (0.0028)	−0.28 (0.20)	6.60 (0.17)	3
J140623.02+273103.3	DA	39.7	33,913 (278)	7.80 (0.05)	Pure H	0.56 (0.02)	0.0155 (0.0006)	−0.54 (0.04)	6.77 (0.01)	
J140704.33+634944.6	DA	27.5	30,573 (289)	7.58 (0.07)	Pure H	0.46 (0.03)	0.0181 (0.0010)	−0.59 (0.05)	6.80 (0.06)	
J140705.79+054259.0	DA	34.1	33,857 (352)	7.40 (0.07)	Pure H	0.41 (0.02)	0.0212 (0.0011)	−0.27 (0.05)	6.24 (0.25)	
J140706.04+022053.9	DA	28.0	34,594 (413)	7.79 (0.07)	Pure H	0.55 (0.03)	0.0156 (0.0009)	−0.50 (0.05)	6.75 (0.02)	
J140807.44+005423.8	DA	4.7	31,202 (1579)	7.88 (0.38)	Pure H	0.59 (0.18)	0.0146 (0.0042)	−0.74 (0.26)	6.89 (0.20)	
J140857.37+415213.8	DA	50.3	30,897 (148)	7.54 (0.04)	Pure H	0.45 (0.01)	0.0187 (0.0005)	−0.54 (0.03)	6.75 (0.04)	
J140919.84+000854.0	DOZ	21.3	78,506 (6931)	8.05 (0.39)	Pure He	0.72 (0.18)	0.0132 (0.0044)	0.77 (0.33)	5.81 (0.18)	6
J141028.66−020048.1	DA	37.9	42,191 (751)	7.75 (0.08)	Pure H	0.55 (0.03)	0.0165 (0.0010)	−0.11 (0.06)	6.49 (0.04)	
J141035.47+080254.7	DA	18.1	34,279 (652)	7.50 (0.12)	Pure H	0.44 (0.04)	0.0195 (0.0018)	−0.32 (0.09)	6.51 (0.26)	
J141057.73−020236.6	DA+M	24.9	31,408 (501)	7.63 (0.12)	Pure H	0.48 (0.04)	0.0175 (0.0016)	−0.57 (0.08)	6.80 (0.09)	1,2
J141127.11+035429.6	DB	50.4	37,462 (540)	7.72 (0.04)	Pure He	0.50 (0.02)	0.0161 (0.0005)	−0.34 (0.04)	6.63 (0.04)	

Table 2.1 – Atmospheric and stellar parameters of hot white dwarfs from SDSS DR12 (continued)

SDSS Name	Type	S/N	$T_{\rm eff}$ (K)	$\log g$	Composition	$M/M_{\odot}$	$R/R_{\odot}$	$\log L/L_{\odot}$	$\log \tau_{\rm cool}$	Notes
J141134.70+102839.7	DA+M	17.0	32,366 (834)	7.38 (0.18)	Pure H	0.40 (0.06)	0.0213 (0.0029)	−0.35 (0.13)	6.30 (0.65)	1,2
J141139.90+485553.1	DA	24.4	37,641 (700)	7.78 (0.10)	Pure H	0.56 (0.04)	0.0159 (0.0012)	−0.34 (0.07)	6.64 (0.03)	
J141227.74+140522.4	DA	6.9	68,134 (13,622)	8.02 (0.68)	Pure H	0.73 (0.30)	0.0138 (0.0085)	0.57 (0.63)	5.91 (0.64)	
J141229.64+590112.8	DA	71.1	45,540 (478)	7.72 (0.04)	Pure H	0.55 (0.02)	0.0170 (0.0006)	0.05 (0.03)	6.39 (0.02)	
J141231.52+264054.9	DA+M	16.2	30,800 (630)	7.81 (0.16)	Pure H	0.55 (0.07)	0.0153 (0.0018)	−0.72 (0.11)	6.90 (0.05)	1,2
J141258.17+045602.2	DB	33.2	31,272 (531)	7.92 (0.06)	Pure He	0.58 (0.03)	0.0138 (0.0006)	−0.79 (0.05)	6.93 (0.02)	
J141301.92+335654.7	DA	5.7	36,107 (2292)	8.15 (0.36)	Pure H	0.74 (0.20)	0.0120 (0.0033)	−0.66 (0.26)	6.70 (0.18)	
J141307.57+121537.4	DA	38.3	39,721 (590)	7.83 (0.07)	Pure H	0.58 (0.03)	0.0154 (0.0008)	−0.28 (0.05)	6.58 (0.02)	
J141317.77+542341.6	DA	37.4	56,896 (1537)	7.27 (0.09)	Pure H	0.43 (0.02)	0.0251 (0.0019)	0.77 (0.08)	<5.00	
J141349.47+571716.3	DB	27.9	30,172 (583)	7.89 (0.07)	Pure He	0.56 (0.04)	0.0140 (0.0007)	−0.83 (0.06)	6.98 (0.03)	
J141413.98+562434.6	DA	16.0	32,319 (534)	7.76 (0.12)	Pure H	0.53 (0.05)	0.0160 (0.0014)	−0.60 (0.08)	6.83 (0.04)	
J141420.07+175353.0	DA	14.4	41,922 (1558)	7.98 (0.16)	Pure H	0.66 (0.08)	0.0138 (0.0017)	−0.28 (0.13)	6.50 (0.05)	
J141536.41+011718.2	DAO	62.8	52,477 (1003)	7.69 (0.07)	$\log N_{\rm He}/N_{\rm H} = -3.11$	0.56 (0.03)	0.0176 (0.0011)	0.33 (0.06)	6.19 (0.05)	4
J141618.58+621538.3	DA	20.3	31,106 (387)	7.76 (0.09)	Pure H	0.53 (0.04)	0.0159 (0.0011)	−0.67 (0.06)	6.88 (0.03)	
J141621.78+322638.5	DB	34.9	35,011 (512)	7.81 (0.05)	Pure He	0.53 (0.02)	0.0150 (0.0006)	−0.52 (0.04)	6.77 (0.02)	
J141621.94+135224.2	DAO	31.4	73,498 (20,311)	7.07 (0.78)	$\log N_{\rm He}/N_{\rm H} = -0.35$	0.44 (0.21)	0.0320 (0.0229)	1.43 (0.81)	<5.00	2,4
J141639.31+510042.5	DA	31.8	46,049 (1087)	7.64 (0.09)	Pure H	0.52 (0.03)	0.0182 (0.0014)	0.13 (0.08)	6.32 (0.14)	
J141646.01+345050.1	DA+M	39.5	64,517 (2220)	7.20 (0.11)	Pure H	0.44 (0.03)	0.0274 (0.0026)	1.07 (0.11)	<5.00	1
J141708.06+355846.0	DA	11.2	50,920 (4152)	7.96 (0.31)	Pure H	0.67 (0.14)	0.0142 (0.0035)	0.09 (0.26)	6.27 (0.11)	
J141740.22+130148.5	DA+M	87.4	35,105 (190)	7.24 (0.03)	Pure H	0.36 (0.01)	0.0239 (0.0005)	−0.11 (0.02)	5.34 (0.17)	1,2
J141749.04+195545.7	DA	55.4	66,178 (1428)	7.46 (0.07)	Pure H	0.52 (0.02)	0.0223 (0.0013)	0.93 (0.06)	5.10 (0.49)	
J141842.32+104908.2	DAO	69.6	110,232 (3334)	6.77 (0.13)	$\log N_{\rm He}/N_{\rm H} = -1.21$	0.50 (0.02)	0.0485 (0.0062)	2.50 (0.13)	<5.00	4,5
J142120.94−010054.7	DA	69.2	42,675 (413)	7.71 (0.04)	Pure H	0.54 (0.02)	0.0170 (0.0006)	−0.06 (0.03)	6.46 (0.03)	
J142212.94+205452.5	DA	24.8	39,844 (785)	7.87 (0.09)	Pure H	0.60 (0.04)	0.0150 (0.0011)	−0.29 (0.07)	6.58 (0.02)	
J142241.90+513537.8	DAO+M	23.0	67,148 (2135)	7.34 (0.11)	$\log N_{\rm He}/N_{\rm H} = -2.60$	0.48 (0.03)	0.0246 (0.0023)	1.04 (0.10)	<5.00	1,4,7
J142254.15−020719.9	DA	26.7	40,162 (859)	7.64 (0.10)	Pure H	0.51 (0.04)	0.0178 (0.0014)	−0.13 (0.08)	6.48 (0.12)	
J142340.59+383649.2	DA	5.5	34,625 (2177)	6.87 (0.39)	Pure H	0.27 (0.09)	0.0313 (0.0092)	0.10 (0.28)	<5.00	
J142349.45+221537.6	DA	32.0	43,664 (974)	7.78 (0.09)	Pure H	0.57 (0.04)	0.0161 (0.0012)	−0.07 (0.08)	6.46 (0.04)	
J142355.06+240924.3	DA+M	40.5	31,668 (196)	7.29 (0.04)	Pure H	0.37 (0.01)	0.0229 (0.0008)	−0.32 (0.03)	5.88 (0.23)	1
J142440.79+330439.5	DO	24.1	51,061 (767)	8.15 (0.14)	Pure He	0.73 (0.08)	0.0119 (0.0013)	−0.06 (0.10)	6.29 (0.04)	
J142505.05+543650.3	DA	13.0	35,439 (836)	7.43 (0.14)	Pure H	0.42 (0.04)	0.0209 (0.0022)	−0.21 (0.10)	6.23 (0.49)	
J142559.72+365800.7	DA+M	23.4	30,215 (327)	7.38 (0.08)	Pure H	0.39 (0.03)	0.0212 (0.0014)	−0.47 (0.06)	6.43 (0.32)	1,2
J142646.84+091656.8	DA	43.4	51,986 (1075)	7.71 (0.08)	Pure H	0.56 (0.03)	0.0174 (0.0011)	0.30 (0.07)	6.21 (0.05)	
J142718.43+450759.8	DA	11.0	39,179 (1487)	8.14 (0.18)	Pure H	0.74 (0.10)	0.0122 (0.0017)	−0.50 (0.14)	6.58 (0.06)	
J142724.38+545925.5	DA	33.1	30,526 (183)	7.79 (0.05)	Pure H	0.54 (0.02)	0.0155 (0.0005)	−0.72 (0.03)	6.91 (0.01)	
J142737.33−000050.0	DA	22.1	35,589 (553)	7.77 (0.09)	Pure H	0.55 (0.04)	0.0159 (0.0011)	−0.44 (0.06)	6.71 (0.03)	
J142831.24−030309.0	DA+M	9.9	51,009 (4835)	7.59 (0.32)	Pure H	0.52 (0.12)	0.0191 (0.0049)	0.35 (0.28)	6.12 (0.39)	1,7
J142835.21+134007.5	DA	19.5	32,409 (389)	7.91 (0.08)	Pure H	0.60 (0.04)	0.0143 (0.0009)	−0.69 (0.06)	6.84 (0.02)	
J142946.77+404904.0	DA	40.3	36,296 (342)	7.83 (0.05)	Pure H	0.57 (0.02)	0.0153 (0.0006)	−0.43 (0.04)	6.69 (0.01)	
J143030.82+034413.7	DA	16.0	33,679 (619)	7.65 (0.12)	Pure H	0.49 (0.05)	0.0174 (0.0016)	−0.45 (0.09)	6.72 (0.10)	
J143037.70+132321.3	DA	40.8	50,055 (1062)	7.49 (0.08)	Pure H	0.48 (0.03)	0.0208 (0.0013)	0.39 (0.07)	5.70 (0.44)	
J143155.98+635830.5	DA	8.2	60,486 (8123)	7.83 (0.46)	Pure H	0.63 (0.20)	0.0160 (0.0063)	0.49 (0.42)	6.07 (0.48)	
J143156.60+370630.2	DA	107.3	35,951 (130)	7.85 (0.02)	Pure H	0.58 (0.01)	0.0150 (0.0002)	−0.47 (0.01)	6.70 (0.01)	
J143227.25+363215.2	DB	12.1	31,725 (1839)	7.65 (0.20)	Pure He	0.46 (0.08)	0.0167 (0.0025)	−0.59 (0.17)	6.81 (0.27)	
J143231.22+065222.2	DA+M	10.4	30,775 (798)	8.06 (0.20)	Pure H	0.68 (0.11)	0.0128 (0.0019)	−0.88 (0.14)	6.94 (0.10)	1,2
J143251.76+362943.3	DA	4.5	30,458 (1535)	7.75 (0.39)	Pure H	0.53 (0.17)	0.0159 (0.0048)	−0.71 (0.27)	6.90 (0.24)	
J143318.25+103726.7	DA	27.4	39,127 (676)	7.98 (0.08)	Pure H	0.65 (0.04)	0.0137 (0.0009)	−0.40 (0.06)	6.59 (0.02)	
J143318.25+245434.4	DA	18.5	55,840 (2778)	7.70 (0.18)	Pure H	0.57 (0.06)	0.0176 (0.0026)	0.44 (0.16)	6.12 (0.17)	
J143356.00+283026.5	DAO	29.8	46,683 (1517)	7.01 (0.13)	$\log N_{\rm He}/N_{\rm H} = -1.68$	0.34 (0.03)	0.0299 (0.0033)	0.58 (0.12)	<5.00	4
J143432.71+454235.4	DA	32.6	30,460 (208)	7.75 (0.05)	Pure H	0.53 (0.02)	0.0159 (0.0006)	−0.70 (0.04)	6.90 (0.02)	

Table 2.1 – Atmospheric and stellar parameters of hot white dwarfs from SDSS DR12 (continued)

SDSS Name	Type	S/N	$T_{\rm eff}$ (K)	$\log g$	Composition	$M/M_{\odot}$	$R/R_{\odot}$	$\log L/L_{\odot}$	$\log \tau_{\rm cool}$	Notes
J143504.37+510822.9	DA	16.8	36,019 (804)	7.71 (0.12)	Pure H	0.52 (0.05)	0.0167 (0.0016)	−0.38 (0.09)	6.67 (0.07)	
J143514.15+103631.1	DAO	78.6	73,489 (2327)	7.11 (0.08)	$\log N_{\rm He}/N_{\rm H} = -1.94$	0.45 (0.02)	0.0308 (0.0023)	1.40 (0.09)	<5.00	4,5
J143606.70+544008.1	DA	30.7	57,079 (1816)	7.63 (0.11)	Pure H	0.55 (0.04)	0.0188 (0.0018)	0.53 (0.10)	6.03 (0.18)	
J143641.61+284451.3	DA	95.7	33,565 (129)	7.91 (0.03)	Pure H	0.61 (0.01)	0.0143 (0.0003)	−0.63 (0.02)	6.79 (0.01)	
J143736.67+362213.3	DA	14.8	41,128 (1414)	7.87 (0.16)	Pure H	0.60 (0.07)	0.0150 (0.0018)	−0.24 (0.12)	6.54 (0.05)	
J143751.27+161039.0	DA	24.4	36,791 (660)	7.74 (0.10)	Pure H	0.54 (0.04)	0.0164 (0.0012)	−0.35 (0.07)	6.66 (0.05)	
J143918.37+481301.3	DA	14.1	30,327 (1277)	7.97 (0.33)	Pure H	0.63 (0.17)	0.0136 (0.0034)	−0.85 (0.22)	6.94 (0.19)	
J143925.15+015914.1	DA	28.8	49,327 (1584)	7.55 (0.12)	Pure H	0.50 (0.04)	0.0197 (0.0020)	0.32 (0.10)	6.03 (0.45)	
J143947.62−010606.8	DA+M	66.8	59,352 (4334)	7.34 (0.24)	Pure H	0.46 (0.07)	0.0238 (0.0049)	0.80 (0.23)	<5.00	1,2
J143954.32−015644.2	DA	20.9	46,246 (1506)	7.90 (0.13)	Pure H	0.63 (0.06)	0.0148 (0.0015)	−0.04 (0.11)	6.39 (0.04)	
J144021.47+313749.7	DA	25.5	31,736 (354)	7.36 (0.08)	Pure H	0.39 (0.02)	0.0217 (0.0013)	−0.37 (0.06)	6.23 (0.35)	
J144028.46−012040.8	DA	8.7	31,793 (858)	7.99 (0.20)	Pure H	0.64 (0.10)	0.0134 (0.0020)	−0.78 (0.13)	6.87 (0.06)	
J144108.42+011020.0	DA	63.5	31,634 (130)	7.28 (0.03)	Pure H	0.37 (0.01)	0.0230 (0.0005)	−0.32 (0.02)	5.86 (0.16)	
J144146.72−011359.2	DA	27.9	32,379 (316)	7.98 (0.07)	Pure H	0.64 (0.04)	0.0135 (0.0007)	−0.74 (0.05)	6.84 (0.02)	
J144205.41+122926.7	DB	25.9	32,904 (836)	7.73 (0.09)	Pure He	0.49 (0.04)	0.0159 (0.0010)	−0.57 (0.07)	6.81 (0.07)	
J144307.83+340523.5	DA+M	13.2	32,688 (670)	7.28 (0.14)	Pure H	0.37 (0.04)	0.0231 (0.0024)	−0.26 (0.10)	5.76 (0.66)	1
J144334.13+001239.9	DA	27.6	44,310 (1165)	7.70 (0.11)	Pure H	0.54 (0.04)	0.0172 (0.0015)	0.01 (0.09)	6.41 (0.09)	
J144431.49+441133.8	DA	5.0	30,410 (1067)	8.08 (0.28)	Pure H	0.69 (0.15)	0.0126 (0.0026)	−0.91 (0.19)	6.96 (0.15)	
J144438.95+490619.4	DA	27.4	42,571 (1009)	7.66 (0.10)	Pure H	0.52 (0.04)	0.0177 (0.0014)	−0.03 (0.08)	6.43 (0.12)	
J144452.97+141206.8	DA	16.7	86,912 (14,527)	6.54 (0.27)	Pure H	0.38 (0.08)	0.0545 (0.0134)	2.18 (0.41)	<5.00	
J144510.28+141344.9	DAO	72.1	48,341 (688)	6.86 (0.06)	$\log N_{\rm He}/N_{\rm H} = -3.45$	0.31 (0.01)	0.0341 (0.0015)	0.76 (0.05)	<5.00	4,5
J144541.71+411441.5	DA	5.9	30,513 (1033)	7.41 (0.26)	Pure H	0.40 (0.08)	0.0207 (0.0041)	−0.47 (0.18)	6.52 (0.71)	
J144544.76−013633.8	DA	16.5	54,981 (3762)	7.44 (0.24)	Pure H	0.48 (0.08)	0.0219 (0.0043)	0.60 (0.21)	5.23 (1.09)	
J144816.19+065827.9	DA	28.3	49,291 (1485)	7.73 (0.11)	Pure H	0.56 (0.04)	0.0170 (0.0016)	0.19 (0.10)	6.30 (0.07)	
J144843.57+083522.2	DAO	85.4	64,960 (1702)	6.98 (0.07)	$\log N_{\rm He}/N_{\rm H} = -2.67$	0.39 (0.02)	0.0335 (0.0021)	1.26 (0.07)	<5.00	4,5
J144846.71+253839.2	DA	20.3	30,000 (286)	7.78 (0.08)	Pure H	0.54 (0.03)	0.0156 (0.0009)	−0.75 (0.05)	6.93 (0.02)	
J144852.98+011530.0	DA	26.8	33,041 (289)	7.05 (0.06)	Pure H	0.30 (0.02)	0.0271 (0.0012)	−0.10 (0.04)	<5.00	
J144856.93+462427.5	DA	29.2	34,273 (385)	7.27 (0.07)	Pure H	0.37 (0.02)	0.0234 (0.0012)	−0.17 (0.05)	5.58 (0.38)	
J144913.28+005503.4	DA	21.3	43,251 (1400)	7.59 (0.14)	Pure H	0.50 (0.05)	0.0187 (0.0021)	0.04 (0.11)	6.31 (0.31)	
J144916.85+093723.0	DA	45.4	38,535 (500)	7.21 (0.06)	Pure H	0.36 (0.02)	0.0248 (0.0011)	0.09 (0.05)	<5.00	
J144932.33+093112.2	DA	14.6	32,255 (539)	7.97 (0.12)	Pure H	0.64 (0.06)	0.0136 (0.0012)	−0.74 (0.08)	6.85 (0.03)	
J144943.68+530444.1	DA	20.5	34,089 (562)	7.12 (0.11)	Pure H	0.32 (0.03)	0.0259 (0.0019)	−0.09 (0.07)	<5.00	
J145005.60+295354.2	DA	21.4	31,243 (928)	7.38 (0.18)	Pure H	0.40 (0.06)	0.0212 (0.0030)	−0.41 (0.13)	6.38 (0.64)	7
J145109.40+544924.5	DA	15.5	34,607 (617)	8.06 (0.11)	Pure H	0.69 (0.06)	0.0128 (0.0010)	−0.67 (0.08)	6.75 (0.03)	
J145140.85−012523.9	DA	38.2	36,779 (428)	7.70 (0.06)	Pure H	0.52 (0.02)	0.0168 (0.0008)	−0.33 (0.05)	6.64 (0.04)	
J145202.06+333232.7	DA	51.3	31,042 (141)	7.93 (0.03)	Pure H	0.61 (0.02)	0.0141 (0.0003)	−0.78 (0.02)	6.90 (0.01)	
J145338.29+425446.4	DA	27.7	57,330 (2209)	7.73 (0.13)	Pure H	0.58 (0.05)	0.0173 (0.0020)	0.46 (0.12)	6.10 (0.10)	
J145406.45+413624.3	DA	7.1	33,648 (1603)	7.70 (0.31)	Pure H	0.51 (0.13)	0.0167 (0.0040)	−0.49 (0.22)	6.75 (0.15)	
J145428.28+002804.0	DA	21.8	32,013 (412)	7.72 (0.09)	Pure H	0.51 (0.04)	0.0165 (0.0011)	−0.59 (0.06)	6.83 (0.04)	
J145444.80+230241.3	DA	12.7	48,586 (2850)	7.76 (0.22)	Pure H	0.57 (0.09)	0.0165 (0.0030)	0.14 (0.19)	6.33 (0.16)	
J145451.08+231413.3	DA	30.6	30,914 (215)	7.84 (0.05)	Pure H	0.57 (0.03)	0.0150 (0.0006)	−0.73 (0.04)	6.90 (0.01)	
J145500.80−022735.3	DA	21.6	37,002 (842)	7.95 (0.12)	Pure H	0.63 (0.06)	0.0140 (0.0013)	−0.48 (0.09)	6.66 (0.03)	
J145515.58+152519.9	DA	30.5	54,719 (1462)	7.82 (0.10)	Pure H	0.61 (0.04)	0.0159 (0.0012)	0.31 (0.08)	6.19 (0.04)	
J145533.98+023459.1	DA	16.9	31,902 (390)	7.77 (0.09)	Pure H	0.54 (0.04)	0.0158 (0.0010)	−0.63 (0.06)	6.85 (0.03)	7
J145537.59+522020.3	DA	24.9	30,411 (230)	7.82 (0.06)	Pure H	0.56 (0.03)	0.0152 (0.0007)	−0.75 (0.04)	6.92 (0.01)	
J145539.98+120602.5	DA	23.1	82,839 (7018)	6.80 (0.17)	Pure H	0.42 (0.04)	0.0425 (0.0067)	1.88 (0.22)	<5.00	
J145545.57+041508.7	DA	64.0	150,000 (7500)	7.44 (0.07)	Pure H	0.75 (0.02)	0.0272 (0.0021)	2.53 (0.12)	<5.00	
J145600.80+574150.6	DA	67.9	31,667 (114)	7.76 (0.03)	Pure H	0.53 (0.01)	0.0159 (0.0003)	−0.64 (0.02)	6.86 (0.01)	
J145602.56+403516.5	DA	35.9	30,481 (173)	7.79 (0.04)	Pure H	0.54 (0.02)	0.0155 (0.0005)	−0.73 (0.03)	6.91 (0.01)	
J145606.73+491116.5	DAO	61.8	75,293 (4174)	6.74 (0.10)	$\log N_{\rm He}/N_{\rm H} = -1.15$	0.37 (0.03)	0.0434 (0.0040)	1.74 (0.14)	<5.00	4,5

Table 2.1 – Atmospheric and stellar parameters of hot white dwarfs from SDSS DR12 (continued)

SDSS Name	Type	S/N	$T_{\rm eff}$ (K)	$\log g$	Composition	$M/M_{\odot}$	$R/R_{\odot}$	$\log L/L_{\odot}$	$\log \tau_{\rm cool}$	Notes
J145614.05+020952.1	DA	20.1	30,595 (333)	7.74 (0.08)	Pure H	0.52 (0.04)	0.0162 (0.0010)	−0.69 (0.06)	6.89 (0.03)	
J145641.13+170415.2	DA	75.0	31,180 (98)	7.97 (0.02)	Pure H	0.63 (0.01)	0.0137 (0.0002)	−0.80 (0.02)	6.90 (0.01)	
J145726.28+364340.5	DA	37.6	37,620 (457)	7.75 (0.06)	Pure H	0.54 (0.03)	0.0163 (0.0008)	−0.32 (0.05)	6.64 (0.03)	
J145757.29+292503.2	DA	20.3	52,118 (2318)	7.61 (0.16)	Pure H	0.53 (0.06)	0.0188 (0.0025)	0.37 (0.14)	6.14 (0.24)	
J145817.44+353516.8	DA	7.1	43,850 (3464)	7.93 (0.33)	Pure H	0.64 (0.16)	0.0143 (0.0038)	−0.16 (0.27)	6.45 (0.13)	
J145907.15+404135.7	DA	32.9	39,252 (574)	7.67 (0.07)	Pure H	0.52 (0.03)	0.0173 (0.0010)	−0.19 (0.05)	6.54 (0.06)	
J150115.80+043326.8	DA	19.8	32,397 (437)	7.44 (0.09)	Pure H	0.42 (0.03)	0.0204 (0.0015)	−0.38 (0.07)	6.48 (0.27)	
J150320.07+572243.9	DA	5.2	30,295 (1330)	7.87 (0.35)	Pure H	0.58 (0.17)	0.0146 (0.0038)	−0.79 (0.24)	6.93 (0.17)	
J150409.88+513729.1	DA	20.3	57,854 (3084)	7.57 (0.18)	Pure H	0.53 (0.06)	0.0198 (0.0030)	0.60 (0.16)	5.92 (0.41)	
J150422.28+621718.5	DA	42.8	55,008 (1149)	7.62 (0.07)	Pure H	0.54 (0.02)	0.0189 (0.0012)	0.47 (0.07)	6.07 (0.11)	5
J150430.84+062457.8	DA	35.8	30,451 (175)	7.89 (0.04)	Pure H	0.59 (0.02)	0.0144 (0.0005)	−0.79 (0.03)	6.93 (0.01)	
J150437.41+281331.2	DA	17.9	47,609 (1734)	7.23 (0.14)	Pure H	0.39 (0.04)	0.0250 (0.0027)	0.46 (0.12)	<5.00	
J150440.22+580421.7	DA	3.2	33,794 (3074)	7.32 (0.58)	Pure H	0.39 (0.18)	0.0224 (0.0101)	−0.23 (0.42)	5.91 (1.39)	
J150449.99+015923.8	DA	5.3	36,193 (2928)	8.27 (0.47)	Pure H	0.81 (0.26)	0.0109 (0.0041)	−0.73 (0.35)	6.73 (0.29)	7
J150452.11+164128.3	DA	40.3	35,125 (302)	7.86 (0.05)	Pure H	0.59 (0.02)	0.0149 (0.0006)	−0.52 (0.04)	6.73 (0.01)	
J150459.70+543008.7	DA	6.1	39,779 (3180)	7.83 (0.38)	Pure H	0.58 (0.17)	0.0154 (0.0046)	−0.27 (0.29)	6.58 (0.23)	
J150647.67+403504.9	DA	5.0	31,975 (1607)	7.66 (0.36)	Pure H	0.49 (0.14)	0.0172 (0.0047)	−0.55 (0.25)	6.80 (0.20)	
J150704.43+384430.1	DA	25.9	31,218 (310)	7.66 (0.07)	Pure H	0.49 (0.03)	0.0171 (0.0010)	−0.60 (0.05)	6.83 (0.05)	
J150716.68+344010.3	DA	39.0	68,105 (2858)	7.13 (0.11)	Pure H	0.44 (0.03)	0.0296 (0.0029)	1.23 (0.12)	<5.00	5
J150748.06+381521.6	DAO	15.3	56,442 (4743)	7.13 (0.35)	$\log N_{\rm He}/N_{\rm H} = -0.87$	0.39 (0.09)	0.0284 (0.0084)	0.87 (0.30)	<5.00	4,5
J150805.30+402354.5	DA	5.7	33,070 (1797)	7.34 (0.36)	Pure H	0.39 (0.11)	0.0221 (0.0060)	−0.28 (0.26)	6.06 (1.10)	
J150816.81+420103.3	DA	41.8	34,372 (257)	7.79 (0.05)	Pure H	0.55 (0.02)	0.0156 (0.0005)	−0.51 (0.03)	6.76 (0.01)	
J150909.60−010826.9	DAB	69.6	30,502 (496)	8.15 (0.07)	$\log q_{\rm H} = -17.15$	0.70 (0.04)	0.0117 (0.0006)	−0.97 (0.06)	7.02 (0.06)	3
J150927.22+292206.3	DO	39.0	49,846 (200)	8.05 (0.07)	Pure He	0.68 (0.04)	0.0128 (0.0007)	−0.04 (0.05)	6.35 (0.02)	
J150950.76+323826.8	DO+M	10.5	50,283 (2376)	7.52 (0.44)	Pure He	0.45 (0.16)	0.0194 (0.0065)	0.34 (0.30)	5.38 (1.38)	1
J151026.47+610656.9	DOZ	41.2	84,315 (5633)	6.97 (0.22)	Pure He	0.37 (0.06)	0.0331 (0.0060)	1.70 (0.20)	<5.00	6,8
J151132.20+451732.6	DA	34.5	51,829 (1351)	7.46 (0.09)	Pure H	0.48 (0.03)	0.0213 (0.0016)	0.47 (0.08)	5.51 (0.59)	
J151208.03+111607.7	DA	15.1	59,289 (5065)	6.95 (0.27)	Pure H	0.37 (0.06)	0.0334 (0.0079)	1.09 (0.26)	<5.00	
J151215.72+065156.3	DOZ	60.1	110,058 (2719)	7.17 (0.17)	Pure He	0.50 (0.04)	0.0304 (0.0049)	2.09 (0.15)	<5.00	6,8
J151243.85+581035.6	DA	16.5	41,365 (1718)	7.61 (0.18)	Pure H	0.50 (0.07)	0.0183 (0.0027)	−0.05 (0.15)	6.40 (0.28)	
J151302.41+560742.2	DA	7.7	32,064 (925)	7.92 (0.21)	Pure H	0.61 (0.10)	0.0141 (0.0022)	−0.72 (0.14)	6.85 (0.05)	
J151336.16+144929.7	DA	18.6	32,694 (471)	7.82 (0.10)	Pure H	0.56 (0.05)	0.0153 (0.0011)	−0.62 (0.07)	6.82 (0.03)	
J151338.54+254744.3	DA	20.2	33,936 (548)	7.71 (0.10)	Pure H	0.52 (0.04)	0.0166 (0.0013)	−0.48 (0.07)	6.75 (0.05)	
J151402.58+005245.5	DA	28.4	62,228 (2517)	7.63 (0.14)	Pure H	0.56 (0.05)	0.0190 (0.0022)	0.69 (0.13)	5.93 (0.19)	
J151418.75+273722.2	DA	18.9	37,096 (672)	7.78 (0.10)	Pure H	0.55 (0.04)	0.0159 (0.0012)	−0.36 (0.07)	6.66 (0.03)	
J151445.18+013635.2	DA	22.4	31,742 (482)	7.22 (0.11)	Pure H	0.35 (0.03)	0.0241 (0.0019)	−0.28 (0.07)	5.51 (0.51)	
J151447.15+335708.4	DA	9.3	71,644 (11,078)	6.99 (0.42)	Pure H	0.42 (0.10)	0.0343 (0.0130)	1.45 (0.45)	<5.00	
J151539.02+075846.6	DA	8.8	30,938 (735)	7.31 (0.18)	Pure H	0.37 (0.05)	0.0225 (0.0030)	−0.38 (0.12)	6.05 (0.73)	
J151551.01+280704.5	DA	10.0	52,168 (4078)	7.53 (0.28)	Pure H	0.50 (0.10)	0.0202 (0.0046)	0.44 (0.25)	5.90 (0.73)	7
J151606.34+274647.0	DA	13.8	40,581 (1397)	7.95 (0.16)	Pure H	0.64 (0.08)	0.0141 (0.0017)	−0.31 (0.12)	6.55 (0.04)	
J151709.68+435647.8	DA	15.9	74,657 (7930)	6.86 (0.26)	Pure H	0.40 (0.06)	0.0387 (0.0090)	1.62 (0.29)	<5.00	
J151711.17+424816.5	DA	6.6	43,302 (3952)	6.98 (0.38)	Pure H	0.32 (0.09)	0.0300 (0.0091)	0.46 (0.31)	<5.00	
J151729.45+433028.6	DB	32.0	32,075 (1460)	8.04 (0.14)	Pure He	0.64 (0.08)	0.0127 (0.0013)	−0.81 (0.12)	6.90 (0.07)	
J151747.98−011049.6	DA	29.1	34,085 (414)	7.67 (0.08)	Pure H	0.50 (0.03)	0.0172 (0.0010)	−0.45 (0.05)	6.72 (0.05)	
J151748.56+131927.0	DA	27.0	30,889 (221)	7.85 (0.05)	Pure H	0.57 (0.03)	0.0149 (0.0006)	−0.74 (0.04)	6.90 (0.01)	
J151752.86+531455.5	DA+M	20.5	30,204 (342)	7.95 (0.09)	Pure H	0.62 (0.05)	0.0138 (0.0009)	−0.85 (0.06)	6.94 (0.02)	1
J151905.96+500702.9	DA	25.5	31,233 (213)	7.97 (0.05)	Pure H	0.63 (0.03)	0.0136 (0.0005)	−0.80 (0.03)	6.90 (0.01)	7
J151957.09+233658.7	DA	22.4	40,322 (850)	7.93 (0.10)	Pure H	0.63 (0.05)	0.0142 (0.0011)	−0.32 (0.08)	6.56 (0.03)	
J152041.16+243019.4	DAB	33.2	40,398 (1802)	7.57 (0.16)	$\log q_{\rm H} = -15.89$	0.45 (0.06)	0.0182 (0.0022)	−0.10 (0.13)	6.22 (0.55)	3
J152041.95+495140.8	DA	53.1	30,061 (109)	7.42 (0.03)	Pure H	0.40 (0.01)	0.0205 (0.0005)	−0.51 (0.02)	6.58 (0.08)	

Table 2.1 – Atmospheric and stellar parameters of hot white dwarfs from SDSS DR12 (continued)

SDSS Name	Type	S/N	$T_{\rm eff}$ (K)	$\log g$	Composition	$M/M_{\odot}$	$R/R_{\odot}$	$\log L/L_{\odot}$	$\log \tau_{\rm cool}$	Notes
J152054.49+431032.1	DA	28.9	41,605 (774)	7.75 (0.08)	Pure H	0.55 (0.03)	0.0165 (0.0011)	−0.14 (0.07)	6.51 (0.04)	
J152101.47+565718.4	DA	28.1	79,595 (5076)	7.08 (0.16)	Pure H	0.46 (0.04)	0.0326 (0.0049)	1.59 (0.18)	<5.00	
J152116.07+245016.4	DA+M	18.9	32,696 (567)	7.48 (0.12)	Pure H	0.43 (0.04)	0.0198 (0.0018)	−0.39 (0.09)	6.55 (0.28)	1,2
J152120.52+122533.6	DA	24.4	33,134 (404)	7.88 (0.08)	Pure H	0.59 (0.04)	0.0147 (0.0009)	−0.63 (0.06)	6.81 (0.02)	
J152138.99+103015.7	DA	73.0	56,062 (1102)	7.24 (0.07)	Pure H	0.42 (0.02)	0.0257 (0.0015)	0.77 (0.06)	<5.00	
J152154.23+280540.1	DA	14.6	34,476 (860)	7.66 (0.15)	Pure H	0.50 (0.06)	0.0173 (0.0020)	−0.42 (0.11)	6.70 (0.13)	
J152226.05−012327.0	DAO	45.4	69,957 (5149)	6.88 (0.15)	$\log N_{\rm He}/N_{\rm H} = -1.04$	0.39 (0.04)	0.0375 (0.0050)	1.48 (0.19)	<5.00	4,5
J152251.08+052349.4	DA	41.2	30,887 (174)	7.76 (0.04)	Pure H	0.53 (0.02)	0.0159 (0.0005)	−0.68 (0.03)	6.89 (0.01)	
J152259.25+082837.2	DAO	14.2	60,150 (5165)	7.81 (0.30)	$\log N_{\rm He}/N_{\rm H} = -2.73$	0.62 (0.12)	0.0162 (0.0042)	0.49 (0.27)	6.07 (0.25)	4,7
J152318.77+004948.0	DA	17.7	45,361 (1828)	7.41 (0.16)	Pure H	0.45 (0.05)	0.0218 (0.0027)	0.26 (0.13)	5.51 (0.79)	
J152340.79+243451.0	DA+M	12.8	37,791 (1458)	7.88 (0.20)	Pure H	0.60 (0.09)	0.0147 (0.0022)	−0.40 (0.15)	6.64 (0.06)	1
J152359.29+381159.1	DA	11.4	36,060 (1179)	8.06 (0.18)	Pure H	0.69 (0.10)	0.0128 (0.0018)	−0.60 (0.13)	6.69 (0.05)	
J152359.74+021841.7	DA	43.2	49,893 (1062)	7.65 (0.08)	Pure H	0.54 (0.03)	0.0181 (0.0012)	0.26 (0.07)	6.23 (0.10)	
J152422.17+073351.2	DAO	29.3	49,645 (1779)	7.46 (0.14)	$\log N_{\rm He}/N_{\rm H} = -1.13$	0.48 (0.05)	0.0212 (0.0024)	0.39 (0.12)	5.58 (0.75)	4
J152537.60+064909.8	DA	21.9	48,711 (2243)	7.79 (0.18)	Pure H	0.59 (0.07)	0.0161 (0.0023)	0.12 (0.15)	6.33 (0.09)	
J152623.30+394636.3	DA	7.5	30,194 (719)	7.68 (0.19)	Pure H	0.49 (0.08)	0.0168 (0.0024)	−0.67 (0.13)	6.89 (0.11)	
J152658.85+021510.4	DA	19.3	47,674 (2052)	7.41 (0.16)	Pure H	0.45 (0.06)	0.0219 (0.0028)	0.35 (0.14)	5.37 (0.86)	
J152710.76+105818.9	DA	19.1	41,659 (1135)	7.75 (0.12)	Pure H	0.55 (0.05)	0.0164 (0.0015)	−0.14 (0.10)	6.51 (0.06)	
J152728.26+002201.7	DA	23.3	57,414 (2630)	7.57 (0.16)	Pure H	0.53 (0.05)	0.0198 (0.0026)	0.58 (0.14)	5.92 (0.38)	
J152744.11+100722.4	DA+M	50.3	32,548 (443)	7.83 (0.09)	Pure H	0.57 (0.04)	0.0152 (0.0011)	−0.63 (0.07)	6.83 (0.02)	1,2
J152759.11+012406.2	DA	61.9	35,401 (161)	7.78 (0.03)	Pure H	0.55 (0.01)	0.0158 (0.0003)	−0.45 (0.02)	6.72 (0.01)	
J152810.28+252458.3	DA	25.3	65,604 (2923)	7.51 (0.14)	Pure H	0.54 (0.05)	0.0212 (0.0026)	0.87 (0.14)	5.51 (0.71)	
J152826.04+155916.5	DA+M	35.3	57,596 (1525)	7.61 (0.09)	Pure H	0.55 (0.03)	0.0191 (0.0015)	0.56 (0.08)	6.00 (0.16)	1
J152839.44+011300.0	DA	70.1	51,817 (577)	7.68 (0.04)	Pure H	0.55 (0.01)	0.0178 (0.0006)	0.31 (0.04)	6.21 (0.03)	
J152840.10+052737.6	DA	13.7	90,187 (11,096)	7.55 (0.34)	Pure H	0.61 (0.10)	0.0219 (0.0070)	1.46 (0.36)	5.15 (0.97)	
J152943.01+183722.8	DO	30.5	54,633 (2236)	8.41 (0.31)	Pure He	0.89 (0.18)	0.0097 (0.0025)	−0.12 (0.24)	6.13 (0.08)	
J152959.38+482242.3	DA	32.0	31,452 (232)	7.45 (0.05)	Pure H	0.42 (0.02)	0.0202 (0.0009)	−0.44 (0.04)	6.56 (0.13)	
J153046.59+044439.6	DAO	24.4	74,818 (7721)	7.13 (0.25)	$\log N_{\rm He}/N_{\rm H} = -2.29$	0.46 (0.06)	0.0305 (0.0070)	1.42 (0.28)	<5.00	4,5
J153102.40+534900.5	DAO	53.2	68,680 (3201)	6.95 (0.11)	$\log N_{\rm He}/N_{\rm H} = -2.21$	0.40 (0.03)	0.0350 (0.0035)	1.39 (0.13)	<5.00	4,5
J153127.86+133917.4	DA	11.5	76,029 (12,119)	6.76 (0.36)	Pure H	0.38 (0.09)	0.0428 (0.0138)	1.74 (0.43)	<5.00	
J153133.11+343327.5	DOZ	63.9	72,546 (1303)	8.12 (0.10)	Pure He	0.74 (0.05)	0.0125 (0.0010)	0.59 (0.08)	5.88 (0.05)	6
J153139.31+233020.1	DA	20.0	52,806 (2468)	7.97 (0.17)	Pure H	0.68 (0.08)	0.0141 (0.0019)	0.14 (0.15)	6.23 (0.06)	
J153246.18+423138.4	DA	60.0	40,585 (365)	7.79 (0.04)	Pure H	0.57 (0.02)	0.0159 (0.0005)	−0.21 (0.03)	6.55 (0.01)	
J153321.57+514057.1	DAB	17.0	41,177 (4271)	7.29 (0.55)	$\log q_{\rm H} = -15.55$	0.35 (0.17)	0.0222 (0.0090)	0.11 (0.39)	<5.00	3
J153323.08+292928.4	DA	44.9	34,191 (258)	7.81 (0.05)	Pure H	0.56 (0.02)	0.0154 (0.0005)	−0.53 (0.03)	6.77 (0.01)	
J153352.49+415135.6	DA	9.8	31,847 (717)	7.41 (0.16)	Pure H	0.41 (0.05)	0.0209 (0.0026)	−0.39 (0.12)	6.42 (0.54)	
J153404.30+412026.1	DA+M	43.9	35,304 (412)	7.72 (0.07)	Pure H	0.53 (0.03)	0.0165 (0.0009)	−0.42 (0.05)	6.70 (0.03)	1,2
J153437.70−004719.4	DA	33.3	30,279 (184)	7.88 (0.05)	Pure H	0.58 (0.02)	0.0146 (0.0005)	−0.79 (0.03)	6.93 (0.01)	
J153713.19+211649.6	DA+M	10.7	40,220 (1947)	7.70 (0.22)	Pure H	0.53 (0.09)	0.0171 (0.0030)	−0.16 (0.18)	6.53 (0.14)	1
J153718.44+151059.6	DA	43.1	38,754 (438)	7.75 (0.05)	Pure H	0.55 (0.02)	0.0163 (0.0007)	−0.27 (0.04)	6.60 (0.02)	
J153938.10+270605.8	DA	49.3	34,893 (351)	7.10 (0.06)	Pure H	0.32 (0.02)	0.0264 (0.0011)	−0.03 (0.04)	<5.00	2
J154005.73+121937.7	DA+M	22.9	33,458 (327)	7.85 (0.06)	Pure H	0.58 (0.03)	0.0150 (0.0007)	−0.59 (0.04)	6.80 (0.01)	1
J154028.81+385407.6	DA	22.4	75,066 (4936)	7.61 (0.21)	Pure H	0.59 (0.07)	0.0200 (0.0037)	1.06 (0.20)	5.65 (0.38)	
J154108.22+171433.8	DA+M	47.6	69,316 (2186)	7.17 (0.09)	Pure H	0.45 (0.02)	0.0289 (0.0025)	1.24 (0.10)	<5.00	1
J154126.42+371647.7	DA	26.5	41,313 (972)	7.63 (0.10)	Pure H	0.51 (0.04)	0.0180 (0.0015)	−0.07 (0.08)	6.44 (0.15)	
J154201.48+502532.0	DB	48.4	32,668 (419)	7.78 (0.04)	Pure He	0.51 (0.02)	0.0153 (0.0005)	−0.62 (0.04)	6.84 (0.03)	
J154204.08+120650.3	DA	39.3	44,058 (808)	7.81 (0.08)	Pure H	0.58 (0.03)	0.0158 (0.0009)	−0.07 (0.06)	6.45 (0.03)	
J154218.18+081301.8	DA	48.3	62,460 (1474)	7.36 (0.08)	Pure H	0.48 (0.03)	0.0239 (0.0015)	0.90 (0.07)	<5.00	
J154221.86+553957.2	DA+M	11.1	42,914 (2357)	7.48 (0.23)	Pure H	0.46 (0.08)	0.0206 (0.0037)	0.11 (0.19)	5.96 (0.85)	1
J154318.28+492240.7	DA	45.7	33,954 (215)	7.79 (0.04)	Pure H	0.55 (0.02)	0.0157 (0.0005)	−0.53 (0.03)	6.77 (0.01)	

Table 2.1 – Atmospheric and stellar parameters of hot white dwarfs from SDSS DR12 (continued)

SDSS Name	Type	S/N	$T_{\rm eff}$ (K)	$\log g$	Composition	$M/M_{\odot}$	$R/R_{\odot}$	$\log L/L_{\odot}$	$\log \tau_{\rm cool}$	Notes
J154415.24+513310.2	DA	55.5	33,610 (194)	7.81 (0.04)	Pure H	0.56 (0.02)	0.0154 (0.0004)	−0.56 (0.03)	6.79 (0.01)	
J154448.25+455039.1	DA	45.5	50,179 (891)	7.69 (0.07)	Pure H	0.55 (0.02)	0.0175 (0.0010)	0.24 (0.06)	6.25 (0.05)	
J154456.80+451521.9	DA	76.4	71,907 (1702)	7.39 (0.06)	Pure H	0.51 (0.02)	0.0238 (0.0012)	1.14 (0.06)	<5.00	5
J154459.10+370729.6	DA	22.9	35,555 (673)	7.36 (0.11)	Pure H	0.40 (0.03)	0.0220 (0.0018)	−0.16 (0.08)	5.93 (0.50)	
J154526.36+125955.6	DA	33.3	46,007 (837)	7.67 (0.07)	Pure H	0.53 (0.03)	0.0178 (0.0010)	0.10 (0.06)	6.35 (0.08)	
J154549.80+195503.8	DA	33.5	46,515 (1044)	7.77 (0.09)	Pure H	0.57 (0.04)	0.0163 (0.0012)	0.05 (0.07)	6.38 (0.04)	2
J154557.81+245106.1	DA	7.5	39,315 (2901)	7.86 (0.35)	Pure H	0.60 (0.16)	0.0150 (0.0042)	−0.31 (0.27)	6.59 (0.20)	
J154605.13+124713.8	DA+M	22.2	37,417 (785)	7.78 (0.11)	Pure H	0.55 (0.05)	0.0159 (0.0013)	−0.35 (0.08)	6.65 (0.04)	1
J154624.26+200406.1	DA	28.7	34,075 (410)	7.89 (0.08)	Pure H	0.60 (0.04)	0.0145 (0.0008)	−0.59 (0.05)	6.77 (0.02)	
J154626.16+143754.8	DA	72.5	36,623 (245)	7.91 (0.04)	Pure H	0.61 (0.02)	0.0144 (0.0004)	−0.47 (0.03)	6.68 (0.01)	
J154640.17+135529.2	DA	33.2	30,590 (218)	7.28 (0.05)	Pure H	0.36 (0.02)	0.0229 (0.0009)	−0.38 (0.04)	5.94 (0.28)	
J154644.44+502902.0	DA	10.0	31,971 (791)	7.74 (0.18)	Pure H	0.52 (0.08)	0.0162 (0.0021)	−0.61 (0.12)	6.84 (0.08)	
J154651.71−020422.5	DA	8.2	30,528 (903)	7.36 (0.23)	Pure H	0.39 (0.07)	0.0215 (0.0037)	−0.44 (0.16)	6.34 (0.77)	
J154655.34+144156.0	DA	22.4	32,300 (363)	7.83 (0.08)	Pure H	0.57 (0.04)	0.0151 (0.0009)	−0.65 (0.05)	6.84 (0.02)	
J154728.82+290206.8	DA	22.1	34,645 (433)	7.95 (0.08)	Pure H	0.63 (0.04)	0.0139 (0.0008)	−0.60 (0.05)	6.75 (0.02)	
J154752.33+423210.8	DOA	41.0	95,843 (6853)	7.03 (0.27)	$\log N_{\rm He}/N_{\rm H} = -0.26$	0.42 (0.07)	0.0328 (0.0075)	1.91 (0.24)	<5.00	4,8
J154758.63+413613.8	DA	19.0	120,787 (25,564)	6.88 (0.20)	Pure H	0.56 (0.10)	0.0448 (0.0092)	2.59 (0.47)	<5.00	
J154814.06+424504.8	DA	16.2	31,261 (421)	7.82 (0.10)	Pure H	0.56 (0.05)	0.0152 (0.0011)	−0.70 (0.07)	6.88 (0.03)	
J154828.89+103708.3	DA	9.1	50,942 (5216)	7.12 (0.37)	Pure H	0.37 (0.10)	0.0277 (0.0085)	0.67 (0.33)	<5.00	
J154829.86+203139.0	DOA	53.4	53,061 (615)	8.07 (0.09)	$\log q_{\rm H} = -16.91$	0.69 (0.05)	0.0127 (0.0009)	0.06 (0.06)	6.27 (0.03)	3
J154830.53+405242.6	DAO	39.6	60,554 (2586)	6.75 (0.12)	$\log N_{\rm He}/N_{\rm H} = -2.89$	0.33 (0.03)	0.0398 (0.0041)	1.28 (0.12)	<5.00	4
J154907.10+412621.4	DA	6.4	35,599 (2388)	7.79 (0.38)	Pure H	0.56 (0.17)	0.0157 (0.0047)	−0.45 (0.28)	6.71 (0.18)	
J154922.16+334601.1	DA	32.2	36,820 (533)	7.79 (0.08)	Pure H	0.56 (0.03)	0.0157 (0.0009)	−0.39 (0.06)	6.67 (0.02)	
J154943.01+231916.6	DA	71.7	30,043 (88)	7.91 (0.02)	Pure H	0.60 (0.01)	0.0142 (0.0002)	−0.83 (0.02)	6.95 (0.01)	
J154949.99+205043.4	DA	44.7	57,253 (1334)	7.56 (0.08)	Pure H	0.53 (0.02)	0.0200 (0.0013)	0.59 (0.07)	5.91 (0.23)	5
J155035.19+402558.6	DA	82.3	55,472 (644)	7.61 (0.04)	Pure H	0.54 (0.01)	0.0191 (0.0007)	0.49 (0.04)	6.04 (0.06)	
J155108.24+454313.3	DA	36.3	43,992 (707)	7.69 (0.07)	Pure H	0.54 (0.03)	0.0173 (0.0009)	0.00 (0.05)	6.42 (0.05)	
J155117.94+044551.6	DA	4.8	46,743 (6611)	7.10 (0.55)	Pure H	0.36 (0.15)	0.0277 (0.0125)	0.52 (0.47)	<5.00	
J155124.56+031153.2	DA	16.0	45,280 (2083)	7.68 (0.18)	Pure H	0.54 (0.07)	0.0175 (0.0026)	0.06 (0.15)	6.38 (0.14)	
J155205.60+433825.9	DA+M	17.9	33,993 (659)	7.68 (0.12)	Pure H	0.51 (0.05)	0.0170 (0.0016)	−0.46 (0.09)	6.73 (0.08)	1,2
J155232.50+202715.2	DA+M	53.6	31,390 (129)	7.90 (0.03)	Pure H	0.60 (0.01)	0.0143 (0.0003)	−0.74 (0.02)	6.88 (0.01)	1
J155251.08+573924.9	DOZ	35.6	109,566 (3905)	8.72 (0.22)	Pure He	1.09 (0.11)	0.0075 (0.0016)	0.87 (0.19)	<5.00	6
J155356.79+483228.6	DO	29.7	72,375 (3078)	8.07 (0.23)	Pure He	0.72 (0.11)	0.0129 (0.0025)	0.62 (0.18)	5.91 (0.09)	8
J155425.33+201315.6	DA+M	22.6	41,521 (1140)	7.51 (0.12)	Pure H	0.47 (0.04)	0.0199 (0.0019)	0.02 (0.10)	6.17 (0.38)	1,2
J155435.60+163527.8	DA	19.0	40,674 (1181)	7.67 (0.13)	Pure H	0.52 (0.05)	0.0174 (0.0018)	−0.13 (0.10)	6.50 (0.13)	
J155508.79+314905.3	DA	39.9	56,015 (1367)	7.62 (0.08)	Pure H	0.54 (0.03)	0.0189 (0.0014)	0.50 (0.08)	6.05 (0.13)	
J155521.13+411650.1	DA+M	28.4	31,147 (283)	7.73 (0.07)	Pure H	0.52 (0.03)	0.0162 (0.0008)	−0.65 (0.05)	6.87 (0.03)	1,2
J155552.39+172920.1	DA	45.2	34,758 (256)	7.80 (0.04)	Pure H	0.56 (0.02)	0.0155 (0.0005)	−0.50 (0.03)	6.74 (0.01)	
J155605.26+320506.9	DA	96.7	31,458 (79)	8.31 (0.02)	Pure H	0.83 (0.01)	0.0105 (0.0002)	−1.01 (0.01)	7.13 (0.04)	
J155712.05+151534.3	DA+M	20.9	43,315 (1845)	7.77 (0.18)	Pure H	0.57 (0.08)	0.0162 (0.0023)	−0.08 (0.15)	6.47 (0.11)	1,2
J155735.37+155817.1	DA+M	30.1	45,104 (922)	7.67 (0.08)	Pure H	0.53 (0.03)	0.0176 (0.0012)	0.06 (0.07)	6.38 (0.08)	1
J155745.39+554609.7	DA	32.5	60,500 (2191)	7.59 (0.12)	Pure H	0.54 (0.04)	0.0196 (0.0021)	0.67 (0.11)	5.88 (0.32)	
J155808.02+053004.3	DA	30.6	54,406 (1895)	7.43 (0.12)	Pure H	0.47 (0.04)	0.0220 (0.0021)	0.58 (0.10)	5.16 (0.82)	
J155832.58+261852.5	DA	11.0	39,491 (1822)	7.88 (0.22)	Pure H	0.61 (0.10)	0.0148 (0.0025)	−0.32 (0.17)	6.59 (0.07)	
J155859.26+083644.5	DA	21.7	37,251 (822)	7.88 (0.12)	Pure H	0.60 (0.06)	0.0147 (0.0013)	−0.43 (0.09)	6.66 (0.03)	
J155904.62+035623.4	DA+M	28.8	36,116 (1952)	7.49 (0.30)	Pure H	0.44 (0.10)	0.0199 (0.0045)	−0.22 (0.22)	6.38 (0.67)	1,2
J155912.40+211839.9	DA	29.4	66,289 (2788)	7.29 (0.13)	Pure H	0.47 (0.04)	0.0257 (0.0030)	1.06 (0.13)	<5.00	
J155919.10+240722.0	DAO	52.2	89,274 (4605)	7.09 (0.15)	$\log N_{\rm He}/N_{\rm H} = -1.59$	0.50 (0.03)	0.0332 (0.0049)	1.80 (0.16)	<5.00	4,5
J155920.76+335511.6	DA	32.8	66,917 (3314)	7.31 (0.16)	Pure H	0.47 (0.04)	0.0252 (0.0034)	1.06 (0.15)	<5.00	
J155935.17+325003.1	DA	10.7	58,364 (4915)	8.05 (0.30)	Pure H	0.72 (0.15)	0.0134 (0.0033)	0.27 (0.26)	6.10 (0.12)	

Table 2.1 – Atmospheric and stellar parameters of hot white dwarfs from SDSS DR12 (continued)

SDSS Name	Type	S/N	$T_{\rm eff}$ (K)	$\log g$	Composition	$M/M_{\odot}$	$R/R_{\odot}$	$\log L/L_{\odot}$	$\log \tau_{\rm cool}$	Notes
J160024.21+274321.1	DA	32.1	34,913 (437)	7.83 (0.08)	Pure H	0.57 (0.03)	0.0152 (0.0009)	−0.51 (0.05)	6.74 (0.02)	
J160025.09+374716.1	DOZ	16.8	65,670 (3913)	8.21 (0.36)	Pure He	0.78 (0.19)	0.0115 (0.0034)	0.34 (0.27)	5.96 (0.11)	6
J160046.56+362937.0	DB	7.4	36,313 (3279)	7.70 (0.32)	Pure He	0.49 (0.13)	0.0163 (0.0039)	−0.38 (0.26)	6.66 (0.30)	
J160116.32+093446.3	DA	5.1	32,817 (1684)	7.26 (0.35)	Pure H	0.36 (0.10)	0.0235 (0.0061)	−0.24 (0.24)	5.63 (1.14)	
J160136.70+050528.0	DA+M	15.0	49,740 (3885)	7.95 (0.30)	Pure H	0.66 (0.14)	0.0142 (0.0034)	0.05 (0.25)	6.30 (0.10)	1,2
J160151.60+195246.9	DA	37.1	35,743 (362)	7.72 (0.06)	Pure H	0.53 (0.02)	0.0166 (0.0007)	−0.39 (0.04)	6.69 (0.03)	
J160216.04+125841.6	DA	13.7	31,674 (529)	7.61 (0.12)	Pure H	0.47 (0.04)	0.0178 (0.0016)	−0.54 (0.09)	6.77 (0.11)	
J160236.07+381950.5	DAO	70.2	80,331 (3478)	7.28 (0.11)	$\log N_{\rm He}/N_{\rm H} = -2.38$	0.51 (0.03)	0.0270 (0.0026)	1.44 (0.12)	<5.00	4,5
J160246.45+303914.5	DA	96.8	59,125 (690)	7.54 (0.04)	Pure H	0.53 (0.01)	0.0205 (0.0007)	0.67 (0.04)	5.77 (0.15)	
J160301.36+265442.3	DA	19.6	72,798 (4855)	7.05 (0.18)	Pure H	0.44 (0.04)	0.0325 (0.0054)	1.43 (0.20)	<5.00	
J160304.54+052338.6	DA	13.1	31,792 (758)	7.18 (0.17)	Pure H	0.34 (0.05)	0.0247 (0.0030)	−0.25 (0.12)	5.33 (0.73)	
J160336.97+040615.2	DA	8.0	30,821 (832)	7.98 (0.21)	Pure H	0.64 (0.11)	0.0135 (0.0021)	−0.83 (0.14)	6.92 (0.07)	
J160415.06+504459.3	DA	41.9	47,989 (827)	7.66 (0.07)	Pure H	0.54 (0.02)	0.0179 (0.0010)	0.18 (0.06)	6.29 (0.07)	
J160417.19+454715.2	DA	37.5	31,145 (212)	7.65 (0.05)	Pure H	0.49 (0.02)	0.0172 (0.0007)	−0.60 (0.04)	6.83 (0.03)	
J160446.43+363011.5	DA	7.3	46,566 (4916)	7.34 (0.41)	Pure H	0.42 (0.12)	0.0231 (0.0077)	0.35 (0.34)	<5.00	
J160523.16+425901.5	DA	21.2	31,949 (435)	7.68 (0.10)	Pure H	0.50 (0.04)	0.0169 (0.0012)	−0.57 (0.07)	6.81 (0.06)	
J160530.50+322521.2	DA	39.4	32,129 (216)	7.80 (0.05)	Pure H	0.55 (0.02)	0.0154 (0.0005)	−0.64 (0.03)	6.85 (0.01)	
J160550.54+060738.0	DA	66.2	52,841 (778)	7.57 (0.05)	Pure H	0.52 (0.02)	0.0195 (0.0009)	0.43 (0.05)	6.04 (0.15)	
J160551.75+353223.3	DA	19.3	33,533 (508)	7.65 (0.10)	Pure H	0.49 (0.04)	0.0174 (0.0013)	−0.46 (0.07)	6.73 (0.08)	
J160634.37+431847.2	DA	7.6	50,388 (5113)	7.41 (0.37)	Pure H	0.46 (0.12)	0.0221 (0.0067)	0.45 (0.32)	5.20 (1.37)	
J160655.28+424526.3	DA+M	31.3	31,353 (229)	7.84 (0.05)	Pure H	0.57 (0.03)	0.0150 (0.0006)	−0.71 (0.04)	6.88 (0.01)	1
J160659.76+421708.5	DA+M	23.7	33,715 (462)	7.83 (0.09)	Pure H	0.57 (0.04)	0.0152 (0.0010)	−0.57 (0.06)	6.79 (0.02)	1
J160721.16+380746.8	DA	6.2	51,937 (6522)	7.90 (0.46)	Pure H	0.64 (0.21)	0.0149 (0.0058)	0.16 (0.40)	6.26 (0.38)	
J160738.12+435759.9	DA	34.6	31,597 (203)	7.79 (0.05)	Pure H	0.55 (0.02)	0.0156 (0.0005)	−0.66 (0.03)	6.86 (0.01)	
J160748.21+073229.1	DA	25.8	58,995 (2414)	7.44 (0.14)	Pure H	0.49 (0.05)	0.0222 (0.0024)	0.73 (0.12)	5.20 (0.93)	
J160822.28+084552.0	DA	32.1	34,591 (403)	7.87 (0.07)	Pure H	0.59 (0.03)	0.0148 (0.0008)	−0.55 (0.05)	6.75 (0.02)	
J160828.70+422101.8	DAO	57.6	84,978 (7071)	6.82 (0.14)	$\log N_{\rm He}/N_{\rm H} = -0.96$	0.43 (0.04)	0.0421 (0.0053)	1.92 (0.20)	<5.00	4,5
J160904.61+035000.2	DA	43.9	41,189 (536)	7.77 (0.06)	Pure H	0.56 (0.02)	0.0161 (0.0007)	−0.17 (0.05)	6.53 (0.02)	
J160915.41+122515.9	DB	11.0	30,201 (2724)	7.62 (0.32)	Pure He	0.44 (0.13)	0.0170 (0.0040)	−0.66 (0.26)	6.86 (0.39)	
J160929.96+443857.1	DA	4.7	36,982 (2873)	8.34 (0.42)	Pure H	0.85 (0.24)	0.0104 (0.0035)	−0.74 (0.32)	6.72 (0.33)	
J161009.84+550211.5	DB	21.5	32,807 (841)	7.76 (0.09)	Pure He	0.51 (0.04)	0.0154 (0.0010)	−0.60 (0.07)	6.83 (0.05)	
J161015.19+053943.8	DA	18.1	43,601 (1587)	7.29 (0.15)	Pure H	0.40 (0.05)	0.0237 (0.0027)	0.26 (0.12)	<5.00	
J161030.32+274052.1	DA	21.8	31,649 (441)	7.45 (0.10)	Pure H	0.42 (0.03)	0.0202 (0.0016)	−0.43 (0.07)	6.56 (0.26)	2
J161044.76+082152.2	DA	15.2	81,702 (8006)	7.48 (0.29)	Pure H	0.57 (0.08)	0.0227 (0.0059)	1.32 (0.29)	5.22 (0.89)	
J161114.17+071140.7	DAO	27.8	79,899 (9000)	6.72 (0.24)	$\log N_{\rm He}/N_{\rm H} = -2.20$	0.39 (0.06)	0.0452 (0.0096)	1.88 (0.30)	<5.00	4
J161126.34+052357.6	DO	23.3	46,449 (318)	7.72 (0.10)	Pure He	0.52 (0.04)	0.0164 (0.0013)	0.05 (0.07)	6.36 (0.14)	
J161134.87+062239.3	DA	25.3	33,751 (404)	7.28 (0.08)	Pure H	0.37 (0.02)	0.0232 (0.0013)	−0.20 (0.05)	5.67 (0.41)	
J161143.45+520355.0	DA+M	14.3	50,167 (4849)	7.88 (0.36)	Pure H	0.63 (0.16)	0.0150 (0.0045)	0.11 (0.31)	6.30 (0.26)	1,2
J161143.86+205805.2	DAO	17.5	90,984 (11,864)	6.67 (0.26)	$\log N_{\rm He}/N_{\rm H} = -1.59$	0.42 (0.07)	0.0493 (0.0118)	2.18 (0.34)	<5.00	4
J161149.05+041937.8	DA	118.6	30,324 (53)	7.87 (0.01)	Pure H	0.58 (0.01)	0.0146 (0.0001)	−0.79 (0.01)	6.93 (0.01)	
J161208.84+175525.2	DA	7.1	52,401 (6668)	7.07 (0.45)	Pure H	0.37 (0.12)	0.0291 (0.0109)	0.76 (0.40)	<5.00	
J161210.90+084732.7	DA	31.5	30,183 (215)	7.70 (0.06)	Pure H	0.50 (0.02)	0.0166 (0.0007)	−0.68 (0.04)	6.90 (0.03)	
J161226.56+425111.4	DA	44.0	41,744 (521)	7.82 (0.05)	Pure H	0.58 (0.02)	0.0156 (0.0007)	−0.18 (0.04)	6.52 (0.02)	
J161244.37+054340.7	DA	18.9	33,716 (606)	7.73 (0.12)	Pure H	0.52 (0.05)	0.0164 (0.0014)	−0.50 (0.08)	6.76 (0.06)	
J161327.41+161826.3	DA	7.7	30,354 (870)	7.84 (0.22)	Pure H	0.57 (0.11)	0.0149 (0.0025)	−0.77 (0.15)	6.93 (0.07)	
J161342.71+572954.1	DA	20.9	48,823 (1617)	7.38 (0.12)	Pure H	0.44 (0.04)	0.0226 (0.0021)	0.42 (0.10)	5.09 (0.71)	
J161426.15+153222.3	DA	9.9	61,202 (6854)	7.55 (0.38)	Pure H	0.53 (0.13)	0.0204 (0.0067)	0.72 (0.35)	5.74 (0.73)	7
J161426.68+383052.5	DA	16.5	68,266 (5248)	7.95 (0.26)	Pure H	0.70 (0.11)	0.0146 (0.0033)	0.62 (0.24)	5.92 (0.11)	
J161441.98+370548.0	DAO	59.2	53,533 (1179)	7.64 (0.08)	$\log N_{\rm He}/N_{\rm H} = -3.24$	0.54 (0.03)	0.0184 (0.0012)	0.40 (0.07)	6.13 (0.09)	4,5
J161444.30+364612.2	DA	21.7	36,914 (719)	7.91 (0.10)	Pure H	0.62 (0.05)	0.0144 (0.0011)	−0.46 (0.08)	6.67 (0.03)	

Table 2.1 – Atmospheric and stellar parameters of hot white dwarfs from SDSS DR12 (continued)

SDSS Name	Type	S/N	$T_{\rm eff}$ (K)	$\log g$	Composition	$M/M_{\odot}$	$R/R_{\odot}$	$\log L/L_{\odot}$	$\log \tau_{\rm cool}$	Notes
J161455.15+414231.3	DA	6.3	34,704 (1527)	8.09 (0.27)	Pure H	0.70 (0.15)	0.0126 (0.0026)	−0.69 (0.19)	6.75 (0.12)	
J161512.21+110240.0	DOA	57.3	52,322 (603)	8.13 (0.09)	$\log q_{\rm H} = -16.95$	0.72 (0.05)	0.0121 (0.0008)	−0.01 (0.06)	6.27 (0.03)	3
J161613.09+252012.6	DA	27.4	80,075 (4860)	7.38 (0.17)	Pure H	0.54 (0.05)	0.0248 (0.0038)	1.36 (0.18)	<5.00	
J161809.53+112257.3	DA	19.4	65,680 (3294)	7.42 (0.16)	Pure H	0.50 (0.05)	0.0230 (0.0031)	0.95 (0.15)	<5.00	
J161815.53+154715.1	DAO	38.2	66,716 (4389)	7.21 (0.16)	$\log N_{\rm He}/N_{\rm H} = -1.12$	0.45 (0.04)	0.0277 (0.0040)	1.14 (0.18)	<5.00	4,5
J161843.23+294412.3	DA	5.3	36,219 (2343)	7.58 (0.36)	Pure H	0.47 (0.13)	0.0185 (0.0051)	−0.27 (0.26)	6.55 (0.35)	
J161844.39+432750.1	DA	17.3	31,342 (337)	7.63 (0.08)	Pure H	0.48 (0.03)	0.0176 (0.0011)	−0.57 (0.06)	6.80 (0.06)	
J161940.02+222958.3	DA	72.0	36,246 (216)	7.20 (0.03)	Pure H	0.35 (0.01)	0.0247 (0.0006)	−0.02 (0.02)	5.03 (0.16)	
J162005.03+114943.3	DA	64.2	34,368 (177)	7.85 (0.03)	Pure H	0.58 (0.02)	0.0150 (0.0004)	−0.55 (0.02)	6.76 (0.01)	
J162006.23+093129.1	DA	15.4	33,834 (676)	7.85 (0.13)	Pure H	0.58 (0.06)	0.0149 (0.0014)	−0.58 (0.09)	6.78 (0.03)	
J162027.38+145358.7	DA	4.5	30,406 (1308)	8.01 (0.34)	Pure H	0.65 (0.18)	0.0132 (0.0034)	−0.87 (0.23)	6.94 (0.19)	
J162125.86+155034.6	DA	16.8	36,811 (1117)	7.76 (0.16)	Pure H	0.55 (0.07)	0.0161 (0.0020)	−0.37 (0.12)	6.67 (0.08)	
J162130.17+232522.9	DA	14.9	34,348 (768)	7.82 (0.14)	Pure H	0.57 (0.06)	0.0153 (0.0016)	−0.53 (0.10)	6.76 (0.04)	
J162131.89+635118.3	DA	29.2	38,967 (697)	7.85 (0.09)	Pure H	0.59 (0.04)	0.0152 (0.0010)	−0.32 (0.07)	6.60 (0.02)	
J162145.79+173322.0	DA	7.2	46,699 (5029)	7.35 (0.42)	Pure H	0.43 (0.13)	0.0229 (0.0077)	0.35 (0.35)	5.06 (1.42)	
J162157.91+285933.6	DA	6.2	44,602 (4279)	7.62 (0.39)	Pure H	0.51 (0.15)	0.0183 (0.0057)	0.08 (0.32)	6.34 (0.30)	
J162251.73+231302.2	DA	22.2	34,313 (618)	7.88 (0.11)	Pure H	0.59 (0.05)	0.0147 (0.0012)	−0.57 (0.08)	6.76 (0.02)	
J162351.63+403211.3	DA	34.7	43,739 (1523)	7.71 (0.14)	Pure H	0.54 (0.06)	0.0170 (0.0020)	−0.02 (0.12)	6.44 (0.10)	2
J162420.68+474654.3	DA	27.7	38,544 (665)	7.59 (0.08)	Pure H	0.48 (0.03)	0.0185 (0.0013)	−0.17 (0.07)	6.47 (0.14)	
J162448.99+321702.0	DA+M	40.7	68,317 (1948)	7.57 (0.09)	Pure H	0.56 (0.03)	0.0204 (0.0016)	0.91 (0.09)	5.75 (0.20)	1,2
J162451.23+355128.0	DA	30.1	50,640 (1581)	7.68 (0.12)	Pure H	0.55 (0.04)	0.0178 (0.0017)	0.27 (0.10)	6.23 (0.13)	
J162452.46+150030.7	DA	20.2	60,091 (3709)	7.58 (0.21)	Pure H	0.54 (0.07)	0.0198 (0.0035)	0.66 (0.19)	5.86 (0.46)	
J162514.88+302610.8	DA	42.9	62,931 (1975)	7.67 (0.11)	Pure H	0.58 (0.04)	0.0184 (0.0017)	0.68 (0.10)	5.96 (0.10)	
J162540.54+231720.3	DA	36.4	40,290 (684)	7.77 (0.08)	Pure H	0.56 (0.03)	0.0162 (0.0010)	−0.21 (0.06)	6.56 (0.03)	
J162554.69+382600.8	DAO	26.2	68,670 (7093)	7.13 (0.27)	$\log N_{\rm He}/N_{\rm H} = -1.66$	0.44 (0.07)	0.0299 (0.0072)	1.25 (0.29)	<5.00	4,5
J162612.07+140132.1	DA	5.6	39,907 (3357)	7.04 (0.39)	Pure H	0.32 (0.10)	0.0281 (0.0087)	0.26 (0.31)	<5.00	
J162629.90+135614.5	DA	33.7	40,854 (688)	7.85 (0.08)	Pure H	0.59 (0.03)	0.0152 (0.0009)	−0.24 (0.06)	6.55 (0.02)	
J162644.18+091007.8	DA	6.2	31,460 (1441)	8.22 (0.34)	Pure H	0.77 (0.20)	0.0113 (0.0030)	−0.95 (0.24)	6.99 (0.30)	
J162648.55+232603.9	DA+M	28.2	42,705 (981)	7.75 (0.10)	Pure H	0.56 (0.04)	0.0164 (0.0013)	−0.09 (0.08)	6.48 (0.05)	1,2
J162711.08+111935.4	DA	10.1	35,549 (1085)	7.16 (0.18)	Pure H	0.34 (0.05)	0.0254 (0.0032)	−0.03 (0.12)	<5.00	
J162754.70+273646.3	DA	3.9	33,134 (2361)	7.46 (0.47)	Pure H	0.43 (0.17)	0.0201 (0.0072)	−0.36 (0.33)	6.49 (0.72)	
J162838.41+083329.0	DA	23.4	47,599 (1805)	7.78 (0.15)	Pure H	0.58 (0.06)	0.0162 (0.0019)	0.08 (0.12)	6.36 (0.07)	
J162845.71+315627.0	DAO	50.0	84,486 (4350)	7.07 (0.14)	$\log N_{\rm He}/N_{\rm H} = -2.06$	0.48 (0.03)	0.0333 (0.0045)	1.71 (0.16)	<5.00	4,5
J163014.61+165856.3	DO	19.9	49,322 (618)	7.83 (0.19)	Pure He	0.57 (0.08)	0.0152 (0.0022)	0.09 (0.13)	6.36 (0.03)	
J163150.83+212425.6	DA	42.1	37,263 (382)	7.70 (0.05)	Pure H	0.52 (0.02)	0.0169 (0.0007)	−0.31 (0.04)	6.63 (0.03)	
J163200.32−001928.3	DAO	17.9	67,367 (7810)	7.60 (0.37)	$\log N_{\rm He}/N_{\rm H} = -1.04$	0.57 (0.13)	0.0198 (0.0064)	0.86 (0.35)	5.82 (0.31)	4
J163230.54+263354.1	DA	17.3	74,466 (8309)	7.31 (0.27)	Pure H	0.49 (0.08)	0.0258 (0.0064)	1.26 (0.30)	<5.00	5
J163313.10+284215.0	DA	3.9	32,634 (1845)	7.51 (0.39)	Pure H	0.44 (0.14)	0.0194 (0.0057)	−0.42 (0.27)	6.61 (0.50)	
J163348.76+182448.6	DA	68.8	31,545 (110)	7.76 (0.03)	Pure H	0.53 (0.01)	0.0160 (0.0003)	−0.64 (0.02)	6.86 (0.01)	
J163350.80+150822.7	DA	17.7	40,495 (1304)	7.83 (0.15)	Pure H	0.58 (0.07)	0.0154 (0.0018)	−0.24 (0.11)	6.56 (0.05)	
J163421.39+313844.3	DA	31.9	79,205 (4017)	7.31 (0.14)	Pure H	0.51 (0.04)	0.0262 (0.0033)	1.39 (0.15)	<5.00	
J163429.28+113119.1	DA+M	17.7	37,838 (1286)	7.16 (0.17)	Pure H	0.34 (0.05)	0.0256 (0.0033)	0.08 (0.13)	<5.00	1
J163542.56+262257.7	DA	21.3	32,941 (432)	7.69 (0.09)	Pure H	0.51 (0.04)	0.0169 (0.0011)	−0.52 (0.06)	6.77 (0.05)	
J163555.13+111237.5	DA	28.9	35,555 (419)	7.61 (0.07)	Pure H	0.48 (0.02)	0.0180 (0.0009)	−0.33 (0.05)	6.61 (0.07)	
J163608.01+154456.9	DA	4.2	30,423 (1594)	7.40 (0.41)	Pure H	0.40 (0.13)	0.0209 (0.0063)	−0.47 (0.28)	6.49 (0.88)	
J163618.11+190725.1	DA	22.0	30,058 (252)	7.83 (0.07)	Pure H	0.56 (0.03)	0.0151 (0.0007)	−0.78 (0.05)	6.94 (0.02)	
J163618.65+412153.0	DAO	27.3	79,945 (7207)	6.78 (0.20)	$\log N_{\rm He}/N_{\rm H} = -2.21$	0.40 (0.05)	0.0428 (0.0076)	1.83 (0.24)	<5.00	4
J163649.99+132207.1	DA	5.7	35,557 (2418)	7.21 (0.39)	Pure H	0.36 (0.11)	0.0245 (0.0073)	−0.06 (0.28)	5.15 (1.27)	
J163725.02+140118.6	DA	8.5	38,282 (2297)	7.74 (0.30)	Pure H	0.54 (0.12)	0.0165 (0.0039)	−0.28 (0.23)	6.61 (0.15)	
J163757.58+190526.1	DBA	28.5	33,573 (1762)	8.53 (0.18)	$\log N_{\rm He}/N_{\rm H} = 1.12$	0.94 (0.11)	0.0088 (0.0013)	−1.06 (0.16)	7.38 (0.40)	9

Table 2.1 – Atmospheric and stellar parameters of hot white dwarfs from SDSS DR12 (continued)

SDSS Name	Type	S/N	$T_{\rm eff}$ (K)	$\log g$	Composition	$M/M_{\odot}$	$R/R_{\odot}$	$\log L/L_{\odot}$	$\log \tau_{\rm cool}$	Notes
J163800.36+004717.7	DA	13.9	63,273 (4402)	7.41 (0.23)	Pure H	0.49 (0.07)	0.0231 (0.0044)	0.89 (0.21)	<5.00	
J163820.36+331741.6	DA	4.4	31,269 (1707)	7.41 (0.40)	Pure H	0.40 (0.13)	0.0208 (0.0063)	−0.43 (0.28)	6.47 (0.85)	
J163826.30+350011.9	DA	115.6	37,850 (162)	7.96 (0.02)	Pure H	0.64 (0.01)	0.0139 (0.0002)	−0.45 (0.02)	6.63 (0.01)	
J163857.21+233531.4	DA	15.1	41,701 (1979)	7.81 (0.21)	Pure H	0.58 (0.09)	0.0156 (0.0026)	−0.18 (0.17)	6.52 (0.11)	
J163910.11+315947.3	DAO	41.4	65,496 (3244)	7.00 (0.13)	$\log N_{\rm He}/N_{\rm H} = -2.55$	0.40 (0.03)	0.0330 (0.0038)	1.26 (0.14)	<5.00	4,5
J163935.98+252747.9	DA	3.7	33,667 (2687)	8.08 (0.52)	Pure H	0.70 (0.27)	0.0126 (0.0051)	−0.73 (0.38)	6.80 (0.39)	
J163943.60+112419.8	DA	5.0	34,579 (2307)	7.56 (0.41)	Pure H	0.46 (0.15)	0.0187 (0.0058)	−0.35 (0.29)	6.59 (0.39)	
J164000.77+403810.5	DA	7.3	34,670 (1437)	7.71 (0.25)	Pure H	0.52 (0.10)	0.0166 (0.0032)	−0.44 (0.18)	6.72 (0.12)	
J164205.84+382218.1	DA+M	24.1	41,980 (1078)	7.66 (0.11)	Pure H	0.52 (0.04)	0.0176 (0.0016)	−0.06 (0.09)	6.45 (0.13)	1
J164207.36+392753.1	DA	18.4	40,642 (1130)	7.83 (0.13)	Pure H	0.59 (0.06)	0.0154 (0.0015)	−0.23 (0.10)	6.55 (0.04)	
J164224.69+231359.4	DA	53.6	35,719 (256)	7.77 (0.04)	Pure H	0.55 (0.02)	0.0159 (0.0005)	−0.43 (0.03)	6.70 (0.01)	
J164235.82+301900.3	DA	25.0	30,449 (302)	7.28 (0.08)	Pure H	0.36 (0.02)	0.0228 (0.0013)	−0.39 (0.05)	5.97 (0.37)	
J164336.39+233220.5	DA	6.8	30,772 (926)	7.75 (0.23)	Pure H	0.52 (0.10)	0.0161 (0.0028)	−0.68 (0.16)	6.89 (0.10)	
J164401.10+501333.9	DOZ	37.8	64,353 (1493)	7.90 (0.15)	Pure He	0.62 (0.06)	0.0147 (0.0018)	0.53 (0.11)	6.07 (0.06)	6
J164424.24+382830.5	DA	72.7	46,402 (454)	7.55 (0.04)	Pure H	0.49 (0.01)	0.0196 (0.0006)	0.20 (0.03)	6.10 (0.13)	
J164444.56+133125.8	DA	4.0	32,488 (1670)	7.85 (0.36)	Pure H	0.58 (0.17)	0.0149 (0.0040)	−0.65 (0.25)	6.83 (0.18)	
J164453.28+401622.5	DA	38.9	60,691 (2201)	7.33 (0.11)	Pure H	0.46 (0.04)	0.0242 (0.0022)	0.86 (0.11)	<5.00	5
J164459.09+382744.5	DA	17.7	34,102 (571)	7.25 (0.11)	Pure H	0.37 (0.03)	0.0236 (0.0018)	−0.17 (0.07)	5.50 (0.53)	
J164610.76+443321.7	DA	30.7	57,040 (2484)	7.46 (0.14)	Pure H	0.49 (0.05)	0.0217 (0.0024)	0.65 (0.13)	5.39 (0.90)	5
J164622.01+132107.9	DA	8.5	41,223 (2953)	7.86 (0.32)	Pure H	0.60 (0.15)	0.0151 (0.0038)	−0.22 (0.25)	6.54 (0.19)	
J164649.56+120547.0	DA	17.0	83,567 (9930)	7.93 (0.38)	Pure H	0.72 (0.15)	0.0152 (0.0053)	1.01 (0.37)	5.65 (0.27)	
J164703.43+245129.1	DB	6.9	30,642 (2519)	7.96 (0.30)	Pure He	0.60 (0.16)	0.0134 (0.0029)	−0.85 (0.24)	6.97 (0.17)	
J164746.26+131923.4	DA+M	30.2	34,018 (365)	7.84 (0.07)	Pure H	0.57 (0.03)	0.0151 (0.0008)	−0.56 (0.05)	6.77 (0.02)	1
J164927.24+212726.0	DA	16.9	36,849 (823)	7.55 (0.12)	Pure H	0.47 (0.04)	0.0190 (0.0018)	−0.22 (0.09)	6.47 (0.24)	
J164947.18+262409.7	DA	71.8	42,596 (341)	7.76 (0.03)	Pure H	0.56 (0.01)	0.0164 (0.0004)	−0.10 (0.03)	6.49 (0.01)	
J165005.16+390426.3	DA+M	21.9	30,196 (324)	7.76 (0.08)	Pure H	0.53 (0.04)	0.0158 (0.0010)	−0.73 (0.06)	6.92 (0.03)	1,2
J165008.22+370110.3	DA	99.7	41,468 (252)	7.81 (0.03)	Pure H	0.58 (0.01)	0.0157 (0.0003)	−0.18 (0.02)	6.53 (0.01)	
J165012.48+112457.1	DA	27.6	47,726 (2000)	7.15 (0.16)	Pure H	0.37 (0.04)	0.0268 (0.0035)	0.53 (0.14)	<5.00	
J165020.06+403722.6	DA	131.4	39,690 (137)	7.89 (0.02)	Pure H	0.61 (0.01)	0.0147 (0.0002)	−0.32 (0.01)	6.58 (0.01)	
J165029.79+275002.4	DA	20.1	36,442 (778)	7.87 (0.12)	Pure H	0.59 (0.06)	0.0148 (0.0013)	−0.46 (0.09)	6.69 (0.03)	
J165041.51+121544.0	DA	8.9	31,430 (1115)	7.89 (0.31)	Pure H	0.59 (0.15)	0.0145 (0.0034)	−0.74 (0.21)	6.88 (0.12)	
J165048.37+184513.6	DAO	28.5	47,817 (1806)	7.57 (0.15)	$\log N_{\rm He}/N_{\rm H} = -1.62$	0.50 (0.05)	0.0193 (0.0024)	0.25 (0.13)	6.13 (0.41)	4
J165102.23+341254.7	DA+M	15.8	30,601 (467)	7.96 (0.12)	Pure H	0.63 (0.06)	0.0137 (0.0012)	−0.83 (0.08)	6.92 (0.03)	1
J165112.42+415139.2	DA+M	9.7	56,743 (6343)	7.63 (0.39)	Pure H	0.55 (0.15)	0.0188 (0.0061)	0.52 (0.35)	6.03 (0.38)	1
J165144.32+324948.7	DA	30.0	40,457 (725)	7.72 (0.08)	Pure H	0.54 (0.03)	0.0168 (0.0011)	−0.17 (0.06)	6.53 (0.05)	
J165148.74+261530.9	DA	48.7	44,135 (612)	7.87 (0.06)	Pure H	0.61 (0.03)	0.0150 (0.0007)	−0.11 (0.05)	6.45 (0.02)	
J165149.80+295600.7	DA+M	9.8	33,273 (908)	7.62 (0.18)	Pure H	0.48 (0.07)	0.0177 (0.0025)	−0.46 (0.13)	6.72 (0.18)	1
J165156.67+250756.4	DA	4.9	33,202 (2120)	7.68 (0.42)	Pure H	0.50 (0.17)	0.0170 (0.0056)	−0.50 (0.30)	6.76 (0.22)	
J165219.80+364110.6	DA	24.7	36,011 (528)	7.95 (0.08)	Pure H	0.63 (0.04)	0.0140 (0.0009)	−0.53 (0.06)	6.70 (0.02)	
J165226.16+323239.3	DA	28.0	30,580 (255)	7.22 (0.07)	Pure H	0.34 (0.02)	0.0239 (0.0011)	−0.34 (0.04)	5.63 (0.30)	
J165249.28+384123.2	DA	71.0	39,646 (270)	7.88 (0.03)	Pure H	0.60 (0.02)	0.0148 (0.0004)	−0.31 (0.02)	6.58 (0.01)	
J165327.71+273022.1	DA	30.9	31,196 (275)	7.82 (0.07)	Pure H	0.56 (0.03)	0.0152 (0.0007)	−0.70 (0.05)	6.89 (0.02)	
J165520.68+242456.7	DA	9.0	47,842 (3647)	7.77 (0.29)	Pure H	0.58 (0.12)	0.0164 (0.0039)	0.10 (0.25)	6.35 (0.23)	
J165521.62+270248.7	DA	7.2	78,676 (19,918)	6.70 (0.53)	Pure H	0.38 (0.13)	0.0456 (0.0215)	1.86 (0.66)	<5.00	
J165523.06+223552.4	DA	27.5	50,683 (1763)	7.63 (0.13)	Pure H	0.53 (0.04)	0.0185 (0.0020)	0.31 (0.11)	6.19 (0.19)	
J165559.11+341707.4	DA	16.9	34,136 (601)	7.85 (0.11)	Pure H	0.58 (0.05)	0.0150 (0.0012)	−0.56 (0.08)	6.77 (0.03)	
J165605.35+122045.3	DA	25.2	42,818 (1282)	7.62 (0.12)	Pure H	0.51 (0.04)	0.0183 (0.0017)	0.01 (0.10)	6.37 (0.21)	7
J165640.80+211812.8	DA+M	32.5	46,740 (1152)	7.48 (0.10)	Pure H	0.47 (0.03)	0.0208 (0.0016)	0.27 (0.08)	5.78 (0.47)	1,2
J165750.21+390914.6	DA	10.6	36,344 (1673)	7.68 (0.25)	Pure H	0.51 (0.10)	0.0172 (0.0034)	−0.33 (0.19)	6.64 (0.15)	
J165851.11+341853.3	DA	74.2	52,153 (644)	7.78 (0.04)	Pure H	0.59 (0.02)	0.0165 (0.0006)	0.26 (0.04)	6.24 (0.02)	

Table 2.1 – Atmospheric and stellar parameters of hot white dwarfs from SDSS DR12 (continued)

SDSS Name	Type	S/N	$T_{\rm eff}$ (K)	$\log g$	Composition	$M/M_{\odot}$	$R/R_{\odot}$	$\log L/L_{\odot}$	$\log \tau_{\rm cool}$	Notes
J165920.95+235959.8	DAO	30.0	64,265 (3790)	7.06 (0.19)	$\log N_{\rm He}/N_{\rm H} = -1.90$	0.40 (0.04)	0.0312 (0.0051)	1.17 (0.18)	<5.00	4
J165944.10+454557.7	DA	37.7	71,848 (2848)	7.19 (0.12)	Pure H	0.46 (0.02)	0.0286 (0.0031)	1.29 (0.12)	<5.00	
J170103.66+362613.7	DA	7.4	68,336 (9936)	7.90 (0.49)	Pure H	0.68 (0.21)	0.0152 (0.0065)	0.66 (0.45)	5.92 (0.46)	
J170117.67+232026.2	DA	17.3	45,102 (2010)	7.64 (0.18)	Pure H	0.52 (0.06)	0.0180 (0.0026)	0.08 (0.15)	6.35 (0.19)	
J170145.26+190400.4	DA	6.6	32,193 (1135)	7.50 (0.25)	Pure H	0.43 (0.08)	0.0195 (0.0037)	−0.43 (0.18)	6.61 (0.45)	
J170158.21+294639.1	DA	25.7	36,606 (520)	7.79 (0.08)	Pure H	0.56 (0.03)	0.0157 (0.0009)	−0.40 (0.06)	6.68 (0.02)	
J170227.48+455723.8	DA	33.7	37,744 (494)	7.83 (0.07)	Pure H	0.58 (0.03)	0.0153 (0.0008)	−0.37 (0.05)	6.64 (0.02)	
J170239.45+373131.4	DA	27.3	33,438 (367)	7.57 (0.07)	Pure H	0.46 (0.02)	0.0185 (0.0010)	−0.41 (0.05)	6.65 (0.09)	
J170404.97+414109.5	DAO	47.0	42,838 (765)	7.04 (0.08)	$\log N_{\rm He}/N_{\rm H} = -2.11$	0.33 (0.02)	0.0287 (0.0019)	0.40 (0.07)	<5.00	4
J170445.60+291545.9	DA	50.7	41,421 (487)	7.72 (0.05)	Pure H	0.54 (0.02)	0.0168 (0.0007)	−0.13 (0.04)	6.51 (0.03)	
J170508.82+212019.2	DAO	61.7	47,256 (661)	7.69 (0.06)	$\log N_{\rm He}/N_{\rm H} = -2.50$	0.54 (0.02)	0.0175 (0.0008)	0.14 (0.05)	6.33 (0.04)	4,5
J170517.86+334507.5	DA	18.5	37,703 (1128)	7.11 (0.15)	Pure H	0.33 (0.04)	0.0266 (0.0031)	0.11 (0.11)	<5.00	
J170522.49+272650.6	DA	18.6	81,503 (7888)	7.03 (0.23)	Pure H	0.46 (0.06)	0.0343 (0.0074)	1.67 (0.27)	<5.00	
J170530.81+271523.2	DA	46.3	37,236 (313)	7.87 (0.04)	Pure H	0.60 (0.02)	0.0148 (0.0005)	−0.42 (0.03)	6.66 (0.01)	
J170609.90+351543.5	DAO	22.1	68,696 (7263)	7.14 (0.27)	$\log N_{\rm He}/N_{\rm H} = -2.49$	0.44 (0.07)	0.0295 (0.0073)	1.24 (0.30)	<5.00	4,5
J170630.79+232813.6	DA	22.8	68,015 (3843)	7.15 (0.17)	Pure H	0.44 (0.04)	0.0292 (0.0044)	1.22 (0.17)	<5.00	
J170723.85+450009.9	DOZ	24.1	67,602 (2648)	7.80 (0.25)	Pure He	0.59 (0.10)	0.0160 (0.0033)	0.68 (0.19)	5.98 (0.11)	6
J170727.10+203153.2	DB	28.0	42,389 (794)	7.76 (0.08)	Pure He	0.53 (0.03)	0.0158 (0.0009)	−0.14 (0.06)	6.51 (0.07)	
J170843.55+274921.1	DA	32.4	31,467 (236)	7.86 (0.05)	Pure H	0.58 (0.03)	0.0148 (0.0006)	−0.71 (0.04)	6.88 (0.01)	
J171113.24+584719.3	DA	11.8	56,983 (4339)	7.80 (0.27)	Pure H	0.61 (0.11)	0.0162 (0.0037)	0.40 (0.24)	6.14 (0.20)	
J171125.54+272405.1	DA	44.8	47,076 (845)	7.62 (0.07)	Pure H	0.52 (0.02)	0.0185 (0.0011)	0.18 (0.06)	6.27 (0.12)	
J171145.43+555444.3	DA+M	26.1	34,759 (439)	7.65 (0.08)	Pure H	0.50 (0.03)	0.0174 (0.0010)	−0.40 (0.06)	6.68 (0.06)	1,2
J171155.00+324712.1	DA	28.9	50,641 (1527)	7.69 (0.12)	Pure H	0.55 (0.04)	0.0176 (0.0017)	0.26 (0.10)	6.24 (0.11)	5
J171156.07+324233.4	DA	15.3	62,367 (4378)	7.90 (0.24)	Pure H	0.66 (0.10)	0.0152 (0.0031)	0.50 (0.22)	6.03 (0.10)	
J171431.62+425634.9	DA	5.8	31,083 (1255)	7.23 (0.30)	Pure H	0.35 (0.09)	0.0238 (0.0053)	−0.32 (0.21)	5.63 (1.07)	
J171441.07+552711.3	DA	5.6	36,897 (3232)	7.18 (0.47)	Pure H	0.35 (0.13)	0.0250 (0.0091)	0.02 (0.35)	<5.00	
J171505.81+271457.0	DA	13.1	30,295 (499)	7.66 (0.13)	Pure H	0.49 (0.05)	0.0171 (0.0017)	−0.65 (0.09)	6.87 (0.08)	
J171530.68+271431.0	DA	16.3	39,028 (1087)	7.54 (0.13)	Pure H	0.47 (0.04)	0.0192 (0.0021)	−0.11 (0.11)	6.37 (0.31)	
J171600.52+422131.1	DO	18.6	119,695 (5765)	7.72 (0.60)	Pure He	0.67 (0.19)	0.0187 (0.0108)	1.81 (0.48)	<5.00	
J171639.76+582134.1	DA	10.2	32,734 (761)	7.84 (0.16)	Pure H	0.57 (0.07)	0.0150 (0.0018)	−0.63 (0.11)	6.82 (0.04)	
J171703.92+413557.3	DA	11.9	32,431 (625)	7.83 (0.13)	Pure H	0.56 (0.06)	0.0152 (0.0015)	−0.64 (0.09)	6.84 (0.04)	
J171720.52+373605.9	DOZ	41.2	62,750 (1520)	8.18 (0.15)	Pure He	0.76 (0.08)	0.0117 (0.0014)	0.28 (0.11)	6.03 (0.06)	6
J171810.89+382754.5	DA	25.1	46,689 (1687)	7.45 (0.14)	Pure H	0.46 (0.05)	0.0213 (0.0023)	0.29 (0.12)	5.61 (0.70)	
J171831.24+280825.6	DA	5.1	50,169 (7511)	7.33 (0.55)	Pure H	0.43 (0.17)	0.0236 (0.0108)	0.50 (0.48)	<5.00	
J171907.09+390449.2	DA	29.1	43,552 (980)	7.99 (0.09)	Pure H	0.67 (0.05)	0.0137 (0.0010)	−0.22 (0.08)	6.45 (0.03)	
J172016.85+422934.0	DA	6.5	44,193 (4012)	7.51 (0.37)	Pure H	0.48 (0.13)	0.0200 (0.0059)	0.14 (0.30)	6.05 (0.89)	
J172102.37+541448.4	DA	10.9	54,200 (4323)	7.30 (0.28)	Pure H	0.43 (0.08)	0.0243 (0.0056)	0.66 (0.25)	<5.00	
J172109.99+583223.2	DA	9.7	70,475 (8539)	7.19 (0.36)	Pure H	0.46 (0.10)	0.0285 (0.0091)	1.26 (0.36)	<5.00	
J172132.02+324209.5	DA	11.1	30,846 (669)	7.04 (0.17)	Pure H	0.29 (0.04)	0.0270 (0.0033)	−0.22 (0.11)	<5.00	
J172211.68+281538.7	DA	42.8	46,294 (712)	7.74 (0.06)	Pure H	0.56 (0.02)	0.0168 (0.0008)	0.07 (0.05)	6.38 (0.03)	
J172255.94+294234.1	DA	9.1	36,992 (1788)	6.87 (0.26)	Pure H	0.27 (0.06)	0.0319 (0.0064)	0.23 (0.20)	<5.00	
J172406.13+562003.0	DA+M	47.9	34,733 (498)	7.22 (0.09)	Pure H	0.36 (0.03)	0.0243 (0.0015)	−0.11 (0.06)	5.25 (0.42)	1,2
J172415.07+254817.5	DA	34.3	37,187 (451)	7.70 (0.06)	Pure H	0.52 (0.03)	0.0169 (0.0008)	−0.31 (0.05)	6.63 (0.04)	
J172505.57+312909.4	DB	18.1	41,819 (1228)	7.83 (0.15)	Pure He	0.55 (0.07)	0.0149 (0.0017)	−0.21 (0.11)	6.56 (0.07)	
J172643.38+583732.1	DA	86.1	58,634 (767)	8.43 (0.05)	Pure H	0.93 (0.03)	0.0098 (0.0004)	0.01 (0.04)	5.98 (0.02)	
J172649.42+530640.9	DA	14.4	30,748 (497)	7.47 (0.12)	Pure H	0.42 (0.04)	0.0198 (0.0019)	−0.50 (0.09)	6.66 (0.27)	
J172656.57+441143.2	DAO	7.0	67,643 (14,541)	7.58 (0.75)	$\log N_{\rm He}/N_{\rm H} = -1.34$	0.56 (0.26)	0.0201 (0.0139)	0.88 (0.69)	5.79 (0.55)	4
J172704.99+084857.1	DA	31.1	41,516 (775)	7.97 (0.08)	Pure H	0.66 (0.04)	0.0138 (0.0009)	−0.29 (0.06)	6.52 (0.02)	
J172744.57+585415.2	DA+M	7.5	32,291 (1003)	7.76 (0.22)	Pure H	0.53 (0.09)	0.0159 (0.0026)	−0.60 (0.15)	6.83 (0.09)	1
J172822.31+324521.2	DA	28.4	30,721 (247)	7.78 (0.06)	Pure H	0.54 (0.03)	0.0157 (0.0007)	−0.70 (0.04)	6.90 (0.02)	

Table 2.1 – Atmospheric and stellar parameters of hot white dwarfs from SDSS DR12 (continued)

SDSS Name	Type	S/N	$T_{\rm eff}$ (K)	$\log g$	Composition	$M/M_{\odot}$	$R/R_{\odot}$	$\log L/L_{\odot}$	$\log \tau_{\rm cool}$	Notes
J172858.96+441217.6	DA	6.2	38,033 (2437)	7.15 (0.32)	Pure H	0.34 (0.09)	0.0256 (0.0064)	0.09 (0.24)	<5.00	
J172950.36+581808.6	DA	11.8	84,398 (12,253)	7.79 (0.45)	Pure H	0.67 (0.17)	0.0172 (0.0072)	1.13 (0.44)	5.59 (0.51)	
J173003.89+572939.9	DA	6.4	36,146 (2184)	7.87 (0.34)	Pure H	0.59 (0.16)	0.0148 (0.0038)	−0.47 (0.25)	6.70 (0.16)	
J173053.86+350830.4	DA	32.3	61,590 (2506)	7.08 (0.13)	Pure H	0.40 (0.03)	0.0303 (0.0034)	1.07 (0.13)	<5.00	
J173109.86+090040.7	DA	18.7	32,913 (556)	7.65 (0.11)	Pure H	0.49 (0.04)	0.0173 (0.0015)	−0.50 (0.08)	6.76 (0.09)	
J173404.59+584954.9	DA	4.4	33,292 (1950)	7.56 (0.38)	Pure H	0.46 (0.14)	0.0187 (0.0055)	−0.41 (0.27)	6.65 (0.37)	
J173440.52+321540.3	DA	6.2	33,153 (1487)	8.04 (0.30)	Pure H	0.68 (0.16)	0.0129 (0.0029)	−0.74 (0.21)	6.81 (0.14)	
J173444.92+335629.6	DA+M	10.5	34,365 (1028)	7.57 (0.18)	Pure H	0.47 (0.07)	0.0185 (0.0027)	−0.36 (0.14)	6.61 (0.28)	1
J173455.32+650823.5	DA	38.9	31,952 (181)	7.84 (0.04)	Pure H	0.57 (0.02)	0.0150 (0.0005)	−0.68 (0.03)	6.86 (0.01)	
J173502.25+640155.1	DA	35.1	67,900 (2639)	7.31 (0.12)	Pure H	0.48 (0.03)	0.0253 (0.0027)	1.09 (0.12)	<5.00	
J173656.14+582344.6	DA	9.7	54,019 (5014)	7.34 (0.32)	Pure H	0.44 (0.10)	0.0234 (0.0064)	0.62 (0.29)	<5.00	
J173726.07+450223.2	DA	14.8	30,830 (370)	8.51 (0.09)	Pure H	0.95 (0.06)	0.0090 (0.0007)	−1.18 (0.07)	7.60 (0.17)	
J173824.63+581801.6	DO	13.1	60,125 (7838)	8.19 (0.81)	Pure He	0.76 (0.39)	0.0116 (0.0081)	0.20 (0.63)	6.08 (0.90)	
J173842.22+645534.2	DA	62.6	30,331 (103)	7.85 (0.03)	Pure H	0.57 (0.01)	0.0148 (0.0003)	−0.78 (0.02)	6.93 (0.01)	
J174048.41+252305.9	DAO	11.3	82,266 (13,812)	7.66 (0.49)	$\log N_{\rm He}/N_{\rm H} = -1.38$	0.62 (0.16)	0.0194 (0.0087)	1.19 (0.49)	5.53 (0.65)	4
J174102.64+533600.4	DA	9.4	31,447 (894)	7.71 (0.21)	Pure H	0.51 (0.09)	0.0166 (0.0026)	−0.62 (0.15)	6.84 (0.11)	
J174327.81+244118.0	DA	12.7	60,828 (6023)	7.49 (0.33)	Pure H	0.51 (0.11)	0.0214 (0.0060)	0.75 (0.30)	5.49 (1.16)	
J174436.68+264522.5	DA	17.0	31,512 (422)	8.02 (0.10)	Pure H	0.66 (0.05)	0.0131 (0.0010)	−0.82 (0.07)	6.89 (0.03)	
J180234.54+243358.1	DA	13.8	45,632 (2160)	7.84 (0.19)	Pure H	0.60 (0.08)	0.0155 (0.0023)	−0.03 (0.16)	6.41 (0.08)	
J181107.25+225901.6	DA	4.3	35,015 (2654)	8.12 (0.45)	Pure H	0.72 (0.25)	0.0123 (0.0043)	−0.69 (0.33)	6.74 (0.25)	
J181424.12+785402.9	DA	63.8	31,505 (116)	7.81 (0.03)	Pure H	0.55 (0.01)	0.0154 (0.0003)	−0.68 (0.02)	6.87 (0.01)	
J182509.24+775535.3	DA	80.2	81,049 (2376)	7.43 (0.07)	Pure H	0.56 (0.02)	0.0237 (0.0015)	1.34 (0.08)	5.04 (0.35)	5
J183329.18+643151.7	DA+M	25.5	42,894 (2379)	7.38 (0.23)	Pure H	0.43 (0.08)	0.0222 (0.0040)	0.18 (0.19)	5.50 (1.04)	1,2
J183337.45+404027.2	DA+M	30.7	44,616 (1053)	7.86 (0.10)	Pure H	0.61 (0.04)	0.0152 (0.0012)	−0.08 (0.08)	6.44 (0.03)	1
J183458.78+410734.2	DA	17.8	35,156 (740)	7.58 (0.12)	Pure H	0.47 (0.04)	0.0185 (0.0018)	−0.33 (0.09)	6.59 (0.19)	
J183812.40+410836.0	DA	15.7	40,998 (1386)	7.99 (0.15)	Pure H	0.66 (0.08)	0.0136 (0.0016)	−0.33 (0.12)	6.53 (0.04)	
J184117.99+410628.3	DA	14.1	30,835 (588)	7.60 (0.14)	Pure H	0.47 (0.05)	0.0179 (0.0020)	−0.58 (0.10)	6.80 (0.14)	2
J184414.59+414738.7	DA	28.2	52,903 (1775)	7.58 (0.12)	Pure H	0.52 (0.04)	0.0194 (0.0020)	0.42 (0.11)	6.06 (0.26)	2
J192056.80+372118.0	DA	46.0	32,682 (201)	8.12 (0.04)	Pure H	0.72 (0.02)	0.0122 (0.0004)	−0.82 (0.03)	6.85 (0.02)	2
J195403.76+773435.8	DA	12.2	41,397 (2263)	7.41 (0.24)	Pure H	0.43 (0.08)	0.0216 (0.0040)	0.09 (0.19)	5.76 (1.00)	
J200646.49−124410.9	DA	52.2	150,000 (7500)	6.75 (0.06)	Pure H	0.64 (0.03)	0.0556 (0.0037)	3.15 (0.12)	<5.00	
J200909.77−114427.3	DA	74.6	62,879 (1039)	7.62 (0.05)	Pure H	0.56 (0.02)	0.0193 (0.0009)	0.72 (0.05)	5.90 (0.10)	
J200940.55+772345.9	DA	21.9	30,524 (346)	7.60 (0.09)	Pure H	0.46 (0.03)	0.0179 (0.0012)	−0.60 (0.06)	6.82 (0.07)	
J201034.26−112537.9	DA	29.1	38,718 (727)	7.24 (0.09)	Pure H	0.37 (0.03)	0.0242 (0.0015)	0.08 (0.07)	5.02 (0.49)	
J201047.04+781013.8	DA+M	7.0	38,068 (2667)	7.30 (0.35)	Pure H	0.39 (0.11)	0.0232 (0.0062)	0.01 (0.27)	5.42 (1.19)	1
J201322.14+762643.1	DA	12.8	30,522 (564)	7.61 (0.14)	Pure H	0.47 (0.05)	0.0178 (0.0019)	−0.61 (0.10)	6.83 (0.12)	
J202253.34+141153.1	DA	34.2	43,044 (725)	7.77 (0.07)	Pure H	0.57 (0.03)	0.0162 (0.0009)	−0.09 (0.06)	6.48 (0.03)	
J202404.12+131547.3	DA	22.8	35,357 (610)	7.63 (0.10)	Pure H	0.49 (0.04)	0.0178 (0.0014)	−0.35 (0.07)	6.64 (0.10)	
J202434.11+140536.6	DA	6.6	47,769 (5723)	7.24 (0.45)	Pure H	0.39 (0.13)	0.0249 (0.0093)	0.46 (0.39)	<5.00	
J202558.22+145402.3	DA	10.8	38,477 (1958)	6.89 (0.25)	Pure H	0.28 (0.05)	0.0316 (0.0063)	0.29 (0.20)	<5.00	
J202818.28+762232.7	DO	16.9	120,634 (6347)	7.90 (0.68)	Pure He	0.72 (0.24)	0.0158 (0.0105)	1.68 (0.54)	5.06 (0.55)	
J203153.90+140602.7	DA+M	21.5	60,333 (2942)	7.40 (0.16)	Pure H	0.48 (0.05)	0.0230 (0.0030)	0.80 (0.15)	<5.00	1
J203511.97+133212.7	DA	14.2	36,173 (1175)	7.95 (0.18)	Pure H	0.63 (0.09)	0.0140 (0.0019)	−0.52 (0.13)	6.69 (0.04)	
J203512.62+145640.1	DA+M	21.1	42,819 (1389)	7.82 (0.14)	Pure H	0.59 (0.06)	0.0156 (0.0017)	−0.13 (0.11)	6.49 (0.05)	1
J203624.84+774903.9	DA	20.2	49,812 (2466)	7.88 (0.19)	Pure H	0.63 (0.08)	0.0151 (0.0023)	0.10 (0.16)	6.31 (0.07)	
J203652.53+141323.7	DA	13.9	35,041 (834)	7.75 (0.14)	Pure H	0.54 (0.06)	0.0162 (0.0017)	−0.45 (0.10)	6.72 (0.06)	
J203658.52−054728.7	DA	15.7	35,652 (799)	7.55 (0.13)	Pure H	0.46 (0.04)	0.0190 (0.0019)	−0.28 (0.10)	6.52 (0.24)	
J203722.16−051303.0	DA	11.6	38,813 (1593)	7.85 (0.20)	Pure H	0.59 (0.09)	0.0151 (0.0023)	−0.33 (0.15)	6.61 (0.07)	
J204111.84+002053.6	DA	5.3	30,458 (1047)	8.21 (0.27)	Pure H	0.77 (0.16)	0.0114 (0.0024)	−0.99 (0.19)	7.05 (0.30)	
J204158.97+000325.4	DO	20.9	79,003 (6716)	7.56 (0.37)	Pure He	0.53 (0.12)	0.0199 (0.0063)	1.14 (0.32)	<5.00	

Table 2.1 – Atmospheric and stellar parameters of hot white dwarfs from SDSS DR12 (continued)

SDSS Name	Type	S/N	$T_{\rm eff}$ (K)	$\log g$	Composition	$M/M_{\odot}$	$R/R_{\odot}$	$\log L/L_{\odot}$	$\log \tau_{\rm cool}$	Notes
J204415.26−010115.9	DA	9.9	31,007 (789)	7.43 (0.19)	Pure H	0.41 (0.06)	0.0205 (0.0030)	−0.46 (0.14)	6.55 (0.54)	
J204420.37+153852.6	DA	9.7	30,230 (1127)	8.24 (0.36)	Pure H	0.79 (0.21)	0.0111 (0.0031)	−1.03 (0.25)	7.12 (0.42)	
J204558.62−005832.3	DA	13.6	45,083 (1887)	7.95 (0.17)	Pure H	0.65 (0.08)	0.0142 (0.0019)	−0.12 (0.14)	6.42 (0.05)	
J204723.36+001245.1	DA	15.3	39,134 (999)	7.82 (0.12)	Pure H	0.58 (0.05)	0.0155 (0.0015)	−0.29 (0.09)	6.60 (0.04)	
J205054.88+161208.4	DA	9.2	50,049 (3985)	8.02 (0.30)	Pure H	0.70 (0.15)	0.0135 (0.0033)	0.01 (0.25)	6.28 (0.11)	
J205440.40+154816.5	DA	42.7	31,711 (174)	7.86 (0.04)	Pure H	0.58 (0.02)	0.0148 (0.0004)	−0.70 (0.03)	6.87 (0.01)	
J205749.78−001818.3	DA	12.8	32,547 (726)	7.65 (0.15)	Pure H	0.49 (0.06)	0.0173 (0.0020)	−0.52 (0.11)	6.77 (0.12)	
J205808.00+003156.4	DA	10.8	50,862 (3156)	7.78 (0.23)	Pure H	0.59 (0.09)	0.0164 (0.0031)	0.21 (0.20)	6.27 (0.17)	
J205930.25−052848.9	DAO	22.9	91,480 (8973)	7.31 (0.30)	$\log N_{\rm He}/N_{\rm H} = -1.32$	0.55 (0.08)	0.0272 (0.0079)	1.67 (0.31)	<5.00	4,5
J210402.30+000410.9	DA	21.9	34,478 (461)	7.77 (0.08)	Pure H	0.54 (0.04)	0.0159 (0.0010)	−0.49 (0.06)	6.75 (0.03)	
J210402.49+104754.7	DA	15.1	48,255 (2237)	7.91 (0.18)	Pure H	0.64 (0.08)	0.0147 (0.0021)	0.02 (0.15)	6.34 (0.06)	
J210702.29−064757.5	DA+M	15.4	32,887 (702)	7.62 (0.14)	Pure H	0.48 (0.05)	0.0178 (0.0020)	−0.48 (0.10)	6.73 (0.14)	1
J210739.32+004253.4	DA	9.6	33,827 (1015)	7.22 (0.19)	Pure H	0.35 (0.06)	0.0242 (0.0034)	−0.16 (0.13)	5.33 (0.83)	
J210829.59+003116.0	DA	31.1	30,447 (203)	8.27 (0.05)	Pure H	0.80 (0.03)	0.0109 (0.0004)	−1.04 (0.04)	7.14 (0.09)	
J210928.32−053843.2	DA	36.5	39,261 (584)	7.70 (0.07)	Pure H	0.53 (0.03)	0.0169 (0.0009)	−0.21 (0.06)	6.56 (0.05)	
J211043.24+093756.8	DA+M	15.7	30,189 (397)	7.84 (0.10)	Pure H	0.57 (0.05)	0.0149 (0.0011)	−0.78 (0.07)	6.93 (0.02)	1
J211056.57+102015.7	DA	12.2	76,120 (9319)	6.93 (0.34)	Pure H	0.42 (0.08)	0.0368 (0.0113)	1.61 (0.36)	<5.00	7
J211149.59−053938.3	DBA	9.7	36,930 (4070)	7.87 (0.35)	$\log N_{\rm He}/N_{\rm H} = 1.23$	0.56 (0.16)	0.0144 (0.0038)	−0.46 (0.30)	6.71 (0.31)	4
J211507.83+103006.9	DA	11.4	36,160 (1167)	7.39 (0.18)	Pure H	0.41 (0.06)	0.0215 (0.0029)	−0.15 (0.13)	6.05 (0.72)	
J211711.78+112304.2	DO	4.3	47,965 (4350)	7.70 (0.85)	Pure He	0.51 (0.36)	0.0167 (0.0113)	0.12 (0.58)	6.29 (0.26)	
J211742.25−060810.2	DA	23.5	36,789 (657)	8.42 (0.10)	Pure H	0.90 (0.06)	0.0097 (0.0008)	−0.81 (0.08)	6.84 (0.18)	
J211813.25+114956.4	DA	36.3	77,652 (4212)	7.60 (0.14)	Pure H	0.60 (0.04)	0.0202 (0.0025)	1.12 (0.15)	5.57 (0.25)	5
J211927.20+045343.3	DAO	24.8	84,031 (15,462)	6.80 (0.32)	$\log N_{\rm He}/N_{\rm H} = -1.02$	0.42 (0.09)	0.0426 (0.0127)	1.91 (0.46)	<5.00	4,5
J212234.88+054239.0	DA	98.9	36,220 (145)	7.69 (0.02)	Pure H	0.51 (0.01)	0.0170 (0.0003)	−0.35 (0.02)	6.65 (0.01)	
J212403.11+114230.1	DB	10.7	30,404 (1231)	8.03 (0.14)	Pure He	0.63 (0.08)	0.0128 (0.0013)	−0.90 (0.11)	6.98 (0.08)	
J212411.99−072648.7	DA	132.5	69,478 (1135)	7.63 (0.05)	Pure H	0.58 (0.01)	0.0193 (0.0008)	0.89 (0.05)	5.82 (0.04)	5
J212717.87+053527.6	DAO	52.5	95,289 (4583)	7.14 (0.16)	$\log N_{\rm He}/N_{\rm H} = -1.84$	0.52 (0.04)	0.0323 (0.0050)	1.89 (0.16)	<5.00	4,5
J212721.51+053434.5	DOA	46.7	78,304 (3904)	8.03 (0.25)	$\log N_{\rm He}/N_{\rm H} = 0.16$	0.71 (0.11)	0.0134 (0.0028)	0.79 (0.20)	5.83 (0.10)	4
J212805.54−062519.0	DA	17.7	38,983 (996)	7.59 (0.12)	Pure H	0.48 (0.04)	0.0186 (0.0018)	−0.14 (0.10)	6.45 (0.22)	
J213019.79+061204.5	DA+M	28.2	32,214 (355)	7.37 (0.08)	Pure H	0.39 (0.02)	0.0216 (0.0013)	−0.34 (0.06)	6.23 (0.33)	1,2
J213156.16+061347.3	DA	31.7	37,265 (481)	7.72 (0.07)	Pure H	0.53 (0.03)	0.0166 (0.0009)	−0.32 (0.05)	6.64 (0.04)	
J213301.40+122831.2	DA	69.7	34,154 (149)	7.79 (0.03)	Pure H	0.55 (0.01)	0.0157 (0.0003)	−0.52 (0.02)	6.76 (0.01)	
J213516.29−003149.0	DA	26.4	38,932 (797)	7.62 (0.10)	Pure H	0.50 (0.04)	0.0181 (0.0014)	−0.17 (0.08)	6.50 (0.14)	
J213559.73+005453.8	DO	22.7	59,589 (1988)	7.91 (0.23)	Pure He	0.62 (0.10)	0.0144 (0.0026)	0.37 (0.17)	6.16 (0.09)	
J213803.15+113629.1	DA	7.8	68,166 (11,220)	7.71 (0.56)	Pure H	0.60 (0.21)	0.0180 (0.0090)	0.80 (0.52)	5.86 (0.70)	7
J213932.48+112611.2	DO	6.8	49,601 (1074)	8.42 (0.36)	Pure He	0.89 (0.21)	0.0096 (0.0028)	−0.30 (0.26)	6.27 (0.09)	
J214001.04−075052.0	DA	71.1	31,783 (96)	7.78 (0.02)	Pure H	0.54 (0.01)	0.0157 (0.0003)	−0.65 (0.02)	6.86 (0.01)	
J214148.62−011027.1	DA	21.6	65,729 (4543)	6.96 (0.20)	Pure H	0.39 (0.05)	0.0342 (0.0061)	1.29 (0.21)	<5.00	
J214223.31+111740.3	DOZ	24.5	92,135 (11,534)	8.16 (0.35)	Pure He	0.79 (0.16)	0.0122 (0.0037)	0.99 (0.34)	5.53 (0.22)	6
J214249.28+104733.0	DA	8.0	43,479 (3810)	7.83 (0.37)	Pure H	0.59 (0.16)	0.0155 (0.0046)	−0.11 (0.30)	6.47 (0.26)	
J214536.28−003544.1	DA+M	6.6	31,109 (1168)	7.61 (0.28)	Pure H	0.47 (0.11)	0.0179 (0.0038)	−0.57 (0.20)	6.80 (0.23)	1
J214538.85+113627.1	DA	5.1	33,467 (1899)	7.21 (0.37)	Pure H	0.35 (0.11)	0.0242 (0.0068)	−0.18 (0.26)	5.35 (1.21)	
J214557.28+001535.9	DA	13.2	50,762 (3266)	7.23 (0.23)	Pure H	0.40 (0.07)	0.0254 (0.0048)	0.59 (0.20)	<5.00	
J214815.48+112419.9	DA	17.9	31,006 (437)	7.09 (0.11)	Pure H	0.31 (0.03)	0.0261 (0.0020)	−0.24 (0.07)	5.08 (0.38)	
J215004.71+001103.3	DA	43.7	73,892 (3916)	6.98 (0.12)	Pure H	0.42 (0.03)	0.0349 (0.0036)	1.51 (0.14)	<5.00	5
J215102.28+125806.9	DA	6.8	39,427 (2600)	7.56 (0.31)	Pure H	0.48 (0.11)	0.0190 (0.0046)	−0.10 (0.24)	6.38 (0.48)	
J215244.90+111222.8	DA	16.6	55,798 (3250)	6.93 (0.19)	Pure H	0.35 (0.04)	0.0336 (0.0055)	0.99 (0.18)	<5.00	
J215359.65+125725.6	DA	5.6	37,598 (3142)	6.65 (0.43)	Pure H	0.23 (0.08)	0.0377 (0.0117)	0.41 (0.31)	<5.00	
J215429.39+064836.9	DA	36.6	30,017 (167)	7.82 (0.04)	Pure H	0.55 (0.02)	0.0152 (0.0005)	−0.77 (0.03)	6.94 (0.01)	
J215514.43−075833.7	DB	16.3	35,438 (1429)	8.11 (0.16)	Pure He	0.69 (0.09)	0.0121 (0.0014)	−0.68 (0.12)	6.76 (0.06)	

Table 2.1 – Atmospheric and stellar parameters of hot white dwarfs from SDSS DR12 (continued)

SDSS Name	Type	S/N	$T_{\rm eff}$ (K)	$\log g$	Composition	$M/M_{\odot}$	$R/R_{\odot}$	$\log L/L_{\odot}$	$\log \tau_{\rm cool}$	Notes
J215628.19+204728.2	DO	67.7	51,235 (301)	8.01 (0.05)	Pure He	0.65 (0.02)	0.0133 (0.0005)	0.04 (0.03)	6.32 (0.01)	
J215630.45+123654.0	DA	15.1	30,428 (401)	7.83 (0.10)	Pure H	0.56 (0.05)	0.0150 (0.0011)	−0.76 (0.07)	6.92 (0.02)	
J215711.87−004435.0	DA	31.1	59,475 (2063)	7.50 (0.12)	Pure H	0.52 (0.04)	0.0211 (0.0020)	0.70 (0.11)	5.63 (0.62)	
J220119.86+002409.0	DA	35.0	43,704 (840)	7.77 (0.08)	Pure H	0.57 (0.03)	0.0162 (0.0010)	−0.06 (0.06)	6.46 (0.03)	
J220210.50−071245.5	DA	7.2	47,194 (4845)	7.02 (0.39)	Pure H	0.34 (0.10)	0.0298 (0.0095)	0.60 (0.34)	<5.00	
J220313.29+113236.1	DB+M	19.6	33,793 (1160)	8.16 (0.13)	Pure He	0.72 (0.08)	0.0116 (0.0011)	−0.80 (0.10)	6.84 (0.07)	1
J220509.56+212239.4	DA	66.5	32,582 (135)	7.34 (0.03)	Pure H	0.39 (0.01)	0.0221 (0.0005)	−0.31 (0.02)	6.08 (0.14)	
J220514.08−005841.6	DA	13.0	32,682 (728)	7.77 (0.15)	Pure H	0.54 (0.07)	0.0159 (0.0018)	−0.59 (0.11)	6.82 (0.06)	
J221315.05+224140.6	DAO	21.4	94,904 (10,922)	6.92 (0.34)	$\log N_{\rm He}/N_{\rm H} = -1.34$	0.48 (0.08)	0.0400 (0.0130)	2.07 (0.36)	<5.00	4
J221325.49+114514.5	DA	75.7	30,865 (100)	7.78 (0.03)	Pure H	0.54 (0.01)	0.0157 (0.0003)	−0.70 (0.02)	6.89 (0.01)	
J221331.52+134223.2	DA	14.8	31,415 (500)	7.58 (0.12)	Pure H	0.46 (0.04)	0.0182 (0.0016)	−0.54 (0.08)	6.76 (0.12)	
J221501.38+051833.3	DA	53.3	58,029 (1426)	7.64 (0.08)	Pure H	0.55 (0.03)	0.0187 (0.0013)	0.55 (0.07)	6.01 (0.11)	5
J221512.18+213905.5	DA	89.3	42,384 (302)	7.82 (0.03)	Pure H	0.59 (0.01)	0.0156 (0.0004)	−0.15 (0.02)	6.50 (0.01)	
J221557.60+064551.9	DA	8.1	34,862 (1638)	7.47 (0.28)	Pure H	0.44 (0.10)	0.0200 (0.0043)	−0.27 (0.21)	6.41 (0.67)	
J221703.09+223330.8	DAO	61.3	40,690 (440)	7.87 (0.06)	$\log N_{\rm He}/N_{\rm H} = -1.32$	0.60 (0.03)	0.0149 (0.0007)	−0.26 (0.05)	6.55 (0.01)	9
J221950.18+123116.0	DA	30.1	32,160 (313)	7.72 (0.07)	Pure H	0.52 (0.03)	0.0164 (0.0008)	−0.59 (0.05)	6.82 (0.03)	
J222155.13+011026.1	DA	15.8	32,759 (755)	7.62 (0.16)	Pure H	0.48 (0.06)	0.0178 (0.0021)	−0.49 (0.11)	6.73 (0.16)	2
J222203.32−003138.0	DA	67.6	70,917 (2229)	7.31 (0.08)	Pure H	0.48 (0.02)	0.0254 (0.0018)	1.17 (0.09)	<5.00	5
J222209.42−011406.8	DA	24.1	30,661 (378)	7.87 (0.09)	Pure H	0.58 (0.05)	0.0146 (0.0010)	−0.77 (0.06)	6.91 (0.02)	
J222318.51+000557.0	DA	97.5	51,924 (481)	7.70 (0.03)	Pure H	0.56 (0.01)	0.0176 (0.0005)	0.31 (0.03)	6.21 (0.02)	
J222337.26+074438.1	DA	25.2	34,143 (431)	7.97 (0.08)	Pure H	0.64 (0.04)	0.0137 (0.0008)	−0.64 (0.06)	6.77 (0.02)	
J222433.02+222134.8	DA	23.8	56,697 (2701)	7.41 (0.16)	Pure H	0.47 (0.06)	0.0224 (0.0029)	0.67 (0.14)	<5.00	
J222528.27+125441.2	DA	26.1	40,017 (841)	7.69 (0.10)	Pure H	0.53 (0.04)	0.0171 (0.0013)	−0.17 (0.08)	6.53 (0.08)	
J222634.96+003905.3	DA	7.3	52,475 (5787)	7.97 (0.41)	Pure H	0.67 (0.19)	0.0141 (0.0048)	0.14 (0.35)	6.24 (0.20)	
J222644.64+141823.5	DA	27.4	42,170 (881)	7.61 (0.09)	Pure H	0.50 (0.03)	0.0185 (0.0013)	−0.01 (0.07)	6.37 (0.17)	
J222644.66+390114.1	DA	83.4	47,028 (462)	7.86 (0.04)	Pure H	0.61 (0.02)	0.0153 (0.0005)	0.01 (0.03)	6.38 (0.01)	5
J222650.26−011120.8	DA	89.1	40,614 (259)	7.74 (0.03)	Pure H	0.55 (0.01)	0.0165 (0.0004)	−0.17 (0.02)	6.54 (0.01)	
J222816.29+134714.4	DA	21.5	34,589 (497)	7.65 (0.09)	Pure H	0.49 (0.03)	0.0175 (0.0012)	−0.40 (0.06)	6.68 (0.07)	
J222833.82+141036.8	DB	14.6	35,538 (1400)	7.99 (0.16)	Pure He	0.62 (0.08)	0.0132 (0.0015)	−0.60 (0.12)	6.76 (0.05)	
J222950.26+212134.7	DO	18.1	51,256 (1341)	8.03 (0.21)	Pure He	0.66 (0.11)	0.0131 (0.0021)	0.03 (0.15)	6.32 (0.05)	
J223025.48+122748.6	DA	23.8	97,935 (10,661)	7.02 (0.19)	Pure H	0.51 (0.05)	0.0366 (0.0069)	2.04 (0.27)	<5.00	
J223114.41−001150.1	DAO	56.2	63,305 (2448)	7.37 (0.12)	$\log N_{\rm He}/N_{\rm H} = -0.86$	0.48 (0.04)	0.0238 (0.0023)	0.92 (0.11)	<5.00	4,5
J223123.29+220823.3	DA	17.3	55,641 (3282)	7.84 (0.21)	Pure H	0.63 (0.09)	0.0157 (0.0027)	0.33 (0.18)	6.17 (0.10)	
J223143.32+123012.6	DA	36.3	49,697 (1203)	7.42 (0.09)	Pure H	0.46 (0.03)	0.0220 (0.0015)	0.42 (0.07)	5.27 (0.55)	
J223236.70+073523.4	DAO	20.7	52,023 (2873)	7.76 (0.26)	$\log N_{\rm He}/N_{\rm H} = -1.19$	0.58 (0.10)	0.0166 (0.0036)	0.26 (0.21)	6.24 (0.17)	4,5
J223239.16+230628.6	DA	28.1	47,084 (1267)	7.57 (0.10)	Pure H	0.50 (0.03)	0.0193 (0.0017)	0.22 (0.09)	6.15 (0.32)	
J223354.70+054706.6	DA	19.5	38,898 (940)	7.74 (0.12)	Pure H	0.54 (0.05)	0.0165 (0.0015)	−0.25 (0.09)	6.59 (0.07)	
J223405.82+232510.9	DA	50.6	38,591 (359)	7.82 (0.05)	Pure H	0.58 (0.02)	0.0154 (0.0005)	−0.32 (0.03)	6.62 (0.01)	
J223824.51+071055.7	DA	25.4	47,612 (1265)	7.77 (0.10)	Pure H	0.58 (0.04)	0.0164 (0.0014)	0.10 (0.09)	6.35 (0.05)	
J223839.71+234639.7	DA	41.2	32,282 (183)	7.75 (0.04)	Pure H	0.53 (0.02)	0.0161 (0.0005)	−0.60 (0.03)	6.83 (0.01)	
J223906.48+215700.1	DA	34.6	37,603 (513)	7.76 (0.07)	Pure H	0.55 (0.03)	0.0161 (0.0009)	−0.33 (0.05)	6.64 (0.03)	
J223939.44+225925.9	DO	31.6	45,630 (186)	7.80 (0.07)	Pure He	0.55 (0.03)	0.0154 (0.0008)	−0.03 (0.05)	6.44 (0.04)	
J224020.37+141231.7	DA	9.7	39,703 (2099)	7.32 (0.25)	Pure H	0.40 (0.08)	0.0230 (0.0043)	0.07 (0.19)	5.43 (1.05)	
J224032.61+233746.7	DA	43.7	36,760 (346)	7.81 (0.05)	Pure H	0.57 (0.02)	0.0155 (0.0006)	−0.40 (0.04)	6.68 (0.01)	
J224131.91+131644.6	DA	59.8	32,173 (133)	7.96 (0.03)	Pure H	0.63 (0.02)	0.0138 (0.0003)	−0.73 (0.02)	6.85 (0.01)	
J224314.00+220128.7	DA	89.3	30,621 (75)	7.89 (0.02)	Pure H	0.59 (0.01)	0.0145 (0.0002)	−0.78 (0.01)	6.92 (0.01)	
J224426.01+140353.9	DA	13.8	30,245 (442)	7.68 (0.12)	Pure H	0.50 (0.05)	0.0168 (0.0014)	−0.67 (0.08)	6.89 (0.06)	
J224520.14+322456.3	DA	39.4	30,342 (198)	7.10 (0.05)	Pure H	0.31 (0.01)	0.0259 (0.0009)	−0.29 (0.03)	5.17 (0.19)	
J224556.68+003334.9	DA	30.7	33,967 (428)	7.83 (0.08)	Pure H	0.57 (0.04)	0.0152 (0.0009)	−0.56 (0.06)	6.78 (0.02)	
J224610.37+241619.3	DA	25.6	31,361 (325)	7.68 (0.08)	Pure H	0.50 (0.03)	0.0169 (0.0010)	−0.60 (0.05)	6.83 (0.05)	

Table 2.1 – Atmospheric and stellar parameters of hot white dwarfs from SDSS DR12 (continued)

SDSS Name	Type	S/N	$T_{\rm eff}$ (K)	$\log g$	Composition	$M/M_{\odot}$	$R/R_{\odot}$	$\log L/L_{\odot}$	$\log \tau_{\rm cool}$	Notes
J224653.72−094834.5	DA	67.7	92,846 (3065)	7.31 (0.09)	Pure H	0.56 (0.03)	0.0273 (0.0023)	1.70 (0.10)	<5.00	5
J224726.39+063225.8	DA	28.5	69,964 (3671)	6.96 (0.14)	Pure H	0.40 (0.03)	0.0348 (0.0044)	1.42 (0.15)	<5.00	
J224742.57−003317.5	DA	9.0	63,782 (8054)	7.30 (0.40)	Pure H	0.46 (0.11)	0.0251 (0.0090)	0.97 (0.39)	<5.00	
J224829.60+223355.9	DA+M	10.3	62,938 (7039)	7.56 (0.37)	Pure H	0.54 (0.13)	0.0203 (0.0064)	0.76 (0.34)	5.75 (0.66)	1
J224915.53−101950.2	DA+M	12.0	36,297 (1406)	7.65 (0.21)	Pure H	0.50 (0.08)	0.0176 (0.0029)	−0.32 (0.16)	6.62 (0.18)	1
J224925.29+065646.5	DA	95.6	135,327 (6692)	6.82 (0.03)	Pure H	0.60 (0.03)	0.0498 (0.0019)	2.88 (0.11)	<5.00	
J224930.59+054327.6	DA+M	28.2	37,447 (459)	7.83 (0.06)	Pure H	0.58 (0.03)	0.0153 (0.0007)	−0.38 (0.05)	6.65 (0.02)	1,2
J225008.69+224528.7	DA	32.1	121,789 (15,844)	6.77 (0.11)	Pure H	0.54 (0.06)	0.0503 (0.0057)	2.70 (0.29)	<5.00	
J225020.59+274934.9	DA	47.5	86,830 (4135)	6.80 (0.09)	Pure H	0.43 (0.02)	0.0431 (0.0035)	1.98 (0.12)	<5.00	
J225117.28+310939.8	DA+M	18.6	41,031 (620)	7.89 (0.07)	Pure H	0.62 (0.03)	0.0147 (0.0008)	−0.26 (0.05)	6.54 (0.02)	1
J225124.07+311627.7	DBA	22.5	40,228 (1893)	7.73 (0.14)	$\log q_{\rm H} = -17.17$	0.51 (0.06)	0.0161 (0.0017)	−0.21 (0.13)	6.55 (0.17)	3
J225125.52+321858.4	DA	18.6	39,544 (1034)	7.36 (0.12)	Pure H	0.42 (0.04)	0.0222 (0.0020)	0.04 (0.09)	5.67 (0.61)	
J225334.79−090553.9	DA+M	4.9	32,453 (1899)	7.99 (0.41)	Pure H	0.65 (0.21)	0.0135 (0.0042)	−0.74 (0.29)	6.84 (0.26)	1
J225359.45−100732.3	DA	11.0	37,028 (1592)	7.83 (0.23)	Pure H	0.58 (0.10)	0.0153 (0.0027)	−0.40 (0.17)	6.67 (0.09)	
J225651.33+135718.8	DA	40.0	58,096 (1646)	7.42 (0.10)	Pure H	0.48 (0.04)	0.0224 (0.0016)	0.71 (0.08)	5.03 (0.77)	
J230052.67+252040.3	DA	17.3	48,325 (2327)	7.86 (0.19)	Pure H	0.62 (0.08)	0.0153 (0.0023)	0.06 (0.16)	6.34 (0.07)	
J230101.07+063754.8	DA	6.9	39,197 (2669)	7.76 (0.33)	Pure H	0.55 (0.14)	0.0162 (0.0042)	−0.25 (0.25)	6.59 (0.21)	
J230228.03+231747.9	DA	24.3	41,554 (1062)	7.49 (0.11)	Pure H	0.46 (0.04)	0.0202 (0.0018)	0.04 (0.09)	6.10 (0.39)	
J230255.02−084005.6	DA	67.1	73,628 (2334)	7.34 (0.08)	Pure H	0.50 (0.03)	0.0250 (0.0017)	1.22 (0.09)	<5.00	5
J230309.98+072216.2	DAO	69.2	84,032 (3258)	7.84 (0.11)	$\log N_{\rm He}/N_{\rm H} = -2.11$	0.69 (0.04)	0.0165 (0.0016)	1.09 (0.11)	5.62 (0.07)	4,5
J230348.46+261859.6	DA	20.4	35,722 (597)	7.55 (0.09)	Pure H	0.46 (0.03)	0.0189 (0.0014)	−0.28 (0.07)	6.53 (0.16)	
J230410.96+232236.1	DA	20.8	31,572 (410)	7.19 (0.10)	Pure H	0.34 (0.03)	0.0245 (0.0016)	−0.27 (0.06)	5.41 (0.43)	
J230501.78+063225.1	DA	62.0	55,269 (865)	7.68 (0.05)	Pure H	0.56 (0.02)	0.0180 (0.0008)	0.43 (0.05)	6.11 (0.05)	
J230757.75+221026.5	DA	10.2	49,108 (4324)	7.38 (0.33)	Pure H	0.45 (0.10)	0.0225 (0.0060)	0.42 (0.28)	5.10 (1.33)	
J230921.24−003204.7	DA	59.5	36,396 (254)	8.25 (0.04)	Pure H	0.80 (0.02)	0.0111 (0.0003)	−0.71 (0.03)	6.71 (0.02)	
J230953.43+011213.4	DA	78.6	31,364 (93)	8.45 (0.02)	Pure H	0.92 (0.01)	0.0094 (0.0002)	−1.11 (0.02)	7.44 (0.05)	
J231133.88+144119.9	DA	27.6	38,427 (691)	7.74 (0.09)	Pure H	0.54 (0.04)	0.0164 (0.0011)	−0.28 (0.07)	6.61 (0.04)	
J231511.53+145131.5	DA	22.0	32,815 (365)	7.38 (0.08)	Pure H	0.40 (0.02)	0.0214 (0.0012)	−0.32 (0.05)	6.26 (0.30)	
J232548.64+522957.6	DA	3.9	33,012 (2273)	7.99 (0.46)	Pure H	0.65 (0.24)	0.0135 (0.0048)	−0.71 (0.33)	6.82 (0.35)	
J232635.01+143401.5	DA	33.0	36,602 (450)	7.81 (0.07)	Pure H	0.57 (0.03)	0.0155 (0.0008)	−0.41 (0.05)	6.68 (0.02)	
J232846.78+152005.5	DA	32.1	31,250 (258)	7.81 (0.06)	Pure H	0.55 (0.03)	0.0154 (0.0007)	−0.69 (0.04)	6.88 (0.02)	
J232937.54+524437.8	DA	16.3	32,158 (516)	8.30 (0.11)	Pure H	0.83 (0.07)	0.0106 (0.0009)	−0.96 (0.08)	7.04 (0.19)	
J233050.00+142653.3	DA	38.5	32,410 (208)	7.15 (0.04)	Pure H	0.33 (0.01)	0.0252 (0.0008)	−0.20 (0.03)	5.18 (0.18)	
J233052.97+143037.5	DA	19.5	99,677 (12,801)	7.17 (0.25)	Pure H	0.55 (0.07)	0.0317 (0.0078)	1.95 (0.33)	<5.00	
J233211.11+462541.4	DA	9.0	70,909 (9908)	7.44 (0.43)	Pure H	0.52 (0.13)	0.0229 (0.0090)	1.08 (0.43)	<5.00	
J233212.24+491102.9	DA	10.5	33,126 (780)	7.53 (0.16)	Pure H	0.45 (0.05)	0.0190 (0.0023)	−0.41 (0.11)	6.62 (0.28)	
J233338.74+093347.7	DA	11.8	50,636 (3689)	7.79 (0.27)	Pure H	0.59 (0.11)	0.0162 (0.0036)	0.19 (0.23)	6.28 (0.20)	
J233433.30+151359.6	DA	5.2	35,283 (2015)	7.50 (0.33)	Pure H	0.44 (0.12)	0.0197 (0.0050)	−0.27 (0.24)	6.44 (0.61)	
J233507.10−083354.0	DA	31.3	31,550 (218)	7.92 (0.05)	Pure H	0.61 (0.03)	0.0141 (0.0005)	−0.75 (0.03)	6.88 (0.01)	
J233626.06+070053.3	DA	15.1	39,715 (1570)	7.60 (0.18)	Pure H	0.49 (0.07)	0.0183 (0.0027)	−0.12 (0.15)	6.45 (0.28)	
J233751.37+133548.0	DA	73.6	57,573 (924)	7.57 (0.05)	Pure H	0.53 (0.02)	0.0198 (0.0009)	0.59 (0.05)	5.92 (0.13)	5
J233924.56+144750.8	DA	25.6	67,151 (3617)	7.15 (0.16)	Pure H	0.44 (0.04)	0.0290 (0.0042)	1.19 (0.16)	<5.00	
J233933.43+061245.5	DAO	24.1	57,925 (3778)	6.85 (0.20)	$\log N_{\rm He}/N_{\rm H} = -2.87$	0.34 (0.05)	0.0363 (0.0062)	1.13 (0.20)	<5.00	4
J233937.11+444651.2	DA	4.2	30,230 (1378)	7.40 (0.36)	Pure H	0.40 (0.12)	0.0208 (0.0055)	−0.49 (0.24)	6.52 (0.82)	
J234150.77−005718.5	DA	10.7	38,000 (1390)	7.58 (0.18)	Pure H	0.48 (0.06)	0.0186 (0.0027)	−0.19 (0.14)	6.48 (0.31)	
J234307.78+140711.3	DA	15.8	61,770 (3927)	7.59 (0.21)	Pure H	0.55 (0.07)	0.0196 (0.0036)	0.70 (0.20)	5.86 (0.38)	
J234401.31+465644.3	DA	8.7	39,703 (2539)	7.90 (0.30)	Pure H	0.62 (0.14)	0.0146 (0.0034)	−0.32 (0.23)	6.58 (0.12)	
J234403.21+004306.9	DA	15.1	30,266 (383)	7.91 (0.10)	Pure H	0.60 (0.05)	0.0142 (0.0010)	−0.81 (0.07)	6.94 (0.02)	
J234409.85+431323.4	DA	10.5	33,597 (994)	7.00 (0.20)	Pure H	0.29 (0.05)	0.0282 (0.0041)	−0.04 (0.14)	<5.00	
J234421.01+442912.2	DA	9.8	40,556 (2163)	7.48 (0.24)	Pure H	0.46 (0.08)	0.0203 (0.0038)	0.00 (0.19)	6.11 (0.83)	

Table 2.1 – Atmospheric and stellar parameters of hot white dwarfs from SDSS DR12 (continued)

SDSS Name	Type	S/N	$T_{\rm eff}$ (K)	$\log g$	Composition	$M/M_{\odot}$	$R/R_{\odot}$	$\log L/L_{\odot}$	$\log \tau_{\rm cool}$	Notes
J234528.67+394643.7	DA	40.5	45,069 (673)	7.73 (0.06)	Pure H	0.55 (0.02)	0.0168 (0.0008)	0.02 (0.05)	6.41 (0.03)	
J234536.46−010204.9	DA	12.8	33,400 (757)	7.48 (0.15)	Pure H	0.43 (0.05)	0.0198 (0.0023)	−0.36 (0.11)	6.52 (0.36)	
J234709.29+001858.0	DB	9.2	34,084 (3914)	8.07 (0.44)	Pure He	0.66 (0.24)	0.0125 (0.0041)	−0.72 (0.35)	6.82 (0.36)	
J234911.40+364107.5	DA	8.4	58,998 (6952)	6.82 (0.37)	Pure H	0.34 (0.08)	0.0373 (0.0114)	1.18 (0.35)	<5.00	
J235137.23+010844.2	DAO	22.3	51,040 (1350)	8.13 (0.18)	$\log q_{\rm H} = -16.66$	0.72 (0.10)	0.0121 (0.0016)	−0.05 (0.13)	6.30 (0.06)	3
J235144.29+375542.6	DA	29.1	52,789 (1673)	7.77 (0.12)	Pure H	0.59 (0.05)	0.0165 (0.0016)	0.28 (0.10)	6.23 (0.06)	
J235359.86+233600.6	DA	26.4	30,012 (238)	7.88 (0.06)	Pure H	0.58 (0.03)	0.0145 (0.0007)	−0.81 (0.04)	6.95 (0.01)	
J235452.30+260513.4	DA	25.2	34,149 (378)	7.77 (0.07)	Pure H	0.54 (0.03)	0.0159 (0.0008)	−0.51 (0.05)	6.76 (0.02)	
J235545.27+370553.7	DA	11.4	36,451 (1093)	7.92 (0.17)	Pure H	0.62 (0.08)	0.0143 (0.0018)	−0.49 (0.12)	6.68 (0.04)	
J235636.10+233858.4	DA	32.4	34,143 (343)	7.21 (0.06)	Pure H	0.35 (0.02)	0.0243 (0.0011)	−0.14 (0.04)	5.28 (0.31)	
J235753.13+284542.9	DBA+M	8.1	42,555 (3424)	7.82 (0.49)	$\log q_{\rm H} = -16.95$	0.55 (0.22)	0.0151 (0.0056)	−0.17 (0.35)	6.53 (0.40)	1,3

(1) The contribution of the main-sequence companion to the spectrum was removed before performing the fit.
(2) At least one line core is filled with emission and was excluded from the fit.
(3) The given parameters were obtained from chemically stratified model atmospheres, which yield a better fit to the hybrid spectrum.
(4) The given parameters were obtained from chemically homogeneous model atmospheres, which yield a better fit to the hybrid spectrum.
(5) The spectrum exhibits the Balmer-line problem and was fitted with the CNO-rich model atmospheres of Gianninas et al. (2010).
(6) The traces of carbon were ignored in the model-atmosphere calculations, and the weak C IV lines were excluded from the fit.
(7) At least one line was excluded from the fit due to the presence of a glitch or to an incomplete wavelength coverage.
(8) The main He II lines are abnormally strong and were excluded from the fit.
(9) The given parameters are meaningless as the hybrid spectrum is actually produced by a DA+DO/DB binary system.

Chapitre 3

On the Spectral Evolution of Hot White Dwarf Stars. II. Time-dependent Simulations of Element Transport in Evolving White Dwarfs with STELUM

A. Bédard[1], P. Brassard[1], P. Bergeron[1], & S. Blouin[2,3]

[1] Département de Physique, Université de Montréal, Montréal, QC H3C 3J7, Canada

[2] Los Alamos National Laboratory, Los Alamos, NM 87545, USA

[3] Department of Physics and Astronomy, University of Victoria, Victoria, BC V8W 2Y2, Canada

Published in *The Astrophysical Journal*

March 2022, Volume 927, Article 128

DOI: 10.3847/1538-4357/ac4497

Abstract

White dwarf stars are subject to various element transport mechanisms that can cause their surface composition to change radically as they cool, a phenomenon known as spectral evolution. In this paper, we undertake a comprehensive theoretical investigation of the spectral evolution of white dwarfs. First, we introduce STELUM, a new implementation of the stellar evolutionary code developed at the Université de Montréal. We provide a thorough description of the physical content and numerical techniques of the code, covering the treatment of both stellar evolution and chemical transport. Then, we present two state-of-the-art numerical simulations of element transport in evolving white dwarfs. Atomic diffusion, convective mixing, and mass loss are considered simultaneously as time-dependent diffusive processes and are fully coupled to the cooling. We first model the PG 1159−DO−DB−DQ evolutionary channel: a helium-, carbon-, and oxygen-rich PG 1159 star transforms into a

pure-helium DB white dwarf due to gravitational settling and then into a helium-dominated, carbon-polluted DQ white dwarf through convective dredge-up. We also compute for the first time the full DO−DA−DC evolutionary channel: a helium-rich DO white dwarf harboring residual hydrogen becomes a pure-hydrogen DA star through the float-up process and then a helium-dominated, hydrogen-bearing DC star due to convective mixing. We demonstrate that our results are in excellent agreement with available empirical constraints. In particular, our DO−DA−DC simulation perfectly reproduces the lower branch of the bifurcation observed in the Gaia color−magnitude diagram, which can therefore be interpreted as a signature of spectral evolution.

Key words: White dwarf stars; Late stellar evolution; Stellar evolutionary models; Stellar diffusion; Stellar convective envelopes; Stellar winds

3.1. Introduction

In the course of their evolution, stars are subject to several physical mechanisms that may alter their chemical composition. Besides the obvious example of nuclear burning, a number of processes give rise to the transport of matter within a star and thereby change the distribution of the elements with depth. These transport mechanisms belong to one of two categories: microscopic processes, which influence individual chemical constituents differentially, and macroscopic processes, which affect the stellar material as a whole (see Salaris & Cassisi 2017 for a recent review).

Microscopic transport, often referred to as atomic diffusion, is the net result of interparticle collisions in the presence of a gradient of some physical quantity. Three types of diffusion can be distinguished: chemical diffusion, gravitational settling, and thermal diffusion, which are induced by composition, pressure, and temperature gradients, respectively. On one hand, both gravitational settling and thermal diffusion tend to separate the atomic species according to their mass, with heavier ions moving toward regions of higher pressure and temperature (that is, toward the center of a star). On the other hand, chemical diffusion tends to homogenize the composition and thus counteract the above-mentioned effect (Thoul et al., 1994; Michaud et al., 2015). Another form of selective transport is radiative levitation, whereby photons transfer part of their net outward momentum to ions of a given type. This

phenomenon also acts against gravitational sedimentation, especially in the outer layers of a hot star (Chayer et al., 1995; Michaud et al., 2015).

As for macroscopic transport, convection is the most common mechanism driving large-scale flows of matter. Besides carrying energy very efficiently, these rapid motions lead to the complete mixing of the various chemical species, thereby impeding the effects of atomic diffusion (Kippenhahn et al., 2012). In addition to ordinary convection, phenomena such as convective overshoot, semiconvection, and thermohaline convection provide additional sources of mixing under certain circumstances (Kippenhahn et al., 1980; Langer et al., 1985; Freytag et al., 1996). Stellar winds and the accompanying mass loss constitute another example of macroscopic transport. In particular, at the surface of a hot star, the radiation field can be strong enough to power a continuous, undifferentiated outflow of material. The impact of such a wind is to slow down atomic diffusion in the outer envelope (Kudritzki & Puls, 2000; Unglaub & Bues, 2000). Obviously, the reverse mechanism, mass accretion, either from the interstellar medium or from a companion, can also influence the surface composition (Alcock & Illarionov, 1980; Koester, 2009).

White dwarf stars provide a unique window on chemical transport in an astrophysical context. In these compact, burnt-out, slowly cooling stellar remnants, gravitational settling is expected to be dominant (Schatzman, 1958; Paquette et al., 1986a) and thus to produce a stratified chemical structure: a carbon/oxygen core, surrounded by a pure-helium mantle, itself surrounded by a pure-hydrogen layer. While pure-hydrogen-atmosphere white dwarfs (type DA [1]) are indeed ubiquitous, atmospheres made of helium (types DO, DB, DC) and/or polluted by trace elements (types DBA, DQ, DZ, and many others) are also observed in significant numbers (Kepler et al. 2019 and references therein). Furthermore, a wealth of evidence suggests that the surface composition of white dwarfs can change as they cool, a phenomenon known as spectral evolution (Bédard et al. 2020, hereafter Paper I, and references therein). Therefore, it is clear that gravitational settling is not the sole transport process at work in degenerate stars.

1. The coolest hydrogen-atmosphere white dwarfs actually belong to the DC spectral class because hydrogen lines disappear below $T_{\rm eff} \sim 5000$ K.

First and foremost, the very existence of hydrogen-deficient white dwarfs is particularly telling. Stellar remnants are expected to retain a "thick" superficial hydrogen layer of fractional mass $q_{\rm H} \equiv M_{\rm H}/M \sim 10^{-4}$ (Iben & Tutukov, 1984; Renedo et al., 2010). The fact that one in four objects enters the cooling sequence with a hydrogen-deficient surface (Paper I) then implies that radical chemical alterations take place in pre-white dwarf evolutionary phases. It is believed that most of these DO white dwarfs descend from helium-, carbon-, and oxygen-rich PG 1159 stars, which themselves are the result of a late helium-shell flash (Althaus et al., 2005b; Werner & Herwig, 2006). The hydrogen deficiency is a direct consequence of this event: the flash produces an extensive convection zone, which causes the superficial hydrogen to be mixed deeply into the stellar envelope and hence almost entirely burned.

At the beginning of the cooling sequence, the idea that gravitational settling leaves only pure-hydrogen and pure-helium atmospheres does not stand up to scrutiny. For instance, some PG 1159 stars keep their surface carbon and oxygen down to an effective temperature $T_{\rm eff} \sim 75{,}000$ K (Werner & Herwig, 2006). In addition, several hot hydrogen-rich DA white dwarfs exhibit atmospheric traces of helium and/or metals (Gianninas et al. 2010; Barstow et al. 2014; Paper I). This indicates that the downward diffusion of heavy elements is initially hampered by a competing transport mechanism. The most likely candidate is a weak radiative stellar wind (Unglaub & Bues, 1998, 2000; Quirion et al., 2012), although radiative levitation is also thought to play some role (Chayer et al., 1995; Dreizler, 1999).

Below $T_{\rm eff} \sim 75{,}000$ K, as stellar winds fade and gravitational settling starts to operate, another remarkable feature emerges: the fraction of helium-dominated white dwarfs gradually declines with decreasing effective temperature, implying that these objects can become hydrogen rich as they cool. More specifically, two-thirds of all hot DO stars turn into DA stars before they reach $T_{\rm eff} \sim 30{,}000$ K (Paper I). This transformation is usually interpreted as the result of the so-called float-up process: a small amount of residual hydrogen, initially diluted into the helium envelope, is slowly carried upward by diffusion, ultimately forming a hydrogen shell at the surface (Fontaine & Wesemael, 1987; Althaus et al., 2005a). This scenario is further supported by the detection, around $T_{\rm eff} \sim 40{,}000 - 50{,}000$ K, of white dwarfs with extremely thin superficial hydrogen layers ($q_{\rm H} \sim 10^{-17} - 10^{-16}$), which represent an intermediate stage in the DO-to-DA transition (Manseau et al. 2016; Paper I).

Going further down the effective temperature scale, element transport produces another striking observational signature: the fraction of helium-dominated white dwarfs reincreases below $T_{\rm eff} \sim 20{,}000$ K (Blouin et al., 2019; Genest-Beaulieu & Bergeron, 2019b; Ourique et al., 2019; Cunningham et al., 2020). This trend suggests that DA stars with newly formed thin hydrogen layers transform back into helium-atmosphere objects. The mechanism at the source of this DA-to-DB/DC spectral metamorphosis is convection. In fact, two similar but distinct phenomena, referred to in the literature as convective dilution and convective mixing, are believed to occur, above and below $T_{\rm eff} \sim 15{,}000$ K, respectively.

In the first case, the amount of hydrogen accumulated at the surface is small enough ($q_{\rm H} \lesssim 10^{-14}$) to allow the development of a convection zone in the underlying helium mantle. As the effective temperature decreases, the convective region grows and erodes the superficial hydrogen layer from below, until the latter is completely diluted into the helium envelope. The observational outcome is a helium-dominated atmosphere with a minute trace of hydrogen, namely, a DBA white dwarf (MacDonald & Vennes, 1991; Rolland et al., 2018, 2020).

In the second case, the superficial hydrogen shell is thicker ($q_{\rm H} \gtrsim 10^{-14}$) and the helium envelope remains convectively stable. Instead, it is in the hydrogen layer that a convection zone appears. When the advective motions reach into the underlying helium, the latter is massively dredged up to the surface, such that the hydrogen ends up being thoroughly mixed in a helium-dominated outer envelope. Although still detectable immediately after the mixing episode, the hydrogen quickly becomes invisible as the effective temperature decreases. Consequently, the white dwarf evolves briefly into a helium-rich DA star and then into a DC star (MacDonald & Vennes, 1991; Chen & Hansen, 2011; Rolland et al., 2018). An analogous phenomenon is thought to be responsible for the existence of carbon-polluted DQ white dwarfs below $T_{\rm eff} \sim 10{,}000$ K: these objects descend from DB stars in which settling carbon (a relic of their PG 1159 past) is dredged up from the deep envelope to the surface by the growing helium convection zone (Pelletier et al., 1986; Dufour et al., 2005; Camisassa et al., 2017).

Finally, 25−50% of cool white dwarfs show atmospheric contamination by heavy elements, especially calcium, magnesium, and iron (Koester et al., 2014a; Coutu et al., 2019). It is now firmly established that these DAZ, DBZ, and DZ stars owe their spectral appearance to the

accretion of tidally disrupted asteroids or planets (Farihi et al., 2010; Jura & Young, 2014). Because such rocky material is expected to sink out of sight on extremely short timescales (Dupuis et al., 1992; Koester, 2009), the existence of so many metal-polluted white dwarfs reveals that this type of accretion is quite frequent.

The above considerations have made evident that the spectral evolution of white dwarfs is governed by a complex interplay between numerous transport mechanisms. This topic has been extensively studied from an empirical perspective in recent years, largely thanks to the Sloan Digital Sky Survey (York et al., 2000) and the Gaia mission (Gaia Collaboration et al., 2016). Nevertheless, our theoretical understanding of the dynamical phenomena giving rise to spectral evolution remains scarce. Several works have attempted to model chemically evolving white dwarfs, but the vast majority of them adopted a crude treatment of chemical transport, either assuming diffusive equilibrium between the various processes or ignoring the feedback of composition changes on the evolution. Detailed evolutionary calculations in which time-dependent transport is fully coupled to white dwarf cooling have seldom been carried out. Moreover, conflicting results have sometimes been reported by different groups from such self-consistent calculations. In this context, we feel that improvements in the modeling of the spectral evolution are greatly needed. This endeavor not only constitutes a remarkable opportunity to further our understanding of element transport in astrophysical objects but is also of crucial relevance for the fields of cosmochronology and asteroseismology, given that the chemical history of degenerate stars impacts their cooling and pulsation properties (Fontaine et al., 2001; Fontaine & Brassard, 2008).

The present paper is the second of a series dedicated to the spectral evolution of white dwarfs. In Paper I, we performed a comprehensive spectroscopic analysis of a large sample of hot white dwarfs in order to improve our empirical knowledge of this phenomenon. In the present work, we turn to the theoretical side of the subject and undertake an extended modeling study of spectral evolution. First, we provide an exhaustive description of our stellar evolutionary code in Section 3.2. Then, we present and discuss the results of our time-dependent simulations of chemical transport in evolving white dwarf models in Section 3.3. Finally, our conclusions are summarized in Section 3.4.

3.2. The STELUM Evolutionary Code

The Montreal white dwarf evolutionary code was introduced some 20 years ago by Fontaine et al. (2001) and subsequently updated by Dufour et al. (2005), Quirion et al. (2012), Van Grootel et al. (2013), and Brassard & Fontaine (2015), among others. In recent years, one of us (P. Brassard) has devoted considerable effort to the development of a new, state-of-the-art version of the code, completely rewritten in modern Fortran and in modular form, with substantially improved capabilities. This revamped implementation of our evolutionary code is named STELUM, for STELlar modeling from the Université de Montréal. STELUM is specifically but not exclusively designed for the modeling of white dwarfs and hot subdwarfs. It can build and evolve complete stellar models, down from the center up to the very surface, in which the transport of chemical species is fully coupled to the evolution. STELUM has already been used in a few works (Rolland et al. 2020; Blouin et al. 2020a,b; Paper I), but has never been properly described. The goal of the present section is to remedy this situation. In the following, we provide a detailed description of the code, with a particular focus on the treatment of element transport.

3.2.1. Stellar Structure and Evolution

STELUM relies on the standard one-dimensional theory of stellar structure and evolution (see the Appendix). Before addressing the physical content of the code, a few aspects of our numerical approach are worth discussing. The fundamental equations are not solved directly in their conventional Lagrangian form; rather, they are first recast in terms of a new independent depth variable. This strategy is motivated by our wish to compute high-precision stellar models down from the center up to the very surface (which is essential to simulate the spectral evolution of white dwarfs properly). While the usual interior mass m is an appropriate independent variable across most of the stellar interior, the quantity $\log q$, where $q = 1 - m/M$ is the exterior mass, is better suited to describe the outermost layers. In order to model both regimes accurately, STELUM adopts the independent mass variable ξ

defined by Equations 1−3 of Tassoul et al. (1990), which we reproduce here for completeness:

$$q = \begin{cases} 1 + c_1\xi^3, & 0.0 \leq \xi \leq 0.4, \\ c_2 + c_3\xi + c_4\xi^2 + c_5\xi^3, & 0.4 \leq \xi \leq 1.0, \\ c_6 \exp\left[15\,(1-\xi)\right], & \xi \geq 1.0, \end{cases} \tag{3.1}$$

where the values of the coefficients are $c_1 = -2.1825397$, $c_2 = 0.64021163$, $c_3 = 2.6984127$, $c_4 = -6.7460317$, $c_5 = 3.4391534$, and $c_6 = 0.03174603$. With this definition, $\xi \propto m^{1/3}$ in the deep interior and $\xi \propto -\log q$ in the outermost layers, as needed.

The numerical solution of the modified structure equations is then carried out using the so-called Galerkin finite-element method, with either linear, quadratic, or cubic elements. The technique is described at length in Brassard et al. (1992) and the details will not be repeated here. Nevertheless, we want to stress that the use of a finite-element scheme to build and evolve stellar models is perhaps the most important and defining feature of STELUM. Indeed, as demonstrated by Brassard et al. (1992) in the context of stellar pulsations, this method outperforms the various finite-difference schemes employed by most evolution and pulsation codes in terms of stability, accuracy, and effectiveness. Furthermore, STELUM relies on an adaptive time-step algorithm, whereby the time step between two successive models of an evolutionary sequence is selected according to a prespecified tolerance for the relative changes in radius, pressure, and temperature averaged over the star.

A number of functions appearing in the basic structure equations must be specified a priori through an appropriate description of the microphysics of the stellar material. This so-called constitutive physics comprises the equation of state, the Rosseland mean opacity, the temperature gradient, and the rates of energy gain/loss due to nuclear reactions, neutrino emission, and gravothermal processes (see the Appendix). In the rest of this section, we give an exhaustive account of how these physical ingredients are handled in STELUM.

The equation of state consists of four tables of thermodynamic data suitable for pure hydrogen, helium, carbon, and oxygen compositions. In order to cover a large domain of the density−temperature plane, each table is made of three parts corresponding to three different physical regimes, connected as smoothly as possible. In the low-density regime, the thermodynamic properties of the partially ionized, nondegenerate, almost ideal gas are obtained by solving the appropriate network of Saha equations including a Coulomb correction term. In

intermediate-density regions where partial ionization, partial electron degeneracy, and nonideal effects all occur, we use the equation of state of Saumon et al. (1995) for hydrogen and helium, an improved version of the equation of state of Fontaine et al. (1977) for carbon, and an unpublished equation of state for oxygen (developed by the late G. Fontaine at the Université de Montréal). Finally, in the high-density regime, the state of the completely ionized, strongly electron-degenerate, highly nonideal plasma is described according to the formalism introduced by Lamb (1974) and improved by Kitsikis et al. (2005), which accounts for both liquid and solid (bcc) phases. For elements heavier than oxygen, we employ the oxygen equation of state scaled to the appropriate atomic weight and charge. For mixtures of multiple species, the thermodynamic data are interpolated in composition following the additive-volume prescription of Fontaine et al. (1977).

The total opacity is a combination of two contributions associated with radiative and conductive heat transfer processes. The default radiative opacities are the OPAL data for pure substances (Iglesias & Rogers, 1996), supplemented at low temperatures with our own hydrogen and helium opacities computed using the model-atmosphere code described in Bergeron et al. (1995, 1997, 2001). For mixtures of multiple species, the pure-element opacities are linearly interpolated in composition; note that the OPAL tables for arbitrary mixtures are also included in STELUM but are not used by default, because they are very time consuming and of little consequence in most applications. Alternatively, the analogous OP data (Badnell et al., 2005) and the low-temperature opacities of Ferguson et al. (2005) are also available. As for the conductive opacities, we rely on the data of Cassisi et al. (2007) and the corrections of Blouin et al. (2020b) in the moderately coupled and moderately degenerate regime. Other available options are the older opacities of Hubbard & Lampe (1969) and Itoh et al. (1983, 1984).

The temperature gradient takes different forms depending on the presence or absence of convection, as determined by the standard Schwarzschild criterion. On one hand, a convectively stable medium is characterized by the radiative temperature gradient,

$$\nabla_{\rm rad} = \frac{3WlP\kappa}{64\pi\sigma GmT^4}, \tag{3.2}$$

where σ is the Stefan−Boltzmann constant, G is the gravitational constant, l is the luminosity, P is the total pressure, T is the temperature, κ is the opacity, and W is a correction factor accounting for the nondiffusive heat transfer at small optical depths (see below). On

the other hand, a convectively unstable region is characterized by the convective temperature gradient, $\nabla_{\rm conv}$, which must be obtained from a model of convection. The default option is the so-called ML2 version of the mixing-length theory, in which the mixing-length parameter is $\alpha = 1.0$ (Böhm-Vitense, 1958; Tassoul et al., 1990). Similarly to the above expression for $\nabla_{\rm rad}$, we incorporate the W factor into the usual equations for $\nabla_{\rm conv}$ in order to consider nondiffusive effects near the surface (see the Appendix). Furthermore, note that the alternative theory of stellar convection introduced by Canuto & Mazzitelli (1991) is also implemented in STELUM.

The atmospheric correction parameter W is inspired by the formalism of Henyey et al. (1965). At the present time, it is evaluated under the assumption of a simple gray atmosphere, in which case it takes the following analytic form:

$$W = 1 + \frac{dH}{d\tau}, \tag{3.3}$$

where τ is the Rosseland optical depth and H is the Hopf function. The latter is approximated with a seventh-order polynomial fit to a numerical solution of its defining integral equation (see the Appendix). We are currently working on implementing in STELUM a more realistic approach, which consists in extracting W from the detailed nongray model atmospheres computed by our group.

The nuclear energy generation rate is defined as the sum of the energy produced per unit mass and unit time by all relevant nuclear reactions. To calculate this, one must supply a reaction network along with individual reaction cross sections and electron screening factors (see the Appendix). The nuclear network of STELUM incorporates the main reactions involved in hydrogen burning (both the PP chain and the CNO cycle) and helium burning. The burning of heavier elements is not presently included. There are three possible levels of sophistication regarding the species tracked in the calculations:

(1) a basic network: H, He, C, O;

(2) a standard network: ^{1}H, ^{2}H, ^{3}He, ^{4}He, ^{12}C, ^{13}C, ^{14}N, ^{15}N, ^{16}O, ^{17}O, ^{20}Ne;

(3) an extended network: ^{1}H, ^{2}H, ^{3}He, ^{4}He, ^{7}Be, ^{7}Li, ^{8}B, ^{12}C, ^{13}C, ^{13}N, ^{14}N, ^{15}N, ^{15}O, ^{16}O, ^{17}O, ^{18}O, ^{17}F, ^{18}F, ^{19}F, ^{20}Ne.

By default, the reaction cross sections are taken from Angulo et al. (1999), but the data of Caughlan & Fowler (1988) and Cyburt et al. (2010) are also available. The electron screening

factors are computed following the prescription of Dewitt et al. (1973) and Graboske et al. (1973).

Similar considerations apply to the neutrino energy-loss rate (see the Appendix). In this case, the leptonic reactions included in STELUM are the pair, photo-, plasma, bremsstrahlung, and recombination neutrino processes. For all these mechanisms, the rates of energy loss are taken from Itoh et al. (1996).

Finally, the gravothermal energy generation rate is defined as the rate at which heat is removed from the stellar material due to changes in its thermodynamic properties. This quantity is a function of time t and is formulated in STELUM as

$$\epsilon_{\rm grav} = \frac{P}{\rho}\frac{\chi_T}{\chi_\rho}\left(\frac{d\ln P}{dt} - \frac{1}{\nabla_{\rm ad}}\frac{d\ln T}{dt}\right) - \sum_{i=1}^{I}\left(u_i + \frac{P}{\rho_i}\right)\frac{dX_i}{dt} + l_{\rm cr}\frac{dm_{\rm cr}}{dt}\,\delta\left(m - m_{\rm cr}\right). \qquad (3.4)$$

In this expression, ρ is the total mass density, χ_T and χ_ρ are standard thermodynamic derivatives, $\nabla_{\rm ad}$ is the adiabatic temperature gradient, X_i, ρ_i, and u_i denote the mass fraction abundance, mass density, and internal energy per unit mass of element i, and I stands for the number of chemical species considered. Besides, note that all time derivatives here and in the rest of the paper are Lagrangian derivatives. The terms involving the derivatives of the pressure and temperature represent the well-known contribution of the expansion/contraction of the star to the energy budget. The terms involving the derivatives of the elemental mass fractions account for changes in internal energy due to changes in chemical composition. Here, dX_i/dt must be deduced from the physics of particle transport, which is discussed extensively in Section 3.2.2.

The last term applies only to crystallizing white dwarfs and represents the energy generated by core crystallization: $l_{\rm cr}$ is the energy released per unit mass, $m_{\rm cr}$ is the mass coordinate of the solidification front, and the δ function indicates that the energy is deposited at $m = m_{\rm cr}$. The crystallized mass $m_{\rm cr}$ is determined by the usual condition on the Coulomb coupling parameter,

$$\Gamma = \frac{\overline{Z^{5/3}}e^2}{a_e k_{\rm B} T} \geq \Gamma_{\rm cr}, \qquad (3.5)$$

where e is the elementary charge, $k_{\rm B}$ is the Boltzmann constant, $\overline{Z^{5/3}}$ is the average of $Z_i^{5/3}$ over all species (with Z_i being the charge of ion i), $a_e = (3/4\pi n_e)^{1/3}$ is the electron-sphere radius (with n_e denoting the electron number density), and $\Gamma_{\rm cr}$ is the value of Γ above which crystallization occurs. The latter quantity, which depends on the local chemical composition,

is obtained from the carbon/oxygen phase diagram of Blouin & Daligault (2021). In principle, $l_{\rm cr}$ comprises only the latent heat released by the phase transition and is simply given by

$$l_{\rm cr} = 0.77 \frac{N_{\rm A} k_{\rm B} T}{\mu_{\rm ion}}, \tag{3.6}$$

where $N_{\rm A}$ is Avogadro's number, $\mu_{\rm ion}$ is the mean molecular weight per ion, and the numerical factor is taken from Salaris et al. (2000). However, in practice, we follow Isern et al. (2000) and add a second term designed to account for the gravitational energy produced by the phase separation of carbon and oxygen upon crystallization. Using Equations 2 and 8 of Isern et al. (2000) and assuming a binary mixture of carbon and oxygen, the previous expression becomes

$$l_{\rm cr} = \left[0.77 + 0.31 \mu_{\rm ion} \left(\Gamma_e - \frac{\langle T \Gamma_e \rangle}{T} \right) \Delta X_{\rm O} \right] \frac{N_{\rm A} k_{\rm B} T}{\mu_{\rm ion}}, \tag{3.7}$$

where $\Gamma_e = \Gamma / \overline{Z^{5/3}}$ is the electron coupling parameter, $\Delta X_{\rm O}$ is the difference in oxygen mass fraction between the solid and liquid phases, and the average $\langle T \Gamma_e \rangle$ is taken over the Rayleigh-Taylor-unstable liquid region just above the crystallization front (see Isern et al. 1997). We again rely on the phase diagram of Blouin & Daligault (2021) to evaluate the degree of oxygen enrichment in the solid core $\Delta X_{\rm O}$ [2].

3.2.2. Element Transport

STELUM incorporates a detailed treatment of element transport, as required to model the chemical evolution of white dwarfs. Several transport phenomena can be considered simultaneously: chemical diffusion, gravitational settling, thermal diffusion, stellar winds, external accretion, ordinary convection, convective overshoot, semiconvection, and thermohaline convection. These mechanisms are all treated as time-dependent diffusive processes, and the feedback of composition changes on the evolution of the star is fully taken into account. As the central purpose of the present paper is to exhibit and exploit these capabilities, we believe it is appropriate to elaborate on the relevant details here.

2. The improvements of Blouin et al. (2020b) to the conductive opacities and of Blouin & Daligault (2021) to the treatment of phase separation were incorporated into STELUM only after the evolutionary sequences presented in Paper I and in this work were computed. Thus, these calculations rely on the uncorrected conductive opacities of Cassisi et al. (2007) and ignore the energy released through phase separation (only the latent heat is included).

The time evolution of the elemental mass fraction X_i at a given radius r is described by the following transport equation:

$$\frac{dX_i}{dt} = S_{\mathrm{nuc},i} - \frac{1}{r^2\rho}\frac{d}{dr}\left(r^2\rho\left[\left(v_i + v_{\mathrm{wind}} + v_{\mathrm{acc}}\right)X_i - D\frac{dX_i}{dr}\right]\right), \tag{3.8}$$

where $S_{\mathrm{nuc},i}$ is a source/sink term accounting for the creation/destruction of element i by nuclear reactions (see the Appendix), v_i is the diffusion velocity of element i, v_{wind} is the stellar wind velocity, v_{acc} is the accretion velocity, and D is the mixing coefficient (also called the macroscopic diffusion coefficient). As before, the time derivative is a Lagrangian derivative. The full chemical evolution is governed by a set of I such equations, one for each atomic species. This form of the transport equation nicely emphasizes the distinction between microscopic and macroscopic transport: the effects of atomic diffusion are contained in v_i, whereas the effects of large-scale motions are captured by v_{wind}, v_{acc}, and D. In the following, we succinctly outline the physics behind each of these terms.

The diffusion velocities are obtained from the formalism of Burgers (1969) describing atomic diffusion in a multicomponent fluid. For a mixture of $I+1$ species (I elements plus the free electrons), one must solve a system of $2I+4$ coupled equations, comprising $I+1$ equations of momentum conservation,

$$\frac{dP_i}{dr} + \rho_i\left(g - g_{\mathrm{rad},i}\right) - n_i Z_i e E = \sum_{j\neq i}^{I+1} K_{ij}\left(v_j - v_i\right) + \sum_{j\neq i}^{I+1} K_{ij} z_{ij}\frac{A_j r_i - A_i r_j}{A_i + A_j}, \tag{3.9}$$

$I+1$ equations of energy conservation,

$$\begin{aligned}\frac{5}{2}n_i k_{\mathrm{B}} T\frac{d\ln T}{dr} = &-\frac{2}{5}K_{ii}z''_{ii}r_i - \frac{5}{2}\sum_{j\neq i}^{I+1}\frac{K_{ij}z_{ij}A_j}{A_i + A_j}\left(v_j - v_i\right)\\ &-\sum_{j\neq i}^{I+1}\frac{K_{ij}}{\left(A_i + A_j\right)^2}\left(3A_i^2 + z'_{ij}A_j^2 + \frac{4}{5}z''_{ij}A_iA_j\right)r_i\\ &+\sum_{j\neq i}^{I+1}\frac{K_{ij}A_iA_j}{\left(A_i + A_j\right)^2}\left(3 + z'_{ij} - \frac{4}{5}z''_{ij}\right)r_j,\end{aligned} \tag{3.10}$$

and two additional equations imposing the constraints of no net mass flow and no net electric current (see for instance Salaris & Cassisi 2017). Note that the index $I+1$ refers to the electrons. In these expressions, E is the electric field, g is the gravitational acceleration, A_i, P_i, n_i, $g_{\mathrm{rad},i}$, and r_i are the atomic weight, partial pressure, number density, radiative acceleration, and residual heat flow of species i, respectively, and K_{ij}, z_{ij}, z'_{ij}, and z''_{ij} are the so-called resistance coefficients, which capture the dynamics of interparticle collisions.

All other symbols have been defined previously. It is instructive to discuss very briefly the physical meaning of the various terms in Equation 3.9. The left-hand side is the total force per unit volume on particles of type i due to the partial pressure gradient, the gravitational field, and the electric field. These contributions collectively give rise to the processes referred to as chemical diffusion and gravitational settling. In the second term, the phenomenon of radiative levitation is accounted for by employing an effective (reduced) gravity $g - g_{\mathrm{rad},i}$. Finally, the last term involving the residual heat flows on the right-hand side represents the contribution of thermal diffusion.

A number of quantities appearing in the Burgers formalism must be specified a priori to close the system. The partial pressure P_i must be expressed in terms of the number density n_i, which is often done through an ideal gas law. Because this approximation breaks down in white dwarf interiors, we add the Coulomb correction term proposed by Beznogov & Yakovlev (2013), so that the partial pressure gradient becomes

$$\frac{dP_i}{dr} = n_i k_{\mathrm{B}} T \left(\frac{d\ln n_i}{dr} + \frac{d\ln T}{dr} \right) - \frac{3}{10} \frac{Z_i^{5/3} e^2}{a_e} \frac{d\ln n_e}{dr} n_i, \tag{3.11}$$

where $n_e \equiv n_{I+1}$. A prescription for the calculation of the radiative acceleration $g_{\mathrm{rad},i}$ is also needed. At the present time, this feature is not included in STELUM (we set $g_{\mathrm{rad},i} = 0$ for all i). Finally, the resistance coefficients K_{ij}, z_{ij}, z'_{ij}, and z''_{ij} are linked to the so-called collision integrals, which must also be known. These are evaluated from the results of Fontaine et al. (2015a), which are based on an improved version of the method described at length in Paquette et al. (1986b). With these quantities specified, the Burgers equations contain $2I + 3$ unknown variables: the $I + 1$ diffusion velocities v_i, the $I + 1$ residual heat flows r_i, and the electric field E. Given that the full system comprises $2I + 4$ equations, the problem is overconstrained. A common approach is to consider the gravitational acceleration g as an additional unknown variable and to compare the derived value with the expected value $g = Gm/r^2$ as a consistency check (Thoul et al., 1994). However, this strategy is problematic when diffusion takes place in electron-degenerate material, such as in white dwarfs. The issue is that Equation 3.9, although appropriate for the nondegenerate ions, cannot be applied to the degenerate electrons, because their partial pressure does not follow a simple analytic formula such as Equation 3.11. A straightforward solution is to drop Equation 3.9 for the electrons and to treat $g = Gm/r^2$ as a known parameter, leaving a closed set of $2I + 3$

equations and $2I + 3$ unknown variables (Pelletier et al., 1986; Paxton et al., 2018). This is the approach adopted in STELUM [3].

The wind velocity follows from simple mass conservation arguments. Assuming that the wind is weak enough so that the stellar mass can be considered constant, the wind velocity is given by

$$v_{\rm wind} = -\frac{\dot{M}_{\rm wind}}{4\pi r^2 \rho}, \tag{3.12}$$

where the mass-loss rate $\dot{M}_{\rm wind}$ must be specified. The mass-loss rate is inherently negative so that the wind velocity is positive (that is, the stellar material is pushed outward). Because mass accretion is the mathematical opposite of mass loss, an identical expression applies to the accretion velocity,

$$v_{\rm acc} = -\frac{\dot{M}_{\rm acc}}{4\pi r^2 \rho}, \tag{3.13}$$

where the accretion rate $\dot{M}_{\rm acc}$ must also be provided. The accretion velocity is directed inward because $\dot{M}_{\rm acc}$ is by definition a positive quantity.

The macroscopic transport coefficient D takes different forms depending on the locally dominant mixing mechanism. In a convection zone, we adopt the mixing coefficient prescribed by Langer et al. (1985),

$$D_{\rm conv} = \frac{1}{3} v_{\rm conv} \ell_{\rm conv}, \tag{3.14}$$

where $\ell_{\rm conv} = \alpha H_P$ is the mixing length (with H_P denoting the pressure scale height) and $v_{\rm conv}$ is the convective velocity obtained from the mixing-length theory (see the Appendix). Just outside a convection zone, mixing due to convective overshoot is included using an exponentially decaying diffusion coefficient, as suggested by Freytag et al. (1996),

$$D_{\rm ov} = D_{\rm conv,0} \ \exp\left(\frac{-2|r - r_0|}{f_{\rm ov}\, H_{P,0}}\right), \tag{3.15}$$

where r_0 is the radial boundary of the convection zone, $H_{P,0}$ and $D_{\rm conv,0}$ are the pressure scale height and convective mixing coefficient at that radius, and $f_{\rm ov}$ is a free parameter controlling the extent of the overshooting region.

3. As pointed out by Paxton et al. (2018), another issue in the application of the Burgers formalism to white dwarfs is that the expression on the left-hand side of Equation 3.10 implicitly assumes an ideal, nondegenerate gas. However, this inconsistency is expected to be of little consequence because it only affects the thermal-diffusion terms, which are generally much smaller than the gravitational-settling terms in white dwarfs.

STELUM also has the capability to model mixing processes arising in the presence of composition gradients. On one hand, the phenomenon of semiconvection occurs in a region that is convectively unstable according to the Schwarzschild criterion but where the composition gradient has a stabilizing effect. Following Langer et al. (1985), the semiconvective diffusion coefficient takes the form

$$D_{\rm sc} = \frac{8}{9}\alpha_{\rm sc}\frac{\sigma T^3}{\rho^2 \kappa c_P}\frac{\nabla_{\rm rad} - \nabla_{\rm ad}}{B - (\nabla_{\rm rad} - \nabla_{\rm ad})}, \tag{3.16}$$

where c_P is the specific heat capacity at constant pressure, B is the so-called Ledoux term (which measures the influence of the composition gradient), and $\alpha_{\rm sc}$ is an adjustable efficiency factor. On the other hand, the reverse situation, a stable thermal structure combined with an unstable chemical structure, leads to the process of thermohaline convection (also called fingering convection). Based on the work of Kippenhahn et al. (1980), the thermohaline mixing coefficient can be expressed as

$$D_{\rm th} = 8\alpha_{\rm th}\frac{\sigma T^3}{\rho^2 \kappa c_P}\frac{B}{\nabla_{\rm rad} - \nabla_{\rm ad}}, \tag{3.17}$$

where $\alpha_{\rm th}$ is another efficiency parameter[4]. We rely on standard quantitative criteria to determine the onset of semiconvective and thermohaline mixing (see for instance Salaris & Cassisi 2017).

Like the structure equations, the I transport Equations 3.8 are first recast in terms of the independent mass variable ξ defined in Equation 3.1. The numerical solution is then performed simultaneously for all atomic species using the implicit Runge-Kutta integrator RADAU5 of Hairer & Wanner (1996), which is particularly well suited for stiff problems. In the present case, the stiffness of the problem is due to the large disparity of diffusive timescales between the center and surface of a star and between the various transport mechanisms. For numerical convenience, our chemical transport formalism is not applied all the way up to the surface, where the diffusive timescales can become extremely short, but only up to a prespecified fractional mass limit $q_{\rm lim}$. Above this layer ($q < q_{\rm lim}$), two choices of boundary conditions are possible. The first option is simply to assume a uniform composition (that is, the composition at $q = q_{\rm lim}$ is imposed everywhere above). The second option is to solve a

4. Note that Equations 3.16 and 3.17 assume that the actual temperature gradient is given by the radiative temperature gradient, which means that we ignore the energy transport associated with semiconvective and thermohaline mixing.

simplified form of the transport equation inspired by Charbonneau (1993) and Turcotte & Charbonneau (1993),

$$\frac{dX_i}{dt} = S_{\mathrm{wind},i} + S_{\mathrm{acc},i} + \frac{1}{r^2\rho}\frac{d}{dr}\left(r^2\rho D_{\mathrm{lim}}\frac{dX_i}{dr}\right), \tag{3.18}$$

where $S_{\mathrm{wind},i}$ and $S_{\mathrm{acc},i}$ are source/sink terms accounting for mass loss and accretion, and D_{lim} is a prespecified diffusion coefficient designed to generate artificial mixing. This method is computationally more expensive but more stable when mass loss or accretion is present. The source/sink terms are given by

$$S_{\mathrm{wind},i} = \frac{\dot{M}_{\mathrm{wind}}}{q_{\mathrm{lim}}M}X_i, \tag{3.19}$$

$$S_{\mathrm{acc},i} = \frac{\dot{M}_{\mathrm{acc}}}{q_{\mathrm{lim}}M}\left(X_{\mathrm{acc},i} - X_i\right), \tag{3.20}$$

where $X_{\mathrm{acc},i}$ is the mass fraction of element i in the accreted material.

3.3. Illustrative Simulations

The aim of this section is to demonstrate the modeling capabilities of STELUM in the framework of the spectral evolution of white dwarfs. To do so, we present two illustrative simulations of this phenomenon. In the first case, we follow the transformation of a helium-, carbon-, and oxygen-rich PG 1159 star into a helium-atmosphere DB white dwarf due to the downward diffusion of heavy elements, and then into a helium-dominated, carbon-polluted DQ white dwarf through the convective dredge-up of settling carbon. This is often called the PG 1159−DO−DB−DQ evolutionary channel. In the second case, we compute the evolution of a hot helium-rich DO white dwarf containing a small amount of hydrogen, which becomes a hydrogen-atmosphere DA star as a consequence of the float-up of hydrogen, and then a helium-atmosphere DC star through the convective mixing of the hydrogen and helium layers. We refer to this as the DO−DA−DC evolutionary channel. As discussed in the Introduction, there is strong empirical evidence that both scenarios indeed occur in nature.

Our adopted computational setup is as follows. For both simulations, we consider a typical mass $M = 0.6\ M_\odot$ and a very high initial effective temperature $T_{\mathrm{eff}} = 90{,}000$ K. The chemical structure consists of a homogeneous, equimassic carbon/oxygen core and a homogeneous envelope of fractional mass $\log q_{\mathrm{env}} = -2.0$. The initial envelope composition is the only parameter that differs between the two simulations and is specified below. The

following element transport mechanisms are taken into account: chemical, gravitational, and thermal diffusion (including nonideal effects), convective and overshoot mixing, and an outward wind in the early evolution. We use mixing-length and overshoot parameters of $\alpha = 1.0$ and $f_{\rm ov} = 0.075$; the reason for this choice will become apparent below. We assume the wind mass-loss law of Blöcker (1995a),

$$\dot{M}_{\rm wind} = -1.29 \times 10^{-15} \left(\frac{L}{L_{\odot}} \right)^{1.86} M_{\odot} \ {\rm yr}^{-1}, \tag{3.21}$$

where L is the total luminosity of the star. This prescription not only has the advantage of computational simplicity, but it also has proven appropriate for hot white dwarfs, even though it was originally developed to model post-AGB stars (see below). In order to capture the chemical evolution of the atmosphere, the transport boundary is placed very high in the envelope, at fractional mass $\log q_{\rm lim} = -14.0$. We assume a uniform composition above this point. Finally, residual nuclear burning is ignored throughout the cooling process.

3.3.1. The PG 1159−DO−DB−DQ Evolutionary Channel

The chain of events linking the PG 1159 stars and DQ white dwarfs is perhaps the best-studied case of spectral evolution and thus constitutes an important benchmark for our demonstration of the capabilities of STELUM. Theoretical calculations of the PG 1159-to-DO transition were performed by a number of authors over the years, namely, Dehner & Kawaler (1995), Unglaub & Bues (2000), Fontaine & Brassard (2002), Althaus & Córsico (2004), and Quirion et al. (2012). The DB-to-DQ transition has also been the focus of detailed modeling, starting with the work of Pelletier et al. (1986) and MacDonald et al. (1998). Later on, simulations of the entire PG 1159−DO−DB−DQ evolution were carried out by the La Plata group in Althaus et al. (2005b), Scóccola et al. (2006), and Camisassa et al. (2017), and by our own group in Dufour et al. (2005) using the ancestor of STELUM (see also Fontaine & Brassard 2005 and Brassard et al. 2007). Obviously, these various sets of models rely on disparate physical and numerical assumptions, especially regarding element transport. An exhaustive discussion of these differences is beyond the scope of the present paper and is thus deferred to a future publication (A. Bédard et al., in preparation). For now, we simply describe the results of our new calculations and make brief qualitative comparisons with previous works wherever appropriate.

In our simulation, the initial envelope composition is a helium/carbon/oxygen mixture typical of PG 1159 stars: $X_{\rm He} = 0.4$, $X_{\rm C} = 0.5$, and $X_{\rm O} = 0.1$ (Werner & Herwig, 2006). Figure 3.1 shows the chemical profile (the elemental mass fractions X_i as a function of fractional mass depth q) at various key points along the evolutionary sequence. The initial model is displayed in panel (a). Note that this starting chemical profile is approximate; the only way to obtain more realistic initial conditions is to compute the full evolution prior to the white dwarf stage, including the late helium-shell flash and associated born-again episode, as done for instance in Althaus et al. (2005b). A video showing the evolving chemical structure is available online as supplementary material.

The early chemical evolution is dominated by the stellar wind, which is strong enough to counteract gravitational settling. Therefore, the carbon and oxygen are temporarily maintained in the outer layers, and the star still exhibits a PG 1159−like surface composition at $T_{\rm eff} \sim 80{,}000$ K, as can be seen in panel (b). However, given the adopted expression for the mass-loss rate, the cooling of the star causes the wind to fade and thus to lose its ability to compete against gravitational settling. As a result, below $T_{\rm eff} \sim 75{,}000$ K, the superficial carbon and oxygen begin to sink rapidly into deeper layers, thereby producing a helium-atmosphere DO white dwarf. After a short transient phase in which a trace amount of carbon is still detectable, the outer envelope becomes completely devoid of heavy elements below $T_{\rm eff} \sim 60{,}000$ K, as displayed in panels (c) and (d), respectively.

It is worth emphasizing that the choice to include a wind in our calculations is far from arbitrary. In an analogous simulation without mass loss (not shown here), the carbon and oxygen diffuse out of the atmosphere in a few years, such that the PG 1159-to-DO transition occurs essentially instantaneously at the onset of the evolution. Such a behavior is clearly at odds with the existence of PG 1159 stars over a wide range of effective temperatures (Werner & Herwig, 2006). This observational evidence necessarily implies that some mechanism, most likely a wind, prevents gravitational settling at the beginning of the cooling sequence. Previous theoretical investigations by Unglaub & Bues (2000) and Quirion et al. (2012) reached a similar conclusion. Moreover, Quirion et al. (2012) examined the effect of changing the mass-loss prescription and found that Equation 3.21 provides the best match to the observed red edge of both the PG 1159 spectroscopic domain and the GW Vir instability strip, hence our use of this particular formula. Interestingly, we also note that our simple

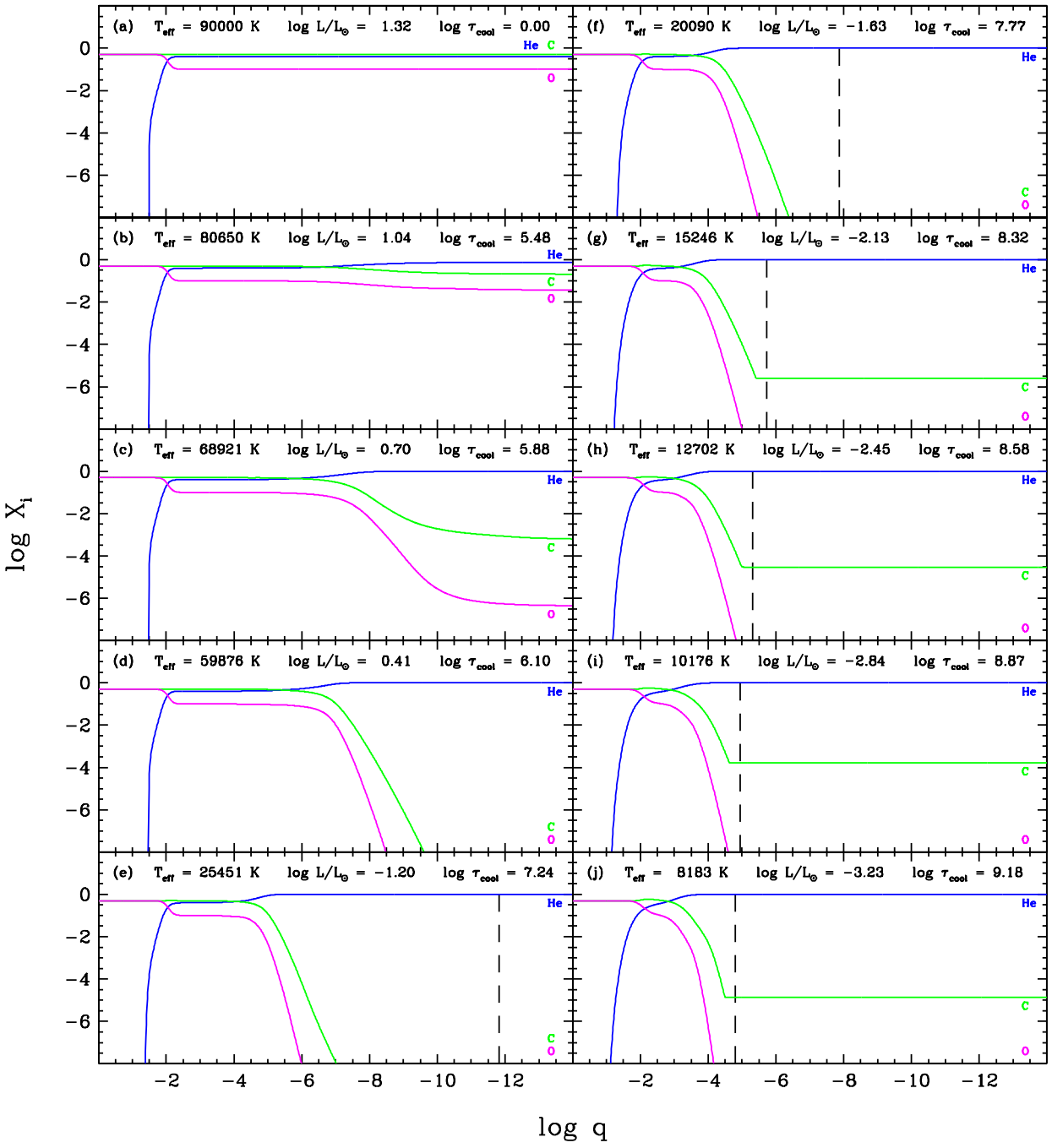

Figure 3.1 – Snapshots of the chemical structure, represented here as the run of the elemental mass fractions with fractional mass depth ($q = 1 - m/M$), at various points along our PG 1159−DO−DB−DQ evolutionary simulation. The hydrogen, helium, carbon, and oxygen abundance profiles are shown as red, blue, green, and magenta curves, respectively. The location of the base of the convection zone is indicated by a dashed black line. Each panel also gives the effective temperature, total luminosity, and cooling age of the displayed model. A video showing the full simulation is available online as supplementary material.

wind model predicts $\log X_{\rm C} \sim -3.0$ at the surface around $T_{\rm eff} \sim 70{,}000$ K, which is broadly consistent with measured carbon abundances of hot DO white dwarfs (Dreizler & Werner, 1996; Reindl et al., 2014a).

During the subsequent evolution, the carbon and oxygen continue to sink further into the star under the influence of gravitational settling and thermal diffusion. The pure-helium layer consequently grows from $\log q_{\rm He} \sim -8.0$ at $T_{\rm eff} \sim 60{,}000$ K to $\log q_{\rm He} \sim -6.0$ at $T_{\rm eff} \sim 25{,}000$ K, as shown in panel (e). However, in this DB white dwarf, element separation is still far from complete: the envelope harbors a double-layered chemical structure, with a pure-helium layer on top of a mantle retaining the initial composition of the PG 1159 progenitor. This is due to the fact that the diffusion timescales are much longer at the bottom than at the top of the envelope. This result was first demonstrated by Dehner & Kawaler (1995) and later corroborated by Fontaine & Brassard (2002) and Althaus & Córsico (2004). As discussed below, it is of fundamental importance for our understanding of DQ white dwarfs. Besides, note that the existence of the double-layered structure is supported independently by asteroseismic analyses of pulsating DB stars (Giammichele et al., 2018; Bischoff-Kim et al., 2019). In particular, the envelope composition profile displayed in panel (e) closely resembles that of the prototypical DB pulsator GD 358 as inferred from asteroseismology.

At this stage of the evolution, our DB white dwarf has a superficial convection zone associated with the recombination of helium, which grows deeper with further cooling (Rolland et al., 2018; Cukanovaite et al., 2019). The location of the base of the convective region is shown by a dashed black line in Figure 3.1. Comparing panels (e) and (f), it can be seen that the deepening of the convection zone occurs much faster than the sinking of carbon and oxygen: between $T_{\rm eff} \sim 25{,}000$ and 20,000 K, the mass extent of the convective region increases by four orders of magnitude, while the chemical profile barely changes. The inevitable outcome is that the helium convection zone eventually catches up with the settling carbon, which is thus brought back to the surface by virtue of the highly efficient convective mixing, as shown in panel (g). Notice that the region in which carbon is uniformly mixed (corresponding to the flat part of the carbon abundance profile) actually extends slightly beyond the formal convective boundary as a result of convective overshoot. As the star cools and the convective motions reach deeper, more carbon-rich layers, the amount of carbon in the helium-rich envelope increases. This is clearly seen in panels (g), (h), and (i): the

surface mass fraction is $\log X_{\rm C} \sim -5.6$, -4.5, and -3.8 at $T_{\rm eff} \sim 15{,}200$, 12,700, and 10,200 K, respectively. The carbon becomes spectroscopically visible, hence making the white dwarf a member of the DQ spectral class.

Then, at even lower effective temperatures, the trend reverses: after a plateau between $T_{\rm eff} \sim 10{,}600$ and 9800 K, the surface carbon abundance starts decreasing, as shown in panel (j). This behavior originates from a combination of two phenomena. First, the base of the convection zone reaches its maximum depth and thereby stops carrying additional carbon to the surface. Second, as originally explained in detail by Pelletier et al. (1986), a change in the average ionization state of carbon makes the slope of the carbon diffusion tail steeper, with the result that carbon partially sinks out of the convective region. This effect is apparent when comparing panels (i) and (j).

The relation between surface carbon abundance and effective temperature predicted by our chemical evolution simulation can be compared to empirically determined atmospheric parameters of DQ stars. Figure 3.2 shows our model prediction as a red curve together with DQ white dwarfs from Coutu et al. (2019) and Blouin & Dufour (2019) as black symbols in the $\log N_{\rm C}/N_{\rm He} - T_{\rm eff}$ diagram (where $N_{\rm C}/N_{\rm He}$ denotes the atmospheric carbon-to-helium number ratio). In the following, we focus solely on the classical, normal-mass DQ stars ($M \leq 0.7\ M_{\odot}$; large circles) and refrain from discussing the more massive objects ($M > 0.7\ M_{\odot}$; small dots). The latter group is believed to be produced by white dwarf mergers and thus constitutes a fundamentally different population (Dunlap & Clemens, 2015; Cheng et al., 2019; Coutu et al., 2019), so our calculations obviously do not apply to these objects. Most classical DQ stars form a tight sequence in the $\log N_{\rm C}/N_{\rm He} - T_{\rm eff}$ diagram, following a clear trend of decreasing carbon abundance with decreasing temperature. Figure 3.2 demonstrates that our simulation perfectly reproduces both the location and the slope of the observed relation. At this time, our calculations cover only the first half of the DQ sequence and cannot be extended to lower effective temperatures due to the unavailability of OPAL radiative opacities for carbon in this region of parameter space. Besides, the absence of objects on the ascending part of the theoretical curve is actually a selection effect: in this temperature range, white dwarfs retain their DB spectral type because the carbon abundance is well below the optical detection limit. Nevertheless, ultraviolet observations of a few cool DB stars have revealed the expected amount of atmospheric carbon (Desharnais et al., 2008).

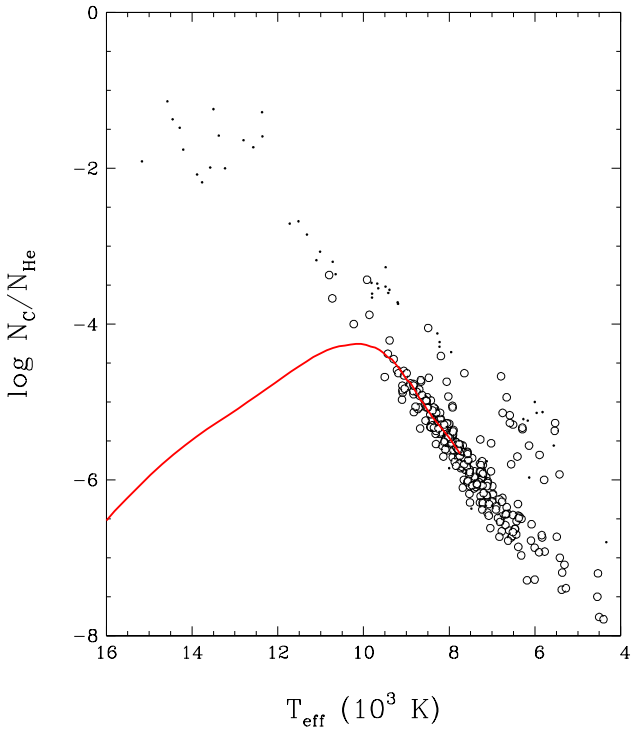

Figure 3.2 – Theoretical and empirical relations between the atmospheric carbon-to-helium number ratio and the effective temperature of DQ white dwarfs. The red curve shows the prediction from our PG 1159−DO−DB−DQ evolutionary simulation, while the black symbols represent empirical atmospheric parameters of DQ stars taken from Coutu et al. (2019) and Blouin & Dufour (2019). The objects with $M \leq 0.7\ M_{\odot}$ and $M > 0.7\ M_{\odot}$ are displayed as large circles and small dots, respectively.

It is important to mention that the agreement between the data and our model is not entirely coincidental. In fact, the height of the predicted curve in the $\log N_{\rm C}/N_{\rm He} - T_{\rm eff}$ diagram depends very sensitively on a number of model parameters, most notably the stellar mass, the depth of the envelope, the initial carbon abundance of the PG 1159 progenitor, and the extent of convective overshoot. For standard values of the first three parameters ($M = 0.6\ M_{\odot}$, $\log q_{\rm env} = -2.0$, $X_{\rm C} = 0.5$), the overshoot efficiency factor $f_{\rm ov}$ can be adjusted to match the location of the observed DQ sequence. We find that $f_{\rm ov} = 0.075$ yields the good agreement shown in Figure 3.2, hence our choice of this specific value. Interestingly, 3D hydrodynamical simulations of convection in white dwarfs favor a higher overshoot parameter, $f_{\rm ov} \sim 0.2-0.4$ (Cunningham et al. 2019; T. Cunningham 2021, private communication). However, these calculations are restricted to shallow convection zones extending no

deeper than $\log q \sim -12.0$. Given that DQ stars have deep convection zones reaching down to $\log q \sim -5.0$, our results indicate that the efficiency of convective overshoot is strongly depth dependent, a conclusion also reached in the context of AGB stars (Herwig, 2000). Therefore, our simulations could potentially be used to calibrate the extent of overshoot mixing in cool white dwarfs, for which 3D hydrodynamical models are currently unavailable. An exhaustive exploration of the model parameter space, which is obviously beyond the scope of the present work, will be the focus of a forthcoming publication (A. Bédard et al., in preparation).

Regardless of this matter, we want to stress that it is still remarkable that our evolutionary sequence successfully reproduces the slope of the empirical $\log N_{\rm C}/N_{\rm He} - T_{\rm eff}$ relation at low temperatures. Indeed, as noted earlier, the dredge-up of carbon in helium-rich white dwarfs and the corresponding DB-to-DQ transition have been the subject of numerous theoretical studies, both by our group (Pelletier et al., 1986; Dufour et al., 2005; Fontaine & Brassard, 2005; Brassard et al., 2007) and by other groups (MacDonald et al., 1998; Althaus et al., 2005b; Scóccola et al., 2006; Camisassa et al., 2017). Among these, only the models of our group have been able to match the observed trend of decreasing carbon abundance with decreasing effective temperature, while other models predict instead a constant or increasing carbon abundance. The differences between previous works and our present calculations will be further discussed in our upcoming paper.

Finally, one last clarification needs to be made. The first generation of DQ models developed in the 1980s assumed chemical structures consisting of a single-layered, helium-dominated envelope atop a pure-carbon core in diffusive equilibrium. In this framework, the trace carbon at the surface is dredged up from the core, a process that can only take place in envelopes much thinner ($\log q_{\rm env} \sim -3.5$) than expected from the standard theory of stellar evolution (Koester et al., 1982; Fontaine et al., 1984; Pelletier et al., 1986). We have known since the work of Dehner & Kawaler (1995) that this scenario contains a major flaw: the envelope of a DQ star has not had the time to achieve complete element separation and is therefore characterized by the double-layered chemical profile discussed above. Consequently, the atmospheric carbon does not come from the core but rather from the PG 1159−like layer at the bottom of the envelope, as clearly seen in Figure 3.1. This distinction is crucial: the

modern paradigm requires more standard envelope masses ($\log q_{\rm env} \sim -2.0$), thereby resolving the conflict between stellar evolution theory and the existence of carbon-polluted white dwarfs. Unfortunately, the misconception that DQ stars have reached diffusive equilibrium and can thus only be explained by thin envelopes is still widespread in the current literature (Koester et al., 2020).

3.3.2. The DO−DA−DC Evolutionary Channel

The DO−DA−DC connection represents another frequently invoked case of white dwarf spectral evolution. Indeed, the DO-to-DA and DA-to-DC transitions have been the topic of many theoretical investigations, although they have often been examined and discussed separately, as two unrelated phenomena. The float-up of residual hydrogen at high effective temperature was first modeled by Unglaub & Bues (1998, 2000). Such calculations were also performed by Althaus et al. (2005a, 2020b), who however placed little emphasis on the chemical transformation itself and focused instead on its implications for stellar pulsations. The convective mixing of the hydrogen and helium layers at low effective temperature has an even longer modeling history, comprising the works of Baglin & Vauclair (1973), Koester (1976), D'Antona & Mazzitelli (1989), MacDonald & Vennes (1991), Althaus & Benvenuto (1998), Chen & Hansen (2011), and Rolland et al. (2018). It is beyond the scope of the present paper to review all of the aforementioned studies and their very diverse levels of sophistication. Nevertheless, while describing our own simulation below, we briefly comment on its similarities and differences with older calculations. For now, we want to point out that this is the first time that the DO−DA−DC evolution is computed as a whole, from beginning to end, including both the float-up process at high temperature and the convective mixing event at low temperature.

Our simulation begins with a helium-dominated envelope containing a small amount of hydrogen: $X_{\rm H} = 0.0001$, $X_{\rm He} = 0.9999$. This initial model would be classified as a normal DO star, given that the optical detection limit of hydrogen in a hot helium-rich atmosphere is $X_{\rm H} \sim 0.01$ (Werner, 1996a). Apart from the initial envelope composition, we use the same computational settings as in our previous simulation. Figure 3.3 details the evolution of the chemical structure, with the starting model shown in panel (a). An important thing to note is that the trace hydrogen profile does not extend down to the base of the envelope, but only down to $\log q = -4.0$, because deeper-lying hydrogen is expected to be burned in

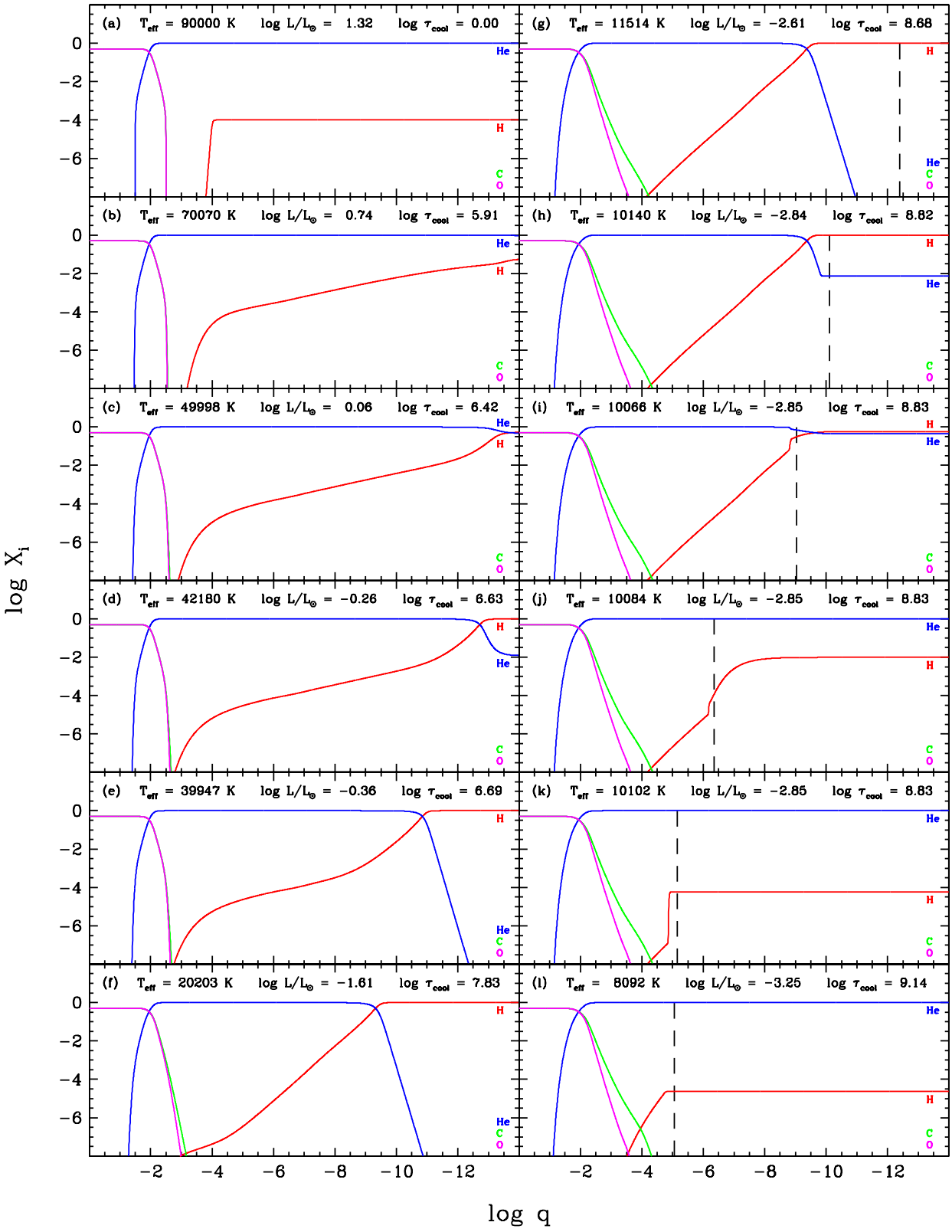

Figure 3.3 – Same as Figure 3.1, but for our DO−DA−DC evolutionary simulation.

previous evolutionary phases (Althaus et al., 2005a). Consequently, the total hydrogen mass is $10^{-8}M$. Once again, a video displaying the full chemical evolution is available online as supplementary material.

Panels (a) to (f) outline the float-up of hydrogen and the associated DO-to-DA transformation taking place in the early cooling phase. At first, the float-up process is considerably slow, because the outer hydrogen-enriched layers are successively peeled off by the stellar wind. Consequently, the hydrogen is still spectroscopically invisible at $T_{\rm eff} \sim 70{,}000$ K. The surface eventually becomes richer in hydrogen than in helium around $T_{\rm eff} \sim 50{,}000$ K. Thereafter, the superficial helium quite rapidly sinks out of sight, leaving a pure-hydrogen atmosphere at $T_{\rm eff} \sim 40{,}000$ K. The hydrogen located deeper in the envelope continues to diffuse upward, such that the pure-hydrogen layer gradually becomes thicker. At $T_{\rm eff} \sim 20{,}000$ K, element separation is complete: the hydrogen and helium layers have reached diffusive equilibrium. Note that at this point, the total hydrogen mass is now $\sim 10^{-9}M$, meaning that $\sim$90% of the hydrogen initially present in the model has been ejected by the wind. The leftovers form a pure-hydrogen layer of thickness $\log q_{\rm H} \sim -10.0$ and an extended diffusion tail underneath.

Interestingly, our simulated DO-to-DA transition occurs at the right time in the evolution, that is, in an effective temperature range where the fraction of DA stars is observed to increase (Paper I). Furthermore, our calculation shows that this transformation takes place on a Myr timescale and thus that there is a nonnegligible probability to observe objects currently transitioning from a helium atmosphere to a hydrogen atmosphere. This is entirely consistent with the recent detection of tens of hot white dwarfs possessing extremely thin hydrogen layers (Manseau et al. 2016; Paper I). In that respect, we must stress once again the important role played by the wind: without the effect of mass loss, gravitational settling would be so efficient that all DO stars containing residual hydrogen would become DA stars practically instantaneously. This scenario is in stark conflict with our empirical knowledge of the spectral evolution of white dwarfs, thereby strongly supporting the existence of stellar winds at the beginning of the cooling sequence. Qualitatively similar results were obtained by Unglaub & Bues (1998, 2000) from transport calculations in static envelope models.

The immediately subsequent evolution is relatively uneventful: because the envelope is in diffusive equilibrium, the chemical profile remains essentially unchanged, as illustrated by

the model with $T_{\rm eff} \sim 11{,}500$ K in panel (g). This model falls within the ZZ Ceti instability strip and is therefore representative of a pulsating DA white dwarf with a thin hydrogen layer, such as Ross 548 (Giammichele et al., 2016).

However, this is the calm before the storm. From that point on, the recombination of hydrogen produces a superficial convection zone, which grows deeper with further cooling (Tremblay et al., 2015). The dashed black line in Figure 3.3 indicates the location of the base of the convective region. A radical chemical transformation follows: the advective motions reach into the underlying helium, which is thus dredged up and thoroughly mixed into the outer hydrogen layer, as can be seen in panel (h). This phenomenon is closely analogous to the dredge-up of carbon that turns a DB star into a DQ star, as featured in our previous simulation. The main difference here is that we are dealing with a runaway process. At a given effective temperature, a helium-rich convection zone is much deeper than a hydrogen-rich convection zone (Rolland et al., 2018). Consequently, the increase in helium abundance results in a more extended convective region, which in turn brings more helium to the outer layers, and so on. In the end, the hydrogen previously accumulated at the surface is entirely diluted in the helium-dominated envelope. This phenomenon is well illustrated in panels (h) to (k): as the base of the convection zone moves inward from $\log q \sim -10.0$ to -5.0, hydrogen goes from dominating the atmospheric composition to becoming a trace element.

A few aspects of this mixing episode are particularly worthy of interest and deserve further comments. First, the chemical transformation occurs extremely rapidly, as indicated by the constant cooling age given in panels (i) to (k). In fact, the timescale for the growth of the convection zone is shorter than the mixing and diffusion timescales. This is obvious in panel (j), where the nonflat hydrogen abundance profile reveals that the convective region has not had the time to achieve complete mixing, and in panel (k), where the steep hydrogen abundance gradient below the convection zone has not yet been smoothed out by chemical diffusion. Second, the mixing event causes a slight increase in effective temperature, from $T_{\rm eff} = 10{,}062$ to 10,102 K, as partly shown in panels (i) to (k). This behavior, highly unusual by white dwarf standards, was also reported in a few earlier studies (Baglin & Vauclair, 1973; D'Antona & Mazzitelli, 1989; Chen & Hansen, 2011). It was explained by Chen & Hansen (2011) as the result of the opacity change in the outer layers and the convective coupling between the core and the envelope. We note in passing that all previous theoretical calculations

of convective mixing (Baglin & Vauclair, 1973; Koester, 1976; D'Antona & Mazzitelli, 1989; MacDonald & Vennes, 1991; Althaus & Benvenuto, 1998; Chen & Hansen, 2011; Rolland et al., 2018) relied on simplified semi-evolutionary approaches and/or instantaneous mixing approximations. To our knowledge, ours is the first fully self-consistent simulation of this phenomenon, including both a detailed time-dependent treatment of element transport and the feedback of composition changes on the evolution of the star.

Once the convection zone stabilizes, the cooling resumes on a more typical timescale, thereby allowing the hydrogen abundance profile below the convection zone to relax toward diffusive equilibrium. The chemical structure of the model with $T_{\rm eff} \sim 8100$ K is displayed in panel (l). The final surface hydrogen mass fraction is $\log X_{\rm H} \sim -4.6$, just below the optical detection limit in this effective temperature range (Rolland et al., 2018). Our DA star has therefore become a DC star. Besides, note that this conversion necessarily involves a short phase during which our model would appear as a so-called helium-rich DA white dwarf.

A few pieces of empirical evidence firmly support the occurrence of such a DA-to-DC transition in real stars. First, this phenomenon is believed to be responsible for the observed increase of the fraction of helium-atmosphere white dwarfs at low effective temperatures (Blouin et al., 2019; Cunningham et al., 2020). Second, it also provides an elegant explanation of the famous bifurcation seen in the Gaia white dwarf sequence (Gaia Collaboration et al., 2018b). This is illustrated in Figure 3.4, which shows the color−magnitude diagram of the Gaia sample of white dwarfs within 100 pc (Gaia Collaboration et al., 2018a) taken from the Montreal White Dwarf Database (MWDD; Dufour et al. 2017). Also displayed are theoretical cooling tracks of 0.6 $M_{\odot}$ white dwarfs with various atmospheric compositions (Holberg & Bergeron 2006; Bergeron et al. 2011; Tremblay et al. 2011; Blouin et al. 2018; Paper I). The red and blue curves correspond to pure-hydrogen and pure-helium atmospheres, respectively, while the green curve assumes the varying surface composition predicted by our simulation. As noted in many previous works, the pure-hydrogen sequence nicely coincides with the upper branch of the bifurcation, while the pure-helium sequence fails to reproduce the lower branch of the bifurcation. It has been demonstrated that the atmosphere of the objects populating the latter region is indeed helium rich, but also likely contains an undetectable amount of hydrogen (or any other electron donor), which is the source of the color and magnitude offset (Bergeron et al., 2019). Figure 3.4 shows that our simulation is in excellent

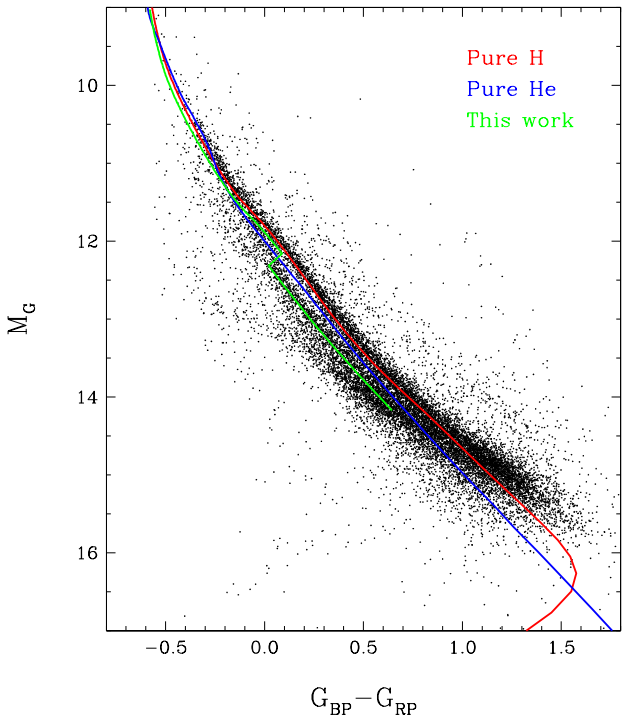

Figure 3.4 – Color−magnitude diagram showing the Gaia sample of white dwarfs within 100 pc taken from the MWDD, together with theoretical cooling tracks of 0.6 $M_\odot$ white dwarfs with various atmospheric compositions: pure hydrogen, pure helium, and the hydrogen−helium mixture predicted by our DO−DA−DC evolutionary simulation, which correspond to the red, blue, and green curves, respectively.

agreement with this interpretation. The green curve initially follows the red curve and heads toward the upper branch, as expected for a DA star, but then abruptly shifts downward and subsequently moves along the lower branch as a result of convective mixing. Both the location and magnitude of the predicted shift are remarkably consistent with the morphology of the observed color−magnitude diagram, indicating that the mixing temperature and hydrogen abundance of our final DC model are realistic. In short, our results confirm that the lower branch of the bifurcation can be ascribed to helium-dominated atmospheres with traces of hydrogen and thus constitutes an observational signature of convectively driven spectral evolution.

Of course, the evolutionary calculation presented here involves several physical parameters whose influence has yet to be examined quantitatively. The most important variable is certainly the mass fraction of hydrogen in the initial model. A larger amount of hydrogen

is expected to result in an earlier DO-to-DA transition, a later DA-to-DC transition, and a larger final hydrogen abundance. Another critical model parameter is the mass-loss law, which dictates the strength of the wind and hence the efficiency of gravitational settling at high effective temperatures. While the expression adopted here (Equation 3.21) was shown to be appropriate for PG 1159 stars, it likely overestimates the mass-loss rate in DO white dwarfs poorer in heavy elements, given that the wind is thought to be metal driven. The use of a more realistic mass-loss law might make the float-up of hydrogen faster. Furthermore, at lower effective temperatures, the convective mixing of the hydrogen and helium layers obviously depends on the extent of convective overshoot. We assumed here the overshoot parameter inferred earlier from our simulation of the DB-to-DQ transformation, but it is not clear that this choice is also suitable for the DA-to-DC transformation. In fact, the latter case probably requires a higher overshoot parameter, because the mixing episode occurs closer to the surface, where convective overshoot is expected to be more efficient. Finally, it would also be interesting to study the effect of hydrogen accretion on the chemical evolution.

3.4. Summary and Conclusion

The aim of this work was to investigate the theory of the spectral evolution of white dwarfs by carrying out numerical calculations of element transport in cooling white dwarfs. To do so, we relied on the STELUM software, which is the latest version of the stellar evolutionary code developed at the Université de Montréal. First, we presented for the first time a thorough description of STELUM. We successively discussed the physical ingredients and numerical techniques used to model the structure and evolution of stars and the transport of chemical species. We emphasized that several transport mechanisms, among which all relevant types of atomic diffusion and convective mixing, are included as time-dependent diffusive processes and are fully coupled to the evolution. We hope that this paper can serve as a valuable reference for future studies using STELUM. Further details about the code can be found in the Appendix or provided upon request to the lead author.

Then, we presented the results of two sophisticated simulations of the chemical evolution of white dwarfs. In the first case, we modeled the PG 1159−DO−DB−DQ evolutionary channel from beginning to end. In the early evolution, the hot PG 1159 star initially retains

a carbon- and oxygen-rich atmosphere due to a stellar wind, but then turns into a pure-helium DO white dwarf once mass loss ceases and gravitational settling becomes efficient. The resulting envelope consists of a double-layered structure: a pure-helium layer atop a PG 1159−like shell. Although the pure-helium layer grows with time, the double-layered structure persists throughout the cooler DB phase because of the long diffusion timescales at the base of the envelope. The superficial helium convection zone eventually reaches into the PG 1159−like shell, thereby bringing a small amount of carbon to the surface and transforming the DB star into a DQ star. At low effective temperatures, the dredged-up carbon partially sinks back below the convective region, and thus the atmospheric carbon abundance decreases with cooling. We demonstrated that our calculation is in excellent quantitative agreement with the well-established empirical relation between the carbon abundance and the effective temperature of cool DQ white dwarfs. We nevertheless pointed out that this portion of the evolution depends sensitively on several model parameters, the most uncertain of which is the extent of convective overshoot.

In the second case, we performed a full-fledged simulation of the DO−DA−DC evolutionary channel. At the outset, the helium-rich envelope of our DO white dwarf model contains a small amount of hydrogen. Gravitational settling causes this hydrogen to diffuse upward, a process that is initially very slow due to the competing effect of the stellar wind. A hydrogen layer gradually forms at the surface, eventually turning the DO star into a DA star. Later on, a superficial convection zone appears and thoroughly dilutes the hydrogen layer into the underlying helium envelope. Consequently, in terms of chemical composition, the final outcome is strikingly similar to the initial state: a helium-dominated atmosphere with an undetectable quantity of hydrogen, which corresponds to the DC spectral type. To our knowledge, this is the first time that this mixing event is computed in a time-dependent and self-consistent way. More quantitatively, for an initial hydrogen mass fraction $X_{\rm H} = 0.0001$, our simulated DO-to-DA and DA-to-DC transformations occur at $T_{\rm eff} \sim 50{,}000$ and 10,000 K, respectively. Although these transition temperatures admittedly depend on the mass-loss and mixing prescriptions, they are both remarkably consistent with the observed variation of the numbers of hydrogen-rich and helium-rich white dwarfs along the cooling sequence. Moreover, we showed that the lower branch of the bifurcation seen in the Gaia color−magnitude diagram

is perfectly matched by the cooling track of our final hydrogen-bearing DC star and can therefore be interpreted as the signature of convective mixing.

Clearly, the results presented in this paper are merely a glimpse of what can be learned from numerical simulations of element transport in cooling white dwarfs. Such calculations hold huge potential for new advances in our theoretical understanding of spectral evolution, and this potential has yet to be fully exploited. An obvious step is the exploration of the model parameter space relevant to the two simulations discussed in Section 3.3, which could provide answers to a number of important questions. How does the carbon content of a PG 1159 star impact the carbon abundance of its DQ progeny? What is the effect of varying the hydrogen content of a hot DO white dwarf on the DO-to-DA and DA-to-DC transitions? What is the ultimate fate of a PG 1159−type object containing hydrogen (a so-called hybrid PG 1159 star)? How do fundamental parameters such as the total stellar mass and the envelope mass influence the transport of chemical species? What are the consequences of changing transport prescriptions such as the strength of the stellar wind, the efficiency of convective mixing, and the extent of convective overshoot? Finally, we note that several other unsettled problems related to the spectral evolution of white dwarfs need to be addressed in future research work. Notable examples include the origin of hydrogen in DBA stars, the carbon abundance pattern of massive DQ stars, and the interplay between the accretion, diffusion, and mixing of metals in DAZ, DBZ, and DZ white dwarfs.

Acknowledgements

We would like to acknowledge the essential contribution of our late colleague Gilles Fontaine to the development of the Montreal white dwarf evolutionary code. This work was supported by the Natural Sciences and Engineering Research Council (NSERC) of Canada and the Fonds de Recherche du Québec − Nature et Technologie (FRQNT). S. Blouin acknowledges support from the Laboratory Directed Research and Development program of Los Alamos National Laboratory (20190624PRD2) and from NSERC's Banting Postdoctoral Fellowship program.

Appendix: Additional Details on the STELUM Code

Equations of Stellar Structure and Evolution

STELUM relies on the standard one-dimensional theory of stellar structure and evolution (see for instance Kippenhahn et al. 2012). Consider a spherical, nonrotating, nonmagnetic star of given total mass M and chemical composition, the latter being specified by I elemental mass fractions X_1,X_2,...,X_I at each depth. The structure and evolution of such an object are governed by the well-known set of four differential equations describing mass conservation, hydrostatic equilibrium, energy conservation, and energy transport. In order to model the atmosphere as well, a fifth equation defining the optical depth must also be included. In Lagrangian form, these equations can be written as

$$\frac{dr}{dm} = \frac{1}{4\pi r^2 \rho}, \tag{3.22}$$

$$\frac{dP}{dm} = -\frac{Gm}{4\pi r^4}, \tag{3.23}$$

$$\frac{dl}{dm} = \epsilon_{\rm nuc} - \epsilon_{\rm neu} + \epsilon_{\rm grav}, \tag{3.24}$$

$$\frac{dT}{dm} = -\frac{GmT}{4\pi r^4 P}\nabla, \tag{3.25}$$

$$\frac{d\tau}{dm} = -\frac{\kappa}{4\pi r^2}. \tag{3.26}$$

In these expressions, the independent variables are the interior mass m and time t (which does not appear explicitly), whereas the five unknown variables are the radius r, total pressure P, luminosity l, temperature T, and Rosseland optical depth τ. As for the remaining quantities, G is the gravitational constant, ρ is the mass density, $\epsilon_{\rm nuc}$, $\epsilon_{\rm neu}$, and $\epsilon_{\rm grav}$ are the rates of energy gain/loss per unit mass due to nuclear reactions, neutrino emission, and gravothermal processes, respectively, $\nabla = d\ln T/d\ln P$ is the logarithmic temperature gradient, and κ is the Rosseland mean opacity. These functions must be specified a priori through an appropriate description of the microphysics of the stellar material, which is the subject of Section 3.2.1. Equations 3.22−3.26 are also supplemented with standard boundary conditions.

Treatment of Convection

In a stellar model, convectively stable regions are characterized by the radiative temperature gradient, $\nabla_{\rm rad}$, given by Equation 3.2. This is a slightly modified version of the standard expression that accounts for the breakdown of the diffusion approximation near the surface through the correction factor W. Convectively unstable layers are characterized instead by the convective temperature gradient, $\nabla_{\rm conv}$, which is evaluated using the mixing-length theory. In this case, too, we adapt the usual equations to incorporate nondiffusive effects. We briefly describe our treatment of convection in the following.

Within the mixing-length formalism, it can be shown that the convective temperature gradient obeys a cubic polynomial equation that only depends on the local properties of the stellar material (see for instance Kippenhahn et al. 2012). In order to write this expression compactly, we first define two dimensionless quantities,

$$U = \frac{c\sigma T^3}{W\rho^2\kappa c_P \ell_{\rm conv}^2}\left(\frac{H_P}{ag}\frac{\chi_\rho}{\chi_T}\right)^{1/2}, \tag{3.27}$$

$$V = \frac{16W}{3bc}. \tag{3.28}$$

Recall that σ is the Stefan−Boltzmann constant, T is the temperature, ρ is the density, κ is the opacity, c_P is the specific heat capacity at constant pressure, χ_T and χ_ρ are standard thermodynamic derivatives, g is the gravitational acceleration, H_P is the pressure scale height, $\ell_{\rm conv}$ is the mixing length, and a, b, and c are numerical constants describing the geometry of the convective cells. It is in these two definitions that we include the effects of nondiffusive energy transfer through the correction factor W.

For purposes of numerical accuracy, the cubic polynomial equation for $\nabla_{\rm conv}$ is formulated differently in the limiting cases $U \gg 1$ and $U \ll 1$, which correspond to the regimes of low and high convective efficiency, respectively. For $U \gg 1$, we solve

$$x^3 + UVx^2 + U^2Vx - UV\left(\nabla_{\rm rad} - \nabla_{\rm ad}\right) = 0, \tag{3.29}$$

where x is related to $\nabla_{\rm conv}$ by

$$\nabla_{\rm conv} = \nabla_{\rm rad} - \frac{x^3}{UV}. \tag{3.30}$$

For $U \ll 1$, we instead solve

$$x^3 + U\left(2V - 3\right)x^2 + 3U^2x - 8UV\left(\nabla_{\rm rad} - \nabla_{\rm ad}\right) - U^3\left(2V + 1\right) = 0, \tag{3.31}$$

where x is now related to $\nabla_{\rm conv}$ by

$$\nabla_{\rm conv} = \nabla_{\rm ad} + \frac{x^2 - U^2}{4}. \tag{3.32}$$

As before, $\nabla_{\rm ad}$ denotes the adiabatic temperature gradient. Note that both forms are entirely equivalent for intermediate convective efficiencies.

Once the convective temperature gradient is known, the convective velocity, which appears in Equation 3.14 for the convective diffusion coefficient, can be computed as

$$v_{\rm conv} = \ell_{\rm conv} \left(\frac{ag}{H_P} \frac{\chi_T}{\chi_\rho} \right)^{1/2} \Big[UV \left(\nabla_{\rm rad} - \nabla_{\rm conv} \right) \Big]^{1/3}. \tag{3.33}$$

Evaluation of the Hopf Function

The Hopf function H enters Equation 3.3 for the atmospheric correction factor W in the gray-atmosphere approximation. It is defined by the integral equation

$$\tau + H(\tau) = \frac{1}{2} \int_0^\infty [t + H(t)] \; E_1(|t - \tau|) \; dt, \tag{3.34}$$

where τ is the optical depth and E_1 is the so-called first exponential integral (Mihalas, 1978). Thus, it cannot be expressed in a closed analytic form. To evaluate the Hopf function efficiently, we rely on a seventh-order polynomial fit to a numerical solution of the above equation. Our fit is given by

$$H = \sum_{k=0}^{7} c_k x^k, \tag{3.35}$$

where x is defined as

$$x = \frac{2}{\pi} \arcsin \Big[\exp \left(-\tau \right) \Big], \tag{3.36}$$

and the values of the coefficients are $c_0 = 0.7104460$, $c_1 = -0.02015790$, $c_2 = -0.08132497$, $c_3 = -0.3250189$, $c_4 = 0.8943672$, $c_5 = -1.1284420$, $c_6 = 0.5274319$, and $c_7 = 0.00004964$.

Treatment of Nuclear Burning and Neutrino Emission

Our treatment of nuclear burning and neutrino emission involves standard formulas (see for instance Kippenhahn et al. 2012), which we explicitly provide here for completeness.

Nuclear burning appears in the equations of stellar structure in the form of a rate of energy generation per unit mass, which is given by

$$\epsilon_{\rm nuc} = \sum_{\mathcal{N}} \frac{R_{\mathcal{N}} Q_{\mathcal{N}}}{\rho}, \tag{3.37}$$

where, for some nuclear reaction $\mathcal{N}$, $R_{\mathcal{N}}$ is the reaction rate per unit volume and $Q_{\mathcal{N}}$ is the energy released by a single reaction (corrected for neutrino losses). The sum runs over all relevant reactions, and ρ denotes the density as usual. Suppose that atomic species i and j are the reactants of reaction $\mathcal{N}$, which can thus be written symbolically as $\nu_i \mathbb{A}_i + \nu_j \mathbb{A}_j \rightarrow$ (products), where ν_i and ν_j are the stoichiometric coefficients and $\mathbb{A}_i$ and $\mathbb{A}_j$ are the chemical symbols. The reaction rate can then be expressed as

$$R_{\mathcal{N}} = \left(\frac{X_i}{A_i}\right)^{\nu_i} \left(\frac{X_j}{A_j}\right)^{\nu_j} \frac{(N_{\mathrm{A}}\rho)^{\nu_i+\nu_j}}{\nu_i!\nu_j!} f_{\mathcal{N}} \langle \sigma v \rangle_{\mathcal{N}}, \tag{3.38}$$

where N_{A} is Avogadro's number, A_i and A_j are the atomic weights, X_i and X_j are the mass fractions, $\langle \sigma v \rangle_{\mathcal{N}}$ is the reaction cross section, and $f_{\mathcal{N}}$ is the electron screening factor.

Energy losses due to the emission of neutrinos through leptonic reactions are considered in a similar fashion. The rate of energy loss per unit mass is given by

$$\epsilon_{\mathrm{neu}} = \sum_{\mathcal{L}} \frac{Q_{\mathcal{L}}}{\rho}, \tag{3.39}$$

where, for some leptonic neutrino-producing process $\mathcal{L}$, $Q_{\mathcal{L}}$ is the energy carried away per unit time and unit volume. Once again, the sum runs over all relevant processes. The physical quantities $Q_{\mathcal{N}}$, $\langle \sigma v \rangle_{\mathcal{N}}$, $f_{\mathcal{N}}$, and $Q_{\mathcal{L}}$ are taken from external sources listed in Section 3.2.1.

Nuclear burning also enters the equations governing element transport in the form of a source/sink term, $S_{\mathrm{nuc},i}$. This term is simply the net rate of change of the elemental mass fraction X_i due to the combined effect of all reactions that add or remove particles of type i. If $\mathcal{N}_i^+$ and $\mathcal{N}_i^-$ denote reactions that create and destroy nuclei of type i with stoichiometric coefficients $\nu_{\mathcal{N}_i^+}$ and $\nu_{\mathcal{N}_i^-}$, respectively, we can write

$$S_{\mathrm{nuc},i} = \frac{A_i}{N_{\mathrm{A}}\rho} \left(\sum_{\mathcal{N}_i^+} \nu_{\mathcal{N}_i^+} R_{\mathcal{N}_i^+} - \sum_{\mathcal{N}_i^-} \nu_{\mathcal{N}_i^-} R_{\mathcal{N}_i^-} \right), \tag{3.40}$$

with the reactions rates given by Equation 3.38.

Chapitre 4

On the Spectral Evolution of Hot White Dwarf Stars. III. The PG 1159−DO−DB−DQ Evolutionary Channel Revisited

A. Bédard[1], P. Bergeron[1], & P. Brassard[1]

[1] Département de Physique, Université de Montréal, Montréal, QC H3C 3J7, Canada

Published in *The Astrophysical Journal*
May 2022, Volume 930, Article 8
DOI: 10.3847/1538-4357/ac609d

Abstract

We continue our comprehensive theoretical investigation of the spectral evolution of white dwarfs based on sophisticated simulations of element transport. In this paper, we focus on the transformation of PG 1159 stars into DO/DB white dwarfs due to the gravitational settling of heavy elements and then into DQ white dwarfs through the convective dredge-up of carbon. We study the impact of several physical parameters on the evolution of the surface carbon abundance over a wide range of effective temperatures. In the hot PG 1159 and DO phases, our calculations confirm that the temperature of the PG 1159-to-DO transition depends sensitively on the stellar mass and the wind mass-loss rate. We show that measured carbon abundances of DOZ white dwarfs are mostly accounted for by our models, with the notable exception of the coolest DOZ stars. In the cooler DB and DQ phases, the predicted atmospheric composition is strongly influenced by the stellar mass, the thickness of the envelope, the initial carbon content, the efficiency of convective overshoot, and the presence of residual hydrogen. We demonstrate that, under reasonable assumptions, our

simulations reproduce very well the observed carbon abundance pattern of DQ stars, which thus allows us to constrain the extent of the overshoot region in cool helium-rich white dwarfs. We also argue that our calculations naturally explain a number of recent empirical results, such as the relative excess of low-mass DQ stars and the presence of trace hydrogen and/or carbon at the surface of most DC and DZ stars.

Key words: White dwarf stars; DO stars; DB stars; DQ stars; Stellar evolutionary models; Atmospheric composition; Stellar diffusion; Stellar convective envelopes; Stellar winds

4.1. Introduction

It is observationally well established that white dwarf stars come in two main groups: those with hydrogen-dominated atmospheres and those with helium-dominated atmospheres. In most cases, the surface is chemically pure, essentially because the strong gravitational field makes the process of gravitational settling highly efficient. Nevertheless, several objects unequivocally show traces of elements other than the primary constituent in their outer layers. Furthermore, multiple studies have demonstrated that a significant fraction of white dwarfs experience radical changes in atmospheric composition as they cool, a phenomenon known as spectral evolution. This empirical evidence indicates that various element transport mechanisms, such as atomic diffusion, convective mixing, stellar winds, and matter accretion, counteract the action of gravitational settling in white dwarf envelopes (see Bédard et al. 2020, 2022b, hereafter Papers I and II, for comprehensive overviews).

One relatively well-studied case of spectral evolution is that of stars possessing helium-rich, carbon-polluted atmospheres. It is often referred to as the PG 1159−DO−DB−DQ evolutionary channel, after the chronological sequence of observed spectral types. The commonly accepted scenario begins with an extremely hot PG 1159 star whose envelope consists of a mixture of helium, carbon, and oxygen in similar proportions. The carbon and oxygen are initially supported in the outer layers by a weak radiative wind. As the star cools, the wind dies and gravitational settling causes the carbon and oxygen to sink out of sight, thereby producing a DO and then DB white dwarf with a pure-helium atmosphere. Then, a convection zone develops in the helium layer and eventually catches up with the settling

carbon, which is thus brought back to the surface. The result is a helium-dominated, carbon-polluted atmosphere corresponding to the DQ spectral class. Finally, as the convective region reaches a maximum depth, the dredged-up carbon partially sinks back into the star, leading to a decline of the surface carbon abundance with decreasing effective temperature.

Several theoretical studies have quantitatively assessed the different phases of this evolutionary scenario by carrying out time-dependent calculations of element transport in stellar models. The PG 1159-to-DO transition was investigated extensively by Unglaub & Bues (2000) and Quirion et al. (2012). They showed that the only viable mechanism allowing PG 1159 stars to keep their peculiar atmospheric composition at the beginning of the cooling sequence is the occurrence of weak mass loss competing against gravitational settling above $T_{\rm eff} \sim 75{,}000$ K. Furthermore, Dehner & Kawaler (1995), Fontaine & Brassard (2002), Althaus & Córsico (2004), and Althaus et al. (2005b) performed similar computations but focused primarily on the chemical structure in the cooler DB phase ($T_{\rm eff} \sim 20{,}000 - 30{,}000$ K). They demonstrated that the resulting DB white dwarf is characterized by a double-layered envelope, with a pure-helium layer on top of a mantle retaining the initial composition of the PG 1159 progenitor. In other words, even at low effective temperatures, element separation is still going on in the envelope, and the state of diffusive equilibrium has not been reached. This is because the diffusion timescales are much longer at the bottom than at the top of the envelope. We note that among the studies quoted above, only those of the La Plata group (Althaus & Córsico, 2004; Althaus et al., 2005b) considered the effect of thermal diffusion, which was shown by Althaus & Córsico (2004) to be nonnegligible for this particular problem.

The DB-to-DQ transition around $T_{\rm eff} \sim 10{,}000$ K has also been the subject of many investigations. The first detailed models of carbon dredge-up were computed by Pelletier et al. (1986), who were able to reproduce very well the trend of decreasing surface carbon abundance with decreasing effective temperature observed among DQ stars (see Coutu et al. 2019 for an up-to-date empirical picture). However, this agreement could only be obtained by assuming envelopes much thinner ($q_{\rm env} = M_{\rm env}/M \sim 10^{-3.5}$) than predicted by the standard theory of stellar evolution ($q_{\rm env} \sim 10^{-2.0}$). Although their work represented a pioneering step forward, it suffered from several shortcomings: (1) they adopted a semi-evolutionary approach in which the feedback of composition changes on the stellar models is ignored, (2)

they used initial chemical structures consisting of a single-layered, pure-helium envelope atop a pure-carbon core (that is, they assumed that complete element separation is achieved in previous evolutionary phases), (3) they ignored thermal diffusion and convective overshoot in the transport equations, and (4) they relied on pieces of constitutive physics, especially radiative opacities, that have since been considerably improved.

MacDonald et al. (1998) carried out analogous calculations into which they incorporated a few upgrades: they adopted a full evolutionary approach in which element transport is coupled to the cooling process, and they employed modern radiative opacities from the OPAL project (Iglesias & Rogers, 1996). They demonstrated that the new opacities result in deeper convection zones, hence making carbon dredge-up possible in thicker helium envelopes. Nevertheless, their computations predicted a monotonic increase of the atmospheric carbon abundance with time, in sharp contrast with the observations, indicating that their models suffered from some unknown issue.

Following the realization by Dehner & Kawaler (1995) that DB white dwarfs harbor double-layered envelopes, it became clear that the next generation of DQ models would need to take into account the full chemical evolution starting from the PG 1159 phase. In this new paradigm, the carbon seen at the surface of DQ white dwarfs is dredged up not from the core, as envisioned by Pelletier et al. (1986), but rather from the PG 1159−like layer at the bottom of the envelope. Our group presented in Dufour et al. (2005) a set of such evolutionary sequences (see also Fontaine & Brassard 2005 and Brassard et al. 2007). These calculations nicely matched the carbon abundance pattern of DQ stars, without the need to invoke very thin envelopes, thanks to the use of the OPAL opacities and the correct treatment of the past chemical history. Similar cooling sequences were published by the La Plata group in Althaus et al. (2005b), Scóccola et al. (2006), and Camisassa et al. (2017). These works incorporated further notable improvements: they computed the full stellar evolution from the main sequence to the white dwarf phase, and they included thermal diffusion and convective overshoot in the element transport scheme. Camisassa et al. (2017) additionally considered the effect of using detailed nongray atmospheres as boundary conditions for the stellar models. Although these calculations are in principle the most sophisticated available, they appear to be affected by a problem akin to that seen in MacDonald et al. (1998): they

fail to reproduce the empirical trend of decreasing surface carbon abundance at low effective temperature.

Finally, it is important to point out that all aforementioned studies ignored nonideal effects in the modeling of atomic diffusion (Beznogov & Yakovlev, 2013), which were recently shown by Koester et al. (2020) to be significant at the bottom of cool DQ envelopes. However, we note that the quantitative results reported by Koester et al. (2020) are flawed because they are based on single-layered envelope models in diffusive equilibrium, an assumption known to be invalid since the work of Dehner & Kawaler (1995). So far, full evolutionary calculations incorporating a nonideal treatment of diffusion have only been performed for hydrogen-rich DA white dwarfs by Althaus et al. (2020a).

In Paper II, we presented and discussed a state-of-the-art simulation of the PG 1159−DO−DB−DQ evolutionary channel that circumvents all of the shortcomings highlighted above. We also demonstrated that our evolutionary sequence, which assumes standard values of the input physical parameters, is in excellent agreement with the observed carbon abundance pattern of DQ white dwarfs. The goal of the present paper is to introduce many more analogous calculations in order to explore the model parameter space relevant to the PG 1159-to-DO and DB-to-DQ transitions in detail. Although this has been done to some extent before, most notably in Pelletier et al. (1986), the theoretical advances achieved since then definitely warrant a new comprehensive investigation. In Section 4.2, we succinctly describe the physical and numerical setup of our simulations. Section 4.3 presents our results regarding the influence of various stellar properties (such as the total mass, the thickness of the envelope, the strength of the wind, and the extent of convective overshoot) on the chemical evolution. We then discuss the astrophysical implications of our findings in Section 4.4. Finally, our conclusions are summarized in Section 4.5.

4.2. Computations

We produce time-dependent simulations of element transport in cooling white dwarfs using the STELUM evolutionary code, which is described at length in Paper II. Briefly, STELUM employs a finite-element scheme to build and evolve complete stellar models, down from the center up to the very surface. Furthermore, it solves the equations governing the transport of chemical species along with the equations of stellar structure in a self-consistent

way. Atomic diffusion, macroscopic mixing, and mass loss or accretion are treated as time-dependent diffusive processes and can all be considered simultaneously. Thanks to these features, STELUM is a powerful tool to study the spectral evolution of white dwarfs from a theoretical perspective. We refer the reader to Paper II for details regarding the constitutive physics and numerical techniques of the code.

In the present work, we start our calculations from very hot white dwarf models ($T_{\rm eff}$ = 90,000 K) consisting of a homogeneous carbon/oxygen core surrounded by a homogeneous helium/carbon/oxygen envelope typical of PG 1159 stars. Unless otherwise stated, our evolutionary sequences include chemical diffusion, gravitational settling, and thermal diffusion through the formalism of Burgers (1969), and take nonideal effects into account following Beznogov & Yakovlev (2013). In the rest of the paper, the nonideal treatment of microscopic diffusion is simply referred to as nonideal diffusion for conciseness. We consider standard convective mixing according to the mixing-length theory, as well as mixing due to convective overshoot using the prescription of Freytag et al. (1996) for the overshoot diffusion coefficient,

$$D_{\rm ov} = D_{\rm conv,0}\ \exp\left(\frac{-2|r-r_0|}{f_{\rm ov}\,H_{P,0}}\right). \tag{4.1}$$

In this expression, r is the radial coordinate, r_0 is the radius of the convective boundary, $D_{\rm conv,0}$ and $H_{P,0}$ are the convective diffusion coefficient and pressure scale height at r_0, and $f_{\rm ov}$ is a numerical factor controlling the extent of the overshoot region [1]. Equation 4.1 is applied both at the upper and lower boundaries of the convection zone, but it is mainly the lower overshoot region that is relevant for this paper. We also include an outward wind in the early evolution using by default the formula of Blöcker (1995a) for the mass-loss rate,

$$\dot{M}_{\rm wind} = -1.29\times10^{-15}\left(\frac{L}{L_\odot}\right)^{1.86} M_\odot\ {\rm yr}^{-1}, \tag{4.2}$$

where L is the surface luminosity. This wind model is admittedly very crude; in particular, it ignores the metallicity dependence predicted by radiative wind theory (Unglaub & Bues, 2000). It is nevertheless commonly employed due to our poor theoretical understanding of the source of mass loss in hot white dwarfs and also because it has the important advantage

1. Note that in the overshoot region, the energy transport is assumed to be purely radiative, meaning that we consider only the particle transport (and not the energy transport) arising from convective overshoot.

of computational simplicity and flexibility. Finally, residual nuclear burning and radiative levitation are ignored throughout our calculations for simplicity.

As will become apparent below, the variation of the atmospheric composition along the PG 1159−DO−DB−DQ evolutionary channel depends sensitively on a number of model parameters. The main parameters studied in this work are the total mass (M), the fractional mass of the envelope ($q_{\rm env}$), the initial carbon mass fraction in the envelope ($X_{\rm C,0}$), the mixing-length parameter (α), the overshoot parameter ($f_{\rm ov}$), and the mass-loss rate ($\dot{M}_{\rm wind}$) [2]. In Section 3.1 of Paper II, we presented in detail a typical PG 1159−DO−DB−DQ evolutionary sequence, which we henceforth refer to as our standard or reference sequence. For this simulation, we assumed $M = 0.6\ M_{\odot}$, $\log q_{\rm env} = -2.0$, $X_{\rm C,0} = 0.5$ (along with $X_{\rm He,0} = 0.4$ and $X_{\rm O,0} = 0.1$), $\alpha = 1.0$, $f_{\rm ov} = 0.075$, and $\dot{M}_{\rm wind}$ given by Equation 4.2. In the following, we present a series of similar calculations in which we vary each of the key parameters one at a time to investigate their individual effect on the chemical evolution.

4.3. Results

4.3.1. The Reference Sequence

For completeness, we first briefly reproduce and discuss here the results of our standard simulation introduced in Section 3.1 of Paper II. Figure 4.1 displays the run of the elemental mass fractions with depth at selected stages along the evolutionary sequence. The depth is measured as the fractional mass above the point of interest, $q = 1 - m/M$, where m is the usual interior mass. This figure is essentially a reduced version of Figure 1 of Paper II. Panels (a) to (c) illustrate the PG 1159-to-DO transition at high effective temperature: because the fading wind gradually loses its ability to compete efficiently against gravitational settling, the surface carbon and oxygen sink into deeper layers, and the initial PG 1159 star thereby becomes a pure-helium DO white dwarf. This transformation necessarily involves a

2. According to pre-white dwarf evolutionary calculations, some of these parameters (especially M, $q_{\rm env}$, and $X_{\rm C,0}$) should be correlated (Miller Bertolami & Althaus, 2006; Althaus et al., 2009b). However, given the historical thin-envelope interpretation of DQ white dwarfs, we prefer here to treat them as independent parameters in order to explore their individual influence on the chemical evolution.

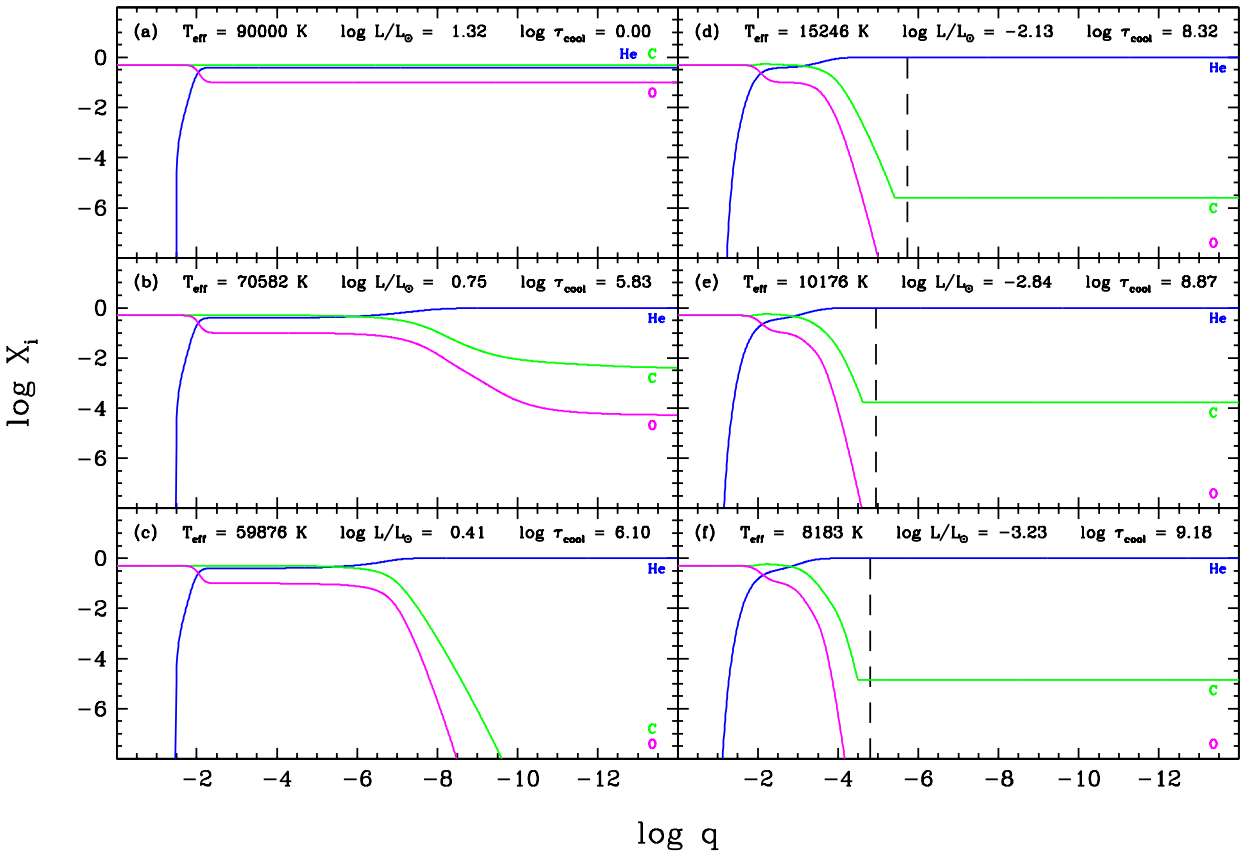

Figure 4.1 – Chemical structure at selected stages along our reference sequence. The elemental mass fraction abundances are shown as a function of the fractional mass depth ($q = 1 - m/M$). The hydrogen, helium, carbon, and oxygen abundance profiles are displayed as red, blue, green, and magenta curves, respectively. The location of the base of the convection zone is indicated by a dashed black line. The effective temperature, surface luminosity, and cooling age are given at the top of each panel.

short intermediate phase in which the model exhibits a helium-dominated yet mildly carbon-polluted atmosphere and would consequently appear as a DOZ white dwarf[3]. Besides, we note that the outer chemical profile of panel (c) is not entirely realistic: at this temperature,

3. In the canonical classification scheme, the letter Z indicates the presence of spectral features of any metal *except* carbon, which is identified distinctly by the letter Q (Wesemael et al., 1993). Therefore, carbon-bearing DO white dwarfs, which exhibit weak C IV lines in addition to the usual strong He II lines, should formally be assigned the spectral type DOQ. However, some carbon-polluted DO white dwarfs also show traces of other heavy elements, such as nitrogen and oxygen, and thus have historically been called DOZ stars (Dreizler & Werner, 1996). In the present work, we continue to use the latter convention, that is,

radiative levitation (which is not included in our calculations) is expected to support minute amounts of metals in the outer envelope (Chayer et al., 1995; Dreizler, 1999). During the DO and DB phases, the pure-helium layer grows as heavy elements diffuse farther downward. Panels (d) to (f) outline the DB-to-DQ transition at low effective temperature: the superficial convection zone (the base of which is indicated by a dashed black line) expands and eventually comes into contact with the PG 1159−like layer at the bottom of the envelope, thereby causing carbon to be dredged up to the surface. The atmospheric carbon abundance of the resulting DQ white dwarf reaches a maximum and then decreases again due to an ionization effect below the convective region: the average ionization state of carbon changes, which causes the carbon diffusion tail to become steeper and thus to move away from the convection zone (Pelletier et al., 1986). Note that the fully mixed region (which corresponds to the flat part of the carbon profile) extends beyond the formal convective boundary as a consequence of convective overshoot.

The chemical evolution of our reference model is summarized in Figure 4.2, where the red line shows the surface carbon abundance (more precisely, the carbon-to-helium number ratio $N_{\rm C}/N_{\rm He}$) as a function of effective temperature. The red points labeled by letters along the curve correspond to the various stages displayed in Figure 4.1. The left and right panels cover the temperature ranges relevant to the PG 1159-to-DO and DB-to-DQ transitions, respectively. In each panel, the dotted black line (read on the right axis) shows a physical quantity related to the transport process responsible for the carbon abundance change. The left panel gives the mass-loss rate, which constitutes a measure of the capacity of the wind to prevent element sedimentation. We can see that the carbon abundance starts to drop abruptly once the mass-loss rate falls below a critical value of $|\dot{M}_{\rm wind}| \sim 10^{-13}\ M_\odot\ {\rm yr}^{-1}$, which occurs around $T_{\rm eff} \sim 80{,}000$ K for the adopted mass-loss law. In our calculations, the carbon abundance subsequently falls to zero, but in reality, a small amount of carbon should be temporarily maintained at the surface by radiative levitation. The right panel displays the location of the base of the superficial convection zone in terms of fractional mass. The correlation between carbon pollution and the inward expansion of the convective region is obvious.

carbon-bearing DO white dwarfs are referred to as DOZ stars even if carbon is the only metal detected in their optical spectra.

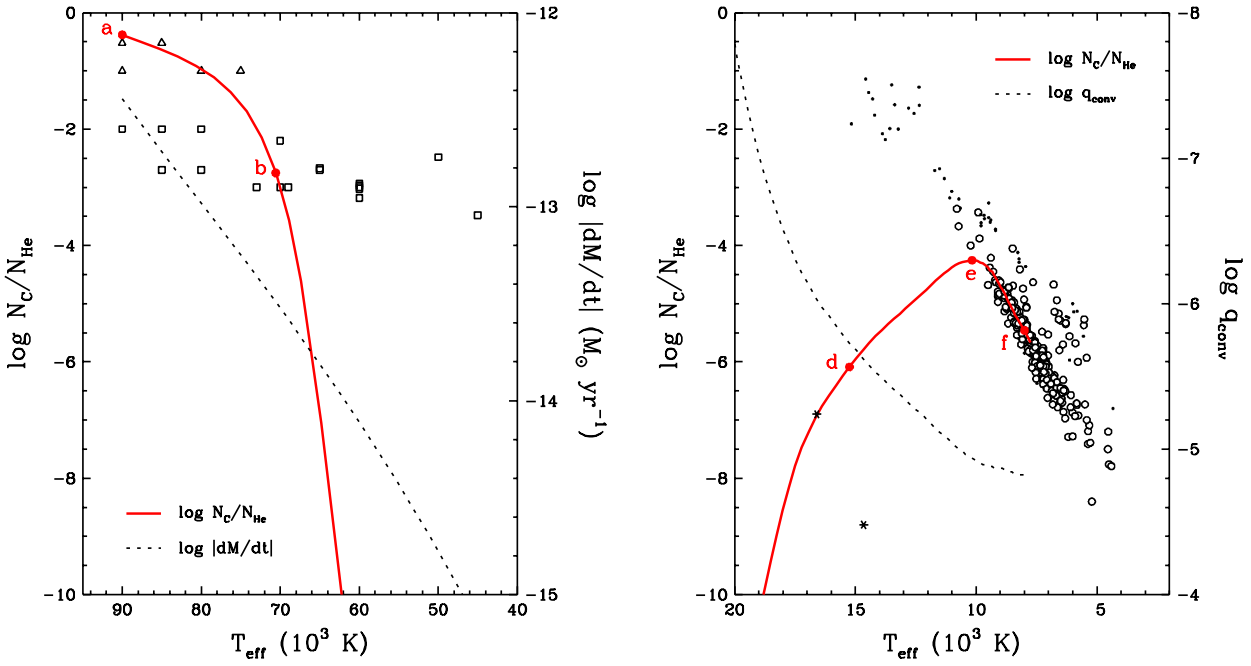

Figure 4.2 – Evolution of the atmospheric carbon-to-helium number ratio as a function of effective temperature in our reference sequence, shown as a red curve. The red points labeled by letters indicate the location of the models displayed in Figure 4.1 along the curve. The dotted black line (read on the right axis) gives the wind mass-loss rate in the left panel and the fractional mass depth of the convection zone in the right panel. Also shown are empirical carbon abundance measurements taken from the literature for several types of objects: PG 1159 stars are represented as triangles (Werner & Herwig, 2006; Werner & Rauch, 2014), DOZ white dwarfs as squares (Dreizler & Werner, 1996; Reindl et al., 2014a; Werner et al., 2014), DB white dwarfs as asterisks (Desharnais et al., 2008), and DQ white dwarfs as large ($M \leq 0.7\ M_{\odot}$) or small ($M > 0.7\ M_{\odot}$) circles (Coutu et al., 2019; Blouin & Dufour, 2019).

Figure 4.2 also compares our predicted carbon abundance pattern with empirically measured carbon abundances for several types of white dwarfs. At high effective temperature, we show the coolest PG 1159 stars from Werner & Herwig (2006) and Werner & Rauch (2014) as triangles, as well as the DOZ white dwarfs from Dreizler & Werner (1996), Reindl et al. (2014a), and Werner et al. (2014) as squares. Note that these carbon-bearing DOZ stars represent only a subset of the whole DO population, which also comprises many pristine DO stars exhibiting pure-helium-line spectra. In particular, the optical detection limit of carbon in a hot helium-rich atmosphere is $\log N_{\rm C}/N_{\rm He} \sim -3.0$ (Dreizler & Werner, 1996),

hence the near absence of objects below this value. Clearly, the population of DOZ white dwarfs cannot be fully explained by our standard sequence alone, a result that has been known for some time. For instance, as pointed out by Reindl et al. (2014a), the two coolest objects, SDSS J0301+0508 and SDSS J2239+2259, have surprisingly high carbon contents for their temperatures. One could allege that radiative levitation may be the solution to this puzzle, but the carbon abundances predicted by existing models of radiative levitation in hot white dwarfs are too low ($-4.5 \lesssim \log N_{\rm C}/N_{\rm He} \lesssim -3.5$; Chayer et al. 1995). Unglaub & Bues (2000) argued that the observed scatter is simply a consequence of the fact that PG 1159 stars have different masses and compositions and therefore undergo the PG 1159-to-DO transition at different effective temperatures. Another possibility, alluded to by Reindl et al. (2014a,b), is that DOZ white dwarfs actually descend from the so-called O(He) stars rather than from the PG 1159 stars. We discuss both ideas in light of our calculations in Section 4.4.1. For now, we nevertheless note that the rudimentary wind model employed in our reference simulation successfully accounts for the disappearance of PG 1159 stars below $T_{\rm eff} \sim 75{,}000$ K, as demonstrated before by Unglaub & Bues (2000) and Quirion et al. (2012). Moreover, it is also roughly consistent with our empirical knowledge of hot DAO white dwarfs, in which the wind is responsible for the helium pollution of the hydrogen-dominated atmosphere (Gianninas et al. 2010; Paper I).

At low effective temperature, the normal-mass DQ white dwarfs ($M \leq 0.7\ M_{\odot}$) from Coutu et al. (2019) and Blouin & Dufour (2019) are represented by large open circles; the remaining, more massive objects are shown as small dots. Our model nicely reproduces the tight sequence formed by classical DQ stars, or at least the first half of it. At this time, we cannot push our calculations to lower effective temperature because of the unavailability of OPAL opacities for carbon in this physical regime. As mentioned in Paper II, this good agreement is not entirely coincidental: it was actually achieved by fine-tuning the overshoot parameter (assuming standard values for the other parameters), hence our choice of $f_{\rm ov} = 0.075$ as default value (see Section 4.3.3). The absence of DQ white dwarfs on the ascending part of the theoretical curve is likely due to the optical visibility limit of carbon, which is $\log N_{\rm C}/N_{\rm He} \sim -4.5$ in this temperature range (Coutu et al., 2019). In other words, the immediate precursors of classical DQ stars appear as genuine DB stars above $T_{\rm eff} \sim 10{,}000$ K. However, their atmospheric carbon can still be detected in the ultraviolet. The two asterisks

in Figure 4.2 represent the two cool DB white dwarfs ($T_{\rm eff}$ < 20,000 K) with ultraviolet carbon abundance measurements from Desharnais et al. (2008). One of them, GD 378, falls directly on the predicted curve and thereby seems entirely consistent with our current understanding of the DB-to-DQ transition, while the other one, GD 408, has an unexpectedly low carbon content. Nevertheless, these two objects also exhibit traces of other metals that probably originate from the accretion of planetary material (Desharnais et al., 2008; Klein et al., 2020, 2021), thus it is not clear whether the detected carbon has been dredged up or accreted.

Finally, it is important to mention that although the PG 1159−DO−DB−DQ scenario satisfactorily describes the evolution of most carbon-polluted white dwarfs, it fails to explain the existence of two known classes of such objects. First, ultraviolet observations have revealed the presence of carbon at the surface of many hot DB stars ($T_{\rm eff}$ > 20,000 K; not shown here), similarly to their cooler counterparts but in even higher amounts ($\log N_{\rm C}/N_{\rm He} \sim -5.5$; Petitclerc et al. 2005; Koester et al. 2014b). It is clear from Figure 4.2 that these objects cannot be accounted for by standard carbon dredge-up, and their origin remains uncertain to this day (Fontaine & Brassard, 2005; Koester et al., 2014b). Second, recent studies have confirmed the existence of a second DQ sequence in the $\log N_{\rm C}/N_{\rm He} - T_{\rm eff}$ diagram populated mainly by the so-called hot and warm DQ white dwarfs, which are generally hotter, more massive, and more carbon-rich than the classical DQ white dwarfs (Coutu et al., 2019; Koester & Kepler, 2019). These peculiar objects, which correspond to the small dots in Figure 4.2, are strongly suspected to be merger products (Dunlap & Clemens, 2015; Coutu et al., 2019), and thus the standard PG 1159−DO−DB−DQ evolutionary channel obviously does not apply in this case. It is beyond the scope of this work to investigate the chemical evolution of hot DB stars and of hot and warm DQ stars, and therefore these questions will be addressed elsewhere.

4.3.2. The PG 1159-to-DO Transition

The PG 1159-to-DO transition is governed by the interplay between atomic diffusion and mass loss in the outermost layers of the envelope. Consequently, it depends mainly on the efficiency of gravitational settling and on the strength of the wind, which are respectively controlled by the total mass and the mass-loss rate. It is also reasonable to expect that the carbon abundance pattern is influenced by the initial carbon content. In contrast, other

parameters such as the thickness of the envelope and the treatment of convective mixing play no role in the transformation. Besides, once the wind has faded, radiative levitation should sustain slight heavy-element pollution, but this phenomenon is disregarded in our models.

Before investigating these effects, we first briefly demonstrate the importance of thermal diffusion at the very high effective temperatures of PG 1159 and DO stars. This was already done by Althaus & Córsico (2004), who however focused mostly on the chemical structure of cooler DB white dwarfs ($T_{\rm eff} \sim 20{,}000 - 30{,}000$ K). Figure 4.3 compares our standard sequence with an analogous calculation in which thermal diffusion was turned off. Note that in this and all subsequent figures, the reference sequence is displayed as a red line. Because thermal diffusion acts in the same direction as gravitational settling, ignoring this process causes the carbon and oxygen to sink more slowly, with the consequence that the temperature of the PG 1159-to-DO transition is erroneously lowered by ∼3000 K. Thus, we reach the same conclusion as Althaus & Córsico (2004): thermal diffusion must be considered when modeling the spectral evolution of hot white dwarfs. This should be kept in mind when referring to previous calculations of the PG 1159-to-DO transition by Unglaub & Bues (2000) and Quirion et al. (2012), which only included gravitational settling.

Figure 4.4 shows how varying the stellar mass impacts the evolution of the carbon abundance. Clearly, the more massive a PG 1159 star is, the earlier it transforms into a DO white dwarf. This behavior is partially due to the simple fact that a more massive star has a stronger gravitational field and thereby experiences more efficient diffusion. However, it must be realized that the mass also has an indirect influence on the strength of the wind: a more massive white dwarf is less luminous and therefore has a lower mass-loss rate by virtue of Equation 4.2. Both effects act in the same direction: faster diffusion and weaker mass loss both accelerate the sedimentation of carbon and oxygen. The net result is significant: the effective temperature of the PG 1159-to-DO transition differs by ∼17,000 K between the models with $M = 0.5$ and 0.7 $M_{\odot}$. This relative difference is in good agreement with the works of Unglaub & Bues (2000) and Quirion et al. (2012), because the inclusion of thermal diffusion (which was ignored in these studies) affects all sequences in a similar way. Therefore, the large temperature dispersion that characterizes the observed carbon abundance pattern of DOZ stars may be explained in part by differences in mass from one object to another, which seems to support the existence of an evolutionary link between PG 1159

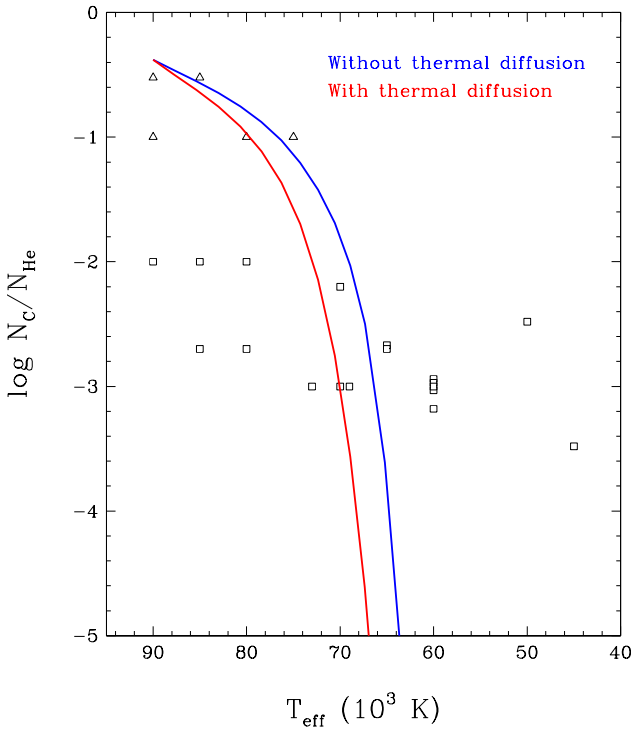

Figure 4.3 – Effect of thermal diffusion on the evolution of the atmospheric carbon-to-helium number ratio at high effective temperature. The red curve shows our reference sequence, which includes thermal diffusion, whereas the blue curve represents an analogous sequence ignoring thermal diffusion. Empirical carbon abundance measurements for PG 1159 stars (Werner & Herwig, 2006; Werner & Rauch, 2014) and DOZ white dwarfs (Dreizler & Werner, 1996; Reindl et al., 2014a; Werner et al., 2014) are displayed as triangles and squares, respectively.

stars and DOZ white dwarfs. Nevertheless, one problem with this interpretation is that it predicts that the hottest DOZ white dwarfs should be the most massive, and vice versa, and yet such a temperature−mass relation is not observed. We come back to this point in Section 4.4.1.

The influence of the initial carbon content on the PG 1159-to-DO transition is illustrated in Figure 4.5. We compare our reference sequence with helium-rich, carbon-poor ($X_{\mathrm{C},0} = 0.3$) and helium-poor, carbon-rich ($X_{\mathrm{C},0} = 0.7$) PG 1159 models. While the carbon abundance is obviously altered at the onset of the evolution, the effect almost vanishes once the carbon starts sinking rapidly into the star. Hence, it appears that the diversity of surface composition seen among PG 1159 stars (Werner & Herwig, 2006) does not translate directly into a

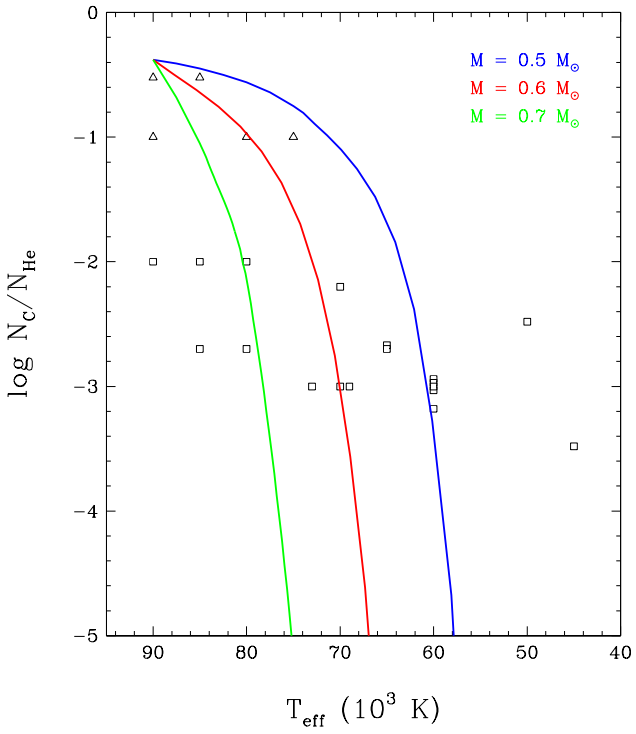

Figure 4.4 – Same as Figure 4.3, but for the effect of the stellar mass. The red curve shows our reference sequence, which assumes $M = 0.6\ M_{\odot}$, whereas the blue and green curves represent analogous sequences assuming $M = 0.5$ and $0.7\ M_{\odot}$, respectively.

scattered distribution of DOZ white dwarfs in the $\log N_{\rm C}/N_{\rm He} - T_{\rm eff}$ diagram. That said, we recall that our simplistic wind model ignores the effect of the heavy-element content on the mass-loss rate and thus on the ability of the wind to counteract gravitational settling. A higher carbon abundance is expected to produce a stronger wind and thereby a later PG 1159-to-DO transition (Unglaub & Bues, 2000). For this reason, the gap between the sequences displayed in Figure 4.5 is likely underestimated.

Given this and other uncertainties regarding the treatment of the wind, we explore in Figure 4.6 the impact of arbitrarily enhancing or reducing the mass-loss law by a factor of 10. For the low mass-loss rate, the wind is too weak to compete against downward diffusion, and thus the PG 1159 star turns into a DO white dwarf very quickly at the onset of the simulation. On the other hand, for the high mass-loss rate, the support mechanism remains highly efficient down to much lower effective temperatures, such that the PG 1159-to-DO transition occurs around $T_{\rm eff} \sim 60{,}000$ K. This behavior is similar to that reported by Quirion et al. (2012). Consequently, a wide range of mass-loss rates could in principle explain the

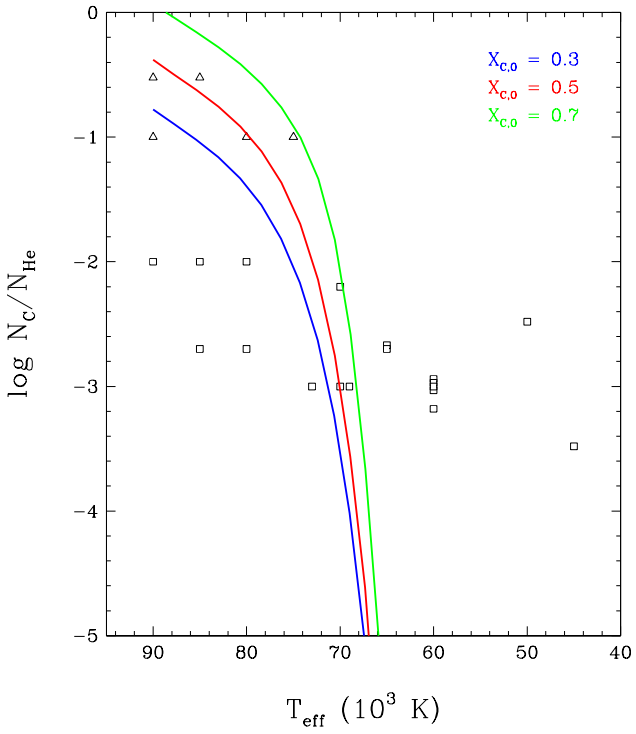

Figure 4.5 – Same as Figure 4.3, but for the effect of the initial carbon mass fraction in the envelope. The red curve shows our reference sequence, which assumes $X_{\rm C,0} = 0.5$, whereas the blue and green curves represent analogous sequences assuming $X_{\rm C,0} = 0.3$ and 0.7, respectively.

existence of DOZ white dwarfs across a wide range of temperatures. However, there is no theoretical justification for such large variations (a factor of 100) in the strength of the wind from one star to another; in particular, the metallicity effect is expected to be much smaller (Unglaub & Bues, 2000). Moreover, this unrealistic scenario still fails to account for the most extreme objects, such as SDSS J0301+0508 and SDSS J2239+2259 at low effective temperature. We further discuss the implications of our results for the origin of DOZ white dwarfs in Section 4.4.1.

4.3.3. The DB-to-DQ Transition

The transformation of a DB white dwarf into a DQ white dwarf involves two competing transport mechanisms: atomic diffusion, which causes heavy elements to sink, and convective mixing, which brings some carbon back to the surface. Several stellar properties come into play in these phenomena. On one hand, the rate of carbon settling at the bottom of the

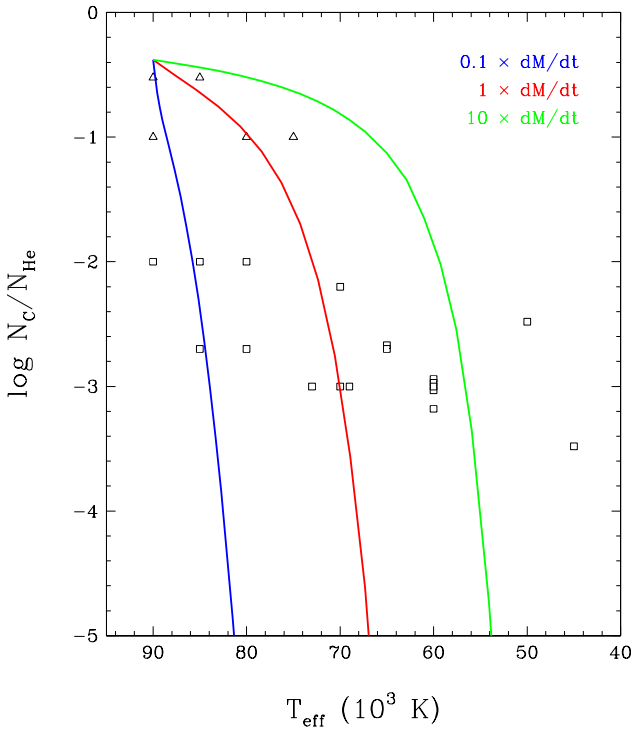

Figure 4.6 – Same as Figure 4.3, but for the effect of the mass-loss rate. The red curve shows our reference sequence, which uses Equation 4.2, whereas the blue and green curves represent analogous sequences using Equation 4.2 divided and multiplied by a factor of 10, respectively.

envelope is controlled by the total mass and the envelope mass. On the other hand, the size of the fully mixed region is determined by the total mass, the mixing-length parameter, and the overshoot parameter. Furthermore, the magnitude of carbon dredge-up in a DQ star should depend to some extent on the carbon abundance of its PG 1159 progenitor. In the following, we investigate the quantitative effect of these parameters on the DB-to-DQ transition. Note that the wind present in the early evolution does not have any impact in later stages (it is completely "forgotten" by the star), hence it is irrelevant in this context. Recall that all figures display our standard simulation as a red line.

Before proceeding with our analysis, it is imperative to connect our current calculations with our previous set of DQ evolutionary models, first presented in Figure 12 of Dufour et al. (2005) and more recently shown in Figure 12 of Coutu et al. (2019). The sequences published in Dufour et al. (2005) ignore three element transport processes that are included in the present work: thermal diffusion, nonideal diffusion, and convective overshoot. Figure

4.7 shows the evolution of the atmospheric carbon abundance before and during the DQ phase for various assumptions regarding these physical ingredients. Our starting point is the blue line, which represents a model computed within the theoretical framework adopted by Dufour et al. (2005). We see that this calculation nicely reproduces the empirical DQ sequence, as demonstrated in Dufour et al. (2005) and Coutu et al. (2019) [4]. The other curves illustrate the impact of successively adding thermal diffusion (green line), nonideal diffusion (cyan line), and convective overshoot with $f_{\rm ov} = 0.075$ (red line, which corresponds to our reference simulation). Both thermal diffusion and nonideal diffusion accelerate the sedimentation of carbon and thereby reduce the amount of carbon caught by the convection zone and dredged up to the surface. According to Figure 4.7, the two processes are of similar magnitude at $T_{\rm eff} \sim 15{,}000$ K, but as the star cools, thermal diffusion becomes negligible while the effects of nonideal diffusion grow stronger, as expected. Our calculations confirm that nonideal diffusion is significant at the bottom of DQ white dwarf envelopes, as first pointed out by Koester et al. (2020). By further including moderate convective overshoot, which extends the homogeneously mixed region, the surface carbon abundance of the model can be brought back into agreement with the observations. In short, the good agreement obtained by Dufour et al. (2005) is somewhat accidental: the effects of thermal and nonideal diffusion are actually important but can be canceled out by convective overshoot.

Figure 4.8 illustrates the impact of varying the stellar mass while keeping all other parameters fixed to their default values. The carbon abundance pattern is highly sensitive to the stellar mass: at a given effective temperature, the carbon-to-helium number ratio differs by more than two orders of magnitude between the models with $M = 0.5$ and $0.7\ M_{\odot}$. A more massive white dwarf undergoes less carbon pollution, primarily because its convection zone is shallower at a given temperature, and secondarily because its stronger gravitational field makes carbon settling more efficient. Note also that the various curves are shifted not only vertically, but also horizontally, such that the maximum carbon abundance is reached at slightly different temperatures. The mass dependence displayed in Figure 4.8 is very similar to that reported by Pelletier et al. (1986). In contrast, the calculations of Camisassa et al.

4. The blue curve in Figure 4.7 actually falls slightly higher in the $\log N_{\rm C}/N_{\rm He} - T_{\rm eff}$ diagram compared to the analogous sequence of Dufour et al. (2005). The reason for this is that we use different values for the initial carbon mass fraction: Dufour et al. (2005) assume $X_{\rm C,0} = 0.43$, whereas we adopt $X_{\rm C,0} = 0.5$, which results in a slightly higher final carbon abundance (see Figure 4.9 and the associated discussion).

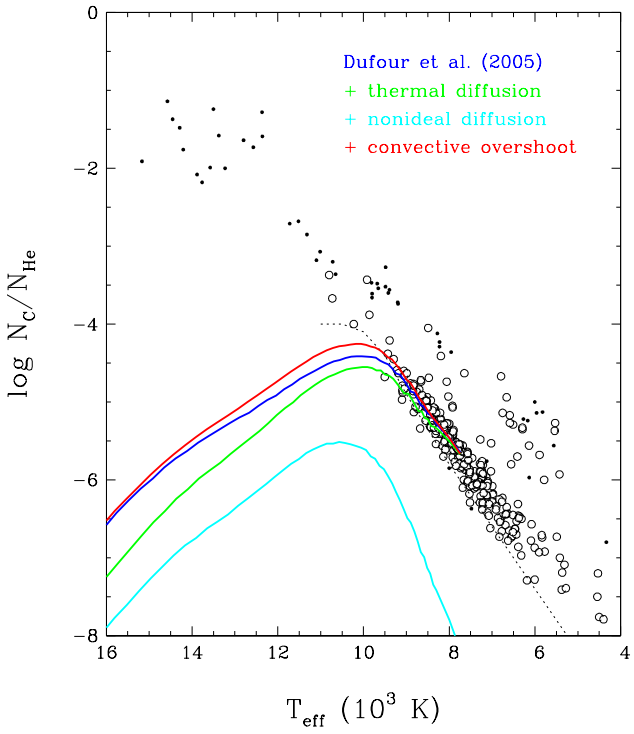

Figure 4.7 – Effect of various element transport processes on the evolution of the atmospheric carbon-to-helium number ratio at low effective temperature. The blue curve shows a sequence ignoring thermal diffusion, nonideal diffusion, and convective overshoot, as in Dufour et al. (2005). The green, cyan, and red curves represent analogous sequences in which these processes are added one by one. The red line corresponds to our reference sequence, which includes all three effects. Empirical carbon abundance measurements for normal-mass ($M \leq 0.7\ M_{\odot}$) and high-mass ($M > 0.7\ M_{\odot}$) DQ white dwarfs (Coutu et al., 2019; Blouin & Dufour, 2019) are displayed as large circles and small dots, respectively. The dotted black line gives the optical detection limit of carbon for a signal-to-noise ratio S/N = 20 based on the DQ model atmospheres of Blouin et al. (2019).

(2017) show a nonmonotonic behavior with mass (see their Figure 10), but the fact that these models do not reproduce the decrease in carbon abundance at low effective temperature prevents us from making a more elaborate comparison. Taken at face value, our results seem to suggest that most DQ white dwarfs span an extremely narrow mass range; this idea is examined more closely in Section 4.4.2.

Figures 4.9 and 4.10 show how the chemical evolution is affected by the main envelope parameters, namely, the initial mass fraction of carbon and the thickness of the envelope.

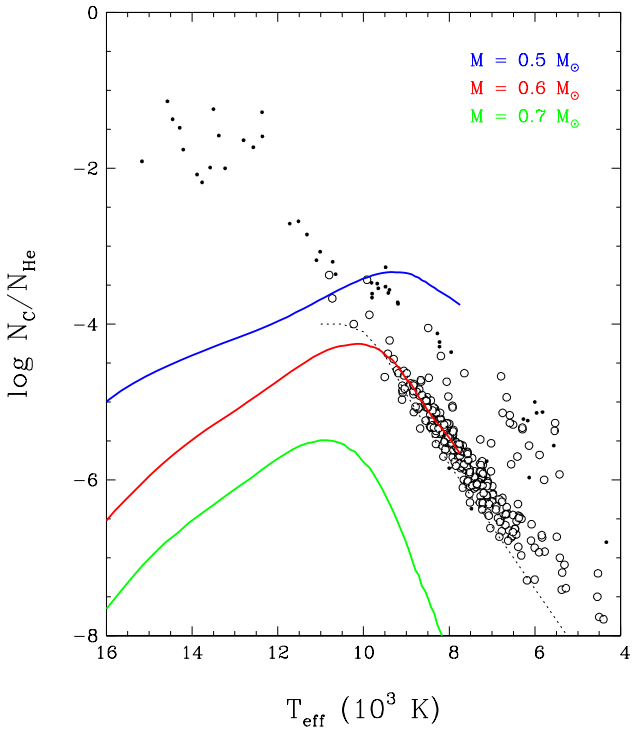

Figure 4.8 – Same as Figure 4.7, but for the effect of the stellar mass. The red curve shows our reference sequence, which assumes $M = 0.6\ M_{\odot}$, whereas the blue and green curves represent analogous sequences assuming $M = 0.5$ and $0.7\ M_{\odot}$, respectively.

The interpretation of Figure 4.9 is quite straightforward: the higher the carbon content of the PG 1159 progenitor, the higher the atmospheric carbon abundance of the DQ progeny. Figure 4.10 shows that thinner envelopes give rise to markedly enhanced carbon enrichment, a trend that has been well known since the work of Pelletier et al. (1986). On the other hand, the results for $\log q_{\rm env} > -2.0$ (not displayed here) are strictly identical to those for $\log q_{\rm env} = -2.0$. This dual behavior can be understood as follows. For $\log q_{\rm env} \lesssim -2.5$, the diffusive timescales at the base of the envelope are short enough that element separation is fully achieved before the onset of convective dredge-up. In other words, the PG 1159−like mantle at the bottom of the envelope is completely disintegrated by diffusion, leaving only a pure-helium layer atop a carbon/oxygen core. In this situation, it is from the core that carbon is brought up to the surface, and thus the magnitude of carbon pollution depends sensitively on the location of the core/envelope boundary. In contrast, for $\log q_{\rm env} \gtrsim -2.5$, the PG 1159−like layer remains intact throughout the DQ phase, and therefore the surface carbon abundance becomes insensitive to the thickness of the envelope. Like the mass in

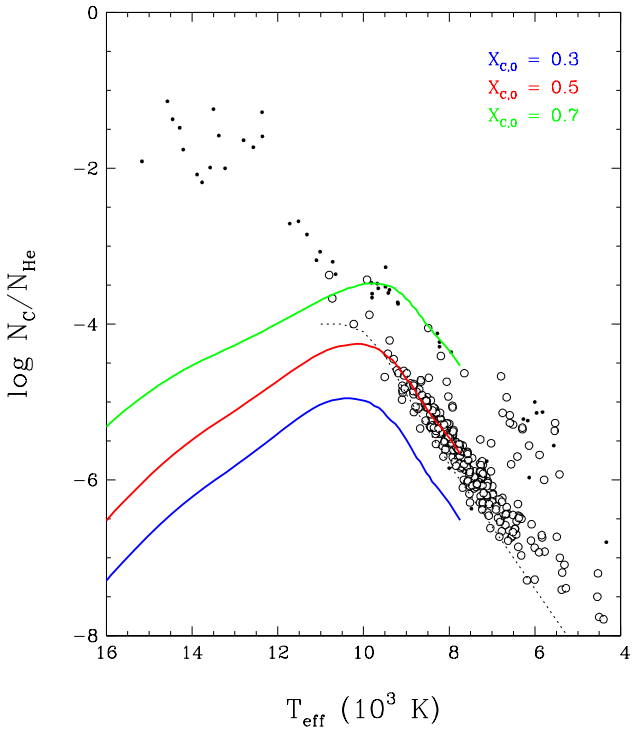

Figure 4.9 – Same as Figure 4.7, but for the effect of the initial carbon mass fraction in the envelope. The red curve shows our reference sequence, which assumes $X_{\rm C,0} = 0.5$, whereas the blue and green curves represent analogous sequences assuming $X_{\rm C,0} = 0.3$ and 0.7, respectively.

Figure 4.8, we note that Figures 4.9 and 4.10 seem to indicate that the DQ population is characterized by an extremely small range of $X_{\rm C,0}$ and $q_{\rm env}$ values, in apparent contradiction with the diversity of carbon abundances measured in PG 1159 stars (Werner & Herwig, 2006). We come back to this point in Section 4.4.2.

Figures 4.11 and 4.12 illustrate how the atmospheric composition is influenced by the treatment of convective mixing, which involves the mixing-length and overshoot parameters. Figure 4.11 simply reaffirms the conclusion of Pelletier et al. (1986) that the adopted version of the mixing-length theory is inconsequential at low effective temperature because convection becomes essentially adiabatic. Nevertheless, the same cannot be said of the extent of convective overshoot. This physical feature is definitely the most poorly understood of all those studied so far, and its effect on the chemical evolution of DQ white dwarfs has seldom been investigated before. Figure 4.12 demonstrates that the impact of the overshoot parameter is substantial. The model without overshoot ($f_{\rm ov} = 0.0$) exhibits a carbon abundance

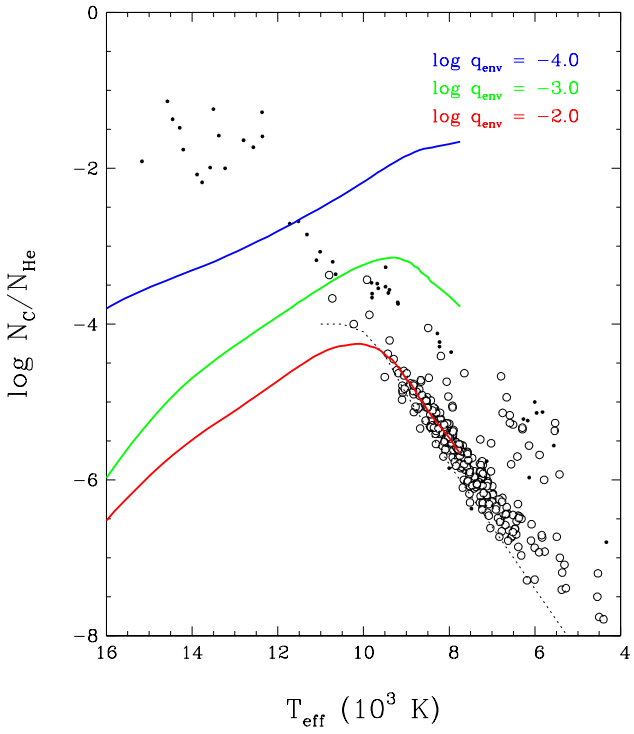

Figure 4.10 – Same as Figure 4.7, but for the effect of the thickness of the envelope. The red curve shows our reference sequence, which assumes $\log q_{\rm env} = -2.0$, whereas the blue and green curves represent analogous sequences assuming $\log q_{\rm env} = -4.0$ and -3.0, respectively.

more than one order of magnitude lower than the reference model at a given temperature (this was already apparent in Figure 4.7). The other theoretical curve displayed in Figure 4.12 assumes $f_{\rm ov} = 0.5$, which is roughly the largest possible value according to recent hydrodynamical simulations of convection in warm DA white dwarfs (Kupka et al., 2018; Cunningham et al., 2019). In this sequence, the extensive overshoot leads to a very strong carbon enrichment, in fact much stronger than observed in cool DQ stars. All in all, the models with $f_{\rm ov} = 0.0$ and 0.5 differ by three to five orders of magnitude in surface carbon abundance depending on the effective temperature.

It thus appears that the extent of convective overshoot is a sizable source of uncertainty in our simulations of the chemical evolution of DQ white dwarfs. However, we can turn the problem around: given standard values of the other important parameters, the overshoot parameter can be calibrated using the observed DQ sequence. This is precisely how we chose the $f_{\rm ov}$ value of our reference simulation: assuming $M = 0.6\ M_{\odot}$, $\log q_{\rm env} = -2.0$, and $X_{\rm C,0} = 0.5$, we find that $f_{\rm ov} = 0.075$ yields the best match to the empirical $\log N_{\rm C}/N_{\rm He} - T_{\rm eff}$

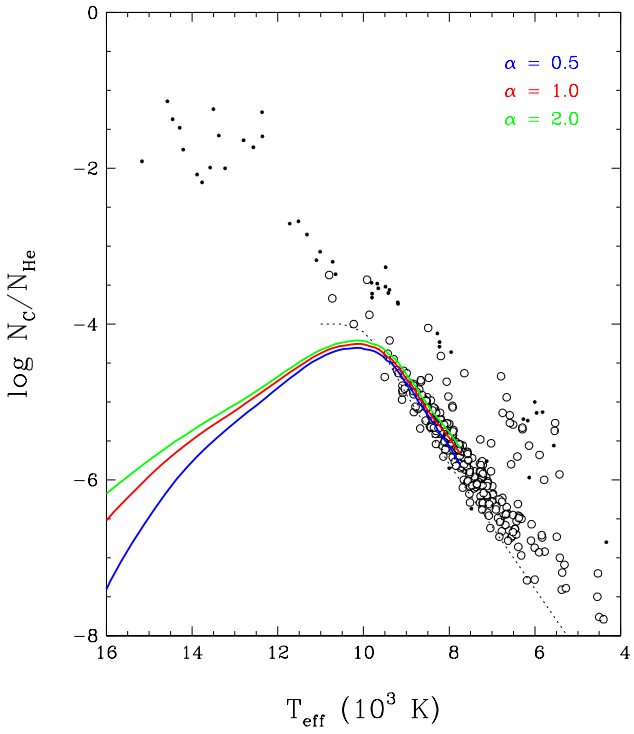

Figure 4.11 – Same as Figure 4.7, but for the effect of the mixing-length parameter. The red curve shows our reference sequence, which assumes $\alpha = 1.0$, whereas the blue and green curves represent analogous sequences assuming $\alpha = 0.5$ and 2.0, respectively.

relation. We want to stress that this is not a firm determination because our assumptions on M, $q_{\rm env}$, and $X_{\rm C,0}$ may not be perfectly accurate. Nevertheless, our approach can still provide some insight into the significance of convective overshoot in cool white dwarfs. This topic is further discussed in Section 4.4.2.

4.3.4. The Effect of Residual Hydrogen

In this section, we present one last simulation, which differs from our standard sequence only by the addition of trace hydrogen in the envelope of the initial model ($X_{\rm H,0} = 10^{-4}$ down to $\log q = -4.0$, for a total hydrogen mass of $10^{-8}M$). We describe this calculation separately and in more detail because the presence of residual hydrogen significantly alters the chemical evolution. This simulation is similar to that presented in Section 3.2 of Paper II, except that the latter was started from an almost pure-helium DO white dwarf, whereas we consider here a PG 1159 star with large amounts of carbon and oxygen. This allows us

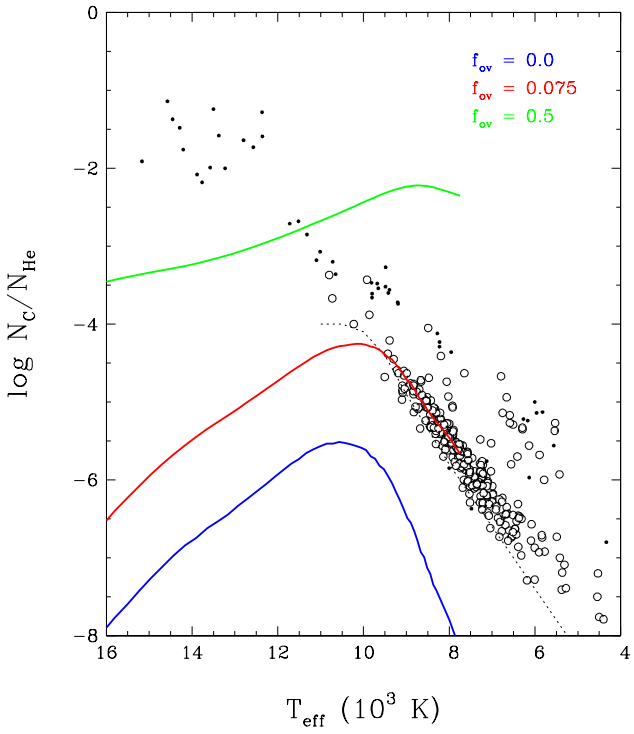

Figure 4.12 – Same as Figure 4.7, but for the effect of the overshoot parameter. The red curve shows our reference sequence, which assumes $f_{\rm ov} = 0.075$, whereas the blue and green curves represent analogous sequences assuming $f_{\rm ov} = 0.0$ and 0.5, respectively.

to study for the first time the effect of hydrogen on the phenomenon of carbon dredge-up at low effective temperatures.

Figure 4.13 shows snapshots of the chemical profile along our evolutionary sequence including hydrogen, similarly to Figure 4.1 for our reference sequence. As can be seen in panels (a) to (d), the sedimentation of carbon and oxygen at high effective temperatures is essentially unaffected by the presence of trace hydrogen. However, a crucial difference is that the hydrogen gradually diffuses upward, eventually forming a thin pure-hydrogen layer at the surface. Consequently, the PG 1159 star transforms briefly into a DO white dwarf and then into a DA white dwarf. For the parameters adopted here, the DO-to-DA transition occurs at $T_{\rm eff} \sim 50{,}000$ K (see Section 3.2 of Paper II for details). It can be seen in panels (c) and (d) that the DA star harbors a triple-layered envelope, with hydrogen-rich, helium-rich, and PG 1159−like layers from top to bottom, which is qualitatively consistent with previous calculations by Althaus et al. (2005a, 2020b). At $T_{\rm eff} \sim 15{,}000$ K, all of the residual hydrogen has reached the surface, and thus the hydrogen and helium layers are in

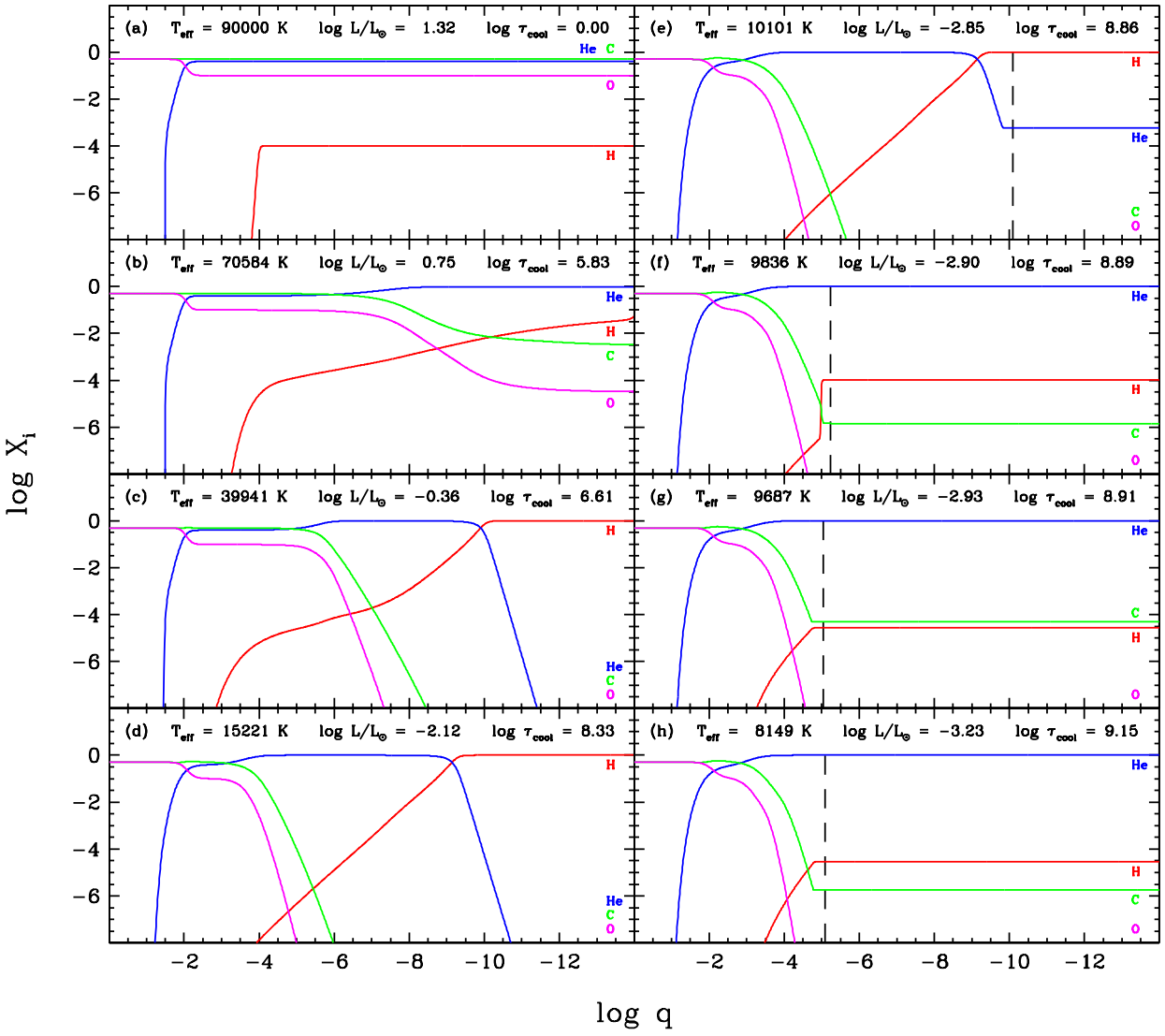

Figure 4.13 – Same as Figure 4.1, but for a sequence including residual hydrogen with an initial mass fraction $X_{\rm H,0} = 10^{-4}$.

diffusive equilibrium. Besides, note that at this point, the total hydrogen mass has decreased to $\sim 10^{-9} M$, because much of the outermost hydrogen-rich material has been ejected by the stellar wind. Furthermore, it is possible that the inclusion of nuclear burning in our calculations would have reduced the hydrogen content even further, as chemical diffusion initially carries some of the hydrogen to great depths (down to $\log q \sim -3.0$) where it should burn (Althaus et al., 2005a; Renedo et al., 2010).

The presence of a superficial pure-hydrogen layer has major repercussions on the subsequent chemical evolution. Going back to Figure 4.1, we notice that at $T_{\rm eff} \sim 15{,}000$ K, our

standard model has already begun to undergo carbon dredge-up by virtue of the deep helium convection zone. In contrast, at the same effective temperature, the outer parts of our model including hydrogen remain devoid of carbon because the thin hydrogen envelope is still convectively stable. Therefore, if a PG 1159 star contains enough residual hydrogen to become a DA rather than DB white dwarf, the onset of carbon dredge-up is delayed. However, the hydrogen layer does eventually become convective. As the star cools, the convection zone expands inward and reaches into the underlying helium reservoir at $T_{\rm eff} \sim 10{,}000$ K, thereby mixing some helium into the hydrogen layer, as illustrated in panel (e) of Figure 4.13. This leads to a runaway mixing event: the higher the surface helium abundance, the deeper the convective region, the more helium is brought to the surface, and so on. The hydrogen very rapidly ends up being completely diluted into a helium-dominated envelope (see Section 3.2 of Paper II for details) [5]. The depth of the convection zone is now such that carbon from the PG 1159−like layer is dredged up to the surface. Because the hydrogen/helium mixing event and the ensuing growth of the convection zone occur on an extremely short timescale, the mass fraction of carbon in the atmosphere goes from 0 to $\sim 10^{-4}$ almost instantaneously near $T_{\rm eff} \sim 10{,}000$ K, as can be seen in panels (f) and (g). Finally, panel (h) shows that the carbon abundance then decreases with cooling, as in the hydrogen-free case. Interestingly, we note that the final hydrogen and carbon abundances are both just below their optical detection limit, and thus the model displayed in panel (h) would not be classified as a DAQ, DQA, DA, or DQ white dwarf, but rather as a plain DC white dwarf.

Figure 4.14 compares our sequences with and without hydrogen in the $\log N_{\rm C}/N_{\rm He} - T_{\rm eff}$ diagram. The presence of residual hydrogen radically modifies the carbon abundance pattern: the increase in carbon abundance is very abrupt rather than gradual. In our calculation, this sudden carbon enrichment occurs at $T_{\rm eff} \sim 10{,}000$ K, but this value is expected to depend on the amount of hydrogen: the thicker the superficial hydrogen layer, the lower the hydrogen/helium mixing temperature, the lower the carbon dredge-up temperature (Rolland et al., 2018; Cunningham et al., 2019). Furthermore, on the descending part of the theoretical

5. Note that the effective temperature of the convective mixing event is ∼200 K lower than in the simulation of Section 3.2 of Paper II. The reason for this is that the initial envelope composition adopted here is slightly different (we include carbon and oxygen), which results in a little less hydrogen being ejected by the wind at high temperature, and thus the remaining hydrogen layer at low temperature is very slightly thicker.

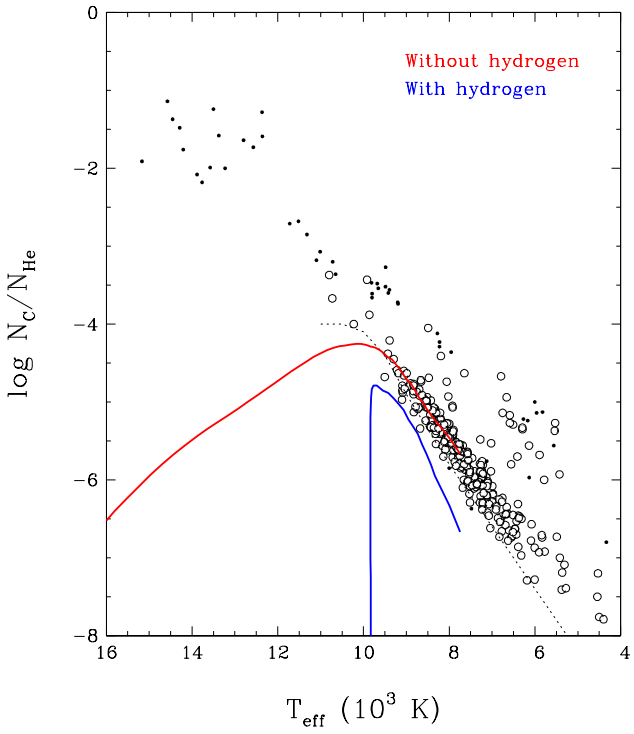

Figure 4.14 – Same as Figure 4.7, but for the effect of residual hydrogen. The red curve shows our reference sequence, which does not include any hydrogen, whereas the blue curve represents an analogous sequence including residual hydrogen with an initial mass fraction $X_{\rm H,0} = 10^{-4}$.

curve, the carbon abundance is somewhat lower when hydrogen is included. This is because the presence of trace hydrogen in the envelope slightly reduces the extent of the convection zone, as is apparent when comparing the last panels of Figures 4.1 and 4.13. Nevertheless, a very small adjustment of the overshoot parameter would be sufficient to bring our sequence with hydrogen in agreement with the observations. In this context, one could be tempted to deduce that perhaps most DQ white dwarfs descend from DA stars with thin hydrogen layers rather than from DB stars. However, we believe that this is highly unlikely. The reason is that such a DA-to-DQ transition involves a ∼0.5 Gyr intermediate phase in which the star appears as a DQA white dwarf, and it is a well-established observational fact that cool DQA white dwarfs are exceedingly rare (Dufour, 2011; Coutu et al., 2019). Therefore, we think that this particular spectral evolution channel only applies to a minority of DQ stars.

4.4. Discussion

4.4.1. The Origin of DOZ White Dwarfs

The transformation of PG 1159 stars into DO white dwarfs is inevitable, given that carbon and oxygen must ultimately sink out of sight under the influence of gravitational settling. However, this does not mean that all DO white dwarfs necessarily descend from PG 1159 stars. In particular, the origin of the subset of DO white dwarfs exhibiting traces of carbon is a question that remains unsettled. Are they simply transitional objects currently in between the PG 1159 and DO phases, or are they the products of an entirely different evolutionary channel?

Based on their element transport calculations, Unglaub & Bues (2000) argued that PG 1159 stars with various masses and compositions transform into DO white dwarfs at various effective temperatures, thereby naturally explaining the large dispersion of the carbon abundance pattern of DOZ white dwarfs. We can take a fresh look at this idea, thanks to our improved chemical evolution simulations and to the increased number of empirical carbon abundance determinations available in the literature. We confirmed the result of Unglaub & Bues (2000) that a relatively small change in the assumed stellar mass leads to a relatively large change in the PG 1159-to-DO transition temperature (that is, a difference of ∼17,000 K between $M = 0.5$ and 0.7 $M_{\odot}$). We showed that part (but not all) of the observational scatter in the $\log N_{\rm C}/N_{\rm He} - T_{\rm eff}$ diagram might be due to the intrinsic width of the DO mass distribution. Furthermore, we found that variations in the adopted wind mass-loss rate (which are theoretically expected from variations in the heavy-element content) also have a considerable impact on the PG 1159-to-DO transition temperature. Nevertheless, for a given mass, the empirical data can be explained only if individual objects have mass-loss rates differing by more than a factor of 100, which is unreasonably high. Still, Figures 4.4 and 4.6 suggest that most of the measured carbon abundances can be accounted for with realistic parameters if we consider both the mass and wind effects simultaneously. This is reasonable because the PG 1159 population is characterized by both a range of masses and a range of metallicities at a given mass (Werner & Herwig, 2006). Therefore, according to our calculations, it remains plausible that most DOZ white dwarfs originate from PG 1159 stars.

However, there are still a few issues with this scenario. For instance, if the carbon abundance pattern does reflect the width of the DO mass distribution, then Figure 4.4 indicates that the hottest DOZ white dwarfs should be the most massive, and vice versa. Such a temperature−mass relation is not observed in spectroscopic studies (Dreizler & Werner, 1996; Reindl et al., 2014a; Werner et al., 2014), which casts doubts on the above interpretation. Moreover, the coolest PG 1159 and DOZ stars are separated by a surprisingly large temperature gap. On one hand, the coolest known PG 1159 star, HS 0704+6153, has $T_{\rm eff}$ = 75,000 K (Werner & Herwig, 2006), and our models predict that it should turn into a pure-helium DO white dwarf before it reaches $T_{\rm eff}$ = 60,000 K (see Figure 4.4). On the other hand, DOZ white dwarfs exist down to much lower effective temperatures: SDSS J0301+0508 and SDSS J2239+2259 have $T_{\rm eff}$ = 50,000 and 45,000 K, respectively (Reindl et al., 2014a). Our calculations indicate that a very high mass-loss rate is likely required to produce such objects. Yet a very high mass-loss rate should also produce PG 1159 stars cooler than $T_{\rm eff} \sim$ 75,000 K, in contradiction with the observations (see Figure 4.6). In other words, none of our models connects HS 0704+6153 with SDSS J0301+0508 and SDSS J2239+2259 in a satisfactory way. Given these difficulties, it appears that our current theoretical framework fails to establish a clear evolutionary link between PG 1159 stars and at least some DOZ white dwarfs.

An alternative possibility, raised by Reindl et al. (2014a,b) on the basis of their spectroscopic analysis of hot white dwarfs and pre-white dwarfs, is that DOZ stars do not belong to the standard PG 1159−DO−DB−DQ evolutionary channel, but instead descend from the so-called O(He) stars. These objects represent a second type of hydrogen-deficient pre-white dwarfs alongside the PG 1159 stars. Their formation is not fully understood, but they are thought to result from low-mass white dwarf mergers (Reindl et al., 2014b). Observationally, they differ from PG 1159 stars by their much lower carbon and oxygen abundances, which are in fact similar to those of DOZ white dwarfs ($\log N_{\rm C}/N_{\rm He} \sim -2.5$). Thus, in this scenario, the carbon abundance would remain approximately constant throughout the O(He) and DOZ phases, thanks to the wind. In terms of the input parameters of our simulations, this would amount to assuming a low initial carbon mass fraction and a high mass-loss rate so that the theoretical curve would pass through the DOZ data points roughly horizontally in the $\log N_{\rm C}/N_{\rm He} - T_{\rm eff}$ diagram. Although this hypothesis effectively removes the need

to invoke a DO population with wildly different mass-loss rates, the fact remains that the coolest carbon-polluted objects require a very high mass-loss rate. Given that the wind is likely metal driven and apparently fades below $T_{\rm eff} \sim 75{,}000$ K in PG 1159 stars, it is highly doubtful that it persists down to $T_{\rm eff} \sim 45{,}000$ K in the much less carbon-rich DOZ white dwarfs. Another problem is that the number counts of O(He) and DOZ stars exhibiting traces of carbon are largely inconsistent. The region of the temperature−gravity plane where O(He) stars are found (80,000 K $\leq T_{\rm eff} \leq$ 200,000 K, $5.00 \leq \log g \leq 6.75$) contains a total of 27 confirmed hydrogen-deficient objects, among which only six are carbon-bearing O(He) stars (see Figure 3 of Reindl et al. 2014a and references therein). In contrast, on the white dwarf cooling sequence, DOZ stars account for more than half of the hydrogen-deficient population above $T_{\rm eff} = 60{,}000$ K (Paper I). Clearly, these objects cannot all descend from O(He) stars.

All things considered, we are still unable to draw a definitive conclusion regarding the origin of DOZ white dwarfs. That said, we can identify a number of avenues to improve the situation. First, it is possible that our ability to interpret the observations is hampered by our simplified treatment of the stellar wind, which is by far the most uncertain feature in our modeling of the PG 1159-to-DO transition. In this context, advances in our theoretical understanding of the source of mass loss in hot white dwarfs are greatly needed. Furthermore, the wind might not be the only transport mechanism acting against the downward diffusion of carbon: the process of radiative levitation might also play a role. More specifically, we can imagine that the wind dominates at very high temperatures but then dies out (perhaps around $T_{\rm eff} \sim 75{,}000$ K), after which radiative levitation takes over and continues to provide some support against gravitational settling. As a result, the amount of carbon in the outer layers remains nonzero, such that PG 1159 stars naturally evolve into DOZ white dwarfs for a long period of time (possibly down to $T_{\rm eff} \sim 45{,}000$ K). The main issue with this scenario is that the surface carbon abundances predicted by existing theoretical calculations of radiative levitation are too low by one and a half orders of magnitude ($-4.5 \lesssim \log N_{\rm C}/N_{\rm He} \lesssim -3.5$; Chayer et al. 1995). However, these results were obtained under the assumption of local equilibrium between gravitational and radiative forces; it is entirely plausible that such an equilibrium has not yet been reached in hot white dwarfs. Therefore, we believe that future

chemical evolution simulations should include a time-dependent, nonequilibrium treatment of radiative levitation.

A clearer picture of carbon pollution in hot helium-rich white dwarfs may also be achieved through improvements on the observational front. First, the effective temperatures, stellar masses, and carbon abundances derived from optical spectroscopic analyses have large uncertainties, typically in the range 5000−20,000 K, 0.05−0.25 $M_{\odot}$, and 0.2−0.5 dex, respectively (Reindl et al., 2014a; Werner et al., 2014) [6]. It is possible that these uncertainties preclude us from discerning the temperature−mass relation expected from our models for DOZ white dwarfs. Ultraviolet spectroscopy could help improve this situation, as it usually provides more precise and accurate atmospheric parameters for these objects (Werner et al., 2018). Second, the total number of analyzed objects is currently relatively low. Hopefully, the ongoing spectroscopic follow-up of Gaia white dwarf candidates (Kilic et al., 2020; Tremblay et al., 2020) will reveal new DOZ stars and thereby increase the density of data points in the $\log N_{\rm C}/N_{\rm He} - T_{\rm eff}$ diagram.

4.4.2. The Physical Properties of DQ White Dwarfs

The carbon abundance pattern of cool DQ white dwarfs is better understood than that of their hot DOZ counterparts. Moreover, their temperature, mass, and carbon abundance estimates are usually much more precise, with typical uncertainties of ∼200 K, ∼0.05 $M_{\odot}$, and ∼0.1 dex, respectively (Coutu et al., 2019). Thus, the comparison between our various models and the observations should allow us to make meaningful inferences about the physical properties of DQ stars. Nevertheless, we are faced with two major difficulties in the interpretation of the empirical DQ sequence.

The first difficulty is of theoretical nature and is obvious from Figures 4.8 to 4.12: the parameter space is highly degenerate. Indeed, the predicted evolution of the surface carbon abundance in the DQ phase is affected in a very similar way by the stellar mass, the thickness of the envelope, the initial carbon content, and the extent of convective overshoot. As such, the effect of a change in one of these parameters can be canceled out by varying the

6. The error on the effective temperature actually becomes smaller for cooler objects. For instance, the two coolest DOZ white dwarfs, SDSS J0301+0508 and SDSS J2239+2259, have uncertainties of 1000 − 2000 K in $T_{\rm eff}$ (Reindl et al., 2014a). For this reason, the existence of DOZ stars down to $T_{\rm eff} \sim 45{,}000$ K is a robust result.

other parameters. This means that our standard set of parameter values ($M = 0.6\ M_{\odot}$, $\log q_{\rm env} = -2.0$, $X_{\rm C,0} = 0.5$, and $f_{\rm ov} = 0.075$) is not the only one that provides a good match to the observed DQ sequence. For instance, a smaller amount of overshoot can be compensated by either a lower mass, a thinner envelope, a higher initial carbon abundance, or any combination thereof (see Figures 4.8 to 4.12). Fortunately, some of these parameters are subject to additional constraints. First, it is a well-known fact that the mass distribution of white dwarfs is very sharply peaked at $M \sim 0.6\ M_{\odot}$ (Genest-Beaulieu & Bergeron, 2019a; Tremblay et al., 2019a; Kilic et al., 2020). Second, pre-white dwarf evolutionary calculations predict that PG 1159 stars should have $\log q_{\rm env} \sim -2.0$ (Miller Bertolami & Althaus, 2006; Althaus et al., 2009b) [7]. Third, spectroscopic studies show that young PG 1159 stars (in which diffusion has not yet modified the surface composition) typically have $X_{\rm C}/X_{\rm He} \sim 1.2 - 1.5$ (Werner & Herwig, 2006). Therefore, our assumptions on the total mass, the envelope mass, and the initial composition rest on solid grounds (although we take a closer look at the $M = 0.6\ M_{\odot}$ hypothesis in the next subsection). On the other hand, the efficiency of overshoot in DQ stars is poorly known, but because it is the sole remaining unconstrained property, it can be probed by calibrating $f_{\rm ov}$ on the observations. This approach effectively provides a new way to investigate convective overshoot in cool white dwarfs. Still, we want to emphasize that our "best-fitting" value of the overshoot parameter, $f_{\rm ov} = 0.075$, is only approximate, as it depends on our assumptions on M, $q_{\rm env}$, and $X_{\rm C,0}$, as well as on the possible presence of trace hydrogen (see Figure 4.14). In addition, it may change following improvements in the input physics of our models, especially regarding the outer boundary condition: we currently assume a gray atmosphere, while Camisassa et al. (2017) showed that a nongray atmosphere results in a deeper convection zone (and thus likely requires less overshoot) [8].

7. In these calculations, the predicted value of $\log q_{\rm env}$ actually varies between -2.5 and -1.5 depending on the stellar mass, but we argued in Section 4.3.3 that the exact value is of no consequence for the chemical evolution of DQ white dwarfs if $\log q_{\rm env} \gtrsim -2.5$.

8. According to Figure 9 of Camisassa et al. (2017), the effect of replacing an Eddington atmosphere with a detailed nongray atmosphere is quite large: the convection zone becomes half an order of magnitude deeper in terms of fractional mass at low effective temperature. However, the effect of upgrading to a detailed nongray atmosphere is expected to be much smaller in our models because we assume a gray atmosphere, which is a better approximation than an Eddington atmosphere.

The second difficulty is of observational nature. In Figures 4.7 to 4.12, a dotted black line indicates the optical detection limit of carbon for S/N = 20 (which is the median value for the DQ sample of Coutu et al. 2019), kindly computed by S. Blouin using his DQ model atmospheres (Blouin et al., 2019) [9]. The curve closely follows the base of the observed DQ sequence, which implies that the apparent narrowness of the sequence is probably a visibility effect rather than a true feature of the DQ population. In other words, the very tight distribution of DQ stars in the $\log N_{\rm C}/N_{\rm He} - T_{\rm eff}$ diagram cannot be interpreted as evidence that all carbon-polluted white dwarfs share the exact same mass and chemical structure. Rather, carbon-polluted white dwarfs are likely characterized by a small yet finite range of M and $X_{\rm C,0}$ values, but only the most carbon-polluted ones appear as DQ stars, whereas the others are classified as DC stars because their atmospheric carbon remains optically undetectable. This view is confirmed by the fact that some optically featureless objects do exhibit carbon features in the ultraviolet (Weidemann & Koester, 1995), although their actual carbon content is highly uncertain (Dufour, 2011). Furthermore, the idea of a range of masses and progenitor abundances is more in line with model-atmosphere analyses of PG 1159, DO, DB, and DQ stars (Werner & Herwig, 2006; Reindl et al., 2014a; Genest-Beaulieu & Bergeron, 2019b; Coutu et al., 2019) and also with our discussion of the carbon abundance pattern of DOZ white dwarfs in Section 4.4.1. Therefore, although our calculations show that all white dwarfs descending from PG 1159 stars will inevitably experience the convective dredge-up of settling carbon at low effective temperature, only a fraction of them will actually be identified as DQ white dwarfs based on optical spectroscopy. This fraction cannot be determined at the present time, as this would require knowledge of the true width of the entire carbon abundance distribution, including both DQ and DC stars. However, we can infer from our results that the objects that do become DQ white dwarfs are probably those with lower masses, more carbon-rich progenitors, and/or thinner envelopes. This has an important consequence on our assessment of the extent of convective overshoot: our "best-fitting" value of the overshoot parameter, $f_{\rm ov} = 0.075$, might be overestimated because it is based on the most carbon-polluted members of the white dwarf population originating from PG 1159 stars. As such, this value should be regarded as an upper limit.

9. The limit is not very sensitive to the assumed S/N. In particular, the theoretical limit, corresponding to an infinite S/N, is only ∼0.3 dex lower than the limit for S/N = 20.

In spite of all these challenges, one robust conclusion that can be drawn from our study is that convective overshoot in cool DQ and DC white dwarfs is somewhat less significant than expected from recent hydrodynamical simulations ($f_{\rm ov} \sim 0.2 - 0.4$; Kupka et al. 2018; Cunningham et al. 2019). While this result may seem puzzling, it is in fact perfectly reasonable upon further thought. Hydrodynamical simulations of convective overshoot have so far been performed only for warm DA white dwarfs ($T_{\rm eff} = 11{,}000 - 18{,}000$ K). These objects have shallow, nonadiabatic convection zones extending no deeper than $\log q \sim -12.0$. On the other hand, cool DQ and DC white dwarfs have deep, adiabatic convection zones reaching down to $\log q \sim -5.0$ (see Figure 4.1). As pointed out by Herwig (2000) in the context of AGB stars, the efficiency of overshoot is expected to be different in these two regimes: under adiabatic conditions, the convective flows have a higher velocity, and thus when they penetrate the radiative region, they have less time to exchange heat with the surroundings, which causes them to decelerate more quickly. Therefore, as a white dwarf cools and its convection zone deepens and becomes increasingly adiabatic, we do expect the relative extent of its overshoot region (as measured by $f_{\rm ov}$) to decrease. This behavior is partially borne out by the coolest hydrodynamical simulations currently available (T. Cunningham 2021, private communication).

Our finding has an important implication for the study of cool metal-polluted white dwarfs. These objects owe their surface composition to the accretion of planetary material, and thus the measured heavy-element abundances can be used to deduce the accretion rate and the composition of the accreted matter. This calculation involves the amount of mass contained within the convectively mixed region, concisely called the mixed mass, as well as the diffusion timescales of the relevant metals at the base of this region (Dupuis et al., 1993a; Koester, 2009). The mixed mass is usually evaluated directly from the mixing-length theory, without considering convective overshoot. Cunningham et al. (2019) demonstrated that the inclusion of overshoot (as predicted by their hydrodynamical simulations) leads to a large increase in the inferred accretion rates of warm hydrogen-rich white dwarfs. A similar effect is also expected for helium-rich white dwarfs but has never been assessed due to the unavailability of overshoot calculations for these objects. Our semi-empirical constraint on the overshoot parameter provides for the first time a quantitative estimate of the true mixed mass in cool helium-rich white dwarfs ($T_{\rm eff} \lesssim 10{,}000$ K), which is essential for an accurate

determination of the accretion rates of DZ stars. In our coolest models with $f_{\rm ov} = 0.075$, the boundary of the fully mixed region is located ∼0.8 pressure scale height below the convection zone. Therefore, when evaluating DZ accretion rates, we recommend computing the mixed mass and diffusion timescales assuming an overshoot region extending at most 0.8 pressure scale height below the convection zone predicted by the mixing-length theory. We stress that this prescription should actually provide an upper limit on the accretion rates, given that our estimate of the overshoot parameter is itself an upper limit. Besides, we note that metal-accreting white dwarfs can be subject to additional mixing associated with the process of thermohaline convection (Deal et al., 2013; Wachlin et al., 2017; Bauer & Bildsten, 2018, 2019). However, this mixing mechanism was found to be negligible in helium-dominated envelopes (Deal et al., 2013; Bauer & Bildsten, 2019), hence it does not affect our interpretation.

So far, we have restricted our discussion to the white dwarfs forming the well-defined DQ sequence, but other more unusual objects also deserve a few comments. There are a few cool DQ stars that lie well above the sequence (and thereby coincidentally appear to blend with the massive DQ stars originating from mergers). Our evolutionary calculations suggest that these objects can be explained in three possible ways: low masses, carbon-rich progenitors, and/or thin envelopes. The first possibility is ruled out by the empirical results of Coutu et al. (2019) and Blouin & Dufour (2019), according to which most of them have typical masses. Furthermore, it is unclear why only a small subgroup of DQ white dwarfs would be characterized by thinner-than-average envelopes. Consequently, the most likely explanation is that they descend from exceptionally carbon-rich PG 1159 stars. Other interesting objects are the two cool DB stars for which Desharnais et al. (2008) obtained carbon abundance measurements from ultraviolet spectroscopy and which are shown as asterisks in Figure 4.2. Although we cannot conclude anything about these objects because of their metal accretion history, they still highlight the fact that ultraviolet spectroscopy of cool DB white dwarfs could be a valuable tool to further our understanding of the carbon dredge-up phenomenon. This is also true for cooler DC white dwarfs, according to the above discussion.

4.4.3. The Observed Mass Distribution of DQ White Dwarfs

In recent years, the advent of the Gaia mission has revolutionized the empirical determination of white dwarf masses. In particular, Coutu et al. (2019) relied on new trigonometric

parallax measurements from Gaia to obtain for the first time the detailed mass distribution of a large sample of DQ stars (303 objects, or an almost 20-fold increase with respect to the previous analysis of Dufour et al. 2005). Surprisingly, they found that the mass distribution of DQ white dwarfs peaks at $M \sim 0.55\ M_{\odot}$ and thus appears shifted by $-0.05\ M_{\odot}$ relative to that of their DB precursors. This difference may seem small but is in fact significant given the high precision of the Gaia data. Koester & Kepler (2019) independently obtained the same result using an almost identical dataset but a distinct model-atmosphere grid. The offset is illustrated in Figure 4.15, which compares the mass distributions of DB stars from Genest-Beaulieu & Bergeron (2019b) and of DQ stars from Coutu et al. (2019) and Blouin & Dufour (2019), both in absolute (left panel) and relative (right panel) terms. Coutu et al. (2019) argued that the systematic shift is likely not real and is possibly caused by the inadequate treatment of ultraviolet opacities in current DQ model atmospheres. They pointed out that this idea is supported by the case of the well-known DQ white dwarf Procyon B, for which their model-derived mass of $0.554 \pm 0.013\ M_{\odot}$ is slightly lower than the precise dynamical mass of $0.592 \pm 0.006\ M_{\odot}$ obtained by Bond et al. (2015).

Our chemical evolution simulations offer a new perspective on this apparent problem. First, as discussed in the previous subsection, DQ stars presumably represent a particularly carbon-rich subset of the whole carbon-polluted white dwarf population. Second, our calculations shown in Figure 4.8 predict that the surface carbon abundance is very sensitive to the stellar mass, in the sense that carbon enrichment is more significant in lower-mass models. The obvious conclusion is that trace carbon is preferentially detected in low-mass objects and therefore that DQ white dwarfs are naturally expected to have lower-than-average masses. For this reason, it appears plausible that the mass shift observed by Coutu et al. (2019) and Koester & Kepler (2019) is real after all. Figure 4.15 seems to support this interpretation: in the left panel, the DQ mass distribution (black histogram) fits the low-mass part of the DB mass distribution (red histogram) relatively well, as anticipated if low-mass and high-mass DB stars generally evolve into DQ and DC stars, respectively, at low effective temperature. That said, one must be careful when comparing the absolute distributions because the DB and DQ samples were constructed using slightly different selection criteria (although they are both largely based on the sample of spectroscopically confirmed white dwarfs from the Sloan Digital Sky Survey). The relative distributions displayed in the right

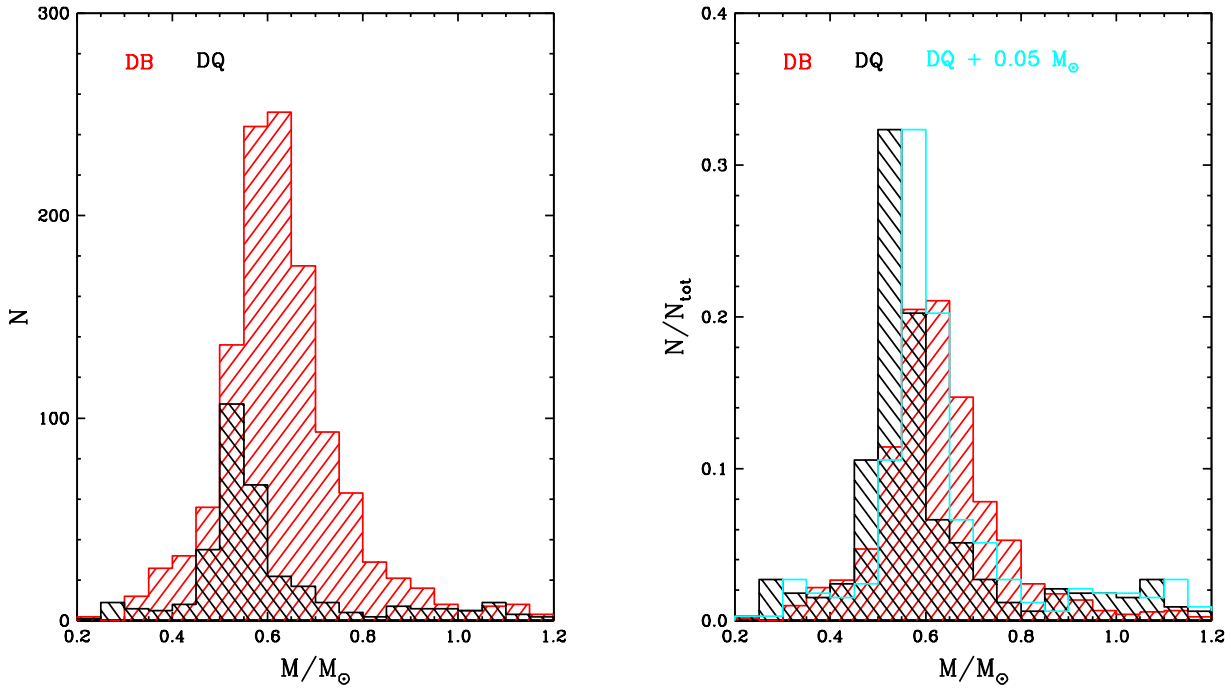

Figure 4.15 – Left panel: absolute mass distributions of DB white dwarfs from Genest-Beaulieu & Bergeron (2019b) and of DQ white dwarfs from Coutu et al. (2019) and Blouin & Dufour (2019), shown as red and black histograms, respectively. In both cases, we use the so-called photometric masses and exclude all objects with parallax measurement errors larger than 25%. Right panel: same as the left panel, but for the relative mass distributions. Also displayed as a cyan histogram is the DQ distribution shifted by +0.05 $M_{\odot}$.

panel allow a fairer comparison; we can see that DQ white dwarfs (black histogram) are significantly overrepresented in the range 0.45 $M_{\odot} \lesssim M \lesssim$ 0.55 $M_{\odot}$ and underrepresented in the range 0.60 $M_{\odot} \lesssim M \lesssim$ 0.80 $M_{\odot}$ relative to their DB progenitors (red histogram), which is consistent with the above considerations [10]. Besides, we note that if most DQ stars truly have $M \sim 0.55\ M_{\odot}$, then assuming $M = 0.6\ M_{\odot}$ in our simulations probably led us to overestimate the amount of convective overshoot needed to reproduce the observed carbon abundance pattern (see Section 4.4.2). Thus, we reiterate that our estimate of the overshoot

10. Another difference between the two mass distributions is the presence of a small bump around $M \sim 1.0\ M_{\odot}$ in the DQ distribution. This bump contains the so-called hot and warm DQ stars resulting from white dwarf mergers (Coutu et al., 2019) and is thus irrelevant to the present discussion.

parameter, $f_{\rm ov} = 0.075$, actually provides an upper limit on the extent of the overshoot region.

Of course, we cannot entirely rule out that issues in DQ model atmospheres are responsible for at least part of the systematic offset. As mentioned above, the case of Procyon B does point in that direction. Nevertheless, even if we artificially increase the masses of all DQ stars by 0.05 $M_{\odot}$, as illustrated in the right panel of Figure 4.15 (cyan histogram), our remarks remain valid: the relative mass distributions of DB and DQ stars have markedly different shapes, with the DQ distribution showing both a clear excess at $M \sim 0.55\ M_{\odot}$ and a clear deficit in the range $0.65\ M_{\odot} \lesssim M \lesssim 0.80\ M_{\odot}$. We interpret this as the natural consequence of the more efficient carbon dredge-up in lower-mass white dwarfs.

4.4.4. Tales of Spectral Evolution

The evolutionary simulations presented in Paper II and in this paper have allowed us to identify and analyze a number of possible scenarios of white dwarf spectral evolution. One conclusion that stands out is that the sequence of events and the final outcome are primarily dictated by the initial envelope composition and thus by the type of progenitor star. There is of course the trivial case of white dwarfs that inherit a standard "thick" hydrogen layer and thereby retain their DA character throughout their life. Although this case is thought to apply to roughly 75% of the white dwarf population (Paper I), it is of little interest to the present work given that it does not involve any spectral transformation. On the other hand, the chemical diversity of helium-dominated stellar remnants gives rise to an array of spectral evolution channels, which we now better understand thanks to our calculations. At this point, we feel that it is appropriate to give an overview of the emerging picture. The different evolutionary paths can be divided into four categories, according to the presence or absence of hydrogen and carbon in the envelope of the progenitor.

(1) The simplest case is that of an almost pure-helium object, containing virtually no hydrogen and only traces of heavy elements. These characteristics are observed in some O(He) stars (Reindl et al., 2014b). With such an initial composition, the formation of a superficial hydrogen layer through diffusion obviously cannot take place, and the dredge-up of settling carbon by the helium convection zone is expected to be insignificant. Consequently, the star always preserves its essentially pure-helium atmosphere as it cools down and successively becomes a DO, DB, and DC white dwarf.

(2) A more interesting evolution occurs if the progenitor possesses a small amount of residual hydrogen, as seen in some other O(He) stars (Reindl et al., 2014b). In this second scenario, which we modeled in detail in Section 3.2 of Paper II, the white dwarf experiences two major transformations. First, at high temperatures, the hydrogen diffuses upward and accumulates at the surface, thereby turning the DO star into a DA star. Then, at low temperature, the thin hydrogen layer becomes convective and mixes with the underlying helium reservoir. As a result, the hydrogen is thoroughly diluted into the helium-rich envelope, and the spectral type accordingly changes from DA to DC. The effective temperature at which this mixing episode occurs depends on the total hydrogen content: the thicker the hydrogen layer, the lower the mixing temperature (Rolland et al., 2018; Cunningham et al., 2019). Furthermore, note that the atmosphere of a DC white dwarf produced by this evolutionary channel contains an invisible yet nonzero amount of hydrogen, the exact abundance also being determined by the total hydrogen content.

(3) The third possibility is a progenitor with significant quantities of carbon and oxygen, namely, a PG 1159 star (Werner & Herwig, 2006). The details of the ensuing chemical evolution were extensively studied in the present work: in essence, the sedimentation of carbon and oxygen produces a pure-helium atmosphere, which remains so until the convection zone brings a small amount of carbon back to the surface. As we have seen, the outcome is either a DQ or a DC white dwarf, depending on whether the final carbon abundance is above or below the optical detection limit (as determined by the stellar mass, the thickness of the envelope, the initial carbon abundance, and the extent of convective overshoot). As in the previous case, a DC star formed in this way does not have a pure-helium atmosphere, but this time the contaminant is carbon instead of hydrogen.

(4) Finally, the fourth possible type of progenitor is a combination of the two previous ones: a PG 1159 star with trace hydrogen. The spectral evolution of such an object, which was investigated in Section 4.3.4 of the present paper, combines all of the above-mentioned phenomena. At high temperatures, the carbon and oxygen sink out of sight while the hydrogen floats to the surface, thus giving rise to a quick PG 1159-to-DO-to-DA transition. At low temperatures, the presence of a thin hydrogen layer prevents

carbon dredge-up at first, but once the convective mixing of the hydrogen and helium layers occurs, the convection zone very suddenly expands inward and reaches into the carbon reservoir. Because the hydrogen is ultimately diluted and thus "hidden" in the helium-dominated envelope, the DA white dwarf becomes either a DQ or a DC white dwarf, once again depending on the magnitude of carbon enrichment. In the end, this evolutionary channel produces a helium-rich atmosphere polluted by both hydrogen and carbon. Besides, we note that the hydrogen/helium mixing event and the concomitant onset of carbon dredge-up are expected to be further delayed in objects with higher hydrogen contents. As an extreme example, in the so-called hybrid PG 1159 stars (which show hydrogen lines in addition to the usual helium, carbon, and oxygen lines), the surface hydrogen mass fraction is typically $X_{\rm H} \sim 0.1$ (Werner & Herwig, 2006); assuming a homogeneous composition down to $\log q \sim -4.0$ (Althaus et al., 2005a), this corresponds to a total hydrogen mass of $\sim 10^{-5} M$. Once all this hydrogen has floated up, the superficial hydrogen layer will be so thick that it will never mix with the underlying helium layer (Rolland et al., 2018), such that the DA-to-DQ/DC transition will never take place. Therefore, hybrid PG 1159 stars will remain DA white dwarfs at low effective temperature.

All these considerations have a particularly interesting implication concerning the surface composition of DC and DZ white dwarfs. Through a comprehensive model-atmosphere analysis relying on Gaia parallax measurements, Bergeron et al. (2019) found that the assumption of a pure-helium atmosphere leads to a global overestimation of the masses of DC stars by $\sim 0.1\ M_{\odot}$. Coutu et al. (2019) reported a similar problem for DZ stars (which differ from their DC counterparts only by their metal accretion history). In both cases, it was argued that more reasonable masses could only be obtained by including an undetectable amount of hydrogen or carbon in the model atmospheres (see Bergeron et al. 2019 and Coutu et al. 2019 for details). The results of our simulations, combined with our knowledge of pre-white dwarf objects, are perfectly consistent with this empirical requirement. Indeed, the majority of the pre-white dwarf population consists of carbon-rich PG 1159 stars (see Figure 3 of Reindl et al. 2014a and references therein). Moreover, most O(He) stars, when observed at sufficiently high S/N, reveal traces of hydrogen (Reindl et al., 2014b). In other words, there exist very few (if any) white dwarf progenitors with virtually pure-helium envelopes, which

suggests that the first spectral evolution channel described above is extremely uncommon. In this context, our calculations predict that nearly all DC and DZ white dwarfs should have atmospheres containing invisible amounts of either hydrogen, carbon, or both. Our work therefore lends strong theoretical support to the results of Bergeron et al. (2019) and Coutu et al. (2019) regarding the surface composition of cool helium-rich white dwarfs.

4.5. Conclusions

In this paper, we presented an in-depth theoretical investigation of the PG 1159−DO−DB−DQ evolutionary channel based on state-of-the-art simulations of element transport in evolving white dwarfs. We examined the influence of several stellar parameters and physical processes on the variation of the atmospheric carbon abundance over a very large range of effective temperatures. Our study represents a significant improvement over previous works, as it is the only one to date that combines a sophisticated treatment of element transport, an extensive exploration of the parameter space, and a good agreement with observations of cool DQ stars. Our main conclusions can be summarized as follows:

(1) At high effective temperatures, thermal diffusion must be considered in order to model the PG 1159-to-DO transformation properly. The inclusion of this process accelerates the sedimentation of carbon and oxygen and thereby leads to an earlier PG 1159-to-DO transition by ∼3000 K in terms of temperature.

(2) The effective temperature at which a PG 1159 star turns into a DO white dwarf primarily depends on the stellar mass and the wind mass-loss rate, in the sense that the spectral change takes place at lower temperature if the mass is lower and/or the wind is stronger. In particular, for our standard mass-loss law (Equation 4.2), the transition temperature is $T_{\rm eff} \sim$ 66,000, 75,000 and 83,000 K for $M \sim$ 0.5, 0.6, and 0.7 $M_{\odot}$, respectively.

(3) The observed carbon abundance pattern of DOZ white dwarfs appears mostly consistent with the idea that these objects represent an intermediate evolutionary stage between the PG 1159 and DO stars, provided that the PG 1159 population is characterized by a reasonable range of masses and mass-loss rates. Nevertheless, there are a few problems with this interpretation, the most serious being that the existence

of relatively cool DOZ white dwarfs ($T_{\rm eff} \sim 45{,}000 - 50{,}000$ K) cannot be explained satisfactorily within our current theoretical framework. Radiative levitation, which we did not take into account, might play a more important role than expected.

(4) At low effective temperatures, thermal diffusion, nonideal diffusion, and convective overshoot all have a significant impact on the chemical evolution. Thermal diffusion and nonideal diffusion both enhance the rate of carbon settling and thereby reduce the magnitude of carbon dredge-up, while convective overshoot makes the homogeneously mixed region deeper and thus has the opposite effect.

(5) The surface carbon abundance in the DB and DQ phases is highly sensitive to a number of physical parameters, namely, the stellar mass, the thickness of the envelope, the initial carbon content, and the extent of convective overshoot. More specifically, a lower mass, a thinner envelope, a higher initial carbon abundance, and more efficient overshoot all result in more important carbon pollution. In our standard model, which assumes $M = 0.6\ M_{\odot}$, $\log q_{\rm env} = -2.0$, $X_{\rm C,0} = 0.5$, and $f_{\rm ov} = 0.075$, the carbon abundance reaches a maximum at $T_{\rm eff} \sim 10{,}000$ K and then decreases, hence closely matching the empirical DQ sequence.

(6) The chemical evolution is also substantially altered if a small amount of residual hydrogen is present in the PG 1159 progenitor. In this case, the hydrogen initially diffuses upward and accumulates at the surface. This thin hydrogen layer first delays the onset of carbon dredge-up but then mixes with the underlying helium layer, which leads to a rapid expansion of the convection zone and therefore a sudden carbon enrichment of the outer envelope. The carbon abundance subsequently decreases, as in the hydrogen-free case.

(7) The comparison between the predicted and observed composition of DQ stars allowed us to constrain for the first time the extent of the overshoot region in cool helium-rich white dwarfs ($T_{\rm eff} \lesssim 10{,}000$ K). Our inferred upper limit on the overshoot parameter, $f_{\rm ov} \leq 0.075$, implies that the overshoot region extends at most 0.8 pressure scale height below the convection zone predicted by the mixing-length theory. This result should be taken into account in the determination of metal accretion rates of DZ stars.

(8) Our calculations offer an elegant explanation for the difference between the empirically derived mass distributions of DB and DQ white dwarfs: although all DB stars likely

experience carbon dredge-up, this phenomenon is more significant (and thus more easily detected) in lower-mass objects, which translates into a relative excess and deficit of low-mass and high-mass DQ stars, respectively.

(9) Given the fact that the vast majority of helium-rich pre-white dwarf objects show traces of hydrogen and/or carbon, our simulations predict that the atmospheres of nearly all cool helium-rich white dwarfs should contain small (potentially invisible) amounts of hydrogen and/or carbon. This result is perfectly in line with recent model-atmosphere analyses of DC and DZ stars.

(10) There are many ways by which our understanding of the PG 1159−DO−DB−DQ evolutionary channel could be further improved in the future. On the hot end, more theoretical work on the source of winds and on the effects of radiative levitation would be highly desirable. Moreover, the identification and analysis of new DOZ stars in the sample of Gaia white dwarf candidates would be beneficial as well. On the cool end, the most promising avenue to obtain a more accurate picture of the carbon-bearing white dwarf population is definitely to investigate the atmospheric carbon content of DB and DC stars through ultraviolet spectroscopy.

Finally, we want to point out that our knowledge of carbon pollution in helium-rich white dwarfs is still far from complete. For instance, the chemical evolution of very massive DQ stars remains unclear. Although the emergence of the hot DQ white dwarfs at $T_{\rm eff} \sim 25{,}000$ K can be explained by the convective dredge-up of carbon in extremely thin helium envelopes ($\log q_{\rm env} \sim -8.0$; Althaus et al. 2009a), no model so far has been able to reproduce the carbon abundance pattern of their alleged progeny, the warm DQ white dwarfs (Brassard et al., 2007; Coutu et al., 2019). Furthermore, the presence of trace carbon at the surface of some hot DB stars ($T_{\rm eff} > 20{,}000$ K) is even more mysterious. One hypothesis that has been proposed is that a residual stellar wind retards the gravitational settling of carbon down to $T_{\rm eff} \sim 20{,}000$ K (Fontaine & Brassard, 2005); however, there is currently no physical basis for the occurrence of such a cool wind. In fact, no known mechanism provides a satisfactory explanation for the phenomenon (Koester et al., 2014b). Therefore, it appears that the theory of the spectral evolution of white dwarfs still faces many fascinating challenges.

Acknowledgements

We are grateful to Simon Blouin for a careful reading of our manuscript and for providing us with the optical detection limit of carbon based on his DQ model atmospheres. We also thank Tim Cunningham for helpful discussions regarding convective overshoot in hydrodynamical simulations. This work was supported by the Natural Sciences and Engineering Research Council (NSERC) of Canada and the Fonds de Recherche du Québec − Nature et Technologie (FRQNT).

Chapitre 5

On the Spectral Evolution of Hot White Dwarf Stars. IV. The Diffusion and Mixing of Residual Hydrogen in Helium-rich White Dwarfs

A. Bédard[1], P. Bergeron[1], & P. Brassard[1]

[1] Département de Physique, Université de Montréal, Montréal, QC H3C 3J7, Canada

Submitted to *The Astrophysical Journal*

Abstract

In the framework of our extensive modeling study of the spectral evolution of white dwarfs, we present here a new set of detailed calculations of the transport of residual hydrogen in helium-rich white dwarfs. First, we investigate the so-called float-up process at high effective temperature, whereby the upward diffusion of trace hydrogen leads to the formation of a hydrogen atmosphere. We examine the dependence of this phenomenon on the initial hydrogen abundance and on the strength of the radiative wind that opposes gravitational settling. Combined with our empirical knowledge of spectral evolution, our simulations provide new quantitative constraints on the hydrogen content of the hot helium-dominated white dwarf population. Then, we study the outcome of the so-called convective dilution process at low effective temperature, whereby the superficial hydrogen layer is mixed within the underlying helium-rich envelope. In stark contrast with previous works, we demonstrate that our models successfully reproduce the observed atmospheric composition of cool DBA stars, thereby solving one of the most important problems of spectral evolution theory. This major improvement is due to our self-consistent modeling of the earlier float-up process, which predicts the existence of a massive hydrogen reservoir underneath the thin superficial

layer. We conclude that the trace hydrogen detected at the surface of DBA white dwarfs is, in most cases, of primordial origin rather than the result of external accretion.

Key words: White dwarf stars; DO stars; DA stars; DB stars; Stellar evolutionary models; Atmospheric composition; Stellar diffusion; Stellar convective envelopes; Stellar winds

5.1. Introduction

The evolution of white dwarf stars is often viewed as a simple phenomenon, given that these stellar remnants are almost devoid of energy sources and thereby continuously cool with time. Moreover, as a result of their extreme compactness, the process of gravitational settling effectively removes all heavy elements from their outer layers, which are thus usually characterized by a high degree of chemical purity. Nevertheless, a closer look at these objects reveals many complexities, and in particular a surprisingly rich variety of surface compositions. Besides the standard atmospheres made of pure hydrogen (type DA [1]), atmospheres dominated by helium (types DO, DB, DC) and/or contaminated by trace elements (types DBA, DQ, DZ, and many others) are also quite common among the white dwarf population. Even more interestingly, the nature of the main surface constituent can change with time, from helium to hydrogen and from hydrogen to helium. This so-called spectral evolution is thought to arise from a collection of chemical transport mechanisms, such as atomic diffusion, convective mixing, stellar winds, and matter accretion, which can compete against gravitational settling in different phases of the life of a white dwarf. The study of this intricate phenomenon is fascinating in its own right, but is also of key importance for the use of white dwarfs as cosmochronometers, given that the envelope composition influences the cooling rate. It has been the purpose of the present series of papers to improve our understanding of spectral evolution, both empirically (Bédard et al. 2020, hereafter Paper I) and theoretically (Bédard et al. 2022b,a, hereafter Papers II and III).

From an empirical point of view, the most straightforward way to investigate the atmospheric transformations is to track the fraction of helium-rich white dwarfs as a function of effective temperature. This has been done repeatedly over the years using increasingly

1. Although hydrogen-atmosphere white dwarfs are generally of type DA, the coolest of them are actually of type DC given that hydrogen lines disappear below $T_{\rm eff} \sim 5000$ K.

sophisticated datasets, models, and techniques (Sion 1984; Fleming et al. 1986; Greenstein 1986; Fontaine & Wesemael 1987; Dreizler & Werner 1996; Bergeron et al. 1997, 2001, 2011; Napiwotzki 1999; Eisenstein et al. 2006a; Tremblay & Bergeron 2008; Krzesinski et al. 2009; Giammichele et al. 2012; Limoges et al. 2015; Blouin et al. 2019; Genest-Beaulieu & Bergeron 2019b; Ourique et al. 2019; Cunningham et al. 2020; McCleery et al. 2020; Paper I; López-Sanjuan et al. 2022). At high temperature, we have shown in Paper I that the fraction of helium-atmosphere objects gradually decreases from ∼24% at $T_{\rm eff} \gtrsim 70{,}000$ K to ∼8% at $T_{\rm eff} \sim 30{,}000$ K. At low temperature, the most recent analyses have established that this proportion remains roughly constant down to $T_{\rm eff} \sim 20{,}000$ K and then rises again among cooler stars. Although there are mild differences from one study to another, the general view is that the incidence of helium-dominated atmospheres reaches ∼20−40% at the end of the cooling sequence (see Figure 9 of López-Sanjuan et al. 2022 for a compilation of modern results). Taken together, these numbers suggest that (1) ∼15−30% of white dwarfs initially have a helium-rich atmosphere but experience a helium-to-hydrogen transition at high temperature and a hydrogen-to-helium transition at low temperature, and that (2) ∼5−10% of white dwarfs retain a helium-rich surface throughout their entire evolution. As for the remaining objects, they likely always possess a standard hydrogen-dominated atmosphere.

The commonly accepted physical interpretation of spectral evolution dates back, in essence, to Fontaine & Wesemael (1987). In their scenario, the transformation of a hot helium-atmosphere DO/DB white dwarf into a hydrogen-atmosphere DA white dwarf is the consequence of the so-called float-up process. The basic assumption is that a small amount of residual hydrogen is initially diluted (and thus hidden) within the hot helium-rich envelope. As the star cools, this hydrogen gradually diffuses upward under the influence of gravitational settling and eventually forms a thin pure-hydrogen layer at the surface. At lower temperature, the conversion of this hydrogen-atmosphere DA white dwarf into a helium-atmosphere DB/DC white dwarf is directly linked to the development of a convection zone in the envelope. Two similar but distinct mechanisms are usually invoked. On one hand, the so-called convective dilution process is believed to take place if the mass of the superficial hydrogen shell is smaller than $\sim 10^{-14} M$ (where M is the total mass of the star). In this case, the underlying helium mantle becomes convectively unstable; the convective motions then erode the hydrogen layer from below until the latter is completely diluted within the helium-rich

envelope. On the other hand, a superficial hydrogen layer thicker than $\sim 10^{-14} M$ gives rise to the so-called convective mixing process. In this case, it is in the hydrogen layer, rather than in the helium shell underneath, that a convection zone forms. The convective region deepens with cooling and ultimately reaches the helium mantle, which results in a thorough mixing of the hydrogen and helium layers. Because the helium reservoir is always orders of magnitude more massive, both mechanisms produce a helium-dominated surface with merely a trace of hydrogen. Convective dilution and convective mixing occur over different but complementary temperature ranges (30,000 K $\gtrsim T_{\rm eff} \gtrsim$ 14,000 K and 14,000 K $\gtrsim T_{\rm eff} \gtrsim$ 6000 K, respectively; Rolland et al. 2018, 2020; Cunningham et al. 2020), so it is thought that both phenomena contribute to the observed spectral evolution.

From these considerations, it is clear that the spectral evolution of a white dwarf depends primarily on its total hydrogen content. Canonical models of stellar evolution predict that the mass of hydrogen left on the cooling sequence should be $\sim 10^{-4} M$ (Iben & Tutukov, 1984; Renedo et al., 2010). Such a "thick" hydrogen layer precludes any of the atmospheric transformations described above and is thus probably representative of those standard white dwarfs which perpetually exhibit a hydrogen-rich surface. In contrast, the stars entering the cooling sequence with a helium-rich atmosphere must have lost nearly all of their hydrogen in previous evolutionary phases, most likely through either a late helium-shell flash (Iben et al., 1983; Herwig et al., 1999; Althaus et al., 2005b; Werner & Herwig, 2006) or a stellar merger (Zhang & Jeffery, 2012; Reindl et al., 2014b). However, the majority of these objects must retain at least some hydrogen, given that they later develop a superficial hydrogen layer. The amount of hydrogen left in the star largely determines when (or alternatively, at what effective temperature) the spectral changes take place. At high temperature, the more hydrogen is contained within the helium-rich envelope, the earlier the float-up process leads to a DO/DB-to-DA transition. At low temperature, the thicker the superficial hydrogen layer, the later convective dilution or mixing occurs and produces a DA-to-DB/DC transition. Furthermore, the amount of hydrogen present in the star also dictates the hydrogen abundance in the helium-rich envelope after convective dilution or mixing has happened. Therefore, the total hydrogen content of helium-dominated white dwarfs is a central question in the study of spectral evolution (Fontaine & Wesemael, 1987; MacDonald & Vennes,

1991; Tremblay & Bergeron, 2008; Bergeron et al., 2011; Koester & Kepler, 2015; Rolland et al., 2018, 2020; Cunningham et al., 2020).

Placing quantitative constraints on the total mass of residual hydrogen cannot be done from empirical analyses alone, given that these only probe the composition of the visible atmosphere, which represents a tiny portion of the stellar envelope. To achieve this purpose, one must turn to theoretical modeling. The ideal approach is to model the spectral transformations through evolutionary calculations in which element transport is self-consistently taken into account. Nevertheless, this is notoriously challenging from a numerical point of view, mainly because of the huge disparity between the cooling and transport timescales of white dwarfs. For this reason, most theoretical studies of spectral evolution published so far have made some approximations in the treatment of chemical transport.

The float-up scenario at high temperature was investigated by MacDonald & Vennes (1991), who however did not simulate the float-up process per se. They instead relied on sequences of static envelope models in diffusive equilibrium, where all of the hydrogen is assumed to have already reached the surface. This assumption was later shown to be incorrect: although gravitational settling is highly efficient in the very outer layers, it operates on a much longer timescale at the bottom of the envelope, where hydrogen can thus remain hidden for a long period of time (Dehner & Kawaler, 1995; Fontaine & Brassard, 2002; Althaus & Córsico, 2004). For this reason, the study of MacDonald & Vennes (1991) only provides a crude lower limit on the mass of hydrogen required for the DO/DB-to-DA transition to take place ($\gtrsim 10^{-15} M$). The first detailed calculations of the diffusion of hydrogen in hot helium-rich white dwarfs were performed by Unglaub & Bues (1998, 2000). These authors still used static envelope models but solved the full time-dependent transport problem. They demonstrated that the DO/DB-to-DA transition indeed occurs extremely rapidly under the influence of gravitational settling alone, but can be significantly delayed by mass loss due to a weak radiative wind. As such, they showed that the float-up phenomenon is primarily governed by three parameters: the initial hydrogen abundance, the wind mass-loss rate, and the stellar mass. Nevertheless, they explored a limited region of the parameter space, as they only considered a few (relatively large) hydrogen abundance values and did not vary the mass-loss law. For instance, they found that at $M = 0.6\ M_{\odot}$, hot DO white dwarfs with initial hydrogen mass fractions $X_{\mathrm{H},0} \sim 10^{-2}$ and 10^{-3} (where the index 0 refers to values

at the beginning of the cooling sequence) turn into DA white dwarfs at $T_{\rm eff} \sim 85{,}000$ and 70,000 K, respectively [2]. Until recently, the work of Unglaub & Bues (1998, 2000) remained the sole theoretical investigation of the kind. In Paper II, we presented full evolutionary calculations including a self-consistent, time-dependent treatment of element transport, with the specific aim of modeling the spectral evolution of white dwarfs. In particular, we analyzed in detail a single simulation of the float-up process and the associated DO/DB-to-DA transition, leaving a thorough examination of the parameter space for future work. We note that Althaus et al. (2005a, 2020b) carried out similar computations but barely discussed the chemical transformation itself, as they were mostly interested in its consequences for stellar pulsations. All in all, the float-up of residual hydrogen remains poorly studied, and therefore the hydrogen content of hot helium-rich white dwarfs remains poorly constrained.

On the other hand, the convective dilution and convective mixing mechanisms at low temperature have been the topic of several theoretical papers (Baglin & Vauclair 1973; Koester 1976; D'Antona & Mazzitelli 1989; MacDonald & Vennes 1991; Althaus & Benvenuto 1998; Chen & Hansen 2011; Rolland et al. 2018, 2020; Paper II). The most puzzling result of these works is the long-standing problem of the origin of hydrogen in cool DBA stars. These helium-dominated, hydrogen-bearing objects are mostly found in the range 20,000 K $\gtrsim T_{\rm eff} \gtrsim$ 12,000 K (where they account for the majority of the helium-rich white dwarf population) and typically have surface hydrogen abundances (by number) in the range $-6.5 \lesssim \log N_{\rm H}/N_{\rm He} \lesssim -4.0$ (Beauchamp et al., 1996; Voss et al., 2007; Bergeron et al., 2011; Koester & Kepler, 2015; Rolland et al., 2018; Genest-Beaulieu & Bergeron, 2019b). They are commonly believed to be the outcome of the convective dilution process. Yet, traditional models of this phenomenon predict final hydrogen abundances that are orders of magnitude lower than those measured in DBA white dwarfs. Consequently, an additional source of hydrogen (that is, besides the thin pure-hydrogen layer once present at the surface) must be invoked to explain these observations. It has often been proposed that the hydrogen is externally accreted, either from the interstellar medium (MacDonald & Vennes, 1991; Voss

2. While in this paper we generally express the hydrogen abundance as a mass fraction (simply because this is the input quantity of our calculations), Unglaub & Bues (1998, 2000) instead use number fractions. In the text, we refer to their calculations assuming $N_{\rm H,0}/N_{\rm He,0} = 10^{-1}$ and 10^{-2}, which approximately correspond to $X_{\rm H,0} \sim 10^{-2}$ and 10^{-3}, respectively, given their adopted composition (see Section 7 of Unglaub & Bues 2000).

et al., 2007) or from water-rich comets, asteroids, or planets (Farihi et al., 2013; Veras et al., 2014; Raddi et al., 2015; Gentile Fusillo et al., 2017). In recent years, the second hypothesis has been shown to successfully account for the composition of some DBA white dwarfs, especially those with very large hydrogen abundances ($\log N_{\rm H}/N_{\rm He} \gtrsim -4.0$). Nevertheless, the accretion scenario faces a difficulty when applied to the bulk of the DBA population: it requires that accretion begins only after convective dilution has happened. Otherwise, the superficial hydrogen layer built up by accretion rapidly becomes too thick to be altered by convection, and thus the star retains a hydrogen-dominated atmosphere (Bergeron et al., 2011; Koester & Kepler, 2015; Rolland et al., 2018). Meanwhile, Rolland et al. (2020) put forward a completely different paradigm: they suggested that the source of hydrogen is internal rather than external. More specifically, they argued that the residual hydrogen located at great depths, where the diffusion timescales are very long, does not have enough time to float to the surface. Once convective dilution has taken place, this reservoir of hydrogen finds itself mixed within the convection zone and thereby affects the final atmospheric composition [3]. Rolland et al. (2020) tested this idea quantitatively and demonstrated that it is promising. However, they relied on static envelope models with approximate chemical profiles, so a more detailed theoretical investigation is definitely warranted.

In this paper, we study the transport of residual hydrogen in hot helium-rich white dwarfs with the aim of constraining the hydrogen content of these objects. To do so, we carry out state-of-the-art simulations of the float-up process analogous to that introduced in Paper II. We examine, in particular, how the initial hydrogen abundance influences the DO/DB-to-DA transition. We can then estimate the range of hydrogen content that characterizes the helium-dominated white dwarf population based on the empirical results of Paper I. Furthermore, a secondary purpose of the present work is to revisit the problem of the surface composition of cool DBA white dwarfs using our improved evolutionary models. More specifically, we investigate the convective dilution scenario proposed by Rolland et al. (2020) using the realistic chemical profiles obtained from our float-up simulations. In Section 5.2, we describe the physical ingredients of our computations. Then, our results are presented in Section 5.3 and discussed in Section 5.4. Finally, our conclusions are summarized in Section 5.5.

3. Rolland et al. (2020) refer to this phenomenon as a dredge-up process, but we argue in Section 5.3.2 that this term is somewhat of a misnomer as we really are dealing with a dilution process.

5.2. Computations

As in the previous papers of this series, we use the STELUM evolutionary code to perform our spectral evolution simulations. A thorough description of the constitutive physics and numerical techniques of the code can be found in Paper II. Briefly, we build complete white dwarf models, from the center to the surface, and evolve them over time while allowing the chemical structure to change. The transport of chemical elements is modeled using a time-dependent diffusive approach and is self-consistently coupled to the evolution of the star, meaning that the feedback of composition changes on the cooling process is taken into account. The transport mechanisms included in our calculations are atomic diffusion, large-scale mixing due to convection, and a weak radiative wind.

Our starting models have a mass $M = 0.6\ M_{\odot}$, an effective temperature $T_{\rm eff} = 90{,}000$ K, a homogeneous carbon/oxygen core, and a homogeneous hydrogen-deficient envelope. We study two families of models characterized by different initial envelope compositions: a largely helium-dominated plasma and a helium/carbon/oxygen mixture. These two compositions are representative of the two classes of hydrogen-deficient white dwarf progenitors, the O(He) stars and the PG 1159 stars, respectively (Werner & Herwig, 2006; Reindl et al., 2014b). In both cases, we also include a uniform trace of hydrogen in the envelope. The initial mass fraction of hydrogen $X_{\rm H,0}$ is an input parameter and the values considered in this work span the range $-7.0 \leq \log X_{\rm H,0} \leq -2.0$ (in steps of 0.5 dex). The initial mass fractions of carbon and oxygen are $X_{\rm C,0} = X_{\rm O,0} = 0.001$ for the O(He)-type models, and $X_{\rm C,0} = 0.5$ and $X_{\rm O,0} = 0.1$ for the PG 1159-type models. The remaining material is helium ($X_{\rm He,0} = 1 - X_{\rm H,0} - X_{\rm C,0} - X_{\rm O,0}$). The exact proportions of carbon and oxygen are inconsequential, given that these elements quickly sink into the star and leave behind a hydrogen/helium mixture; nevertheless, our two types of composition are expected to power stellar winds of different strengths, an effect that we take into consideration below. In terms of the fractional mass depth $q = 1 - m/M$ (where m is the usual interior mass), we set the base of the envelope at $\log q = -2.0$; however, we include residual hydrogen only above $\log q = -4.0$, because deeper-lying hydrogen is burned in pre-white dwarf evolutionary phases (Althaus et al., 2005a; Renedo et al., 2010).

The float-up process is essentially governed by an interplay between atomic diffusion, which carries hydrogen upward, and the radiative wind, which tends to maintain a homogeneous composition in the outer layers. Thus, these two transport mechanisms must be treated as realistically as possible. Our simulations include the three types of particle diffusion (chemical diffusion, gravitational settling, and thermal diffusion) following the formalism of Burgers (1969) and using the diffusion coefficients of Fontaine et al. (2015a). In particular, we have shown in Paper III (see also Althaus & Córsico 2004) that thermal diffusion, which is often considered negligible in white dwarfs, has a significant impact on spectral evolution at high temperature. Unlike in our previous papers, we ignore here the nonideal term of Beznogov & Yakovlev (2013) in the diffusion equations, as it becomes important only at low temperature.

Ideally, the wind would be handled through the theory of radiation-driven winds, but this approach is highly impractical in an evolutionary context. One must then resort to approximate analytic formulas to evaluate the wind mass-loss rate efficiently along an evolutionary sequence. In the case of hot white dwarfs, a few studies have demonstrated that the simple mass-loss law of Blöcker (1995a),

$$\dot{M}_{\rm wind} = -1.29 \times 10^{-15} \left(\frac{L}{L_\odot}\right)^{1.86} M_\odot \ {\rm yr}^{-1}, \tag{5.1}$$

where L is the surface luminosity, accounts relatively well for the observed properties of PG 1159 stars and their descendants (Unglaub & Bues 2000; Quirion et al. 2012; Paper III). Therefore, we adopt this expression for our PG 1159-type models, and we henceforth refer to it as the strong wind or the high mass-loss rate. As for objects with almost pure-helium envelopes, the situation is even less clear, because there exists no definite constraint on the strength of their winds. The best we can do is to use Equation 5.1 scaled by a numerical factor chosen according to our knowledge of the winds of their direct precursors, the O(He) stars. Based on a rough comparison between the estimated mass-loss rates of individual O(He) (Reindl et al., 2014b) and PG 1159 (Koesterke & Werner, 1998; Herald et al., 2005) pre-white dwarfs, we simply set the mass-loss rate of our helium-dominated models to one-tenth the value given by Equation 5.1. This is admittedly nothing more than an educated guess, but this allows us to investigate the effect of the wind prescription on the float-up of

hydrogen. In the following, this reduced version of the mass-loss law is called the weak wind or the low mass-loss rate.

Furthermore, we also extend some of our calculations to lower effective temperatures, where the chemical evolution is dominated by the helium convection zone and thus depends on the treatment of convective mixing. We rely on the so-called ML2 version of the mixing-length theory, in which the mixing-length parameter is $\alpha = 1.0$ (Böhm-Vitense, 1958; Tassoul et al., 1990). For our purpose, which is to study cool DBA stars, the details of the mixing-length model are somewhat inconsequential because convection becomes adiabatic below $T_{\rm eff} \sim 20{,}000$ K (Rolland et al., 2018; Cukanovaite et al., 2019). Much more important is the prescription for mixing due to overshoot beyond the formally convective region. As in our previous works, we use the overshoot coefficient of Freytag et al. (1996),

$$D_{\rm ov} = D_{\rm conv,0}\ \exp\left(\frac{-2|r - r_0|}{f_{\rm ov}\, H_{P,0}}\right), \tag{5.2}$$

where r is the radial coordinate, r_0 is the radius of the convective boundary, $D_{\rm conv,0}$ and $H_{P,0}$ are the mixing coefficient and pressure scale height at r_0, and $f_{\rm ov}$ is a numerical parameter. In this framework, it is the value of $f_{\rm ov}$ that controls the extent of the overshoot region. Unfortunately, this parameter constitutes another rather poorly constrained physical ingredient in our models. According to hydrodynamical simulations of convective overshoot in hydrogen-rich white dwarfs, the depth of the overshoot region in these objects is relatively well represented by $f_{\rm ov} \sim 0.4$ (Kupka et al. 2018; Cunningham et al. 2019; T. Cunningham 2021, private communication). Analogous calculations for helium-rich white dwarfs are not yet available but are not expected to be significantly different. Consequently, we adopt $f_{\rm ov} = 0.4$ as our default value. Nevertheless, it is possible that this value is appropriate only for the thin nonadiabatic convection zones ($\log q_{\rm conv} \lesssim -12.0$, where $q_{\rm conv}$ is the location of the base in terms of fractional mass depth) found in relatively hot objects ($T_{\rm eff} \gtrsim 20{,}000$ K). Indeed, based on observations and models of carbon-polluted DQ stars, we have shown in Paper III that cool helium-dominated white dwarfs ($T_{\rm eff} \lesssim 10{,}000$ K), which have much thicker convection zones ($\log q_{\rm conv} \sim -5.0$), must have $f_{\rm ov} \leq 0.075$. We interpreted this result as evidence that the relative extent of the overshoot region decreases as the convection zone deepens and becomes increasingly adiabatic. To account for this possibility, we also carry out calculations in which the overshoot parameter varies with the depth of the formally convective region: we assume $f_{\rm ov} = 0.4$ for $\log q_{\rm conv} \leq -12.0$, $f_{\rm ov} = 0.05$ for $\log q_{\rm conv} \geq -6.0$,

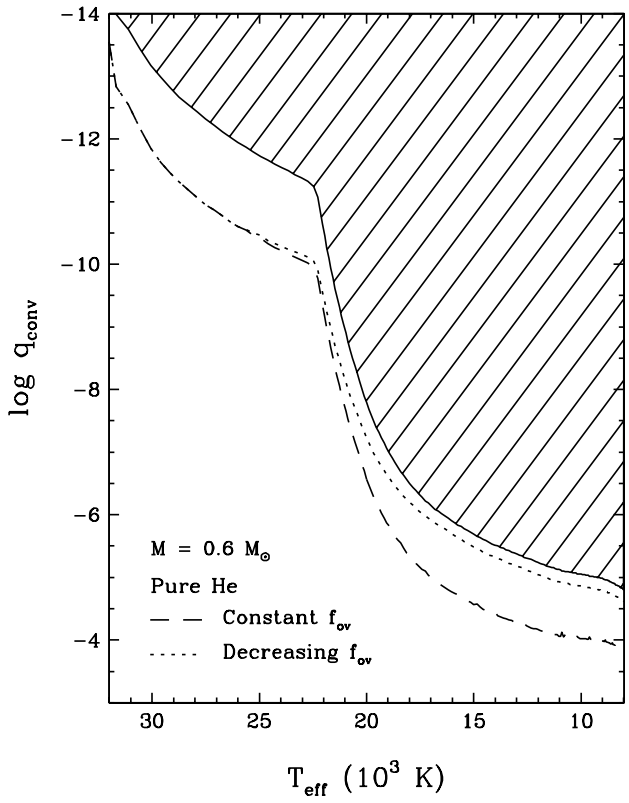

Figure 5.1 – Extent of the convectively mixed region as a function of effective temperature in a white dwarf model with a mass $M = 0.6\ M_{\odot}$ and a pure-helium envelope. The position inside the star is measured in terms of the fractional mass depth ($q = 1 - m/M$). The hatched area represents the formally convective zone, while the dashed and dotted curves show the base of the overshoot region for a constant and decreasing overshoot parameter, respectively (see text for details).

and a linear interpolation in between. For reference, Figure 5.1 illustrates the extent of the convectively mixed region as a function of effective temperature in a pure-helium envelope for both treatments of the overshoot parameter.

For simplicity, our simulations do not include residual nuclear burning, which is expected to play a minor role in the phenomena investigated here. The main consequence of nuclear burning would be to reduce slightly the hydrogen content of our white dwarf models as they evolve, because a small amount of hydrogen is expected to be carried below $\log q = -4.0$ by chemical diffusion (due to the sharp composition gradient there; see for instance Figure 5.2) and thus burned. We simply ignore this effect here, given that it would not affect the

float-up process. On the other hand, it would likely have a small impact on the hydrogen abundance in the DBA phase; we bear this in mind in our discussion in Section 5.4. Besides, note that nuclear burning of deep-lying hydrogen is also expected to maintain the strong hydrogen abundance gradient at $\log q = -4.0$; in order to mimic this effect, we artificially prevent hydrogen from diffusing below this region.

Finally, it is important to discuss briefly the outer boundary condition of the chemical structure. We do not simulate element transport up to the very surface (which is set at $\log q \sim -18.5$ in our models), as this would require an enormous amount of computing time. Rather, the transport calculations are only performed up to a fractional mass limit $q_{\rm lim}$, above which the composition is assumed to be uniform. As in our previous papers, we adopt $\log q_{\rm lim} = -14.0$. We currently cannot place the transport boundary higher in the envelope, because this gives rise to numerical instabilities. For this reason, at low effective temperature, we are unable to model the convective dilution mechanism per se, given that this phenomenon involves very thin hydrogen layers that cannot be resolved in our calculations. Nevertheless, we can still compute the subsequent evolution of the chemical profile under the assumption that convective dilution has occurred. This approach has been used in all other theoretical studies of convective dilution published so far (MacDonald & Vennes, 1991; Rolland et al., 2018, 2020) and is again used below.

5.3. Results

5.3.1. The Float-up Process

In this section, we describe the results of our simulations of the float-up process. We focus only on the evolution of the hydrogen abundance profile; see Section 3.2 of Paper II for a depiction of the full chemical structure in a similar calculation. That said, it should be mentioned that there is a small difference between the models of the present paper and that of Paper II with regard to the float-up process. Because the latter model was computed primarily for illustrative purposes, artificial mixing was included near the transport boundary ($\log q \lesssim -13.0$) to improve numerical convergence, which caused the atmospheric helium-to-hydrogen transition to be slightly delayed. We do not include such artificial mixing in the present work, and thus the quantitative results displayed below supersede those of Paper II.

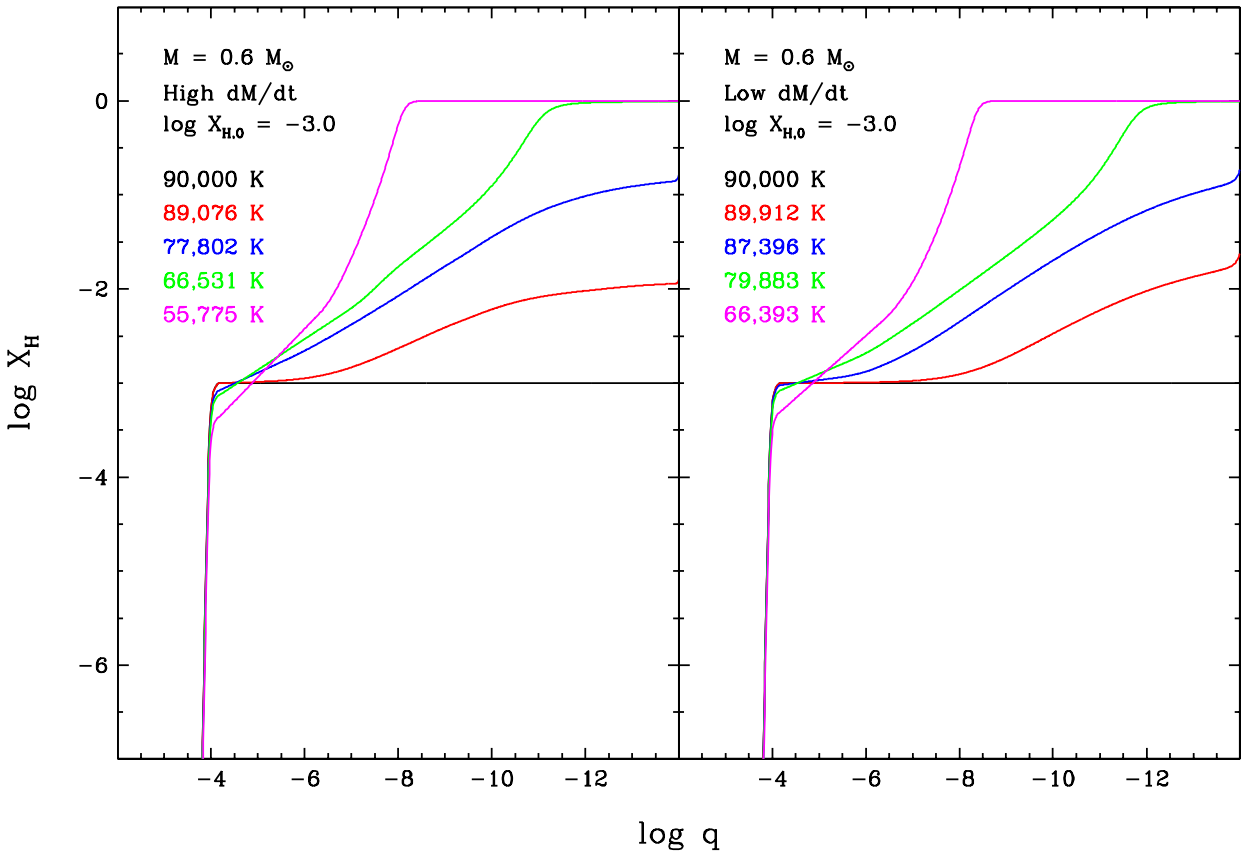

Figure 5.2 – Evolution of the hydrogen abundance profile due to the float-up process in a white dwarf model with a mass $M = 0.6\ M_{\odot}$, a high (left panel) or low (right panel) mass-loss rate (see Section 5.2 for details), and an initial hydrogen abundance $\log X_{\rm H,0} = -3.0$. The hydrogen abundance is expressed as a mass fraction, while the position inside the star is measured in terms of the fractional mass depth ($q = 1 - m/M$). Each curve represents a selected stage along the evolutionary sequence and is labeled with the corresponding value of the effective temperature.

Figure 5.2 shows the evolution of the hydrogen abundance profile (the hydrogen mass fraction $X_{\rm H}$ as a function of the fractional mass depth q) for the initial condition $\log X_{\rm H,0} = -3.0$ and for both the PG 1159-type, strong-wind and O(He)-type, weak-wind models. Let us first concentrate on the strong-wind case, which is displayed in the left panel. At the outset of the simulation, hydrogen diffuses upward rapidly due to the highly efficient gravitational settling: the surface hydrogen abundance has already risen by ∼1 dex at $T_{\rm eff} \sim 89{,}100$ K. However, it can be seen that mass loss causes the composition of the outer layers to remain

nearly uniform. Consequently, as soon as a small abundance gradient is established, the float-up process is considerably slowed down by the wind. The surface hydrogen abundance has increased by another ∼1 dex at $T_{\rm eff} \sim 77{,}800$ K, and the outer envelope has become hydrogen dominated at $T_{\rm eff} \sim 66{,}500$ K. As more hydrogen from the inner envelope is carried upward by diffusion, the superficial pure-hydrogen layer thickens; for instance, it extends down to $\log q \sim -8.0$ at $T_{\rm eff} \sim 55{,}800$ K. This specific evolutionary sequence falls within the parameter space studied by Unglaub & Bues (1998, 2000). The two sets of calculations are in good agreement: for the same parameters ($M = 0.6\ M_{\odot}$, $\log X_{\rm H,0} = -3.0$, and $\dot{M}_{\rm wind}$ given by Equation 5.1), they both predict that the atmosphere becomes richer in hydrogen than in helium around $T_{\rm eff} \sim 70{,}000$ K (see Figure 19 of Unglaub & Bues 2000). In fact, the DO-to-DA transition happens slightly earlier in our model, but this is likely due the fact that we take thermal diffusion into account, while this transport mechanism was ignored by Unglaub & Bues (1998, 2000).

In the weak-wind case, which is shown in the right panel, the chemical evolution is qualitatively very similar but occurs much faster because gravitational settling encounters less resistance. In particular, the surface has already become hydrogen dominated at $T_{\rm eff} \sim$ 79,900 K, which is ∼13,000 K hotter than in the strong-wind case. Notice also that the lower mass-loss rate results in a more pronounced abundance gradient in the outer layers of the first few models.

Figure 5.3 is identical to Figure 5.2, but for $\log X_{\rm H,0} = -4.5$. All other things being equal, reducing the initial hydrogen abundance has the obvious consequence of increasing the time required for the star to develop a hydrogen-rich atmosphere. The hydrogen abundance profile initially behaves as in the previous example, but then becomes much steeper near the surface, as shown at $T_{\rm eff} \sim 62{,}300$ and 76,500 K for the high and low mass-loss rates, respectively. This is because the wind fades with cooling and thereby looses its ability to compete against gravitational settling before the DO-to-DA transition is achieved. Hydrogen then continues to diffuse upward, such that a very thin pure-hydrogen layer has formed at $T_{\rm eff} \sim 46{,}800$ and 59,300 K for the high and low mass-loss rates, respectively. Therefore, assuming a lower hydrogen content not only delays the DO-to-DA transition, but also allows the emergence of a much thinner superficial hydrogen layer as a result of the reduced influence of the wind in these later phases.

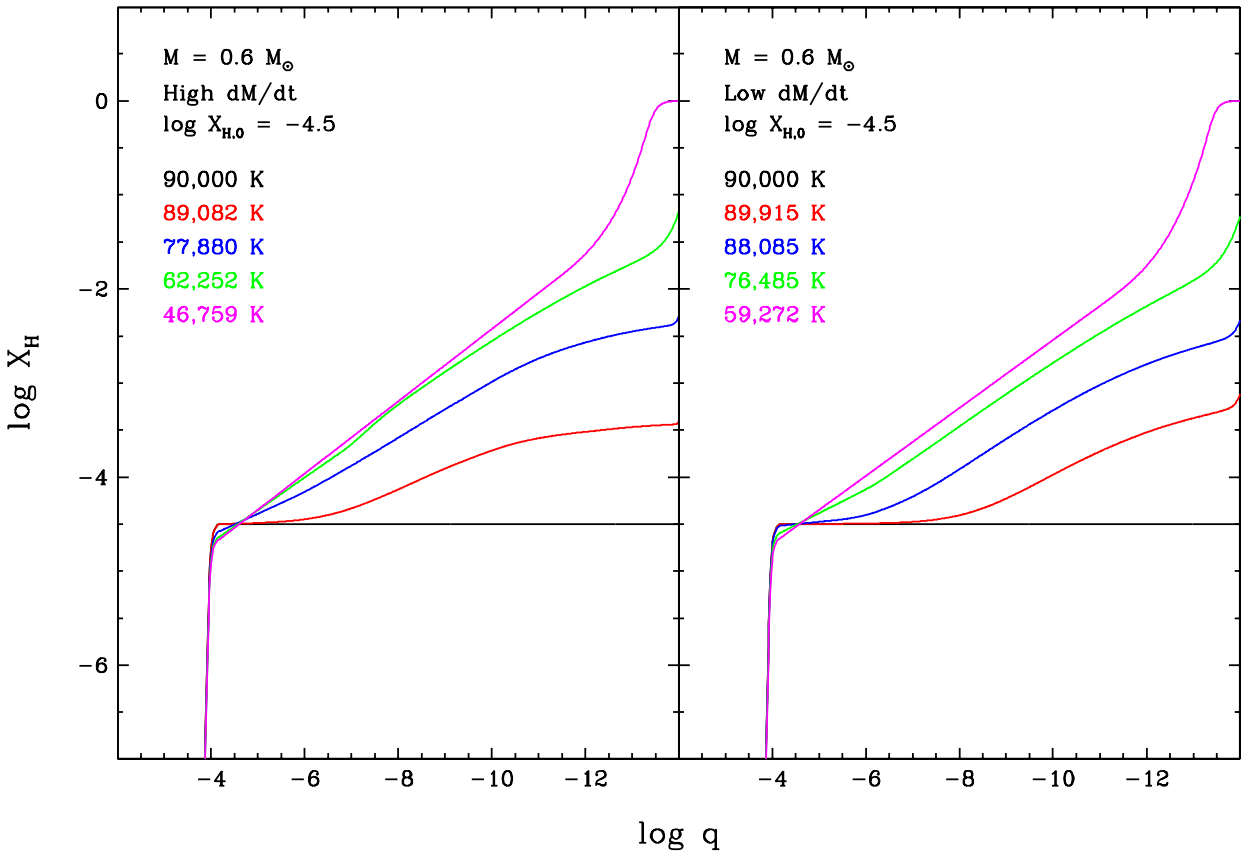

Figure 5.3 – Same as Figure 5.2, but for $\log X_{\mathrm{H},0} = -4.5$.

Another important difference with the previous example arises after the development of the outer pure-hydrogen layer: at this point, the large abundance gradient begins to drive a very small semiconvection zone around $\log q \sim -13.25$. This semiconvective region is not in a steady state: as soon as convection mixes hydrogen and helium, the composition gradient is destroyed, which causes the convection zone to disappear. Diffusion then quickly rebuilds the composition gradient, which causes the convection zone to reappear, and the cycle starts again. This oscillatory behavior occurs on an extremely short timescale (that is, less than a day); for this reason, we are numerically unable to follow the float-up process beyond this stage [4]. Nevertheless, it is likely that this semiconvective instability subsequently prevents the hydrogen located deeper in the envelope from reaching the superficial pure-hydrogen layer, which thus stops growing and remains very thin.

4. In principle, STELUM has the ability to model semiconvective mixing properly (see Paper II), but the adopted scheme becomes unstable in the outer envelope, where diffusion timescales are very short.

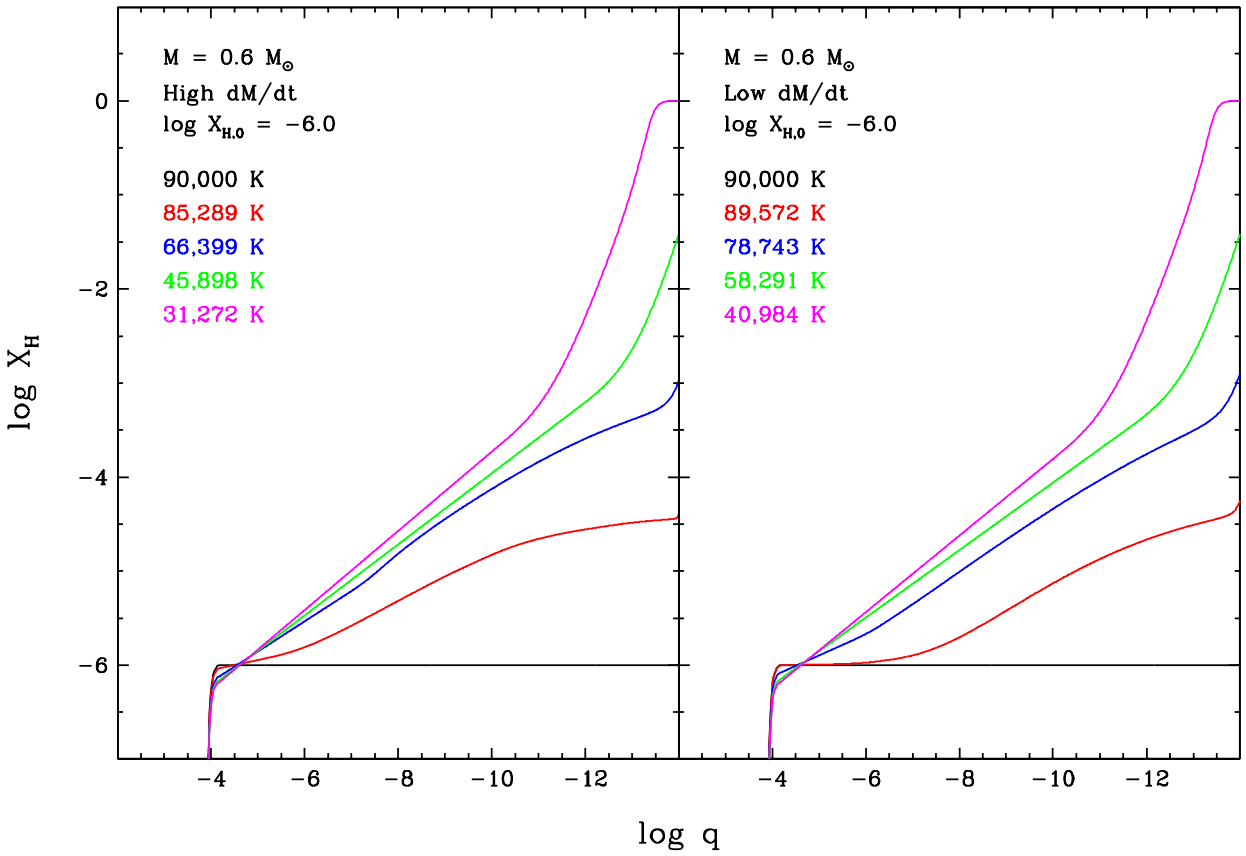

Figure 5.4 – Same as Figure 5.2, but for $\log X_{\rm H,0} = -6.0$.

Figure 5.4 illustrates the chemical evolution for an even lower initial hydrogen abundance, $\log X_{\rm H,0} = -6.0$. This simulation is similar to the previous one, except that the atmospheric transformation happens even later: the thin hydrogen layer emerges at $T_{\rm eff} \sim 31{,}300$ and 41,000 K for the high and low mass-loss rates, respectively. In the strong-wind case, the float-up process is so slow that the DO star first becomes a DB star before turning into a DA white dwarf. After the DO/DB-to-DA transition, the same oscillatory semiconvective instability as before arises and precludes us from computing the subsequent chemical evolution. In fact, we find that all of our models with $\log X_{\rm H,0} \leq -4.5$ experience this instability near the surface just after the formation of their hydrogen layer. Given that this phenomenon likely inhibits the upward diffusion of hydrogen, these stars should retain very thin hydrogen shells as they continue to cool. Notice that our calculations predict the existence of an extended hydrogen diffusion tail underneath the superficial layer, as envisioned by Rolland et al. (2020); this internal reservoir actually contains most of the hydrogen present in the white dwarf.

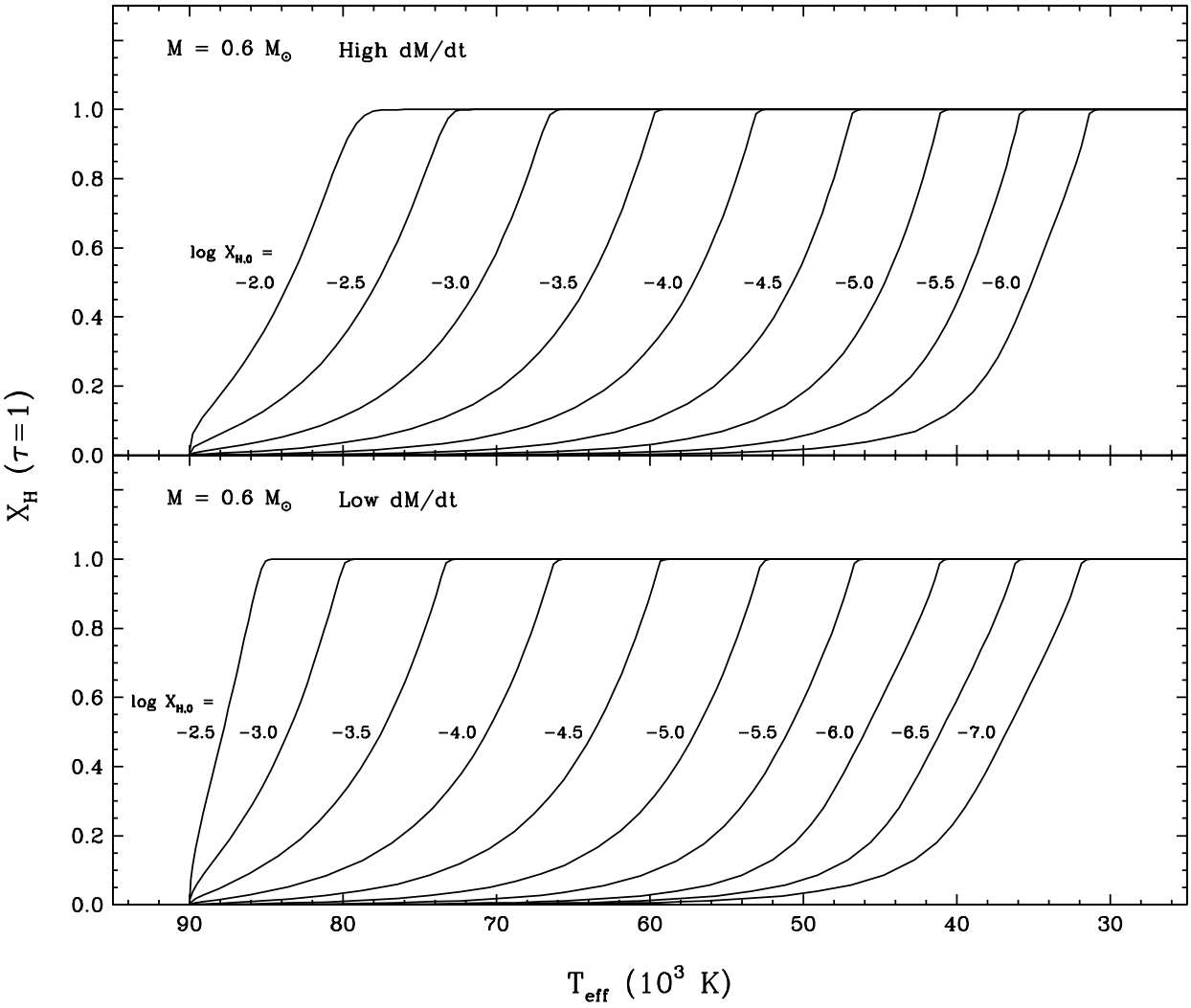

Figure 5.5 – Atmospheric hydrogen abundance as a function of effective temperature throughout the float-up process in white dwarf models with a mass $M = 0.6\ M_{\odot}$, a high (top panel) or low (bottom panel) mass-loss rate (see Section 5.2 for details), and various initial hydrogen abundances given in the figure. The hydrogen abundance is expressed as a mass fraction.

Figure 5.5 displays the variation of the surface hydrogen abundance with effective temperature in all of our simulations. The top and bottom panels show our PG 1159-type, strong-wind and O(He)-type, weak-wind models, respectively. This figure clearly demonstrates that the transformation of a helium-rich atmosphere into a hydrogen-rich atmosphere depends sensitively on the amount of hydrogen left in the star at the beginning of the cooling sequence. In essence, two curves differing by 0.5 dex in initial hydrogen abundance are

shifted by ∼7000 K in effective temperature (although this shift becomes smaller for the most hydrogen-deficient models). We also note that in a given simulation, the increase in surface hydrogen abundance is quite gradual, such that there is a broad temperature range over which both hydrogen and helium are present in the atmosphere. It is therefore not surprising that white dwarfs exhibiting spectral signatures of this transitional stage have been discovered in fairly large numbers (Manseau et al. 2016; Paper I). Furthermore, as mentioned earlier, the strength of the wind also has a marked impact on the speed of the float-up process: the curves are globally shifted by ∼13,000 K in effective temperature as a result of a change of a factor of 10 in the mass-loss law. Besides, note that the rightmost curve of each panel corresponds to the most hydrogen-deficient model in which the formation of a hydrogen-dominated atmosphere is possible. For lower initial hydrogen abundances, the emergence of the standard helium convection zone at $T_{\rm eff} \sim 32{,}000$ K (see Figure 5.1) halts the float-up process, hence such stars always retain a helium-dominated atmosphere.

In order to examine the influence of the initial hydrogen content on the DO/DB-to-DA transition more quantitatively, let us define the transition temperature $T_{\rm trans}$ as the effective temperature for which $X_{\rm H} = X_{\rm He}$ at the surface. Figure 5.6 displays the predicted transition temperature as a function of the assumed initial hydrogen abundance for our two wind prescriptions. The two horizontal dashed lines approximately delimit the range of "observed" transition temperatures, that is, the range of effective temperatures over which the fraction of helium-atmosphere white dwarfs is observed to decrease continuously (Paper I). Combining our theoretical results with this empirical constraint allows us to infer the range of hydrogen content of the hot helium-rich white dwarf population. We find that the observed spectral evolution can be explained by $-6.0 \lesssim \log X_{\rm H,0} \lesssim -3.0$ if we assume a high mass-loss rate or by $-7.0 \lesssim \log X_{\rm H,0} \lesssim -4.0$ if we assume a low mass-loss rate. Accordingly, the stars that never develop a hydrogen-dominated atmosphere must have had $\log X_{\rm H,0} \lesssim -6.0$ or -7.0. Although it is clear that the treatment of the wind constitutes a major source of uncertainty, this is the first time, to our knowledge, that such constraints are obtained.

Finally, we recall that all of the calculations presented in this paper assume a fixed stellar mass $M = 0.6\ M_{\odot}$, while it is well known that hot DO and DB stars actually span a small mass range, mostly between $M = 0.5$ and $0.7\ M_{\odot}$ (Reindl et al. 2014a; Paper I).

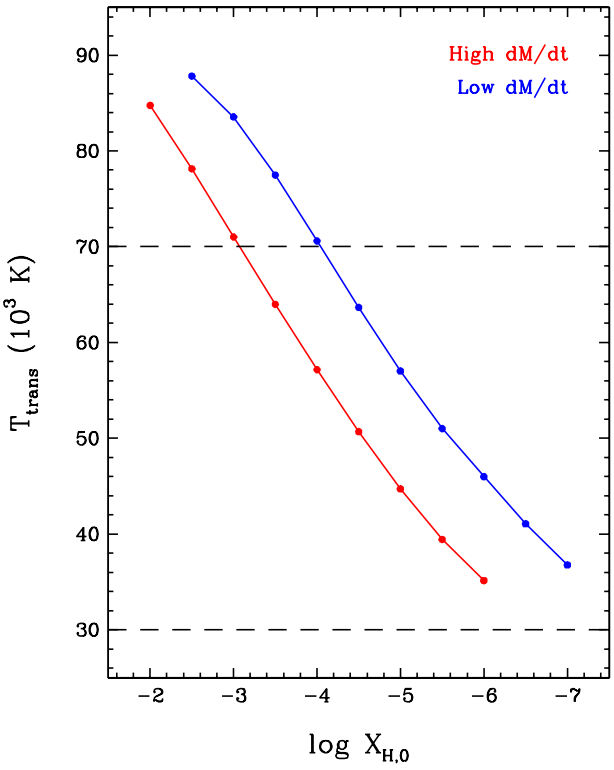

Figure 5.6 – Relation between the DO/DB-to-DA transition temperature and the initial hydrogen abundance for white dwarf models with a mass $M = 0.6\ M_{\odot}$ and a high (red curve) or low (blue curve) mass-loss rate (see Section 5.2 for details). The hydrogen abundance is expressed as a mass fraction. The two dashed black lines approximately delimit the range of empirical DO/DB-to-DA transition temperatures derived in Paper I.

The mass influences the transport of hydrogen in two ways: in a more massive white dwarf, gravitational settling is more efficient (because of the stronger gravitational field) and the radiative wind is weaker (because of the lower surface luminosity), with the result that the float-up process is faster. Thus, the fact that different objects undergo the DO/DB-to-DA transition at different effective temperatures might be partly due to differences in stellar mass (and not only to differences in hydrogen content). We carried out a few test calculations and found that varying the stellar mass by $\pm 0.1\ M_{\odot}$ changes the transition temperature by $\pm 4000-6000$ K (depending on the hydrogen content), which is smaller than the effect of varying the initial hydrogen abundance by ± 0.5 dex. Therefore, considering a range of masses might reduce the range of hydrogen abundances required to explain the observed spectral evolution, but this effect is expected to be small.

5.3.2. The Convective Dilution Process

In this section, we present evolutionary calculations at lower effective temperature with the aim of studying the implications of our float-up simulations for our understanding of cool DBA white dwarfs. These objects have long been thought to be the products of the convective dilution process in DA white dwarfs with extremely thin hydrogen layers, yet previous models of this phenomenon have failed to reproduce their observed atmospheric composition. As stated in Section 5.2, we cannot model the convective dilution mechanism per se within our current theoretical framework. Indeed, our choice of transport boundary ($\log q_{\rm lim} = -14.0$) prevents us from resolving the very outer parts of the envelope where convective dilution is expected to take place. Nevertheless, one way around this problem is to assume that convective dilution does occur, without paying attention to the specifics of the process, and to follow the ensuing chemical evolution [5]. To achieve this in practice, we take the last stellar model of a given float-up simulation and artificially dilute its hydrogen-rich layer within a small helium-rich region underneath. We then feed this modified model back into our code and resume the evolutionary calculation. In this regime, element transport is entirely dominated by the rapidly expanding helium convection zone, so we turn off atomic diffusion and mass loss for computational simplicity. We apply this procedure only to our most hydrogen-deficient simulations with $\log X_{\rm H,0} \leq -5.0$, for which the superficial hydrogen layer remains thin and thus the assumption of convective dilution is safe. We want to stress that our crude description of the convective dilution mechanism does not affect the evolution of the hydrogen abundance profile at later times. This is because the bulk of the hydrogen is still located in the diffusion tail ($-10.0 \lesssim \log q \lesssim -4.0$; see for instance Figure 5.4), hence making the details of the outer stratification unimportant for our purpose. Furthermore, note that our method incorporates a number of significant improvements over that of Rolland et al.

5. Note that our transport boundary condition necessarily leads us to overestimate the thickness of the pure-hydrogen layer at the surface. By definition, our float-up simulations can only produce hydrogen-layer masses larger than $10^{-14}M$ (see for instance Figure 5.4), while true hydrogen-layer masses are likely smaller than that. In fact, it is thought that only hydrogen-layer masses smaller than $10^{-14}M$ give rise to convective dilution (Rolland et al., 2018, 2020), so our only way to study the outcome of this process is to assume that it takes place and to induce it artificially. This should not be interpreted as a physical statement that convective dilution occurs for hydrogen-layer masses larger than $10^{-14}M$, but rather as a numerical procedure designed to overcome the shortcomings related to our transport boundary condition.

(2018, 2020): (1) we use realistic chemical profiles obtained from comprehensive calculations of the float-up process, (2) we rely on a full evolutionary approach in which white dwarf cooling and element transport are self-consistently coupled, and (3) we include mixing due to convective overshoot.

Figure 5.7 displays the evolution of the hydrogen abundance profile at low effective temperature for the simulation started from the initial condition $\log X_{\rm H,0} = -6.0$. The left and right panels show the results obtained under the assumption of a constant and decreasing overshoot parameter, respectively, as described in Section 5.2. In both panels, the first curve represents the chemical structure prior to convective dilution (in this case, this corresponds to the last model displayed in the left panel of Figure 5.4), while the other four curves illustrate the chemical structure at $T_{\rm eff} \sim$ 22,000, 20,000, 18,000, and 14,000 K. Within the convection zone and the overshoot region, the convective motions mix hydrogen and helium very efficiently and thereby produce a flat hydrogen abundance profile. As the star cools and the convection zone grows inward, the hydrogen finds itself diluted within increasingly helium-rich layers, thus causing the surface hydrogen abundance to decrease. However, and this is a key point for what follows, the presence of the hydrogen reservoir in the deep envelope prevents the surface hydrogen abundance from dropping to exceedingly low values. Indeed, it is clear from Figure 5.7 that the amount of hydrogen in the atmosphere is essentially set by the amount of hydrogen at the base of the convectively mixed region, which is nonzero given the broad hydrogen diffusion tail shaped by the float-up process. On another note, it is also apparent that the treatment of convective overshoot has a substantial impact on the atmospheric composition below $T_{\rm eff} \sim$ 20,000 K. More specifically, if the overshoot parameter is assumed to decrease with cooling, the homogeneously mixed region is less extended and therefore the surface hydrogen abundance is higher (by almost 0.5 dex), as expected from Figure 5.1.

Figure 5.8 displays the surface hydrogen abundance as a function of effective temperature following convective dilution in our most hydrogen-deficient models. The top and bottom panels correspond to the cases of a constant and decreasing overshoot parameter, respectively. The dotted parts of the curves indicate the region where the results are unreliable due to our artificial treatment of convective dilution; modeling this region correctly would require a better understanding of the details of the mechanism. Nevertheless, for the reasons

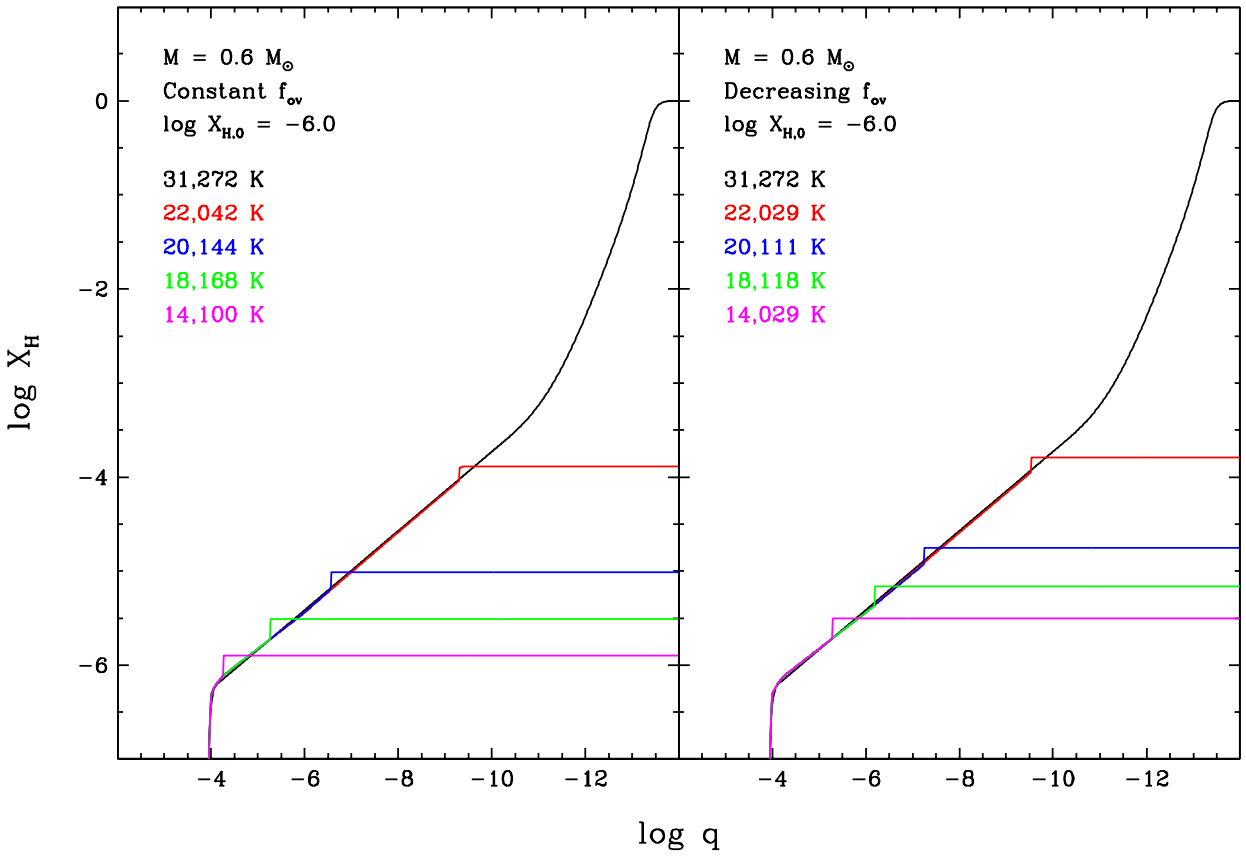

Figure 5.7 – Evolution of the hydrogen abundance profile following the convective dilution process in a white dwarf model with a mass $M = 0.6\ M_{\odot}$, a constant (left panel) or decreasing (right panel) overshoot parameter (see Section 5.2 for details), and an initial hydrogen abundance $\log X_{\rm H,0} = -6.0$. The hydrogen abundance is expressed as a mass fraction, while the position inside the star is measured in terms of the fractional mass depth ($q = 1 - m/M$). Each curve represents a selected stage along the evolutionary sequence and is labeled with the corresponding value of the effective temperature.

given above, the solid parts of the curves are physically accurate. In both panels, we also display as circles the DBA white dwarfs with empirically derived atmospheric parameters from Rolland et al. (2018) and Genest-Beaulieu & Bergeron (2019b). We express here the hydrogen abundance as the hydrogen-to-helium number ratio $N_{\rm H}/N_{\rm He}$, which is the usual observational quantity. This figure shows that regardless of the large uncertainty associated with the overshoot prescription, our simulations nicely reproduce the range of atmospheric compositions measured in cool DBA stars. This is in stark contrast with traditional models

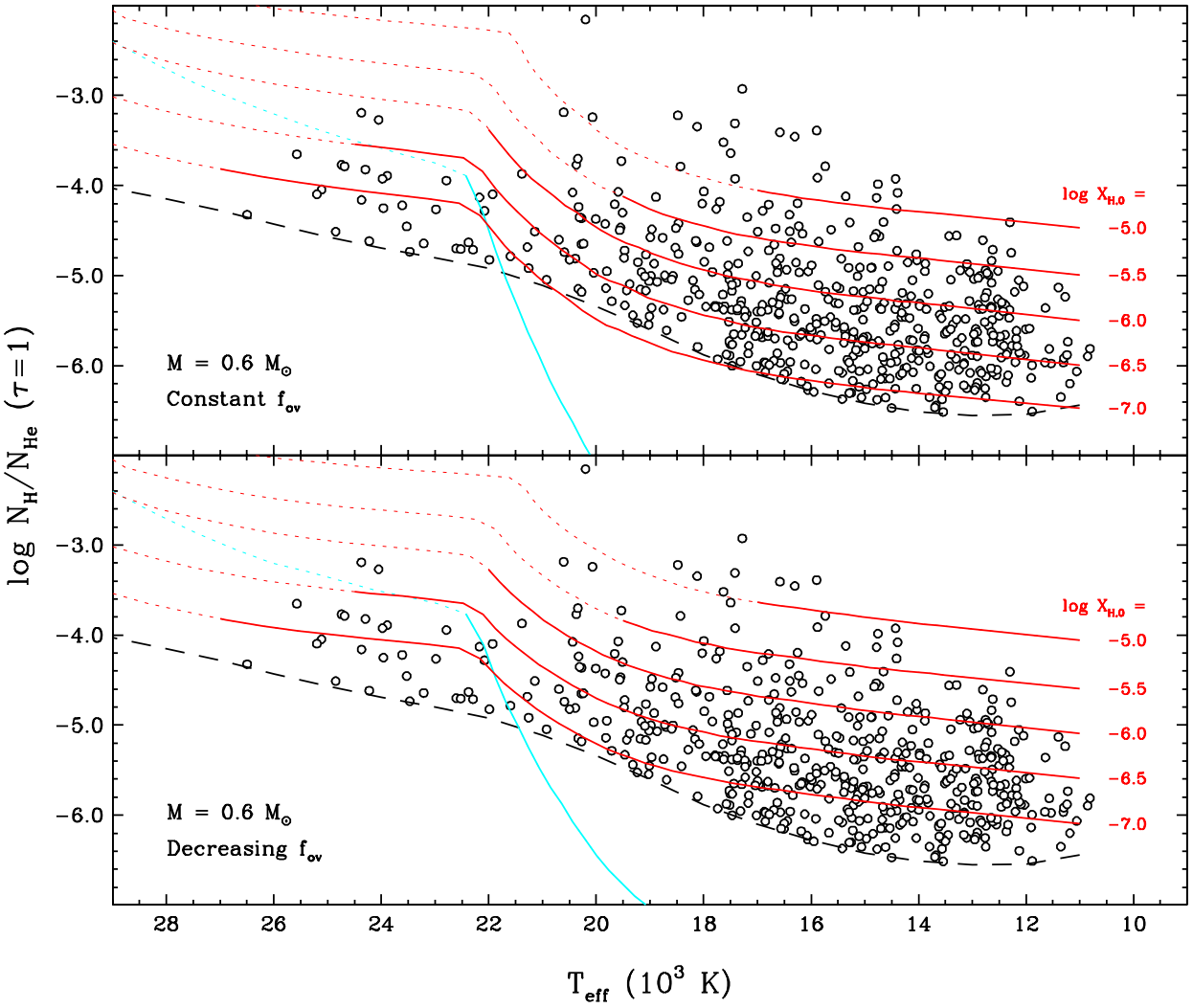

Figure 5.8 – Atmospheric hydrogen abundance as a function of effective temperature following the convective dilution process in white dwarf models with a mass $M = 0.6\ M_{\odot}$, a constant (top panel) or decreasing (bottom panel) overshoot parameter (see Section 5.2 for details), and various initial hydrogen abundances given in the figure (red curves). The instantaneous hydrogen abundance (the vertical axis) is measured in terms of the hydrogen-to-helium number ratio, while the initial hydrogen abundance (the label of each curve) is expressed as a mass fraction. For comparison, we display a second sequence with $\log X_{\mathrm{H},0} = -6.0$ in which the deep hydrogen reservoir was artificially removed (cyan curves). The dotted parts of the curves indicate the region where the results are unreliable due to our artificial treatment of convective dilution. Also shown are empirical atmospheric parameters of DBA white dwarfs (Rolland et al. 2018; Genest-Beaulieu & Bergeron 2019b; black circles) and the optical detection limit of hydrogen in a helium-rich atmosphere (dashed black line).

of the convective dilution process, which predict much lower surface hydrogen abundances (MacDonald & Vennes, 1991; Rolland et al., 2018, 2020). This is illustrated in Figure 5.8 by the cyan lines, which are evolutionary sequences with $\log X_{\rm H,0} = -6.0$ in which we artificially removed the deep hydrogen reservoir before convective dilution, thereby replicating the behavior of these older models.

The crucial feature of the present calculations is the use of accurate chemical profiles obtained from a detailed assessment of the float-up process. Indeed, the problem of traditional models lies with their assumption that the thin pure-hydrogen layer that undergoes convective dilution represents the whole hydrogen content of the white dwarf. In other words, they presume that gravitational settling is so efficient that a complete separation of hydrogen and helium has been previously achieved, such that that there remains no hydrogen below the superficial layer. Consequently, when the thin pure-hydrogen shell is diluted within the much more massive pure-helium envelope, the surface hydrogen abundance becomes extremely low. It turns out, as first suggested by Rolland et al. (2020) and as convincingly demonstrated here, that this assumption is far from accurate: there is actually a large amount of residual hydrogen "hidden" below the superficial layer. Upon convective dilution, this hydrogen reservoir finds itself mixed within the convection zone and thus determines the atmospheric composition. Rolland et al. (2020) refer to this phenomenon as a dredge-up process, but we have realized that this expression is somewhat of a misnomer, given that the concept of dredge-up generally involves an increase of the surface abundance of some trace element with time. As illustrated in Figure 5.7, we really are dealing with a dilution process here; the novelty of the current paradigm is simply that the superficial hydrogen layer is diluted within a helium-rich but hydrogen-contaminated (rather than hydrogen-free) envelope. For this reason, we believe that convective dilution remains an appropriate term to describe the phenomenon. Finally, we also note that the comparison between the predicted and observed hydrogen abundances shown in Figure 5.8 is much more satisfactory than that shown in Figure 11 of Rolland et al. (2020), a result that can be ascribed to our improved chemical profiles. Based on this excellent agreement, we can confidently state, for the first time, that the convective dilution scenario does provide a valid explanation for the atmospheric composition of the bulk of DBA white dwarfs.

5.4. Discussion

5.4.1. The Hydrogen Content of Hot DO White Dwarfs

In Paper I, we performed a spectroscopic analysis of a large sample of hot white dwarfs in order to study the spectral evolution of these objects from an empirical perspective. We were able to determine that (1) about one in four stars enter the cooling sequence with a helium-rich atmosphere, and that (2) about two-thirds of them develop a hydrogen-rich atmosphere by the time they reach $T_{\rm eff} \sim 30{,}000$ K. Moreover, we found that different objects experience this DO/DB-to-DA transition at different effective temperatures over the range $70{,}000 \text{ K} \gtrsim T_{\rm eff} \gtrsim 30{,}000$ K. If we interpret the atmospheric transformation as the consequence of the float-up of residual hydrogen, the results of Paper I suggest that the population of hot helium-dominated white dwarfs is characterized by a broad range of hydrogen content. But what is this range exactly? In other words, what is the quantitative relation between the amount of residual hydrogen and the transition temperature? It has been the primary goal of the present work to answer this question through theoretical calculations of element transport in evolving white dwarfs.

Our simulations of the float-up process have indeed provided a completely new way to estimate the hydrogen abundance left in the stellar envelope at the beginning of the cooling sequence, although this inference depends on the rather uncertain treatment of the radiative wind that opposes gravitational settling. As shown in Section 5.3.1, the range of initial hydrogen abundances that best reproduces the observed spectral evolution is $-6.0 \lesssim \log X_{\rm H,0} \lesssim -3.0$ for our strong-wind model and $-7.0 \lesssim \log X_{\rm H,0} \lesssim -4.0$ for our weak-wind model (which are roughly representative of objects with PG 1159-type and O(He)-type progenitors, respectively). As a corollary, the upper limit on the initial hydrogen abundance of those few white dwarfs that always retain a helium-rich surface is $\log X_{\rm H,0} \lesssim -6.0$ and -7.0 for the two mass-loss prescriptions.

Although these constraints are of great significance (as further discussed below), the ultimate quantity of interest is the total mass of hydrogen present in the star, which unfortunately is not straightforward to obtain. The first and foremost reason for this is that the conversion from an abundance to a total mass involves an assumption regarding the depth to which hydrogen is initially mixed. In our simulations, we adopt the maximum possible depth, $\log q = -4.0$, which means that the total mass of hydrogen is simply given

by $M_{\rm H}/M = 10^{-4} X_{\rm H,0}$. Consequently, our models undergoing the DO/DB-to-DA transition in the range 70,000 K $\gtrsim T_{\rm eff} \gtrsim$ 30,000 K are characterized by $-10.0 \lesssim \log M_{\rm H}/M \lesssim -7.0$ in the strong-wind case and $-11.0 \lesssim \log M_{\rm H}/M \lesssim -8.0$ in the weak-wind case. Nevertheless, we cannot exclude the possibility that residual hydrogen is mixed less deeply, which introduces a large uncertainty (that is, 1 dex in $\log M_{\rm H}/M$ for 1 dex in $\log q$). Furthermore, another issue is that the total amount of hydrogen is expected to decrease with time as a result of nuclear burning at the bottom of the envelope and mass loss at the surface. In our calculations, the first effect is ignored, while the second effect is highly uncertain. To illustrate the latter point, we draw attention to the float-up simulation presented in Section 3.2 of Paper II. In that work, we stated that as much as ∼90% of the hydrogen can be ejected by the wind in the course of the evolution. Upon further analysis, we have realized that most of this mass loss occurs at relatively low effective temperature ($T_{\rm eff} \lesssim$ 40,000 K) due to the fact that the decrease in mass-loss rate is then compensated by the increase in evolutionary timescale [6]. In reality, the radiative wind is expected to die out quite quickly with cooling and thus should not have any influence at such a late time, so this particular result is doubtful and likely stems from our extrapolation of the mass-loss law well beyond its domain of validity. Although the calculations of the present paper do not suffer from this problem (given that, as mentioned in Section 5.3.2, we turn off the wind at low effective temperature), the fact remains that our treatment of the wind is very rudimentary. For all of these reasons, we refrain from further interpreting our results in terms of total hydrogen masses.

Despite this limitation, our estimate of the hydrogen abundance in hot helium-rich white dwarfs is still noteworthy as it provides independent information on the phenomena responsible for the hydrogen deficiency in the first place. Two main mechanisms are believed to produce hydrogen-poor pre-white dwarf objects: the occurrence of a late helium-shell flash in a post-AGB star, which then becomes a PG 1159 star (Iben et al., 1983; Herwig et al., 1999; Althaus et al., 2005b; Werner & Herwig, 2006), and the merger of two low-mass white dwarfs, which possibly leads to the formation of a O(He) star (Zhang & Jeffery, 2012; Reindl

6. As a rough example, for a typical model at $T_{\rm eff} \sim$ 30,000 K, the mass-loss rate obtained from Equation 5.1 is $\sim 5 \times 10^{-17} M_{\odot} {\rm yr}^{-1}$ and the evolutionary timescale is $\sim 1 \times 10^{7}$yr, and thus the mass of hydrogen lost in a single timestep may be as large as $\sim 5 \times 10^{-10} M_{\odot}$, which may represent a significant fraction of the total hydrogen content of the star.

et al., 2014b). In both cases, it is practically impossible to detect low hydrogen abundances spectroscopically ($\log X_{\rm H,0} \lesssim -2.0$), because all hydrogen lines are blended with ionized helium lines (Werner, 1996a). For this reason, the exact amount of residual hydrogen can only be assessed through theoretical models of the aforementioned processes, which are extremely challenging to compute and hence come with their share of uncertainties. We can compare our hydrogen abundance constraints, which have been derived from a totally different approach, with the predictions of such calculations. Models of the late helium-shell flash have shown that there exist two common variants of this phenomenon, which are generally referred to as the late thermal pulse (LTP) and very late thermal pulse (VLTP) scenarios (see for instance Werner & Herwig 2006). The LTP version leads to relatively large hydrogen abundances ($\log X_{\rm H,0} \gtrsim -2.0$), so it definitely cannot account for the DO white dwarfs that turn into DA white dwarfs in the range 70,000 K $\gtrsim T_{\rm eff} \gtrsim$ 30,000 K[7]. On the other hand, these objects appear to be well explained by the VLTP version. For instance, according to the VLTP models of Miller Bertolami et al. (2006), the hydrogen abundance immediately after the helium-shell flash is $-5.3 \lesssim \log X_{\rm H,0} \lesssim -3.4$ depending on the adopted constitutive physics (see their Table 2). Our results are entirely consistent with these values, but additionally indicate that the hydrogen content left intact by the VLTP event varies from star to star. The preliminary calculations of Miller Bertolami et al. (2017) suggest that this could be the consequence of differences in main-sequence mass and/or metallicity. Besides, we note that most theoretical studies of the VLTP scenario have claimed that the leftover hydrogen is probably entirely shed off by mass loss in the giant phase before the star returns to the cooling sequence (Iben et al., 1983; Althaus et al., 2005b; Werner & Herwig, 2006); obviously, the spectral evolution of hot white dwarfs strongly challenges this assertion. Finally, as for the channel involving the merger of two low-mass white dwarfs, the available models, such as those of Zhang & Jeffery (2012), usually assume that all of the hydrogen is destroyed and therefore make no prediction regarding the remaining hydrogen content.

7. We do not imply here that the LTP scenario does not occur in nature, but rather that it results in a hydrogen abundance large enough that the star likely develops a hydrogen-rich atmosphere before even reaching the white dwarf cooling sequence. The so-called hybrid PG 1159 stars, in which hydrogen is spectroscopically visible, are extreme examples of such objects.

5.4.2. The Origin of Hydrogen in Cool DBA White Dwarfs

There is a general consensus that the increase in the fraction of helium-rich white dwarfs at low effective temperature is due to the convective dilution and convective mixing processes. On the other hand, the origin of the trace hydrogen seen at the surface of the majority of these objects has been a matter of debate for a few decades. There currently exist two main schools of thought regarding the atmospheric composition of DBA stars: either the hydrogen is primordial, or it has been accreted. The first scenario, in which the surface composition is simply the outcome of convective dilution, potentially has the merit of explaining both the spectral evolution and the DBA phenomenon with a single mechanism. However, the hydrogen abundances predicted by traditional models of the convective dilution process are notoriously much too low (MacDonald & Vennes, 1991; Rolland et al., 2018, 2020). For this reason, most recent works on DBA white dwarfs have favored the second scenario, more specifically the accretion of water-rich planetesimals (Raddi et al., 2015; Gentile Fusillo et al., 2017; Cunningham et al., 2020). Meanwhile, Rolland et al. (2020) suggested that the apparent failure of the primordial hypothesis might only be an unfortunate consequence of the inaccuracy of previous studies of convective dilution. They argued that the atmospheric hydrogen of DBA stars may actually come from an internal reservoir of residual hydrogen, which is expected from the float-up process but has been completely overlooked in the past.

We have investigated this idea using our comprehensive simulations of the float-up process at high effective temperature, which constitute a significant improvement with respect to the preliminary models of Rolland et al. (2020). Our calculations indeed predict the existence of a massive hydrogen reservoir underneath the thin pure-hydrogen layer. As demonstrated in Section 5.3.2, this key feature of the chemical structure effectively resolves the issue of the primordial scenario: following convective dilution, our models closely match the range of surface hydrogen abundances observed among the DBA population. These results compellingly validate the paradigm put forward by Rolland et al. (2020). In a nutshell, the convective dilution mechanism does produce the atmospheric composition of DBA white dwarfs, provided that realistic hydrogen abundance profiles are considered. Furthermore, we want to stress that this conclusion is independent of the details of how the superficial pure-hydrogen layer gets mixed within the underlying helium-rich envelope, because the final surface hydrogen abundance is largely governed by the deep hydrogen reservoir. However, this also implies

that the post-dilution hydrogen abundance of a given simulation is subject to the uncertainties on the total hydrogen content discussed in the previous section (related to initial conditions, nuclear burning, and mass loss), in addition to the uncertainty associated with convective overshoot. In other words, the range of initial hydrogen abundances for which our calculations reproduce the atmospheric composition of DBA stars, $-7.0 \lesssim \log X_{\rm H,0} \lesssim -5.0$, is possibly systematically off and should be taken with caution. Nevertheless, this does not change in any way our main qualitative conclusion: our models provide a clear solution to the long-standing puzzle of the origin of hydrogen in DBA white dwarfs.

In light of this development, it is worth reviewing the strengths and weaknesses of each of the two theories commonly invoked in this context. In principle, the accretion of water-rich planetesimals remains a viable explanation for the surface composition of DBA stars. There is even undeniable observational evidence that this phenomenon indeed occurs in a few objects (Gentile Fusillo et al. 2017 and references therein). The question to be asked is whether water accretion is responsible for the entire DBA population. As mentioned earlier, one drawback of this scenario is the requirement that hydrogen be delivered to the star only after the convective dilution process has taken place. However, this difficulty is not insurmountable: it has recently been pointed out by Hoskin et al. (2020) that the dynamical accretion simulations of Mustill et al. (2018) predict that planetesimals cannot be scattered to within the Roche limit of a white dwarf for the first ∼40 Myr of its cooling lifetime, which corresponds to $T_{\rm eff} \gtrsim 22{,}000$ K according to our evolutionary calculations. This delay in the onset of accretion is exactly what is needed to produce cool DBA white dwarfs. Nevertheless, another complication is that DBA stars represent as much as 60−75% of the DB population (Koester & Kepler, 2015; Rolland et al., 2018). Within the accretion hypothesis, this means that 60−75% of all white dwarfs must accrete water-bearing planetesimals in their first few 100 Myr on the cooling sequence (assuming that the phenomenon is equally common in hydrogen-rich and helium-rich objects), a number which is uncomfortably high. Still, this scenario has generally been favored until now due to the lack of a better alternative, that is, because of the failure of the model based on residual hydrogen to account for the measured abundances of DBA stars.

Now that this problem has been fully resolved, perhaps it is time to question the relevance of the water-accretion interpretation for the bulk of the DBA population. Our calculations

have demonstrated that DBA white dwarfs actually represent an inevitable evolutionary stage of stars retaining a small amount of primordial hydrogen on the cooling sequence. From this new perspective, the chief advantage of the primordial scenario is that it consistently explains (1) the helium-to-hydrogen transformation at high effective temperature, (2) the hydrogen-to-helium transformation at low effective temperature, and (3) the atmospheric composition of DBA white dwarfs. In contrast, the accretion scenario explains only the last item[8]. Furthermore, the results of Paper I indicate that about two-thirds of hot DO stars contain enough residual hydrogen to transform into DA white dwarfs and then into DBA white dwarfs; this is remarkably consistent with the observed proportion of DBA stars among the DB population quoted in the previous paragraph. Therefore, although the accretion of water-rich planetesimals undoubtedly plays a role in some individual cases (especially in the most hydrogen-rich objects with $\log N_{\rm H}/N_{\rm He} \gtrsim -4.0$), it now seems somewhat superfluous to invoke this additional mechanism as the primary source of hydrogen. In short, our study strongly supports the idea that the trace hydrogen seen at the surface of the majority of DBA white dwarfs is of primordial origin.

In recent years, a further argument in favor of water accretion onto DBA stars has often been put forward. It was shown by Gentile Fusillo et al. (2017) that there exists a clear correlation between the presence of hydrogen and the presence of metals in helium-dominated atmospheres. Given that the heavy elements are necessarily accreted, they interpreted this correlation as evidence that the hydrogen is accreted alongside the metals, most plausibly in the form of water. The obvious question then is whether this finding can be reconciled with our above conclusion. We believe so, as there is another possible explanation for the observed correlation. Stating that the presence of hydrogen and the presence of metals are related is equivalent to stating that the absence of hydrogen and the absence of metals are related. In other words, those DB white dwarfs that appear devoid of hydrogen tend to appear devoid of planetary material as well; in the following, we will call them the pure DB white dwarfs. Interestingly enough, this particular property is also found among another class of helium-rich white dwarfs, namely, the cool DQ stars, in which carbon is generally the sole contaminant.

8. One could allege that hydrogen accretion could possibly explain the DO/DB-to-DA transition at high effective temperature, but this would contradict the argument according to which a significant delay in the onset of accretion is necessary to explain the existence of DBA white dwarfs.

These objects likely represent the immediate progeny of the pure DB white dwarfs, and they owe their surface carbon enrichment to the convective dredge-up of primordial carbon from the deep envelope (Paper III). This means that the absence of hydrogen and heavy elements is also eventually associated with a significant carbon enrichment. Thus, there really is something special about the pure DB and DQ stars: not only do they rarely accrete from a companion, but they additionally undergo a more efficient carbon dredge-up than average. We suggest that the source of this correlation lies in the pre-white dwarf evolution: the progenitors of pure DB and DQ white dwarfs might be PG 1159 stars that have experienced a particularly violent late helium-shell flash before settling on the cooling sequence. First, such an event may result in a larger carbon abundance in the envelope of the PG 1159 star and thereby a larger carbon abundance at the surface of the white dwarf at low effective temperature. Second, it is not difficult to imagine that the rapid episodes of expansion and contraction of the pre-white dwarf object may lead to the ejection or engulfment of any small orbiting body and thus prevent the accretion of planetary material at later times. Third, and most importantly, this very active evolutionary phase may deplete the hydrogen content of the star to such a low level that it will never be detectable at any point on the cooling sequence. The conclusion is that we indeed expect the pure DB and DQ white dwarfs to be strongly deficient in both hydrogen and metals (other than carbon), regardless of the composition of their former planetary companions. This, of course, naturally gives rise to the observed trend that DBA stars often exhibit traces of heavy elements, which therefore cannot be taken as a definitive proof of water accretion onto white dwarfs. That said, we recognize that the scenario outlined here is somewhat speculative and will have to be confirmed by models of the late helium-shell flash.

5.5. Summary and Conclusion

In this paper, we presented detailed theoretical calculations of the transport of residual hydrogen in helium-dominated white dwarfs. We first studied the upward diffusion of trace hydrogen at high effective temperature, which eventually leads to the formation of a hydrogen-rich atmosphere. We examined how this float-up mechanism is influenced by the initial hydrogen abundance and the strength of the radiative wind that competes with gravitational settling. We showed that the atmospheric transformation takes place later in the

cooling process when a lower hydrogen content or a higher wind mass-loss rate is assumed. Based on these results, we interpreted the empirical fact that DO/DB stars turn into DA stars over a broad range of effective temperatures as a consequence of the existence of a broad range of hydrogen content among the hot helium-rich white dwarf population. More specifically, we found that the initial hydrogen abundances that best explain the observed spectral evolution are $-6.5 \pm 0.5 \lesssim \log X_{\rm H,0} \lesssim -3.5 \pm 0.5$ if we allow for uncertainties in the strength of the wind. These values are roughly consistent with the level of hydrogen deficiency expected from models of late helium-shell flashes in post-AGB stars. Furthermore, we noted that our simulations predict that the thin hydrogen shell at the surface represents only a small fraction of the total amount of residual hydrogen, as most of it remains "hidden" in the deep envelope for a long period of time.

We then investigated the convective dilution of the superficial hydrogen layer within the underlying helium-dominated envelope at low effective temperature. We demonstrated that our models successfully reproduce the range of atmospheric hydrogen abundances observed among cool DBA white dwarfs, in stark contrast with previous studies. This remarkable improvement is essentially due to the use of realistic chemical profiles obtained from the float-up process, including in particular the deep hydrogen reservoir which had been completely overlooked until the recent work of Rolland et al. (2020). Our calculations are the first to provide a clear solution to the three-decade-old problem of the origin of hydrogen in DBA stars, which was arguably the most serious problem of the theory of the spectral evolution of white dwarfs. This outcome is perhaps the most striking example of the importance of considering a self-consistent, time-dependent treatment of element transport in evolutionary models of white dwarfs. We thus concluded that the atmospheric composition of the majority of DBA stars can be explained solely by the convective dilution of primordial hydrogen, without the need to invoke external accretion. Nevertheless, we noted that the quantitative relation between the initial and final surface hydrogen abundances of a given object is still uncertain, especially because it depends on the location of the base of the hydrogen reservoir and on the efficiency of convective overshoot. Better constraints on these two physical ingredients, as well as on the strength of the wind at high temperature, would definitely help us refine our understanding of the spectral evolution of white dwarfs.

Acknowledgements

We dedicate this paper to the memory of our late colleague, mentor, and friend, Gilles Fontaine, who would certainly have been very enthusiastic about the results presented here. This work was supported by the Natural Sciences and Engineering Research Council (NSERC) of Canada and the Fonds de Recherche du Québec − Nature et Technologie (FRQNT).

Chapitre 6

Conclusions

Dans cette thèse de doctorat, nous nous sommes intéressés à l'évolution spectrale des étoiles naines blanches, avec une attention particulière pour les naines blanches les plus chaudes. Les changements drastiques de composition de surface que subissent ces cadavres stellaires sont généralement interprétés comme le résultat d'une compétition entre divers mécanismes de transport des éléments chimiques dans l'enveloppe stellaire. Néanmoins, malgré de nombreux travaux de recherche échelonnés sur plus de trois décennies, plusieurs lacunes importantes subsistaient dans notre compréhension de ce phénomène complexe.

En premier lieu, nous avons attaqué le problème sous un angle empirique, c'est-à-dire en étudiant les propriétés atmosphériques d'un gros échantillon d'étoiles. Plus spécifiquement, nous avons réalisé au chapitre 2 une analyse spectroscopique détaillée de près de 2000 naines blanches chaudes ($T_{\rm eff} \geq 30{,}000$ K) observées par le SDSS. Pour mener à bien ce projet, nous avons d'abord calculé un nouvel ensemble de modèles d'atmosphères incorporant toute la physique nécessaire, notamment les effets hors-équilibre thermodynamique local et les processus d'élargissement spectral appropriés. Grâce à ces nouveaux modèles, nous avons pu déterminer les paramètres atmosphériques, soit la température effective, la gravité de surface et la composition atmosphérique, de tous les objets de notre échantillon de manière homogène. Nous avons également étendu les modèles évolutifs standards du groupe de Montréal à plus haute température effective, ce qui nous a permis d'évaluer d'autres quantités d'intérêt, telles que la masse stellaire et l'âge de refroidissement. Notre analyse est la plus exhaustive et sophistiquée qui ait été réalisée à ce jour dans cette région de l'espace des paramètres. Afin de mieux contraindre l'incidence de l'évolution spectrale parmi les naines blanches chaudes, nous avons étudié la fréquence relative des atmosphères d'hydrogène et d'hélium en fonction de la température effective. Nous en avons déduit qu'environ une étoile sur quatre arrive

sur la séquence de refroidissement avec une surface riche en hélium. Cependant, pour environ deux tiers de ces objets, la surface devient ultérieurement riche en hydrogène, fort probablement via le flottement de l'hydrogène résiduel initialement dilué dans l'enveloppe. La température effective à laquelle se produit cette transformation semble varier grandement d'une étoile à l'autre (70,000 K $\gtrsim T_{\rm eff} \gtrsim$ 30,000 K), ce qui indique que la quantité d'hydrogène résiduel est loin d'être universelle. Nos résultats ont ainsi fourni de nouvelles contraintes sur la proportion de la population de naines blanches appartenant à chacun des trois canaux évolutifs identifiés dans l'introduction. De plus, nous avons minutieusement examiné les objets de notre échantillon montrant un spectre hybride afin de déterminer la configuration chimique, c'est-à-dire homogène ou stratifiée, de leur atmosphère. Cette analyse a approximativement doublé le nombre total de naines blanches de chaque type ayant été soumises à une caractérisation rigoureuse. Nous avons ainsi confirmé que les étoiles homogènes doivent vraisemblablement leur existence à un vent stellaire, tandis que les étoiles stratifiées représentent un stade intermédiaire du processus de flottement de l'hydrogène.

En second lieu, nous avons étudié les métamorphoses atmosphériques des naines blanches d'un point de vue théorique. Plus spécifiquement, nous avons effectué des simulations numériques de pointe combinant le transport chimique au refroidissement stellaire, ce qui nous a permis de mettre à l'épreuve les scénarios astrophysiques couramment invoqués pour expliquer l'évolution spectrale observée. Au chapitre 3, nous avons tout d'abord introduit notre outil de modélisation, soit le code d'évolution stellaire STELUM. Nous avons décrit en détail les ingrédients physiques et les techniques numériques utilisés par le programme pour construire et faire évoluer des modèles de naines blanches. Nous avons mis un accent particulier sur le traitement du transport des éléments, qui permet de considérer simultanément la diffusion atomique, le mélange dû à la convection, ainsi que l'éjection ou l'accrétion de matière, et ce de façon rigoureuse et cohérente. Nous avons ensuite présenté et analysé deux exemples de simulations dans le but d'illustrer le potentiel remarquable de STELUM pour l'étude de l'évolution spectrale. Premièrement, nous avons modélisé la séquence évolutive bien connue de type PG 1159−DO−DB−DQ, dans laquelle une étoile PG 1159 se transforme en naine blanche DO/DB lorsque le tri gravitationnel prend le dessus sur le vent radiatif déclinant, puis en naine blanche DQ lorsque le mécanisme de dragage convectif enrichit la surface

en carbone. Nous avons démontré que notre calcul reproduit très bien la composition atmosphérique mesurée des étoiles DQ, et en particulier la décroissance de l'abondance de carbone à très basse température effective ($T_{\rm eff} \lesssim 10{,}000$ K). Deuxièmement, nous avons présenté la toute première simulation complète du canal évolutif de type DO−DA−DC, dans lequel une atmosphère riche en hélium devient riche en hydrogène à cause du flottement de l'hydrogène résiduel, puis redevient riche en hélium via le phénomène de mélange convectif. Grâce à ce modèle, il a notamment été établi de manière convaincante que la bifurcation observée dans le diagramme couleur−magnitude des naines blanches découvertes par le satellite Gaia représente une signature du mélange convectif à basse température effective.

Au chapitre 4, nous avons réalisé une étude plus approfondie de l'évolution spectrale de type PG 1159−DO−DB−DQ. Nous avons examiné l'influence de plusieurs paramètres stellaires (tels que la masse totale, l'épaisseur de l'enveloppe et l'abondance initiale de carbone) et mécanismes physiques (tels que le vent radiatif et le dépassement convectif) sur la variation temporelle de l'abondance atmosphérique de carbone. Ce travail est le premier à explorer cet espace des paramètres de façon exhaustive à l'aide d'un traitement réaliste du transport des éléments. À haute température effective, nous avons confirmé que la rapidité de la transition de PG 1159 à DO due au tri gravitationnel dépend principalement de la masse de l'étoile et de l'intensité du vent. Il a également été démontré que le processus de diffusion thermique, qui est souvent considéré comme négligeable dans les naines blanches, joue en fait un rôle significatif dans cette transformation. En outre, nous avons déduit de nos simulations que le carbone détecté à la surface des étoiles de type DOZ peut généralement être expliqué par le scénario étudié, bien que ce ne soit pas le cas pour les objets les plus froids. À basse température effective, il a été établi que les effets non-idéaux et le dépassement convectif ont un impact majeur sur le dragage convectif et la transition de DB à DQ qui en résulte. Nous avons aussi montré que l'abondance de carbone à la surface d'une naine blanche DQ est déterminée par une multitude de paramètres, soit la masse totale, l'épaisseur de l'enveloppe, le contenu initial en carbone et l'étendue du dépassement convectif. En comparant nos modèles à la séquence empirique des étoiles DQ, nous avons obtenu une limite supérieure sur l'étendue du dépassement convectif dans les naines blanches froides dominées par l'hélium ($T_{\rm eff} \lesssim 10{,}000$ K), qui devrait avoir des répercussions notamment sur notre compréhension des corps rocheux accrétés par celles-ci. Enfin, nous avons souligné que nos calculs prédisent

que le dragage convectif est plus efficace dans les objets moins massifs et fournissent donc une explication naturelle au fait que les étoiles DQ ont typiquement des masses plus faibles que la moyenne.

Au chapitre 5, nous nous sommes penchés sur le transport de l'hydrogène résiduel dans les naines blanches chaudes et riches en hélium. Dans un premier temps, nous avons effectué plusieurs simulations du mécanisme de flottement de l'hydrogène afin d'évaluer comment la transition de DO à DA est influencée par la quantité d'hydrogène résiduel et l'intensité du vent radiatif s'opposant au tri gravitationnel. Nous avons montré que la transformation atmosphérique se produit plus tardivement lorsque le contenu initial en hydrogène est plus faible ou le taux de perte de masse est plus élevé. En combinant cette relation théorique aux résultats empiriques du chapitre 2, nous avons obtenu une contrainte inédite sur l'abondance d'hydrogène dans l'enveloppe au tout début de la séquence de refroidissement. Plus précisément, la population d'étoiles DO qui se transforment en étoiles DA est caractérisée par une gamme d'abondances initiales d'hydrogène donnée (en termes de la fraction de masse) par $-6.5 \pm 0.5 \lesssim \log X_{\rm H,0} \lesssim -3.5 \pm 0.5$, où les incertitudes sont dues au traitement du vent. Notre travail a ainsi fourni de nouveaux renseignements sur les phénomènes à l'origine de la carence en hydrogène, comme le flash tardif de l'hélium. Par ailleurs, nous avons souligné que nos calculs prédisent bel et bien l'existence d'un réservoir massif d'hydrogène demeurant longuement « caché » dans l'enveloppe d'hélium en-dessous de la mince couche d'hydrogène pur à la surface. Dans un second temps, nous avons étudié l'évolution de la composition atmosphérique suite à la dilution convective de cette couche d'hydrogène dans l'enveloppe d'hélium à plus basse température effective. Nous avons démontré que nos modèles reproduisent parfaitement les abondances d'hydrogène mesurées à la surface des naines blanches DBA, contrairement aux modèles traditionnels de la dilution convective. Cette amélioration remarquable est due à notre modélisation détaillée du processus de flottement à haute température effective, qui donne lieu à une structure chimique réaliste dont le réservoir profond d'hydrogène est la composante essentielle. Nos calculs sont les premiers à offrir une solution claire au problème vieux de trois décennies de l'origine de l'hydrogène dans les étoiles DBA, sans doute le problème le plus sérieux de la théorie de l'évolution spectrale. Nous avons conclu que l'existence de la grande majorité des naines blanches DBA peut être expliquée

uniquement par la dilution convective de l'hydrogène primordial et ne constitue donc pas une manifestation de l'accrétion de comètes, d'astéroïdes ou de planètes riches en eau.

Bien que les avancées réalisées dans cette thèse aient indéniablement repoussé les frontières de notre connaissance de l'évolution spectrale des naines blanches, beaucoup de travail reste à accomplir dans ce champ de recherche. Du côté empirique, la révolution la plus importante depuis l'avènement du SDSS est présentement en cours dans le domaine. En effet, le satellite Gaia a jusqu'à maintenant identifié plus de 300,000 nouvelles candidates naines blanches (Gentile Fusillo et al., 2021), qui seront éventuellement confirmées et caractérisées grâce aux grands relevés spectroscopiques des prochaines années, notamment WEAVE (*William-Herschel-Telescope Enhanced Area Velocity Explorer* ; Dalton et al. 2012), 4MOST (*4-meter Multi-Object Spectroscopic Telescope* ; de Jong et al. 2014) et DESI (*Dark Energy Spectroscopic Instrument* ; DESI Collaboration et al. 2016). Ceci permettra entre autres d'augmenter significativement la précision des statistiques portant sur la fréquence relative des atmosphères d'hydrogène et d'hélium en fonction de la température effective. Toutefois, dans le cas spécifique des étoiles chaudes, il faudra également améliorer certaines composantes physiques des modèles d'atmosphère pour assurer la fiabilité des résultats. En effet, l'analyse du chapitre 2 a révélé certains problèmes dans l'évaluation des masses stellaires, particulièrement pour les objets riches en hélium. Il est possible que cette difficulté soit causée par des lacunes dans le traitement de l'élargissement des raies d'hélium ionisé, qui devra donc être révisé.

Du côté théorique, nous avons incontestablement démontré l'importance d'une description rigoureuse et cohérente du transport des éléments dans les modèles évolutifs de naines blanches. Notre résolution du problème de l'origine de l'hydrogène dans les étoiles DBA est probablement l'exemple le plus frappant de cette constatation. Cependant, notre compréhension de certains mécanismes de transport jouant un rôle crucial dans l'évolution spectrale demeure insuffisante. C'est le cas notamment du vent radiatif à haute température et du dépassement convectif à basse température, qui ont été inclus dans nos simulations à l'aide d'approximations très rudimentaires. Il sera indispensable de développer des modèles plus réalistes de ces phénomènes et d'examiner l'impact de ceux-ci sur la structure chimique des naines blanches. Il pourrait aussi être intéressant d'étudier l'effet de certains processus physiques ayant été carrément ignorés dans les calculs de cette thèse, tels que la lévitation

radiative et le brûlage nucléaire résiduel. Par ailleurs, soulignons que certains problèmes de la théorie de l'évolution spectrale des naines blanches demeurent à ce jour non résolus. Le mystère le plus intriguant est probablement celui des étoiles DQ massives. Bien qu'il soit maintenant admis que ces objets sont les produits de la fusion de deux naines blanches, aucun modèle évolutif n'a encore réussi à reproduire leur composition de surface correctement. Des simulations de pointe telles que celles présentées dans cette thèse pourraient potentiellement permettre de résoudre cette énigme et ainsi de mieux comprendre le résultat des fusions stellaires. Finalement, il est pratiquement certain que la révolution observationnelle mentionnée ci-dessus, de par son ampleur, révèlera de toutes nouvelles classes d'objets aux propriétés atmosphériques jamais vues auparavant. Ces découvertes constitueront autant de nouveaux défis pour la théorie de l'évolution spectrale des étoiles naines blanches.

Bibliographie

Ahumada, R., Prieto, C. A., Almeida, A., et al. 2020, ApJS, 249, 3

Alam, S., Albareti, F. D., Allende Prieto, C., et al. 2015, ApJS, 219, 12

Alcock, C., & Illarionov, A. 1980, ApJ, 235, 541

Althaus, L. G., & Benvenuto, O. G. 1998, MNRAS, 296, 206

Althaus, L. G., & Córsico, A. H. 2004, A&A, 417, 1115

Althaus, L. G., Córsico, A. H., & De Gerónimo, F. 2020a, A&A, 644, A55

Althaus, L. G., Córsico, A. H., Isern, J., & García-Berro, E. 2010, A&A Rv, 18, 471

Althaus, L. G., García-Berro, E., Córsico, A. H., Miller Bertolami, M. M., & Romero, A. D. 2009a, ApJL, 693, L23

Althaus, L. G., Miller Bertolami, M. M., Córsico, A. H., García-Berro, E., & Gil-Pons, P. 2005a, A&A, 440, L1

Althaus, L. G., Panei, J. A., Miller Bertolami, M. M., et al. 2009b, ApJ, 704, 1605

Althaus, L. G., Serenelli, A. M., Panei, J. A., et al. 2005b, A&A, 435, 631

Althaus, L. G., Córsico, A. H., Uzundag, M., et al. 2020b, A&A, 633, A20

Angulo, C., Arnould, M., Rayet, M., et al. 1999, NuPhA, 656, 3

Arcoragi, J. P., & Fontaine, G. 1980, ApJ, 242, 1208

Badnell, N. R., Bautista, M. A., Butler, K., et al. 2005, MNRAS, 360, 458

Baglin, A., & Vauclair, G. 1973, A&A, 27, 307

Bailer-Jones, C. A. L. 2015, PASP, 127, 994

Bailer-Jones, C. A. L., Rybizki, J., Fouesneau, M., Mantelet, G., & Andrae, R. 2018, AJ, 156, 58

Barnard, A. J., Cooper, J., & Smith, E. W. 1974, JQSRT, 14, 1025

Barstow, M. A., Barstow, J. K., Casewell, S. L., Holberg, J. B., & Hubeny, I. 2014, MNRAS, 440, 1607

Barstow, M. A., Good, S. A., Burleigh, M. R., et al. 2003a, MNRAS, 344, 562

Barstow, M. A., Good, S. A., Holberg, J. B., et al. 2003b, MNRAS, 341, 870

Barstow, M. A., & Hubeny, I. 1998, MNRAS, 299, 379

Barstow, M. A., Hubeny, I., & Holberg, J. B. 1998, MNRAS, 299, 520

Bauer, E. B., & Bildsten, L. 2018, ApJL, 859, L19

Bauer, E. B., & Bildsten, L. 2019, ApJ, 872, 96

Beauchamp, A. 1995, PhD thesis, Université de Montréal (Canada)

Beauchamp, A., Wesemael, F., & Bergeron, P. 1997, ApJS, 108, 559

Beauchamp, A., Wesemael, F., Bergeron, P., Liebert, J., & Saffer, R. A. 1996, in ASP Conf. Ser. 96 : Hydrogen Deficient Stars, ed. C. S. Jeffery & U. Heber (San Francisco : Astronomical Society of the Pacific), 295

Bédard, A., Bergeron, P., & Brassard, P. 2022a, ApJ, 930, 8

Bédard, A., Bergeron, P., Brassard, P., & Fontaine, G. 2020, ApJ, 901, 93

Bédard, A., Bergeron, P., & Fontaine, G. 2017, ApJ, 848, 11

Bédard, A., Brassard, P., Bergeron, P., & Blouin, S. 2022b, ApJ, 927, 128

Bergeron, P., Dufour, P., Fontaine, G., et al. 2019, ApJ, 876, 67

Bergeron, P., Leggett, S. K., & Ruiz, M. T. 2001, ApJS, 133, 413

Bergeron, P., & Liebert, J. 2002, ApJ, 566, 1091

Bergeron, P., Ruiz, M. T., & Leggett, S. K. 1997, ApJS, 108, 339

Bergeron, P., Saffer, R. A., & Liebert, J. 1992, ApJ, 394, 228

Bergeron, P., Saumon, D., & Wesemael, F. 1995, ApJ, 443, 764

Bergeron, P., Wesemael, F., Beauchamp, A., et al. 1994, ApJ, 432, 305

Bergeron, P., Wesemael, F., Lamontagne, R., & Chayer, P. 1993, ApJL, 407, L85

Bergeron, P., Wesemael, F., Dufour, P., et al. 2011, ApJ, 737, 28

Beznogov, M. V., & Yakovlev, D. G. 2013, PhRvL, 111, 161101

Bischoff-Kim, A., Provencal, J. L., Bradley, P. A., et al. 2019, ApJ, 871, 13

Blanton, M. R., Bershady, M. A., Abolfathi, B., et al. 2017, AJ, 154, 28

Blöcker, T. 1995a, A&A, 299, 755

Blöcker, T. 1995b, A&A, 297, 727

Blouin, S., & Daligault, J. 2021, PhRvE, 103, 043204

Blouin, S., Daligault, J., Saumon, D., Bédard, A., & Brassard, P. 2020a, A&A, 640, L11

Blouin, S., & Dufour, P. 2019, MNRAS, 490, 4166

Blouin, S., Dufour, P., & Allard, N. F. 2018, ApJ, 863, 184

Blouin, S., Dufour, P., Thibeault, C., & Allard, N. F. 2019, ApJ, 878, 63

Blouin, S., Shaffer, N. R., Saumon, D., & Starrett, C. E. 2020b, ApJ, 899, 46

Blouin, S., & Xu, S. 2022, MNRAS, 510, 1059

Bochanski, J. J., West, A. A., Hawley, S. L., & Covey, K. R. 2007, AJ, 133, 531

Böhm-Vitense, E. 1958, ZA, 46, 108

Bond, H. E., Gilliland, R. L., Schaefer, G. H., et al. 2015, ApJ, 813, 106

Brassard, P., & Fontaine, G. 2015, in ASP Conf. Ser. 493 : 19th European Workshop on White Dwarfs, ed. P. Dufour, P. Bergeron, & G. Fontaine (San Francisco : Astronomical Society of the Pacific), 125

Brassard, P., & Fontaine, G. 2018, STELUM : A Progress Report, Zenodo, doi :10.5281/zenodo.1755252

Brassard, P., Fontaine, G., Dufour, P., & Bergeron, P. 2007, in ASP Conf. Ser. 372 : 15th European Workshop on White Dwarfs, ed. R. Napiwotzki & M. R. Burleigh (San Francisco : Astronomical Society of the Pacific), 19

Brassard, P., Pelletier, C., Fontaine, G., & Wesemael, F. 1992, ApJS, 80, 725

Burgers, J. M. 1969, Flow Equations for Composite Gases (New York : Academic Press)

Camisassa, M. E., Althaus, L. G., Rohrmann, R. D., et al. 2017, ApJ, 839, 11

Canuto, V. M., & Mazzitelli, I. 1991, ApJ, 370, 295

Cassisi, S., Potekhin, A. Y., Pietrinferni, A., Catelan, M., & Salaris, M. 2007, ApJ, 661, 1094

Caughlan, G. R., & Fowler, W. A. 1988, ADNDT, 40, 283

Chandrasekhar, S. 1931, ApJ, 74, 81

Chandrasekhar, S. 1935, MNRAS, 95, 207

Charbonneau, P. 1993, ApJ, 405, 720

Chayer, P., Fontaine, G., & Wesemael, F. 1995, ApJS, 99, 189

Chayer, P., Vennes, S., Dupuis, J., & Kruk, J. W. 2005, ApJL, 630, L169

Chen, E. Y., & Hansen, B. M. S. 2011, MNRAS, 413, 2827

Cheng, S., Cummings, J. D., & Ménard, B. 2019, ApJ, 886, 100

Choi, J., Dotter, A., Conroy, C., et al. 2016, ApJ, 823, 102

Coutu, S., Dufour, P., Bergeron, P., et al. 2019, ApJ, 885, 74

Cox, J. P., & Giuli, R. T. 1968, Principles of Stellar Structure (New York : Gordon and Breach)

Cukanovaite, E., Tremblay, P. E., Freytag, B., et al. 2019, MNRAS, 490, 1010

Cunningham, T., Tremblay, P.-E., Freytag, B., Ludwig, H.-G., & Koester, D. 2019, MNRAS, 488, 2503

Cunningham, T., Tremblay, P.-E., Gentile Fusillo, N. P., Hollands, M., & Cukanovaite, E. 2020, MNRAS, 492, 3540

Cyburt, R. H., Amthor, A. M., Ferguson, R., et al. 2010, ApJS, 189, 240

Dalton, G., Trager, S. C., Abrams, D. C., et al. 2012, in Ground-based and Airborne Instrumentation for Astronomy IV, ed. I. S. McLean, S. K. Ramsay, & H. Takami, Vol. 8446 (Society of Photo-Optical Instrumentation Engineers), 84460P

D'Antona, F., & Mazzitelli, I. 1989, ApJ, 347, 934

De Gerónimo, F. C., Althaus, L. G., Córsico, A. H., Romero, A. D., & Kepler, S. O. 2017, A&A, 599, A21

de Jong, R. S., Barden, S., Bellido-Tirado, O., et al. 2014, in Ground-based and Airborne Instrumentation for Astronomy V, ed. S. K. Ramsay, I. S. McLean, & H. Takami, Vol. 9147 (Society of Photo-Optical Instrumentation Engineers), 91470M

Deal, M., Deheuvels, S., Vauclair, G., Vauclair, S., & Wachlin, F. C. 2013, A&A, 557, L12

Dehner, B. T., & Kawaler, S. D. 1995, ApJL, 445, L141

Desharnais, S., Wesemael, F., Chayer, P., Kruk, J. W., & Saffer, R. A. 2008, ApJ, 672, 540

DESI Collaboration, Aghamousa, A., Aguilar, J., et al. 2016, arXiv e-prints, arXiv :1611.00036

Dewitt, H. E., Graboske, H. C., & Cooper, M. S. 1973, ApJ, 181, 439

Dimitrijevic, M. S., & Sahal-Brechot, S. 1984, JQSRT, 31, 301

Dreizler, S. 1999, A&A, 352, 632

Dreizler, S., & Heber, U. 1998, A&A, 334, 618

Dreizler, S., Heber, U., Napiwotzki, R., & Hagen, H. J. 1995, A&A, 303, L53

Dreizler, S., & Werner, K. 1996, A&A, 314, 217

Dufour, P. 2011, in White Dwarf Atmospheres and Circumstellar Environments, ed. D. W. Hoard (New York : Wiley), 53–88

Dufour, P., Bergeron, P., & Fontaine, G. 2005, ApJ, 627, 404

Dufour, P., Blouin, S., Coutu, S., et al. 2017, in ASP Conf. Ser. 509 : 20th European Workshop on White Dwarfs, ed. P. E. Tremblay, B. Gänsicke, & T. Marsh (San Francisco :

Astronomical Society of the Pacific), 3

Dufour, P., Fontaine, G., Liebert, J., Schmidt, G. D., & Behara, N. 2008, ApJ, 683, 978

Dufour, P., Kilic, M., Fontaine, G., et al. 2012, ApJ, 749, 6

Dufour, P., Liebert, J., Fontaine, G., & Behara, N. 2007, Nature, 450, 522

Dunlap, B. H., & Clemens, J. C. 2015, in ASP Conf. Ser. 493 : 19th European Workshop on White Dwarfs, ed. P. Dufour, P. Bergeron, & G. Fontaine (San Francisco : Astronomical Society of the Pacific), 547

Dupuis, J., Fontaine, G., Pelletier, C., & Wesemael, F. 1992, ApJS, 82, 505

Dupuis, J., Fontaine, G., Pelletier, C., & Wesemael, F. 1993a, ApJS, 84, 73

Dupuis, J., Fontaine, G., & Wesemael, F. 1993b, ApJS, 87, 345

Eggleton, P. P. 1972, MNRAS, 156, 361

Eisenstein, D. J., Liebert, J., Koester, D., et al. 2006a, AJ, 132, 676

Eisenstein, D. J., Liebert, J., Harris, H. C., et al. 2006b, ApJS, 167, 40

Farihi, J. 2016, NewAR, 71, 9

Farihi, J., Barstow, M. A., Redfield, S., Dufour, P., & Hambly, N. C. 2010, MNRAS, 404, 2123

Farihi, J., Gänsicke, B. T., & Koester, D. 2013, Science, 342, 218

Ferguson, J. W., Alexander, D. R., Allard, F., et al. 2005, ApJ, 623, 585

Fleming, T. A., Liebert, J., & Green, R. F. 1986, ApJ, 308, 176

Fontaine, G., & Brassard, P. 2002, ApJL, 581, L33

Fontaine, G., & Brassard, P. 2005, in ASP Conf. Ser. 334 : 14th European Workshop on White Dwarfs, ed. D. Koester & S. Moehler (San Francisco : Astronomical Society of the Pacific), 49

Fontaine, G., & Brassard, P. 2008, PASP, 120, 1043

Fontaine, G., Brassard, P., & Bergeron, P. 2001, PASP, 113, 409

Fontaine, G., Brassard, P., Dufour, P., & Tremblay, P. E. 2015a, in ASP Conf. Ser. 493 : 19th European Workshop on White Dwarfs, ed. P. Dufour, P. Bergeron, & G. Fontaine (San Francisco : Astronomical Society of the Pacific), 113

Fontaine, G., Dufour, P., Chayer, P., Dupuis, J., & Brassard, P. 2015b, in ASP Conf. Ser. 493 : 19th European Workshop on White Dwarfs, ed. P. Dufour, P. Bergeron, & G. Fontaine (San Francisco : Astronomical Society of the Pacific), 117

Fontaine, G., Graboske, H. C., J., & van Horn, H. M. 1977, ApJS, 35, 293

Fontaine, G., & Michaud, G. 1979, ApJ, 231, 826

Fontaine, G., & van Horn, H. M. 1976, ApJS, 31, 467

Fontaine, G., Villeneuve, B., Wesemael, F., & Wegner, G. 1984, ApJL, 277, L61

Fontaine, G., & Wesemael, F. 1987, in IAU Colloq. 95 : Second Conference on Faint Blue Stars, ed. A. G. D. Philip, D. S. Hayes, & J. W. Liebert (Schenectady : Davis Press), 319–326

Fowler, R. H. 1926, MNRAS, 87, 114

Freytag, B., Ludwig, H. G., & Steffen, M. 1996, A&A, 313, 497

Gaia Collaboration, Prusti, T., de Bruijne, J. H. J., et al. 2016, A&A, 595, A1

Gaia Collaboration, Brown, A. G. A., Vallenari, A., et al. 2018a, A&A, 616, A1

Gaia Collaboration, Babusiaux, C., van Leeuwen, F., et al. 2018b, A&A, 616, A10

Gänsicke, B. T., Koester, D., Farihi, J., et al. 2012, MNRAS, 424, 333

García-Berro, E., Torres, S., Althaus, L. G., et al. 2010, Nature, 465, 194

Genest-Beaulieu, C., & Bergeron, P. 2014, ApJ, 796, 128

Genest-Beaulieu, C., & Bergeron, P. 2019a, ApJ, 871, 169

Genest-Beaulieu, C., & Bergeron, P. 2019b, ApJ, 882, 106

Gentile Fusillo, N. P., Gänsicke, B. T., Farihi, J., et al. 2017, MNRAS, 468, 971

Gentile Fusillo, N. P., Tremblay, P. E., Cukanovaite, E., et al. 2021, MNRAS, 508, 3877

Giammichele, N., Bergeron, P., & Dufour, P. 2012, ApJS, 199, 29

Giammichele, N., Fontaine, G., Brassard, P., & Charpinet, S. 2016, ApJS, 223, 10

Giammichele, N., Charpinet, S., Fontaine, G., et al. 2018, Nature, 554, 73

Gianninas, A., Bergeron, P., Dupuis, J., & Ruiz, M. T. 2010, ApJ, 720, 581

Gianninas, A., Bergeron, P., & Ruiz, M. T. 2011, ApJ, 743, 138

Good, S. A., Barstow, M. A., Burleigh, M. R., et al. 2005, MNRAS, 363, 183

Good, S. A., Barstow, M. A., Holberg, J. B., et al. 2004, MNRAS, 355, 1031

Graboske, H. C., Dewitt, H. E., Grossman, A. S., & Cooper, M. S. 1973, ApJ, 181, 457

Green, R. F., Schmidt, M., & Liebert, J. 1986, ApJS, 61, 305

Greenstein, J. L. 1986, ApJ, 304, 334

Hairer, E., & Wanner, G. 1996, Solving Ordinary Differential Equations II : Stiff and Differential Algebraic Problems (Berlin : Springer)

Hamada, T., & Salpeter, E. E. 1961, ApJ, 134, 683

Hansen, B. M. S., Brewer, J., Fahlman, G. G., et al. 2002, ApJL, 574, L155

Hansen, B. M. S., Anderson, J., Brewer, J., et al. 2007, ApJ, 671, 380

Hansen, C. J., Kawaler, S. D., & Trimble, V. 2004, Stellar Interiors : Physical Principles, Structure, and Evolution, 2e éd. (New York : Springer)

Harris, H. C., Munn, J. A., Kilic, M., et al. 2006, AJ, 131, 571

Heber, U., Napiwotzki, R., Lemke, M., & Edelmann, H. 1997, A&A, 324, L53

Henyey, L., Vardya, M. S., & Bodenheimer, P. 1965, ApJ, 142, 841

Herald, J. E., Bianchi, L., & Hillier, D. J. 2005, ApJ, 627, 424

Herwig, F. 2000, A&A, 360, 952

Herwig, F., Blöcker, T., Langer, N., & Driebe, T. 1999, A&A, 349, L5

Holberg, J. B., & Bergeron, P. 2006, AJ, 132, 1221

Holberg, J. B., Barstow, M. A., Buckley, D. A. H., et al. 1993, ApJ, 416, 806

Hollands, M. A., Gänsicke, B. T., & Koester, D. 2018, MNRAS, 477, 93

Hollands, M. A., Koester, D., Alekseev, V., Herbert, E. L., & Gänsicke, B. T. 2017, MNRAS, 467, 4970

Hoskin, M. J., Toloza, O., Gänsicke, B. T., et al. 2020, MNRAS, 499, 171

Hoyer, D., Rauch, T., Werner, K., & Kruk, J. W. 2018, A&A, 612, A62

Hoyer, D., Rauch, T., Werner, K., Kruk, J. W., & Quinet, P. 2017, A&A, 598, A135

Hu, H., Tout, C. A., Glebbeek, E., & Dupret, M. A. 2011, MNRAS, 418, 195

Hubbard, W. B., & Lampe, M. 1969, ApJS, 18, 297

Hubeny, I., & Lanz, T. 1995, ApJ, 439, 875

Hubeny, I., & Lanz, T. 2017a, arXiv e-prints, arXiv :1706.01859

Hubeny, I., & Lanz, T. 2017b, arXiv e-prints, arXiv :1706.01935

Hubeny, I., & Lanz, T. 2017c, arXiv e-prints, arXiv :1706.01937

Hügelmeyer, S. D., Dreizler, S., Homeier, D., et al. 2006, A&A, 454, 617

Hügelmeyer, S. D., Dreizler, S., Werner, K., et al. 2005, A&A, 442, 309

Hummer, D. G., & Mihalas, D. 1988, ApJ, 331, 794

Iben, I., J., Kaler, J. B., Truran, J. W., & Renzini, A. 1983, ApJ, 264, 605

Iben, I., J., & Tutukov, A. V. 1984, ApJ, 282, 615

Iglesias, C. A., & Rogers, F. J. 1996, ApJ, 464, 943

Isern, J., García-Berro, E., Hernanz, M., & Chabrier, G. 2000, ApJ, 528, 397

Isern, J., Mochkovitch, R., García-Berro, E., & Hernanz, M. 1997, ApJ, 485, 308

Itoh, N., Hayashi, H., & Kohyama, Y. 1993, ApJ, 418, 405

Itoh, N., Hayashi, H., Nishikawa, A., & Kohyama, Y. 1996, ApJS, 102, 411

Itoh, N., Kohyama, Y., Matsumoto, N., & Seki, M. 1984, ApJ, 285, 758

Itoh, N., Mitake, S., Iyetomi, H., & Ichimaru, S. 1983, ApJ, 273, 774

Jordan, S., & Koester, D. 1986, A&AS, 65, 367

Jura, M., & Young, E. D. 2014, AREPS, 42, 45

Kalirai, J. S. 2012, Nature, 486, 90

Kepler, S. O., Pelisoli, I., Koester, D., et al. 2015, MNRAS, 446, 4078

Kepler, S. O., Pelisoli, I., Koester, D., et al. 2016, MNRAS, 455, 3413

Kepler, S. O., Pelisoli, I., Koester, D., et al. 2019, MNRAS, 486, 2169

Kilic, M., Bergeron, P., Kosakowski, A., et al. 2020, ApJ, 898, 84

Kilic, M., Munn, J. A., Harris, H. C., et al. 2017, ApJ, 837, 162

Kippenhahn, R., Ruschenplatt, G., & Thomas, H. C. 1980, A&A, 91, 175

Kippenhahn, R., Weigert, A., & Weiss, A. 2012, Stellar Structure and Evolution (Berlin : Springer)

Kitsikis, A., Fontaine, G., & Brassard, P. 2005, in ASP Conf. Ser. 334 : 14th European Workshop on White Dwarfs, ed. D. Koester & S. Moehler (San Francisco : Astronomical Society of the Pacific), 65

Klein, B., Jura, M., Koester, D., & Zuckerman, B. 2011, ApJ, 741, 64

Klein, B., Jura, M., Koester, D., Zuckerman, B., & Melis, C. 2010, ApJ, 709, 950

Klein, B., Blouin, S., Romani, D., et al. 2020, ApJ, 900, 2

Klein, B. L., Doyle, A. E., Zuckerman, B., et al. 2021, ApJ, 914, 61

Kleinman, S. J., Kepler, S. O., Koester, D., et al. 2013, ApJS, 204, 5

Koester, D. 1976, A&A, 52, 415

Koester, D. 2009, A&A, 498, 517

Koester, D., Gänsicke, B. T., & Farihi, J. 2014a, A&A, 566, A34

Koester, D., Girven, J., Gänsicke, B. T., & Dufour, P. 2011, A&A, 530, A114

Koester, D., & Kepler, S. O. 2015, A&A, 583, A86

Koester, D., & Kepler, S. O. 2019, A&A, 628, A102

Koester, D., Kepler, S. O., & Irwin, A. W. 2020, A&A, 635, A103

Koester, D., & Knist, S. 2006, A&A, 454, 951

Koester, D., Liebert, J., & Saffer, R. A. 1994, ApJ, 422, 783

Koester, D., Provencal, J., & Gänsicke, B. T. 2014b, A&A, 568, A118

Koester, D., Rollenhagen, K., Napiwotzki, R., et al. 2005, A&A, 432, 1025

Koester, D., Weidemann, V., & Zeidler, E. M. 1982, A&A, 116, 147

Koesterke, L., & Werner, K. 1998, ApJL, 500, L55

Krzesinski, J., Kleinman, S. J., Nitta, A., et al. 2009, A&A, 508, 339

Krzesiński, J., Nitta, A., Kleinman, S. J., et al. 2004, A&A, 417, 1093

Kudritzki, R.-P., & Puls, J. 2000, ARA&A, 38, 613

Kupka, F., Zaussinger, F., & Montgomery, M. H. 2018, MNRAS, 474, 4660

Lamb, D. Q. 1974, PhD thesis, University of Rochester (USA)

Langer, N., El Eid, M. F., & Fricke, K. J. 1985, A&A, 145, 179

Lanz, T., & Hubeny, I. 1995, ApJ, 439, 905

Latour, M., Fontaine, G., Green, E. M., & Brassard, P. 2015, A&A, 579, A39

Lauffer, G. R., Romero, A. D., & Kepler, S. O. 2018, MNRAS, 480, 1547

Leggett, S. K., Ruiz, M. T., & Bergeron, P. 1998, ApJ, 497, 294

Liebert, J., Bergeron, P., & Holberg, J. B. 2005, ApJS, 156, 47

Liebert, J., Wehrse, R., & Green, R. F. 1987, A&A, 175, 173

Liebert, J., Wesemael, F., Hansen, C. J., et al. 1986, ApJ, 309, 241

Limoges, M. M., & Bergeron, P. 2010, ApJ, 714, 1037

Limoges, M. M., Bergeron, P., & Lépine, S. 2015, ApJS, 219, 19

Löbling, L., Maney, M. A., Rauch, T., et al. 2020, MNRAS, 492, 528

López-Sanjuan, C., Tremblay, P. E., Ederoclite, A., et al. 2022, A&A, 658, A79

MacDonald, J., Hernanz, M., & Jose, J. 1998, MNRAS, 296, 523

MacDonald, J., & Vennes, S. 1991, ApJ, 371, 719

Manseau, P. M., Bergeron, P., & Green, E. M. 2016, ApJ, 833, 127

Manser, C. J., Gänsicke, B. T., Gentile Fusillo, N. P., et al. 2020, MNRAS, 493, 2127

McCleery, J., Tremblay, P.-E., Gentile Fusillo, N. P., et al. 2020, MNRAS, 499, 1890

Mestel, L. 1952, MNRAS, 112, 583

Michaud, G., Alecian, G., & Richer, J. 2015, Atomic Diffusion in Stars (Cham : Springer

International)

Mihalas, D. 1978, Stellar Atmospheres (San Francisco : W. H. Freeman)

Miller Bertolami, M. M., & Althaus, L. G. 2006, A&A, 454, 845

Miller Bertolami, M. M., Althaus, L. G., & Córsico, A. H. 2017, in ASP Conf. Ser. 509 : 20th European Workshop on White Dwarfs, ed. P. E. Tremblay, B. Gänsicke, & T. Marsh (San Francisco : Astronomical Society of the Pacific), 435

Miller Bertolami, M. M., Althaus, L. G., Serenelli, A. M., & Panei, J. A. 2006, A&A, 449, 313

Mustill, A. J., Villaver, E., Veras, D., Gänsicke, B. T., & Bonsor, A. 2018, MNRAS, 476, 3939

Nagel, T., Schuh, S., Kusterer, D. J., et al. 2006, A&A, 448, L25

Napiwotzki, R. 1992, in The Atmospheres of Early-Type Stars, ed. U. Heber & C. S. Jeffery, Vol. 401 (Berlin : Springer), 310

Napiwotzki, R. 1997, A&A, 322, 256

Napiwotzki, R. 1999, A&A, 350, 101

Napiwotzki, R., & Rauch, T. 1994, A&A, 285, 603

Napiwotzki, R., & Schönberner, D. 1995, A&A, 301, 545

Oswalt, T. D., Smith, J. A., Wood, M. A., & Hintzen, P. 1996, Nature, 382, 692

Ourique, G., Kepler, S. O., Romero, A. D., Klippel, T. S., & Koester, D. 2020, MNRAS, 492, 5003

Ourique, G., Romero, A. D., Kepler, S. O., Koester, D., & Amaral, L. A. 2019, MNRAS, 482, 649

Paquette, C., Pelletier, C., Fontaine, G., & Michaud, G. 1986a, ApJS, 61, 197

Paquette, C., Pelletier, C., Fontaine, G., & Michaud, G. 1986b, ApJS, 61, 177

Parsons, S. G., Gänsicke, B. T., Marsh, T. R., et al. 2017, MNRAS, 470, 4473

Pauldrach, A., Puls, J., Kudritzki, R. P., Mendez, R. H., & Heap, S. R. 1988, A&A, 207, 123

Paxton, B., Bildsten, L., Dotter, A., et al. 2011, ApJS, 192, 3

Paxton, B., Cantiello, M., Arras, P., et al. 2013, ApJS, 208, 4

Paxton, B., Marchant, P., Schwab, J., et al. 2015, ApJS, 220, 15

Paxton, B., Schwab, J., Bauer, E. B., et al. 2018, ApJS, 234, 34

Paxton, B., Smolec, R., Schwab, J., et al. 2019, ApJS, 243, 10

Pelletier, C., Fontaine, G., Wesemael, F., Michaud, G., & Wegner, G. 1986, ApJ, 307, 242

Pereira, C., Bergeron, P., & Wesemael, F. 2005, ApJ, 623, 1076

Petitclerc, N., Wesemael, F., Kruk, J. W., Chayer, P., & Billères, M. 2005, ApJ, 624, 317

Preval, S. P., Barstow, M. A., Bainbridge, M., et al. 2019, MNRAS, 487, 3470

Puls, J., Springmann, U., & Lennon, M. 2000, A&AS, 141, 23

Quirion, P. O., Fontaine, G., & Brassard, P. 2012, ApJ, 755, 128

Raddi, R., Gänsicke, B. T., Koester, D., et al. 2015, MNRAS, 450, 2083

Rauch, T., Dreizler, S., & Wolff, B. 1998, A&A, 338, 651

Rauch, T., Reiff, E., Werner, K., et al. 2006, in ASP Conf. Ser. 348 : Astrophysics in the Far Ultraviolet, ed. G. Sonneborn, H. W. Moos, & B. G. Andersson, 194

Reimers, D. 1975, MSRSL, 8, 369

Reindl, N., Geier, S., & Østensen, R. H. 2018, MNRAS, 480, 1211

Reindl, N., Rauch, T., Werner, K., et al. 2014a, A&A, 572, A117

Reindl, N., Rauch, T., Werner, K., Kruk, J. W., & Todt, H. 2014b, A&A, 566, A116

Reindl, N., Bainbridge, M., Przybilla, N., et al. 2019, MNRAS, 482, L93

Renedo, I., Althaus, L. G., Miller Bertolami, M. M., et al. 2010, ApJ, 717, 183

Rolland, B., Bergeron, P., & Fontaine, G. 2018, ApJ, 857, 56

Rolland, B., Bergeron, P., & Fontaine, G. 2020, ApJ, 889, 87

Salaris, M., Althaus, L. G., & García-Berro, E. 2013, A&A, 555, A96

Salaris, M., & Cassisi, S. 2017, RSOS, 4, 170192

Salaris, M., Cassisi, S., Pietrinferni, A., Kowalski, P. M., & Isern, J. 2010, ApJ, 716, 1241

Salaris, M., García-Berro, E., Hernanz, M., Isern, J., & Saumon, D. 2000, ApJ, 544, 1036

Salaris, M., Serenelli, A., Weiss, A., & Miller Bertolami, M. 2009, ApJ, 692, 1013

Saumon, D., Chabrier, G., & van Horn, H. M. 1995, ApJS, 99, 713

Schatzman, E. L. 1958, White Dwarfs (Amsterdam : North-Holland)

Schlafly, E. F., & Finkbeiner, D. P. 2011, ApJ, 737, 103

Schmidt, M. 1975, ApJ, 202, 22

Schöning, T., & Butler, K. 1989, A&AS, 78, 51

Scóccola, C. G., Althaus, L. G., Serenelli, A. M., Rohrmann, R. D., & Córsico, A. H. 2006, A&A, 451, 147

Shamey, L. J. 1969, PhD thesis, University of Colorado at Boulder (USA)

Sion, E. M. 1984, ApJ, 282, 612

Sion, E. M., Greenstein, J. L., Landstreet, J. D., et al. 1983, ApJ, 269, 253

Subasavage, J. P., Jao, W.-C., Henry, T. J., et al. 2017, AJ, 154, 32

Tassoul, M., Fontaine, G., & Winget, D. E. 1990, ApJS, 72, 335

Thoul, A. A., Bahcall, J. N., & Loeb, A. 1994, ApJ, 421, 828

Tremblay, P. E., & Bergeron, P. 2008, ApJ, 672, 1144

Tremblay, P. E., & Bergeron, P. 2009, ApJ, 696, 1755

Tremblay, P. E., Bergeron, P., & Gianninas, A. 2011, ApJ, 730, 128

Tremblay, P. E., Bergeron, P., Kalirai, J. S., & Gianninas, A. 2010, ApJ, 712, 1345

Tremblay, P. E., Cukanovaite, E., Gentile Fusillo, N. P., Cunningham, T., & Hollands, M. A. 2019a, MNRAS, 482, 5222

Tremblay, P. E., Kalirai, J. S., Soderblom, D. R., Cignoni, M., & Cummings, J. 2014, ApJ, 791, 92

Tremblay, P. E., Ludwig, H. G., Freytag, B., et al. 2015, ApJ, 799, 142

Tremblay, P.-E., Fontaine, G., Gentile Fusillo, N. P., et al. 2019b, Nature, 565, 202

Tremblay, P. E., Hollands, M. A., Gentile Fusillo, N. P., et al. 2020, MNRAS, 497, 130

Turcotte, S., & Charbonneau, P. 1993, ApJ, 413, 376

Unglaub, K., & Bues, I. 1998, A&A, 338, 75

Unglaub, K., & Bues, I. 2000, A&A, 359, 1042

Van Grootel, V., Charpinet, S., Brassard, P., Fontaine, G., & Green, E. M. 2013, A&A, 553, A97

Vanderburg, A., Johnson, J. A., Rappaport, S., et al. 2015, Nature, 526, 546

Vauclair, G., Vauclair, S., & Greenstein, J. L. 1979, A&A, 80, 79

Vennes, S., Chayer, P., & Dupuis, J. 2005, ApJL, 622, L121

Vennes, S., Chayer, P., Dupuis, J., & Lanz, T. 2006, ApJ, 652, 1554

Vennes, S., Chayer, P., Thorstensen, J. R., Bowyer, S., & Shipman, H. L. 1992, ApJL, 392, L27

Vennes, S., & Fontaine, G. 1992, ApJ, 401, 288

Vennes, S., Pelletier, C., Fontaine, G., & Wesemael, F. 1988, ApJ, 331, 876

Veras, D., Shannon, A., & Gänsicke, B. T. 2014, MNRAS, 445, 4175

Voss, B., Koester, D., Napiwotzki, R., Christlieb, N., & Reimers, D. 2007, A&A, 470, 1079

Wachlin, F. C., Vauclair, G., Vauclair, S., & Althaus, L. G. 2017, A&A, 601, A13

Wegner, G., & Yackovich, F. H. 1984, ApJ, 284, 257

Weidemann, V., & Koester, D. 1995, A&A, 297, 216

Wenger, M., Ochsenbein, F., Egret, D., et al. 2000, A&AS, 143, 9

Werner, K. 1996a, A&A, 309, 861

Werner, K. 1996b, ApJL, 457, L39

Werner, K., & Dreizler, S. 1994, A&A, 286, L31

Werner, K., Dreizler, S., Heber, U., et al. 1995a, A&A, 293, L75

Werner, K., Dreizler, S., & Wolff, B. 1995b, A&A, 298, 567

Werner, K., & Herwig, F. 2006, PASP, 118, 183

Werner, K., & Rauch, T. 2014, A&A, 569, A99

Werner, K., Rauch, T., & Kepler, S. O. 2014, A&A, 564, A53

Werner, K., Rauch, T., & Kruk, J. W. 2007, A&A, 466, 317

Werner, K., Rauch, T., & Kruk, J. W. 2017, A&A, 601, A8

Werner, K., Rauch, T., & Kruk, J. W. 2018, A&A, 609, A107

Werner, K., Rauch, T., & Reindl, N. 2019, MNRAS, 483, 5291

Werner, K., Rauch, T., Ringat, E., & Kruk, J. W. 2012, ApJL, 753, L7

Wesemael, F., Green, R. F., & Liebert, J. 1985, ApJS, 58, 379

Wesemael, F., Greenstein, J. L., Liebert, J., et al. 1993, PASP, 105, 761

Wesemael, F., Bergeron, P., Lamontagne, R. L., et al. 1994, ApJ, 429, 369

Winget, D. E., Hansen, C. J., Liebert, J., et al. 1987, ApJL, 315, L77

Wolff, B., Jordan, S., Koester, D., & Reimers, D. 2000, A&A, 361, 629

Wyatt, M. C., Farihi, J., Pringle, J. E., & Bonsor, A. 2014, MNRAS, 439, 3371

Xu, S., Jura, M., Koester, D., Klein, B., & Zuckerman, B. 2014, ApJ, 783, 79

Xu, S., Zuckerman, B., Dufour, P., et al. 2017, ApJL, 836, L7

York, D. G., Adelman, J., Anderson, John E., J., et al. 2000, AJ, 120, 1579

Zahn, J. P. 1991, A&A, 252, 179

Zhang, X., & Jeffery, C. S. 2012, MNRAS, 419, 452

Zuckerman, B., Koester, D., Melis, C., Hansen, B. M., & Jura, M. 2007, ApJ, 671, 872

Zuckerman, B., Koester, D., Reid, I. N., & Hünsch, M. 2003, ApJ, 596, 477

Zuckerman, B., Melis, C., Klein, B., Koester, D., & Jura, M. 2010, ApJ, 722, 725

Zuckerman, B., & Reid, I. N. 1998, ApJL, 505, L143